

Edge Race-Tracking Effect on Preform Impregnation during Compression Resin Transfer Molding

Mario Albert Vollmer

Vollständiger Abdruck der von der TUM School of Engineering and Design der
Technischen Universität München zur Erlangung eines
Doktors der Ingenieurwissenschaften (Dr.-Ing.)
genehmigten Dissertation.

Vorsitz: Prof. Dr.-Ing. Veit St. Senner

Prüfer der Dissertation:

1. Prof. Dr.-Ing. Klaus Drechsler
2. Prof. Pierre Mertiny, Ph.D.

Die Dissertation wurde am 17.06.2022 bei der Technischen Universität München
eingereicht und durch die TUM School of Engineering and Design am 12.10.2022
angenommen.

Technische Universität München
TUM School of Engineering and Design
Lehrstuhl für Carbon Composites
Boltzmannstraße 15
D-85748 Garching bei München

Tel.: + 49 (0) 89 / 289 - 15092
Fax: + 49 (0) 89 / 289 - 15097
Email: info.lcc@ed.tum.de
Web: www.asg.ed.tum.de/lcc

Acknowledgement

First of all, I would like to express my gratitude to Prof. Dr.-Ing. Klaus Drechsler for his supervision of my thesis and our discussions about my research at the Chair of Carbon Composites. Furthermore, I would like to thank my mentor Prof. Pierre Mertiny, PhD, for his continuous support and guidance throughout my research activities. Special thanks to Dr.-Ing. Swen Zaremba for countless professional and private discussions, your valuable feedback and advice.

Many thanks to my colleagues at the Chair of Carbon Composites Maximilian Schäfer, Dennis Bublitz and Felix Nusser for discussing, challenging and supporting my research throughout the years. I would also like to acknowledge the help of our technical staff Reiner Rauch and Daniel Amrein. Additionally, I would like to thank all the motivated and skilled students who worked with me on certain aspects of this project Johannes Kil, Dorothea König, Ines Gilch, Nevine Tagscherer, Rupert Ernhofer, Markus Schreiber, Heiko Baumann, Lukas Graßl, Hanno Waller-Ehrat, Felix Nusser, Andreas Prenninger, Minhazur Rahman, Patrick Laubichler, Johannes Stockbauer, Thomas Erschbaumer and Yaping Jiang.

However, industrial research is not possible without the experts from the industry. A special thank you to Christian Hübner from Profol Kunststoffe GmbH for his commitment and help to develop a suitable film material for my research and Maximilian Strohmayer from DEKUMED Kunststoff- und Maschinenvertrieb GmbH & Co. KG for his hands-on mentality which eventually verified our novel process concept. Overall, I thank the German Federal Ministry for Economic Affairs and Energy (BMWi) for funding parts of my research within the framework of the “Central Innovation Program for SMEs (ZIM)” under grant number ZF4004314TA9.

Last but certainly not least, I would like to thank my family for all your love and support. My parents for always being there for me since day one. My deepest gratitude to my wife Carina for always finding the right words and keeping things going (or finally finishing). Ultimately, I thank my sons Otto and Fritz – seeing you smile provides purpose and motivation.

*“If you always do what you’ve always done,
you’ll always get what you’ve always got.”*

Henry Ford

Abstract

Edge race-tracking is a reported issue during manufacturing of structural fiber reinforced plastic (FRP) parts which increases the risk of unsuccessful preform impregnation and raises scrap part rates. While edge race-tracking is studied for certain FRP manufacturing processes, literature provides limited knowledge about its effect during the compression resin transfer molding (CRTM) process. Thus, this work investigates edge race-tracking during CRTM and, furthermore, studies a passive flow control strategy to diminish this effect.

The effect of edge race-tracking during CRTM was first investigated via numerical flow simulations in various process configurations. For all configurations, edge race-tracking was identified to change the preform impregnation pattern and result in an incomplete preform impregnation. While certain process parameters can be strategically designed to diminish edge race-tracking, specific parameter combinations are prone to edge race-tracking, which is why further studies focused on the unfavorable case of preforms of small geometrical aspect ratio. Simulations modeling the passive flow control strategy demonstrated its effectiveness in diminishing edge race-tracking by spatially disconnecting the injection gap from the edge race-tracking channel. The modeled partitioned upper mold design resulted in a manipulated impregnation pattern from the preform's center towards its edges, filling a potential edge race-tracking channel late in the process.

For industrial applications, the passive flow control strategy can be enabled through slider tooling technology. However, conventional sealing concepts are generally strongly worn at movable sliders which increases the risk of production downtime. Therefore in this work, a seal-free tool design is applied, enabled by the encapsulation of the CRTM preform impregnation by film material.

According to the theory of innovative problem solving (TRIZ), a function analysis was performed to identify the effect of a film-integration into the CRTM process and to specify a solution by defining principal process steps of the film-sealed compression resin transfer molding (FS-CRTM) process. FS-CRTM was then characterized by, firstly, identifying a suitable film material. Via literature studies and laboratory tests, a multi-layer film made of polyamide and polypropylene (PA/PP) was identified for FS-CRTM manufacturing, as well as a substitution film made of low-density polyethylene (PE-LD) was specified for laboratory flow visualization experiments. Secondly, flow visualization experiments were conducted to identify dominant process control factors of the FS-CRTM process. Additionally, flow visualization experiments were performed to study the effect of edge race-tracking on FS-CRTM preform impregnation confirming the principle observations of the nu-

merical CRTM simulations. Finally, FS-CRTM experiments were conducted, validating the effect of the passive flow control strategy known from CRTM simulations. However, slight discrepancies between the CRTM simulations and the FS-CRTM experiments were observed, which were traced back to modeling assumptions.

In sum, this work expands the knowledge regarding edge race-tracking during the manufacturing of FRP parts. Edge race-tracking is identified to change the preform impregnation during CRTM as well as FS-CRTM and to increase the risk of an incomplete preform impregnation. However, the investigated passive flow control strategy provides a solution to manipulate the preform impregnation in a way that makes CRTM and FS-CRTM less sensitive to edge race-tracking and, therefore, increases the process robustness during industrial FRP production.

Kurzfassung

Ein bekanntes Problem bei der Herstellung von faserverstärkten Kunststoffbauteilen ist die Rand-Bypassströmung (engl. edge race-tracking). Diese erhöht das Risiko einer unvollständigen Imprägnierung des Faservorformlings und somit die Ausschussrate in der Produktion. Während bestimmte Herstellungsprozesse hinsichtlich einer auftretenden Rand-Bypassströmung untersucht sind, gibt es in der Literatur nur begrenztes Wissen über diesen Effekt beim Compression Resin Transfer Molding (CRTM) Prozess. Aus dieser Wissenslücke heraus wird in dieser Arbeit der Effekt einer Rand-Bypassströmung während CRTM untersucht. Darüber hinaus wird eine passive Flusskontrollstrategie erforscht, um die Auswirkungen der Rand-Bypassströmung im CRTM Prozess zu minimieren.

Zu Beginn der Arbeit wurden die Auswirkungen einer Rand-Bypassströmung mittels numerischen Strömungssimulationen des CRTM Prozesses in verschiedenen Prozesskonfigurationen untersucht. In allen untersuchten Prozesskonfigurationen führte eine Rand-Bypassströmung zu einem veränderten Füllschema der Werkzeugform und resultierte in einer unvollständigen Imprägnierung des Faservorformlings. Während einige Prozessparameter strategisch auslegbar sind, um eine Rand-Bypassströmung zu minimieren, sind spezifische Parameterkombinationen kritisch. Daher fokussierten sich alle weiteren Studien dieser Arbeit auf den kritischen Fall einer Preform mit einem kleinen geometrischen Längen-Dicken-Verhältnis. Simulationen der passiven Flusskontrollstrategie zeigten deren Effektivität, die Auswirkungen einer Rand-Bypassströmung mittels einer räumlichen Trennung des Injektionsspalts vom Bypassströmungskanal zu minimieren. Die hierbei modellierte obere Werkzeugsektion, welche geteilt ausgeführt wurde, resultierte in einem korrigierten Füllschema der Werkzeugform von der Mitte des Faservorformlings zu dessen Rändern. Hierdurch wird ein potentieller Rand-Bypassströmungskanal zu einem späten Zeitpunkt im Prozessablauf gefüllt.

Die untersuchte passive Flusskontrollstrategie kann für industrielle Anwendungen mithilfe eines Schieberwerkzeuges realisiert werden. Jedoch sind konventionelle Dichtungskonzepte bei Schiebern meist starker Abnutzung ausgesetzt, was das Risiko von erhöhtem Wartungsaufwand und Produktionsstillstand nach sich ziehen kann. Um diesem vorzubeugen, wurde in dieser Arbeit ein dichtungsfreies Werkzeugkonzept eingesetzt. Der Einsatz eines dichtungsfreien Werkzeugkonzeptes wurde ermöglicht, indem die Faservorformlingsimprägnierung mit Folien umschlossen und abgedichtet wurde.

Nach dem Ansatz der Theorie des erfinderischen Problemlösens (TRIZ) wurde eine Funktionsanalyse durchgeführt, um die Auswirkungen einer Folienintegration

in den CRTM Prozess zu untersuchen und eine Lösung zu spezifizieren, welche die einzelnen Prozessschritte des Film-Sealed Compression Resin Transfer Molding (FS-CRTM) Prozesses aufzeigt. Anschließend wurde der FS-CRTM Prozess charakterisiert, indem zuerst geeignetes Folienmaterial identifiziert wurde. Anhand einer Literaturrecherche und Laborversuchen wurde eine mehrlagige Folie aus Polyamid und Polypropylen (PA/PP) für eine industrielle FS-CRTM Produktion und eine Substitutionsfolie aus Polyethylen mit geringer Dichte (PE-LD) für Strömungsexperimente im Labor ausgewählt. Des Weiteren wurden dominierende Prozessparameter des FS-CRTM Prozesses mittels Strömungsexperimenten ermittelt. Die generellen Erkenntnisse der numerischen CRTM Simulationen hinsichtlich der Auswirkungen einer Rand-Bypassströmung auf die Imprägnierung des Faservorformlings konnten mittels FS-CRTM Strömungsexperimenten validiert werden. Der Effekt der passiven Flusskontrollstrategie wurde ebenfalls mittels FS-CRTM Strömungsexperimenten untersucht und stimmte in den wesentlichen Erkenntnissen mit den zuvor beschriebenen CRTM Simulationen überein. Einzelne identifizierte Diskrepanzen zwischen den CRTM Simulationen und den FS-CRTM Experimenten wurden auf Modellierungsannahmen zurückgeführt.

Zusammenfassend erweitern die Erkenntnisse dieser Arbeit das bisherige Wissen hinsichtlich Rand-Bypassströmungseffekten bei der Herstellung von faserverstärkten Kunststoffbauteilen. Die Rand-Bypassströmung ist als Ursache einer veränderten Imprägnierung und als erhöhtes Risiko einer unvollständigen Imprägnierung des Faservorformlings im CRTM- sowie FS-CRTM Prozess identifiziert. Das Füllschema in der Werkzeugform kann jedoch mittels der untersuchten passiven Flusskontrollstrategie verändert werden. Hierdurch ist die Imprägnierung des Faservorformlings während des CRTM- sowie FS-CRTM Prozesses weniger störungsempfindlich hinsichtlich einer Rand-Bypassströmung, wodurch die Robustheit dieser Prozesse gesteigert wird.

Contents

Contents	xv
Nomenclature	xvii
List of Figures	xxi
List of Tables	xxxv
1 Introduction	1
2 State of the Art	5
2.1 Liquid Composite Molding (LCM) Technology	5
2.1.1 LCM Process Variants	6
2.1.2 Edge Race-Tracking in LCM Processing	11
2.1.3 Films in LCM Processing	13
2.1.4 Slider Tooling in LCM Processing	17
2.2 Numerical Simulation of Preform Impregnation in LCM	19
2.2.1 Control Volume Finite Element Method	21
2.2.2 Physical Description of LCM Preform Impregnation	23
2.2.3 Equivalent Permeability Approach	26
2.2.4 Numerical Simulation of Compression Resin Transfer Mold- ing (CRTM) in PAM-RTM of ESI Group	34
3 Research Design	39
3.1 Research Questions	39
3.2 Research Approach and Thesis Outline	42
4 Numerical Studies on Edge Race-Tracking during CRTM	45
4.1 Modeling Approach and Evaluation Method	46
4.2 Results and Discussion of the Numerical Race-Tracking Study	50
4.2.1 Edge Race-Tracking during Different CRTM Process Config- urations	50
4.2.2 Investigations of Edge Race-Tracking Severity	67
4.3 Conclusions of the Numerical Race-Tracking Study	72
4.4 Results and Discussion of the Numerical Flow Control Study	75
4.4.1 Passive Flow Control Strategy during Idealized CRTM Pre- form Impregnation	75
4.4.2 Effect of Passive Flow Control Strategy on CRTM Preform Impregnation at Presence of Edge Race-Tracking	77
4.5 Conclusions of the Numerical Flow Control Study	79

5	Enhancement of the CRTM Process	81
5.1	Function Analysis of Film-Integration into CRTM	81
5.2	Process Concept of the Film-Sealed Compression Resin Transfer Molding (FS-CRTM) Process	87
6	Characterization of the FS-CRTM Process	91
6.1	Film Material for the FS-CRTM Process	92
6.1.1	Materials and Methods of Film Specification	93
6.1.2	Results and Discussion of Film Specification for FS-CRTM Manufacturing	98
6.1.3	Results and Discussion of Film Specification for FS-CRTM Flow Visualization Experiments	106
6.1.4	Conclusions of Film Specification	112
6.2	FS-CRTM Injection Experiments with Unrestrained Film Deformation	114
6.2.1	Experimental Setup, Materials and Methods of Unrestrained Film Deformation Experiments	115
6.2.2	Results and Discussion of Unrestrained Film Deformation Experiments	119
6.2.3	Conclusions of Unrestrained Film Deformation Experiments	128
6.3	Experimental Investigations on Factor-Response Correlations	129
6.3.1	Performing and Experimental Plan of the Factor-Response Study	130
6.3.2	Results and Discussion of the Factor-Response Study	137
6.3.3	Conclusions of the Factor-Response Study	154
7	Experimental Studies on Edge Race-Tracking during FS-CRTM	159
7.1	Performing and Experimental Plan of Race-Tracking and Flow Con- trol Study	161
7.2	Results and Discussion	164
7.2.1	Results and Discussion of the Race-Tracking Study	165
7.2.2	Results and Discussion of the Flow Control Study	173
7.3	Conclusions of the Race-Tracking and Flow Control Study	181
8	Summary and Conclusions	185
9	Post-Thesis Achievements and Outlook	197
	Bibliography	201
A	Appendix	221
A.1	Material Characterization	221
A.1.1	Matrix Material	222

A.1.2	Reinforcement Material	226
A.2	Appendix of Numerical Studies on Edge Race-Tracking during CRTM	240
A.2.1	Modeling Approach and Evaluation Method	240
A.2.2	Numerical Race-Tracking Study	245
A.2.3	Numerical Flow Control Study	246
A.3	Appendix of Function Analysis of Film-Integration into CRTM	247
A.4	Methodology of FS-CRTM Flow Visualization Experiments	248
A.4.1	Film-Sealing of Preforms	248
A.4.2	Flow Visualization Setup	251
A.4.3	Experimental Procedure	257
A.5	Appendix of Characterization of the FS-CRTM Process	260
A.5.1	Film Specification for FS-CRTM	260
A.5.2	Unrestrained Film Deformation Experiments	265
A.5.3	Factor-Response Study	272
A.6	Appendix of Experimental Studies on Edge Race-Tracking during FS-CRTM	286
A.6.1	Race-Tracking Study	286
A.6.2	Flow Control Study	294
B	Publications	301
C	Supervised Student Theses	303

Nomenclature

Abbreviations

ABS	Acrylonitrile-butadiene-styrene
AFR	Area filling ratio
Amb.	Ambient
ARTM	Advanced resin transfer molding
BEM	Boundary element method
CNC	Computer numerical control
CPU	Central processing unit (processor)
CRTM	Compression resin transfer molding
CTM	Compression transfer molding
CVFEM	Control volume finite element method
DMTA	Dynamic-mechanical-thermal analysis
DoE	Design of experiment
DSC	Differential scanning calorimetry
engl.	Englisch
ETFE	Ethylene tetrafluoroethylene
Exp.	Experiment
FC	Flow control
FDM	Finite difference method
FEM	Finite element method
FRP	Fiber-reinforced plastic
FS-CRTM	Film-sealed compression resin transfer molding
FVF	Fiber volume fraction
HP-RTM	High-pressure resin transfer molding
incl.	Including
I/CM	Injection compression molding
LCM	Liquid composite molding
LTS	Laser triangulation sensor
MCR	Modular Compact Rheometer
MD	Machine direction
MLR	Multiple linear regression
NCF	Non-crimp fabric
NFC	Numerical flow control
NRT	Numerical race-tracking
PA	Polyamide
PC	Polycarbonate

PC-RTM	Pressure-controlled resin transfer molding
PE	Polyethylene
PEI	Polyetherimide
PES	Polyethersulfone
PE-LD	Polyethylene – low density
PHC	Pneumatic-hydraulic converter
PMMA	Polymethylmethacrylate
PP	Polypropylene
PTFE	Polytetrafluoroethylene
PVC	Polyvinyl chloride
PVF	Polyvinyl fluoride
RQ	Research question
RT	Race-tracking
RTM	Resin transfer molding
RT/CM	Resin transfer/compression molding
SD	Standard deviation
TD	Transversal direction
temp.	Temperature
TITTP	Time of initial through-thickness penetration
TPE	Thermoplastic elastomer
TRIZ	Theory of innovative problem solving
UTM	Universal testing machine
UV	Ultraviolet
VARI	Vacuum assisted resin infusion
VARTM	Vacuum assisted resin transfer molding
VFR	Volume filling ratio
WCM	Wet compression molding

Symbols

AFR_{bottom}	%	Area filling ratio of preform bottom side
C	-	Carman-Kozeny coefficient (material parameter)
E^*	MPa	Complex modulus of viscoelastic material
E'	MPa	Storage modulus of viscoelastic material
E''	MPa	Loss modulus of viscoelastic material
f_i	-	Filling factor
f_c	kN	Compression force
$f_{c,t}$	kN	Target compression force
H	mm	Height of flow domain
h_{ig}	mm	Height of injection gap
h_p	mm	Height of preform
$h_{p,f}$	mm	Final height of preform
$h_{p,u}$	mm	Uncompressed height of preform
h_{ig}	mm	Height of injection gap
$h_{ig,t}$	mm	Target height of injection gap
\dot{h}_c	mm/s	Rate of change of cavity height
\dot{h}_p	mm/s	Rate of change of preform thickness
\mathbf{K}	m^2	Permeability
$K_{\text{ch,eq}}$	m^2	Equivalent permeability of edge race-tracking channel
$K_{\text{ig,eq}}$	m^2	Equivalent permeability of injection gap
$K_{p,i}$	m^2	In-plane permeability of preform
$K_{p,t}$	m^2	Transversal (out-of-plane) permeability of preform
K_{11}	m^2	Primary (larger) principal in-plane permeability
K_{22}	m^2	Secondary (smaller) principal in-plane permeability
K_{33}	m^2	Principal out-of-plane (through-thickness) permeability
l_p	mm	Length of preform
m	-	Carman-Kozeny exponent (material parameter)
n	-	Number of experiments
\vec{n}	-	Normal vector on control surface
p	Pa	Pressure
p_f	Pa	Fluid pressure
p_p	kPa	Pot (injection) pressure
$p_{p,t}$	kPa	Target pot (injection) pressure
p_v	kPa	Vent pressure
$p_{v,t}$	kPa	Target vent pressure
p_{stg}	kPa	Stagnation pressure
$p_{\text{stg,t}}$	kPa	Target stagnation pressure
p_v	kPa	Vent pressure

$p_{v,t}$	kPa	Target vent pressure
Q	m^3/s	Flow rate
Q_2	-	Ratio of variation of response predicted by model
R_{CP}	-	Radius of cone-plate (DSC measurement setup)
R_2	-	Ratio of variation of response explained by model
t	s	Time
T_g	$^{\circ}C$	Glass transition temperature
T_m	$^{\circ}C$	Melting temperature (corresponds to T_{pm})
t_{np}	-	Normalized process time
T_{pm}	$^{\circ}C$	Peak melting temperature
\vec{v}	m/s	Volume averaged flow velocity
$V_{f,p}$	%	Fiber volume fraction of preform
W	mm	Width of flow domain
y_{max}	mm	y -distance of maximum z -deformation in yz -plane
α	-	Shear rate coefficient
α_{CP}	$^{\circ}$	Angle of cone-plate (DSC measurement setup)
β	$^{\circ}$	Permeability angle between K_{11} and coordinate system
$\dot{\gamma}$	s^{-1}	Shear rate
Δ	-	Differential value
ϵ	-	Strain
$\dot{\epsilon}$	s^{-1}	Strain rate
η	Pas	Dynamic viscosity
η_{eff}	Pas	Effective viscosity
σ_p	Pa	Stress acting on preform (compaction stress)
σ_{tot}	Pa	Total stress
∇	-	Gradient

List of Figures

1-1	Hypothesis of an enhanced CRTM process design to diminish edge race-tracking.	3
2-1	Schematic illustrating the principal steps of the resin transfer molding (RTM) process.	7
2-2	Schematic illustrating the principal steps of the compression resin transfer molding process at which the upper mold marginally compacts the preform prior to resin injection, denoted CRTM-1.	9
2-3	Schematic illustrating the principal steps of the compression resin transfer molding process at which an empty space (injection gap) is formed between upper mold and preform prior to resin injection, denoted CRTM-2.	10
2-4	Comparison of an undisturbed RTM preform impregnation (top row) and a RTM preform impregnation in the presence of edge race-tracking (bottom row).	12
2-5	Functions of films for FRP materials grouped in functional classes (light gray) and their characteristics (white).	14
2-6	Tooling and preform concept of the Film-RTM process – approach after Häffelin.	16
2-7	Applications of slider tooling in LCM: (a) To enable FRP parts with undercuts; (b) To enhance preform impregnation.	18
2-8	Discretization scheme of CVFEM in three-node triangular elements and polygonal control volumes.	22
2-9	Flow front identification during CVFEM simulations by using the nodal parameter of filling factor.	22
2-10	Progressions of equivalent permeability over injection gap height calculated by equation (2-8) and (2-9).	28
2-11	Progressions of equivalent permeability for a channel width of $W = 2$ mm over gap height, calculated by Equations (2-10) to (2-14).	32
2-12	Progressions of equivalent permeability for a channel width of $W = 4$ mm over injection gap height, calculated by Equations (2-10) to (2-14).	33
3-1	Outline of the present work.	43

4-1	Impregnation pattern of preform (a) as well as of preform plus 2 mm wide edge race-tracking channel (b) at characteristic process times; normalized process time (t_{np}): injection of 1.5 s between t_{np} of 0 and 1 as well as compression of 1.53 s between t_{np} of 1 and 2; results obtained by numerical simulations of CRTM process configuration 1: small geometrical aspect ratio, high injection gap height, and lateral inlet.	53
4-2	Characteristic process parameters over normalized process time of numerical simulations without and with edge race-tracking of CRTM process configuration 1: small geometrical aspect ratio, high injection gap height, and lateral inlet.	54
4-3	Impregnation pattern of preform (a) as well as of preform plus 2 mm wide edge race-tracking channel (b) at characteristic process times; normalized process time (t_{np}): injection of 4.5 s between t_{np} of 0 and 1 as well as compression of 1.53 s between t_{np} of 1 and 2; results obtained by numerical simulations of CRTM process configuration 2: large geometrical aspect ratio, high injection gap height, and lateral inlet.	57
4-4	Characteristic process parameters over normalized process time of numerical simulations without and with edge race-tracking of CRTM process configuration 2: large geometrical aspect ratio, high injection gap height, and lateral inlet.	58
4-5	Impregnation pattern of preform (a) as well as of preform plus 2 mm wide edge race-tracking channel (b) at characteristic process times; normalized process time (t_{np}): injection of 1.5 s between t_{np} of 0 and 1 as well as compression of 0.91 s between t_{np} of 1 and 2; results obtained by numerical simulations of CRTM process configuration 3: small geometrical aspect ratio, low injection gap height, and lateral inlet.	61
4-6	Characteristic process parameters over normalized process time of numerical simulations without and with edge race-tracking of CRTM process configuration 3: small geometrical aspect ratio, low injection gap height and lateral inlet.	62
4-7	Impregnation pattern of preform (a) as well as of preform plus 2 mm wide edge race-tracking channel (b) at characteristic process times; normalized process time (t_{np}): injection of 1.5 s between t_{np} of 0 and 1 as well as compression of 1.53 s between t_{np} of 1 and 2; results obtained by numerical simulations of CRTM process configuration 4: small geometrical aspect ratio, high injection gap height and central inlet.	65

4-8	Characteristic process parameters over normalized process time of numerical simulations without and with edge race-tracking of CRTM process configuration 4: small geometrical aspect ratio, high injection gap height and central inlet.	66
4-9	Impregnation pattern of preform (a) as well as of preform plus 2 mm wide (b) and plus 4 mm wide edge race-tracking channel (c) at characteristic process times; normalized process time (t_{np}): injection of 1.5 s between t_{np} of 0 and 1 as well as compression of 1.53 s between t_{np} of 1 and 2; results obtained by numerical simulations of CRTM process configuration 1: small geometrical aspect ratio, high injection gap height, and lateral inlet.	68
4-10	Volume filling ratio (VFR) over normalized process time of numerical simulations without, with a 2 mm and 4 mm wide edge race-tracking channel of CRTM process configuration 1: small geometrical aspect ratio, high injection gap height, and lateral inlet.	69
4-11	Pressure at inlet during the CRTM injection phase of numerical simulations without, with a 2 mm and 4 mm wide edge race-tracking channel of the CRTM process configuration 1: small geometrical aspect ratio, large injection gap and, lateral inlet.	70
4-12	Force on tool at the end of process of numerical simulations without, with a 2 mm and 4 mm wide edge race-tracking channel of the CRTM process configuration 1: small geometrical aspect ratio, high injection gap height and lateral inlet.	71
4-13	Preform filling pattern during a simulation without an edge race-tracking channel and with applied passive flow control strategy of CRTM process configuration 4: of small geometrical aspect ratio, high injection gap height, and central inlet; normalized process time (t_{np}): injection of 1.5 s between t_{np} of 0 and 1 and compression of 1.73 s between t_{np} of 1 and 2.	76
4-14	Comparison of VFR between simulations without and with passive flow control strategy at occurrence of edge race-tracking of CRTM process configuration 4: small geometrical aspect ratio, high injection gap height, and central inlet.	77
4-15	Location of macro void in blue and gray at the end of the process of simulations of CRTM process configuration 4: small geometrical aspect ratio, high injection gap height, and central inlet as well as with edge race-tracking: (a) without passive flow control strategy; (b) with passive flow control strategy.	78

5-1	Component analysis: Illustration of the main-function of the technical system (top row) and listing of components of the super system (green) as well as the technical system (blue).	82
5-2	Functional model of the technical system “mold” (blue), the target “resin system” (orange), and the super system “CRTM manufacturing” (green) including all interactions between the individual components.	83
5-3	Classification of useful (black arrows) and harmful (red dashed/dotted arrows) functions as well as components to be trimmed (crossed out in red) of the technical system “mold” and the super system “CRTM manufacturing”.	84
5-4	Enhanced functional model of the CRTM manufacturing at which the new component film-sealing is integrated, entitling this process variant the film-sealed compression resin transfer molding (FS-CRTM) process.	85
5-5	Schematic illustrating the principal steps of the film-sealed compression resin transfer molding (FS-CRTM) process.	88
6-1	(a) Test equipment of solubility investigations: 1) hot stage, 2) control device of hot stage, 3) microscope with positioning table and 4) data acquisition and control computer of microscope; (b) Setup of sample for solubility investigations.	96
6-2	Schematic illustration of strain (a) and stress (b) during the three phases of a stress relaxation test: (I) load increase, (II) constant strain loading and (III) strain recovery.	98
6-3	Storage modulus of monolayer films (shown as average in black as well as spread between maximum and minimum measured values in gray).	101
6-4	Weld seam investigations of PP, PVF and PA films via the dye-test adhered to the standard ASTM F1929.	104
6-5	Storage modulus of monolayer films and PA/PP multilayer film (shown as average in black as well as spread between maximum and minimum measured values in gray).	107
6-6	Storage modulus of PA/PP multilayer film for FS-CRTM manufacturing at process temperature of 80 °C to 120 °C and substituting PE-LD film for FS-CRTM flow visualization experiments at ambient temperature (Amb. temp.) (shown as average in black as well as spread between maximum, and minimum measured values in gray).	109

6-7	Relaxed stress after 20 s of constant strain load at four different strain levels of the PA/PP film at lower (80 °C) and upper (120 °C) process temperature and the substitution PE-LD film at test temperature (23.5 °C) (shown as mean and standard deviation of five measurements and of ten measurements for PA/PP at 120 °C, at 4%, and 6%).	110
6-8	Strain recovery after different relaxation strain loads of PA/PP film at lower (80 °C) and upper (120 °C) process temperature and substitution PE-LD film at ambient temperature (23.5 °C): (a) five seconds and (b) 120 seconds after load cycle.	111
6-9	Hypothesis of the three stages of unrestrained film deformation during FS-CRTM injection trials: (a) before injection, (b) during injection and (c) after injection.	115
6-10	Test setup of experiments to study the unrestrained film deformation.	116
6-11	Experimental plan of the unrestrained film deformation study.	118
6-12	Illustration of the three-dimensional film deformation of experiment #6 over time during injection (top row) and after injection (bottom row) – depicted in the longitudinal yz -plane at the center of the inlet at $x = 0$ (left column) and at the transversal xz -plane at $y_{max} = 70.6$ mm, position of maximum z -deformation recorded in the yz -plane (right column).	120
6-13	Maximum z -deformation of film (a) and y -length of film lift-off (b) in the yz -plane at $x = 0$ plotted over time after injection start of the three replicates at central factor setting.	122
6-14	Effect of pot pressure variation on the out-of-plane film deformation during the injection phase – depicted in the longitudinal yz -plane at the center of the inlet at $x = 0$ (left column) and at the transversal xz -plane position of maximum z -deformation recorded in the yz -plane at $y_{max}(\#7) = 38.1$ mm, $y_{max}(\#6) = 70.6$ mm and $y_{max}(\#3) = 75.0$ mm (right column).	124
6-15	Maximum z -deformation of film (a) and y -length of film lift-off (b) in the yz -plane at $x = 0$ plotted over time after injection start of the experiments with varying pot pressures.	125
6-16	Effect of vent pressure variation on the out-of-plane film deformation during the injection phase – depicted in the longitudinal yz -plane at the center of the inlet at $x = 0$ (left column) and at the transversal xz -plane position of maximum z -deformation recorded in the yz -plane at $y_{max}(\#5) = 44.8$ mm, $y_{max}(\#6) = 70.6$ mm and $y_{max}(\#2) = 60.9$ mm (right column).	126

6-17	Maximum z -deformation of film (a) and y -length of film lift-off (b) in the yz -plane at $x = 0$ plotted over time after injection start of the experiments with varying vent pressures.	127
6-18	Factors, responses as well as control and disturbance variables of flow visualization experiments investigating the injection phase of the FS-CRTM process.	132
6-19	Test plan of the factor-response study investigating the injection phase of the FS-CRTM process.	133
6-20	Factors, responses as well as control and disturbance variables of flow visualization experiments investigating the injection phase of the FS-CRTM process.	136
6-21	Test plan of the factor-response study investigating the injection phase of the FS-CRTM process.	136
6-22	(a) Effects of injection time model; (b) predictions of injection time model at medium factor setting ($p_{stg} = 350$ kPa, $p_v = -47.5$ kPa, $h_{ig} = 1.39$ mm).	139
6-23	Predictions of flow rate model at medium factor setting ($p_{inj} = 350$ kPa, $p_v = -47.5$ kPa, $h_{ig} = 1.39$ mm).	141
6-24	(a) Effects of injection pressure model; (b) predictions of injection pressure model at medium factor setting ($p_{stg} = 350$ kPa, $p_v = -47.5$ kPa, $h_{ig} = 1.39$ mm).	141
6-25	Fluid pressure progression at inlet over time after injection start of FS-CRTM flow experiments at low and high stagnation pressure level ($p_{v,t} = -90$ kPa).	143
6-26	Fluid pressure development and AFR of preform top side over time after injection start of FS-CRTM flow experiments at low and high injection gap height level ($p_{v,t} = -90$ kPa).	143
6-27	(a) Effects of ratio of area filling ratio (AFR) of preform top side model; (b) predictions of AFR of preform top side model ($p_{stg} = 350$ kPa; $p_v = -47.5$ kPa; $h_{ig} = 1.98$ mm).	144
6-28	Flow front progression during the injection phase at high (a) and low (b) level of injection gap height ($p_{stg,t} = 100$ kPa; $p_{v,t} = -90$ kPa).	145
6-29	Flow front progression at low (a) and high (b) level of stagnation pressure ($p_{v,t} = -90$ kPa; $h_{ig,t} = 1.98$ mm).	146
6-30	(a) Effects of compression time model; (b) predictions of compression time model at medium factor setting ($f_c = 17.31$ kN, $p_v = -47.5$ kPa, $h_{ig} = 1.39$ mm).	148
6-31	(a) Compression force over time after injection start; (b) compression time over (maximum) compression force of additional experiments.	149

6-32	(a) Effects of time of initial through-thickness penetration (TITTP) model; (b) predictions of TITTP model at medium factor setting ($f_c = 17.31$ kN, $p_v = -47.5$ kPa, $h_{ig} = 1.39$ mm).	151
6-33	Area filling ratio of preform bottom side of the additional experiments: (a) during the first 20 s of the process; (b) until gel time of representative snap-cure resin system. For legend of both plots see (b).	152
6-34	Impregnation pattern on bottom side of preform of experiment vc-#1 ($AFR_{bottom} =$ area filling ratio of preform bottom side).	153
7-1	Hypothesized FS-CRTM flow experiment scenarios of preforms of small geometrical aspect ratio: (a) without edge race-tracking (rt) channel; (b) with edge race-tracking channel; (c) applying a passive flow control strategy to diminish the edge race-tracking effect. . . .	160
7-2	Overview of important process variables during FS-CRTM experiments of the race-tracking study: (a) no race-tracking channel – vc-#3; (b) medium race-tracking channel width – mrt-#3; (c) wide race-tracking channel width – wrt-#1 (LTS = laser triangulation sensor).	166
7-3	Flow front progression of FS-CRTM experiments of the race-tracking study: (a,b) no race-tracking (rt) channel – vc-#3; (c,d) medium race-tracking channel width – mrt-#3; (e,f) wide race-tracking channel width – wrt-#1 ($AFR =$ area filling ratio).	167
7-4	Area filling ratio of preform bottom side: (a) during the first 25 s of the process; (b) until gel time of representative snap-cure resin system. For legend of both plots see (b).	170
7-5	Maximum recorded force of the three experimental scenarios of the race-tracking study. Bar heights give the mean value, and the error bars indicate the standard deviation of three repetitions.	172
7-6	Overview of important process variables during FS-CRTM experiments of the flow control study: (a) no race-tracking channel – fcs-#1; (b) medium race-tracking channel width – fcs-mrt-#3; (c) wide race-tracking channel width – fcs-wrt-#2 (LTS = laser triangulation sensor).	175
7-7	Flow front progression of FS-CRTM experiments of the flow control study: (a,b) no race-tracking (rt) channel – fcs-#1; (c,d) medium race-tracking channel width – fcs-mrt-#3; (e,f) wide race-tracking channel width – fcs-wrt-#2 ($AFR =$ area filling ratio).	176

7-8	Time of initial through-thickness penetration (TITTP) and corresponding gap height of FS-CRTM experiments without a race-tracking channel from the race-tracking study and the flow control study. Shown are mean values and standard deviations for experiments in triplicate.	178
7-9	Preform impregnation on the bottom side of the three experimental scenarios of the flow control study at 23 s: (a) complete filling of experiment without a race-tracking channel fcs-#1; unimpregnated corner sections of experiments with a medium fcs-mrt#3 (b) and wide fcs-wrt#2 (c) race-tracking channel.	180
7-10	Flow scenarios derived from FS-CRTM experiments: (a) without edge race-tracking (rt) channel; (b) with edge race-tracking channel; and (c) with applied passive flow control strategy of a localized, central injection gap and pre-compaction of the preform edge. . . .	182
9-1	(a) Tooling system and partially impregnated film-sealed flat preform, (b) final three-dimensional demonstrator of post-thesis FS-CRTM industrialization project.	198
A-1	Isothermal viscosity measurements over time of three temperatures - epoxy resin system: Araldite [®] LY 3585 and Aradur [®] 3475 (mean of tests performed in triplicate; standard deviations shown as error bars).	224
A-2	Principal permeability tensor as ellipsoid (a); in-plane permeabilities rotated by β (b).	226
A-3	Superposition of flow front positions of RTM flow experiments with numerical simulations at different time steps.	229
A-4	Measured out-of-plane and adjusted (+40%) in-plane permeability of the reinforcement material: Permeability over fiber volume fraction.	230
A-5	Permeability angle over fiber fiber volume fraction (mean of three measurements; standard deviations shown as error bars).	232
A-6	Compaction behavior of the reinforcement material: Compaction stress over fiber volume fraction and strain (experimental data: mean of three measurements; standard deviations shown as error bars).	233
A-7	Fill time of edge race-tracking channel: Simulation result (blue) vs. experimental result (orange) for different channel width (W) and fiber volume fractions ($V_{f,p}$) (bar height represents mean of three experiments or numerical simulations; standard deviations shown as error bars).	235
A-8	Superposition of RTM race-tracking flow experiments with numerical simulations: edge race-tracking channel width = 2 mm.	238

A-9	Superposition of RTM race-tracking flow experiments with numerical simulations: edge race-tracking channel width = 4 mm.	239
A-10	Comparison of CRTM simulation results calculated with different PAM-RTM versions 2019.0, 2019.5 and 2020.5, all used in this work – CRTM process configuration 4 of small geometrical aspect ratio, large injection gap and central inlet as well as with a 2 mm wide race-tracking channel.	240
A-11	Geometry dimensions of simulation models at process start (simulated as half models) at which the channel domain is defined as preform domain for simulations without an edge race-tracking channel: (a) numerical race-tracking study – process configuration 1, 3 and 4; (b) numerical flow control study; (c) numerical race-tracking study – process configuration 2.	241
A-12	Comparison of CRTM simulation results calculated with a coupling frequency of 0.05 s and 0.075 s, the maximum deviation of coupling frequency between two comparing simulations in this work (see Table A-3) – CRTM process configuration 1 of small geometrical aspect ratio, large injection gap and lateral inlet.	242
A-13	Comparison of CRTM simulation results calculated with and without gravitation – CRTM process configuration 1 of small geometrical aspect ratio, large injection gap and lateral inlet.	243
A-14	Comparison of CRTM simulation results at presence of edge race-tracking calculated with and without gravitation – CRTM process configuration 1 of small geometrical aspect ratio, large injection gap and lateral inlet.	243
A-15	Comparison of evaluation methods – CRTM process configuration 1 of small geometrical aspect ratio, large injection gap and lateral inlet (both simulations calculated in PAM-RTM version 2020.5). . .	244
A-16	Comparison of evaluation methods – CRTM process configuration 4 of small geometrical aspect ratio, large injection gap and central inlet (both simulations calculated in PAM-RTM version 2020.5). . .	244
A-17	Pressure at inlet during the CRTM injection phase of numerical simulations of the CRTM process configuration 2 of large geometrical aspect ratio, large injection gap, and lateral inlet: without and with 2 mm wide edge race-tracking channel.	245
A-18	Pressure at inlet during the CRTM injection phase of numerical simulations of the CRTM process configuration 3 of small geometrical aspect ratio, small injection gap, and lateral inlet: without and with 2 mm wide edge race-tracking channel.	245

A-19	Pressure at inlet during the CRTM injection phase of numerical simulations of the CRTM process configuration 4 of small geometrical aspect ratio, large injection gap, and central inlet: without and with 2 mm wide edge race-tracking channel.	246
A-20	Pressure at inlet during the CRTM injection phase of numerical simulations of the CRTM process configuration 4 of small geometrical aspect ratio, small injection gap, and central inlet: without and with applied flow control strategy.	246
A-21	Abstraction of the system “CRTM manufacturing” via a tree diagram and definition of the investigated technical system (blue), super system (green) and target (orange).	247
A-22	Interactions of the components of the technical system (blue), target (orange), and super system (green); + interaction, - no interaction.	247
A-23	Abstraction of the system “FS-CRTM manufacturing”.	248
A-24	Components of the film-sealing station for preforms.	249
A-25	Schematic illustration of preform shapes including fluid transition zone and preform fixation on lower side of preforms with a race-tracking channel.	250
A-26	Features and components of a film-sealed preform package.	251
A-27	Flow visualization test rig grouped in its three main units. Inset on top right illustrates the cavity unit with labeling of its main components and sensors.	252
A-28	Schematic of flow visualization test rig. For a list of abbreviations and further details, see Tables A-4 and A-5.	254
A-29	Loss modulus of monolayer films and PA/PP multilayer film (shown as average in black as well as spread between maximum and minimum measured values in gray).	260
A-30	Loss modulus of monolayer films and PA/PP multilayer film - zoom in at process temperature range of FS-CRTM process (shown as average in black as well as spread between maximum and minimum measured values in gray).	261
A-31	Storage and loss modulus of PP monolayer film manufactured by Profol - machine direction (MD) vs. transversal direction (TD) (shown as average in black as well as spread between maximum and minimum measured values in gray).	261
A-32	Storage and loss modulus of PA monolayer film manufactured by mf-Folien - machine direction (MD) vs. transversal direction (TD) (shown as average in black as well as spread between maximum and minimum measured values in gray).	262

A-33 Storage and loss modulus of PVF monolayer film manufactured by DuPont - machine direction (MD) vs. transversal direction (TD) (shown as average in black as well as spread between maximum and minimum measured values in gray).	262
A-34 Storage and loss modulus of TPE monolayer film manufactured by Infiana - machine direction (MD) vs. transversal direction (TD) (shown as average in black as well as spread between maximum and minimum measured values in gray).	263
A-35 Loss modulus of PA/PP multilayer film for FS-CRTM at process temperature of 80 °C to 120 °C and substituting PE-LD film for FS-CRTM flow visualization experiments at ambient temperature (Amb. temp.) (shown as average in black as well as spread between maximum and minimum measured values in gray).	263
A-36 Storage and loss modulus of PA/PP multilayer film manufactured by Profol - machine direction (MD) vs. transversal direction (TD) (shown as average in black as well as spread between maximum and minimum measured values in gray).	264
A-37 Storage and loss modulus of PE-LD monolayer film manufactured by Sokufol - machine direction (MD) vs. transversal direction (TD) (shown as average in black as well as spread between maximum and minimum measured values in gray).	264
A-38 Three-dimensional z-deformation of ARAMIS measurement area of experiment #6 at injection end.	265
A-39 Illustration of the three-dimensional film deformation of experiment #1 over time during injection (top row) and after injection (bottom row) – depicted in the longitudinal yz -plane at the center of the inlet at $x = 0$ (left column) and at the transversal xz -plane at $y_{max} = 71.0$ mm, position of maximum z -deformation recorded in the yz -plane (right column).	268
A-40 Illustration of the three-dimensional film deformation of experiment #4 over time during injection (top row) and after injection (bottom row) – depicted in the longitudinal yz -plane at the center of the inlet at $x = 0$ (left column) and at the transversal xz -plane at $y_{max} = 75.0$ mm, position of maximum z -deformation recorded in the yz -plane (right column).	269

A-41	Effect of injection pressure variation on the out-of-plane film deformation after injection – depicted in the longitudinal yz -plane at the center of the inlet at $x = 0$ (left column) and at the transversal xz -plane position of maximum z -deformation recorded in the yz -plane at $y_{max}(\#7) = 38.1$ mm, $y_{max}(\#6) = 70.6$ mm and $y_{max}(\#3) = 75.0$ mm (right column).	270
A-42	Effect of vent pressure variation on the out-of-plane film deformation after injection – depicted in the longitudinal yz -plane at the center of the inlet at $x = 0$ (left column) and at the transversal xz -plane position of maximum z -deformation recorded in the yz -plane at $y_{max}(\#5) = 44.8$ mm, $y_{max}(\#6) = 70.6$ mm and $y_{max}(\#2) = 60.9$ mm (right column).	271
A-43	Overview plot of response model: injection time (p_{stg} = stagnation pressure, h_{ig} = injection gap height, p_v = vent pressure; \sim indicates the transformed model as described in Chapter 6.3.2). . .	275
A-44	Overview plot of response model: flow rate (p_{stg} = stagnation pressure, h_{ig} = injection gap height, p_v = vent pressure; \sim indicates the transformed model as described in Chapter 6.3.2).	275
A-45	Overview plot of response model: injection pressure (p_{stg} = stagnation pressure, h_{ig} = injection gap height, p_v = vent pressure; \sim indicates the transformed model as described in Chapter 6.3.2). . .	276
A-46	Overview plot of response model: area filling ratio on preform top side (p_{stg} = stagnation pressure, h_{ig} = injection gap height, p_v = vent pressure; \sim indicates the transformed model as described in Chapter 6.3.2).	276
A-47	Predictions of ratio of injection gap filling model ($p_{stg} = 350$ kPa, $p_{vent} = -47.5$ kPa, $h_{ig} = 0.79$ mm).	277
A-48	Overview plot of response model: compression time (f_c = compression force, h_{ig} = injection gap height, p_v = vent pressure; \sim indicates the transformed model as described in Chapter 6.3.2). . .	283
A-49	Overview plot of response model: time of initial through-thickness penetration (TITTP) (f_c = compression force, h_{ig} = injection gap height, p_v = vent pressure).	283
A-50	Overview plot of response model: time of initial through-thickness penetration (TITTP) (without factor interactions, f_c = compression force, h_{ig} = injection gap height, p_v = vent pressure). . . .	284
A-51	Overview plot of response model: time of 50% AFR on preform bottom side (f_c = compression force, h_{ig} = injection gap height, p_v = vent pressure).	284

A-52 Overview plot of response model: time of 90% AFR on preform bottom side (f_c = compression force, h_ig = injection gap height, p_v = vent pressure).	285
A-53 Area filling ratio of preform bottom side for repetition experiments of the full factorial experimental design investigating the compression and holding phase of the FS-CRTM process.	285
A-54 Overview of important process variables during FS-CRTM experiments of the race-tracking study: (a) no race-tracking channel – vc-#1; (b) no race-tracking channel – vc-#2; (c) medium race-tracking channel width – mrt-#1 (LTS = laser triangulation sensor).	290
A-55 Overview of important process variables during FS-CRTM experiments of the race-tracking study: (a) medium race-tracking width – mrt-#2; (b) wide race-tracking width – wrt-#2; (c) wide race-tracking width – wrt-#3 – no pictures of the preform top side were recorded during the injection of wrt-#3 due to issues of the data acquisition equipment (LTS = laser triangulation sensor).	291
A-56 Flow front progression of FS-CRTM experiments of the race-tracking study: (a,b) no race-tracking (rt) channel – vc-#1; (c,d) no race-tracking channel – vc-#2; (e,f) medium race-tracking channel width – mrt-#1 (AFR = area filling ratio).	292
A-57 Flow front progression of FS-CRTM experiments of the race-tracking study: (a,b) medium race-tracking (rt) channel width – mrt-#2; (c,d) wide race-tracking channel width – wrt-#2; (e) wide race-tracking channel width – wrt-#3 – no pictures of the preform top side were recorded during the injection of wrt-#3 due to issues of the data acquisition equipment (AFR = area filling ratio).	293
A-58 Overview of important process variables during FS-CRTM experiments of the flow control study: (a) no race-tracking channel – fcs-#2; (b) no race-tracking channel – fcs-#3; (c) medium race-tracking channel width – fcs-mrt-#1 (LTS = laser triangulation sensor).	297
A-59 Overview of important process variables during FS-CRTM experiments of the flow control study: (a) medium race-tracking channel width – fcs-mrt-#2; (b) wide race-tracking channel width – fcs-wrt-#1; (c) wide race-tracking channel width – fcs-wrt-#3 (LTS = laser triangulation sensor).	298
A-60 Flow front progression of FS-CRTM experiments of the flow control study: (a,b) no race-tracking (rt) channel – fcs-#2; (c,d) no race-tracking channel – fcs-#3; (e,f) medium race-tracking channel width – fcs-mrt-#1 (AFR = area filling ratio).	299

A-61 Flow front progression of FS-CRTM experiments of the flow control study: (a,b) medium race-tracking (rt) channel width – fcs-mrt-#2; (c,d) wide race-tracking channel width – fcs-wrt-#1; (e,f) wide race-tracking channel width – fcs-wrt-#3 (AFR = area filling ratio). . . 300

List of Tables

2-1	Cross sections and assumptions of equations to calculate the equivalent permeability of an injection gap.	27
2-2	Cross sections and assumptions of equations to calculate the equivalent permeability of an edge race-tracking channel.	31
4-1	CRTM process configurations investigated in the numerical race-tracking study.	51
6-1	Properties of investigated monolayer films.	100
6-2	Rating of investigated monolayer films for the FS-CRTM process towards fulfillment of specific requirements: ++ = excellent; + = good; - = poor; -- = inappropriate.	102
6-3	Factor levels of flow visualization experiments investigating the compression and holding phase of the FS-CRTM process – additional experiments.	137
6-4	Summary of factor-response correlations of the FS-CRTM process (factors listed in first column, responses listed in first row – AFR = area filling ratio, compr. = compression, TITTP = time of initial through-thickness penetration).	154
7-1	Process conditions of experiments for the race-tracking (RTS) and flow control (FCS) studies.	164
A-1	Coefficient of the Carman-Kozeny Equation (A-1) for the determined principle permeabilities presented in Figure A-4.	231
A-2	Flow rate of CRTM simulations of the numerical race-tracking study (NRT study) and numerical flow control study (NFC study).	240
A-3	Coupling frequency between fluid and solid mechanics solver in PAM-RTM of CRTM simulations of the numerical race-tracking study (NRT study) and numerical flow control study (NFC study).	242
A-4	List of abbreviations (I / II) and further details on flow visualization setup of Figure A-28.	255
A-5	List of abbreviations (II / II) and further details on flow visualization setup of Figure A-28.	256
A-6	Preform data and process factors of the FS-CRTM experiments with unrestricted film deformation.	266
A-7	Process responses of the FS-CRTM experiments with unrestricted film deformation.	267

A-8	Preform data of the factor-response study investigating the injection phase of the FS-CRTM process.	272
A-9	Factors of flow visualization experiments investigating the injection phase of the FS-CRTM process.	273
A-10	Responses of flow visualization experiments investigating the injection phase of the FS-CRTM process.	274
A-11	Preform data of the factor-response study investigating the compression and holding phase of the FS-CRTM process.	277
A-12	Factors of flow visualization experiments investigating the compression and holding phase of the FS-CRTM process.	278
A-13	Responses of flow visualization experiments investigating the compression and holding phase of the FS-CRTM process.	279
A-14	Preform data of the factor-response study investigating the compression and holding phase of the FS-CRTM process – additional experiments.	280
A-15	Factors of flow visualization experiments investigating the compression phase of the FS-CRTM process – additional experiments.	281
A-16	Responses of flow visualization experiments investigating the compression and holding phase of the FS-CRTM process – additional experiments.	282
A-17	Preform data of experiments of the race-tracking study.	286
A-18	Theoretical race-tracking channel widths of preforms of the race-tracking study (neglecting preform placing tolerances).	287
A-19	Process factors of experiments of the race-tracking study.	288
A-20	Process responses of experiments of the race-tracking study.	289
A-21	Preform data of experiments of the flow control study.	294
A-22	Theoretical race-tracking channel widths of preforms of the flow control study (neglecting preform placing tolerances).	294
A-23	Process factors of experiments of the flow control study.	295
A-24	Process responses of experiments of the flow control study.	296

1 Introduction

The world is changing: All over the globe people are protesting to show their concern about ongoing climate change and their desire to initiate a sustainable management of our environmental resources. At the Paris climate conference (COP21) in 2015, the global community agreed to limit the global warming to the symbolic number of 1.5 °C [1]. More specifically, in 2019, the European Commission rolled out their Green Deal which sets the goal to make Europe the first climate-neutral continent by 2050 [2]. To achieve this goal, specific actions have to be taken by different industry sectors. Nowadays, the transport sector makes up to 25% of the greenhouse gas emissions in the European Union [3] and is therefore a focus area to achieve the set goals. The so-called green transition in the automotive sector is ongoing by an increased effort to switch from conventional fossil fuel cars to alternative driving concepts, such as electromobility and hydrogen fuel cells [4]. Besides alternative driving concepts, a reduction of the vehicle mass directly reduces the greenhouse gas emission for all driving concepts and provides a supplementary strategy towards a climate neutral transport sector [5–7].

Light-weight materials are increasingly used to raise the efficiency and sustainability of modern cars [6]. One promising material for automotive applications is fiber-reinforced plastic (FRP) due to its excellent weight-specific mechanical properties. Over the last two decades, raw materials as well as manufacturing processes and equipment have been optimized to meet the requirements of automotive serial production. About a decade ago, a breakthrough was achieved by the design of the BMW i3 in which nearly 50% of its body structure is made out of FRP materials [8]. In recent years, FRP parts were also applied to other small to medium volume cars such as the BMW 7 Series [9], Audi A8 [10, 11] and BMW iX [12, 13].

For FRP parts, the manufacturing process is of high importance. While for, e.g., metal materials the properties of the finished parts are commonly unchanged compared to the properties of the initial virgin material, the properties of FRP parts are formed during its manufacturing. During the production process, the raw materials, i.e. fibers and matrix, are united to form the structure and shape of the desired FRP part. Therefore, the manufacturing process is a crucial factor to ensure the quality of the material and the finished FRP part. [14] Besides others, the compression resin transfer molding (CRTM) process has seen an increased use in the automotive industry due to its potential to manufacture high quality FRP parts in an economic and automated way [10, 15–17].

In addition to other measures, a greening of the automotive industry requires an optimization of existing production processes and development of new ones [4].

In this context, process efficiency must be enhanced to ensure a minimal scrap rate during high-volume serial productions of the automotive industry. One often reported issue, leading to increased scrap rates during FRP manufacturing, is the edge race-tracking effect [14]. A gap between preform edge and cavity wall of the mold, created due to e.g. preform cutting and placement tolerances, leads to a locally increased flow velocity which drastically changes the preform impregnation pattern and increases the risk of unimpregnated preform sections [14, 18–20]. While edge race-tracking has been reported in literature to cause unsuccessful preform impregnations during CRTM processing [21, 22], edge race-tracking has not yet been studied in detail for the CRTM process. So far, knowledge about the effects of edge race-tracking and strategies to diminish them have been transferred to CRTM processing from studies of related FRP processes [10, 23] without validating them specifically for CRTM.

The present work aims to contribute to sustainable CRTM manufacturing by increasing the process robustness towards edge race-tracking. Specific process characteristics are intended to be exploited by a modified sealing and tooling concept to diminish the edge race-tracking effect during CRTM processing. Figure 1-1 illustrates the core idea which sets the starting point for the research presented in this work. The CRTM process characteristic of an actuated upper mold shall be enhanced by partitioning the upper mold into different sections that can be individually actuated. This can be put in effect by the known technology of slider tooling enabling a pre-compaction of the preform edge and a localized, central injection gap in which the resin is distributed above the preform. Thus, the partitioned upper mold design enables a spatial disconnection of the injection gap and a potential edge race-tracking channel. During the compression phase, the central mold section is closed to distribute the resin inside the preform, filling potential edge race-tracking channels late in the process. However, most conventional sealing concepts for slider tools are subject to considerable wear, therefore, a new sealing concept shall be introduced in the CRTM process. As known from a related FRP manufacturing process [24], a film material is intended to be introduced into the CRTM process to seal the preform impregnation space inside the mold, making conventional mold sealing redundant and enabling seal-free mold designs. [25] In brief, the overall research objective of this work is defined as:

Increasing process robustness towards edge race-tracking during CRTM preform impregnation by investigating, enabling and validating a passive flow control strategy via the use of film-sealing and slider tooling.

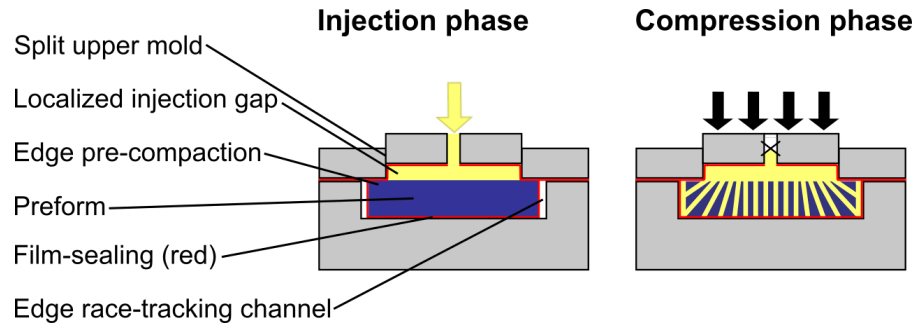


Fig. 1-1 Hypothesis of an enhanced CRTM process design to diminish edge race-tracking. cf. [26]

2 State of the Art

The aim of this work is to broaden the knowledge on preform impregnation patterns and advanced fabrication strategies in the presence of edge race-tracking during the compression resin transfer molding (CRTM) process. In this context, the following chapter provides an overview of current knowledge in the field relevant for the later presented original research studies.

The first Section 2.1 describes the liquid composite molding (LCM) technology, in which CRTM is integrated. Furthermore, Section 2.1 provides a literature review on the edge race-tracking effect and presents current process enhancement trends in LCM technology by introducing thin polymeric films and slider tooling.

The second Section 2.2 covers numerical flow simulations to model the preform impregnation in LCM processes. At the beginning, the often applied control volume finite element method (CVFEM) is described before the basic physics of a LCM preform impregnation is explained. Moreover, the equivalent permeability approach is discussed, needed to model edge race-tracking in the used software package PAM-RTM by ESI Group (Rungis, France). At the end of the second section, the CRTM modeling module in PAM-RTM is presented to provide background knowledge for the following research studies.

2.1 Liquid Composite Molding (LCM) Technology

A wide variety of manufacturing processes for fiber-reinforced plastic (FRP) materials exist, each characterized by specific advantages and limitations which need to be balanced to find the most suitable process based on the characteristics of the desired part (e.g. geometry, structure, etc.) and business case (e.g. desired production rate, available manufacturing equipment, etc.) involved. LCM is a class of manufacturing processes for composite parts in which a stationary fiber structure in the shape of the future part, commonly called “preform”, is placed inside a one-sided or closed mold and impregnated with a liquid polymer resin system. The intention of all LCM processes is to fill the empty spaces between the fibers with resin and displace potential gases to completely saturate the preform. After a successful preform impregnation, the resin is cured and the FRP part can be demolded. [14, 15, 27, 28] A detailed explanation about two specific LCM processes, frequently used in the automotive industry and studied in this work, is presented in Subsection 2.1.1

Uncertainties¹ concerning LCM processes, e.g. raw materials, environmental or process conditions, can lead to a poor robustness of the process and result in increased rejection rates during industrial production [28–30]. Uncertainty during fabric cutting, assembly and placement may result in inhomogeneous permeability distribution inside the mold and, in the worst case, to a fiber free channel between preform edge and mold wall, commonly referred to as “edge race-tracking”. Edge race-tracking is reported to strongly disturb the resin flow inside LCM molds bearing high risk of an unsuccessful preform impregnation. [14, 18–20, 28–30] Subsection 2.1.2 provides a literature review on the edge race-tracking effect and strategies to diminish this effect in LCM processing.

Numerous attempts to enhance LCM processes are reported in literature. One promising attempt is the integration of thin polymeric films in closed mold LCM processes in order to e.g. seal the injection space, thus, making conventional mold sealing concepts obsolete. [24, 31] An overview of the functions thin polymeric films can take and how they have been successfully integrated in closed mold LCM processes is given in Subsection 2.1.3. Another promising attempt is the use of slider tooling technology to enable complex part geometries or enhance the flow control during LCM processes. Regarding this topic, Subsection 2.1.4 provides basic knowledge about slider tooling and current applications in LCM technologies.

2.1.1 LCM Process Variants

The class of LCM processes can be subdivided into the application of a one-sided or closed mold. While for the latter variant the preform is covered at all sides by rigid tool walls, the preform can also be simply placed in a one-sided mold and covered on the other side with a thin non-porous film. Due to the flexible, deformable character of the film, the preform can only be impregnated applying pressure levels below the surrounding atmospheric pressure. The rigid, matched mold of the closed mold concept enables the resin to be injected at elevated pressure levels. There are numerous process variants for both categories, but some of the most common are, for the category of one-sided mold processes, vacuum-assisted resin transfer molding (VARTM), Seemann’s composite resin infusion molding (SCRIMP), and controlled atmospheric pressure resin infusion (CAPRI), as well as, for the category of closed mold processes, resin transfer molding (RTM), wet compression molding (WCM), and compression resin transfer molding (CRTM). [14, 27, 32, 33]

¹ “Uncertainty: A range of values within which it is estimated that the true value of a quantity of interest lies. It is typically aimed to form the narrowest possible range that encompasses all possible sources of error, including the intrinsic randomness of the system, inaccuracy due to a lack of knowledge, deficiencies of equipment, etc.” [29]

Due to the specific characteristics of closed mold processes, such as tight geometrical tolerances, good surface quality, and short injection times, these processes have been applied in medium to high-volume serial production in the automotive industry. Especially the RTM and CRTM process have shown potential to meet the high requirements for automotive serial productions. [10, 17] Therefore, both processes are explained and discussed further in this subsection.

Resin Transfer Molding (RTM)

The resin transfer molding (RTM) process has been used in a wide variety of industries since the middle of last century. Figure 2-1 illustrates the principle process steps of the RTM process. A fiber structure in a shape close to the desired part (preform) is manufactured in an upstream process, reducing the mold/press cycle time at the RTM process to the duration of the preform impregnation and resin curing.

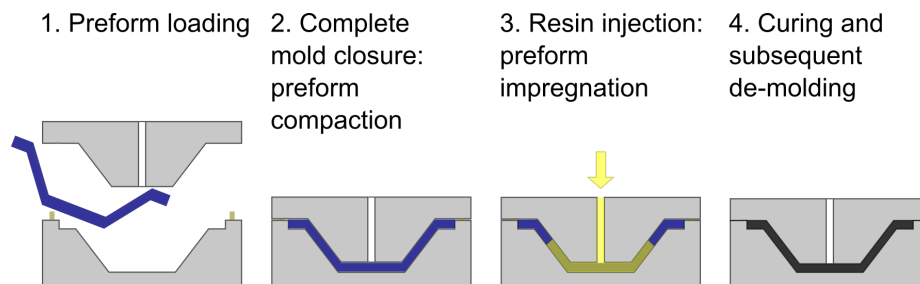


Fig. 2-1 Schematic illustrating the principal steps of the resin transfer molding (RTM) process.

At the beginning of this process the preform is loaded into the cavity formed by a rigid, matched mold, as shown in the first step of Figure 2-1. In the second step, the mold is closed compacting the preform inside the cavity to the final part thickness. During the third, and most important, step, resin is injected into the cavity to impregnate the preform. Especially for shell structures, the resin flows predominantly in an in-plane direction during RTM, which can lead to long flow distances of the resin. The complete preform compaction prior to the injection comes along with an increased resistance against resin flow inside the fiber structure (reduced permeability). In some cases, the long flow distances through a preform of low permeability increases the effort to realize adequate RTM impregnation times. Different strategies exist to quickly and evenly distribute the resin inside the preform, such as increased injection pressure, use of resin runners or multiple inlet injection. [14, 27, 34]

High mold clamping forces are required during the RTM process to withstand the compression forces of the preform and sealing material as well as the fluid

pressure present during the injection. The process equipment has to be adequately designed to cope with these forces to maintain a complete mold closure throughout the process, ensure tight part tolerances and prevent resin from leaking from the cavity. Finally, at the fourth step of the RTM process (Figure 2-1), the resin system is cured at an increased or isothermal temperature level enabling the de-molding of a near net-shaped part. [14, 27, 34]

Advantages of RTM include:

- Tight geometrical tolerances due to rigid, matched tooling (incl. tight mechanical properties due to consistent fiber volume fraction) [14, 34].
- Good surface finish replicated by the finish of the cavity walls inside the mold [14, 27, 34].
- Complex part geometries and direct inclusion of inserts can be realized [14, 34].
- High fiber volume fractions are achievable needed for structural parts [34].
- Mitigating the need for machining operations after de-molding due to (near) net-shape manufacturing [14, 27, 34].
- Flexibility in used raw material types (i.e. reinforcement or resin) [14, 34].
- Closed injection atmosphere prevents exposure to volatile chemical vapor [14].
- Lower mold clamping forces compared to compression resin transfer molding (CRTM) [35].
- High potential of process automation [15].

Limitations of RTM include:

- Sensitivity of mold design, i.e. position of inlet(s) and vent(s) [14].
- Sensitivity of impregnation result on preform quality, i.e. preform cutting and placement [14, 29].
- Risk of movement of preform (known as “washout”) leading to a decrease in mechanical performance of the part [14].
- Increased costs due to rigid, matched mold and potential need of press equipment [15].

Compression Resin Transfer Molding (CRTM)

While the RTM process is generally suitable for serial productions, the general high flow resistance inside the preform for parts of high fiber volume fraction (FVF) can

be a limitation for some industries at which short cycle times are required, such as in the automotive industry. The compression resin transfer molding² (CRTM) process, as an enhancement of the RTM process, has been developed to integrate the movement of the mold as a process control variable, adjusting the flow resistance inside the mold during preform impregnation and realizing short mold filling times. [15, 27]

In literature, two CRTM variants are distinguished by their relative position between upper mold and preform. Figure 2-2 and 2-3 illustrates the principle process steps of the two CRTM variants denoted according to [15] as CRTM-1 and CRTM-2, respectively. As for the RTM process, the preform is placed during the first step inside a rigid, matched mold for both CRTM variants. During the second step, the upper mold is not fully closed as in RTM but only partially closed, to marginally compact the preform for CRTM-1 or to enable an empty space above the preform, denoted “injection gap”, for CRTM-2. Due to the minimal preform compaction and therefore decreased flow resistance of the preform at CRTM-1 compared to conventional RTM, a fast resin injection can be realized which partially impregnates the preform pre-dominantly in an in-plane direction, as illustrated in Figure 2-2. [15, 36–38]

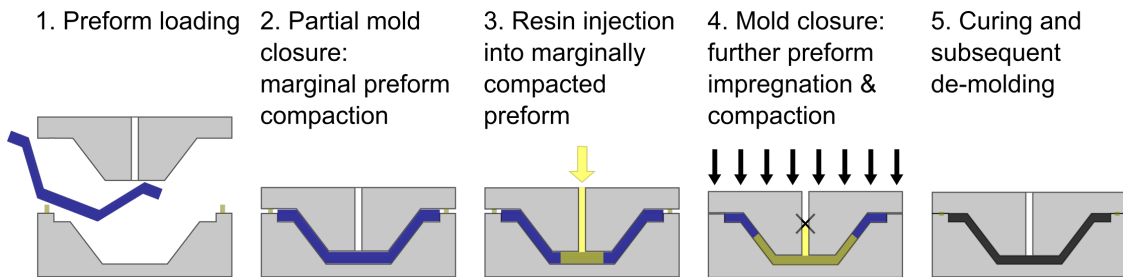


Fig. 2-2 Schematic illustrating the principal steps of the compression resin transfer molding process at which the upper mold marginally compacts the preform prior to resin injection, denoted CRTM-1.

By creating an injection gap above the preform, the CRTM-2 variant in Figure 2-3 enables an even lower overall flow resistance inside the cavity, which leads to a distribution of the resin mainly above the preform while the preform is only minorly impregnated during the injection phase. After a defined amount of polymeric resin is injected for both CRTM variants, the upper mold is fully closed, often referred to in literature as the compression phase. The compression phase distributes the resin further inside the preform leading to its complete saturation, and compresses

² In literature also referred to as: injection compression molding (I/CM), advanced resin transfer molding (ARTM), compression transfer molding (CTM), injection/compression liquid composite molding, resin transfer/compression molding (RT/CM), ultra resin transfer molding, pressure controlled resin transfer molding (PC-RTM).

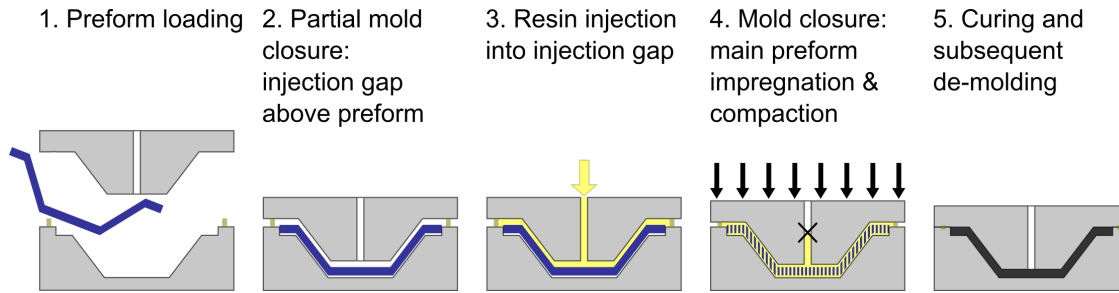


Fig. 2-3 Schematic illustrating the principal steps of the compression resin transfer molding process at which an empty space (injection gap) is formed between upper mold and preform prior to resin injection, denoted CRTM-2.

the part to final thickness. While an in-plane squeeze flow is initiated during the compression phase of CRTM-1, a three-dimensional flow occurs inside the cavity of CRTM-2 due to the presence of the two flow domains (i) injection gap and (ii) preform. The permeability of the injection gap is generally orders of magnitude higher than the preform, which is why the resin is first predominantly distributed inside the injection gap until it is completely filled or until the upper tool gets in contact with the preform. Subsequently, the preform is saturated, at the CRTM-2 variant, by a complex flow pattern, including in-plane and out-of-plane flow components. As for the RTM process, the resin inside the saturated preform is finally cured in both CRTM variants at increased or isothermal temperature and eventually de-molded. [15, 36–38]

As an enhancement of the conventional RTM process, CRTM inherits many advantages such as possibility of near net-shape fabrication, high potential to automate manufacturing of parts with high FVF as well as tight part tolerances and good surface finish due to the rigid, matched mold. Furthermore, the integration of the mold position into the CRTM process control can enable significant reduction of injection pressure and mold filling time. Nevertheless, more process variables, as for RTM, lead to a more complex process control. On the practical side, a more complex mold sealing concept is required to seal the cavity during the resin injection of the partially opened mold and increased wear of the sealing due to the relative movement of the tool segments is an undesirable outcome. Advanced process equipment is needed to adjust and control the resin injection and mold closure during the CRTM process. Finally, literature studies have shown that higher mold clamping forces occur during the CRTM process than for RTM. [15, 35]

Even though the CRTM-2 process variant is reported to be of higher complexity, due to a more intricate three-dimensional preform impregnation pattern and additional process variables concerning the injection gap, this process variant is also recorded to provide the highest potential to decrease injection pressures and

impregnation time. Therefore, the CRTM-2 variant is chosen to be studied in this work and for simplicity is denoted CRTM in the remainder of this document.

2.1.2 Edge Race-Tracking in LCM Processing³

A frequently reported issue in closed mold liquid composite molding processes is so-called edge race-tracking, which is theoretically preventable, yet with an effort that is usually not practical. Specifically, the preform dimensions need to be negatively toleranced in relation to the cavity in-plane dimensions to enable the preform to be placed inside the cavity and to minimize the risk of fiber pinching, which can be damaging to the mold. Thus, a small channel or area is created between the preform edge and the cavity wall that has low resistance to resin flow. During injection, local inhomogeneous flow front velocities develop inside the cavity that drastically change the preform impregnation pattern. This effect is commonly referred to as edge effect or (edge) race-tracking. [14]

Multiple studies investigated the effect of edge race-tracking on the preform impregnation during RTM. In flow visualization experiments of the edge race-tracking effect, Hammami et al. [19] and Bickerton and Advani [20] showed that the preform impregnation pattern is drastically changed due to an advancing flow inside the edge race-tracking channel and an additional lateral flow from the channel into the preform. Besides changes to the flow pattern, Bickerton and Advani [20] observed in their experiments that the presence of an edge race-tracking channel also reduces the injection pressure at constant flow-rate injection or the filling time of injections at constant pressure. Han and Lee [18] performed experiments in which a flat preform was placed centrally in a cavity surrounded by edge race-tracking channels. Injecting the resin into the preform-free space, the flow advances along the edge race-tracking channels around the preform and eventually fills it transversely from all four sides. As a consequence, an encapsulated dry preform section is formed in the center of the preform. The flow advances until a pressure equilibrium is reached between the fluid pressure of the impregnated preform sections and the gas pressure in the encapsulated dry preform section. At the point of pressure equalization, the dry preform section cannot be further compressed, commonly referred to as a dry spot or macro void. Parts containing macro voids are typically rejected in industrial FRP production and therefore need to be avoided by appropriate process control strategies. Figure 2-4 compares an illustration of an ideal, undisturbed RTM preform impregnation, in the top row, with a case at which edge race-tracking is present, similar as studied by Han and Lee [18], forming a central macro void.

³ This subsection has been previously published in [26].

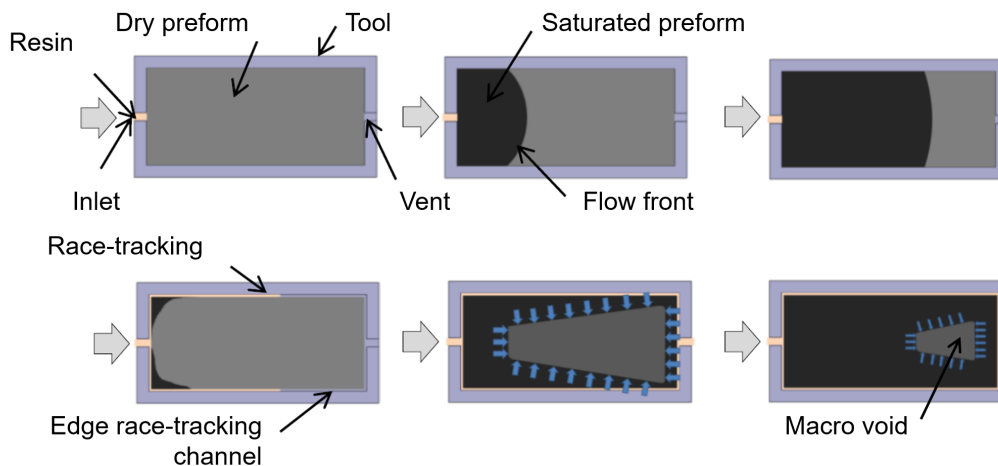


Fig. 2-4 Comparison of an undisturbed RTM preform impregnation (top row) and a RTM preform impregnation in the presence of edge race-tracking (bottom row). [39]

Different attempts have been presented in literature to control the preform impregnation and diminish the edge race-tracking effect during RTM processing. These can be divided into passive and active process control strategies. In passive strategies, the objective is to reduce the lateral inwards or outwards flow between the preform edge and a potential race-tracking channel by manipulating one of the three involved factors: preform edge, race-tracking channel or injected resin. A well-established approach is to increase the resistance to resin flow of the preform edge by circumferentially increasing its fiber volume fraction (over-compacting or pinch-off) [34, 40]. This can be achieved through design features of the tool such as a reduced cavity height [41] or incorporation of additional material [42–44]. Instead of over-compacting the preform edge to reduce a lateral race-tracking flow, the preform edge can be sealed by applying sealant between individual layers [45] or on top of the preform before the tool is closed [46]. As for the preform edge, the race-tracking channel can be sealed by blocking it with impermeable material prior to the preform injection [47–49], or the flow resistance of the channel can be increased by filling it with low permeable material [44, 49, 50]. Other passive strategies involve local heating or cooling of the tool cavity to change the resin viscosity and therefore adjust the local flow front velocity inhomogeneity caused by the race-tracking effect [51, 52].

In contrast to passive strategies, active process control strategies use sensors to detect the actual flow front progression inside the tool and take corrective action in case a disturbed flow is detected, to prevent the formation of macro voids. Nielsen and Pitchumani [53] presented an active control strategy in which a flow disturbance is tracked in real-time and corresponding data is processed by a controller. The

controller employs an artificial neural network, trained by process simulations, to adjust the injection pressure of three inlet ports along the inlet side of the mold. Lee et al. [54] presented an active control method at which the flow is observed via sensors feeding the information back to a control unit that either adjusts the injection pressure or opens auxiliary gates. The latter attempt to sense the flow front shape and correct a disturbed flow by strategically opening or closing auxiliary gates was also investigated by other researchers and was shown to prevent macro void formation due to flow disturbances such as edge race-tracking [55–59]. Edge race-tracking occurs in industrial FRP production sporadically due to tolerances of preform cutting and placement inside the cavity. The presented active control strategies have the clear advantage that they can sense and adjust the flow in real time but are complex in tool and controller design, adding costs for associated sensors and actuators. In contrast, passive strategies are static means to control the resin flow. Nevertheless, one passive strategy in particular, the over-compaction or pinch-off of the preform edge, has been proven to be effective and easy to implement, which is why it is a common control strategy for RTM applications [17, 23, 39, 60].

Despite the extensive investigations on edge race-tracking effects during RTM, a knowledge gap exists about the edge race-tracking effect in the CRTM process, even though this effect has been reported in literature [21, 22] to cause unsuccessful CRTM impregnation. Furthermore, no effective strategy on how edge race-tracking can be diminished during CRTM processing has yet been presented in literature.

2.1.3 Films in LCM Processing

Films are thin sheet materials which are diversely used in FRP manufacturing. In the context of this work, polymeric films are focused on, which consist of a pure organic material type or a blend of multiple materials. Furthermore, the film's structure can be composed of one or multiple layers of different material, with the former herein being referred to as monolayer film and the latter as multilayer film. Extrusion technology is commonly used to manufacture films. Polymer granulate is melted and pressed through a thin and wide die after which a chemical or thermal curing is initiated. After extrusion, the polymeric compound is stretched by rolls or via air pressure to form a film of desired thickness. [61–63]

Bruckbauer [31] grouped the function of films for FRP materials in four main groups, as shown in Figure 2-5 and exemplarily explained for specific functions in this paragraph. For different purposes, films are either permanently bonded to the FRP material or remain separate and are removed after their desired use. Modifying the surface of a FRP part with films can help to protect the part from e.g. chemicals and ultraviolet (UV) radiation or improve its flame resistance. By

printing circuit paths onto films, which are embedded in a FRP part, sensors can be integrated to realize e.g. process monitoring of the structure in use. Furthermore, films are integrated in FRP structures to prepare for downstream production steps. Thermoplastic film surfaces can for example be co-cured on a thermoset FRP part to enable weldable part surfaces. [31]

Functions of films	
Surface modification	<ul style="list-style-type: none"> - Chemical protection - UV protection - Moisture barrier - Corrosion protection - Flame protection - Surface finish - Electromagnetic shielding
Carrier	<ul style="list-style-type: none"> - Circuits - Sensors - Lightning protection
Process aid material	<ul style="list-style-type: none"> - Seal - Release agent - Protective film - Handling aid
Preparation for production steps	<ul style="list-style-type: none"> - Joining layer - Separation layer - Assembling aid

Fig. 2-5 Functions of films for FRP materials grouped in functional classes (light gray) and their characteristics (white). cf. [31]

The use of films as process aid material is the most common application in FRP manufacturing. During the vacuum assisted resin transfer molding (VARTM) process, the preform is placed on a one-sided mold and covered by film material. The film acts as a seal to evacuate the preform and shape it to the tool. Resin is infused into the preform over at least one inlet and outlet, driven by the pressure gradient between resin inlet at ambient and outlet at vacuum pressure level. One of the biggest advantages of this process, especially for large structures, is its cost efficiency due to the need of only one-sided tools and the use of cost-effective film material to enclose the injection space of the preform. The right choice of the film as process aid material is a key process parameter at VARTM. Besides thermoplastic films also silicon rubber or thermoplastic elastomer (TPE) bagging materials are used. Depending on the manufacturing conditions during the VARTM process, different thermoplastic film materials are chosen, such as polyethylene (PE), polypropylene (PP), polyamide (PA), polyvinylchlorid (PVC), polytetrafluoroethy-

lene (PTFE), polyvinyl fluoride (PVF) or ethylene tetrafluoroethylene (ETFE). [64–66]

In the wide range of FRP manufacturing technologies, films are utilized to fulfill different functions. Covering the mold with shape adaptive films before e.g. placing and injecting the preform on top of it allows to work without chemical release agents and reduces mold contamination. For this purpose, the Fraunhofer IFAM (Bremen, Germany) developed a highly elastic thermoplastic elastomer (TPE) film, commercially distributed by Infiana (Forchheim, Germany). The so-called Flex^{PLAS}[®] film is plasma coated to increase its release properties from cured thermoset FRP parts. [67, 68]

Closed mold LCM processes, at which the mold concept consists of a rigid, matched mold, are conventionally run without films as a functional layer. In recent years, the benefits of films have been utilized to improve closed mold processes such as resin transfer molding (RTM), compression resin transfer molding (CRTM) or wet compression molding⁴ (WCM).

To increase the process robustness during WCM, Bockelmann [70] used film materials as carrier material with multiple deep drawn cavities spread evenly over the preform's surface. The carriers, filled with matrix material, are placed below the preform and inserted into the tool. During the tool closure, the carriers are squeezed and the matrix material impregnates the preform. Bockelmann [70] showed that the matrix dosing via the carriers in the film enable a more even and precise preform impregnation than during conventional WCM, at which the resin is dosed on top of the preform. In addition to the use of the film as matrix carrier, Bockelmann also intended to bond the used film STRECH-VACTM 250 [71] manufactured by Richmond Aircraft Products (CA, USA) to the part. Therefore, the film can be used as surface modification or preparation for downstream production steps. [31]

Another example of film integration in a closed mold LCM process is the concept of Film-RTM by Häffelin [24]. To enhance the resin transfer molding process, the preform is encapsulated by two films as shown in Figure 2-6. Connecting elements to the inlet and the cavity pressure control system are integrated into the film package. The film-package is then sealed air- and liquid-tight by welding the two films at the edges. Häffelin highlights the benefits of an evacuated film package, which are e.g. increased transport stiffness and protection of the preform from environmental impacts. During the Film-RTM process, the preform is injected on the inside the of the film-sealed preform package. The film acts as a barrier layer between resin and

⁴ During wet compression molding, fabric layers are stacked and resin is dosed onto the flat fabric stack. Both, fabric stack and dosed resin, are placed inside a rigid, matched mold. During the mold closure the fabric is draped into the final part shape and impregnated by resin before the resin is cured under elevated or isothermal temperature. [69]

mold wall and makes the use of conventional release agent obsolete. Furthermore, the injection inside the film-sealed preform package enables a seal-free tool design. The used polycarbonate (PC) and acrylonitrile-butadiene-styrene (ABS) multilayer film was specially designed to co-cure to the matrix system to improve the part's surface quality and prepare for downstream production steps. [24]

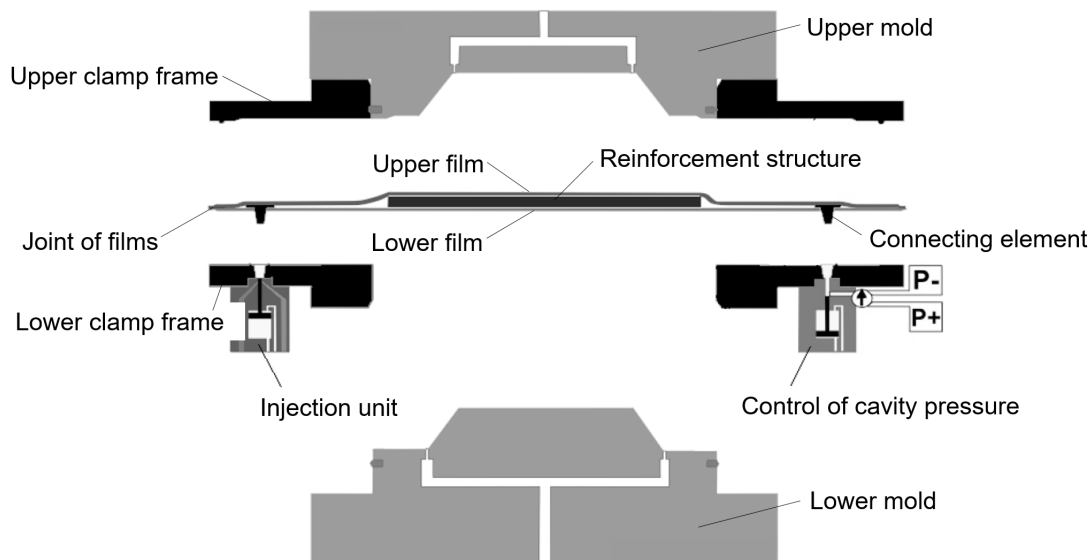


Fig. 2-6 Tooling and preform concept of the Film-RTM process – approach after Häffelin. cf. [24]

Ruiz and Trochu [72] as well as Chang [73] integrated a flexible film in-between two rigid mold halves to create a cavity with two separated chambers. In one of the two chambers, the reinforcement structure is placed and impregnated while the pressure acting across the film can be adjusted by the pressure level inside the other chamber. By using a gas or fluid as compression medium, the pressure level above the film can be adjusted during the preform impregnation to manipulate the preform saturation in the lower chamber. Additionally, the used compaction medium can be heated and cooled to control the curing cycle during the FRP manufacturing. The film is used as a process aid material to separate the two chambers and realize a preform impregnation which combines characteristics of the VARTM and CRTM processes. [72, 73]

Finally, Stewart [74] suggested to use film material to separate sections of a mold, which are equipped with movable sliders, from the liquid polymeric resin. Stewart's LCM mold design with an integrated film is shown in Figure 2-7(b) and further explained in the following subsection.

2.1.4 Slider Tooling in LCM Processing

Together with the injection and press equipment, the tool or mold is a crucial component of the manufacturing apparatus during LCM processing. For closed mold LCM processes, the cavity of the mold defines the negative shape of the future part. During the LCM process, the preform is placed inside the mold and a liquid resin system is injected to impregnate the preform and fill the cavity to eventually form the FRP part. A LCM mold has to be designed considering mechanical, rheological, and thermal aspects. The mechanical design has to ensure that the mold is stiff enough to enable the required part tolerances and that the opening and closing mechanism of the mold enables a proper loading of the preform and demolding of the cured part. The rheological design ensures that the preform is completely impregnated during the LCM process, and the thermal design of the mold guarantees that heat is transferred to or from the raw materials during injection and curing of the resin system. [34]

Movable mold sections, so-called “sliders”, can be incorporated into a LCM mold as part of the mechanical or rheological design. Figure 2-7 presents two examples of slider tooling used in LCM manufacturing due to part geometry as well as process control constraints. Sections of parts, which cannot be demolded in the main opening direction of the mold, are commonly called “undercuts” and need to be released in a supplementary demolding direction. Mold inserts are used in manual processes, while sliders enable the automation of the manufacturing of the FRP part with undercuts as exemplary shown Figure 2-7(a). The picture shows a mold designed by Alpex (Mils, Austria) which enables HP-RTM manufacturing of an automotive wheel geometry with undercuts [75, 76]. The mechanical design of this mold enables the demolding of the wheel manufactured via four automated sliders which are actuated in a perpendicular plane to the main demolding direction of the part. Figure 2-7(b) shows an example in which sliders are applied according to rheological design aspects. Stewart [74] patented a mold design in which sliders are utilized to actively promote the resin flow during a LCM process by strategically moving sections of the upper mold to promote the resin flow inside the mold. A similar theoretical approach of an enhanced rheological mold design, the so-called “articulated tooling”, is suggested by Choi and Dharan [77, 78] for the manufacturing of FRP parts.

Sliders can be applied in any direction or plane inside the mold as long as the design allows the slider to be actuated. The actuation of a slider can commonly be done in two different ways – passively or actively controlled. The passive control is generally realized via an inclined column or a slider bolt which move into or inside a inclined hole of the slider and actuate it in an angled plane in regard

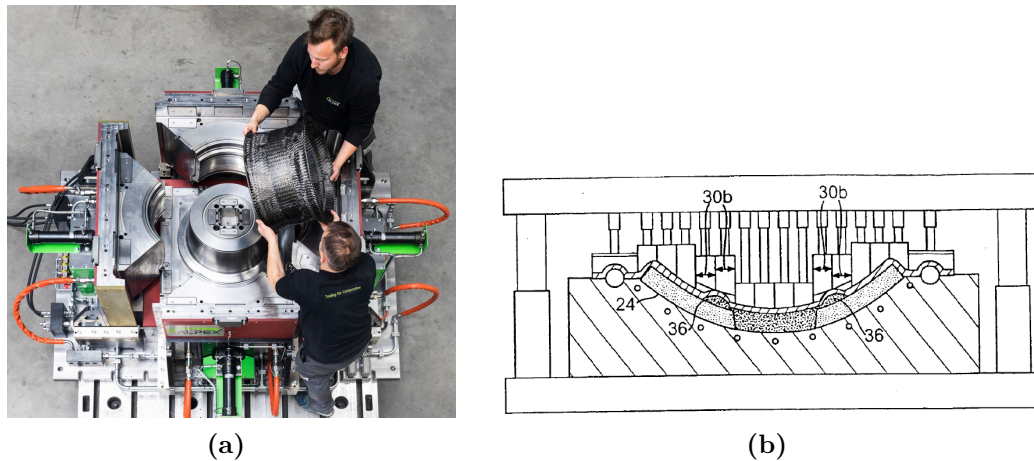


Fig. 2-7 Applications of slider tooling in LCM: (a) To enable FRP parts with undercuts [75, 76]; (b) To enhance preform impregnation [74].

to the demolding direction during the opening and closing of the mold. The main advantage of a passively controlled slider is its simple and compact design. However, the actuated stroke of the slider as well as the slider size is limited and it can only be actuated during the opening and closing of the mold. Larger slider components or movement distances can be realized via an actively controlled slider. For this control variant hydraulic cylinders are commonly used. Cylinders can be purchased in different configurations and stroke lengths which increase the mold design flexibility of actively controlled sliders and enable a movement of the slider independent of the mold opening or closing movement. However, the cylinder is generally mounted outside of the mold and, therefore, increases the size of the mold as well as the complexity of the mold and its actuation mechanism. [79, 80]

Just as during the actuated CRTM tool movement [15, 27], the actuation of the slider components increase the effort to realize a vacuum and liquid-tight sealing of the mold. Furthermore, the increased friction due to the relative movement between slider and its neighboring mold components can result in a stronger wear of conventional sealing concepts which are applied between mold segments, resulting in increased production downtime. A solution to this problem provides the separation of the sealing and mold design by spatially separating the injection space inside the mold from the actuated sliders via film material. While Bruckbauer [31] generally suggests film material as a process aid material to seal LCM processes, Häffelin [24] validated this idea for a static mold during Film-RTM. Furthermore, Stewart [74] incorporated a film in his tool design for an active flow control strategy for LCM processing which is enabled via sliders and sealed by film material (see Figure 2-7b).

Generally, slider tooling can increase the design freedom of the mold during LCM manufacturing. However, sliders make a mold design and process control generally

more complex and more expensive. Therefore, the trade-off between technological and economical benefits versus the effort of designing and operating a slider tool must be considered for a given application.

2.2 Numerical Simulation of Preform Impregnation in LCM

Virtual simulations enable a fast and cost-effective prediction of LCM manufacturing processes at an early stage of the design process. Without the need of cost-intensive trial-and-error experiments, designers can analytically or numerically optimize injection strategies, i.e. injection pressure, flow rate, position and number of inlets, vents, flow media or flow channels. If the raw materials are characterized, insights of the mold filling via numerical simulations enable the design of a robust process by investigating e.g. flow front progression, pressure gradient, temperature distribution and degree of cure as a function of time. [14, 20, 81, 82]

During the modeling of isothermal LCM processes, at which little to no heat transfer and chemical reaction takes place, the filling and the subsequent curing process can be modeled separately. The focus of this work is to investigate the preform impregnation during the isothermal CRTM process as applied in the automotive industry. Therefore, in the context of this work, the focus is set to understand and improve the mold filling of the CRTM process while part curing is disregarded. [14, 20, 81, 82]

Analytical or semi-analytical methods exist to analyze the preform impregnation of simple part geometries. More complex geometries are commonly investigated using numerical simulation methods. Various numerical methods are available to simulate the preform impregnation during LCM processes such as the finite difference method (FDM), the boundary element method (BEM), the finite element method (FEM), or the control volume finite element method (CVFEM). [14, 83–85]

The finite difference method (FDM) is commonly used to analyze regular geometries or problem domains which are discretized in a regular grid of nodes. Due to the regular grid, FDM is an efficient solution method at which a set of discrete equations is applied to each node. The equations of differential form are solved to analyze the physics of the investigated problem. In contrast to FDM, only the boundary of the observed problem domain is discretized in the boundary element method (BEM), not its complete surface or volume. This leads to a reduced number of nodes and usually to a reduced numerical effort compared to other methods which discretize the complete problem domain. LCM filling simulations by FDM or

BEM are based on the moving grid approach, at which only the region of the fluid inside the problem domain is discretized. With progressing flow the fluid domain needs to be re-meshed at each time step. The re-meshing at each time step makes the moving grid approaches accurate at predicting the exact flow front position but is also reported to result in high computational effort. [84, 85]

The finite element method (FEM) is a numerical method suitable to discretize complex geometries or problem domains in small and simple shaped elements, the so-called finite elements. The non-overlapping finite elements are connected at common nodes which are characterized by equations that describe the physics of the problem domain. It is stated that mass conservation, essential to accurately simulate LCM filling processes, is not always fulfilled across element boundaries in standard FEM but which can be overcome by additional computational effort. As for the FEM, the control volume finite element method (CVFEM) discretizes a geometry or problem domain in small finite-sized elements of simple shapes. CVFEM provides similar geometrical freedom as FEM due to the related discretization into non-overlapping elements at which vortice nodal points are defined. Further, CVFEM enables the creation of control volumes which surround each node. In contrast to standard FEM, the CVFEM satisfies the mass conservation across elements. FEM and CVFEM are fixed grid approaches in which the complete problem domain is initially meshed and the progressing flow front is calculated to progress through the meshed problem domain. Numerical methods of the fixed grid approach are reported to be more stable at simulating merging fluid flows making these methods suitable for optimization of complex LCM filling patterns. [84, 85]

By using numerical methods the filling process of fibrous structures during LCM processes can be investigated on different scales. Depending on the intended goal, the problem domain is intentionally limited to a certain discretization size to minimize the computational time of the simulation. The most detailed investigations on fibrous structures are done on the micro-scale, i.e. discretizing domains in the order of micrometers. The impregnation of single tows and the development of micro voids inside fiber bundles are studied on this scale. Fabric structures and their permeability⁵ are studied in simulations on the meso-scale, i.e. in the order of millimeters. Macro-flow simulations investigate the preform impregnation of complete parts in the order of centimeters to meters. The filling pattern of the preform on the macro-scale is often described by applying Darcy's law according to Equation (2-1) in which the preform is described as a homogeneous porous medium. [85–87]

In the context of this work, the effect of edge race-tracking on the preform impregnation in the CRTM process is investigated. Therefore, numerical simulations on

⁵ The permeability of a porous material is defined as the inverse of the quantity describing the medium's resistance to fluid flow. [14]

the macro scale are performed using the commercial software package PAM-RTM of ESI Group (Rungis, France). PAM-RTM uses the numerical control volume finite element method which is explained in detail in the following subsection 2.2.1. The physical description of flow processes by applying Darcy's law, as used in PAM-RTM, is described in subsection 2.2.2. Furthermore, the approach of equivalent permeabilities is discussed in Subsection 2.2.3, an approach needed to simulate fibrous-free spaces, such as an injection gap or edge race-tracking channel, in simulation environments applying Darcy's law. Finally in Subsection 2.2.4, the simulation scheme to model the CRTM process via the used software package PAM-RTM is explained.

2.2.1 Control Volume Finite Element Method

The control volume finite element method (CVFEM) is a widely used numerical calculation methods to simulate the preform impregnation of LCM processes. Especially the efficient simulation of complex geometries and the easy implementation of physical relations governing the flow in LCM processes have contributed to the broad application of this method in research [36, 88–98] and in commercial software packages such as PAM-RTM (ESI Group, Rungis, France), RTM Worx (Polyworx, Nijverdal, Niederlande), LIMS (University of Delaware, Newark, DE, USA) and My-RTM (Estern Switzerland University of Applied Sciences, Rapperswil, Switzerland) [82, 84, 85, 99].

At the beginning of the CVFEM modeling process, the geometry to be filled, or more general the problem domain, is meshed into non-overlapping finite elements. As illustrated in Figure 2-8, the mesh consists of nodes at the vertices of the elements as well as element borders connecting the nodes with each other. In a second step, the mesh is further partitioned by connecting the centroid of each element to the center points of the element borders creating a polygonal control volume around each node, as seen in Figure 2-8. The borders of each control volume are referred to as control surface. [82, 91, 93, 99]

Each control volume represents a discrete problem domain in which the pressure driven flow is numerically solved by considering specific boundary conditions. To be able to track the fluid flow, a filling factor f_i is associated to each node of each control volume. The filling factor represents the ratio between fluid volume present in the control volume and total available volume of the control volume at a certain point in time. [82, 91, 93, 99]

As illustrated in Figure 2-9, the filling state of the problem domain can be split into three regions. The fully filled control volumes of $f_i = 1$ represent the satu-

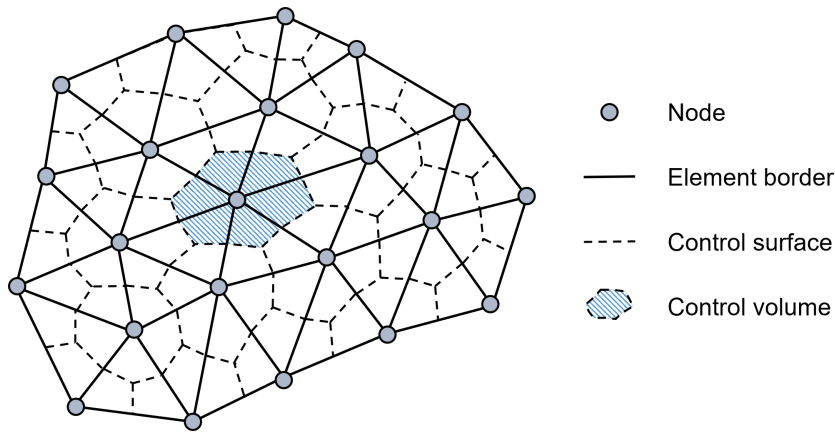


Fig. 2-8 Discretization scheme of CVFEM in three-node triangular elements and polygonal control volumes. cf. [81, 91, 100]

rated section of the problem domain and empty control volumes of $f_i = 0$ represent the unsaturated problem domain. Control volumes which are only partially filled ($0 < f_i < 1$) representing the region of the flow front. [82, 91, 93, 99]

Due to the assumption in CVFEM that each control volume is equally filled over its volume, the determination of the flow front is strongly dependent on the element size. Therefore, the exact flow front position cannot be identified inside the range of partially filled control volumes which can lead to deviations between real and numerical flow front positions, as illustrated in Figure 2-9. The flow front progression over discrete time steps is evaluated by applying and solving the governing equations at each node which is presented in the following subsection. [82, 91, 93, 99]

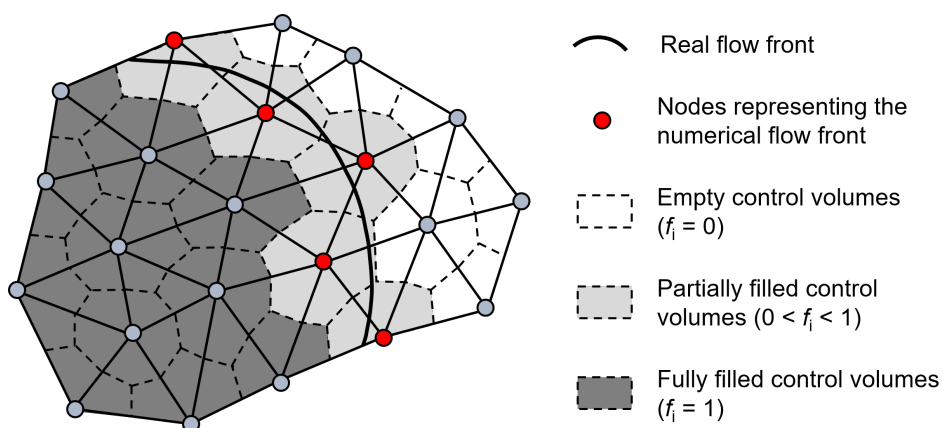


Fig. 2-9 Flow front identification during CVFEM simulations by using the nodal parameter of filling factor. cf. [81, 91, 100]

2.2.2 Physical Description of LCM Preform Impregnation

In the following, the modeling approach including the main equations describing the physics of the preform impregnation of the conventional resin transfer molding (RTM) process is explained according to [82, 84, 85, 93, 101, 102]. Based on the modeling approach of RTM, an enhanced method to describe the more complex preform impregnation pattern during the compression resin transfer molding (CRTM) process is explained according to [85, 90, 92, 93, 103, 104]. While the exact CRTM calculation method of the commercial software PAM-RTM, used in this work, is not made available by ESI Group, the presented approach provides the reader with essential knowledge to comprehend the fundamentals underlying numerical CRTM simulations.

RTM Modeling

The preform impregnation during RTM, at which the mold is fully closed prior to resin injection, can be represented by a flow through a homogeneous porous medium. The equations describing the physics of such a flow can be formulated by Darcy's law in combination with the continuity equation. Assuming negligible inertia effects, Darcy's law is stated as:

$$\vec{v} = -\frac{\mathbf{K}}{\eta} \cdot \nabla p \quad (2-1)$$

where \vec{v} is the volume averaged flow velocity, \mathbf{K} is the permeability tensor⁶ of the porous medium (preform), η is the viscosity⁷ of the fluid (resin system) and ∇p is the pressure gradient of the fluid. Assuming that the mold around the preform is stiff and non-deformable and that the resin as well as the preform are incompressible, the problem domain can be further described by applying the continuity equation:

$$\nabla \vec{v} = 0 \quad (2-2)$$

The velocity of the continuity equation in (2-2) can now be substituted by Darcy's law (2-1) resulting in the governing equation of a numerical RTM simulation:

⁶ The general second order permeability tensor \mathbf{K} can be diagonalized, consisting of two principal in-plane permeabilities K_{11} and K_{22} and of one principal out-of-plane (or through-thickness) permeability K_{33} [14].

⁷ Viscosity is defined as the resistance of a fluid against deformation or flow [14].

$$\nabla \left(\frac{\mathbf{K}}{\eta} \cdot \nabla p \right) = 0 \quad (2-3)$$

This second order differential equation (2-3) can now be solved to derive the pressure field by prescribing boundary conditions. The applied boundary conditions are that (i) the known inlet pressure or inlet flow rate is applied at the nodes of the inlet, that (ii) the known outlet pressure is assigned at the nodes of the flow front, and that (iii) a flow velocity of zero, normal to the impermeable tool walls, is defined. The solved pressure field of Equation (2-3) allows calculation of the flow front progression by calculating the flow rate Q_{ij} between two neighboring control volumes i and j via the following formula:

$$Q_{ij} = \int_{s_{ij}} \frac{\mathbf{K}}{\eta} \cdot \nabla p \cdot \vec{n}_{ij} ds \quad (2-4)$$

where s_{ij} represents the shared control surface of the two neighboring control volume i and j and \vec{n}_{ij} defines the normal vector of their shared control surfaces.

The flow front progression during a CVFEM simulation is evaluated in sequences of quasi-steady-state time steps. At each sequence the potential time steps to completely fill ($f_i = 1$) each individual control volume in the flow front region is calculated. To ensure that no control volume is overfilled, the time step of the following sequence is defined by the shortest calculated time step. After progressing the flow over one quasi-steady-state time step, the new pressure field inside the fluid domain is solved and the subsequent time increment is calculated to further increase the flow until the complete problem domain (mold) is filled.

CRTM Modeling

In the following, a simulation method will be explained describing a CRTM process similar as simulated in PAM-RTM (version 2019.5), used for the majority of simulation conducted in this work. PAM-RTM enables the simulation of a CRTM process at which the upper tool is not completely in contact with the preform, creating an injection gap above the preform. Furthermore, the process steps are serially simulated at which (i) the resin is injected while the tool position is fixed and (ii) the tool is lowered at a constant closing speed.

During the injection phase, the fluid flow can be modeled according to the previously presented RTM modeling approach. The cavity domain is hereby modeled in two different domains, the injection gap and the preform domain, between which resin can flow from one to the other. Even though the empty space of the injection

gap is not actually a porous medium, it can be virtually treated as one by assigning an equivalent permeability to this domain, so that the fluid flow can be calculated via Darcy's law. Further details on the equivalent permeability approach are given in Subsection 2.2.3.

One of the main assumptions of the presented RTM approach is that the porous medium does not deform during the preform impregnation. The previously presented continuity Equation (2-2) is based on this assumption and is therefore not valid during the compression phase of the CRTM process. During the tool closure of the CRTM process, the control volumes are compressed, leading to a reduction of their effective volumes. In consequence, control volumes of complete filling have to release part of their stored incompressible fluid to the neighboring control volume, resulting in a new source of fluid flow. To consider this, a infinitesimal volumetric strain rate $\dot{\epsilon}$ can be assigned in a fixed global coordinate system as a new source term in the continuity equation:

$$\nabla \vec{v} = -\dot{\epsilon} \quad (2-5)$$

To simplify this attempt, three assumptions are made, i.e. (i) the preform deformation during one calculation step is moderately small, (ii) the preform deforms only in the through-thickness direction, and (iii) the preform deforms uniformly over its thickness. Based on these assumptions the strain rate can be replaced by the rate of change of preform thickness (or closing speed) $\dot{h}_p(x,t)$ divided by the uncompressed thickness of the preform $h_{p,u}(x)$:

$$\nabla \vec{v} = -\frac{\dot{h}_p(x,t)}{h_{p,u}(x)} \quad (2-6)$$

Darcy's law (2-1) can now be applied in the adapted continuity equation of (2-6) to form the governing equation of the fluid flow in the CRTM compression phase:

$$\nabla \left(\frac{\mathbf{K}(h)}{\eta} \cdot \nabla p \right) = \frac{\dot{h}_p(x,t)}{h_{p,u}(x)} \quad (2-7)$$

In contrast to the governing equation during the RTM process (2-3), the permeability $\mathbf{K}(h)$ in Equation (2-7) changes in the CRTM compression phase due to the change of preform thickness. By knowing the tool kinematics, the permeability at each time step can be correlated to the current preform thickness by applying an analytical model or experimentally determined values. Equation (2-7) can now be solved to determine the pressure at each node and the flow progression can be calculated via Darcy's law (2-1). As for the RTM approach, the time dependent

flow front progression in the CRTM compression phase is modeled by computing the presented calculation scheme at sequential quasi-steady-state time steps until the complete problem domain is filled.

2.2.3 Equivalent Permeability Approach

As explained earlier, filling simulations based on Darcy's law assume a flow through a homogeneous porous medium. This assumption is true for the impregnation of the preform as a porous fibrous structure, but not necessarily true for other flow domains potentially present inside a mold, such as an edge race-tracking channel or a CRTM injection gap. Edge race-tracking channels and injection gaps are generally free of fibers. Therefore, these flow domains are in reality not porous media but generally treated as a "virtual porous media" to simplify LCM modeling approaches based on Darcy's law. [14, 15, 85]

To be able to model the flow inside a virtual porous medium, an equivalent permeability has to be assigned. Based on the shape of the virtual porous medium and its boundary conditions, different formulas to calculate the equivalent permeability are derived by correlating Darcy's law with a Poiseuille flow. [14, 15, 105]

In PAM-RTM, the flow during the CRTM process is modeled via different three-dimensional, volumetric flow domains, i.e. for the preform, the injection gap and the potential edge race-tracking channels. Therefore, each flow domain needs to be characterized by a permeability tensor \mathbf{K} , consisting of components in all three principal directions K_{11} , K_{22} and K_{33} . In the following chapter, formulas used in literature are presented and discussed which enable the calculation of equivalent permeabilities of a CRTM injection gap and an edge race-tracking channel.

Equivalent Permeability Formulas to Model a CRTM Injection Gap

Two Equations, (2-8) and (2-9), are used in literature to calculate the equivalent permeability $K_{ig,eq;x,y}$ of an injection gap. The cross sections and boundary conditions of the assumed flow domains are presented in Table 2-1. Both equations are derived based on a flow between two parallel plates. Therefore, the flow domain is characterized by a significantly larger in-plane than out-of-plane dimension (width $W \gg$ height H) which is generally true for an injection gap between preform and upper tool wall at the CRTM process.

$$K_{ig,eq;x,y} = \frac{H^2}{12} \quad (2-8)$$

$$K_{ig,eq;x,y} = \frac{\alpha \cdot H^3 + 4 \cdot H^2 \cdot \sqrt{K_{p,t}} + 6 \cdot \alpha \cdot H \cdot K_{p,t}}{12(\sqrt{K_{p,t}} + \alpha \cdot H)} \quad \text{with } \alpha = \sqrt{\frac{\eta_{eff}}{\eta}} \quad (2-9)$$

Equation (2-8) is derived by a fully developed, pressure driven Poiseuille flow between two impermeable walls [14, 15, 105] while Equation (2-9) considers potential penetration of fluid from the gap domain into the subjacent preform [105] (see Table 2-1). Therefore, the equivalent gap permeability in Equation (2-9), which considers a drainage from the gap into the preform, is dependent on the out-of-plane (transversal) preform permeability $K_{p,t}$. Furthermore, Equation (2-9) considers shear-rate dependent behavior of the resin by the coefficient α , at which η_{eff} is the effective viscosity inside the porous medium which can differ from the measured dynamic viscosity η . However, Bley [106] has shown that the shear-rate dependent behavior of the resin has no significant effect on $K_{ig,eq;x,y}$ in Equation (2-9) which correlates with literature studies [107, 108] that assume $\alpha = 1$.

Tab. 2-1 Cross sections and assumptions of equations to calculate the equivalent permeability of an injection gap. c.f. [100]

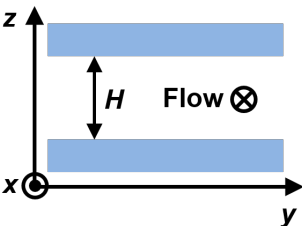
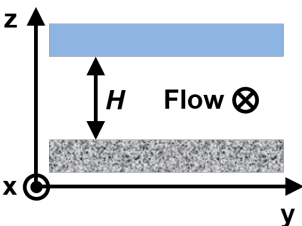
Gap cross section	Assumptions	Equation
	<ul style="list-style-type: none"> • Planar flow between two parallel plates • Flow direction out-of-plane in x-direction • Both walls impermeable 	<ul style="list-style-type: none"> • Equation (2-8)
	<ul style="list-style-type: none"> • Planar flow between two parallel plates • Flow direction out-of-plane in x-direction • Upper wall impermeable • Lower wall permeable 	<ul style="list-style-type: none"> • Equation (2-9)

Figure 2-10 compares progressions of two curves representing the equivalent permeability for gap heights between 0.1 mm to 6.0 mm calculated by Equation (2-8) and (2-9). An out-of-plane permeability of the preform of $K_{p,t} = 1.91 \cdot 10^{-12} \text{ m}^2$ is set as a base to calculate Equation (2-9), which is the permeability of an activated preform during gap injection as experimentally determined (see Appendix A.1.2) and used in this work.⁸ Based on [106–108] α was set to unity to calculate the equivalent permeabilities of Equation (2-9).

As seen in Figure 2-10 the calculated equivalent permeabilities of the two equations hardly differ from each other over the complete investigated gap height range which correlates to findings in literature [15, 109]. A non-linear trend of the curve progression is recorded in the semi-logarithmic plot. Up to 1 mm of gap height, the equivalent permeability changes over half of its total range, indicating a strong increase in flow resistance inside the gap during the final mold closure of the CRTM process.

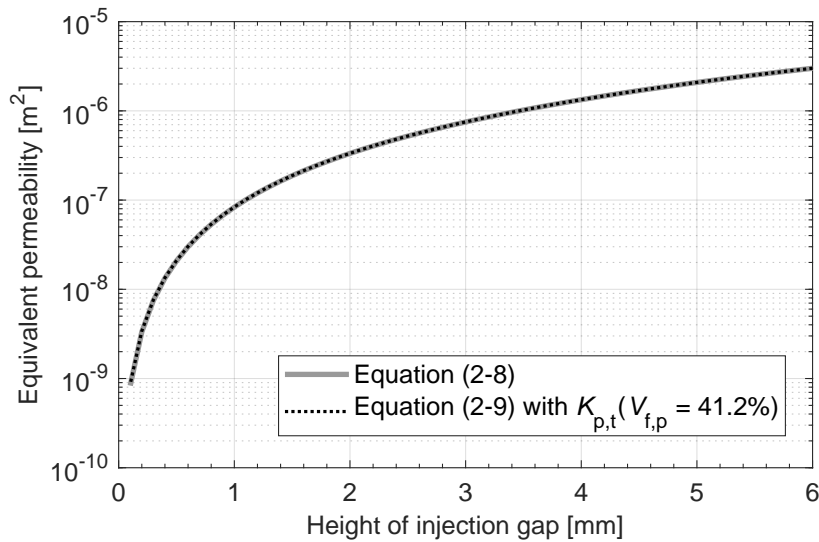


Fig. 2-10 Progressions of equivalent permeability over injection gap height calculated by equation (2-8) and (2-9) – equation (2-9) calculated with $K_{p,t}(V_{f,p} = 41.2\%) = 1.91 \cdot 10^{-12} \text{ m}^2$ and $\alpha = 1$.

While Equation (2-9) has been used only in a few studies [90, 108], most researchers [19, 36, 92–95, 109–115] apply Equation (2-8) to simulate an injection gap during LCM processing. Baskaran et al. [115] has used Equation (2-8) to simulate the filling of injection gaps of three different CRTM setups in PAM-RTM. Only the injection phase at a static mold position was investigated by Baskaran et al. neglecting the compression phase of the CRTM process. The flow front progression inside

⁸ At an unloaded state, the activated preform is characterized by a fiber volume fraction of 41.2%.

the injection gap and the preform penetration on the lower side at the end of the injection phase are compared between simulations and experiments. A good correlation was found. [115]

A CRTM injection gap is generally characterized by large in-plane dimensions, spreading over the complete preform surface. Therefore, the assumptions of flow between two parallel plates apply to both in-plane directions, and Equations (2-8) as well as (2-9) can be applied to calculate the equivalent permeability in x and y -direction of the injection gap. No statement about the out-of-plane equivalent permeability of the injection gap is found in literature.

Equivalent Permeability Formulas to Model Edge Race-Tracking

Equations (2-10) to (2-14) are used in literature to simulate the edge race-tracking effect during LCM processing. These equations are based on a flow through a rectangular duct or channel of height H and width W , as schematically illustrated in Table 2-2. While Equations (2-10) to (2-13) assume a channel at which all four sides are impermeable, Equation (2-14) considers potential lateral penetration from the channel into the preform by the boundary condition of one permeable channel wall.

$$K_{\text{ch,eq;x}} = \frac{H \cdot W}{8 \cdot \pi} \quad (2-10)$$

$$\begin{aligned} K_{\text{ch,eq;x}} &= \frac{H^2}{96} \left[1 - \frac{192 \cdot H}{\pi^5 \cdot W} \cdot \tanh\left(\frac{\pi \cdot W}{2 \cdot H}\right) \right] & \text{if } W \leq H \\ K_{\text{ch,eq;x}} &= \frac{W^2}{96} \left[1 - \frac{192 \cdot W}{\pi^5 \cdot H} \cdot \tanh\left(\frac{\pi \cdot H}{2 \cdot W}\right) \right] & \text{if } W > H \end{aligned} \quad (2-11)$$

$$K_{\text{ch,eq;x}} = \frac{H^2}{12} \left[1 - \frac{192 \cdot H}{\pi^5 \cdot W} \sum_{n=1,3,5,\dots}^{\infty} \frac{\tanh\left(\frac{n \cdot \pi \cdot W}{2 \cdot H}\right)}{n^5} \right] \quad (2-12)$$

$$\begin{aligned} K_{\text{ch,eq;x}} &= \frac{1}{HW} \sum_{n=1,3,5,\dots}^{\infty} \frac{8}{n \cdot \pi \cdot \beta_n^3} [W + \\ &\frac{(\cosh(\beta_n \cdot W) - 1)^2 - \sinh^2(\beta_n \cdot W)}{\beta_n \cdot \sinh^2(\beta_n \cdot W)}] \quad \text{with } \beta_n = \frac{n \cdot \pi}{H} \end{aligned} \quad (2-13)$$

$$K_{\text{ch,eq;x}} = \frac{1}{HW} \sum_{n=1,3,5,\dots}^{\infty} \frac{8}{n \cdot \pi \cdot \beta_n^3} \left[W - \frac{\sinh(\beta_n \cdot W)}{\beta_n} - \frac{1 - K_{\text{p,i}} \cdot \beta_n^2 - \frac{\sqrt{K_{\text{p,i}}}}{\alpha} \cdot \beta_n \cdot \sinh(\beta_n \cdot W) - \cosh(\beta_n \cdot W)}{\sinh(\beta_n \cdot W) + \frac{\sqrt{K_{\text{p,i}}}}{\alpha} \cdot \beta_n \cdot \cosh(\beta_n \cdot W)} \cdot \frac{\cosh(\beta_n \cdot W) - 1}{\beta_n} \right]; \text{ with } \alpha = \sqrt{\frac{\eta_{\text{eff}}}{\eta}}; \beta_n = \frac{n \cdot \pi}{H} \quad (2-14)$$

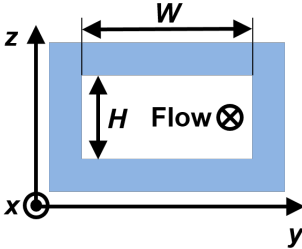
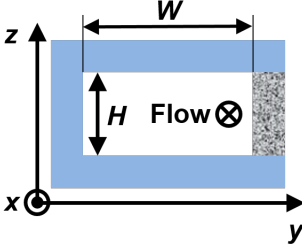
Hammami et al. [109] derived Equation (2-10) by assuming a flow through a cylinder and correlated it to a rectangular channel of identical cross section. Young and Lai [89] as well as Yang et al. [116] used Equation (2-11) to calculate the equivalent permeability of an edge race-tracking channel by neglecting slip boundary conditions of a fully developed flow through a rectangular duct and correlated it with Darcy's law. Likewise, Bickerton and Advani⁹ [20] as well as Advani and Sozer [14] assumed a fully developed, steady-state flow along a rectangular duct to derive Equation (2-12) but based it on different flow rate formula as used for Equation (2-11). Ni et al. [105] present Equation (2-13) to calculate the equivalent permeability of a rectangular duct of impermeable walls without further explanation on its exact derivation. In the same paper, Ni et al. [105] derived Equation (2-14) based on a Poiseuille flow through a rectangular duct with the boundary condition of one permeable wall and correlated the Poiseuille flow to Darcy's law.

Figures 2-11 and 2-12 present curves of equivalent permeabilities based on Equations (2-10) to (2-14) for a channel height between 0.1 mm to 6.0 mm. While the calculations for Figure 2-11 were based on a channel width of 2 mm, the curves presented in Figure 2-12 correspond to a width of 4 mm, which are the two channel widths investigated in this work. The curves calculated with Equation (2-14) consider preform permeability values characteristic for preforms used in this work (see Appendix A.1.2).

In the CRTM process the preform undergoes a compression and therefore changes its permeability. Two curves are presented in each figure to consider the effect of changed preform permeability on the equivalent permeability, calculated with Equation (2-14). On the upper limit, the uncompressed preform at a fiber volume fraction ($V_{\text{f,p}}$) of 41.2% is characterized by an in-plane preform permeability of $K_{\text{p,i}} = 2.72 \cdot 10^{-11} \text{ m}^2$. On the lower limit, the compressed preform at the final part thickness corresponding to a fiber volume fraction of 53.6% is characterized

⁹ Note that Bickerton and Advani [20] state π^2 while Advani and Sozer [14] use π^5 in Equation (2-12). Based on the latest issues of their original sources [117, 118] Equation (2-12) is printed and used in this work according to Advani and Sozer [14].

Tab. 2-2 Cross sections and assumptions of equations to calculate the equivalent permeability of an edge race-tracking channel. c.f. [100]

Channel cross section	Assumptions	Equations
	<ul style="list-style-type: none"> • Flow through a rectangular channel • Flow direction out-of-plane in x-direction • All walls impermeable 	<ul style="list-style-type: none"> • Equation (2-10) • Equation (2-11) • Equation (2-12) • Equation (2-13)
	<ul style="list-style-type: none"> • Flow through a rectangular channel • Flow direction out-of-plane in x-direction • One wall permeable • Other walls impermeable 	<ul style="list-style-type: none"> • Equation (2-14)

by $K_{p,i} = 5.79 \cdot 10^{-12} \text{ m}^2$. Additionally, α is set to unity at both calculations of Equation (2-14), according to literature [106–108].

Figures 2-11 and 2-12 show that the equivalent permeability of all equations increase with increased channel height, except for Equation (2-13) at a channel width of 2 mm if the channel height is larger than 4.7 mm. Comparing Figures 2-11 and 2-12 shows that for Equations (2-10) and (2-11) the equivalent permeabilities are larger for an increased channel width. Equations (2-12) and (2-14) are nearly identical up to 1 mm and Equation (2-13) up to 2 mm channel height, while beyond these heights a higher equivalent permeability is recorded at increased channel width.

Even though all Equations (2-10) to (2-14) calculate an equivalent permeability for an identical edge race-tracking channel, the spread of the curves in Figure 2-11 as well as in Figure 2-12 varies quite significantly from each other. Nevertheless, Equations (2-12) and (2-14) are observed to agree well with each other within the investigated widths and heights. Furthermore, no significant difference is identified between the upper and lower limit of the preform permeability used for Equation (2-14) over the investigated dimensions of an edge race-tracking channel.

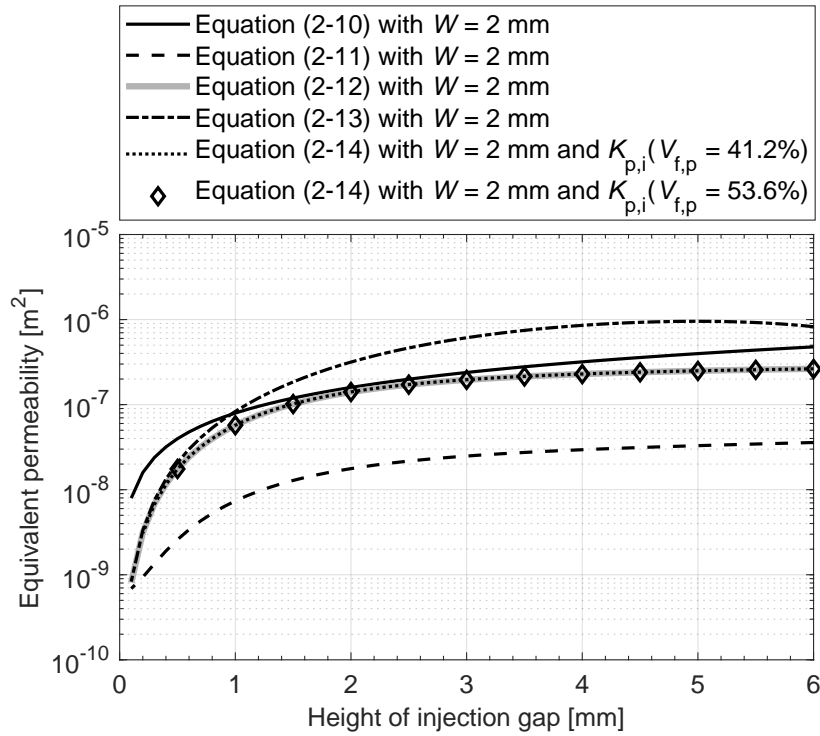


Fig. 2-11 Progressions of equivalent permeability for a channel width of $W = 2$ mm over gap height, calculated by Equations (2-10) to (2-14) – Equation (2-14) calculated with $\alpha = 1$ as well as once with $K_{p,i}(V_{f,p} = 41.2\%) = 2.72 \cdot 10^{-11} \text{ m}^2$ and once with $K_{p,i}(V_{f,p} = 53.6\%) = 5.79 \cdot 10^{-12} \text{ m}^2$.

In the following paragraphs, papers are reviewed which investigate the accuracy of the presented equivalent permeability equations by comparing experiments with numerical simulations. Hammami et al. [109] studied the edge race-tracking effect by the approach of Equation (2-10). The filling pattern of preforms of biaxial fabric with a fiber volume fraction of 37% were investigated in the presence of an edge race-tracking channel of 1 mm to 6 mm on one side along the preform length. The comparison of simulations and experiments shows that Equation (2-10) neglects a transverse flow from the channel into the preform. Therefore, Equation (2-10) is only valid for limited cases such as for scenarios of low transversal preform permeability or minimal flow front advancement in the race-tracking channel. [109]

Young and Lai [89] compared edge race-tracking simulations using Equation (2-11) with experiments. While the measured preform permeability is reported with a variance of 10%, the fitting of the simulations and experiments with channel width of 1 mm, 2 mm and 3 mm are within a variance of 30%. Similarly, Yang et al [116] reported “reasonable correspondence” between numerical simulation using Equation (2-11) and conducted experiments of the edge race-tracking effect.

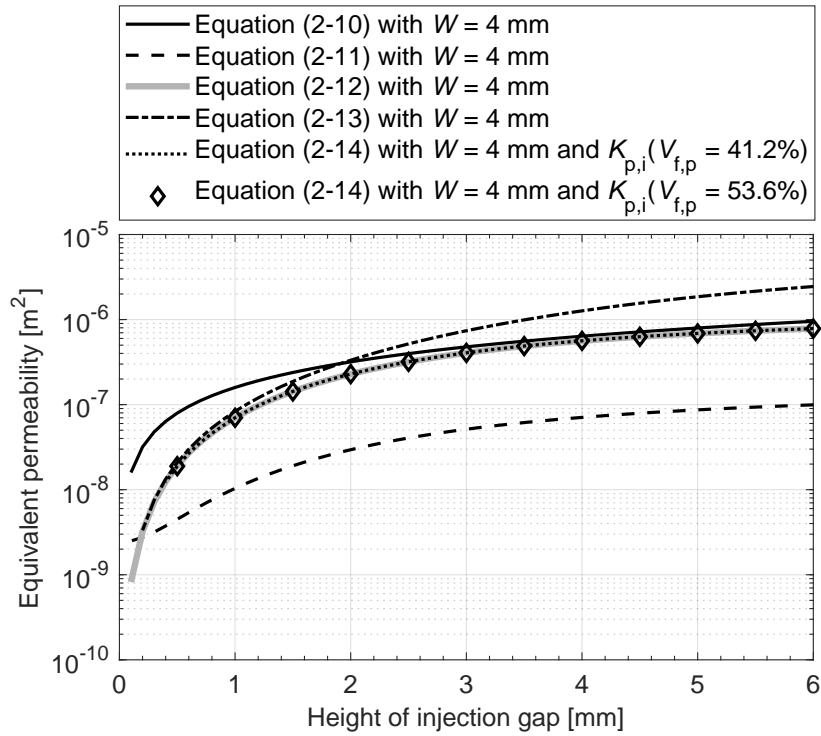


Fig. 2-12 Progressions of equivalent permeability for a channel width of $W = 4$ mm over injection gap height, calculated by Equations (2-10) to (2-14) – Equation (2-14) calculated with $\alpha = 1$ as well as once with $K_{p,i}(V_{f,p} = 41.2\%) = 2.72 \cdot 10^{-11} \text{ m}^2$ and once with $K_{p,i}(V_{f,p} = 53.6\%) = 5.79 \cdot 10^{-12} \text{ m}^2$.

Bickerton and Advani [20] used Equation (2-12) to simulate the edge race-tracking effect of channels between 0 to 8 mm and preforms of different fiber volume fractions permeabilities between 5.5% to 16.6%. No statement on the used transversal channel permeability is stated in the paper. The comparison between simulations and experiments shows good agreement. Martin et al. [21] simulated a CRTM process without injection gap in the presence of edge race-tracking which is modeled with Equation (2-12). Good agreement between simulation and experiments is reported. No comparison between simulation and experiments could be found for the approach of Equation (2-13).

Ni et al. [105] conducted experiments at which the preform was placed in the center of the preform neighbored by edge race-tracking channels of 6.35 mm and 19.05 mm on each longitudinal side. The channels are modeled by using Equation (2-14) in the numerical simulations and correlated with the flow front progression of the experiments.

While Equations (2-10) to (2-14) are all derived to model the flow in an edge race-tracking channel in longitudinal direction, no statement is found in literature about which equation has been used to model the transversal (in-plane) and out-

of-plane component of an edge race-tracking channel. However, investigations on the influence of the transversal (in-plane) equivalent permeability are found in literature. Yang et al. [116] report that a stronger flow from the edge race-tracking channel into the preform occurs for increased transversal equivalent permeability of the channel without stating the used values for transversal (in-plane) equivalent permeability. Sheard et al. [119] used an iterative approach between simulation and experiments to match their flow front progressions and to determine an optimal equivalent permeability of the channel. Experiments with different channel widths and preform fiber volume fractions are well matched with simulations at which the longitudinal and transversal component of the equivalent permeability of the channel are equated ($K_{ch,eq;x} = K_{ch,eq;y}$). [119]

2.2.4 Numerical Simulation of Compression Resin Transfer Molding (CRTM) in PAM-RTM of ESI Group

PAM-RTM is a commercially available software package to simulate LCM processes such as resin transfer molding (RTM), vacuum assisted resin transfer molding (VARTM), vacuum assisted resin infusion (VARI) and compression resin transfer molding (CRTM) [120, 121]. The software is characterized by an intuitive usage due to its graphical user interface [122] and distributed by ESI Group (Rungis, France). PAM-RTM is widely used for industrial [114, 120, 123] and research purposes [39, 113, 115, 122, 124].

The numerical method of control volume finite element method (CVFEM) is used in PAM-RTM to simulate the filling pattern of LCM processes, which is described in Chapter 2.2.1. A non-conforming finite element approach is used which are characterized by good numerical stability and potential for parallelization of computations [114, 125]. The flow pattern in PAM-RTM is modeled according to Darcy's law which is a widely used approach to simulate the macro-flow during the preform impregnation of LCM processes (see Chapter 2.2.2).

In the context of this work, the preform impregnation during CRTM process is studied in depth. As described in Chapter 2.1.1, the flow pattern inside the mold during the CRTM is of complex nature as it is generally superimposed of an in-plane and out-of-plane flow at which the permeability of the preform is changed continuously throughout the process. [15]

Since 2010 a CRTM module has existed in PAM-RTM which is limited to 2D elements. Models of two-dimensional elements are not able to adequately simulate an out-of-plane flow which introduces uncertainties on how accurate the complex flow pattern of the CRTM process inside the preform and injection gap can be

modeled using this approach. Therefore, ESI further developed its CRTM module to be able to simulate the process via three-dimensional elements. First introduced in version 2018.0, the 3D CRTM module of PAM-RTM enables the modeling of a three-dimensional flow and an interaction of fluid pressure and preform compaction during the CRTM process. [114, 121, 126]

A CRTM process with injection gap between preform and upper tool is modeled in PAM-RTM in two stages. First, a defined amount of resin is injected. Second, after the injection gate is closed, the upper mold closes and initiates a further resin distribution and preform compaction. Two new features, the fluid-solid coupling and the inter-penetrating mesh, have been introduced at the 3D CRTM module to model the deformation of the preform and the flow inside the injection gap during tool closure. [114, 121, 126] Both features are explained in the following.

Fluid-Solid Coupled Solver

The fluid-solid mechanics coupling in PAM-RTM enables the modeling of the interaction between fluid flow and preform deformation during the CRTM process. During the injection and compression phase of the CRTM process, the fluid and/or the mold applies a pressure to the preform which results in a change of preform thickness. This change of preform thickness goes along with a changed preform permeability that, in turn, alters the continuous flow progression. These complex interactions are modeled in PAM-RTM by an iterative, quasi-static approach to couple the fluid and solid mechanics solver. [114, 121]

During one fluid-solid coupling iteration of the simulation, the fluid solver first calculates the pressure field of the fluid and the resulting flow front progression inside a fixed, quasi-static grid according to Darcy's law (see Chapter 2.2.2). Next, the calculated pressure field of the fluid is transferred to the solid solver, which computes the preform deformation based on Terzaghi's principle. [114, 121] By assuming a pure through-thickness preform deformation, the one-dimensional Terzaghi's principle can be stated as: [15, 127]

$$\sigma_{tot} = \sigma_p + p_f \quad (2-15)$$

Equation (2-15) correlates the total stress σ_{tot} applied across the thickness of the problem domain to the sum of the compression stress exhibited to the porous medium (i.e. preform) σ_p and the fluid pressure p_f inside the pores of the porous medium.

Finally, the calculated preform deformation is transferred from the solid solver back to the fluid solver. This enables an update of the preform's geometry and permeability as input for the next fluid-solid coupling iteration starting with further flow front progression. [114, 121]

Interpenetrating Mesh

During the compression phase of a CRTM process with injection gap, the upper mold closes and displaces the resin inside the injection gap until it has vanished. To simulate this process characteristic, a new functionality is introduced at the 3D CRTM module of PAM-RTM, the so-called inter-penetrating mesh technology. Two meshes are defined at the inter-penetrating mesh technology, one for the upper mold and one for the injection gap. The impermeable mold mesh can now be moved through the permeable mesh representing the injection gap and displace the fluid inside the injection gap. [114, 121]

Based on the position of the lower nodes of the mold mesh, the solver calculates which elements of the injection gap mesh are filled or not. Furthermore, the lowest position of the moving mold mesh defines the volume of remaining fluid inside the partially cut elements of the injection gap. [114, 121]

Certain assumptions are made at the 3D CRTM module of PAM-RTM which are explained and discussed in the following:

Only Darcy flow: All flow domains are modeled according to a flow through porous medium governed by Darcy's law. The approach of Darcy's law is true for the flow domain representing the fibrous structure of the preform. Other flow domains, such as edge race-tracking channels or an injection gap at CRTM, are non-porous media but are treated as virtual porous media in PAM-RTM according to the equivalent permeability approach, as described in Chapter 2.2.3. [114, 121, 128]

Constant equivalent permeability of injection gap: At the 3D CRTM module of PAM-RTM the equivalent permeability of the injection gap can only be assigned as a constant value and not as a function of gap height. Yet, according to the derived formulas of the equivalent permeability of the injection gap its values are dependent on the height of injection gap as seen in Figure 2-10. Therefore, a changing equivalent permeability during mold closure and gap vanishing cannot be accurately modeled in PAM-RTM and is commonly over-estimated during mold closure if the injection gap's permeability is defined by the height of the injection gap present at process start. [114, 121, 128]

Only out-of-plane preform deformation: According to ESI's CRTM modeling guidelines [128] all nodes of the preform have to be restrained in their in-plane movement, so that the preform is only free to deform in through-thickness direction. Therefore, the shear behavior of the preform is neglected in the 3D CRTM module of PAM-RTM. Especially, preforms of complex three-dimensional shape are exposed to normal as well as to shear stress during their deformation [129]. Additionally, calculated tool forces in the CRTM process are changed if only preform normal stresses are considered and shear stresses are neglected [129].

In [130] the first version of the 3D CRTM module of PAM-RTM version 2018.0 is studied towards its capabilities and limitations for process optimization. While simulations in PAM-RTM are reported to model the principle preform impregnation mechanisms during CRTM, a lack of adjustable process variables is noted at the initial version of 2018.0 which has partially been improved in subsequent releases. [130] Generally, CRTM simulations are possible in PAM-RTM with injection gap and since version 2020.0 also without injection gap [130, 131]. Resin injection at defined flow rate or pressure can be modeled while the exact resin volume has to be regulated by defining the maximum injection time (end of injection) [128]. The tool closing can be initiated velocity-controlled at a constant or, since version 2018.5, variable tool closing speed [132]. A force-controlled tool closure cannot be modeled [130]. While the resin curing stage of the process could not be modeled at the first release of the 3D CRTM module in version 2018.0, heat transfer between tool and resin is implemented in version 2019.5 and a variable viscosity curve can be defined since 2020.0 [130, 131, 133]. Post-processing of the CRTM simulation has been improved in PAM-RTM by providing the tool force history since version 2020.0 and filling factor history as well as history of contained resin volume for each modeled flow domain (e.g. injection gap or preform) since version 2020.5 [131, 134].

Numerical simulation software, such as the 3D CRTM module of PAM-RTM, are an efficient tool to virtually investigate preform filling patterns during LCM manufacturing processes. The accuracy of such tools must always be validated by comparing the outcome of simulations with real manufacturing trials or flow experiments. Dereims et al. [114] initiated a first validation of the 3D CRTM module of PAM-RTM by comparing simulations with flow experiments in a truncated pyramid tool. The presented results show quantitative and qualitative compliance between simulations and experiments during the injection phase and correlate quantitatively during the compression phase. The authors conclude that the flow front progression simulations correspond well with the performed experiments. [114] Furthermore, Vita et al. [124] compared numerical CRTM simulations in PAM-RTM with ex-

periments of a planar part geometry and reports good correspondence based on a deviation of less than 5% [124].

3 Research Design

As presented in Chapter 1, the overall research objective of this work is defined as:

Increasing process robustness towards edge race-tracking during CRTM preform impregnation by investigating, enabling and validating a passive flow control strategy via the use of film-sealing and slider tooling.

Based on this general objective, four research sub-objectives are formulated in the following to structure the research presented in this work and to fulfill the overall research objective. In Section 3.1, a set of research questions are presented in accordance with the four research sub-objectives. Furthermore, the research approach and outline of this work is presented in Section 3.2.

3.1 Research Questions

The first research sub-objective is to investigate the effect which race-tracking between preform edge and mold cavity wall has on the preform impregnation during the compression resin transfer molding (CRTM) process and how to diminish the edge race-tracking effect by conducting numerical simulation studies on the CRTM process.

As the literature review in Chapter 2.1.2 shows, edge race-tracking is a widely studied effect in the context of resin transfer molding (RTM) processing but has not yet been investigated for CRTM. Therefore, the hypothesis is drawn that if race-tracking is a known issue for RTM, it also impacts the preform impregnation during its process variant CRTM. In the presence of edge race-tracking, the complex character of the CRTM flow pattern is expected to change differently for different geometrical preform or design parameters.

Furthermore, Chapter 2.1.2 presents that lowering the permeability at the preform edge via its over-compacting (pinching-off), is a common strategy to diminish edge race-tracking during RTM. However, due to the fact that no studies exist on edge race-tracking during CRTM, also no such strategy has yet been studied for this process. In this context a second hypothesis regarding the first sub-objective is drawn that if the upper mold could be partitioned during CRTM processing, a passive flow control strategy could be put into effect, pre-compacting the preform edge and enabling a localized, central injection gap which is separated from the edge race-tracking channels.

Both hypotheses regarding the first research sub-objective shall be validated by answering the following two main research questions (RQ) in which the first research question is broken down in two more-specific research sub-questions:

RQ 1: How does edge race-tracking impact the CRTM process?

RQ 1.1: How does edge race-tracking impact the flow pattern at different CRTM process configurations?

RQ 1.2: How does the severity of edge race-tracking affect CRTM process responses?

RQ 2: How does the passive flow control strategy impact the flow pattern during CRTM preform impregnation in the absence and presence of edge race-tracking?

For industrial applications, the suggested passive flow control strategy can be enabled via the use of the slider tooling technology. As discussed in Chapter 2.1.4, a known drawback of this technology is the increased wear of conventional sealing concepts placed between the sliding mold components. Therefore, a seal-free tool design is sought in this work by using film material to spatially separate preform impregnation and mold components. In this context, the second research sub-objective is to specify a process concept of an enhanced CRTM process, called film-sealed compression resin transfer molding (FS-CRTM), which integrates films to seal the preform impregnation space inside the mold.

A literature study in Chapter 2.1.3 revealed that films have been used in liquid composite molding (LCM) processes such as resin infusion, i.e. vacuum assisted resin transfer molding (VARTM), for decades. Recently, films have been also introduced into matched mold LCM processes such as wet compression molding (WCM) and resin transfer molding (RTM). A process fusion between VARTM and CRTM has been investigated, but the integration of films into the matched mold CRTM process has not yet been studied. Therefore, the third research question is stated as follows:

RQ 3: How can film material be functionally integrated in the matched mold CRTM process to seal the preform impregnation space?

The third research sub-objective is to make a recommendation of films that can be integrated in the CRTM process and help to understand the characteristics of FS-CRTM preform impregnation by investigating its individual process phases.

Chapter 2.1.3 showed that a wide range of film materials are used for manufacturing fiber-reinforced plastic (FRP) parts, which are chosen based on requirements defined by the specific manufacturing process. In literature, no film has yet been integrated into the matched mold CRTM process. A film to be integrated into the

CRTM process has to meet specific requirements derived from industrial CRTM processing conditions.

In the context of this work, the novel FS-CRTM process shall be investigated via flow visualization experiments on a laboratory scale at room temperature. Thus, a second film, used during FS-CRTM flow visualization experiments, has to feature comparable mechanical properties at room temperature, as the identified process film features during industrial FS-CRTM manufacturing at elevated temperature.

Different experimental and simulative studies have been reported in literature which investigate the conventional CRTM process and its key process factors [15, 110, 112, 115, 135–139]. The FS-CRTM is a novel LCM manufacturing technique which has not been studied in literature. The film-sealing layer during FS-CRTM processing introduces a pressure gradient acting across the flexible film which is not present during conventional CRTM processing. This pressure gradient is expected to influence the overall FS-CRTM preform impregnation and could be used as an additional control factor compared to conventional CRTM.

To answer the third research sub-objective, the following two research questions are formulated:

RQ 4: Which film material is suitable to be used in FS-CRTM manufacturing and with which second film material can it be substituted in FS-CRTM flow visualization experiments?

RQ 5: How does the preform impregnation during FS-CRTM take place and which are dominant process factors to control the preform impregnation?

The fourth research sub-objective is to investigate means for diminishing the edge race-tracking effect during FS-CRTM preform impregnation by experimentally studying the effect of edge race-tracking and by investigating the effectiveness of slider tooling technology to locally pre-compact the preform edge as well as to isolate the injection gap from the edge race-tracking channel during preform impregnation.

A numerical simulation study conducted in the context of this work showed that edge race-tracking affects the preform impregnation pattern during conventional CRTM. However, no experimental investigation of the edge race-tracking effect during either conventional CRTM nor FS-CRTM exists. Furthermore, the numerical simulation study showed that a passive flow control strategy helps to diminish the edge race-tracking effect during conventional CRTM processing. The passive flow control strategy intends to pre-compact the preform edge and isolate a central injection gap from the edge race-tracking channel. Due to the fact that neither the FS-CRTM process nor the edge race-tracking effect during FS-CRTM has been

studied in literature, also no strategy for diminishing the edge race-tracking effect is known for FS-CRTM processing. Therefore, the final two research questions shall be answered to achieve the fourth research sub-objective:

RQ 6: How does edge race-tracking affect the preform impregnation during FS-CRTM processing?

RQ 7: How effective is the attempt to diminish the edge race-tracking effect during FS-CRTM processing by applying the passive flow control strategy?

3.2 Research Approach and Thesis Outline

The present work is structured as depicted in Figure 3-1. The motivation and objective of this work is derived in Chapter 1 based on recent developments in the manufacturing of fiber-reinforced plastic (FRP) parts for automotive applications. A literature study is presented in Chapter 2 which examines the state of the art of FRP manufacturing techniques used in the automotive industry. Furthermore, a numerical method to simulate the preform impregnation by such manufacturing techniques is explained and discussed. Based on Chapter 1 and 2, the research design of this work is presented in Chapter 3. The research design specifies the overall research objective into four sub-objectives. Identified research gaps are presented which are aimed to be closed by answering seven main research questions in the context of this work.

Chapter 4 presents a numerical simulation study on the CRTM process which investigates the edge race-tracking effect during CRTM processing and, thus, aims to answer research question 1 and 2. Via numerical filling simulations in the CRTM module of the commercial software PAM-RTM (ESI Group, Rungis, France), the preform impregnation at different process configurations was studied on an ideal case (no edge race-tracking) and compared to simulations considering edge race-tracking. In case a negative effect of edge race-tracking during CRTM was identified, a potential flow control strategy to diminish race-tracking via local pre-compaction of the preform edge and injecting the resin into a localized, central injection gap, was simulatively evaluated.

To industrially implement the identified passive flow control strategy from Chapter 4, Chapter 5 evaluates the integration of a film material into the CRTM process to seal the preform injection space inside the mold. In Chapter 5, the research question 3 is answered via an abstract evaluation of the CRTM process showing the effect a film integration has on the individual components of the process. The abstract

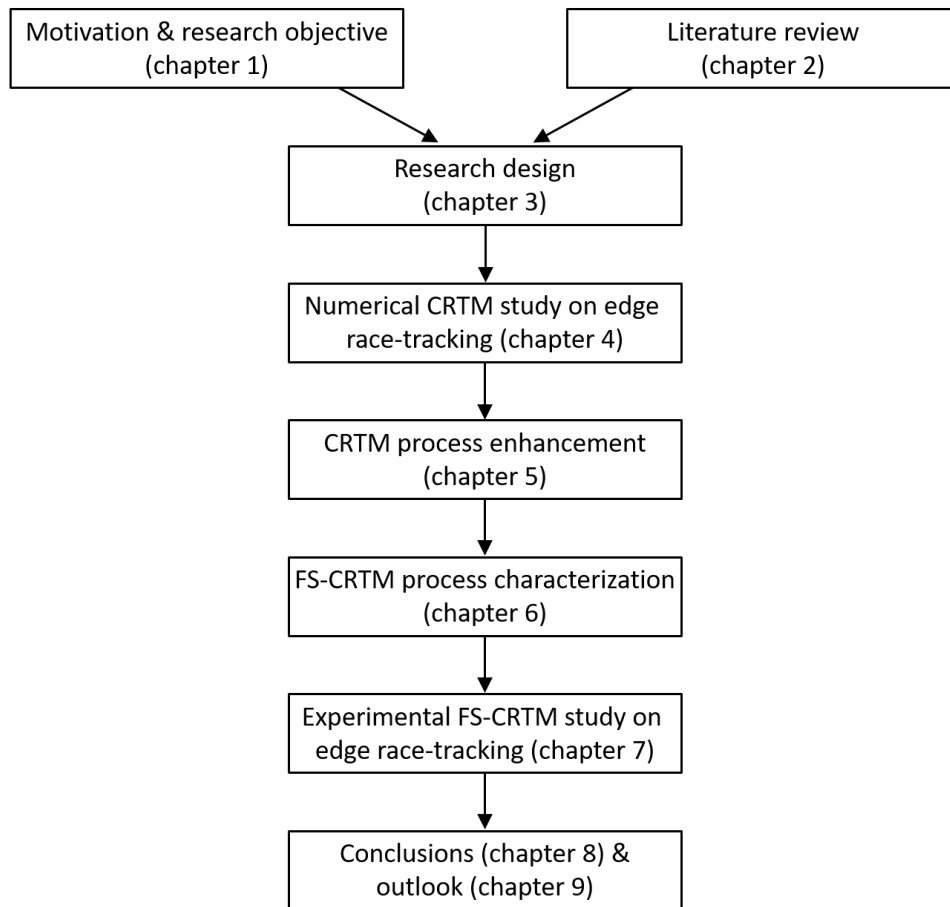


Fig. 3-1 Outline of the present work.

solution of the enhanced CRTM process is then transferred into a concrete process concept of the film-sealed compression resin transfer molding (FS-CRTM) process. The novel FS-CRTM process is characterized in Chapter 6, by answering research question 4 and 5. Suitable films are identified via a literature study and further selected via laboratory tests. Eventually, two films are identified, one for industrial FS-CRTM manufacturing and one which substitutes this film in flow visualization experiments at laboratory conditions. Using this substitution film, flow visualization experiments were performed in the context of this work to study the FS-CRTM process. The FS-CRTM process characterization of Chapter 6 is finalized by performing a full-factorial experimental plan on each of the two phases of the FS-CRTM process, the (i) injection and (ii) compression phase, to identify dominant process control factors.

After the FS-CRTM process has been characterized in Chapter 6, the edge race-tracking effect during FS-CRTM processing is studied in Chapter 7. Flow visualization experiments were performed to answer research question 6 and 7. The effects

of edge race-tracking were studied by comparing the preform impregnation during FS-CRTM at ideal conditions (no edge race-tracking) with the preform impregnation of experiments in which edge race-tracking occurs. Furthermore, the passive flow control strategy from Chapter 4 was applied in FS-CRTM flow experiments to verify its effectiveness to diminish edge race-tracking and answer the overall research objective of this work.

Finally, the work is concluded by summarizing the answers to all seven research questions in Chapter 8 and giving a guideline for future research on edge race-tracking during the (film-sealed) compression resin transfer molding process in Chapter 9.

4 Numerical Study on Edge Race-Tracking during CRTM¹

Edge race-tracking is a widely studied effect in the context of the resin transfer molding (RTM) process. It is caused by high permeable areas between the preform edge and the mold cavity wall resulting in inhomogeneous flow front velocities during cavity filling. Edge race-tracking has been shown to drastically change the filling pattern of the preform during RTM and to increase the risk of an incomplete preform impregnation due to macro void formation. [14, 18–20] To date, there is no literature available that investigates the edge race-tracking effect during the compression resin transfer molding (CRTM) process, even though this process has been widely used in the industry over the last decade [10, 17, 141] and edge race-tracking has been reported to cause unsuccessful part manufacturing during CRTM processing [21, 22]. To start closing this gap, a numerical simulation study is presented in this chapter, termed “numerical race-tracking” study, investigating the effect of edge race-tracking during CRTM processing.

Different passive [34, 40, 41, 43–47, 49–52] and active [53–59] control strategies are reported in literature to diminish the edge race-tracking effect during RTM and to increase its process robustness. A well proven and often applied passive strategy in the industry is by over-compacting or pinching-off the preform edge in order to lower its permeability [34, 40–44]. Because research on edge race-tracking during CRTM is limited, no such strategy has yet been reported in the technical literature. Therefore, a second numerical study, termed “numerical flow control study”, investigates the following hypothesis. Edge race-tracking effects can be reduced during CRTM by pre-compacting the preform edge and thus separating the central injection gap from edge race-tracking channels, which can be achieved by implementing a partitioned upper mold.

The present chapter is split in five subsections. The first Subsection 4.1 presents the modeling approach and evaluation methods of the two numerical simulation studies. Further, the results of the numerical race-tracking study are presented and discussed in Subsection 4.2 followed by its conclusion in Subsection 4.3. The results of the numerical flow control study are discussed in Subsection 4.4 and the drawn conclusions are given in Subsection 4.5.

¹ Parts of the introduction have been previously published in [140].

4.1 Modeling Approach and Evaluation Method²

Two numerical CRTM process simulation studies are presented in this chapter using the commercial software package PAM-RTM (version 2019.0, 2019.5 and 2020.5; ESI Group, Rungis, France). PAM-RTM computes the fluid flow during CRTM simulations based on Darcy's law (Equation 2-1). To be able to correlate the flow front progression with the acting pressure, the materials used during the manufacturing process need to be carefully characterized with the goal of providing input data for the simulation, i.e. the preform permeability \mathbf{K} and the resin viscosity η . Importantly, the preform permeability needs to be characterized for different fiber volume fractions since the preform undergoes a compaction during its impregnation in the CRTM process.

The software versions 2019.0 and 2019.5, used for the majority of the presented flow simulations, only permit entering a constant viscosity value. The snap-cure resin system used for all numerical flow simulations [142] was found to have an approximate constant viscosity of 0.01 Pas during the simulated CRTM process times, as presented in Appendix A.1.1. The reinforcement structure [143] was characterized as explained in Appendix A.1.2. The identified permeabilities in the material's principle directions for relevant fiber volume fractions are presented in Figure A-4. The angle between the principle in-plane permeabilities K_{11} and the coordinate system of the reinforcement was measured as presented in Figure A-5 and is approximated to be constant at 0° over relevant fiber volume fractions, as discussed in Appendix A.1.2. Besides permeability, the compaction behavior of the fabric needs to be provided to the software to enable the simulation of the preform deformation during the CRTM process. The compaction stress at a constant mold closing velocity of $\dot{h}_c = 1$ mm/s was characterized as discussed in Appendix A.1.2 and is illustrated in Figure A-6.

The software tool models the fluid flow of all three flow domains, i.e. preform, injection gap and race-tracking channel, using Darcy's law. In the conducted numerical studies, the equivalent permeabilities in all three dimensions of the injection gap was calculated using equation (2-8) based on the constant gap height value during the injection phase, as presented in Figure A-11 in Appendix A.2.1. As discussed and verified in Appendix A.1.2, the equivalent permeabilities in all three dimensions of the edge race-tracking channel was calculated in the two numerical studies according to Equation (2-12). While the width of the race-tracking channel is constant during a CRTM simulation, the channel height changes in accordance to the preform height. As discussed in Chapter 2.2.4, the software only permits entering a permeability curve dependent on fiber volume fraction (FVF) and not directly

² Parts of this subsection have been previously published in [140].

by height. Therefore, a fictive FVF had to be assigned to the channel. Preliminary tests showed numerical issues at low fictive FVF of the channel and identified an appropriate level for stable simulations at 4% at an uncompressed height of 2.6 mm which enabled the correlation of equivalent permeabilities to the deformed state of the channel according to Equation (2-12). To ensure an equal deformation of the two neighboring flow domains, preform and channel, the compaction stress curve of the preform was also assigned to the flow domain of the race-tracking channel.

The pressure inside the three flow domains, i.e. preform, injection gap and, edge race-tracking channel, prior to injection was set to 20 kPa by defining this pressure level to the outlet and closing the outlet after an insignificant resin amount of 10^{-10} m³ has exited. The resin was injected into the injection gap at a predefined constant flow rate over a time of 1.5 s for all simulations of small and of 4.5 s for the simulations of large geometrical aspect ratio. To ensure a comparable preform impregnation in regard to the injected resin volume, the flow rate had to be adapted for each simulation model by (i) the resin volume exiting at the outlet and (ii) the channel's fictive fiber volume fraction for simulations with an edge race-tracking channel. For the latter correction of the flow rate, a complete channel filling was assumed at final channel height of 2 mm correlating to a fictive FVF of the channel of 5.2%. The flow rates of all simulations are presented in Table A-2 in Appendix A.2.1.

After the injection, the mold-closure is initiated by a constant closing velocity of 1 mm/s until one of the software's abort criteria is fulfilled: (i) complete impregnation of all defined flow domains (except injection gap) or (ii) reaching of predefined maximum process time. A final FVF of the preform of 53.6% at a height of 2 mm was sought by the predefined theoretically injected resin volume. While the reference simulation of each process configuration was simulated until complete preform impregnation, the comparing simulation with an edge race-tracking channel was simulated until process end time (maximum process time) of the corresponding reference simulation of identical process configuration.

The geometrical dimensions of the models for both studies are presented in Figure A-11 in Appendix A.2.1. The lay-up of the preform was modeled as (0₃/90₃). The lateral as well as the central inlet were defined to be of identical area (37 mm²) while the central inlet was modeled of round, and the lateral of squared shape. The latter spanned over the complete thickness of the injection gap and was located at the center of one gap side. All domains were meshed with three-dimensional (tetrahedral) elements. Preliminary tests were performed to identify a mesh size which enables to adequately model the three-dimensional flow during the CRTM process. Hence, the flow domains were in-plane meshed by triangles and a mesh size of 2 mm refined at the central inlet. Further, the tetrahedral elements were defined

by an out-of-plane mesh size of 0.14 mm for the preform and edge race-tracking channel as well as 0.06 mm for the injection gap.

All presented results of the numerical race-tracking study were calculated via the PAM-RTM version 2019.5 except for the “force on tool” results which cannot be evaluated in this version which is why a selection of simulations was recalculated with version 2020.5 to obtain these specific results. The software versions 2019.5 and 2020.5 were shown to result in numerical instabilities during simulations for the numerical flow control study, therefore version 2019.0 was used instead. To verify comparability, a model of the numerical race-tracking study was simulated with all three used software versions showing identical results as illustrated in Figure A-10 in Appendix A.2.1. All simulations, regardless of the used software version, were calculated on four processors (CPUs).

The coupling frequency between the fluid and solid mechanics solver of all simulations was targeted at 0.05 s. A low value of the coupling frequency was defined to ensure the best as possible modeling of the preform compaction and its effect on the resin flow during the CRTM process. Numerical issues at the targeted coupling frequency forced the software to abort three simulations of the presented numerical studies before the process had been finished, which is why these simulations had to be recalculated at a coupling frequency as close as possible to their comparing simulation. The coupling frequency of all presented simulations are listed in Table A-3 in Appendix A.2.1. To investigate the effect of the coupling frequency on the modeled CRTM process, a sensitivity study was performed simulating one model without race-tracking at different coupling frequencies over the complete applied range of the numerical studies. Figure A-12 shows the results of the largest frequency discrepancy between two comparing simulations. The general curve progressions is shown to be nearly identical, only locally deviating during phases of strong preform compaction recorded by a maximum deviation of 2% in volume filling ratio (VFR) of the preform. Hence, the sensitivity study showed that the coupling frequency effects the results of CRTM flow simulations. However, the discrepancy in the two comparing simulations is shown to be on a moderate scale which is not considered to significantly impact potential flow pattern changes due to edge race-tracking.

The investigated CRTM flow control strategy intends to pre-compact the preform edge to the final part thickness prior to process start and to inject the resin into a localized, central injection gap. An edge pre-compaction of 10 mm width was defined for the numerical flow control study presented in this chapter. Accordingly, the dimensions of the injection gap were adapted as presented in Figure A-11(b) in Appendix A.2.1. The pre-compaction of the preform edge section cannot be realized via any standard function of the employed simulation software. A workaround

was identified by manually manipulating the input files of the mechanical solver. A constant out-of-plane deformation velocity was assigned to all nodes on the preform top side inside the pre-compaction zone. These nodes are deformed to the final preform thickness during the first three coupling steps between fluid and solid solver and held at this position for the rest of the process time. It was ensured that the resin does not flow in the edge pre-compaction region during the first three coupling steps. This approach enabled a realistic preform deformation after 0.15 s with a reduced preform height at the preform edge to the final thickness, a transition of a gradually compacted preform at the edge of the injection gap, and a fully un-compacted preform at the central section. Correspondingly, permeability values were assigned to all elements according to their compaction state.

All simulations of the two numerical studies were calculated without gravitation due to observed numerical instabilities at specific model configurations. To validate this assumption one exemplary CRTM simulation of the numerical race-tracking study without race-tracking and one with a 2 mm wide race-tracking channel was calculated with and without gravitation. As shown in Figure A-13 in Appendix A.2.1, the effect of gravity shows no significant effect on the presented process parameters of a CRTM simulation in absence of edge race-tracking. Figure A-14 shows that the progression of the VFR curve of the channel and of the injection gap at a CRTM simulation with edge race-tracking are marginally changed while the VFR curve of the preform is unchanged. These results show that gravitation can be neglected for the intended investigations of the CRTM preform impregnation in the presence of edge race-tracking.

Due to limited post-processing options of the CRTM simulations in the simulation software of version 2019.0 and 2019.5, a script was developed in the context of this work to evaluate all relevant data from the obtained simulation outputs [144]. The script was programmed using Python (Python Software Foundation, Wilmington, DE, USA) to calculate the history of the VFR of each flow domain, i.e. preform, injection gap and race-tracking channel, which enables evaluating the resin flow from one flow domain into the other throughout the CRTM process. At each time step, the script sums up the filling factor of each node of a flow domain and divides it by the number of all these nodes, which reveals the main limitation of this method, assuming a regular grid. Besides the VFR history, the script also calculates the cavity height and preform thickness history as mean and standard deviation of all nodes at the lowest layer of the upper mold and at the upper layer of the preform domain. The script was presented at the ESI Forum in 2019 [144]. Since version 2020.5 of PAM-RTM, the filling factor history of all flow domains can be evaluated in the post-processing environment of PAM-RTM. Figure A-15 and Figure A-16 in Appendix A.2.1 compares the results of the VFR of all flow domains of simulations

with lateral and central inlet, respectively. The results show that at both scenarios the edge race-tracking channel, which consists of a homogeneous grid, is equally evaluated by the post-processing tool used in this work and the one of PAM-RTM. The curve progression of the injection gap and preform is observed to deviate between the two evaluation methods, which is traced back to the refined grid size at the zone of the central inlet. Nevertheless, the effect of edge race-tracking is evaluated in the two numerical studies by comparing two models only differing by absence or presence of edge race-tracking, resulting in identical VFR deviations due to grid size inhomogeneity at both comparing simulations. Therefore, the developed post-processing script [144] is concluded to be applicable for the numerical race-tracking and the numerical flow control study – always considering the script’s specific limitations.

4.2 Results and Discussion of the Numerical Race-Tracking Study

The numerical race-tracking study (NRT study) presented in this section investigates the effect of edge race-tracking during CRTM processing via numerical flow simulations. The CRTM impregnation pattern can change significantly by different configurations of process parameters. Therefore, the effect of race-tracking is investigated at different process configuration settings in the first Subsection 4.2.1. Furthermore, the effect of increased race-tracking severity, due to an increased race-tracking channel width, is studied in the second Subsection 4.2.2.

4.2.1 Edge Race-Tracking during Different CRTM Process Configurations

The CRTM process with injection gap is defined by a large number of process variables of which some are reported to drastically change the preform impregnation pattern. Edge race-tracking is expected to affect the preform impregnation differently at different settings of these CRTM process parameters. Hence, numerical simulations are presented in these subsections at which three process parameters are separately changed on two levels resulting in four investigated process configurations as listed in Table 4-1. The changed process parameters and why they are chosen to be investigated are explained in the following.

Geometrical aspect ratio (preform length l_p versus final preform height $h_{p,f}$)
Literature studies [36–38] have shown that the preform impregnation pattern dur-

Tab. 4-1 CRTM process configurations investigated in the numerical race-tracking study.

CRTM process configuration	Geometrical aspect ratio	Injection gap height (h_{ig})	Inlet position
1	small (105)	high ($h_{ig} = 0.928$ mm)	lateral
2	large (315)	high ($h_{ig} = 0.928$ mm)	lateral
3	small (105)	low ($h_{ig} = 0.309$ mm)	lateral
4	small (105)	high ($h_{ig} = 0.928$ mm)	central

ing the CRTM process with injection gap, change depending on the geometrical aspect ratio of the preform. For small geometrical aspect ratio, the resin is reported to be first distributed inside the injection gap in in-plane direction until it is completely filled, and subsequently impregnates the preform predominantly in out-of-plane direction during mold-closure [37, 38]. For structures of large geometrical aspect ratio, the permeability of the injection gap is reported to be not low enough to distribute the resin completely above the preform before the upper mold is in contact with the preform, resulting in a superimposed preform impregnation with out-of-plane and in-plane flow components [36, 37]. While the final preform height of the presented numerical simulations is set to $h_{p,f} = 2$ mm for all simulations, the preform length is changed from $l_p = 210$ mm at small setting to $l_p = 630$ mm at large setting corresponding in a geometrical aspect ratio of 105 and 315, respectively.

Injection gap height

The objective of the injection gap is to distribute the resin over the largest possible area above the preform to ease the adjacent preform impregnation via a short out-of-plane flow distance in the overflow area. In theory, the upper limit of an injection gap that is completely filled by the injected resin, is defined by the volume of the injected resin. Therefore, the maximum injection gap height (h_{ig}) of simulations of the NRT study is $h_{ig} = 0.928$ mm based on the resin volume resulting of the predefined final preform thickness of $h_{p,f} = 2$ mm and final fiber volume fraction of $V_{f,p} = 53.6\%$. Even though a further increase of the injection gap height would reduce its equivalent permeability according to Equation (2-8), the preform overflow would be reduced due to a larger volume of the injection gap compared to the constant injected resin [37]. Literature studies [36, 93, 115] confirm on the one hand that a large gap height reduces the overflow preform surface, but show on the other hand that a low gap height results in an increased preform impregnation during injection. The latter observation is explained by the progression of the equivalent permeability at changed injection gap heights in Figure 2-10. This figure shows that especially for small gap heights below one millimeter, the permeability is drastically reduced, resulting in an increased flow resistance inside the gap and

an increased impregnation of the below situated preform. Therefore, the effect of edge race-tracking on the CRTM preform impregnation pattern is investigated at the maximum gap height of 0.928 mm (high setting) and at the small setting of $h_{ig} = 0.309$ mm representing one third of the gap volume of the high setting.

Inlet position

With respect to edge race-tracking, a long known strategy for LCM processes, such as RTM, is to place the inlet centrally on the preform to delay a potential occurrence of edge race-tracking and ensure an undisturbed preform impregnation until the flow front reaches the edge race-tracking channels. RTM injections with a lateral inlet are reported to show an increased tendency of edge race-tracking, due to the direct connection between inlet and edge race-tracking channel. [145] The commonly aimed distribution of the resin inside the injection gap prior to the main preform impregnation during CRTM is expected to lower the influence of the inlet position at occurrence of edge race-tracking and is therefore investigated via numerical CRTM simulations with a lateral and central inlet position.

For each of the four investigated process configurations, two simulations (i) without and (ii) with an edge race-tracking channel of two millimeter are presented and compared. The graph of each quantitative comparison, as exemplary shown in Figure 4-2, display the mean cavity and preform height as well as the volume filling ratio (VFR) of the three flow domains, i.e. preform, injection gap, and race-tracking channel, over normalized process time. The graphs, quantitatively comparing the simulations, displays the injection phase of the process between zero and unity and the compression phase between unity and two. The height of the injection gap at each time step is indirectly shown by the difference between cavity and preform height of the specific simulation. The qualitative comparison, as exemplary shown in Figure 4-1, illustrates the preform filling patterns at characteristic times of the comparing CRTM simulations of each process configuration.

Process Configuration 1: Small Geometrical Aspect Ratio, High Injection Gap Height, and Lateral Inlet

In the following paragraphs, numerical CRTM simulations of preforms of small geometrical aspect ratio are presented at which the resin is laterally injected into an injection gap of high height. As shown in Figure 4-1(a), the resin flow of the simulated process configuration 1 without race-tracking is observed to first fill the injection gap while slightly penetrating the preform before the major part of the preform is impregnated predominantly in out-of-plane direction. This flow pattern correlates well with literature reports [37, 38] of the CRTM impregnation of preforms of small geometrical aspect ratio with high injection gap.

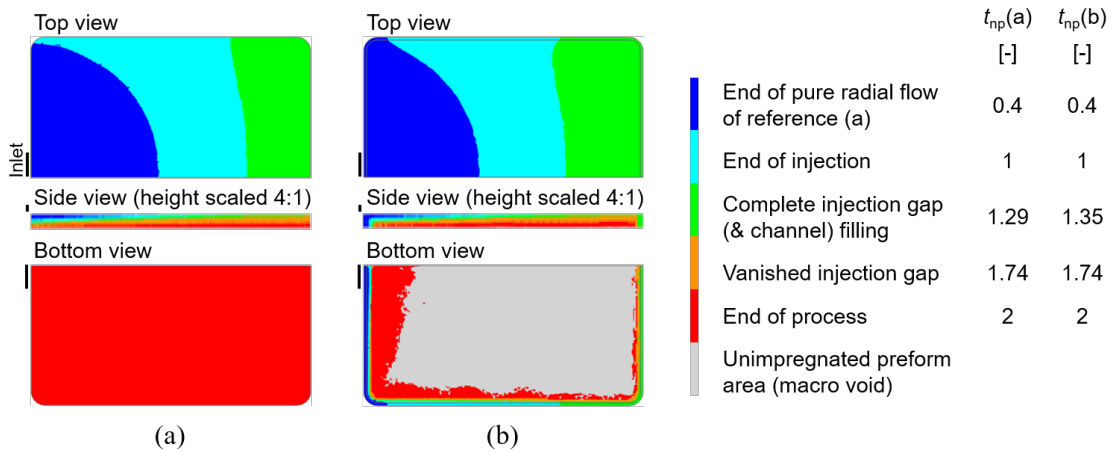


Fig. 4-1 Impregnation pattern of preform (a) as well as of preform plus 2 mm wide edge race-tracking channel (b) at characteristic process times; normalized process time (t_{np}): injection of 1.5 s between t_{np} of 0 and 1 as well as compression of 1.53 s between t_{np} of 1 and 2; results obtained by numerical simulations of CRTM process configuration 1: small geometrical aspect ratio, high injection gap height, and lateral inlet.

The filling progression of the individual flow domains of the simulation without race-tracking is quantitatively shown in Figure 4-2 by the curves marked with a cross. The displayed VFR of the injection gap shows a near-linear increase interrupted by a steeper increase at 0.46 normalized process time. While the general near-linear increase is explained by the injection at constant flow rate, the intermediate steeper increase is traced back to the limitation of the evaluation method while filling the refined mesh at the center of the preform and can therefore be neglected. At the end of the injection phase, the injection gap is not completely filled, even though its height is chosen so that the gap volume is equal to the volume of injected resin. The incomplete gap filling is explained by the simultaneously occurring impregnation of the preform seen at the slight increase of the preform's VFR during the injection phase.

After the complete amount of resin is injected at a normalized process time of unity, the upper mold starts to close at a constant closing speed of 1 mm/s seen by the linear decrease of the cavity height in Figure 4-2. The changed slope of the injection gap's VFR curve around a normalized process time of unity is explained by the changed source of flow promotion from injection at constant flow rate to mold-closure movement. The reduction of cavity height further distributes the resin inside the high-permeable injection gap which is completely filled at a normalized process time of 1.29. At this time, the VFR of the preform is recorded to be only filled up to 28% but increases strongly afterwards correlating to the observed predominantly out-of-plane flow front progression in Figure 4-1(a).

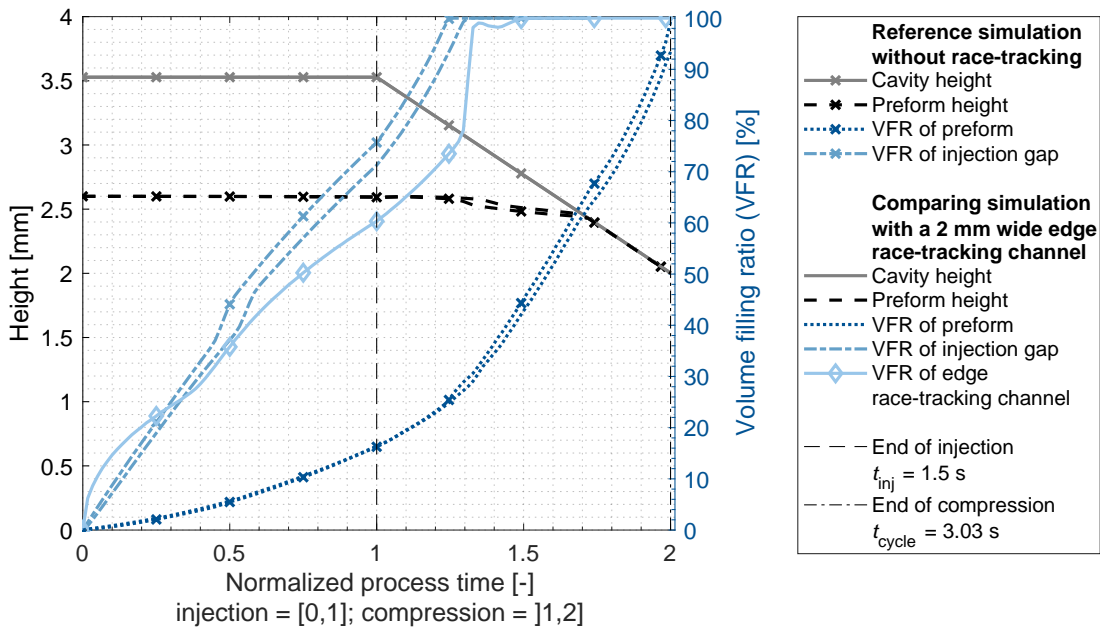


Fig. 4-2 Characteristic process parameters over normalized process time of numerical simulations without and with edge race-tracking of CRTM process configuration 1: small geometrical aspect ratio, high injection gap height, and lateral inlet.

The preform height is recorded in Figure 4-2 to stay constant during the injection and at the beginning of the compression phase. The observed preform reduction after a normalized process time of 1.29 correlates with the time of complete filling of the injection gap. After this time the preform is predominantly impregnated in out-of-plane direction, as observed in Figure 4-1(a), forming an out-of-plane fluid pressure gradient which compacts the preform until the injection gap vanishes at a process time of 1.74. After this time the upper mold is in contact with the preform, further distributing the resin inside the preform and compacting the preform.

The process setting of the comparing simulation is identical except that the model includes a two millimeter wide edge race-tracking channel resulting in a impregnation pattern of the preform and edge race-tracking channel as depicted in Figure 4-1(b). Comparing the preform impregnation patterns on the preform top side of the simulation without race-tracking in Figure 4-1(a) and with the simulation with race-tracking in (b) shows that the presence of a race-tracking channel changes the first two illustrated flow front shapes (dark and light blue) due to a slight advancing of the flow in the channel. The observed advancing flow inside the race-tracking channel results of the 2.4 times higher equivalent permeability inside the channel than inside the injection gap. The quantitative evaluation in Figure 4-2 shows an increase of the channel's VFR from process start which is confirmed by the qualitative observation that the race-tracking channel is filled early in the process due

to its lateral position of the inlet next to the channel (see side view of Figure 4-1(b) – dark blue).

Compared to the simulation without edge race-tracking, the injection gap's VFR of the simulation with edge race-tracking is recorded to progress slightly slower due to the additional filling of the race-tracking channel. This results in a slightly delayed complete filling of the injection gap in presence of edge race-tracking at a normalized process time of 1.35. At the same time, the VFR of the race-tracking channel increases up to 98% which correlates to its complete filling. The offset to 100% of the channel's VFR is traced back to numerical problems, which is also seen by the unphysical reduction of VFR at a normalized process time of 1.41 and is to be neglected. The identical times of complete filling of injection gap and race-tracking channel is explained by their spacial connection and their permeabilities which are in a comparable range while the filling of the preform is delayed due to the preform's permeability which is three orders of magnitudes lower.

After the injection gap and the race-tracking channel are filled, the VFR of the preform strongly increases in Figure 4-2 similarly as for the reference simulation without race-tracking but on a slightly reduced level. The offset is explained by the additional fiber-free volume of the race-tracking channel which is completely filled with resin at this point in time while the same amount of resin has been injected into the cavity at both simulations. Due to the increased overall porosity inside the cavity at presence of a fiber-free race-tracking channel, the final VFR of the preform is recorded to 93.4%, revealing that the preform is not completely filled if edge race-tracking occurs.

The qualitative comparison of the two simulations in Figure 4-1 shows a change in preform impregnation pattern at presence of edge race-tracking. Comparing the two preform impregnation patterns demonstrates that while the preform of the reference simulation in (a) is predominantly impregnated in out-of-plane direction after the injection gap is filled, the preform of the simulation with edge race-tracking in (b) is impregnated by a superimposed flow of an out-of-plane and in-plane component. As for the reference simulation, the mold-closure forces the resin inside the injection gap to impregnate the preform in out-of-plane direction while the resin inside the race-tracking channel additionally impregnates the preform in in-plane direction, as observed in Figure 4-1(b).

Furthermore, the preform impregnation pattern of the simulation with edge race-tracking in Figure 4-1(b) shows an unimpregnated preform section (gray) at the end of the process correlating to the reduced final VFR of the preform of 93.4% recorded in Figure 4-2. The observed macro void (unimpregnated preform section) spans over a large section of the preform bottom side and is characterized by its

small height, barely visible in the side view of Figure 4-1(b). This shape results of the observed superimposed preform impregnation of central out-of-plane flow from the injection gap and lateral in-plane flow from the race-tracking channel caused by the early filling of the injection gap and race-tracking channel.

Process Configuration 2: Large Geometrical Aspect Ratio, High Injection Gap Height, and Lateral Inlet

The second investigated CRTM process configuration consists of preforms of large geometrical aspect ratio at which the resin is laterally injected into an injection gap of high height. The preform impregnation pattern at characteristic process times of the reference simulation without an edge race-tracking channel is shown in Figure 4-3(a). The graph depicts that the resin is not distributed above the complete preform before the injection gap vanishes (green). After the upper mold is in contact with the preform, the flow front inside the preform is observed to equalize over the preform's thickness before a predominantly in-plane advancement of a nearly uniform flow front over the thickness of the preform is recorded. This flow pattern correlates well with descriptions of the CRTM impregnation pattern of preforms with large geometrical aspect ratio and large injection gap in literature [36, 37].

The progression of the VFR of the individual flow domains, i.e. injection gap and preform, of the reference simulation without edge race-tracking are presented by the curves marked with a cross in Figure 4-4. Due to the increased preform length more resin needs to be injected resulting in an increased injection time at identical flow rate at both investigated process configurations. A longer injection time of the resin results in more resin penetrating from the injection gap into the preform leading to an increased VFR of the preform from 16.2% to 27.3% and a reduced VFR of the gap from 75.7% to 55.4% between the previously presented simulation of process configuration 1 and the here presented simulation of process configuration 2, respectively. Furthermore, the flow front is recorded to reach the bottom of the preform at the inlet zone already during the injection phase, as shown in light blue in Figure 4-3(a).

During the compression phase, the VFR of the gap and the preform further increase, as seen in Figure 4-4. While the VFR of the preform increases to 100% at process end, the VFR of the gap is observed to reach a plateau at 85.7% between a normalized process time of 1.57 and 1.71. The observed plateau of the gap's VFR results from (i) the modeling and evaluation method of the simulation as well as from (ii) the out-of-plane compaction state of the preform which differs at different zones of the preform.

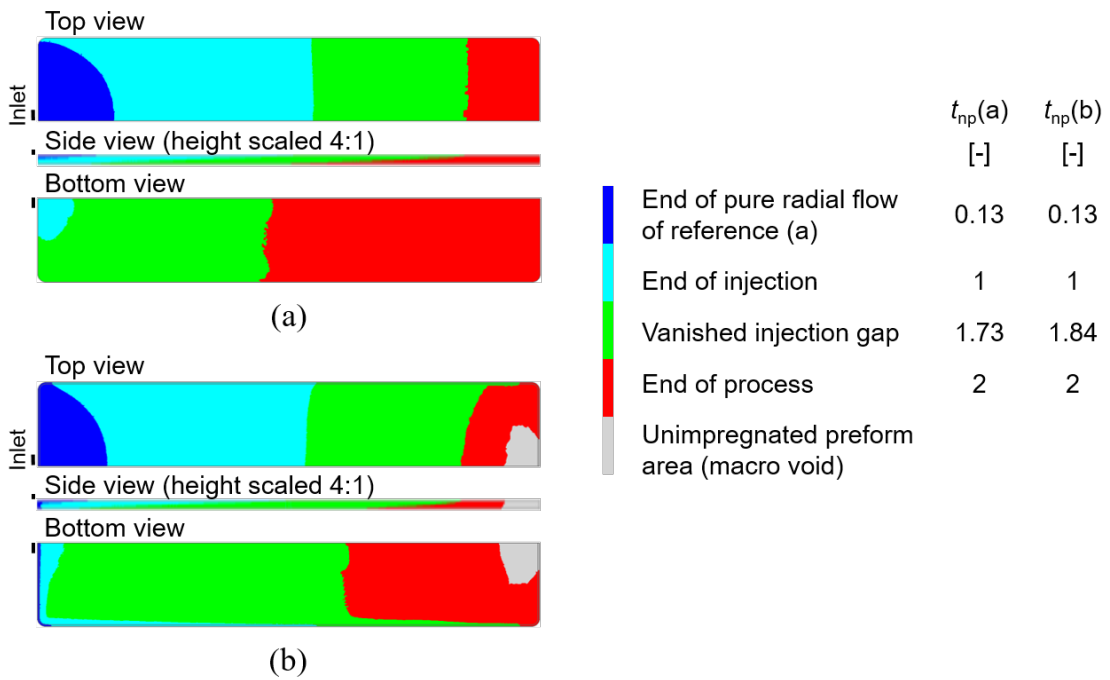


Fig. 4-3 Impregnation pattern of preform (a) as well as of preform plus 2 mm wide edge race-tracking channel (b) at characteristic process times; normalized process time (t_{np}): injection of 4.5 s between t_{np} of 0 and 1 as well as compression of 1.53 s between t_{np} of 1 and 2; results obtained by numerical simulations of CRTM process configuration 2: large geometrical aspect ratio, high injection gap height, and lateral inlet.

The developed evaluation method of the CRTM simulations calculates the VFR of the gap as the average of all nodes of the gap below the lowest upper cavity position [144] to account for the inter-penetrating mesh technology applied in the simulation software (see Chapter 2.2.4). To model the resin flow from the gap into the preform, the lowest layer of nodes of the flow domain representing the injection gap are shared and equal to the upper nodes of the flow domain representing the preform. Additionally, a mechanical contact condition is applied between the lower surface of the upper mold and the upper surface of the preform (including their containing nodes) to model the preform compaction during the CRTM process. Therefore, all upper nodes of the preform (equal to all lower nodes of the injection gap) will always remain below the lowest nodes of the upper mold. This can lead to a state at which the lower nodes of the injection gap are still considered in the calculation of the gap's VFR even though the gap has already vanished in some sections of the preform.

Based on these modeling and evaluation assumptions, the observed plateau of the gap's VFR is reached when the in-plane flow inside the injection gap above the preform stagnates at a normalized process time of 1.57. At this point in time the

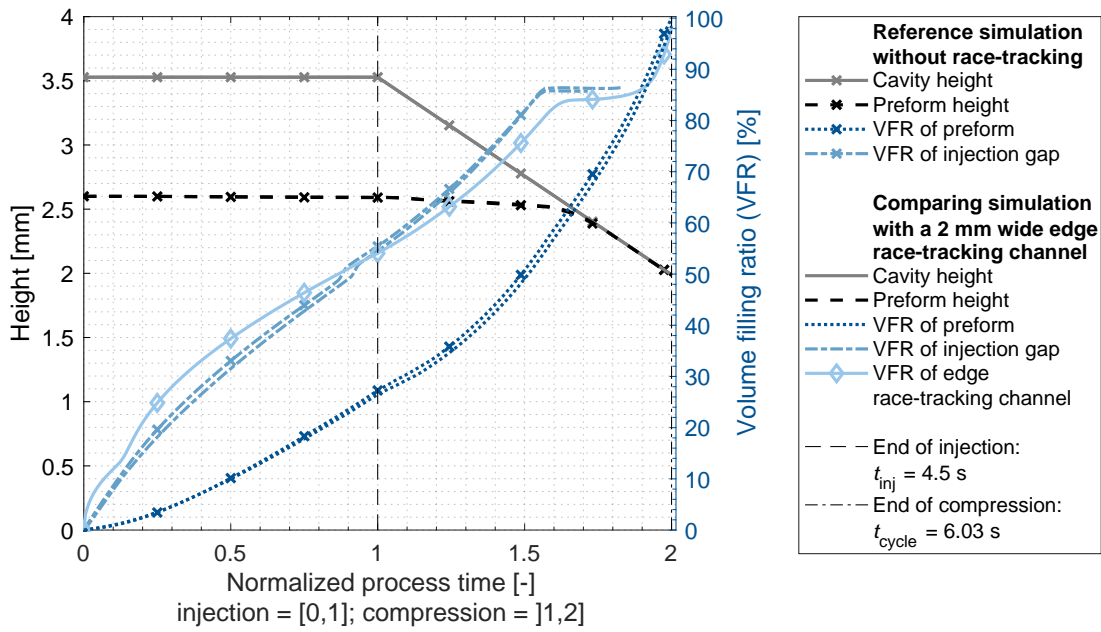


Fig. 4-4 Characteristic process parameters over normalized process time of numerical simulations without and with edge race-tracking of CRTM process configuration 2: large geometrical aspect ratio, high injection gap height, and lateral inlet.

upper mold is at a position of 2.65 mm and is therefore almost in contact with the unimpregnated and uncompressed preform of 2.6 mm at the flow front position of the gap. The remaining volume of resin inside the gap seems to be too low to further promote a flow above the preform before the upper mold is for the first time in contact with the preform at a height of 2.6 mm. While the upper mold is now in contact with the preform over the preform's unimpregnated zone, the preform in its impregnated zone has undergone a compaction due to the acting fluid pressure and is at this time not yet in contact with the upper mold. Due to the modeling assumption, discussed in the previous paragraph, a biased VFR of the gap is calculated at this point including all upper nodes of the preform (lowest nodes of the gap) resulting in the observed plateau while in reality the nodes in contact with the upper mold should be excluded and the VFR of the localized gap should be equal to 100%. During further mold-closure the remaining localized injection gap reduces also until the gap eventually vanishes when the upper mold is in contact with the preform over its complete surface at a normalized time of 1.71, indicated by the end time of the plateau. The absolute value of the VFR of the gap is therefore biased in the region of the observed plateau, but is purposely illustrated in the evaluation graphs of the simulations of this work to present (i) the time at which the in-plane flow above the preform stagnates at the beginning of the plateau and (ii) the time at which the upper mold is in contact with the complete preform surface at the end of the plateau.

The preform impregnation pattern of the comparing simulation with edge race-tracking is shown Figure 4-3(b). The flow inside the race-tracking channel is shown to slightly advance the flow on top of the preform due to an approximately 2.4 times higher equivalent permeability in the channel (at uncompressed state) than inside the injection gap above the preform. The advancement of the flow inside the channel is shown to be more dominant on the bottom side of the preform due to an equivalent permeability of the channel that is three orders of magnitudes higher than the in-plane permeability of the preform.

Due to the location of the lateral inlet above the race-tracking channel, the channel is filled from the beginning of the process, as depicted in Figure 4-4. The additional filling of the race-tracking channel reduces the VFR of the injection gap of the simulation with edge race-tracking compared to the simulation without race-tracking. Furthermore, the flow progression is delayed, which is illustrated by a shift of the biased jump in curve progression due to the filling of the refined mesh at the central inlet section from a normalized process time of 0.87 for the simulation without race-tracking to 0.89 for the simulation with race-tracking.

Figure 4-4 shows that the plateau of the gap's VFR is reached at an identical normalized process time of 1.57 compared to the simulation without race-tracking, but on a slightly higher level. The identical start time of the plateau is explained by the identical mold kinematics and preform dimensions at both simulations resulting in a stagnation of the flow inside the injection gap at a height of 2.65 mm shortly before the upper mold gets in contact with the preform in its unimpregnated and uncompressed sections of 2.6 mm height. The higher level of the plateau is explained by a lateral filling from the slightly advancing flow inside the race-tracking channel towards the center of the injection gap (and the preform) in the zone of the advanced channel flow as observed in Figure 4-3(b).

As depicted in Figure 4-4, the progression of the VFR of the race-tracking channel is observed to reach a temporary plateau at a normalized process time of 1.62. While the previously discussed plateau of the gap's VFR is traced back to limitations of the modeling and evaluation method, the plateau of the channel's VFR is explained by physical phenomena during the flow progression of the presented CRTM process configuration. From the beginning of the process, the injection gap and the race-tracking channel are similarly filled due to their spacial connection and their comparable equivalent permeability. After the flow front inside the injection gap stagnates, the gap does not fully vanish due to compressed preform sections at its impregnated sections providing a resin reservoir from which resin is further distributed into the neighboring flow domains, further increasing the channel's VFR until a normalized process time of 1.62. Subsequently, the flow inside the race-tracking channel is observed to stay nearly constant during the ongoing

out-of-plane equalization of the flow front inside the preform. After the flow front inside the preform has equalized, the flow front inside the preform and race-tracking channel is observed to further advance predominantly in in-plane direction after a normalized process time of 1.8 due to an increased and equalized pressure at the flow front.

At the end of the process the channel as well as the preform are recorded to be not completely impregnated in Figure 4-4 indicated by a final VFR value 98.1% and 98.4%, respectively. The cause for the unimpregnated preform and channel section is traced back to (i) the overall increased porosity inside the cavity due to the fiber-free volume of the edge race-tracking channel and (ii) the injection of the same resin volume as for the reference simulation without race-tracking. In contrast to process configuration 1 at which the edge race-tracking channel is completely filled during the process and only the final VFR of the preform is reduced at process end, the investigations of process configuration 2 show that the final VFR of the preform and edge race-tracking channel are both reduced at process end. The incomplete filling of the two flow domains is correlated to their impregnation pattern resulting in a formed macro void at the end of the process which spans over sections of both flow domains, as seen in Figure 4-3(b). The macro void is located opposite of the inlet next to the preform zones lastly filled. The in-plane progression of the equalized flow front over the preform thickness at process end, visible at the side view of Figure 4-3(b), results in a compacted void size of limited in-plane dimensions but extending over the preform's complete thickness.

The progression of the mean preform height in Figure 4-4 is observed to be not influenced by edge race-tracking. It is recorded to insignificantly change during the injection due to the high equivalent permeability of the injection gap which results in a low injection pressure. During the gap closure of the compression phase between a normalized process time of unity and 1.71, the mean preform thickness reduces, which is traced back to the preform compaction in the impregnated preform zone. The majority of the preform compaction is observed to take place after the gap vanishes and the upper mold is in contact with the preform, compacting the preform down to its final thickness of 2 mm.

Process Configuration 3: Small Geometrical Aspect Ratio, Low Injection Gap Height, and Lateral Inlet

The third investigated CRTM process configuration studies the edge race-tracking effect of preforms of small geometrical aspect ratio at a lateral resin injection into an injection gap of low height. The preform impregnation pattern of the reference simulation without edge race-tracking is shown in Figure 4-5(a). Even though the

here investigated preform is of small aspect ratio, it is observed to be not completely overflowed before the gap vanishes (orange) due to the low equivalent permeability of the injection gap at low gap height. After the flow inside the injection gap stagnates, the flow front inside the preform is observed to equalize over the preform's thickness and eventually progresses predominantly in in-plane direction nearly uniformly over the preform's thickness. The described preform impregnation pattern of the investigated CRTM configuration 3, shown in Figure 4-5(a), is observed to be similar to the preform impregnation pattern of the previously investigated CRTM configuration 2, illustrated in Figure 4-3(a).

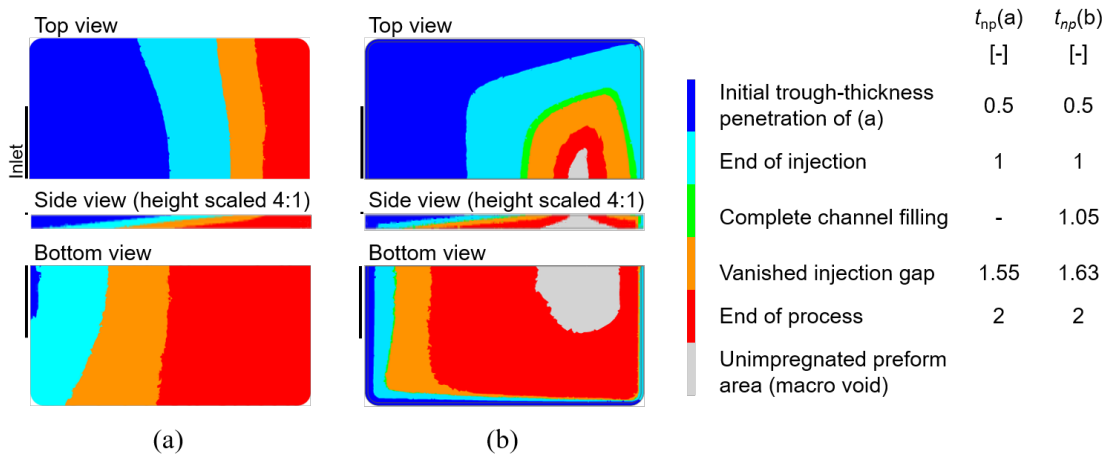


Fig. 4-5 Impregnation pattern of preform (a) as well as of preform plus 2 mm wide edge race-tracking channel (b) at characteristic process times; normalized process time (t_{np}): injection of 1.5 s between t_{np} of 0 and 1 as well as compression of 0.91 s between t_{np} of 1 and 2; results obtained by numerical simulations of CRTM process configuration 3: small geometrical aspect ratio, low injection gap height, and lateral inlet.

Figure 4-6 shows the cavity and mean preform height as well as the VFR of the two flow domains, i.e. injection gap and preform, of the reference simulation without race-tracking of process configuration 3 by curves marked with a cross. The low gap height setting of 0.309 mm is indirectly shown by the difference between the cavity and preform height at process start. While the cavity height is predefined to a constant value during the injection, the averaged preform height is observed to decrease during the injection due to an increased injection pressure during the flow rate controlled injection into the injection gap of low height and, according to Equation (2-8), also of low equivalent permeability.

As observed in the qualitative flow front progression of Figure 4-5(a), the injection gap is not completely filled before the upper mold gets into contact with the preform. This observed fact is characterized in the quantitative overview of the simulation results in Figure 4-6 by reaching the plateau of the gap's VFR curve

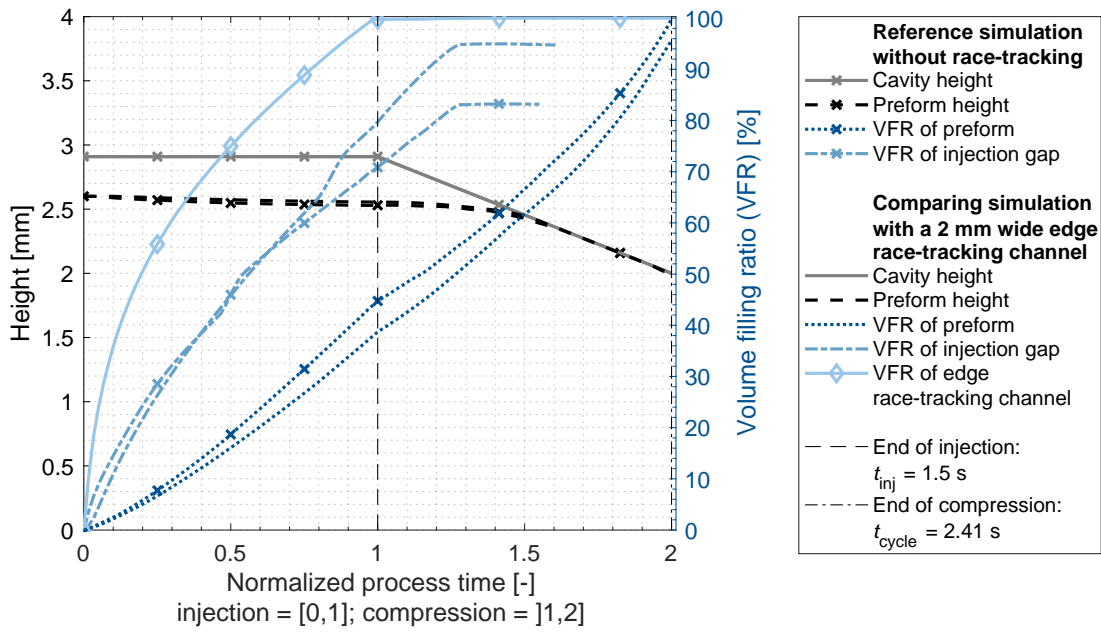


Fig. 4-6 Characteristic process parameters over normalized process time of numerical simulations without and with edge race-tracking of CRTM process configuration 3: small geometrical aspect ratio, low injection gap height and lateral inlet.

after a normalized process time of 1.28. The plateau results of limitations of the modeling and evaluation method discussed in detail for the previous CRTM process configuration 2. The stagnation of the in-plane flow inside the injection gap occurs at a cavity height of 2.65 mm, shortly before the upper mold gets in contact with the unimpregnated and uncompressed preform zone of a height of 2.6 mm.

While the preform of the initially investigated CRTM configuration 1 reached only a VFR of 16.2% at the end of the injection, the preform impregnation of the now investigated configuration 3 is characterized by a VFR of the preform of 44.7% at the end of the injection. The increased preform impregnation during the injection phase of process configuration 3 is caused by a lowered equivalent permeability of the injection gap according to Equation (2-8) resulting of the reduced injection gap height. The lowered equivalent permeability of the injection gap leads to an increased injection pressure during the flow rate controlled injection, as seen by comparing the recorded pressure at inlet of the simulations without race-tracking of the process configuration 1 in Figure 4-11 and process configuration 3 in Figure A-18 in Appendix A.2.2. Consequently, the increased fluid pressure inside the gap during the injection of process configuration 3 results in the observed increased impregnation of the neighboring preform, according to Darcy's law (Equation 2-1). During the subsequent compression phase the preform's VFR is observed to further increase until complete filling of 100% at the end of the process.

Comparing the qualitative preform impregnation pattern of the reference simulation without edge race-tracking in Figure 4-5(a) with the simulation with edge race-tracking in (b) shows a significant influence of the race-tracking effect on the preform impregnation pattern. A fast filling of the race-tracking channel is observed which strongly advances the flow inside the injection gap (preform top side) and preform. The advancement of the flow inside the race-tracking channel during process configuration 3 is explained by the value of the equivalent permeability of the channel (at uncompressed state) which is two orders of magnitudes higher than the equivalent permeability of the injection gap and four orders of magnitude higher than the preform's in-plane permeability (at uncompressed state). The channel's fast filling is quantitatively depicted in Figure 4-6 by a steep increase of its VFR from the beginning of the process reaching a complete filling of 100% at a normalized process time of 1.05.

In the first third of the injection phase, the gap's VFR of the simulation with edge race-tracking is recorded in Figure 4-6 to be below the corresponding VFR curve of the reference simulation without edge race-tracking due to the additional filling of the edge race-tracking channel. Subsequently, the two curves are on a comparable level before the gap's VFR of the simulation with race-tracking increases more steeply during the last third of the injection phase and eventually reaches a plateau during the compression phase at a VFR value of 94.8%. The increased progression of the gap's VFR curve in the last third of the injection phase and during the compression phase as well as the increased final value of the plateau is traced back to the fast filling of the race-tracking channel in the early stages of the process which results in an additional lateral filling of the injection gap from the race-tracking channel toward the center of the injection gap as seen in the top view of Figure 4-5(b). Even though the level of the final VFR of the gap increases, the point in time at which the in-plane filling of the gap stagnates at 1.28 is comparable with the reference simulation without race-tracking due to the sole dependency of the upper mold's first contact with the preform in its unimpregnated and uncompressed sections.

The preform's VFR of the simulation with edge race-tracking is observed in Figure 4-6 to increase on a lower slope during the injection due to a reduced injection pressure as for the simulation without race-tracking as shown in Figure A-18 in Appendix A.2.2. The reduced injection pressure at constant flow rate results of the presence of the edge race-tracking channel with a significantly higher equivalent permeability as the other flow domains, i.e. preform and injection gap. The reduced injection pressure explains also the slightly increased mean preform thickness of the simulation with edge race-tracking as recorded in Figure 4-6. During the compression phase the offset between the VFR curves of the simulation with-

out and with edge race-tracking narrows down while a reduced final VFR of the preform of 95.7% is recorded in Figure 4-6. The partially filled preform at the end of the process with race-tracking can be traced back to (i) the presence of the fiber-free volume of the edge race-tracking channel which is completely filled at this point while (ii) the same amount of resin has been injected as for the simulation without a race-tracking channel. The reduced VFR of the preform is observed in Figure 4-5(b) as a formed, localized macro void spanning over the complete thickness of the preform. The position and shape of the macro void is explained by the resin flow of the investigated CRTM process configuration at which (i) the race-tracking channel is filled early in the process, additionally filling the injection gap and preform laterally and (ii) at which the injection gap vanishes before the gap is completely filled resulting in an out-of-plane equalization and final dominant in-plane progression of a nearly uniform flow front over the preform's thickness.

Process Configuration 4: Small Geometrical Aspect Ratio, High Injection Gap Height, and Central Inlet³

The last investigated CRTM process configuration 4 defines preforms of small geometrical aspect ratio at which the resin is centrally injected into an injection gap of high height. Figure 4-7 depicts a qualitative overview of the preform filling patterns at characteristic times of the two CRTM simulations without (a) and with edge race-tracking (b). Comparing the two graphs reveals that the initial flow pattern of both simulations are identical until the end of the pure radial flow (dark blue). The quantitative comparison of the two simulations in Figure 4-8 confirms this observation by overlapping VFR curves of gap and preform until the end of the radial flow at a normalized process time of 0.9. Note that the initially steep increase of the injection gap's VFR is attributed to a limitation of the evaluation script over-predicting the VFR due to the refined mesh at the inlet section, and can thus be neglected. The subsequent constant slope of the VFR curve of the injection gap until 0.9 is explained by the predefined process setting to inject the resin centrally into the gap at a constant flow rate. Due to the process design, the resin flows at the process start radially inside the injection gap while only marginally penetrating the preform located below as seen in the side views of Figure 4-7. Since the injection gap has a low flow resistance to the resin, the fluid pressure during the flow rate controlled injection is low, recorded by a maximum pressure at inlet of 22.2 kPa during the radial flow as shown in Figure A-19 in Appendix A.2.2. According to Darcy's law, Equation (2-1), the observed marginal impregnation at the preform surface is explained by the low acting fluid pressure during resin injec-

³ The following paragraphs of this subsection have been previously published in [140].

tion and its comparably low permeability in the uncompressed state, three order of magnitudes lower than the permeability of the injection gap. Additionally, the low fluid pressure explains that the preform undergoes no significant deformation during the radial filling of the injection gap, as seen in Figure 4-8.

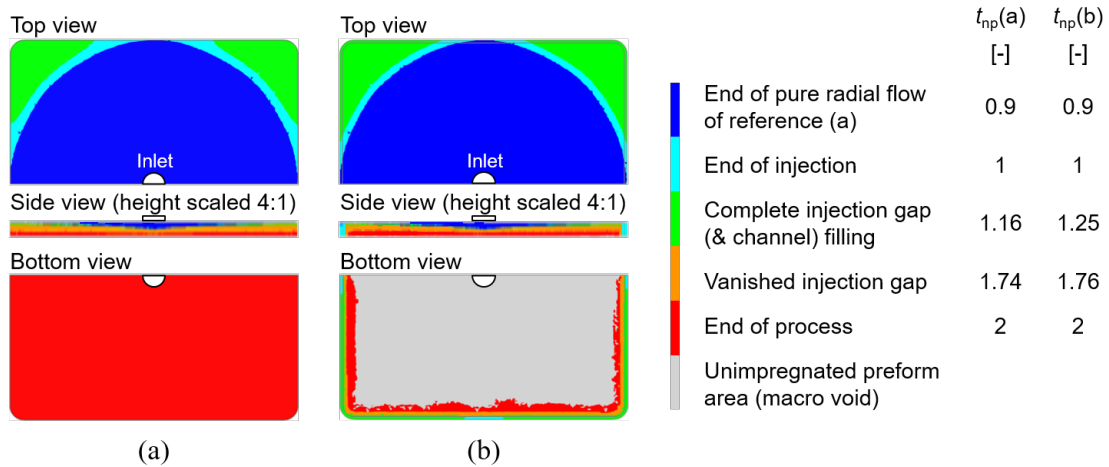


Fig. 4-7 Impregnation pattern of preform (a) as well as of preform plus 2 mm wide edge race-tracking channel (b) at characteristic process times; normalized process time (t_{np}): injection of 1.5 s between t_{np} of 0 and 1 as well as compression of 1.53 s between t_{np} of 1 and 2; results obtained by numerical simulations of CRTM process configuration 4: small geometrical aspect ratio, high injection gap height, and central inlet. [140]

For the simulation with an edge race-tracking channel, the radial flow inside the injection gap overflows the preform edge at a normalized process time of 0.9 and fills the race-tracking channel due to the spatial connection. This is observed in the side view of Figure 4-7(b) in light blue as well as in Figure 4-8 by a steep increase of the channel's VFR after a normalized process time of 0.9. At the same time, the VFR of the gap is reduced in comparison to the simulation without edge race-tracking due to the additional filling of the edge race-tracking channel. Therefore, the time of complete gap filling is delayed for the simulation with edge race-tracking.

After the injection ends (at a normalized process time of unity), the upper mold in both simulations is closed at a constant velocity shown by the linear reduction of the cavity height in Figure 4-8. The mold movement further distributes the resin inside the highly permeable flow domains of the gap as well as the channel and further impregnates the preform. While the VFR of the preform is only insignificantly increased until complete filling of the gap and the channel in Figure 4-8, the slope of the preform's VFR increases strongly afterwards in both simulations. Simultaneously, a reduction of preform height is recorded for both simulations caused by fluid pressure during the closing of the gap and the contact of preform and cavity after the gap has vanished. While the preform of the simulation without race-tracking

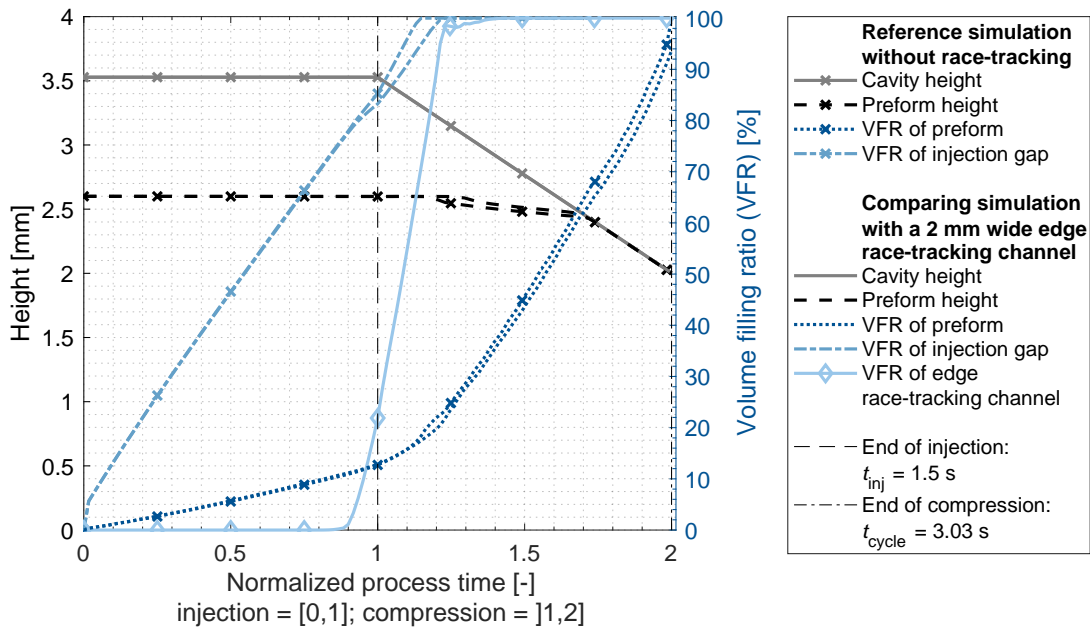


Fig. 4-8 Characteristic process parameters over normalized process time of numerical simulations without and with edge race-tracking of CRTM process configuration 4: small geometrical aspect ratio, high injection gap height and, central inlet. [140]

in Figure 4-7(a) is predominantly impregnated in out-of-plane direction during the cavity-closure, the corresponding simulation in Figure 4-7(b) shows an additional lateral flow component from the race-tracking channel towards the preform center.

After complete filling of the injection gap and race-tracking channel, the quantitative comparison between the two VFR curves of the preform in Figure 4-8 shows a similar increase but slightly lower values for the simulation with edge race-tracking. The reduced values are traced back to the additional fiber-free volume of the race-tracking channel, which is completely filled at this time, reducing the volume of resin inside the preform. For the same reason, the preform of the simulation with edge race-tracking is not completely filled at the end of the process even though the same resin volume was injected into the cavity at both simulations. The reduced final VFR of 93.7% indicates an incomplete impregnation of the preform for the simulation with edge race-tracking, which is identified in Figure 4-7(b) to be located on the preform bottom side. The formed macro void is shown to be of large in-plane and small out-of-plane dimensions. The out-of-plane dimension is so small that it is barely visible in the side view of Figure 4-7(b). The shape of the macro void is a result of the superimposed flows of the dominant out-of-plane preform filling from the injection gap and the lateral in-plane flow from the race-tracking channel towards the preform center.

4.2.2 Investigations of Edge Race-Tracking Severity

To further investigate the effect of edge race-tracking on the CRTM process, this subsection investigates how the edge race-tracking severity, at increasing channel width, affects different CRTM process responses. For this purpose, the first CRTM process configuration of small geometrical aspect ratio, high injection gap height and lateral inlet is chosen and modeled in three scenarios (i) without an edge race-tracking channel, (ii) with a two and (iii) with a four millimeter wide edge race-tracking channel. The process configurations of all three simulations are identical except for the race-tracking channel width which reduces the in-plane dimension of the preform as shown in Figure A-11(a) in Appendix A.2.1.

The flow front progressions of the three simulated process scenarios at characteristic process times are presented in Figure 4-9. Comparing the first two illustrated flow front progression steps (dark and light blue) of the reference simulation without race-tracking in (a) with the one with a two millimeter wide race-tracking channel in (b) shows that the presence of edge race-tracking leads to a slight advancing flow inside the channel. This has been observed for all previously investigated CRTM process scenarios due to the slightly higher equivalent permeability of the channel than the equivalent permeability of the injection gap and due to the multiple order of magnitudes lower permeability of the preform. Furthermore, a comparison of the flow front progressions in (b) and (c) reveals that an increase of the edge race-tracking channel width leads to an even stronger advancement of the flow inside the edge race-tracking channel. The increased advancing flow is explained by the increased equivalent permeability at an increased channel width according to Equation (2-12). While the values of the equivalent permeability of the injection gap and the permeability of the preform are constant at all presented simulations, the equivalent permeability of the edge race-tracking channel nearly doubles (at an uncompressed state) from $1.7 \cdot 10^{-7} \text{ m}^2$ to $3.2 \cdot 10^{-7} \text{ m}^2$.

The qualitative observation of an advancing flow inside the race-tracking channel with increased channel width is confirmed by the quantitative evaluation of the channel's VFR depicted in Figure 4-10. The VFR of the race-tracking channel is recorded to increase faster for the simulation with a four than with a two millimeter wide race-tracking channel. The flow inside the race-tracking channel is observed to effect also the impregnation of the neighboring flow domains of injection gap and preform. The flow front progression inside the injection gap is observed to be more strongly affected than the flow front progression inside the preform, identified by comparing the flow on the preform top side of the three different process scenarios in Figure 4-9 (identical to the flow inside the injection gap) and the flow on the preform bottom side. As discussed in the previous subsection, the observed difference is

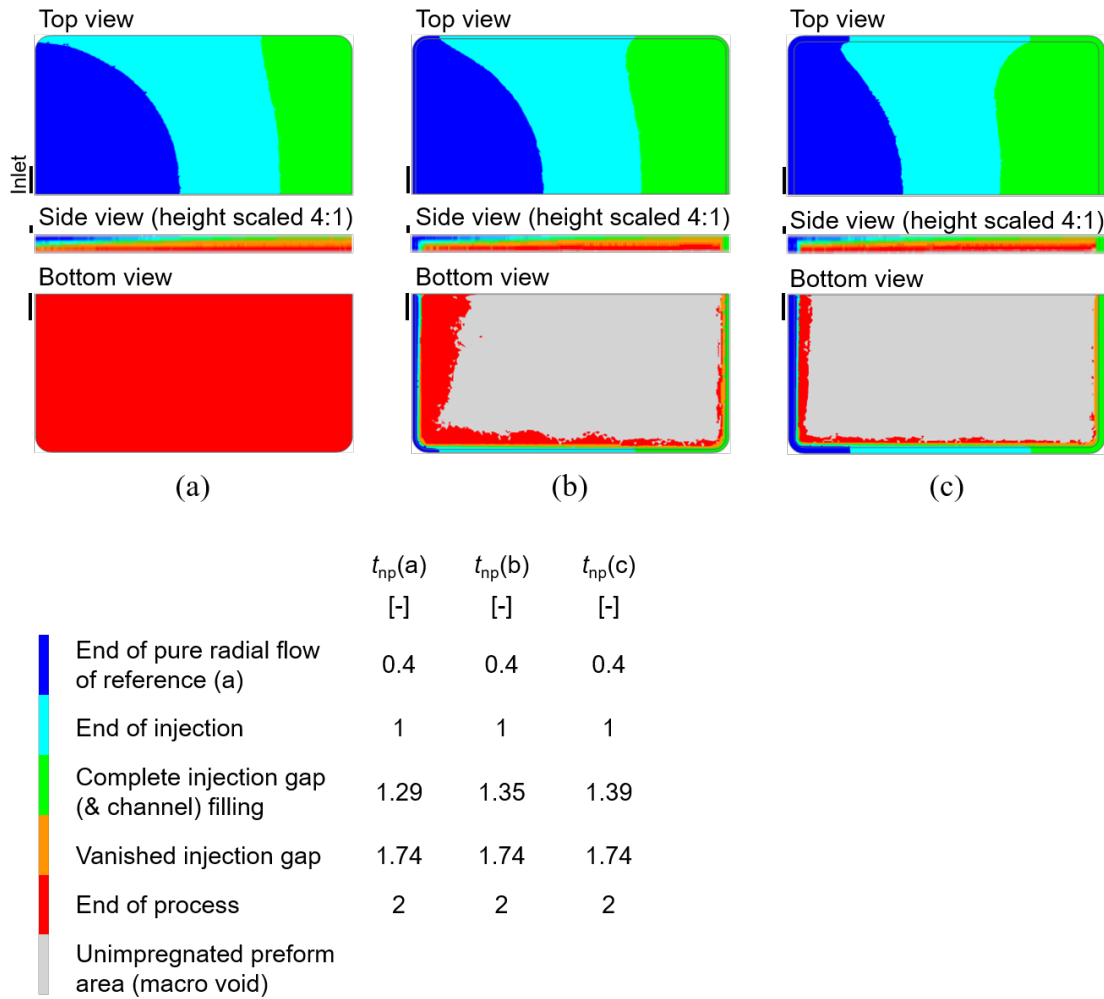


Fig. 4-9 Impregnation pattern of preform (a) as well as of preform plus 2 mm wide (b) and plus 4 mm wide edge race-tracking channel (c) at characteristic process times; normalized process time (t_{np}): injection of 1.5 s between t_{np} of 0 and 1 as well as compression of 1.53 s between t_{np} of 1 and 2; results obtained by numerical simulations of CRTM process configuration 1: small geometrical aspect ratio, high injection gap height, and lateral inlet.

explained by the large variation of the permeabilities of the two neighboring flow domains being in a comparable range for the injection gap but around four order of magnitudes lower for the preform as compared to the race-tracking channel.

The quantitative evaluation of the flow domains in Figure 4-10 illustrates also that the injection gap is filled slower at increased race-tracking channel width observed by a reduced slope of the gap's VFR curve. This is explained by the additional filling of the race-tracking channel and the channel's increased volume with increased width. Due to the same reason, the time of complete gap filling is shifted to a later point in time, delaying also the time of complete filling of the race-tracking

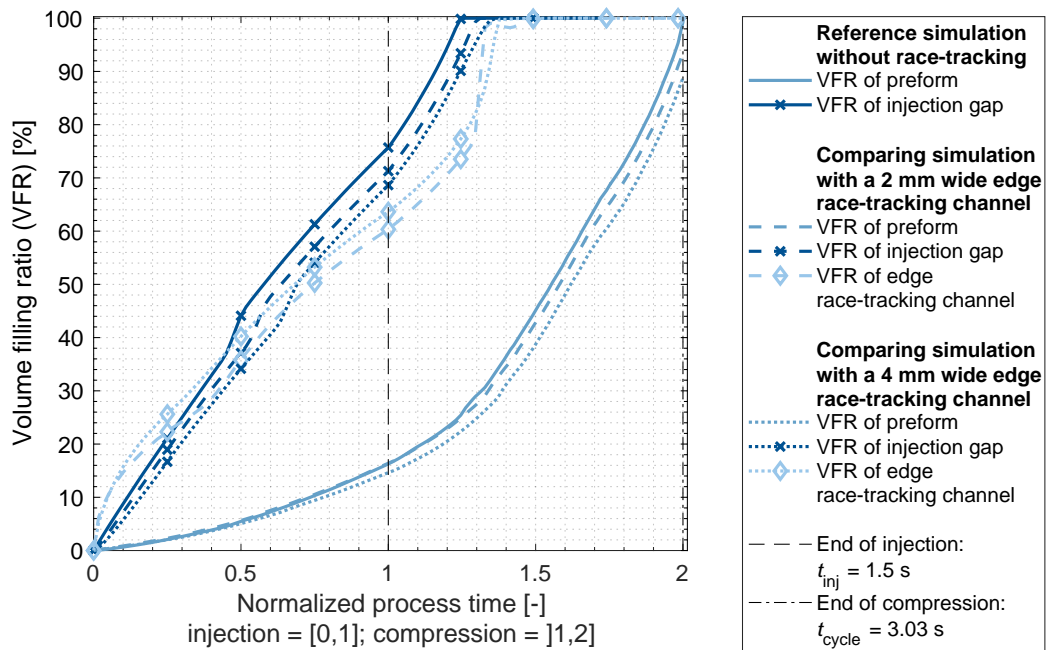


Fig. 4-10 Volume filling ratio (VFR) over normalized process time of numerical simulations without, with a 2 mm and 4 mm wide edge race-tracking channel of CRTM process configuration 1: small geometrical aspect ratio, high injection gap height, and lateral inlet.

channel due to their spacial connection and their comparable levels of equivalent permeability.

Until time of complete gap and channel filling, the VFR of the preform is observed in Figure 4-10 to be on a similar progression for the simulation without and with a two millimeter wide race-tracking channel while the simulation with a four millimeter wide race-tracking channel shows a reduced value with progressing process time. After the injection gap and edge race-tracking channel are completely filled, a clear difference between the preform's VFR of the individual simulations is observed which shows a reduced VFR of the preform with increased race-tracking channel width. This is correlated to the fact that the same amount of resin is injected at all three simulations but by increasing the fiber-free volume of the race-tracking channel less resin is available to impregnate the preform after the channel is completely filled. For the same reason, the final VFR of the preform is recorded in Figure 4-10 to be reduced from 100% for the reference simulation without race-tracking to 93.4% for the simulation with a two millimeter wide race-tracking channel and to 88.8% with a four millimeter wide race-tracking channel. The reduced final VFR of the preform is depicted in the overview of the qualitative flow front progressions in Figure 4-9(b) and (c) by a macro voids (gray) of increased in-plane and out-of-plane dimensions for increased channel width.

Figure 4-11 depicts the pressure at inlet during the injection phase of the three modeled CRTM process scenarios (i) without race-tracking, (ii) with a two and (iii) with a four millimeter wide race-tracking channel. The graph shows that the pressure at inlet during the resin injection of constant flow rate is reduced with increasing race-tracking channel width. This is explained by the reduced flow resistance inside the race-tracking channel that is even lower than inside the high-permeable injection gap. Furthermore, according to Equation (2-12) the equivalent permeability of the edge race-tracking channel reduces with increasing channel width, further reducing the recorded pressure at inlet.

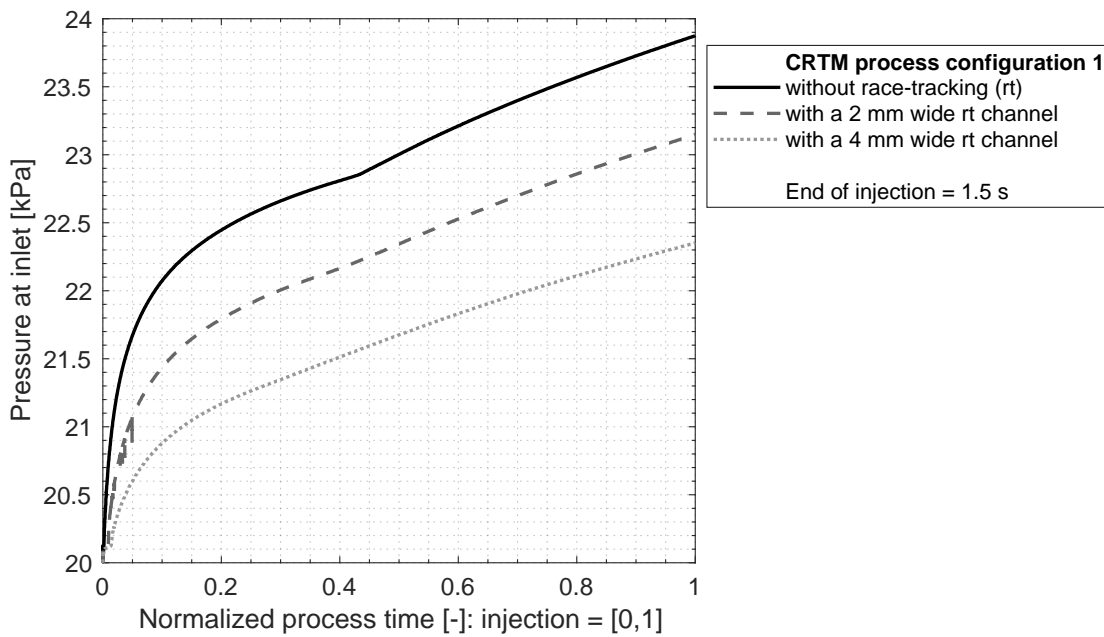


Fig. 4-11 Pressure at inlet during the CRTM injection phase of numerical simulations without, with a 2 mm and 4 mm wide edge race-tracking channel of the CRTM process configuration 1: small geometrical aspect ratio, large injection gap and, lateral inlet.

Due to the lateral inlet position, the resin is injected close to the edge race-tracking channel which results in a filling of the edge race-tracking channel and a reduced recorded pressure at inlet from process start on. The pressures at inlet of the other previously investigated CRTM process configurations with lateral inlet show also a reduced pressure at presence of race-tracking as illustrated in Figures A-17 and A-18 in Appendix A.2.2. The recorded pressures at inlet of the CRTM process configuration with central inlet (furthest away from the edge race-tracking channel) in Figure A-19 in Appendix A.2.2 shows that the pressure at inlet is identical until a normalized process time of 0.9 at which the flow front reaches the edge race-tracking channel. All these observations strengthen the conclusion that the pressure at inlet is reduced after the flow front reaches the edge race-tracking channel.

Figure 4-12 shows the maximum force at the end of the process acting on the upper mold calculated for the three investigated simulations (i) without race-tracking, (ii) with a two and (iii) with a four millimeter wide edge race-tracking channel. A strong reduction of force by -56.6% and -63.2% is recorded between the simulation without race-tracking and the simulations with a two as well as a four millimeter wide race-tracking channel, respectively. The strong reduction of force is traced back to the increased overall porosity inside the cavity due to the presence of the fiber-free volume of the edge race-tracking channel, resulting in an incomplete filling of the preform and a reduced final pressure inside the cavity. The increase of the race-tracking channel width from 2 mm to 4 mm, which further increases the overall porosity inside the cavity, is recorded to only minorly reduce the maximal force in comparison to the reduction at absence and presence of race-tracking.

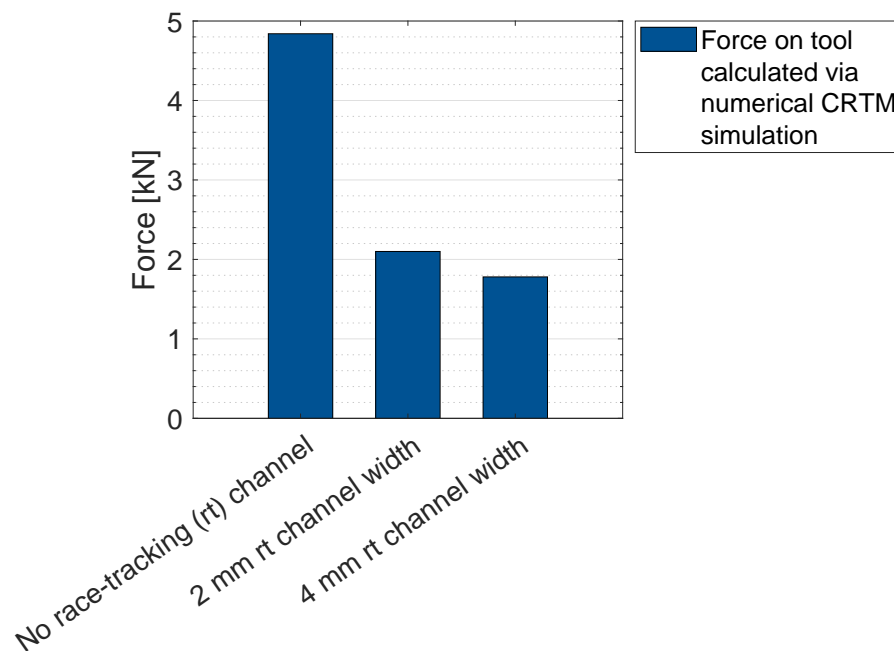


Fig. 4-12 Force on tool at the end of process of numerical simulations without, with a 2 mm and 4 mm wide edge race-tracking channel of the CRTM process configuration 1: small geometrical aspect ratio, high injection gap height and lateral inlet.

It has to be noted that the calculated maximum force values of the simulations with edge race-tracking is overestimating the force due to the assumption of identical compaction behavior of the preform and the edge race-tracking channel, as discussed in Subsection 4.1. In reality the compaction of the fiber-free volume of the race-tracking channel would not result in a compaction force acting on the upper mold except for the component of the acting fluid pressure inside the channel. Nevertheless, this assumption was necessary to ensure a uniform compaction of the preform and race-tracking channel height. Considering that the presented forces for the two simulations with an edge race-tracking channel are overestimated further

highlights the strong force reduction at the end of process between the simulation without and with edge race-tracking.

4.3 Conclusions of the Numerical Race-Tracking Study

The numerical race-tracking study (NRT study) investigated the edge race-tracking effect during CRTM preform impregnation. It was split in two parts, the first of which studied the effect of edge race-tracking at different process configurations. The process parameters (i) geometrical aspect ratio of the preform (length/width versus height), (ii) injection gap height and (iii) inlet position were individually changed on two levels. For each resulting CRTM process configuration a reference simulation without race-tracking was compared to a simulation with a two millimeter wide edge race-tracking channel. The second part of the NRT study investigated the effect of edge race-tracking severity at which simulations of identical process settings were compared only differentiating in the presence and the width of an edge race-tracking channel.

Comparing only the reference simulations without race-tracking of the different investigated process configurations with each other showed that the preform impregnation during the CRTM process with injection gap is of complex character, strongly depending on the specific settings of individual process parameters. The performed simulations showed that besides process design parameters, such as injection gap height, also preform parameters, such as geometrical aspect ratio, strongly influence the exact preform impregnation pattern during the CRTM process. Furthermore, the simulations showed that the resin flow pattern during CRTM is caused by a superposition of in-plane and out-of-plane flow. Generally, two flow phases are present during CRTM processing with injection gap. First, the resin is distributed mainly in in-plane direction above the preform inside the injection gap during which the preform is impregnated mainly in out-of-plane direction from its top surface. The extent of the preform impregnation during this first flow phase depends on predefined process design parameters, at which the preform impregnation increases by e.g. a longer injection time at constant flow rate or an increased injection pressure due to reduced equivalent permeability of the injection gap.

Adjacently, the final complete impregnation of the preform takes place during the second flow phase. The impregnation pattern was observed to occur in two scenarios depending on two specific CRTM process parameters, i.e. injection gap height and geometrical aspect ratio of the preform. Preforms of small geometrical aspect ratio and high injection gap height were shown to be characterized by a complete filling

of the injection gap before the upper mold is in contact with the preform which leads to the development of a final impregnation of the preform by a predominantly out-of-plane resin flow, which correlates well with the CRTM flow description in literature [37, 38]. In contrast, preforms of large geometrical aspect ratio and high injection gap height as well as preforms of small geometrical aspect ratio with low injection gap height, are characterized by a partially filled injection gap at the time at which the upper mold gets in contact with the preform leading to a subsequent equalization of the flow front over the preform's thickness and final preform impregnation predominantly in in-plane direction. While this flow front progression was previously described in [36, 37] for preforms of large geometrical aspect ratio with high injection gap height, the presented NRT study showed that it is also develops for CRTM process configurations with preforms of small geometrical aspect ratio and low injection gap height.

Comparing the simulations of the NRT study without and with edge race-tracking of the different investigated process configurations showed that edge race-tracking drastically changes the preform impregnation during the CRTM process with injection gap. The development of the changed resin flow was traced back to the acting (equivalent) permeabilities in the three flow domains, i.e. injection gap, edge race-tracking channel and preform. Generally, the preform of structural parts are in the fiber volume fraction range of 50% to 60% and is characterized by a permeability which is multiple orders of magnitudes lower than the equivalent permeabilities of the injection gap and the edge race-tracking channel. Therefore, the resin is primarily distributed inside the high-permeable flow domains of injection gap and edge race-tracking channel. The ratio between the equivalent permeability of the injection gap and race-tracking channel defines how strong the flow is advancing in the individual domains due to a higher local flow front velocity, according to Darcy's law (Equation 2-1). A potential advancing flow in one of the flow domains results in a lateral filling of the other two flow domains due to their spacial connection, which is identified as the main cause of the observed changes of the preform impregnation pattern at presence of edge race-tracking. Furthermore, the simulation results of all investigated CRTM process scenarios revealed that the preform is not completely impregnated at the end of the process due to the increased overall porosity inside the cavity as a result of the fiber-free volume of the edge race-tracking channel and the fact that the same resin volume is injected as during the reference simulation without a channel.

The second part of the NRT study showed that edge race-tracking does not only influence the flow pattern during a CRTM process with injection gap, but also has an effect of certain process responses. The equivalent permeability of the edge race-tracking channel was shown to influence the injection pressure of a resin in-

jection at constant flow rate as soon as the flow front reaches the race-tracking channel. The maximum force acting on the upper mold was identified to decrease significantly between simulations without and with race-tracking while the width increase from a two to a four millimeter wide race-tracking channel was shown to only marginally reduce the maximum force. The force reduction is traced back to the reduction of fluid stagnation pressure inside the mold at the end of process resulting of the increased overall porosity inside the cavity at presence of a fiber-free edge race-tracking channel, while the injected resin volume was unchanged between the simulation at absence and presence of edge race-tracking. The reduced final volume filling ratio (VFR), or in other words the size of the formed macro void, at the end of process was shown to increase at increased channel width, while the position and shape of the macro void is dependent on the CRTM process setting always located next to the preform's lastly filled region.

Generally, the NRT study showed that the CRTM flow pattern as well as certain process responses are changed in the presence of edge race-tracking. Even though the change of flow pattern and process responses could not be prevented, it was observed that the initiation of these effects could be delayed by placing the inlet from its lateral position, close to the race-tracking channel, to the center of the preform, furthest away from the race-tracking channel. Furthermore, the simulations show that in the attempt to diminish edge race-tracking effects, it has to be ensured that the filling of the race-tracking channel is not only delayed, but that the preform is majorly impregnated before the resin starts to fill the edge race-tracking channel. Based on the presented simulations of the NRT study, this can be achieved for CRTM process configurations with a central inlet and a small injection gap or with a central inlet and a large preform aspect ratio. These process configurations are characterized by a limited flow inside the injection gap which can be designed to stagnate before reaching the edge race-tracking channel. The subsequent equalization of the flow over the preform thickness and final predominantly in-plane impregnation of the preform are suitable to initiate a preform impregnation pattern that wets out the majority of the preform before filling the edge race-tracking channel. However, the simulations of the presented fourth CRTM process configuration (small aspect ratio of preform and high injection gap height) showed that the relocation of the inlet to a central position is not sufficient enough to prevent a resin flow from the injection gap into the edge race-tracking channel. A potential solution to delay the filling of the edge race-tracking channel could be to spatially separate the injection gap from the edge race-tracking channel. A partitioned upper mold design is anticipated to enable the spatial separation of the two flow domains for CRTM process configurations of small aspect ratio and high injection

gap heights and is investigated in depth in the following numerical flow control study.

4.4 Results and Discussion of the Numerical Flow Control Study

The results of the previous subsection show that edge race-tracking changes the preform impregnation pattern and leads in all investigated CRTM process configurations to a reduced final volume filling ratio of the preform. In this section, a numerical flow control study (NFC study) is presented which investigates a passive flow control strategy for the CRTM process intended to diminish the edge race-tracking effect during the studied CRTM process configuration 4. A numerical simulation was performed and is presented in Subsection 4.4.1 to investigate the flow pattern manipulation of the passive flow control strategy during an idealized CRTM process without edge race-tracking. The potential of the passive flow control strategy to diminish the edge race-tracking effect during CRTM is studied via numerical simulations in Subsection 4.4.2.

4.4.1 Passive Flow Control Strategy during Idealized CRTM Preform Impregnation⁴

The NFC study investigates a strategy to control the resin flow during a CRTM process with injection gap, which is intended to passively guide the flow during preform impregnation, and hence, diminish the edge race-tracking effect. To first analyze the neat resin flow resulting from the applied flow control strategy, a CRTM simulation without an edge race-tracking channel was performed, as illustrated in Figure 4-13.

Firstly, the passive flow control strategy is designed to pre-compact the preform edge to the final part thickness to locally reduce the preform permeability. As seen in Figure 4-13(a), the outer 10 mm of the preform are compacted over the first three coupling steps of the simulation to the final part thickness ($h_{p,f}$). The depicted preform half section of the simulation also illustrates the resulting preform shape in the central preform section below the injection gap where a transition of preform thickness is observed from the reduced height ($h_{p,f}$) of the edge pre-compaction section of 2 mm to the uncompressed preform thickness ($h_{p,u}$) of 2.6 mm at the center of the preform.

⁴ This subsection has been previously published in [140].

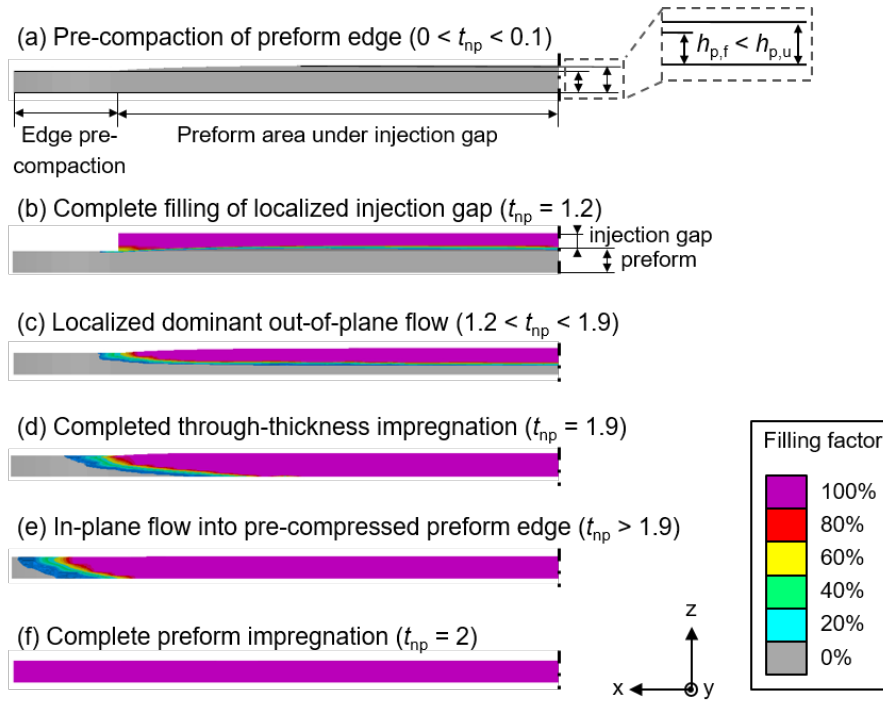


Fig. 4-13 Preform filling pattern during a simulation without an edge race-tracking channel and with applied passive flow control strategy of CRTM process configuration 4: of small geometrical aspect ratio, high injection gap height and, central inlet; normalized process time (t_{np}): injection of 1.5 s between t_{np} of 0 and 1 and compression of 1.73 s between t_{np} of 1 and 2. [140]

Secondly, the flow control strategy intends to inject the resin into a localized, central injection gap. As shown in Figure 4-13(b), the resin fills the highly permeable gap during the injection and at the beginning of the compression phase, while only marginally penetrating the preform. After the central injection gap is completely filled, the ongoing closure movement of the upper mold forces the resin to penetrate the preform mainly in the out-of-plane direction at the preform section below the injection gap and only insignificantly in the in-plane direction outwards into the pre-compacted preform edge, as seen in Figure 4-13(c) and (d). After the central preform section under the injection gap is completely filled in through-thickness direction, a predominantly in-plane flow is initiated, wetting out the remaining dry preform at the edge pre-compaction section, as shown in Figure 4-13(e). The observed preform filling pattern of the CRTM simulation with applied flow control strategy shows a clear tendency to fill a potential race-tracking channel, located at the edge of the preform, late in the filling process.

4.4.2 Effect of Passive Flow Control Strategy on CRTM Preform Impregnation at Presence of Edge Race-Tracking⁵

To investigate the potential of the flow control strategy to diminish the edge race-tracking effect, another simulation was performed which contained a two millimeter wide edge race-tracking channel. Figure 4-14 illustrates the VFR of the flow domains of a reference simulation of process configuration 4, previously presented in the numerical race-tracking study of Chapter 4.2.1, and a corresponding simulation with applied flow control study, both simulations feature edge race-tracking. Besides the difference of the applied flow control strategy, process settings for both simulations are identical.

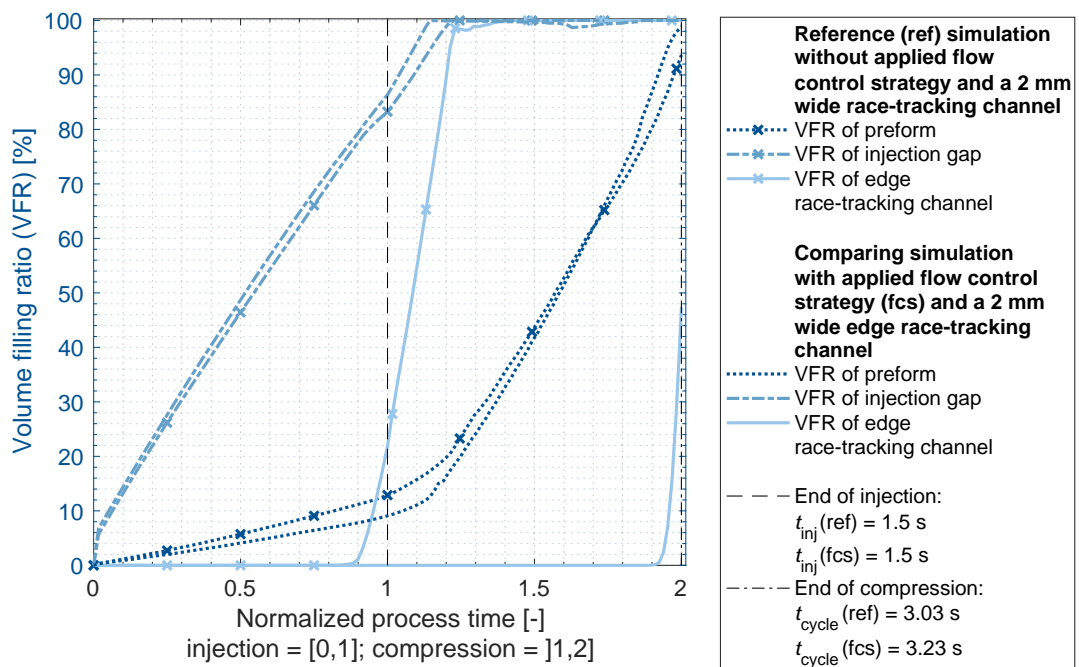


Fig. 4-14 Comparison of VFR between simulations without and with passive flow control strategy at occurrence of edge race-tracking of CRTM process configuration 4: small geometrical aspect ratio, high injection gap height, and central inlet. [140]

For both simulations, the volume of the injection gaps are defined to be identical to the injected resin volume. Therefore, at the simulation with applied flow control strategy, the height of the localized, central injection gap is increased as shown in A-11(b) in Appendix A.2.1. The increased gap height results in a higher permeability of the injection gap according to Equation (2-8) and a reduced injection pressure during injection at constant flow rate, as shown in Figure A-20 in Appendix A.2.3.

⁵ This subsection has been previously published in [140].

The reduced acting fluid pressure, in combination with the reduced overflow preform surface due to the increased gap height, results in a reduced initial VFR of the preform and an increased VFR of the injection gap for the simulation with applied flow control strategy, as recorded in Figure 4-14. The majority of the preform impregnation is observed to occur after complete filling of the injection gap when the VFR of the preform is recorded to rise steeply for each of the two simulations.

A clear difference between the two simulations is observed by comparing the VFR of the race-tracking channels in Figure 4-14. While for the reference simulation the spatial connection between the injection gap and the edge race-tracking channel results in a complete filling of the edge race-tracking channel at the end of the injection and beginning of the compression phase, the applied flow control strategy is shown to delay the filling of the edge race-tracking channel to the end of the compression phase. Furthermore, the applied flow control strategy shows to reduce the final VFR of the race-tracking channel to below 50%. This is attributed to a changed filling pattern of first impregnating the central preform section predominantly in out-of-plane direction and subsequently impregnating the preform edge predominantly in the in-plane direction, filling the edge race-tracking channel late in the process. Due to the reduced final VFR of the race-tracking channel of the simulation with applied flow control strategy, more fluid fills the preform leading to an increased final VFR of the preform of 98.9% compared to 93.7% for the reference simulation for which the race-tracking channel is completely filled.

Additionally, the location of the macro voids are changed, as illustrated in Figure 4-15, from one flat but wide macro void spreading over nearly the complete bottom side of the reference simulation in 4-15(a) to multiple localized macro voids at the outermost radii of the preform for the simulation with applied flow control strategy in 4-15(b).

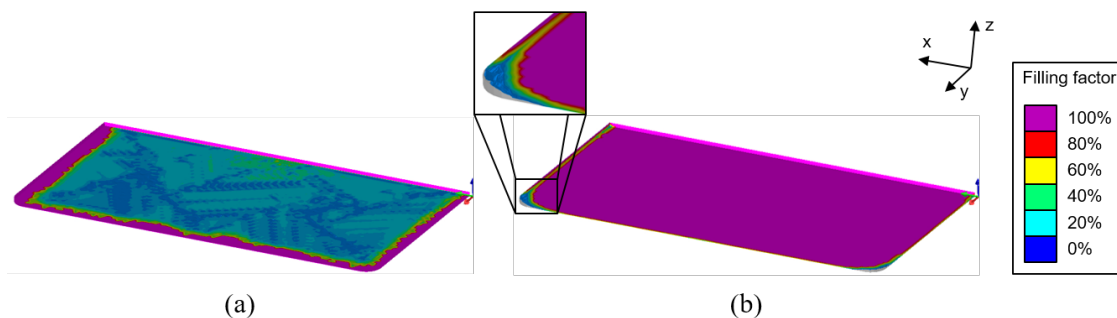


Fig. 4-15 Location of macro void in blue and gray at the end of the process of simulations of CRTM process configuration 4: small geometrical aspect ratio, high injection gap height, and central inlet as well as with edge race-tracking: (a) without passive flow control strategy; (b) with passive flow control strategy. [140]

4.5 Conclusions of the Numerical Flow Control Study⁶

To diminish the edge race-tracking effect at CRTM process configurations of small aspect ratio and high injection gap height, the NFC study investigated a passive flow control strategy at which the upper mold is partitioned. The partitioned upper mold design enables the preform edge to be pre-compacted and to inject the resin into a localized, central injection gap which is spatially not in contact with a potential edge race-tracking channel.

Simulation of the investigated flow control strategy at a preform of small geometrical aspect ratio without edge race-tracking, revealed a passively manipulated flow pattern of central predominantly out-of-plane preform impregnation with a subsequent predominantly in-plane filling of the pre-compacted preform edge. A final CRTM simulation with applied flow control strategy and an edge race-tracking channel confirmed that the spatial disconnection of the localized, central injection gap and the edge race-tracking channel leads to a delayed and reduced channel filling and an increased final VFR of the preform. Furthermore, the position of the reduced macro voids is relocated towards the outer edges of the preform.

While the conventional CRTM process design for preforms of small aspect ratio and with a high injection gap height is shown to be sensitive to edge race-tracking, the investigated passive flow control strategy was demonstrated to diminish the edge race-tracking effect and to increase the process robustness of the CRTM process. Even though the presence of an edge race-tracking channel still causes a slightly reduced final VFR of the preform, the flow manipulation ensures that the majority of the part is impregnated and that formed macro voids are located at the edge of the part, which is often machined off during industrial part manufacturing.

A partitioned upper mold concept, required to enable the flow control strategy for CRTM processes, can be realized by using slider-tooling technology. As discussed in Chapter 2.1.4, one of the main challenges of this technology is the sealing of the sliding tool components. Conventional sealing concepts located in between the sliding tool components may be subject to rapid wear resulting in increased maintenance. Novel sealing concepts, using thin films to seal the preform injection space inside closed mold LCM processes (see Chapter 2.1.3), are a promising solution to enable a seal-free tool design. The enhancement of the conventional CRTM process to be sealed by thin films is studied in depth in the following chapter of this work to overcome current design limitations and to implement the presented passive flow control strategy in industrial manufacturing processes.

⁶ Parts of this section have been previously published in [140].

The presented NRT study and NFC study expands current knowledge of preform impregnation patterns during CRTM with injection gap and provides a flow control strategy to increase process robustness of CRTM with edge race-tracking. Nevertheless, the conclusions derived from the two presented numerical studies have to be verified by experiments which is done for an enhanced CRTM process, the so-called film-sealed compression resin transfer molding process, in Chapter 7 of this work.

5 Enhancement of the CRTM Process

The numerical simulations, presented in the previous Chapter 4, showed promising results to minimize the edge race-tracking effect during CRTM manufacturing via a passive flow control strategy that can be enabled by a partitioned upper mold design. The different sections of the upper mold are intended to be actuated separately from each other to create a pre-compaction of the outer preform edge and a localized, central injection gap which is spatially disconnected from potential edge race-tracking channels. Such a mold design can be enabled via the slider tooling technology. However, slider tooling is known to be difficult to be sealed in conventional tool designs (see Chapter 2.1.4). Therefore, an innovative sealing method for the CRTM process is analyzed in this chapter by using film sheets to seal the injection space enabling to design seal-free molds. The effect of an integration of the film material in CRTM manufacturing is studied in the Subsection 5.1 on an abstract level via a function analysis. The derived abstract model of the novel process variant, the film-sealed compression resin transfer molding (FS-CRTM) process, is then, in Subsection 5.2, transferred into a concrete concept by defining a sequence of process steps which shows the practical integration of the film.

5.1 Function Analysis of Film-Integration into CRTM

The following section presents a function analysis of CRTM manufacturing to visualize and clarify the effect which an integration of a film material has on the process. The analysis was done by using aspects of the methodology of TRIZ which abbreviates the “theory of innovative problem solving”. In 1946 Genrikh Saulowitsch Altschuller started to analyse patents to identify systematic patterns which has led to the TRIZ methodology of innovative problem solving. Altschuller and his colleagues identified that technical systems develop in certain patterns and that inventions require the overcoming of contradictions. Furthermore, their investigations showed that a large amount of inventions are based on a relatively small amount of solution principles. Based on Altschuller et al.’s studies, a collection of TRIZ methods has evolved which cover the aspects of problem understanding and solving. [146–149]

One method of TRIZ is the function analysis which examines a system by modeling its components and their interactions on an abstract level. Depending on the goal of the specific function analysis, the focus can be set differently. [147] In the

context of this work, the focus of the performed function analysis is how a new feature (the film) can be integrated in a system (CRTM manufacturing) and which effect this new feature has on the interactions of the system. According to [147] the function analysis consists of three steps, (i) the component analysis, (ii) the interaction analysis and (iii) the functional modeling. By identifying useful and harmful functions in the functional model and by using it as the baseline for the subsequent analysis of component trimming, the effect of film-integration in CRTM manufacturing is assessed.

At the beginning of the component analysis, the system “CRTM manufacturing” is modeled on an abstract level via a tree diagram to identify the abstraction level of the function analysis. The tree diagram, presenting the core components¹ of the system “CRTM manufacturing”, is depicted in Figure A-21 in Appendix A.3. The third level of the tree diagram was chosen as abstraction level of the function analysis. At this level the so-called super system is located on which the analysis focuses. The film-integration is intended to seal the impregnation space inside the mold. Therefore, the system “mold”, which includes the component sealing in the conventional CRTM manufacturing, is chosen as technical system. The technical system is assessed in detail by including all its sub-components in the function analysis. The main-function of the technical system “mold” was identified to “shape” the resin system into the form of the future part. Therefore, the component resin system of the super system is defined as target. Figure 5-1 presents the outcome of the component analysis illustrating the correlation of the technical system to the target in the first row and listing all components of the technical system and super system, which surround the technical system.

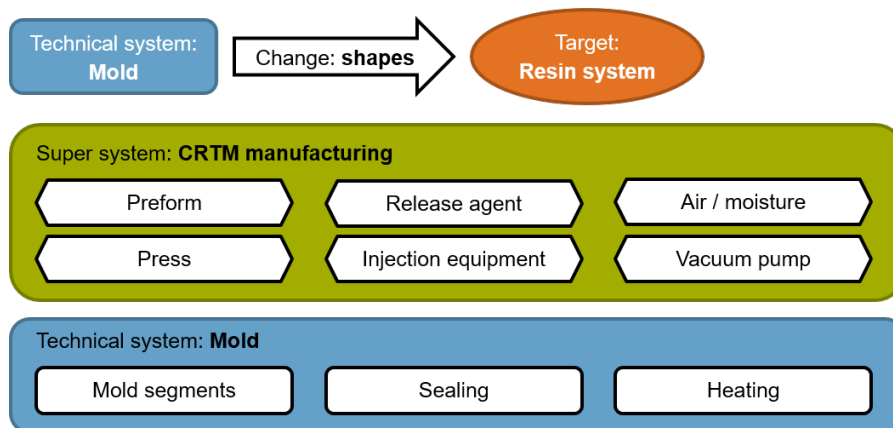


Fig. 5-1 Component analysis: Illustration of the main-function of the technical system (top row) and listing of components of the super system (green) as well as the technical system (blue).

¹ A component is an element or part of a technical or super system [147].

The three sub-components of the mold (mold segments, sealing and heating), the target component (resin system) and the six components of the super system (preform, release agent, air / moisture, press, injection equipment and vacuum pump) are now included in the second step of the function analysis, the interaction analysis. During this analysis step, all interactions² of the components of the technical and super system, as well as of the target component are identified. Figure A-22 in Appendix A.3 presents the interaction matrix which shows which components interact with each other.

The functional modeling is the third step of the function analysis. A model of the technical system is targeted in which all previously identified interactions are transferred into directed functions³. Figure 5-2 presents the functional model of the technical system “mold” (blue) surrounded by the super system “CRTM manufacturing” (green) including the target “resin system” (orange). The functions are depicted by arrows between two components. Each arrow shows the direction of the function going from the function owner to the object of the function at which a parameter is changed or maintained. The specific action of each function is noted above its arrow.

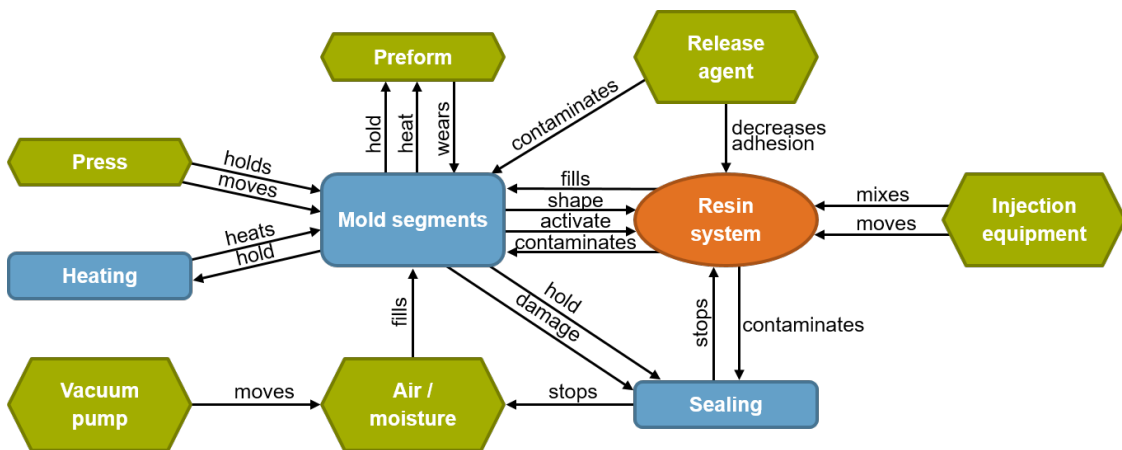


Fig. 5-2 Functional model of the technical system “mold” (blue), the target “resin system” (orange), and the super system “CRTM manufacturing” (green) including all interactions between the individual components. [25]

After all functions are now identified and visualized in Figure 5-2, each function is evaluated and categorized as a useful or harmful function. Figure 5-3 depicts the outcome of the categorization of the functions, presenting useful functions as black

² An interaction specifies that two components are connected (e.g. in terms of space or signal) [147].

³ A function is an action of a component which targets to change or maintain a parameter of another component [147].

arrows and harmful functions as red dashed/dotted arrows. The identified harmful functions are:

- **Preform – wears – mold segments:** Preforms are generally cut to completely fill the cavity during CRTM manufacturing. When the matched mold is closed, fibers or fiber bundles can be trapped between the mold segments. This so-called fiber pinching is reported to damage and wear the mold segments over time. [34]
- **Release agent / resin system – contaminates – mold segments / sealing:** Release agent is used to decrease the adhesion of the resin system to the mold segments and to ease the removal of the cured part. A thin layer of release agent is present between resin system and mold segments during curing. After the cured part is removed from the mold, residues of the release agent can remain on the mold segments which contaminates them over time. Furthermore, sections of cured resin can remain on the mold surface or on the sealing material which also leads to contamination. [34]
- **Air / moisture – fills – mold segments:** Air or moisture inside the mold and the containing preform can lead to void formation during the preform impregnation and subsequent part curing which reduces the mechanical performance of the part. [150, 151]
- **Mold segments – damage – sealing:** Improper placement of the sealing inside the mold can damage the sealing by e.g. pinching which bears the risk of increased wear of the sealing or in the worst case that the mold is no longer air- and liquid-tight during manufacturing.

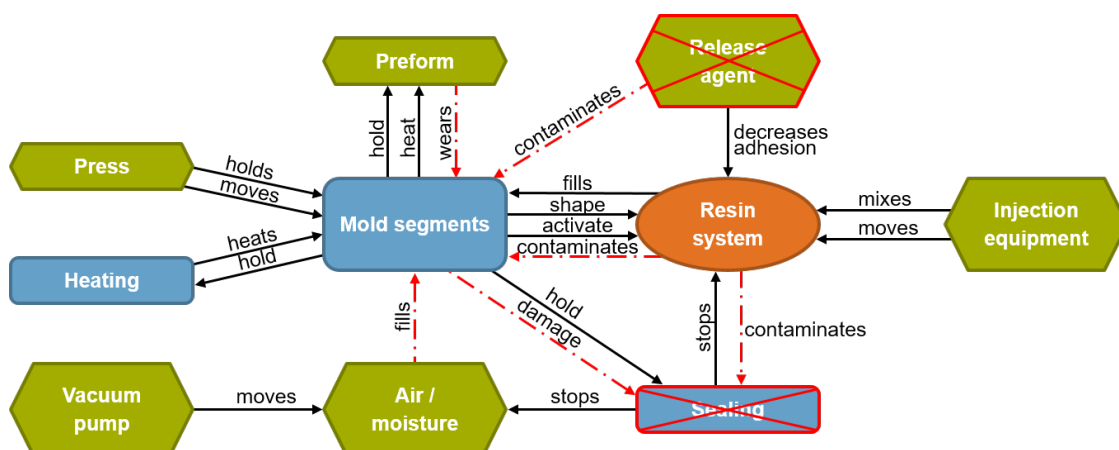


Fig. 5-3 Classification of useful (black arrows) and harmful (red dashed/dotted arrows) functions as well as components to be trimmed (crossed out in red) of the technical system “mold” and the super system “CRTM manufacturing”. [25]

To enhance the CRTM manufacturing, a film is intended to be integrated in the process to seal the preform injection space inside the mold. The trimming approach was applied to identify components in the presented functional model of the CRTM manufacturing which can be replaced by a new “film-sealing” component. The trimmed components, which are crossed out in red in Figure 5-3, are:

- **Sealing:** If the film seals the complete injection space inside the mold, the mold does not need to be air- and liquid-tight making the component “sealing” of the technical system “mold” redundant.
- **Release agent:** As a barrier layer between the resin system and mold segments, the film separates them from each other leading to a case in which no release agent is needed if the film by itself does not adhere to the resin system.

Figure 5-4 presents the enhanced functional model of the CRTM manufacturing in which the new component “film-sealing” is integrated into the super system. The abstract model of the film-sealed compression resin transfer molding (FS-CRTM) process illustrates the main benefits which a film-integration provides for the CRTM manufacturing. Even though an additional component, the film-sealing, was added in Figure 5-4, two components, the release agent and mold sealing, of the conventional CRTM manufacturing model (Figure 5-3) could be taken out. A tree diagram listing all components of the novel FS-CRTM process is presented in Figure A-23 in Appendix A.3.

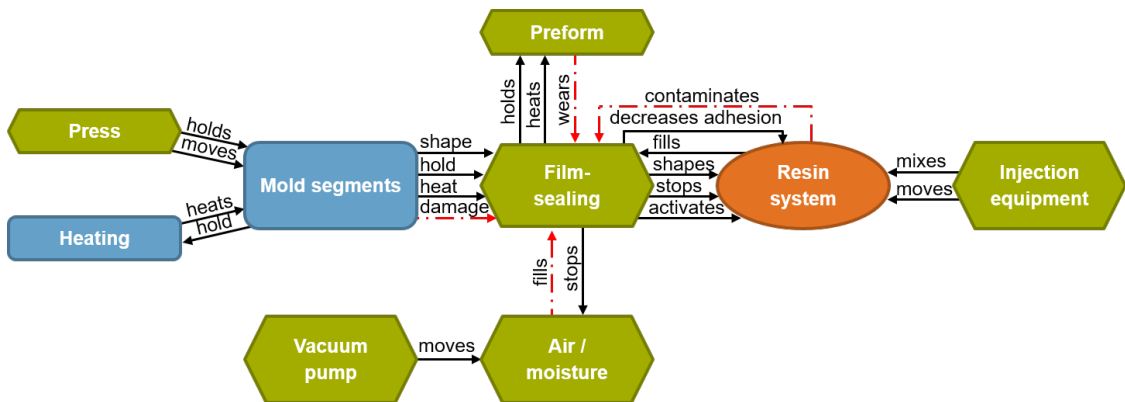


Fig. 5-4 Enhanced functional model of the CRTM manufacturing at which the new component film-sealing is integrated, entitling this process variant the film-sealed compression resin transfer molding (FS-CRTM) process. [25]

The use of release agent is made obsolete at the FS-CRTM process due to the spacial separation of the resin system and the mold segments, visualized in Figure 5-4 by no directly connecting function between these two components. The resin system and the mold segments are now linked by the new component, film-sealing. The

film is intended to be designed to decrease an adhesion to the resin system due to its chosen material type. Thus, the film takes over the former function of the release agent to “decrease adhesion”, as illustrated in Figure 5-4. Furthermore, a sealing of the mold itself is redundant due to the intention of the film to seal the injection space air- and liquid-tight inside the mold. In this context, the film-sealing component is shown in Figure 5-4 to fulfill the functions to “stop” the resin system as well as to “stop” air / moisture, which was previously carried out by the component “sealing” of the system “mold”. Therefore, the FS-CRTM process enables the use of seal-free molds which increases the design freedom of these molds. A seal-free mold eases the integration of known technologies, such as slider tooling, into the automated manufacturing of fiber-reinforced plastic (FRP) parts. Today at conventionally sealed molds, the slider tooling technology is only used to a limited extent due to specific drawbacks. One drawback is an increased effort needed to seal sliders. Another drawback is the increased wear of conventional sealing concepts due to increased friction between movable mold sections (slider) which leads to increased maintenance effort and costs. Especially in regard to the processing of low-viscosity thermoset resin systems, these drawbacks bear major challenges in enabling an economical production without long mold downtime. Via a film-sealing of the preform impregnation space inside the mold, the discussed limitations of the slider tooling technology are eliminated due to the enabled seal-free mold design. This eases the design of tooling concepts which can create the, in Chapter 4 suggested, partitioned upper mold design to pre-compact the outer preform edge while creating a central, localized injection gap which is spatially disconnected from potential edge race-tracking channels.

Figure 5-4 also depicts that all harmful functions of the FS-CRTM process model are directed towards the new film-sealing component. While in conventional CRTM manufacturing, the preform is in direct contact with the mold segments, the film-sealing separates them during FS-CRTM. Therefore, pinched fibers bear now the risk of wearing the film-sealing instead of the mold segments. The identified harmful function of the preform wearing the film-sealing is not only a limitation but can be also seen as an opportunity. If the thickness of the film is chosen to be much thicker than a fiber or fiber bundle, the film can be designed as a buffer which compensates for fibers or fiber bundles pinched between mold segments due to the film’s elastic and plastic deformation behavior. This enables to increase the service life of the mold and reduce preform cutting and placement tolerances.

However, the in Figure 5-4 illustrates a direct contact between the mold and the film-sealing which can lead to damage of the film-sealing at improper handling. If for example wrinkles are formed in the area between two touching mold segments at which film material overlaps, the film can be thinned or even torn in this area

causing a loss of its sealing function and an increased risk of an unsuccessful preform impregnation.

As a barrier layer between resin system and mold, the resin is never in contact with the mold segments during the FS-CRTM process and contaminates only the film-sealing. The discussed three harmful functions of film-wearing, damaging and contamination suggest that the film should be used as a sacrificial material during the FS-CRTM process to take up the presented harmful functions and, therefore, increase the robustness of the process and its manufacturing equipment compared to conventional CRTM. However, this also implies that the film can only be used for a limited amount of manufacturing cycles or even be designed only as a single-use sealing concept which is changed for each manufactured part. If the latter is done, and the film-sealing is not intended to be reused, neither the tool nor the film needs to be cleaned of any contamination, reducing the mold cycle time by the time needed for cleaning.

The last harmful function illustrated in the functional model of the FS-CRTM process in Figure 5-4 is the filling of the film-sealing by air or moisture. Because the preform impregnation takes place inside the film-sealing, this space should be free of air- and moisture to minimize the formation of voids which could reduce the mechanical performance of the finished part. However, the functional model in Figure 5-4 shows that during the FS-CRTM process, not the mold needs to be evacuated but the film-sealing which is a component of the super system, surrounding the mold. Therefore, the FS-CRTM process can be designed so that the evacuation of the preform inside the film-sealing takes place in an upstream process step, which reduces the mold cycle time by the time needed to evacuate the mold during conventional CRTM processing. According to [152, 153] the mold evacuation and cleaning accounts for 20% to 30% of the total mold cycle time. This shows the potential of the FS-CRTM process to gain not only in practicality by focusing all harmful functions in a disposable film-sealing, but to gain also in cost-efficiency by reducing the mold cycle time during the manufacturing of FRP parts.

5.2 Process Concept of the Film-Sealed Compression Resin Transfer Molding (FS-CRTM) Process⁴

The previous section derived a functional model of the film-sealed compression resin transfer molding (FS-CRTM) process on an abstract level. In the following section, the presented abstract solution is transferred into a concrete concept of

⁴ Parts of this section has been previously published in [25].

the FS-CRTM process. The core aspect of the FS-CRTM process is the integration of film material to seal the preform injection space inside the mold. Figure 5-5 illustrates the principal steps of the FS-CRTM process as it is defined in the context of this work. Note that this is one out of many possible ways how a film can be integrated into the CRTM process and that the presented concept is based on the successfully verified Film-RTM process by Häffelin [24] (see Chapter 2.1.3).

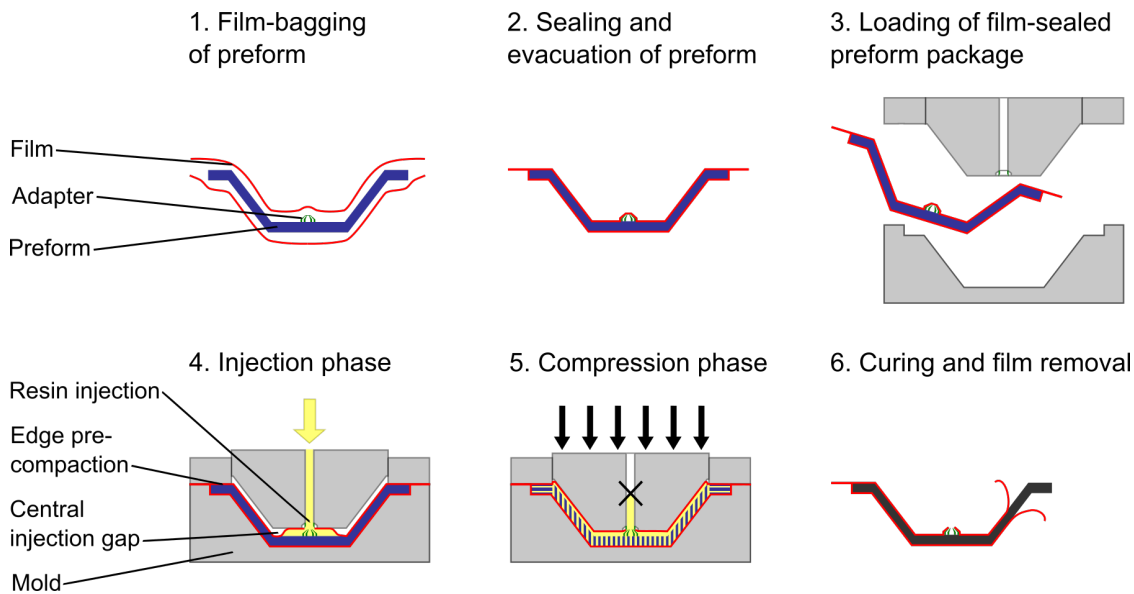


Fig. 5-5 Schematic illustrating the principal steps of the film-sealed compression resin transfer molding (FS-CRTM) process. [25]

To exploit the full potential of the FS-CRTM process, the preform encapsulation and evacuation is done in an upstream process step prior to molding. At the first FS-CRTM process step the preform is bagged within film sheets, as illustrated in Figure 5-5. Additionally, as preparation for later process steps, adapters to evacuate the preform and to inject the resin into the film-sealed preform package during molding can be placed in-between the films. During the second process step, the films are sealed by welding, enabling an evacuation of the preform prior to placing the film-sealed preform package inside the mold (third step). Due to the advantage of the tool not needing to be sealed, more complex tool designs can be created using, for example, slider tooling technology. The slider tooling technology enables for example the production of FRP parts with undercuts in an automated way or to create the passive flow control strategy suggested in Chapter 4. This passive flow control strategy can be implemented by a partitioned upper mold design which enables the pre-compaction of the outer preform edge while the resin is injected into a localized, central injection gap, as illustrated at the fourth step in Figure

5-5. During the injection phase, the film is penetrated, and the resin is injected into the film-sealed preform package. Due to the elastic behavior of the film, it can lift off the preform and expand to allow the resin to be easily distributed inside the injection gap. During the subsequent compression phase, the tool is closed further, distributing the resin to fill the complete preform, as illustrated in the fifth process step in Figure 5-5. Since the film acts as a barrier layer between the preform impregnation space and the cavity wall, the film seals the tool and, additionally, enables a release agent-free FRP production. While the film is used in the context of this work solely as a process aid material, which is intended to be removed after the part is cured (step 6 in Figure 5-5), it can also be designed to co-cure with the resin and remain on the part as a functional layer to enable, for example, a weldable part surface or an integration of sensors [31], as discussed in Chapter 2.1.3.

6 Characterization of the FS-CRTM Process

As presented in Chapter 2.1.3, films have been introduced in various closed mold LCM processes to fulfill different functions. The concept of a novel CRTM variant is presented in the previous chapter at which the film is intended to seal the injection space inside the mold. The so-called film-sealed compression resin transfer molding (FS-CRTM) process concept defines that the preform is film-sealed prior to its placement inside the mold and the resin is injected into the film-sealed preform package. The following chapter aims at characterizing the novel FS-CRTM process.

To successfully implement a film material in an industrial manufacturing process, the film needs to be designed and selected based on requirements of the specific process. Therefore, the first Subsection 6.1 presents the specification of a film material to be used in FS-CRTM manufacturing under industrial conditions. In the context of this work, the FS-CRTM process is intended to be characterized on a laboratory scale via flow visualization experiments. While snap-cure resin systems, as intended to be used during industrial FS-CRTM manufacturing, are processed at elevated temperatures, the flow visualization experiments are performed at ambient temperature to reduce the complexity of the experiments. Thus, a second film material is additionally specified in Subsection 6.1 for the FS-CRTM flow visualization experiments that has comparable characteristics at room temperature than the chosen film for industrial FS-CRTM manufacturing has at elevated process temperatures.

The FS-CRTM concept, as drafted in Chapter 5.2, is based on the CRTM-2 concept (see Chapter 2.1.1) at which the resin is injected into an empty space between preform and upper cavity wall, denoted “injection gap”. To enable a distribution of the resin inside the injection gap, the film, encapsulating the preform, has to be flexible enough to be deformed by the acting fluid pressure and to adapt to the shape of the cavity walls limiting the injection gap above the preform. The film deformation inside the cavity could not be monitored with the available test equipment, which is why experiments were performed in which the upper mold setup was removed to enable a monitoring of the unrestrained film deformation. The unrestrained film deformation experiments are intended to verify the required flexibility of the chosen film material to adapt to the inner cavity walls limiting the injection gap and enable a FS-CRTM injection into an injection gap.

As previously stated, the film acts as a barrier layer during the FS-CRTM process to seal the preform impregnation space inside the mold. Due to the film’s flexibility, a

pressure gradient acts across the film resulting from the pressure level on the film's inner surface (inside the film-sealed preform package) and the ambient pressure acting on the film's outer surface. This pressure gradient across the film is a newly introduced phenomena of the FS-CRTM process which is not present during the conventional CRTM process. The pressure gradient is expected to e.g. compact the preform prior to the injection and lift the film off the preform during the injection. Thus, the characteristics of the complete process could be changed due to the film integration. In this context, Subsection 6.3 presents a study to identify factor-response correlations of the FS-CRTM process to establish guidelines to control the novel process.

6.1 Film Material for the FS-CRTM Process

The first part of this chapter to characterize the newly developed film-sealed compression resin transfer molding process focuses on the specification of a film material to be integrated in the CRTM process. Films used in fiber-reinforced material (FRP) manufacturing often consist of material blends or layers of different materials in order to combine specific characteristics of the individual materials as needed for the desired application [65, 66]. Therefore, in the first step of the presented film specification, a literature study is performed to identify polymer materials suitable for use as film materials in the FS-CRTM process. Further, four monolayer films of pure material types were analyzed by performing different test methods comparing the films according to the defined requirements needed to be integrated in the FS-CRTM process. In a second step, the most suitable materials were combined in a multi-layer film to create an improved solution for FS-CRTM manufacturing.

Further on, flow visualization experiments are planned to characterize the FS-CRTM process. As presented in Appendix A.4, specific laboratory equipment has been developed, which operates at different service conditions than would occur during FS-CRTM manufacturing. To simulate the real FS-CRTM process as closely as possible, a second film needs to be identified that shows similar mechanical behavior during flow visualization experiments as does the multilayer film during FS-CRTM manufacturing.

6.1.1 Materials and Methods of Film Specification¹

Materials

In total, six film types are investigated in this section, five monolayer films and one multilayer film. The films are briefly presented in this subsection and further characterized in the following results and discussion subsection. First, monolayer films of pure material types typically used in FRP manufacturing were studied for their suitability in the FS-CRTM process. These are:

- polypropylene (PP) films, manufactured by Profol (Halfing, Germany), type TA201-2017 and type PB77AB, both with 0.1 mm thickness, were used for welding tests and antistick investigations, respectively, and type TT01AC with 0.08 mm thickness for other remaining tests
- a polyamide (PA), more specifically PA6, film of 0.1 mm thickness manufactured by mf-Folien (Kempten, Germany)
- a polyvinyl fluoride (PVF) film of 0.051 mm thickness type Tedlar[®] MR 20 SM 3 manufactured by DuPont (Buffalo, NY, USA)
- a thermoplastic elastomer (TPE) film of 0.04 mm thickness type Flex^{PLAS[®]} manufactured by Infiana (Forchheim, Germany)

Furthermore, a multilayer film of 0.1 mm thickness is analyzed to be used in FS-CRTM manufacturing. The film, manufactured by Profol (Halfing, Germany), is composed of a PA and a PP layer with thickness of 0.075 mm and 0.02 mm, respectively, joined by a bonding agent layer of 0.005 mm thickness. Finally, a polyethylene low density (PE-LD) film of 0.1 mm thickness is investigated for its use for the flow visualization experiments, manufactured by Sokufol (Limburg, Germany).

Experimental Methods

Differential Scanning Calorimetry

Differential scanning calorimetry (DSC) was employed to thermally analyze the materials and identify physical or chemical transformations at constant pressure. Specifically, for the film specification development for the FS-CRTM process, DSC measurements were performed to determine the melting temperature of the thermoplastic materials, which is indicated by a physical and endothermic transformation of the material from a solid crystalline to a liquid amorphous state. While

¹ This subsection has been previously published in [154], except for “Experimental Methods” – “Stress Relaxation”.

thermoplasts are characterized by a melting temperature range, the peak melting temperature T_{pm} , i.e. the point at which the majority of crystallites of the thermoplastic material melts, is used in this work to compare the different film materials. This temperature is henceforth referred to as melting temperature T_m . [155–157] To perform the measurements, DSC equipment type Q200 (TA Instruments, New Castle, DE, USA) was used. Multiple layers of film material were stacked to fill each sample pan of comparable weight. All samples were heated twice and cooled once at a defined rate. The melting temperature was evaluated using TA Universal Analysis software (TA Instruments). The melting temperature was taken from the second cycle in order to exclude material history effects. The test parameters of the DSC measurements were set as follows:

- Sample weight (without pan) = 5–7 g
- Heating rate = +10 °C/min
- Cooling rate = -10 °C/min
- Temperature limits = > 50 °C above and below the material's expected melting temperature range as found in the technical literature [158]

Dynamic-Mechanical-Thermal Analysis

Dynamic-mechanical-thermal analysis (DMTA) was employed to assess the mechanical properties as a function of temperature and to establish transition temperatures of the investigated materials. Tensile tests via forced vibration were performed applying a small sinusoidal strain load to a sample to elicit a stress response. By tracking both mechanical load and deformation, the viscoelastic² material behavior of the polymer materials was characterized by measuring the complex modulus E^* , which consists of the storage modulus E' (indicating stiffness of the viscoelastic material) and the loss modulus E'' (indicating the energy dissipation during oscillatory loading). [159, 160] DMTA equipment type Q800 (TA Instruments) was used for the analysis of all investigated films. To ensure linear viscoelastic material behavior over the investigated temperature range, strain and frequency sweeps were conducted for each film at the lower and upper limit of the presented temperature range, defining a common strain amplitude and frequency for all tests. Besides storage and loss modulus, the glass transition temperature T_g of the materials was detected via DMTA measurements. Similar to the melting transition, the transition from the glassy state to the rubber-elastic plateau in thermoplastic materials also occurs over a temperature range [159]. In the context of this work, T_g was determined via the peak of the loss modulus curve, evaluated

² Viscosity describes the characteristic properties of fluid while elasticity describes characteristic properties of solid bodies. Polymer materials are characterized by a combination of both property spectra called viscoelasticity.

in the TA Universal Analysis software. All DMTA measurements performed in this study adhered to the standard DIN EN ISO 6721-1 [161] with the following specific test parameters:

- Sample width = 6 mm
- Free clamping length = 20 mm
- Strain amplitude = 0.08 mm
- Frequency = 1 Hz
- Heating rate = 3 °C/min
- Starting temperature = -50 °C
- End temperature = 20 °C below melting temperature of specific material

Antistick Investigation

Film antistick properties were investigated by two test series. First, the solubility of the films in epoxy resin systems was investigated via thermo-optical analysis. During the thermo-optical experiments, images were captured using a microscope to examine a film sample that was exposed to an uncured resin system, or to one of the individual components of the resin system, while a thermal load was applied. The setup for the thermo-optical analysis is shown in Figure 6-1(a). A hot-stage (type HS82, Mettler Toledo, Columbus, OH, USA) was placed under the microscope (type BX 41M-LED, Olympus, Tokyo, Japan). Using the hot stage control device (type HS 1), samples inside the hot stage were heated at maximum heating rate of 20 °C/min to 80 °C or 120 °C and held isothermally for 21 minutes or 4 minutes, respectively. Potential swelling or dissolution of the film samples was qualitatively and quantitatively investigated using the Stream Motion software (Olympus).

As shown in Figure 6-1(b), the film samples were specially prepared for the thermo-optical analysis to ensure that no voids or bubbles were created during heat application, which would have disturbed the observation. First, a thin layer of sealant tape [162] was bonded to a slide. The center of the squared sealant tape was cut out and removed as shown in Figure 6-1(b). A 5 mm long by 0.4 mm wide film sample was placed in the center of the sealant tape and covered by a coverslip, creating a small cavity. The test fluid, i.e, resin, hardener or the mixed resin system, was degassed and injected into the cavity via a syringe shortly before each experiment.

The second test series used peel tests to investigate the films' antistick properties. To simulate a manufacturing environment that closely mimics the FS-CRTM process, one layer of film was placed inside a cavity as the lower layer of a pre-form impregnated via the wet compression molding process. Plates of 530 mm × 280 mm were manufactured at process temperatures of 80 °C and 130 °C. Peel

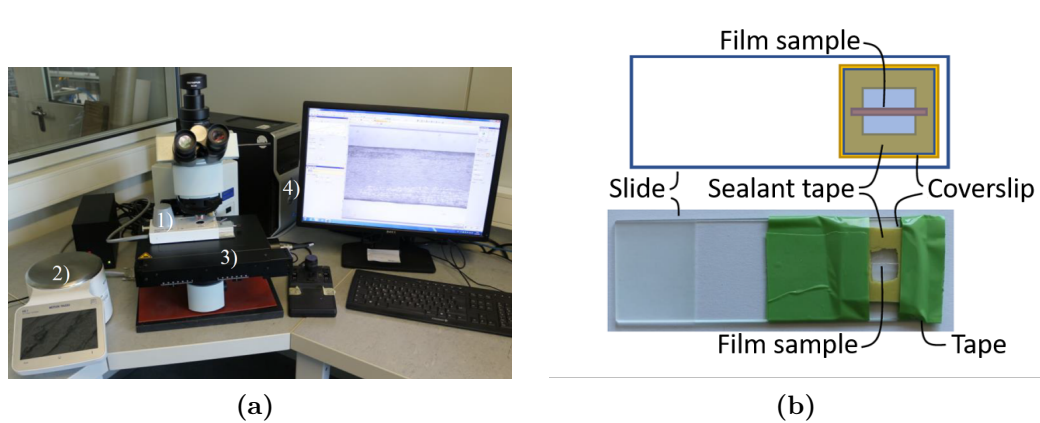


Fig. 6-1 (a) Test equipment of solubility investigations: 1) hot stage, 2) control device of hot stage, 3) microscope with positioning table and 4) data acquisition and control computer of microscope; (b) Setup of sample for solubility investigations. [154]

test samples of 240 mm length, 50 mm width and 2 mm thickness were cut from the manufactured plates. The rig for the peel tests was manufactured after [163] in analogy to the standard DIN EN 1939 [164] and mounted in a universal testing machine (Inspekt table 100, Hegewald & Peschke, Nossen, Germany). The film was peeled off the FRP specimen over a distance of 130 mm, under an angle of 90° and with a velocity of 5 mm/s. The force was recorded via a 20 N load cell (type S2M, Hottinger Baldwin Messtechnik, Darmstadt, Germany).

Welding Tests

As introduced in Chapter 5.2, the FS-CRTM process concept intends to seal the films via welding. The testing of different welding techniques to weld films is described in [165]. It was concluded that impulse welding is the most suitable technique from among those investigated. Based on these results, impulse welding was chosen for the film-sealing of the preforms for FS-CRTM.

Impulse welding equipment hpl ISZ 450 (Hawo GmbH, Obrigheim, Germany) was used for the welding tests presented in this work. This impulse welding equipment can be continuously adjusted at its pulse generator. Measurements were performed on the equipment showing a maximum achievable welding temperature of up to 220°C . Two film sheets of $200\text{ mm} \times 100\text{ mm}$ were stacked and welded on all four sides. The manual welding equipment was modified with a limit stop to ensure repeatable pressure application between the experiments. At a defined level of the pulse generator, the equipment indicates the end of the welding process by sounding an acoustic signal, after which the pressure was maintained for another ten seconds to enable the equipment and sample to cool. All experiments were repeated five times except for the PVF film due to a limited quantity of available sample material. The quality of the welding seam was investigated optically using

a digital microscope with a nine mega pixel resolution (MIRAZOOM MZ 902, OWL Tech Limited, Hong Kong, China). Furthermore, manual peel tests were performed to subjectively investigate the weld seam strength.

During the FS-CRTM process, the weld seam is intended to be air- and liquid-tight. While air tightness is difficult to be measured, the standard ASTM F1929 [166] provides a quick and effective method to test liquid tightness of weld seams. Employing a so-called dye-test, a colored fluid of low viscosity (dye) is injected in between the two welded films and manually pushed toward the weld seams. Without further pressure, untight or permeable weld seam sections can be identified using dye permeation through the weld seam due to capillary forces. The tightness of the weld seam was investigated and documented using the digital microscope (MIRAZOOM MZ 902).

Stress Relaxation

According to Ehrenstein [159], relaxation describes the time-delayed recovery of a material's equilibrium state after a load has been applied. Under static loading, polymer materials behave viscoelastically, observed by its time- and temperature-dependent response. Creep and relaxation tests are common methods used to investigate the viscoelastic response of a polymer material to a defined stress or strain load, respectively. [155, 160, 167]

In the context of this work, relaxation tests under tension load are performed to compare the chosen multilayer film under FS-CRTM manufacturing conditions with the substitution film for the flow visualization experiments under experimental conditions. Figure 6-2 illustrates a schematic strain- and stress-curve of the performed stress relaxation tests under tension load presented in this chapter. During phase I, the specimen is loaded by a constant strain rate to the desired testing load level of the test. During phase II, the strain is kept constant, and the declining stress response is recorded, as shown in Figures 6-2(a) and (b), respectively. After a defined period of time, the sample is unloaded at the beginning of phase III by lowering the acting force to a minimal static force of 0.001 N, as shown in Figure 6-2(b). This load level is low enough to assume that it does not influence the material's strain recovery but is great enough to keep the film under slight tension and ensure a meaningful recording of the strain recovery during phase III, as shown in Figure 6-2(a).

All stress relaxation tests under tension load were performed using the relaxation test program of the DMTA equipment type Q800 (TA Instruments). Samples of the identified PA/PP film to be used for FS-CRTM manufacturing were tested at its lower and upper process temperatures. The material behavior of the PA/PP film was compared with its substitution PE-LD film for the flow visualization experi-

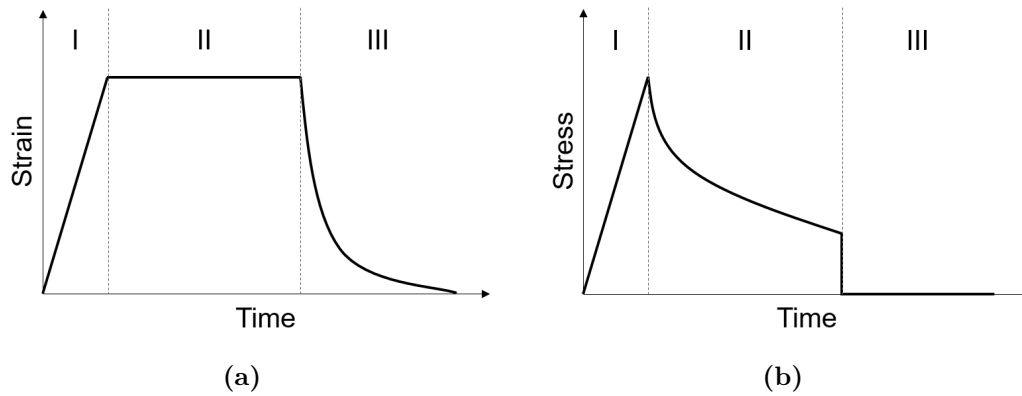


Fig. 6-2 Schematic illustration of strain (a) and stress (b) during the three phases of a stress relaxation test: (I) load increase, (II) constant strain loading and (III) strain recovery.

ments performed at ambient temperature. Tests were performed at four different strain levels and all test scenarios were repeated five times, except when testing the PA/PP film at the upper process temperature, which was repeated ten times due to observed increased fluctuation in the recorded responses. The test parameters for the performed stress relaxation tests were as follows:

- Sample width = 6 mm
- Free clamping length = 20 mm
- Temperature = 80 °C and 120 °C for PA/PP film, 23.5 °C for PE-LD film
- Isothermal holding phase of temperature before test = 300 s
- Strain rate = 1%/s
- Strain load = 1%, 2%, 4% and 6%
- Loading time (phase I and II) = 30 s
- Strain recovery time (phase III) = 360 s

6.1.2 Results and Discussion of Film Specification for FS-CRTM Manufacturing³

The film-sealed compression resin transfer molding (FS-CRTM) process is a newly developed process which introduces a film material in the conventional compression resin transfer molding process to seal the preform impregnation space inside the mold. In Chapter 5.1, a functional analysis of the film integration into the CRTM process is presented and the principle FS-CRTM process steps are introduced in Chapter 5.2. Based on the process design presented in these two chapters, the

³ This subsection has been previously published in [154].

following requirements are derived for a film to be integrated in the FS-CRTM process, which are further explained and discussed in the subsequent subsection:

1. Weldability
2. Elasticity
3. Thermal stability
4. Low gas permeability of air
5. Antistick properties to epoxy resin systems
6. Cost efficiency

The newly developed FS-CRTM process requires the preform to be encapsulated by polymeric films which are welded together to seal the preform air- and liquid-tight (i.e. first requirement). The polymer type as part of the film specification is limited to thermoplasts and thermoplastic elastomers, since these are weldable due to their specific molecular structure [168–170].

After film-sealing and evacuation, the preform package is placed inside the mold as schematically illustrated in Figure 5-5 in Chapter 5.2. The resin is then injected into the film-sealed preform package, forcing the film on the top side of the preform to lift off so that the resin inside the injection gap can be distributed. Once the injection gap has been completely filled, the film that initially covered the top of the preform is deformed to conform to the upper shape of the injection gap as limited by the mold. During the compression phase, the injection gap is closed and the film surface is forced to its original smaller size. The film material requires a certain elasticity to accommodate this deformation.

The elasticity of polymer materials, more specifically the linear viscoelastic behavior, is temperature dependent, which is assessed via the DMTA method. The requirement of high reversible elasticity of the film material (i.e. second requirement), needed to accommodate the deformation during the FS-CRTM injection and compression phase, is best fulfilled while using a film at a temperature of its rubber-elastic state. Thermoplastic polymers can be characterized as having amorphous and semi-crystalline structures, which exhibit different material properties, including temperature-dependent viscoelastic behavior. Typically, the storage modulus of amorphous thermoplasts drops at the glass transition to such a low stiffness that it is commonly recommended that these materials be used only in their glassy state. Semi-crystalline thermoplasts are characterized by a less drastic drop in stiffness at the glass transition due to a crystalline phase. The storage modulus of semi-crystalline thermoplasts at the rubber-elastic state that meets application requirements, permits these materials to be used in their glassy as well as

rubber-elastic states. Hence, for the presented film specification, the group of thermoplasts was limited to semi-crystalline materials used at the temperature range of their rubber-elastic state. The second pre-selected polymeric group, thermoplastic elastomers are commonly used in their rubber-elastic state. [155, 160]

Investigations of Monolayer Films

In the automotive industry, thermoset snap cure resin systems such as [142, 171, 172], characterized by a low viscosity and fast curing times at processing temperature, are commonly used to manufacture structural FRP parts. These resin systems are also intended to be used for the FS-CRTM process and shall be processed at a temperature between 80 °C to 120 °C. Therefore, a film needs to be thermally stable at such temperatures, which is defined as the third requirement.

The broad limits of the desired application range of the rubber-elastic state are the glass transition temperature at its lower end and the melting temperature at its upper end. These lower and upper temperature limits of the four monolayer films, i.e. three films made of semi-crystalline thermoplasts (PP, PA and PVF) and one film made of thermoplastic elastomer (TPE), were characterized via DMTA and DSC measurements and are listed in Table 6-1. The presented glass transition and melting temperatures are well below and above the FS-CRTM processing temperatures of 80 °C to 120 °C, respectively. The glass transition temperature of the TPE film could not be identified via the performed DMTA measurements, and it was concluded that it is below the lowest test temperature of -50 °C, i.e. far below the FS-CRTM process temperature range.

Tab. 6-1 Properties of investigated monolayer films. [154]

Polymer type of film	Glass transition temperature ^I	Melting temperature ^{II}	Gas permeability of air ^{III}
	[°C]	[°C]	[cm ³ /(m ² · d · bar)]
PP	-10 (<i>SD</i> = 0)	164 (<i>SD</i> = 0)	230–260 [173]
PA	19 (<i>SD</i> = 1)	219 (<i>SD</i> = 0)	20–22 [173]
PVF	31 (<i>SD</i> = 1)	192 (<i>SD</i> = 1)	50 [173]
TPE	-	216 (<i>SD</i> = 1)	*

^I Mean and standard deviation (*SD*) of three measurements via the DMTA method, determined via the curve peak of the loss modulus (see Figure A-29).

^{II} Mean and *SD* of three measurements via the DSC method. ^{III} All gas permeability values are based on a film thickness of 0.1 mm [173]. * No value available in data sheet [68] and no information of exact TPE type given by manufacturer to check for literature values.

To ensure a robust FS-CRTM processing, the films should not only be within the rubber-elastic state but also be characterized by a relative constant mechanical

behavior inside the process temperature range of 80 °C to 120 °C. DMTA measurements under tension load were performed to investigate the linear viscoelastic behavior of the four monolayer films. The material's stiffness, characterized by the storage modulus, is shown in Figure 6-3, while the energy dissipation, characterized by the loss modulus, is depicted in Figures A-29 and A-30 in Appendix A.5.1. These presented measurements correspond to samples loaded in machine direction. All materials appear isotropic inside the investigated temperature range of 80 °C to 120 °C by comparing the moduli in machine and transversal direction as presented in Figures A-31 to A-34 in Appendix A.5.1, except for the PVC film which shows slightly lower properties in transversal direction.

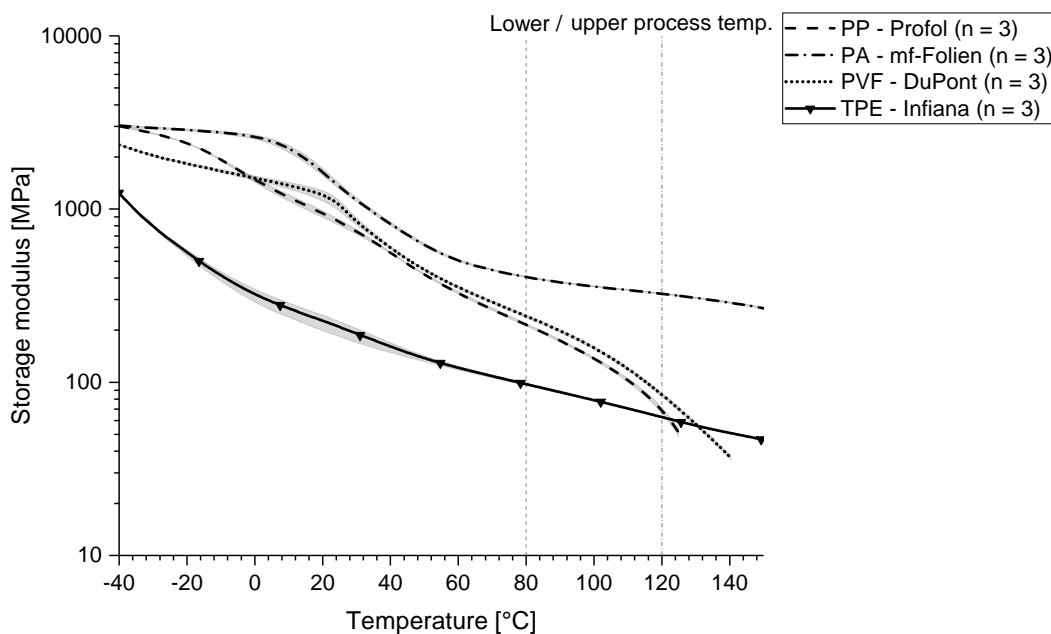


Fig. 6-3 Storage modulus of monolayer films (shown as average in black as well as spread between maximum and minimum measured values in gray). cf. [154]

As seen in Figure 6-3, a decline in the storage modulus over the process temperature range is observed to be strongest for the PVF film from 241 MPa to 85 MPa and for the PP film from 213 MPa to 69 MPa. A moderate drop is measured for the PA film from 405 MPa to 324 MPa, while its overall storage modulus level is at the highest of the investigated films. The storage modulus level of the TPE film is at the lowest level of all four investigated films, while its decline from 98 MPa to 85 MPa over the process temperature range is measured to be the lowest. Therefore, the storage modulus plateau of the rubber-elastic state of the TPE and PA films is identified as being the most suitable for a robust FS-CRTM processing due to the low-recorded decline of the film's storage modulus over the process temperature

range. Based on the performed DMTA results, a rating of the four monolayers materials is presented in Table 6-2 (second column, “Thermal stability”).

Tab. 6-2 Rating of investigated monolayer films for the FS-CRTM process towards fulfillment of specific requirements: ++ = excellent; + = good; - = poor; -- = inappropriate. [154]

Polymer type of film	Thermal stability	Low gas permeability of air	Antistick properties	Weldability	Cost efficiency
PP	-	-	+	++	+
PA	+	++	+	-	+
PVF	-	+	+	++	-
TPE	++	*	+	--	-

* No value available in data sheet [68] and no information of exact TPE type given by manufacturer to check for literature values.

During the FS-CRTM process, the film seals the injection space inside the cavity, and hence prevents (i) resin from exiting the cavity and (ii) air from entering the injection space. Therefore, a film needs to be characterized by low gas permeability of air (i.e. fourth requirement). Gas permeability describes the passage of gas molecules through a solid material such as a polymer film [63]. Referring to the fourth column in Table 6-1, literature values are listed for gas permeability of air for the three semi-crystalline thermoplasts. Values are given for a comparable film thickness of 0.1 mm. Generally, films made of the three semi-crystalline thermoplasts are used in FRP manufacturing [64, 174–176]. More specifically, they are used to cover and evacuate dry or wet fiber material. Therefore, for the intended purpose all three materials are considered suitable in regard to their specific gas permeabilities but should be compared with each other to select the most suitable film for the FS-CRTM process. Comparing the gas permeabilities in Table 6-1 shows that a film made of PA has the lowest permeability value followed by PVF, which is characterized by a permeability that is more than twice as high as PA. A PP film shows the highest permeability of air—over ten times the value of PA. Therefore, as rated in Table 6-2, a film made of PA is most suitable for low gas permeability of air followed by PVF, while PP is rated poorly for fulfilling the investigated requirement.

A film used in the FS-CRTM process is considered purely as process aid material and should be removed from the part after manufacturing. Therefore, the fifth requirement relates to the antistick properties to epoxy resin systems. According to the PVF and TPE film manufacturer, both film types are described as having antistick properties in terms of epoxy resin systems [175, 176], and hence, both are rated good in this category in Table 6-2. Information regarding the PP and PA antistick properties could not be drawn from their data sheets, which motivated

further investigation of these materials. Antistick properties of a film material are established if the film does not adhere to the epoxy resin system during the curing process. According to Bonnet [177], adhesion of two polymers occurs if they are soluble in each other and if both are of polar character to form dipolar adhesion forces. Therefore, the solubility of PP and PA films in two snap cure epoxy resin systems [142, 172] was first investigated via thermo-optical analysis. By comparing the behavior of PP and PA films with soluble polyetherimide (PEI) and polyethersulfone (PES) films, it was ascertained that PP as well as PA films do not dissolve during the curing cycle of the investigated resin systems. These observations correlate well with findings of Bruckbauer [178].

To exclude potential adhesion due to dipolar forces, peel tests can be used to characterize potential adhesion forces. Therefore, PP and PA films were integrated as the outer, lower layer of the preform during plate manufacturing with the epoxy resin system [142]. Peel tests of the PA film showed moderate peel forces of 31 N/m to 42 N/m, which is approximately one order of magnitude lower than peel forces of peel plies peeled off FRP parts [163]. No peel force could be measured for the PP film due to self-releasing of the film in the first two minutes after demolding. The observed self-release is assumed to occur due to thermal contraction of the film after demolding, resulting in shear forces between film and FRP plate higher than potential adhesion forces between the nonpolar PP material and the polar epoxy resin system [179, 180]. In contrast, the minor adhesion force between the PA film and the epoxy resin systems can be explained by the polar character of both materials [179, 180].

Based on these findings, the fifth requirement of antistick properties towards epoxy resin systems was verified also for PP and PA film materials and rated with good in Table 6-2. Because the four films were not compared relatively to each other but absolutely according to their fulfillment of the requirement, all films are rated equally to meet the requirement of antistick properties in terms of epoxy resin systems.

The first requirement, i.e. weldability, is critical to the type of polymeric material for all four monolayer films. Hence, elementary welding tests were performed to confirm the weldability of the specific monolayer films. In a first test series, basic weldability was evaluated of the film materials by optical inspection and manual peel tests of the weld seam. As seen in Figure 6-4, the investigated PP and PVF film exhibited excellent weld seam quality characterized by an evenly melted weld seam. Good adhesion during manual peel tests was ascertained as well. In the case of PA samples, even though adhesion was noted during manual peel tests, the weld seam showed poor quality as observed in Figure 6-4, characterized by inhomogeneous and incomplete melting over the weld seam length. No adherent

weld seam could be created with the TPE film. The poor-to-insufficient weldability of PA and TPE is considered to correlate to their melting temperatures of 219 °C (SD = 0) and 216 °C (SD = 1), respectively, as these melting temperatures are potentially too close to the maximum achievable welding temperature of 220 °C of the used impulse welding equipment, thus preventing the complete melting which is necessary to adequately weld the materials.

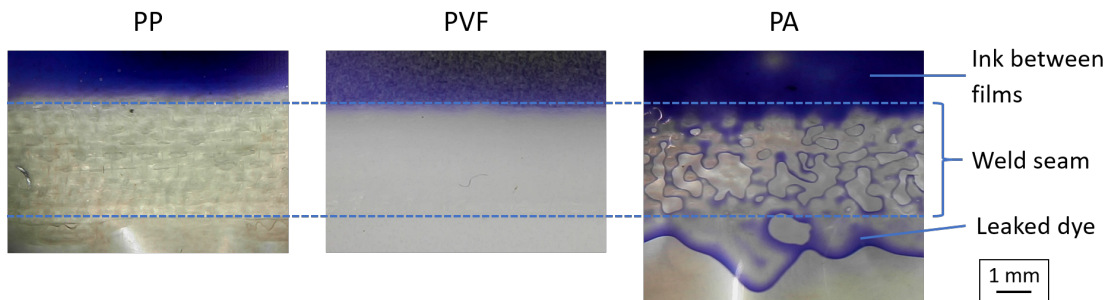


Fig. 6-4 Weld seam investigations of PP, PVF and PA films via the dye-test adhered to the standard ASTM F1929 [166]. [154]

In a second test series, the tightness of a weld seam in terms of liquids was investigated via the dye-test adhered to the standard ASTM F1929 [166]. The weld seams of the PP and PVF films were found to be liquid impermeable while the inhomogeneous weld seams of the PA film was permeable for the test fluid, as seen in Figure 6-4. Based on these results, the weldability of the investigated films with the available equipment is rated as listed in Table 6-2, i.e. the PP and PVF films have excellent weldability, while the PA film is listed as weldable but of poor quality. The TPE film is rated as inappropriate because the material is not weldable with the available equipment.

Besides technical requirements, a film, which is intended for industrial processes, needs to be cost-effective (the sixth and final requirement of the film specification for the FS-CRTM process). The overall process benefits arising from film integration during the FS-CRTM process need to exceed the cost increase due to the additional film material. Identifying an exact cost for the investigated films is difficult due to price variations between suppliers. Based on interviews with manufacturers and suppliers of the investigated films, the four monolayer films are rated relative to each other in terms of their cost efficiency as listed in Table 6-2. Due the large volume of worldwide manufactured PP and PA material, their raw material prices are rather low. Additionally, PP and PA films are used in a wide range of industries, including composite manufacturing [66, 181], making these films quite cost-effective. In contrast, PVF and TPE films are typically used for specific applications in com-

posite manufacturing and other industries, and hence, their produced volume is lower, and their price is consequently much higher.

Considering the ratings of the four monolayer films in fulfilling the set requirements for use in the FS-CRTM process, Table 6-2 indicates that the TPE film is unsuitable, primarily due to the inability of welding it with the available impulse welding equipment. It should be further noted that none of the other three semi-crystalline thermoplastic films is an optimal choice due to at least one poorly rated aspect for each of them. While PVF is rated good to excellent for low gas permeability of air, antistick properties and weldability, thermal stability and cost efficiency are poorly rated. The only two film materials rated good for cost efficiency are PP and PA, making them a desirable material for industrial applications. However, due to the poor weldability of PA as well as the poor thermal stability and high gas permeability of air of PP, both materials exhibit significant weaknesses.

Comparing the PP and PA ratings reveals that the two films are complementary in their qualification for the FS-CRTM process, indicating that a multilayered film made of PA and PP would likely fulfill all requirements for the successful integration of a film material in the FS-CRTM process. With both film featuring good antistick properties and cost efficiency, the PA material is intended to provide a multilayer film with low gas permeability of air and thermal stability, while the PP material would enable a weldable film surface.

Investigations of Multilayer Film

In collaboration with the manufacturer Profol, a cost-effective multilayer PA/PP film was developed consisting of a 0.02 mm thick PP layer that is to be arranged to form the inside of the film sealed preform package to enable optimal welding and antistick properties. The multilayer film was formed by joining the PP layer to a 0.075 mm thick PA layer via a bonding agent. As mentioned above, the PA layer is intended to provide low gas permeability of air and sufficient thermal stability to enable a robust FS-CRTM process.

To verify the operating range of the film between 80 °C to 120 °C, DMTA and DSC measurements were performed to identify the glass transition and melting temperatures of the individual material components of the film. The peak of the loss modulus curve of the PA/PP film as presented in Figure A-29 in Appendix A.5.1, indicates its glass transition at 12 °C ($SD = 2$, $n = 5$) which is considered to be the glass transition of the PA component of the multilayer film due to similar temperatures measured for the PA monolayer film, as listed in Table 6-1. A glass transition temperature of the PP component could not be identified even though a minimal curve deformation is observed at approximately -18 °C, which could theoretically be the PP component, yet the curve deformation is too small

to make a definite judgment. Nevertheless, the operating range of the multilayer film within the rubber-elastic state of both materials is within the highest recorded glass transition and lowest melting temperature, making the glass transition of the PA component the defining temperature at the lower boundary. The DSC measurements of the multilayer film identified two melting temperatures at 161 °C (SD = 0, $n = 5$) and 218 °C (SD = 0, $n = 5$) of the PP and PA component, respectively. Therefore, the process temperature range of the FS-CRTM process between 80 °C to 120 °C is well within the rubber-elastic state of both material components of the multilayer film, which is limited by the measured upper glass transition of 12 °C and lower melting temperature of 161 °C.

Furthermore, the change in mechanical properties, i.e. elasticity, over the process temperature range of the FS-CRTM process between 80 °C to 120 °C is of interest to ensure a thermal stability of the film as judged by a minimal change in the storage modulus. The storage modulus of the PA/PP film and the four previously discussed monolayer films are shown in Figure 6-5⁴ – all measured via the DMTA method under tension load. The curve of the PA/PP film shows a progression similar to the PA monolayer but on a slightly lower level. A decline in the storage modulus from 320 MPa to 228 MPa was recorded over the FS-CRTM process temperature range of 80 °C to 120 °C. The recorded decline in the storage modulus is in the range of the decline of the PA monolayer film and is therefore at a moderate rate compared to the monolayer films and rated as good in regard to the thermal stability requirement. The stiffness level of the film cannot be judged at this stage of the film selection and is evaluated in Chapter 6.2 of this work by FS-CRTM injection experiments of unrestricted film deformation.

In summary, a multilayered film made of PA and PP was designed and manufactured, combining the advantages of the two individual materials to form a film that meets all requirements that were defined for integrating a film as a process aid material in CRTM manufacturing.

6.1.3 Results and Discussion of Film Specification for FS-CRTM Flow Visualization Experiments

In the context of this work, the FS-CRTM preform impregnation is intended to be characterized via flow visualization experiments. The experiments are performed on laboratory test equipment presented in Appendix A.4.2. To reduce the complexity

⁴ The, in Figure 6-5 presented, measurements correspond to samples loaded in machine direction. As the monolayer films (except PVC), the PA/PP film appears isotropic inside the investigated temperature range of 80 °C to 120 °C by comparing the moduli in machine and transversal direction as presented in Figure A-36 in Appendix A.5.1.

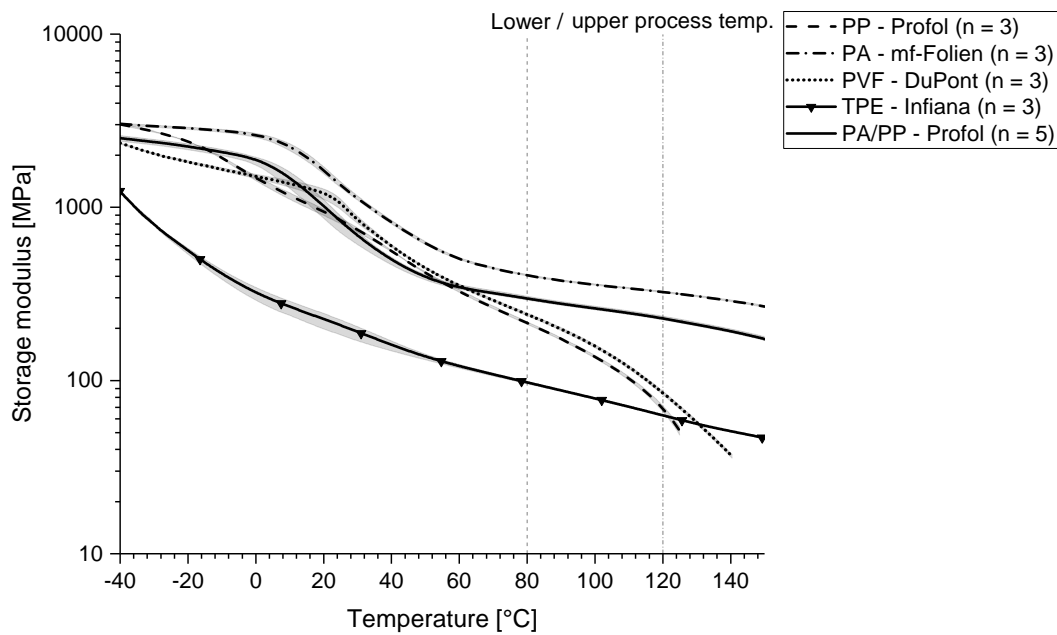


Fig. 6-5 Storage modulus of monolayer films and PA/PP multilayer film (shown as average in black as well as spread between maximum and minimum measured values in gray). [154]

of the experiments, the flow of a reactive epoxy resin system at process temperatures between 80 °C to 120 °C is simulated by using a non-reactive substitution fluid, i.e. sunflower oil, with comparable rheological properties at test temperature of approximately 23.5 °C. Analogue to the substitution of the flow medium, the specified PA/PP multilayer film for FS-CRTM manufacturing needs to be substituted for the flow visualization experiments to ensure comparable mechanical properties at their individual operating temperatures.

As previously explained, the film material is intended to lift off the preform surface during the FS-CRTM injection phase and deform to adapt to the upper shape of the injection gap to enable a fluid distribution above the preform. During the FS-CRTM compression phase, the injection gap is closed, and the film is forced to its original, smaller shape. Ideally, the deformation of the film happens elastically and reversibly. Therefore, the elastic characteristics of the PA/PP film are used as a starting point to select a potential substitution film.

As presented in Figure 6-5, the multilayer PA/PP film is characterized by a storage modulus of 320 MPa to 228 MPa over the FS-CRTM process temperature range from 80 °C to 120 °C. According to Ehrenstein [159], the storage modulus corresponds approximately to the coefficient of elasticity derived from static tests stated in literature. Therefore, a literature review was performed to identify a thermoplast with a coefficient of elasticity at ambient temperature comparable to the storage

modulus of the PA/PP film between 80 °C to 120 °C. Additionally, to exhibit good elasticity, the substitution film material should be a semi-crystalline thermoplast and operated at its rubber-elastic state.

The semi-crystalline thermoplast, polyethylene of low density (PE-LD), has been identified to be a suitable candidate with a coefficient of elasticity of approximately 210 MPa. Furthermore, a PE-LD film operated at a test temperature of approximately 23.5 °C during FS-CRTM flow visualization experiments would be within its rubber-elastic state located between its glass transition temperature at below -40 °C and its melting temperature at approximately 110 °C. Besides general requirements on the mechanical behavior, PE-LD films can be manufactured to be optically transparent which is required to observe the fluid flow during FS-CRTM flow visualization experiments. PE-LD is characterized by a good weldability, which is why PE-LD films are often used as a sealing layer for packaging goods. The material's melting temperature of approximately 110 °C is well below the maximum achievable welding temperature of 220 °C in the utilized welding equipment at the film-sealing station. [158, 173, 182, 183]

Based on the presented pre-selection, an optically transparent PE-LD film of 0.1 mm thickness manufactured by Sokufol (Limburg, Germany) is used for all flow visualization experiments presented in this work. The limits of the film's rubber-elastic state were measured to be within its glass transition temperature at -26 °C (SD = 2, $n = 5$) (evaluated via DMTA measurements, see Figure A-35) and its melting temperature at 112 °C (SD = 0, $n = 5$) (evaluated via DSC measurements).

DMTA tests under tension load were performed to investigate the comparability of the storage modulus of the PE-LD film and the PA/PP multilayer film. As shown in Figure 6-6, the storage modulus of the PE-LD film at 23.5 °C is measured to be 222 MPa (SD = 12, $n = 5$) and is, therefore, located at the lower end of the storage modulus range of 320 MPa to 228 MPa of the PA/PP multilayer film at its process temperature range between 80 °C to 120 °C. The presented comparison is performed via DMTA tests of samples cut in production direction while both films show isotropic properties, identified by comparing measurements of machine and transversal direction in Figures A-36 and A-37 in Appendix A.5.1.

Assuming that the injection gap is completely filled during the injection phase, the film deformation is constrained by the upper shape of the injection gap. Therefore, the defining load factor of the film during the FS-CRTM injection phase is strain, which is why stress relaxation tests were performed to further investigate the comparability of the mechanical behavior of the two films. The yield point of a material characterizes the transition from its linear-elastic to its plastic deformation. To investigate the yield point of the two films, the relaxed stress at different

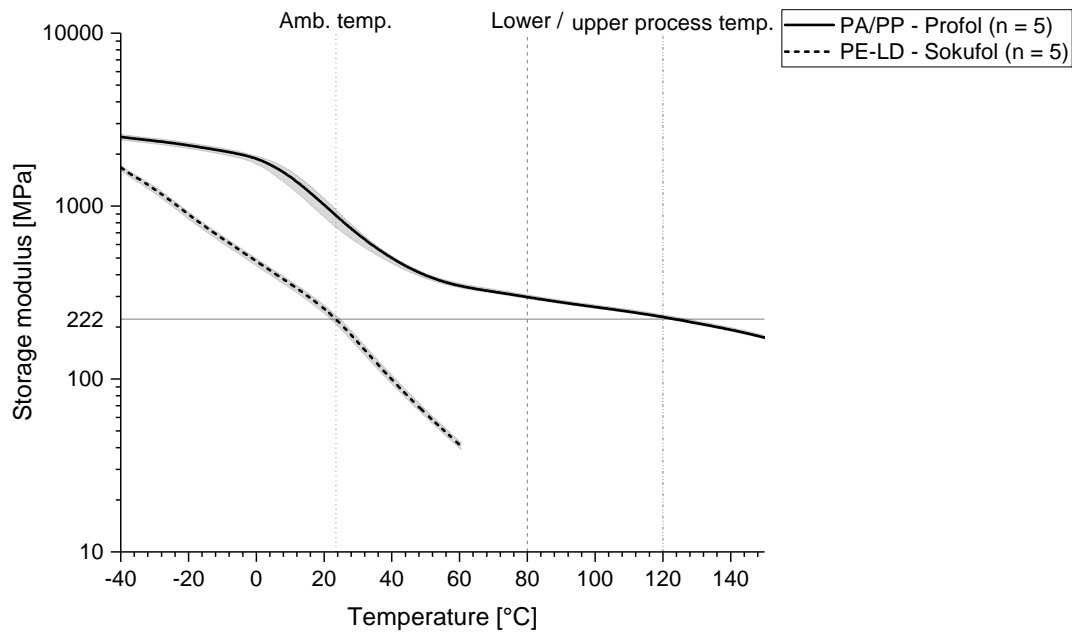


Fig. 6-6 Storage modulus of PA/PP multilayer film for FS-CRTM manufacturing at process temperature of 80 °C to 120 °C and substituting PE-LD film for FS-CRTM flow visualization experiments at ambient temperature (Amb. temp.) (shown as average in black as well as spread between maximum, and minimum measured values in gray).

strains are plotted in Figure 6-7. To consider a certain holding time during the FS-CRTM injection, the relaxed stress is measured after the first 20 seconds of phase II of the stress relaxation test (see Figure 6-2). While the experiments of the PE-LD film were performed at the intended test temperature of 23.5 °C, the PA/PP multilayer film was tested at its lower and upper process temperature limits of 80 °C and 120 °C, respectively. The results show that for both films, the relaxed stress increases linearly with increasing strain from one to four percent. A further increase of four to six percent strain is shown to reduce the stress increase of the PA/PP film at 80 °C and even stagnates for the PA/PP film at 120 °C and PE-LD film at 23.5 °C. These observations indicate a comparable yield point of both films between four to six percent of strain at their specific temperature of use. Moreover, the results of the PA/PP film show a clear dependency of the temperature, observed as a reduction of relaxed stress at increased temperature and an increased standard deviation around the yield point of the PA/PP film at 120 °C and six percent strain.

For semi-crystalline thermoplasts in their rubber-elastic state, plastic deformation can already occur below the yield point [160]. During FS-CRTM manufacturing, plastic deformation and resulting permanent film elongation needs to be minimized to limit the risk of undesired film wrinkling closure of the injection gap,

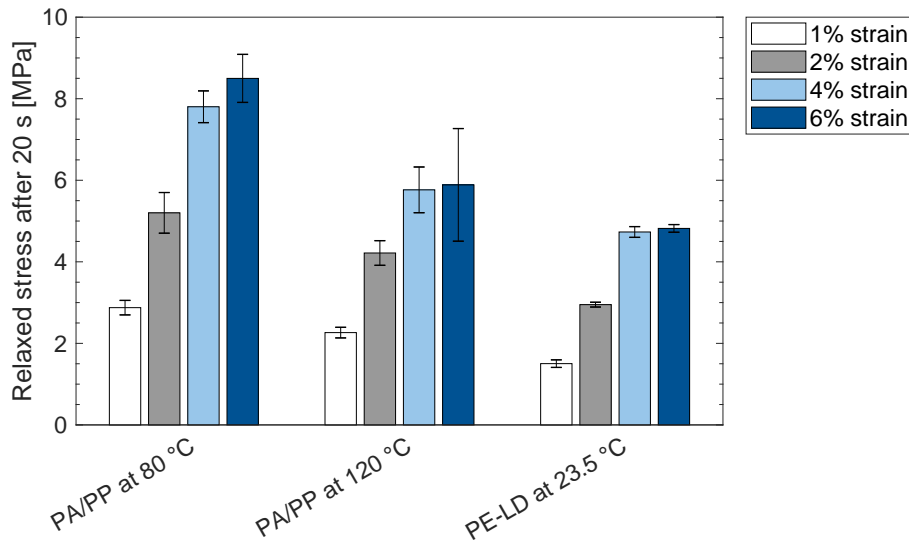


Fig. 6-7 Relaxed stress after 20 s of constant strain load at four different strain levels of the PA/PP film at lower (80 °C) and upper (120 °C) process temperature and the substitution PE-LD film at test temperature (23.5 °C) (shown as mean and standard deviation of five measurements and of ten measurements for PA/PP at 120 °C, at 4%, and 6%).

which could result in imprints on the part surface or out-of-plane fiber undulations. To compare the deformation behavior of the PA/PP and PE-LD films, the stress relaxation experiments were further tracked during phase III (see Figure 6-2) to measure the strain recovery of the film samples after a constant strain load interval of 30 seconds. Figure 6-8 shows the strain recovery after 5 seconds and 120 seconds. These two time limits were chosen in order to investigate the three different kinds of deformation observed for polymeric materials—elastic (impulsively reversible), viscoelastic (time-dependent reversible) and viscous (time-dependent irreversible) deformation [159, 160]. While the strain recovery after five seconds in Figure 6-8(a) presents information about the elastic strain recovery, the difference in strain recovery between 5 (a) and 120 seconds (b) offers knowledge about the viscoelastic deformation. Additionally, the offset of the strain recovery after 120 seconds (b) to a complete strain recovery of 100% provides information about the viscous deformation.

Looking at the elastic strain recovery after five seconds in Figure 6-8(a) shows a clear strain load dependency of the PA/PP film. The temperature increase from 80 °C to 120 °C appears to lower the strain recovery only minimally for strains larger than 2%, but increases its standard deviation. The elastic strain recovery of the PE-LD film shows that it is less dependent on the strain load and is recorded to be constant up to a strain load of 4%. While the PE-LD film recovers elastically up to only 70%, the PA/PP film shows better impulsive recovery of up to 85%

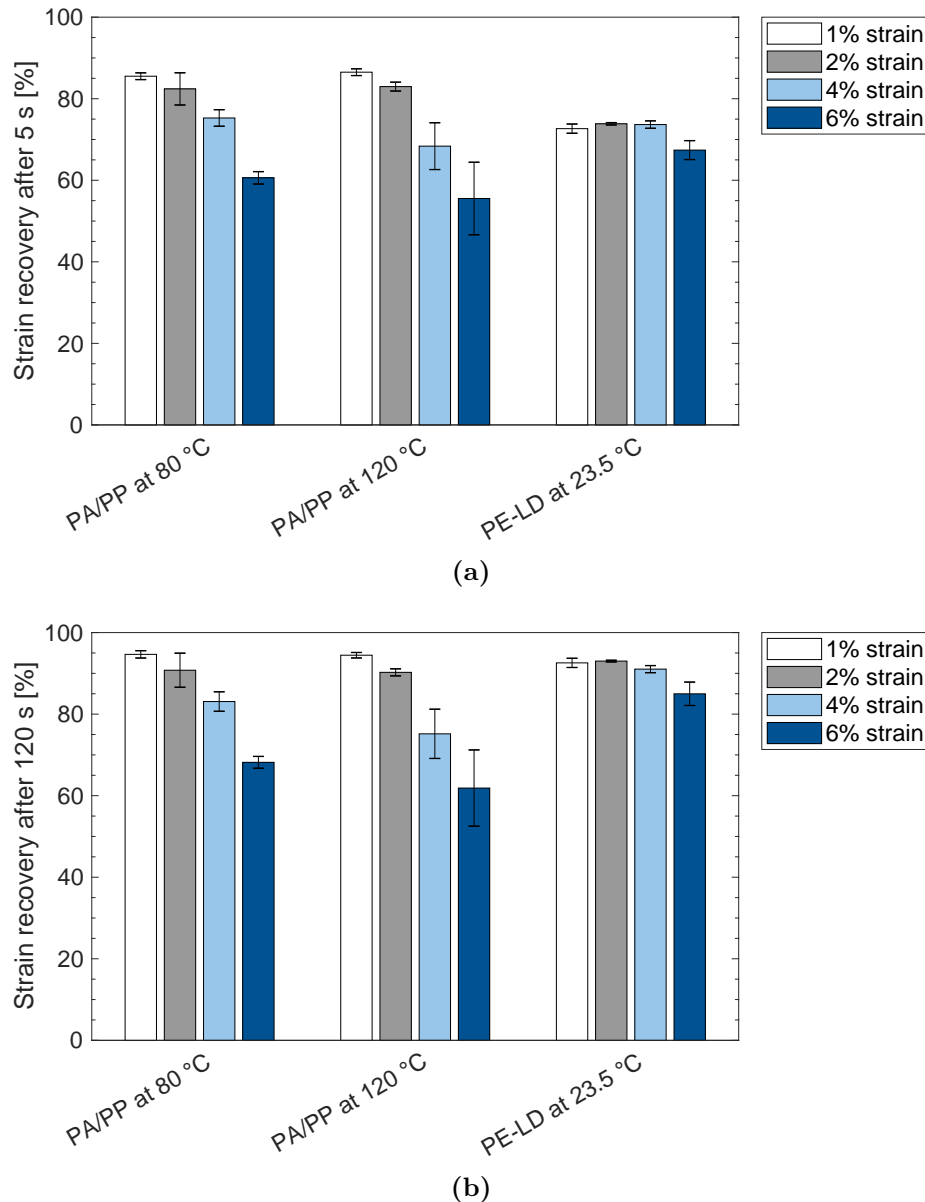


Fig. 6-8 Strain recovery after different relaxation strain loads of PA/PP film at lower (80 °C) and upper (120 °C) process temperature and substitution PE-LD film at ambient temperature (23.5 °C): (a) five seconds and (b) 120 seconds after load cycle.

for small loads below 2% strain, but drops below the elastic recovery of PE-LD at large strain load levels of more than 4%.

Examining the strain recovery after 120 seconds in Figure 6-8(b) illustrates that both films recover to at least 90% at smaller loads of below 2%. Considering the lower elastic component of the PE-LD film recorded after five seconds in (a), the recovery values after 120 seconds in (b) indicates a larger time-dependent viscoelastic recovery component of the PE-LD film than for the PA/PP film. As observed after five seconds in (a), the strain recovery after 120 seconds in (b) illustrates a

clear dependency of the strain recovery on the load level for the PA/PP film and a nearly equal recovery rate of the PE-LD film up to a strain load of 4%.

Hence, the comparability of the strain recovery after applied load is only limited between the two films. While the PE-LD shows a more homogeneous response at increasing strain load, the PA/PP film shows better elastic strain recovery behavior at low load levels. The exact strain load level of the film during FS-CRTM process depends on the gap height, which is defined as being dependent on the process control strategy. Furthermore, the film is not expected to deform equally but to deform more in the corners of the injection gap due to friction between the film and the flat mold surface at the upper slider and side wall of the injection gap, both first in contact with the film. With a lower elastic strain recovery of the PE-LD film, the risk of potential wrinkling is higher in the flow visualization experiments which is why the experiments are expected to give a good indication about the severity of the risk of potential film wrinkles after mold closure.

In summary, a monolayer film, made of PE-LD, was identified to be an adequate substitution of the PA/PP film during FS-CRTM flow experiments performed in this work.

6.1.4 Conclusions of Film Specification⁵

In the first part of this chapter, a film was specified to be integrated in the CRTM process. Based on the defined requirements of weldability and elasticity, the broad group of polymers was narrowed down to semi-crystalline thermoplasts and thermoplastic elastomers, both to be used at a temperature in their rubber-elastic state. Further, four monolayer films made of polypropylene (PP), polyamide (PA), polyvinyl fluoride (PVF) and a thermoplastic elastomer (TPE) were selected for detailed investigations.

Basic welding tests, using the available equipment, showed that the TPE film is not weldable, and that no liquid-tight weld seam could be manufactured using the PA film. Both, the PP and PVF film, showed to be well weldable. Based on literature data, the PA film is characterized by the lowest gas permeability of air, making this material most suitable to prevent air from entering the film-sealed cavity. The antistick properties for epoxy resin systems are sufficient for all film types, enabling a release of the film from the cured part after FS-CRTM manufacturing.

To enable FS-CRTM manufacturing with constant process characteristics, the stiffness of the film is intended to be characterized by a homogeneous progression with minimal drop throughout the process temperature range of 80 °C to 120 °C. DMTA

⁵ Parts of this subsection have been previously published in [154].

tests under tension load were performed for all four monolayer films showing a low storage modulus drop of the TPE and PA film. From an economical point of view, the film has to be cost-effective to enable a good trade-off between cost increase due to the extra film used in the process and the resulting benefits. The PP and PA materials are reported to be most economically worthwhile when comparing the four investigated film materials.

In conclusion, the investigations on the four monolayer films showed that none of them is able to meet all defined requirements, but that a film combining PA and PP is suitable. Therefore, a multilayered film made of PA and PP was designed and manufactured, combining the advantages of the two individual materials to form a film that meets all requirements which were defined for integrating a film as a process aid material in FS-CRTM manufacturing.

In the second part of the presented film specification, a substitution monolayer film, made of PE-LD, has been identified for FS-CRTM flow visualization experiments. DMTA tests were performed to compare the PE-LD film at its test temperature of 23.5 °C with the PA/PP multilayer film of the FS-CRTM manufacturing at its process temperature range of 80 °C to 120 °C. The results show a storage modulus of 222 MPa ($SD = 12$, $n = 5$) of the PE-LD film, comparable to the lower end of the storage modulus range of the PA/PP film. Furthermore, stress relaxation tests were performed indicating a comparable yield point between four to six percent of strain load of the two films.

Investigations on the strain recovery show limited comparability of the PA/PP and PE-LD film. Nevertheless, considering that the purpose of the FS-CRTM flow visualization experiment is to characterize the preform impregnation pattern, the observed limitations of strain recovery are of minor impact on the general comparability between experimental and manufacturing conditions of the FS-CRTM process. The general stiffness and yield point are considered to be the dominant film properties which influence the film's mechanical behavior during the FS-CRTM injection and compression phase, while the strain recovery could result in film wrinkles which rather impact the quality of the cured part than the preform impregnation pattern. Nevertheless, further investigation into the identified strain load dependency of the PA/PP film during the first FS-CRTM manufacturing trials are recommended, in which imprints and fiber undulations at the circumference of the central slider would indicate unintended viscous film deformation of the PA/PP film.

In sum, the identified multilayered PA/PP film enables the industrialization of the FS-CRTM process to further improve high-volume industrial FRP production. Nevertheless, it has to be noted that in the context of the presented selection process

the PA/PP film has not been tested in real FS-CRTM production trials. However, a post-thesis project verified the use of a PA/PP film during FS-CRTM part manufacturing on an industrial scale (see Chapter 9). Based on the identified PA/PP film, a substitution film made of PE-LD material was identified to be used during FS-CRTM flow experiments at room temperature. Among others, the two films show comparable stiffness levels. Thus, this stiffness level has not been validated in this chapter to allow a suitable deformation of the film above the preform during resin injection. Therefore, this validation is going to be done via FS-CRTM flow experiments with unrestrained film deformation presented in the following Section 6.2.

6.2 FS-CRTM Injection Experiments with Unrestrained Film Deformation⁶

The FS-CRTM process is an enhanced FRP manufacturing technique. The newly introduced film seals the injection space inside the mold and acts as a barrier layer between preform/resin and mold surface during preform impregnation. Due to the film's flexibility, a pressure gradient is formed across the film, which either compacts the preform or lifts the film off the preform, creating a space where the resin can overflow the preform.

After a film has been selected in the previous subsection, this subsection investigates how the film deforms during the FS-CRTM injection. More specifically, the goal of this study is to investigate if the stiffness of the film allows the film on the top side of the preform to adapt to the limiting geometry of the mold wall inside the injection gap and how the acting pressure gradient across the film influences its deformation. Therefore, the film deformation in the following study is not restrained by the upper mold, to be able to measure the unrestrained film deformation only governed by the acting pressure gradient across the film.

Based on different acting pressures, film deformation during a FS-CRTM injection is expected to take place in three stages as presented in [186] and illustrated in Figures 6-9(a)-(c). Prior to the injection, the pressure level inside the film-sealed preform package is lowered to below ambient pressure via the vent. A resulting negative pressure gradient across the film results in an adaption of the film to the preform surface shown in Figure 6-9(a). During the injection, fluid is injected into the film-sealed preform package at an injection pressure larger than ambient pressure, partially impregnating and overflowing the preform. The acting positive pressure

⁶ Parts of this section are based on the master's thesis of Prenninger [184] and Laubichler [185], both supervised by Mario Albert Vollmer.

gradient across the film in regions of the injected fluid, leads to an out-of-plane deformation of the film. In preform sections which are not impregnated or overflowed by the fluid, the film further exhibits a negative pressure gradient leading to sections where the film is not lifted off and still adapted to the preform as illustrated in Figure 6-9(b). After the injection, the fluid further impregnates the preform driven by the pressure gradient between fluid and unimpregnated preform (p_{Vent}) leading to a reduction of the out-of-plane film deformation while fluid flows from above the preform into fiber structure, as illustrated in Figure 6-9(c).

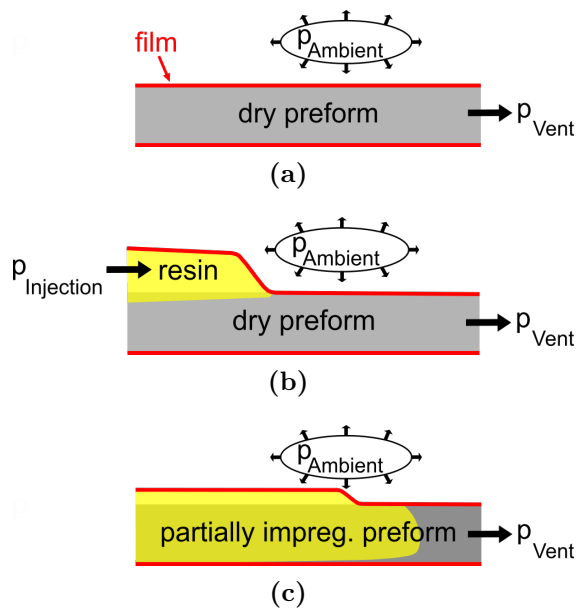


Fig. 6-9 Hypothesis of the three stages of unrestrained film deformation during FS-CRTM injection trials: (a) before injection, (b) during injection and (c) after injection. [186]

6.2.1 Experimental Setup, Materials and Methods of Unrestrained Film Deformation Experiments

Experimental Setup

As described in Appendix A.4, specific laboratory equipment has been developed to investigate the FS-CRTM process. By using this equipment, the preform impregnation can be studied in flow visualization experiments at which all main process variables can be adjusted and monitored. During the experiments of unrestrained film deformation, the laboratory equipment presented in Appendix A.4 was used, except that the movable upper setup of the cavity unit including the central slider was removed. Its absence is seen in Figure 6-10 showing the modified test setup. The removal of the upper cavity unit section was done to ensure that the out-of-

plane film deformation above the preform is not limited by the central slider and only governed by the acting pressure gradient across the film. The unrestrained film deformation was recorded and evaluated via a non-contact measurement system manufactured by GOM (Braunschweig, Germany) consisting of the camera system ATOS Capsule and the evaluation software ARAMIS.

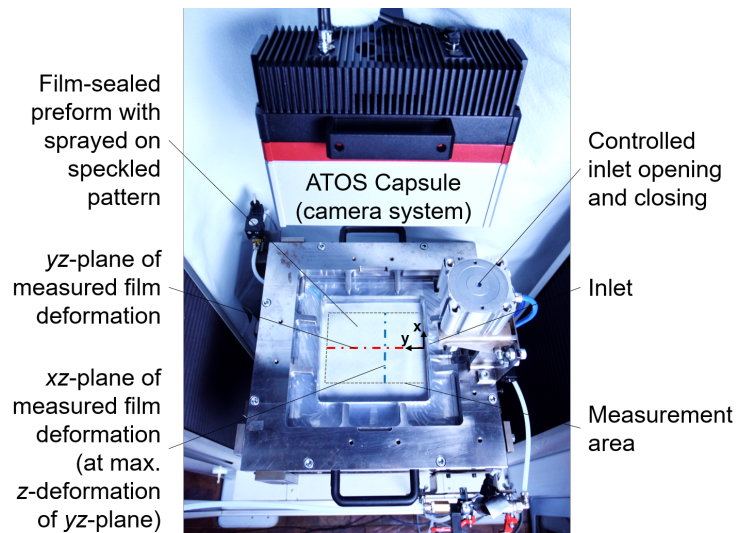


Fig. 6-10 Test setup of experiments to study the unrestrained film deformation. cf. [186]

Materials

The preforms of the experiments consisted of stitched, biaxial, carbon fiber non-crimp fabric (NCF), SIGRATEX[®] C B310-45/ST-E214/5g, manufactured by SGL Group (Wiesbaden, Germany) [143]. Twelve layers were evenly stacked while the lower six layers were flipped and rotated by 90° to enable a symmetrical ($\pm 45_6$)_s lay-up of the preform. The stack was binder-activated for thirty seconds at 170 °C \pm 10 °C via infrared heating and debulked under vacuum pressure. The activated, flat preforms were cut to the cavity dimension of 210 mm \times 210 mm with corner radii of 10 mm. The weight of all preforms is listed in Table A-6 in Appendix A.5.2.

All preforms were film-sealed in a 0.1 mm thick PE-LD film manufactured by Sokufol (Limburg, Germany) as explained in Chapter A.4.1. To enable a non-contact measurement of the film deformation with the ARAMIS system, a speckled pattern was sprayed onto the upper film in the section above the preform. Tensile tests according to DIN EN ISO 527-3 [187] were performed to investigate the effect of the 0.02 mm to 0.03 mm thick painted speckled pattern on the stiffness of the film. The tests showed an increase of the coefficient of elasticity in machine direction by 8% from 226 MPa (SD= 4, $n= 7$) to 244 MPa (SD = 5, $n = 8$)

at a measurement speed of 5 mm/s. The measurement speed was derived by the recorded film deformation velocities measured during the unrestrained deformation experiments. The observed stiffness increase of 8% of the PE-LD film with painted speckled pattern is not considered to compromise the transferability of the results to the PA/PP multilayer film. DMTA measurements in Subsection 6.1 showed that the stiffness of the pure PE-LD film is located on the lower bound of the PA/PP multilayer film at manufacturing conditions showing a total gap of 44% between the stiffness of the PE-LD and the the upper stiffness bound of the PA/PP multilayer film. Therefore, the increased stiffness of 8% of the PE-LD film with sprayed on speckled pattern is well located inside the stiffness range of the PA/PP multilayer film between its manufacturing temperatures of 80 °C to 120 °C.

A non-reactive sunflower oil of type Vita D'Or was used as injection fluid during the unrestrained film deformation experiments. The viscosity of the sunflower oil at the specific temperature of each test is listed in Table A-6 in Appendix A.5.2.

Experimental Method

The non-contact 3D optical measurement system ARAMIS by GOM was used to measure the film deformation during FS-CRTM injection experiments. The camera system ATOS Capsule was deployed to measure a film in an area of 200 mm × 140 mm. The measurement area was positioned to observe the film surface close to the inlet while the origin of the measurement was placed at the center point of the 40 mm wide lateral inlet as shown in Figure 6-10. During the experiments, the ATOS Capsule recorded pictures of 12 megapixel resolution under a inclination angle of 70° and at a measurement rate of 12 Hz.

The software ARAMIS Professional 2018 of GOM was used to evaluate the film deformation. By spraying a stochastic speckled pattern on the film, the software is able to assign coordinates to each pixel of the recorded pictures. Surface pattern as well as deformation of the surface can be evaluated in ARAMIS by comparing and calculating the displacement of individual pixels between sequential pictures. To investigate the three-dimensional deformation of the film during the experiment, splines of the deformation in longitudinal direction at the yz -plane at the center of the inlet at $x = 0$ and in transversal direction at the xz -plane at the maximum z -deformation of the yz -plane were evaluated at specific time steps. The measurement planes are schematically illustrated in Figure 6-10.

To further investigate the deformation of the film, the maximum z -deformation of the yz -plane at each time step was calculated via a MATLAB® (MathWorks, MA, USA) script and plotted over time. Furthermore, the longitudinal progression of the film lift-off was calculated in MATLAB® by plotting the leading y -position of each

z -deformation spline over time. To minimize deviations due to preform swelling during impregnation, the y -length of film lift-off was evaluated at a z -deformation of 0.5 mm.

Experimental Plan

The laboratory equipment for FS-CRTM flow visualization experiments, explained in Appendix A.4.2, was modified for this study, in a way that the film deformation is not restricted in its z -deformation by the upper slider. Therefore, the film deformation is only governed by the acting pressure gradient across the film, defined by the injection and vent pressure. To investigate the effect of these two types of pressure, an experimental plan is defined as illustrated in Figure 6-11. The injection pressure is defined by the target pot pressure ($\Delta p_{p,t}$), which is varied between 100 kPa and 600 kPa relative to the ambient pressure. The lower limit was identified at preliminary FS-CRTM injection tests as the lower pressure level at which the film expands and the fluid is distributed above the preform. The upper limit of the target pot pressure was defined by the available air supply system of the laboratory at which the experiments were performed. The target vent pressure ($\Delta p_{v,t}$) was varied between -5 kPa and -99 kPa relative to the ambient pressure to investigate the effect of minimal and full evacuation of the film-sealed preform package prior to fluid injection. The pot as well as the vent pressure were varied on the central settings of the interacting factor and the center point of the factor settings was tested three times to investigate the repeatability of the test method. All experiments were performed in random order as listed in Figure 6-11.

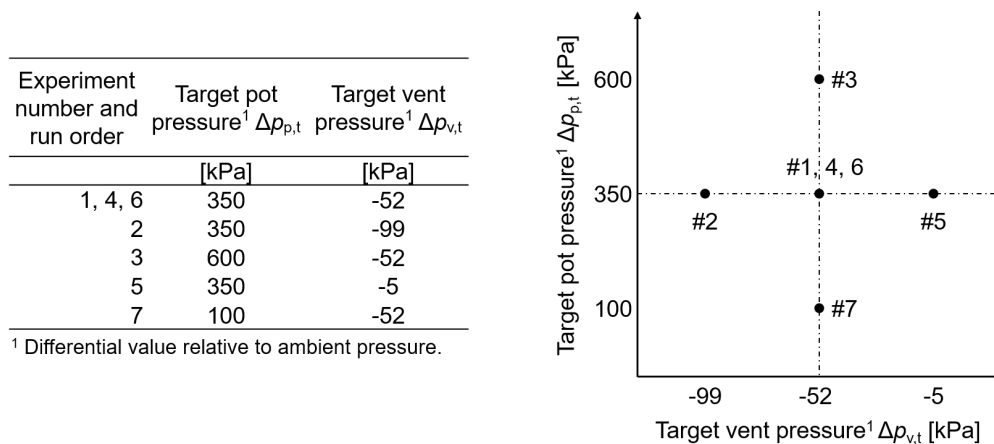


Fig. 6-11 Experimental plan of the unrestrained film deformation study.

6.2.2 Results and Discussion of Unrestrained Film Deformation Experiments

The following paragraphs present and discuss the results of the unrestrained film deformation experiments. First, the three-dimensional deformation of the film during a FS-CRTM injection is compared to the hypothesis of unrestrained film deformation, presented at the beginning of this subsection. Additionally, an investigation on the repeatability of the test method is presented. Finally, the effect of vent and injection (pot) pressure variation on the unrestrained film deformation is discussed.

All measured factors of the experiments are listed in Table A-6 in Appendix A.5.1. Furthermore, Table A-7 (Appendix A.5.1) presents a quantitative overview of the measured process responses of all conducted experiments while the main responses are discussed in detail in the following results and discussion sections.

Three-Dimensional Deformation Shape of Film

The experiments of unrestrained film deformation showed that the film deforms generally in a double-curved out-of-plane shape during the FS-CRTM injection, as exemplary shown for experiment #6 in Figure A-38 in Appendix A.5.2. The exact shape of the film is dependent on the acting pressure gradient across the film influenced by the pre-defined injection (Δp_p) and vent pressure (Δp_v). To investigate the time-dependent progression of the film deformation, a series of splines are plotted illustrating the film shape progression in two characteristic planes. An example is given in Figure 6-12 depicting the film deformation progression of experiment #6, one of the repeatability experiments at central factor setting. The two graphs of the first column, (a) and (c), illustrate the film deformation in the yz -plane at the center of the 40 mm wide lateral inlet at $x = 0$. The second column of Figure 6-12, (b) and (d), shows the film deformation at the transversal xz -plane at $y_{max} = 70.6$ mm, the y -distance of maximum z -deformation measured in the yz -plane. Furthermore, the top row, (a) and (b), shows the film's z -deformation during the injection and the bottom row, (c) and (d), after the injection.

As expected by the hypothesis of the unrestrained film deformation presented in Figure 6-9, the film on the top side of the preform of experiment #6 deforms out-of-plane in positive z -direction during the injection. The graph in Figure 6-12(a) shows that the film is forced in a parabolic shape. An instant z -deformation in the yz -plane is observed at injection start due to the positive pressure gradient acting across the film. The deformation progresses from the lateral inlet positioned slightly below $y = 0$. A time-delayed out-of-plane deformation in the xz -plane is observed in Figure 6-12(b) due to the distance of the transversal plane by $y_{max} = 70.6$ mm

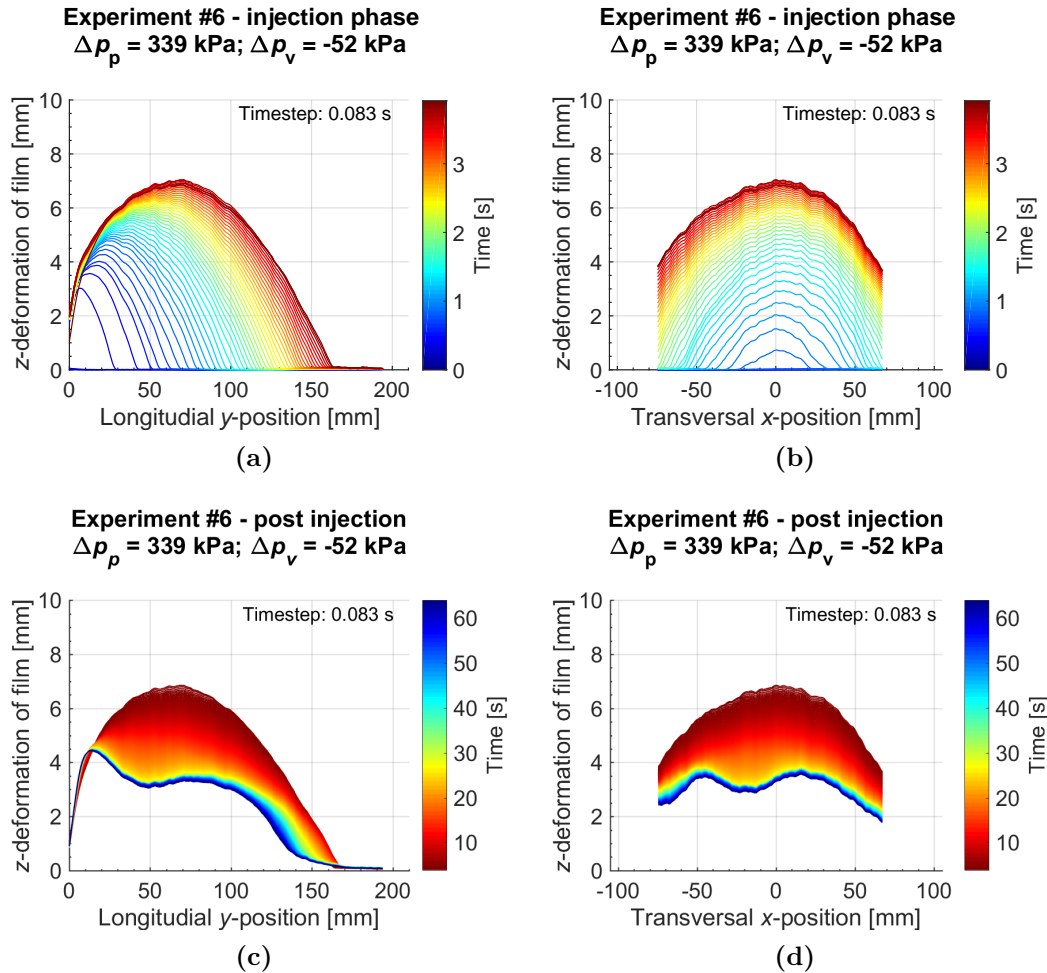


Fig. 6-12 Illustration of the three-dimensional film deformation of experiment #6 over time during injection (top row) and after injection (bottom row) – depicted in the longitudinal yz -plane at the center of the inlet at $x = 0$ (left column) and at the transversal xz -plane at $y_{max} = 70.6$ mm, position of maximum z -deformation recorded in the yz -plane (right column). cf. [185]

to the inlet. The maximum film deformation in both planes is recorded at the end of the injection phase, as depicted in Figures 6-12(a) and (b).

Investigating the areal distribution of the film lift-off, the experiments showed that the film does not lift off the complete preform surface but only detaches locally from the top side of the preform as seen in Figure A-38 in Appendix A.5.2. The circumferential boundary of the film lift-off is either located at constraining sections such as the upper frame or at open sections of the preform surface at which the force across the film is balanced between the acting fluid pressure and the negative pressure gradient at the neighboring unimpregnated preform sections. These observations correlate well with stage II of the hypothesis of the unrestrained film deformation, presented in Figure 6-9(b).

After the injection, the z -deformation of the film reduces, as seen in Figure 6-12(c) and (d). The recorded parabolic film shape at the end of the injection is reduced to an uneven shape with multiple peaks stagnating after approximately 20 seconds (post injection). These observations correlate with stage III of the hypothesis of the unrestrained film deformation, illustrated in Figure 6-9(c). The film reduction after the injection and the correlated reduction of the fluid volume above the preform indicates that the preform below the film is impregnated driven by the pressure gradient between fluid and vent pressure at the unimpregnated preform section. Eventually, Figures 6-12(c) and (d) shows that the film deformation and most likely also the preform impregnation reaches a state of equilibrium after approximately 20 seconds. The incomplete film re-deformation indicates that without further action a certain amount of fluid remains above the preform during a FS-CRTM injection.

Experimental Repeatability

To investigate the repeatability of the test method, experiments of the central factor setting were conducted in triplicate. The presented film deformation shapes over time during the injection of experiment #6 in Figures 6-12(a) and (b) correlates well with its replicates #1 shown in Figures A-39(a) and (b) as well as #4 in Figures A-40(a) and (b) in Appendix A.5.2. After the injection, the film shapes of all repetition experiments collapse and stagnate at different film deformation shapes as seen by comparing experiment #6 in Figures 6-12(c) and (d) with #1 in Figures A-39(c) and (d) as well as #4 in Figures A-40(c) and (d). The only constant characteristic of the three shapes after film collapse is the peak in the yz -plane close to the inlet between $10 \text{ mm} < y < 20 \text{ mm}$. The film in this section is recorded for all three experiments to be strongly deformed during the injection start, indicating a potential plastic deformation of this film section which results in a poor re-deformation and the observed peaks.

To further investigate the deformation shapes, the maximum z -deformation of each spline as well as the y -length of the film lift-off is plotted over time in Figure 6-13. Even though the curves of experiment #1 show noise, caused by a poor quality of its sparkled pattern, a general trend of both curves of experiment #1 is evaluable. Figure 6-13(a) shows a nearly identical maximum z -deformation during the injection phase of all three experiments, peaking at approximately 7 mm. After the injection, the maximum z -deformation of the film decreases and stagnates for all three experiments after approximately 20 seconds, as previously discussed for experiment #6. The difference of the film's z -deformation at the yz -plane after the injection can be explained by the observed uneven shape of film reduction, result-

ing in local variation depending on the film deformation shape in the transversal plane.

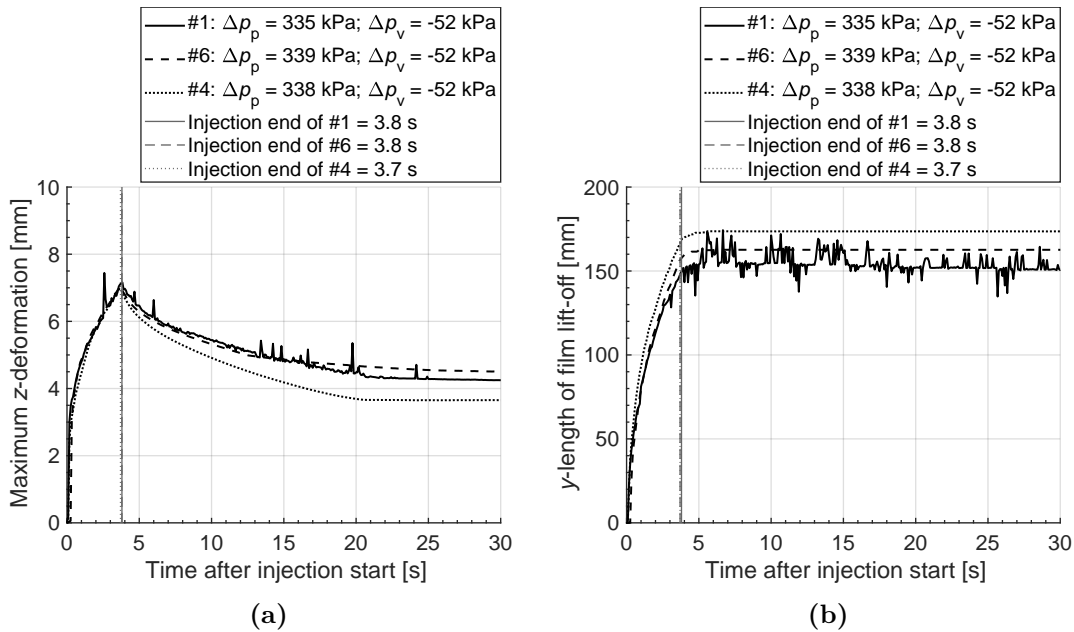


Fig. 6-13 Maximum z -deformation of film (a) and y -length of film lift-off (b) in the yz -plane at $x = 0$ plotted over time after injection start of the three replicates at central factor setting. cf. [185]

The y -length of the film lift-off of the three repeated experiments is depicted in Figure 6-13(b). During the injection the y -length increases similarly and reaches its maximum value at approximately two seconds after injection end, at which level the y -length of all three experiments stagnate. The recorded increase during the injection is explained by the acting positive pressure gradient across the film which vanishes after the injection resulting in the observed stagnation of the y -length. The recorded minimal increase after injection end is explained by the remaining impulse of the fluid due to the pressure-driven lateral injection. The deviation of the stagnated y -length between 150 mm to 170 mm shows a moderate repeatability of the y -length of the film lift-off. This needs to be considered during the interpretation of the process variation experiments at which experiments at the upper and lower limit setting was only conducted once.

A good repeatability of the test method during the injection phase is observed by the presented results of the three experiments showing nearly identical injection end times and maximum z -deformation as well as comparable y -length progression of the film's out-of-plane deformation. The collapse of the film after the injection proved to be not repeatable and is anticipated to be influenced by other factors such as e.g. pre-tension of the film during clamping via the upper frame or by local plastic deformation of the film during the injection. Therefore, during the

following investigation of the process parameter variation, only the progression of the film deformation shape during the injection phase is considered and discussed. The deformation shapes after injection are excluded but presented as additional information in Figures A-41 and A-42 in Appendix A.5.2.

Variation of Pot Pressure

To investigate the effect of injection pressure variation, experiments at three levels of pot pressure were carried out – all at constant vent pressure of medium level. The recorded film deformation shapes during injection are presented in Figure 6-14. The observations show that the film shapes in both planes are changed from a rather triangular shape with rounded tip at the lower pot pressure level to a parabolic shape at the medium and high pot pressure level.

Besides film shapes, the injection end time varied also with changed pot pressure, as indicated by the vertical lines in Figure 6-15. The injection end time is observed to be dependent on the pre-defined pot pressure while for higher pot pressures a shorter injection time is recorded. Figure 6-15(a) depicts the maximum z -deformation of the three experiments at varied pot pressure. The highest maximum z -deformation at injection end of 8 mm is recorded for experiment #7 with the lowest pot pressure level. The experiments of medium and high pot pressure level showed an equal maximum z -deformation of approximately 7 mm at injection end. Contrary, the y -length of the film lift-off after injection is measured to be shortest for experiment #7 of low pot pressure compared to the equal y -lengths at medium and high pot pressure level as shown in Figure 6-15(b).

The observations indicate that a stable double-curved parabolic film shape with constant z -deformation and y -length at injection end can be realized by choosing a pot pressure above a certain threshold level. A further increase of pot pressure is not observed to change the spacial distribution of the injected fluid above the preform but influences its temporal distribution indicated by the observed reduction of injection end time. Pot pressures below this threshold level result in rather triangular film shapes accumulating the majority of the fluid close to the inlet.

Variation of Vent Pressure

Figure 6-16 depicts the z -deformation of the film above the preform of experiments at three levels of vent pressure – all conducted at medium pot pressure level. While experiment #5 at high vent pressure level of -5 kPa, simulating minimal evacuation of the preform, show a triangular shape with rounded tip, the experiments of

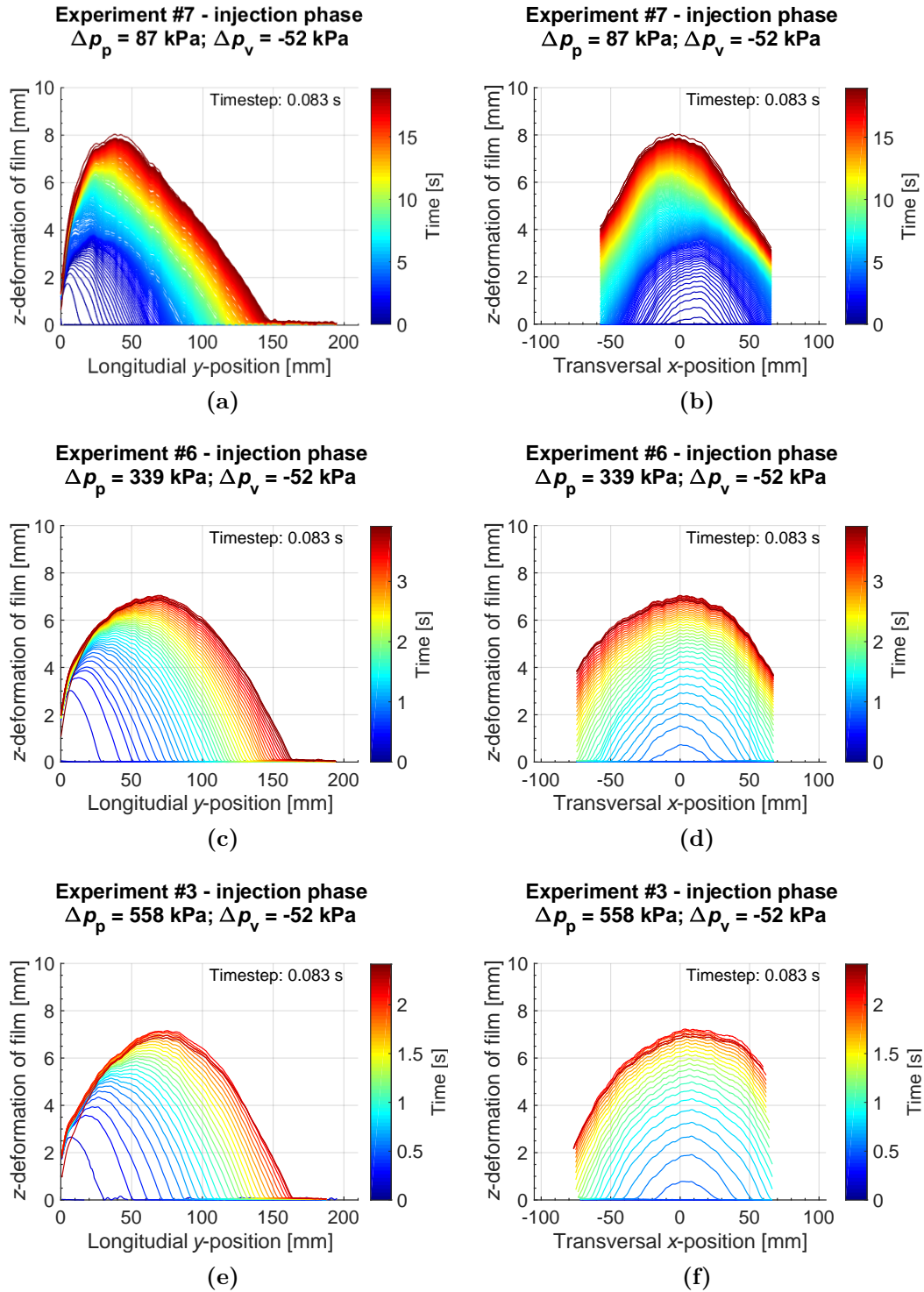


Fig. 6-14 Effect of pot pressure variation on the out-of-plane film deformation during the injection phase – depicted in the longitudinal yz -plane at the center of the inlet at $x = 0$ (left column) and at the transversal xz -plane position of maximum z -deformation recorded in the yz -plane at $y_{max}(\#7) = 38.1$ mm, $y_{max}(\#6) = 70.6$ mm and $y_{max}(\#3) = 75.0$ mm (right column). cf. [185]

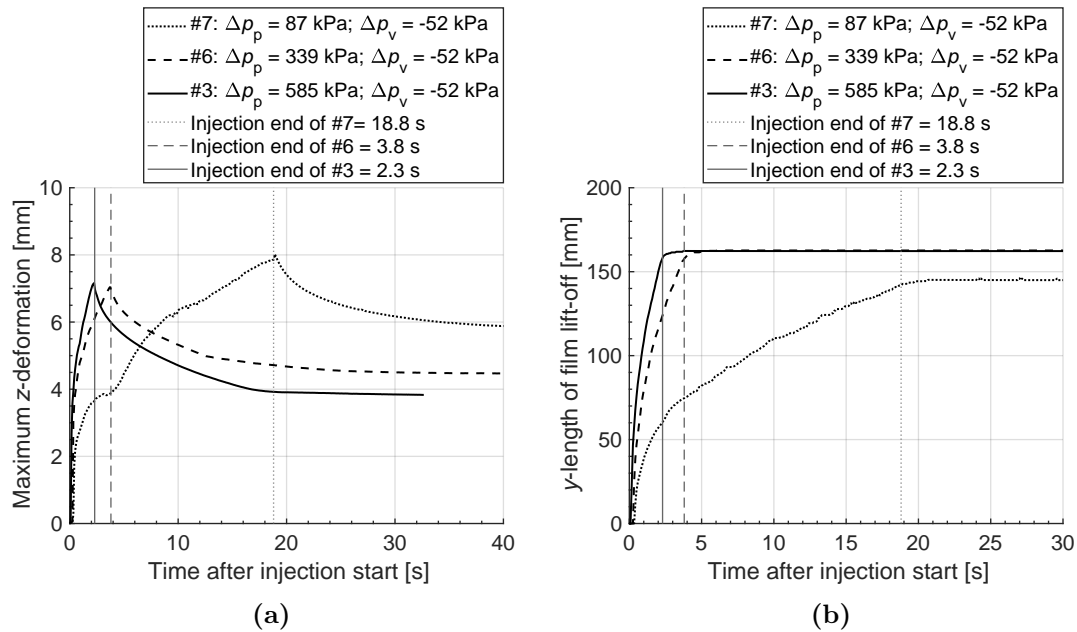


Fig. 6-15 Maximum z -deformation of film (a) and y -length of film lift-off (b) in the yz -plane at $x = 0$ plotted over time after injection start of the experiments with varying pot pressures. cf. [185]

medium and low vent pressure level, of -52 kPa and -99 kPa, exhibited a parabolic shape of the film.

The maximum z -deformation over time, recorded in the yz -plane at $x = 0$, is plotted in Figure 6-17(a). The maximum z -deformation is registered for all experiments at injection end, as previously observed for the experiments with pot pressure variation. While a similar increase in the first second of the injection is recorded for the experiments of medium and low vent pressure level, the two experimental settings separate afterwards showing a stronger increase and higher maximum z -deformation at injection end for the the experiment of low setting. Contrary, the experiment of high vent pressure (minimal vacuum) shows the highest z -deformation of the compared vent pressure variation experiments. This observation indicates a non-linear trend of the maximum z -deformation depending on the applied vent pressure.

As illustrated in both plots of in Figure 6-17, the injection time of all three experiments of varied vent pressure is nearly identical, which indicates an independence of the injection time from the vent pressure level. Figure 6-17(b) depicts the y -length of film lift-off for the experiments with vent pressure variation. The curves show a common progression trend which increases during the injection phase and stagnates shortly after the injection end, as previously observed during the experiments of pot pressure variation in Figure 6-15(b). Figure 6-17(b) exhibits a faster increase and higher final y -length of film lift-off with higher vent pressure. The y -length at

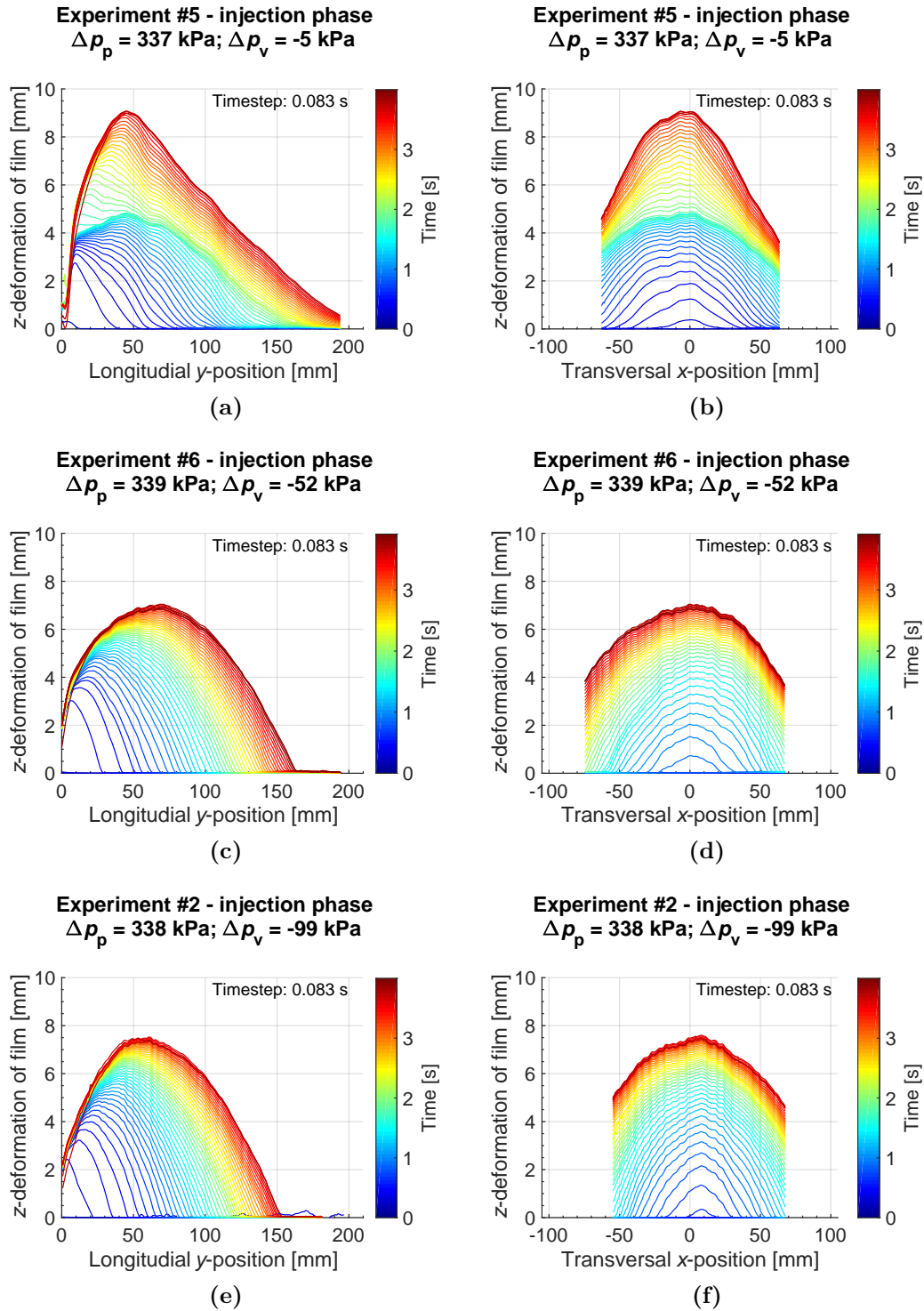


Fig. 6-16 Effect of vent pressure variation on the out-of-plane film deformation during the injection phase – depicted in the longitudinal yz -plane at the center of the inlet at $x = 0$ (left column) and at the transversal xz -plane position of maximum z -deformation recorded in the yz -plane at $y_{max}(\#5) = 44.8 \text{ mm}$, $y_{max}(\#6) = 70.6 \text{ mm}$ and $y_{max}(\#2) = 60.9 \text{ mm}$ (right column). cf. [185]

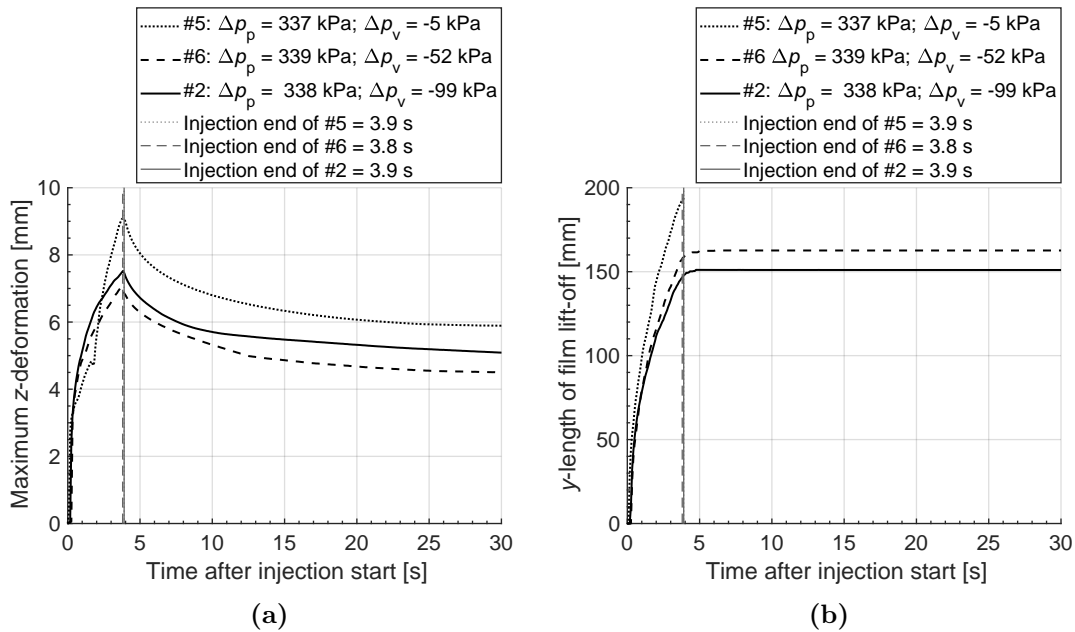


Fig. 6-17 Maximum z -deformation of film (a) and y -length of film lift-off (b) in the yz -plane at $x = 0$ plotted over time after injection start of the experiments with varying vent pressures. cf. [185]

experiment #5, at which the preform is not evacuated, exceeded even the length of the ARAMIS measurement area of 200 mm which indicates a complete overflow of the 210 mm long preform. The reduced y -length with decreased vent pressure correlates with the hypothesis, introduced at the beginning of this subsection, that an applied vent pressure creates a negative pressure gradient across the film which hinders the film to lift off the preform.

The hypothesis of an increased negative pressure gradient acting across the film with lowered vent pressure explains also the slight change of the parabolic shape between medium to low vent pressure level shown in 6-16(c), (d) and (e),(f), respectively. The reduction from medium to low vent pressure level increases the acting negative pressure gradient at the unimpregnated preform sections and consequently constrains the y -length of the film deformation, as recorded in Figure 6-17(b). Considering the reduced y -length, the previously discussed increased z -deformation level between medium to low vent pressure level, recorded in 6-17(a), is explained if a comparable amount of fluid is assumed to be situated below the films of both experiments.

Therefore, the presented experiments indicate, as for the pot pressure, that a certain threshold level needs to be exceeded for the vent pressure to form a stable double-curved parabolic film shape. A further decrease of vent pressure beyond this threshold is observed to decrease the maximum flow front progression (y -length), explained by an increased pressure gradient across the film in the unimpregnated

preform section, which needs to be overcome by the fluid pressure to lift-off the film.

6.2.3 Conclusions of Unrestrained Film Deformation Experiments

The presented study on unrestrained film deformation showed a good repeatability of the film deformation during the injection of FS-CRTM experiments. While maximum z -deformations are recorded to be nearly identical, slight deviation of flow front progression is observed during the repeatability experiments. The incomplete film re-deformation after injection indicates that without further action a certain amount of fluid remains above the preform after a FS-CRTM injection. These observations lead to the conclusion that by simply injecting the fluid into a film-sealed preform package without subsequent mold closure, the preform cannot be completely impregnated.

Furthermore, the investigations on injection (pot) and vent pressure variation showed that a certain pressure level needs to be exceeded for both process factors to form an unrestrained film deformation of parabolic shape. While an additional increase above the threshold level of the pot pressure is observed to not further change the film shape, a further reduction below the threshold of the vent pressure hinders the in-plane expansion (y -length) and increases the maximum z -deformation. Therefore, the flow front progression seems to be mainly controlled by the vent pressure level while the flow front progression can only be increased up to a certain stagnation level by increasing the injection (pot) pressure at FS-CRTM experiments of unrestrained film deformations.

Besides investigating the shape of the film deformation during FS-CRTM injection, the goal of this study is to investigate if the stiffness of the film is low enough to enable a complete filling of the injection gap by adapting to its inner geometry limited by the mold walls.

The presented experiments showed, that the unrestrained film deformation only locally lifts off the preform surface. A restrained deformation, forced by the upper mold surface present during real FS-CRTM injections, is expected to lead to an increased in-plane distribution of the fluid inside the injection gap. In this context, the measured maximum z -deformation during experiments of unrestrained film deformation has to be larger than an injection gap height during FS-CRTM manufacturing.

A theoretical upper limit of the injection gap volume is defined by the injected volume of the fluid. Aiming at a complete overflow of the preform and complete filling

of the injection gap by the fluid, the gap can theoretically be filled up to the point at which its volume is equal to the fluid volume, assuming an idealized scenario at which no fluid penetrates the preform. 123.9 ml (SD = 0.7) of fluid were injected at all presented experiments of this study which corresponds to a maximal gap height of 2.8 mm, calculated for an injection gap covering the complete preform surface. All experiments at injection (pot) and vent pressure variation show a maximal z -deformation far above the maximal theoretical gap height of 2.8 mm, indicating an early restraint of the film's z -deformation during FS-CRTM manufacturing at which a physical injection gap is present. The restraint in z -direction is intended to promote the in-plane distribution of the fluid, leading to an increased in-plane distribution of the fluid inside the injection gap as recorded during unrestrained film deformation experiments.

In conclusion, the unrestrained film deformation study showed that the stiffness level of the PE-LD film is adequate to enable an adaption of the film to the upper contour of the injection gap during FS-CRTM trials and that consequently also the stiffness of the identified PA/PP film at its desired process temperatures is suitable for FS-CRTM manufacturing.

6.3 Experimental Investigations on Factor-Response Correlations

The following section presents studies investigating the phases of the FS-CRTM process – (i) the injection as well as (ii) compression and holding phase. The studies are designed to identify factor-response correlations of the FS-CRTM process and give insight into the preform impregnation during FS-CRTM processing. Specifically developed laboratory equipment was utilized to perform flow visualization experiments according to the methodology explained in Appendix A.4. Due to the boundary conditions of the used test setup, flow visualization experiments could only be performed on preforms of small geometrical aspect ratio. Thus, the results and conclusions presented in this section are limited to FS-CRTM processing of preforms of small aspect ratio.

While the utilized test setup as well as film-sealing and experimental procedure is presented in Appendix A.4, the preforming and experimental design is explained in the following Subsection 6.3.1. The results of the factor-response study are presented and discussed in Subsection 6.3.2. Finally, conclusions are drawn in Subsection 6.3.3 and dominant process factors are presented for the FS-CRTM impregnation of preforms of small geometrical aspect ratio.

6.3.1 Preforming and Experimental Plan of the Factor-Response Study

Materials and Preforming

As frequently utilized for structural FRP parts in the automotive industry [9, 10, 188, 189], a carbon fiber non-crimp fabric (NCF) was used to manufacture the preforms for the factor-response study. Specifically, the stitched, biaxial NCF SIGRATEx® C B310-45/ST-E214/5g, manufactured by SGL Group (Wiesbaden, Germany) [143], was applied. Two lay-ups were manufactured. Twelve layers and fifteen layers were evenly stacked while a symmetrical lay-up was formed by rotating the lower six or seven layers by 90° for the experiments of the two full factorial test plans and for the additional experiments, respectively. Due to deformation of the test rig, the mold did not completely close during the experiments of the full factorial design, resulting in a slightly reduced fiber volume fraction (FVF) of approximately 55%. The out-of-plane deformation of the test rig was compensated during the additional experiments by programming the position control of the universal testing machine (UTM) to close the mold -0.15 mm below the nominal position of a completely closed mold leading to a FVF of approximately 60%. The pre-applied binder of the NCF [143] was activated via infrared heating at 170 °C ± 10 °C, while the preform was simultaneously vacuum-debulk. To investigate the FS-CRTM process with ideal preform impregnation conditions, it was essential that edge race-tracking was minimized during the performed experiments. As suggested in [190], the preforms were intended to be cut larger in their in-plane dimensions to prevent edge race-tracking. Via the CNC cutting table (M-1200 CV, Zünd, Altstätten, Germany), the preforms were cut to a theoretical dimension of 210 mm × 210 mm, 0.2 mm larger than nominal, with corner radii of R10.1. While the used CNC cutting table proved to cut single layers with tight tolerances, the cutting of thicker preforms proved to result in larger tolerances. Thus, the preforms of the factor-response study were recorded to be cut up to 0.7 mm larger than the programmed theoretical in-plane dimensions. The exact dimensions of all preforms are listed in Tables A-8, A-11 and A-14 in Appendix A.5.3. The preform dimensions resulted in an geometrical aspect ratio (in-plane versus out-of-plane dimension) of approximately 100 for the experiments of the full factorial designs and approximately 50 for the additional experiments at the final closing position of the mold.

All preforms were film-sealed as explained in Appendix A.4.1 by using the, in Subsection 6.1.3 identified, PE-LD film to substitute the PA/PP multilayer film designed for industrial FS-CRTM manufacturing (see Chapter 6.1.2). The 0.1 mm thick PE-LD film was manufactured by Sokufol (Limburg, Germany).

A non-reactive fluid was used during the FS-CRTM flow experiments substituting a reactive resin system which would be used during industrial FS-CRTM manufacturing. Sunflower oil of type Vita D'Or was used as substitution fluid. The specific viscosities of the sunflower oil are measured according to the procedure explained in Appendix A.1.1 and are listed in Tables A-9, A-12 and A-15 in Appendix A.5.3 for each performed experiment.

Experimental Design

To screen dominant process parameters and investigate the preform impregnation of the FS-CRTM process, two experimental series were conducted on the phases of the FS-CRTM process – (i) the injection, as well as (ii) compression and holding phase. A full-factorial experiment design was chosen in which each factor is individually changed on two levels while the other factors are kept constant. Additionally, the center point of the experimental design (medium setting of each factor) was tested multiple times at both series to evaluate the reproducibility of the test method. By the chosen experimental design, effects of specific factors and factor interactions can be identified. [191] The full factorial design is favorable due to its characteristic to be orthogonal⁷ and balanced⁸ but comes along with an increased amount of experiments compared to e.g. a design of experiment (DoE) attempt. Nonetheless, due to the relative small amount of factors (three) at both test series, the number of experiments at the chosen full factorial design at two levels was manageable. The multiple linear regression (MLR) approach was utilized to model the system which allows to describe effects and interactions of factors on investigated responses [191]. The commercial software package MODDE[®] Version 12 (Sartorius Stedim Data Analytics, Umeå, Sweden) was used to set up the experimental design and perform the MLR analysis based on the performed experiments. Due to limitations of the model validity for the compression phase, additional FS-CRTM flow experiments were performed to qualitatively validate the results of the MLR model. The experimental designs for the injection as well as the compression and holding plan are explained in the following.

Experimental Design – FS-CRTM Injection Phase: Figure 6-18 lists the identified factors, responses, control and disturbance variables, for FS-CRTM flow experiments to investigate the injection phase. The factors as well as control and disturbance variables influence the listed responses. Therefore, they have to be adequately managed during the FS-CRTM flow experiments to minimize potential

⁷ An experimental design is orthogonal if the pattern of factors is independent of each other [191].

⁸ An experimental design is balanced if the factor levels of each factor is equally divided in regard to all other factors [191].

errors of the MLR model and ensure meaningful predictions of the factor-response correlations.

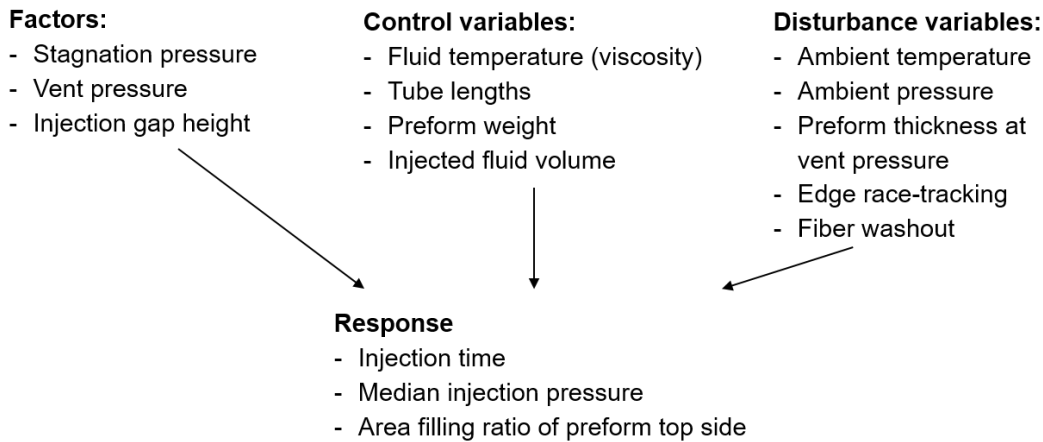


Fig. 6-18 Factors, responses as well as control and disturbance variables of flow visualization experiments investigating the injection phase of the FS-CRTM process.

Factors are input parameters of an experiment and are varied individually on two levels at the selected experimental design. Three factors were identified which were expected to influence the FS-CRTM process during its injection phase: (i) the stagnation pressure of the fluid (p_{stg}), (ii) the vent pressure (p_v), applied to the film-sealed preform package, and (iii) the injection gap height (h_{ig}), between the upper side of the preform and the lower side of the upper film after it is expanded to the upper mold. The stagnation pressure is a measure of the fluid pressure inside the feeding line. It is recorded close to the inlet and provides a relevant measure of the acting fluid pressure prior to mold injection, neglecting the occurring pressure losses inside the tubes and the injection equipment, specifically the pneumatic-hydraulic converter (PHC). Preliminary designs were conducted to correlate pre-defined pot pressures to acting stagnation pressures. Furthermore, the lower stagnation pressure level of 100 kPa was identified in preliminary tests to be high enough to ensure a reasonable injection time and a reproducible film deformation inside the injection gap. The upper stagnation pressure level of 600 kPa was defined by the limiting pressure level of the pneumatic supply line at the laboratory. The vent pressure limits were set on the lower level to -90 kPa to represent a nearly complete mold evacuation as applied during industrial applications [17, 23, 39] and on the upper level to -5 kPa to represent a nearly unevacuated mold. Both, the stagnation and vent pressure, were measured as differential value relative to the ambient pressure. The injection gap height, as third factor, is varied between 0.79 mm on its lower level and 1.98 mm on its upper level. The upper level represents an injection volume that is 10% larger than the injected fluid volume ensuring that the injection

gap is not completely filled during the injection phase. In contrast, the lower level represents a height at which the volume of the injection gap is 45% of the volume of the injected fluid, intended to simulate a full filling of the injection gap during the injection phase. The targeted factor settings ($p_{stg,t}$; $p_{v,t}$; $h_{ig,t}$) of the individual experiments are listed in Figure 6-19 which also illustrates the design space of the full factorial design on the right.

Experiment number	Target stagnation pressure ¹	Target vent pressure ¹	Target injection gap height
	($p_{stg,t}$)	($p_{v,t}$)	($h_{ig,t}$)
	[kPa]	[kPa]	[mm]
1,12	600	-90	0.79
2,13	600	-90	1.98
3,14	100	-90	0.79
4,18	100	-90	1.98
5,6,11,20	350	-47.5	1.39
7,16	100	-5	0.79
8,17	100	-5	1.98
9,19	600	-5	1.98
10,15	600	-5	0.79

¹ Differential value relative to ambient pressure.

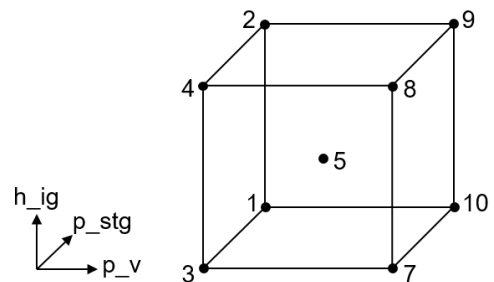


Fig. 6-19 Test plan of the factor-response study investigating the injection phase of the FS-CRTM process.

As listed in Figure 6-18, four control variables were identified which have to be kept constant during the performed FS-CRTM flow experiments. A change in fluid temperature directly influences the viscosity of the substitution fluid (sunflower oil) which, according to Darcy’s law (2-1), changes the preform impregnation pattern during the FS-CRTM flow experiments. To ensure a comparable fluid viscosity between the experiments, the fluid reservoir was temperature-controlled and all fluid containing equipment, which was not temperature-controlled, was filled last in the preparatory work of the experiments to limit the exposure time of the fluid to a potentially different ambient temperature. Difference in tube lengths would change the stagnation pressure at a pre-defined pot pressure due to frictional losses inside the tubes connecting the injection equipment and mold inlet. A standardized test setup ensured that all tube lengths were kept constant. The preform weight was controlled by manufacturing all preforms of the experimental study on the injection as well as compression and holding phase from the same material batch. Furthermore, CNC cutting equipment was used to minimize tolerances of the preform in-plane dimensions and their effect on the preform weight. The injected fluid volume was controlled by a limit stop which defined the piston stroke of the PHC during the loading of the fluid. Therefore, all control variables were regulated by a

standardized experimental setup ensuring a reproducible experimental procedure as explained in Appendix A.2.1.

Figure 6-18 lists five disturbance variables. The impact of each of the listed disturbance variables on the FS-CRTM flow experiments has to be minimized to ensure a robust experimental procedure and meaningful results. The laboratory, at which the experiments were performed, was not temperature-controlled, which is why the ambient temperature could vary between experiments. A fluctuating ambient temperature was identified to be most critical towards changing the temperature and consequently the viscosity of the injected fluid (sunflower oil). Thus, the fluid was temperature-controlled and its exposure to the ambient temperature was minimized, as explained in the last paragraph. The influence of a changing ambient pressure was minimized by measuring the factors, stagnation and vent pressure, not absolute but relative to the ambient pressure. The thickness of a film-sealed preform depends on the pressure gradient acting across the film, defined by the applied vent pressure level inside the film-sealed preform package. Therefore, the injection gap would also change if the cavity height was kept constant for experiments of different vent pressures. To minimize the influence of the preform thickness on the injection gap height, the preform thickness of each preform was measured prior to each experiment at its defined vent pressure level and the position of the upper mold was adjusted to ensure comparable injection gap heights between experiments. As suggested in [190], the edge race-tracking effect was minimized by cutting the in-plane preform dimensions larger than the cavity dimensions. Fiber washout was eliminated by a standardized film-sealing procedure of the preform which includes a fluid transition zone guiding the fluid onto the preform, as presented in Appendix A.4.1.

Finally, three responses of the FS-CRTM process are listed in Figure 6-18 which were all measured during the flow experiments. The first response, injection time, was calculated between the injection start, recorded by the initiation of the operator in the control software, and the time at which the injection piston was empty, recorded by the activation of the converter-empty bottom at the PHC. The injection pressure, as second response, was monitored at the feeding line of the inlet and calculated as median between injection start and injection end. As described in Appendix A.2.1, the preform impregnation on the preform top side is monitored via an industrial camera. The impregnation of the preform top side can be directly correlated to the fluid flow inside the injection gap above the preform. Therefore, the area filling ration (AFR) of the preform top side at the end of the injection phase is chosen as third process response to investigate the FS-CRTM injection phase.

Experimental Design – FS-CRTM Compression and Holding Phase: Figure 6-20 lists the identified factors, responses as well as control and disturbance variables of the FS-CRTM experiments to investigate the compression and holding phase. As for the injection phase, the factors, vent pressure and injection gap height, are expected to influence the FS-CRTM preform impregnation during the compression and holding phase. The third factor of the injection phase, stagnation pressure, is only influencing the fluid flow during the injection phase, which is why this factor is not included in the investigations on the compression and holding phase. For all experiments investigating the compression and holding phase the stagnation pressure was set at 300 kPa. During the here investigated compression and holding phase the movement of the upper mold is influencing the fluid flow. The movement of the upper mold is controlled via the UTM and the compression force is recorded between test setup of upper mold and the moving traverse of the UTM. Therefore, the compression force (f_c) is listed as third factor in Figure 6-20. All experiments investigating the compression and holding phase were force-controlled at which the upper mold was closed at a constant closing speed (\dot{h}_c) of 0.1667 mm/s up to a pre-defined maximum compression force. After reaching the pre-defined compression force the closing speed was automatically reduced so that the compression force was kept constant until the mold was completely closed. Preliminary velocity-controlled FS-CRTM flow experiments at a constant closing speed of 0.1667 mm/s were performed to identify the maximal compression force and the relaxed compression force. Knowing the maximal compression force of the preliminary tests, a slightly lower compression force of 19.8 kN, corresponding to a pressure of 450 kPa, was defined as the upper limit for the force-controlled experiments. A slightly higher force than the relaxed compression force of the preliminary tests of 15.4 kN was defined as the lower limit for the force-controlled experiments which corresponds to a pressure of 350 kPa. Figure 6-21 lists the targeted factor setting ($f_{c,t}$; $p_{v,t}$; $h_{ig,t}$) of all performed FS-CRTM flow experiments to investigate the compression and holding phase and illustrates the experimental design space on the right.

The identified control and disturbance variables for the experiments investigating the compression and holding phase are identical to the ones for the injection phase.

Four responses were defined to investigate the FS-CRTM compression and holding phase. First, the compression time between injection end and complete mold closure is measured for all experiments. Further, the time of initial through-thickness penetration (TITTP) is recorded by monitoring the preform impregnation on the preform bottom side via an industrial camera. Conclusions on the preform impregnation pattern are desired by evaluating the time at which 50% and 90% of the

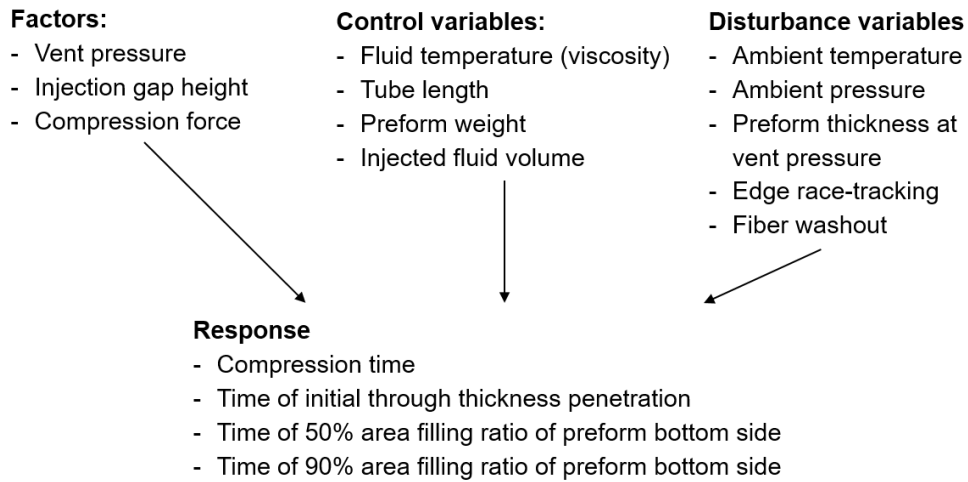


Fig. 6-20 Factors, responses as well as control and disturbance variables of flow visualization experiments investigating the injection phase of the FS-CRTM process.

preform bottom side is impregnated (time of 50% / 90% area filling ratio of preform bottom side).

Additional experiments were performed to further investigate the correlation between the factor, compression force, and the response, compression time. Therefore, the factors stagnation pressure, vent pressure and injection gap height were kept constant at levels listed in Table 6-3. The only factor varied was the compression force which was varied on three levels. On each level, experiments were repeated three times. First, the experiments were conducted velocity-controlled at $\dot{h}_c = 0.1667$ mm/s to gain insight on the maximum compression force. Further, an increase in compression time, compared to the velocity-controlled experiments, was

Experiment number	Target compression force (f_c,t)	Target vent pressure ¹ (p_v,t)	Target injection gap height (h_ig,t)
	[kN]	[kPa]	[mm]
1	15.4	-5	1.98
2	19.8	-5	0.79
3, 12	19.8	-90	0.79
4, 6, 9	17.6	-47.5	1.39
5	19.8	-5	1.98
7, 13	15.4	-5	0.79
8	19.8	-90	1.98
10	15.4	-90	0.79
11	15.4	-90	1.98

¹ Differential value relative to ambient pressure.

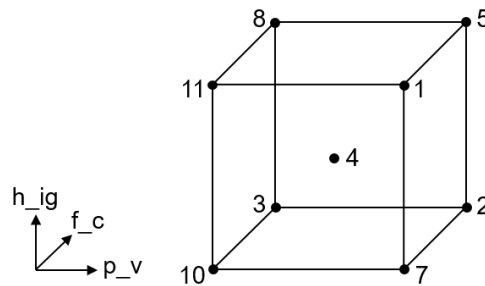


Fig. 6-21 Test plan of the factor-response study investigating the injection phase of the FS-CRTM process.

investigated by conducting force-controlled experiments at a medium of 24.2 kN and low compression force level of 22 kN, corresponding to a pressure of 550 kPa and 500 kPa, respectively.

All experiments investigating the factor-response correlations of the FS-CRTM process were performed at a constant closing speed of 0.1667 mm/s either until complete mold closure (velocity-controlled) or until a pre-defined force limit was reached (force-controlled). The difference in cavity height and fabric layers of the preform required an adjustment of the injected fluid volume. For the experiments of the full factorial design investigating the injection phase 78.2 cm³ (SD = 0.5), for the compression and holding phase 78.2 cm³ (SD = 0.8) and for the additional experiments 93.6 cm³ (SD = 0.4) were injected, measured via five dosed injections prior to each test series.

6.3.2 Results and Discussion of the Factor-Response Study

This subsection presents the findings of two studies investigating effects and interactions of factors during FS-CRTM processing. Flow visualization experiments with preforms of small aspect ratio were conducted according to the methodology explained in Appendix A.4. The process factors of the performed experiments, as listed in Tables A-9, A-12 and A-15 in Appendix A.5.3, were recorded to match the target values, presented in the previous subsection. Two full factorial experimental designs were set up to investigate separately (i) the injection as well as (ii) compression and holding phase of the FS-CRTM process. Multi-linear regression (MLR) analysis was performed in the software MODDE[®] to model the correlation of factors on individual responses. The exact response values of each experiment is listed in Tables A-10, A-13 and A-16 in Appendix A.5.3.

Tab. 6-3 Factor levels of flow visualization experiments investigating the compression and holding phase of the FS-CRTM process – additional experiments.

Process factor	Level
Target stagnation pressure ^I (p _{stg,t})	300 kPa
Target vent pressure ^I (p _{v,t})	-90 kPa
Target injection gap height (h _{ig,t})	1.42 mm
	3 × velocity-controlled
Target compression force (f _{c,t})	3 × force-controlled ^{II} : 24.2 kN 3 × force-controlled ^{II} : 22 kN

^I Differential value relative to ambient pressure.

^{II} Constant closing speed of $\dot{h}_c = 0.1667$ mm/s until force limit is reached.

For each response model an “overview plot” is presented in Appendix A.5.3 consisting of four graphs. The first graph in the top left depicts the “replicate plot” which shows the response of each experiments, grouping the replicates under the same index to ease the identification of potential outliers. The second graph on the top right shows the “summary of fit plot”, in which four basic model statistics are presented. The first presented statistic represents the model fit or R² value, showing the percentage of the variation of the response explained by the model. The second model statistic in the summary of fit plot estimates the prediction precision of the model given as Q² value, representing the percentage of the variation of the response predicted by the model. The third statistic in the summary of fit plot provides a measure of the validity of the model while the fourth model statistic illustrates the reproducibility value representing the variation of the response under the same conditions compared to the total variation of the response. Further, the “coefficient plot” is depicted as third graph on the lower left of the overview plot. It shows the value of each coefficient of the MLR model and its uncertainty level. The significance of each coefficient is indicated by a bar of large distance from the y-axis and an uncertainty level that does not cross the y-axis. On the fourth graph, on the lower right of the overview plot, the raw residuals are plotted over their normal probability to check if the residuals are normally distributed indicated by residuals aligned on a straight, diagonal line. [191, 192]

The response models are presented in this subsection by “effect plots” showing the effects in sorted and descending order. The effects are computed in MODDE[®] as two times the corresponding coefficient of the MLR model and contain, therefore, all model terms (coefficients) of each factor and factors’ interactions. Each effect is considered to be significant if its uncertainty level is smaller than the magnitude of the effect. Furthermore, the “prediction plot” is presented for each model showing the predicted correlation between factor and response as well as the uncertainty level of the model at a pre-defined setting of all factors. The uncertainty level of all plots represents the 95% confidence interval. [192]

Injection Phase – Injection Time and Flow Rate

Based on the performed FS-CRTM flow experiments, a response model of the injection time was calculated to investigate which factors influence this specific response. The model was box-cox⁹ transformed by the exponent $\lambda = -1.39$. The overview plot, presented in A-43 in Appendix A.5.3, shows similar response values of the replicated experiments and indicates a well fitted transformed response model.

⁹ The box-cox transformation describes a mathematical transformation to increase the model quality of the response in dependence of its factors. The mathematical formula of the box-cox transformation is $z = y^\lambda, \lambda \neq 0$ & $z = \ln(y), \lambda = 0$. [191]

Figure 6-22(a) depicts the effect plot of the transformed injection time model. The factors stagnation pressure (p_{stg}) and injection gap height (h_{ig}) are listed to be significant effects of the presented MLR model while all other effects are shown to be not significant. By comparing the magnitude of the significant effects, it is clear that the stagnation pressure has the strongest impact while the injection gap height is recorded to influence the investigated response, injection time, only minimally. The observed dependency of the injection time by the stagnation pressure and the injection gap height can be explained by describing the flow inside the injection gap via Darcy’s law (Equation 2-1). Even though Darcy’s law has been derived for fluid flow through a porous medium, which the injection gap is not, literature studies have shown that the equivalent approach can be applied to model the flow inside an injection gap via Darcy’s law (see Chapter 2.2.3). The flow velocity, which correlates to the injection time of a defined fluid volume, is, by Darcy’s law, dependent on the viscosity of the fluid, the equivalent permeability of the injection gap and the acting pressure gradient. While the viscosity of the fluid was controlled to be constant, the permeability and pressure were varied at the performed experiments. Applying the equivalent permeability approach, Equation (2-8) describes the permeability of the injection gap to be dependent on its height. Therefore, a reduced injection gap height decreases the permeability, slowing down the fluid flow and increasing the injection time. The stagnation pressure is assumed to influence the acting fluid pressure during the injection. According to Darcy’s law an increased stagnation and consequently injection pressure would, therefore, lead to an increased velocity of the flow and to a reduced injection time.

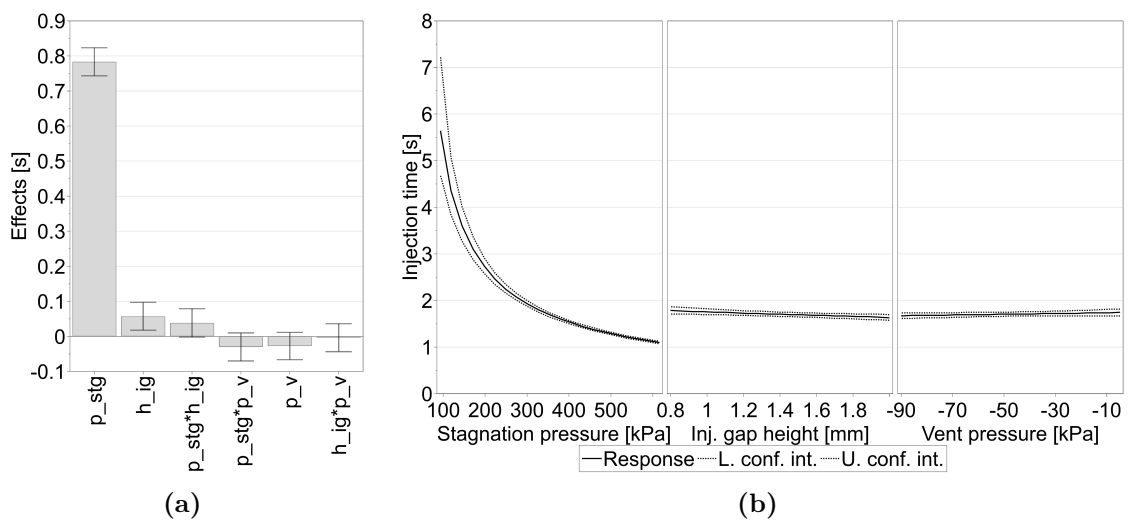


Fig. 6-22 (a) Effects of injection time model; (b) predictions of injection time model at medium factor setting ($p_{stg} = 350$ kPa, $p_v = -47.5$ kPa, $h_{ig} = 1.39$ mm).

The prediction plot of the injection time model is depicted in Figure 6-22(b) for medium factor setting ($p_{stg} = 350$ kPa, $p_v = -47.5$ kPa, $h_{ig} = 1.39$ mm).

The insignificant effect of vent pressure (p_v) is predicted to minimally change the injection time over the range of investigated vent pressure level which is lower than its upper and lower uncertainty levels. A slight increase in injection time is predicted for reduced injection gap heights. Comparing the magnitude of changed injection time over the range of investigated injection gap height with the magnitude of changed injection time over the range of investigated stagnation pressure, shows that the stagnation pressure has a stronger influence on the injection time. A strong non-linear reduction of injection time and reducing upper and lower confidence interval levels are predicted for an increasing stagnation pressure. While it was stated in the last paragraph, that the significant factors are identical to the influencing coefficient of Darcy's law, the correlations are not. Even though Darcy's law states a linear dependency of the injection time on the pressure, the prediction of the MLR model shows a non-linear trend. Furthermore, Darcy's law, in combination with the equivalent permeability approach, assumes a non-linear dependency of the injection time on the injection gap height while the presented model states a linear correlation.

By knowing the pre-defined injected fluid volume and the measured injection time of each experiment an additional response, the flow rate, was calculated and modeled. The MLR model of the flow rate was box-cox transformed ($\lambda = -1.44$). The overview plot of the transformed model is presented in Figure A-44 in Appendix A.5.3 indicating a good fit of the response model.

As for the injection time model, the coefficients of stagnation pressure as well as injection gap height are significant, as shown in the coefficient plot in Figure A-44 in Appendix A.5.3. The predictions in Figure 6-23 for medium factor setting ($p_{stg} = 350$ kPa, $p_v = -47.5$ kPa, $h_{ig} = 1.39$ mm) show a similar correlation between vent pressure and flow rate as well as injection gap height and flow rate as observed for the injection time prediction in Figure 6-22(b). However, a near-linear correlation is predicted between the flow rate and the stagnation pressure at which an increasing stagnation pressure results in an increasing flow rate.

Injection Phase – Median Injection Pressure

The injection pressure, calculated as median over the injection time, was chosen as second response to be modeled. The MLR model was box-cox transformed in MODDE[®] by $\lambda = 0.265$. The overview plot, depicted in Figure A-45 in Appendix A.5.3, presents a well fitted model.

The effect plot, in Figure 6-24(a), illustrates that the factors, stagnation pressure (p_{stg}) and injection gap height (h_{ig}), are both significant effects of the presented MLR model of the injection pressure. The third factor vent pressure (p_v) and all

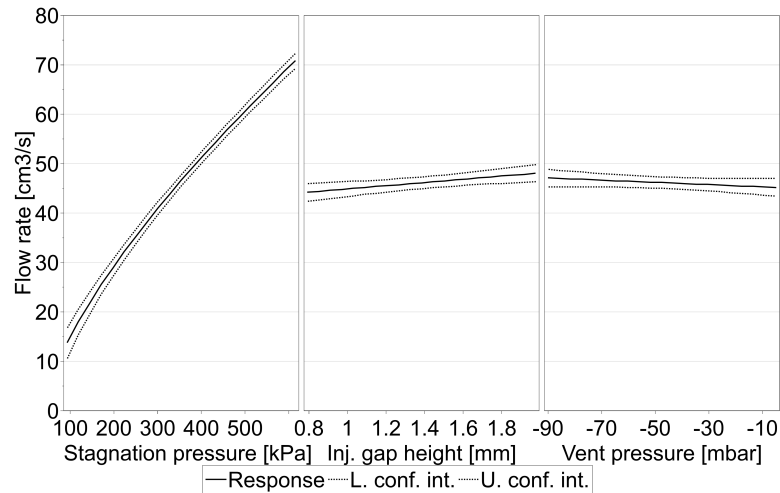


Fig. 6-23 Predictions of flow rate model at medium factor setting ($p_{inj} = 350$ kPa, $p_v = -47.5$ kPa, $h_{ig} = 1.39$ mm).

interactions are reported to be not significant. The large value of the stagnation pressure indicates that it has the strongest effect while the second significant effect, injection gap height, with a magnitude of approximately three times its uncertainty level, is predicted to also influence the response but on a lower level.

Figure 6-24(b) shows the predictions of the injection pressure model at medium factor setting ($p_{stg} = 350$ kPa, $p_v = -47.5$ kPa, $h_{ig} = 1.39$ mm). The observed change in injection pressure over the investigated vent pressure range is far smaller than its upper and lower uncertainty limit, showing the insignificance of this factor. A linear decrease of injection pressure is predicted for an increasing in-

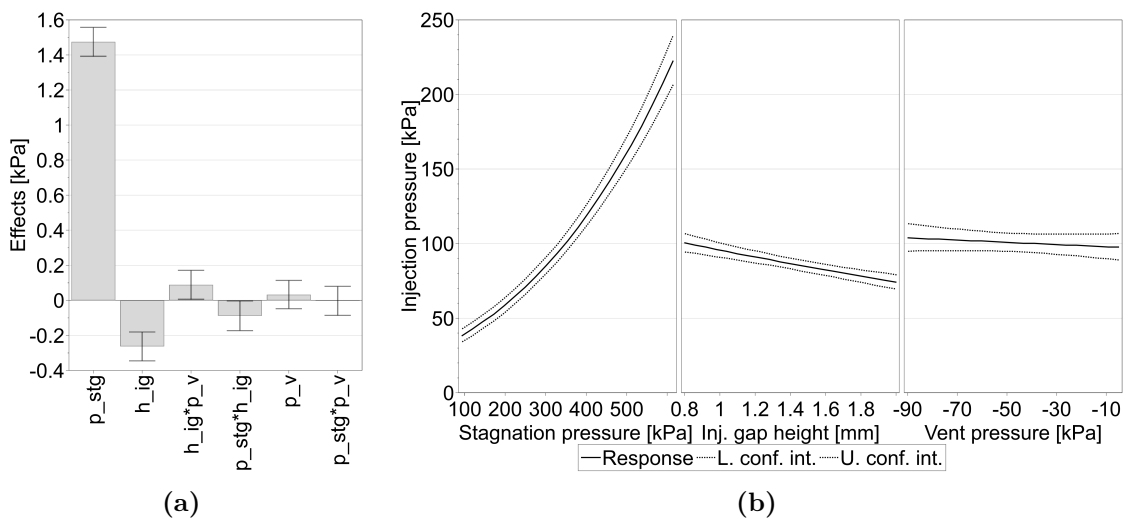


Fig. 6-24 (a) Effects of injection pressure model; (b) predictions of injection pressure model at medium factor setting ($p_{stg} = 350$ kPa, $p_v = -47.5$ kPa, $h_{ig} = 1.39$ mm).

jection gap height while the injection pressure is predicted to increase non-linearly with increasing stagnation pressure. Comparing the magnitudes of changed injection pressure for all three factors indicates that the stagnation pressure has the strongest effect on the stagnation pressure inside the investigated ranges of factors.

While the MLR model reveals which factors influence the injection pressure response, detailed experimental results are presented in the following to give further insight into specific factor-response correlations observed during the flow experiments. Figure 6-25 depicts the pressure level progressions, recorded at the inlet, of FS-CRTM flow experiments at high level of stagnation pressure (600 kPa) and low level of stagnation pressure (100 kPa). The time scale is illustrated as time after injection start, so that for all experiments the injection start is located at 0 s. Thus, the recorded pressure level before 0 s represents the pre-defined stagnation pressure. After the injection start at 0 s, the pressure level is recorded to drop drastically for FS-CRTM injections at presence of an injection gap. Ignoring the short time spans of initial pressure drop and of a short reduction at the injection end for high stagnation pressure, the pressure during the injection (p_{inj}) is recorded to be constant. The results reveal also that the injection pressure level differs for different pre-defined stagnation pressure levels. As predicted by the MLR model, a higher injection pressure plateau is recorded for a higher stagnation pressure. The absolute pressure drop, between the stagnation pressure prior to injection start and the pressure plateau during the injection, is observed to be larger for the experiments of high level than of low level of stagnation pressure. Generally, the pressure drop is explained by a transition from a static pressure (stagnation pressure) to a dynamic fluid flow during the injection (injection pressure). The larger pressure drop for a higher stagnation pressure is explained by a faster fluid flow during these injections, indicated by the much shorter injection time at an identical injected fluid volume.

Figure 6-26 presents results of two exemplary experiments at high and low level of injection gap height while all other factors are identical for both experiments. Besides the progression of the fluid pressure at the inlet, the plot shows the area filling ratio (AFR) on the top side of the preform which can be correlated to the extend to which the injection gap is filled. The predicted factor-response correlation of higher injection pressure for lower injection gap height is observed by a lower pressure drop after injection start for experiment #3 than for #4. Additionally, a slightly longer injection time for a lower injection gap height is recorded in Figure 6-26 as predicted by the MLR model for the injection time response. In contrast to the constant pressure plateau for high injection gap heights at experiment #4, the pressure increases after an initial plateau for experiment #3. The observed pressure increase starts at the same time as the area filling ratio indicates a complete filling of the injection gap (AFR = 96%) at 4.8 s. Therefore, the injection pressure is

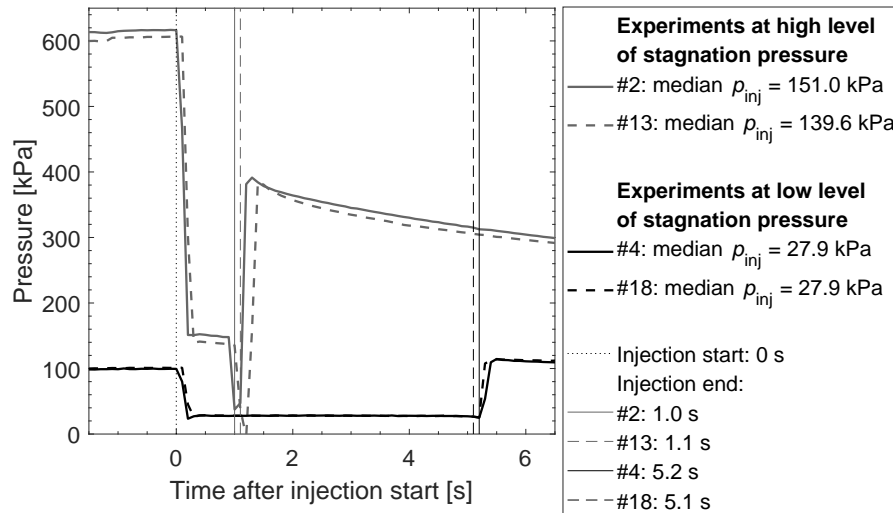


Fig. 6-25 Fluid pressure progression at inlet over time after injection start of FS-CRTM flow experiments at low and high stagnation pressure level ($p_{v,t} = -90$ kPa).

correlated to the filling state of the injection gap. During the filling of the injection gap, the pressure is observed to remain at a nearly constant level, while the pressure is recorded to rise after the injection gap is completely filled. This conclusion is strengthened by the observations of experiment #4 at which the injection gap is not completely filled during the injection and a constant pressure plateau is recorded without any pressure increase at the end of its injection phase.

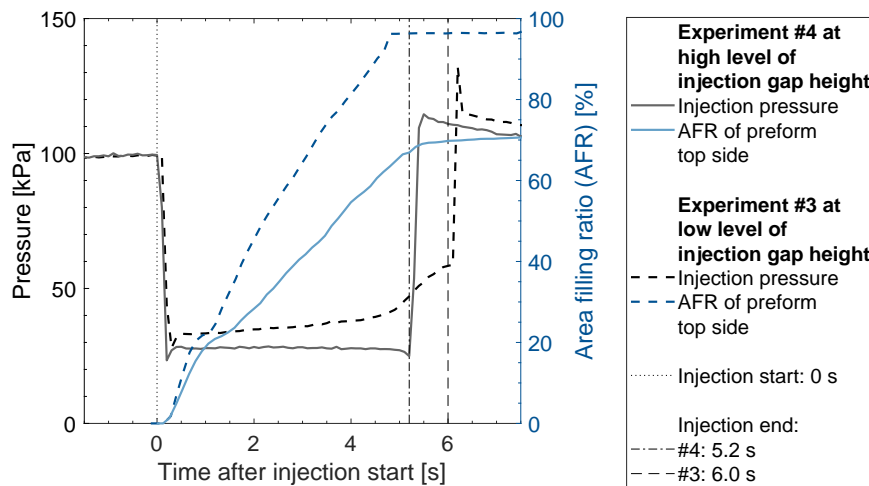


Fig. 6-26 Fluid pressure development and AFR of preform top side over time after injection start of FS-CRTM flow experiments at low and high injection gap height level ($p_{v,t} = -90$ kPa).

Injection Phase – Area Filling Ratio of Preform Top Side

Based on the performed experiments a MLR model was calculated to investigate the correlation between the factors and the response area filling ratio (AFR) of the preform top side at the end of injection. The AFR of the preform top side correlates to the filling of the injection gap which cannot be directly measured. To increase the model quality, the MLR model was extended to include a squared term of injection gap height and the model was negatively log-transformed by $-10 \times \log(100 - y)$. The transformed response model of the AFR of preform top side is well fitted indicated by the model statistics presented in the overview plot in Figure A-46 in Appendix A.5.3.

Figure 6-27(a) depicts the effect plot of the response model of the AFR of the preform top side. The factors stagnation pressure (p_stg), injection gap height (h_ig) and the squared term of the injection gap height (h_ig*h_ig) are stated to be significant effects. Comparing the magnitude of the three significant effects, the injection gap height's linear and squared term are identified to have the strongest effect on the response AFR of the preform top side. The third factor, vent pressure (p_v), and the interactions of all factors are not significant in the MLR model.

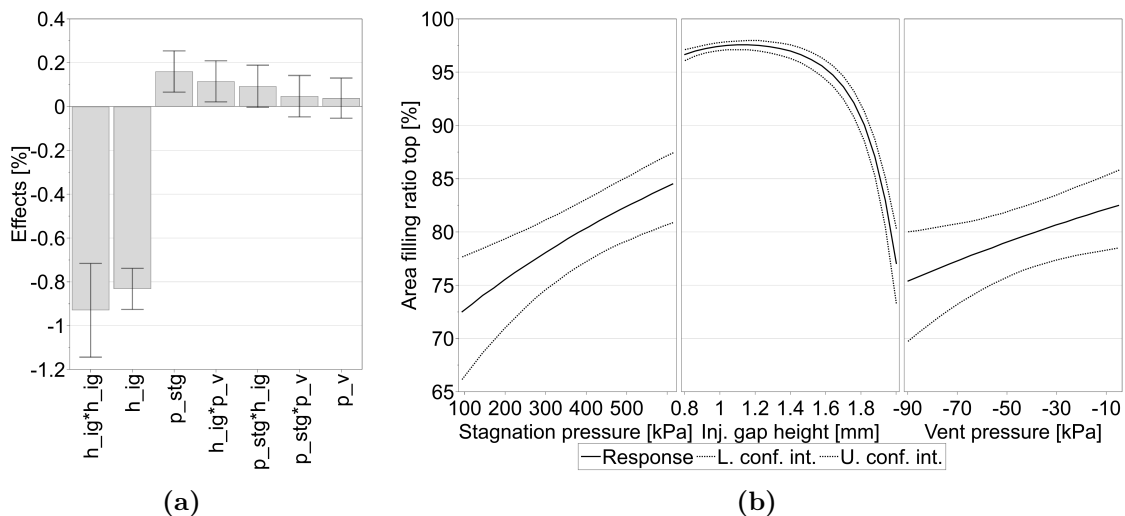


Fig. 6-27 (a) Effects of ratio of area filling ratio (AFR) of preform top side model; (b) predictions of AFR of preform top side model ($p_stg = 350$ kPa; $p_v = -47.5$ kPa; $h_ig = 1.98$ mm).

Prediction plots at medium factor setting of stagnation and vent pressure are shown in Figure 6-27(b) and in Figure A-47 in Appendix A.5.3 for high and low setting of injection gap height, respectively. At both prediction plots, the prediction of the AFR of the preform top side shows a minor change compared to its confidence level between an injection gap height of 0.8 mm to 1.5 mm while a further increase of injection gap height is predicted to result in a strong response reduction. As explained

in Appendix A.4.3, an AFR of the top preform side of 95% or above represents a complete filling due to limitations of the used evaluation method. Therefore, the injection gap is predicted to be completely filled for injection gap heights below 1.5 mm. This results of the pre-defined boundary conditions of the target injection gap height at which the upper limit represents a volume of the injection gap that is 10% larger than the injected fluid volume while the lower boundary of the injection gap height represents a volume that is 65% smaller than the injected fluid volume. Therefore, experiments in which only the injection gap height is changed a high setting of the injection gap height leads to an incomplete filling of the injection gap (AFR of the preform top side), as visualized for experiment #4 in Figure 6-28(a), and a low injection gap height results in a complete filling of the injection gap, as visualized for experiment #3 in Figure 6-28(b). Furthermore, this explains why at a high injection gap height, at which the injection gap is not completely filled, the stagnation pressure is predicted to also effect the AFR on the preform top side (see Figure 6-27b). In contrast, the injection gap height at a low setting is observed to always cause a full filling of the injection gap, resulting in a prediction model, shown in Figure A-47 in Appendix A.5.3, at which no other factor than the injection gap height is predicted to influence the response AFR of the preform top side at injection end.

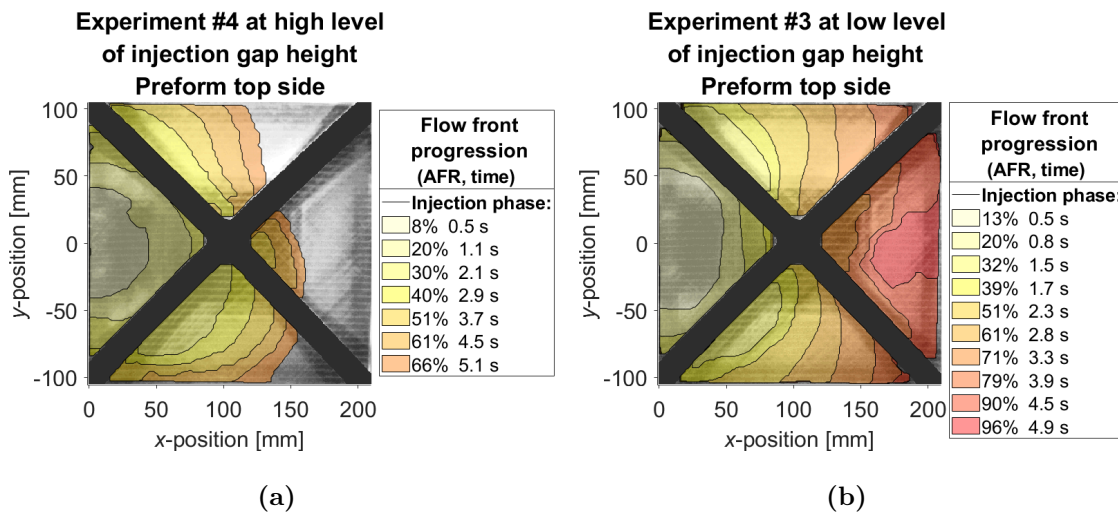


Fig. 6-28 Flow front progression during the injection phase at high (a) and low (b) level of injection gap height ($p_{stg,t} = 100$ kPa; $p_{v,t} = -90$ kPa).

The predicted effect of stagnation pressure on the AFR of the preform top side at a high level of injection gap height is further illustrated by the flow front progression graphs of Figure 6-29. The presented MLR model at high injection gap height level predicts in Figure 6-27(b) that with increasing stagnation pressure the AFR on the preform top side increases. As identified at previous response models, an increased stagnation pressure leads (i) to an increased injection pressure and

(ii) to a reduced injection time. Generally, on the one hand, an increased injection pressure is expected to promote the preform impregnation due to a higher acting fluid pressure and on the other hand a reduced injection time is expected to reduce the preform impregnation due to time constraints. Additionally, an increased impregnation of the preform correlates to a reduced filling of the injection gap and a reduced recorded AFR of the preform top side. Therefore, the predicted increase in AFR on the preform top side with increasing stagnation pressure indicates that the resulting reduced injection time has a larger influence on the preform impregnation, as visualized by experiment #4 and #2 in Figure 6-29. While experiment #4 at low level of stagnation pressure in Figure 6-29(a) is recorded to have a final AFR of 66% at its injection end after 6s, experiment #2 at high level of stagnation pressure in Figure 6-29(b) has an increased final AFR of 83% and a shorter injection time of 1 s.

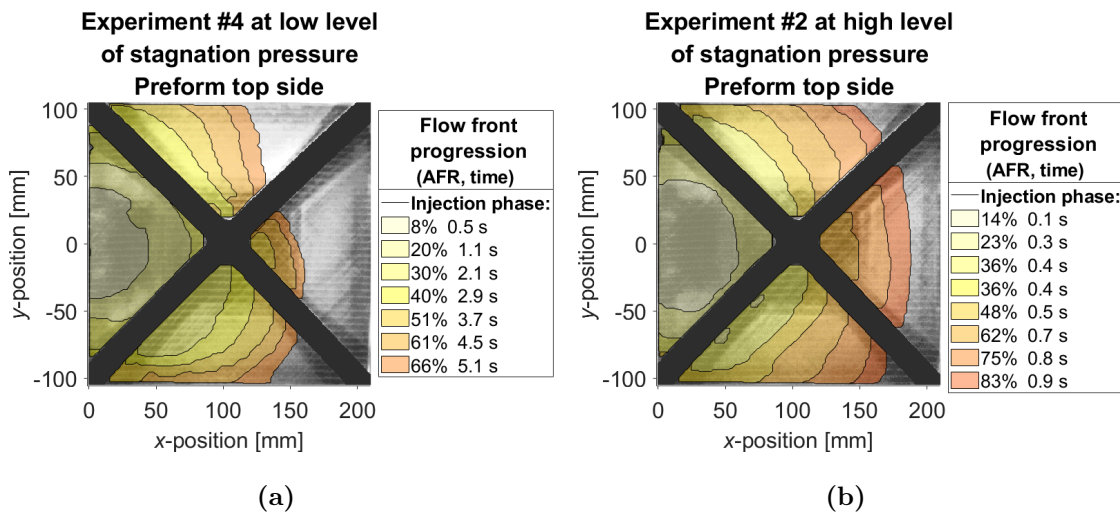


Fig. 6-29 Flow front progression at low (a) and high (b) level of stagnation pressure ($p_{v,t} = -90$ kPa; $h_{ig,t} = 1.98$ mm).

Compression and Holding Phase – Compression Time

A second full factorial experimental design was set up to investigate the compression and holding phase of the FS-CRTM process. Due to limited resources of the NCF material, the experiments were anticipated to be conducted once except for the center point which was planned to be repeated three times to verify the reproducibility of the experimental method.

The overview plot of the compression time model is presented in Figure A-48 in Appendix A.5.3. The replicate plot on the top left shows a good reproducibility of the center point experiments (#4, #6 and #9). Two additional preforms enabled experiment #3 and #7 to be repeated. While the reproducibility of experiment #3

by #12 was shown to be good a larger gap between the repetitions #7 and #13 is recorded. The limited reproducibility of the latter two experimental settings is expected to be caused by the specific experimental procedure of the FS-CRTM flow experiments. As defined in the experimental plan (Figure 6-21), experiments #7 and #13 are conducted at high vent pressure setting, small injection gap height and low compression force. At a high vent pressure the gas inside the film-sealed preform package can only exit the package through a porous cord at a preform corner opposite of the inlet. As identified during the investigations of the injection phase, a small injection gap height results in a complete filling of the injection gap during the injection phase. This early, complete filling of the injection gap also results in the cord becoming soaked with fluid early in the process. Thus, the fluid is expected to block the pores of the cord reducing its anticipated functionality to provide a passage for the gas. The fact that the preform is not evacuated (high level of vent pressure) at the experimental setting of experiment #7 and #13 in combination of limited venting of the preform during the process due to the fluid-soaked cord and a small acting compression force leads to an unstable process setting which resulted in the observed large fluctuation of the two repetitions. The concept of venting the film-sealed preform package by a cord is, therefore, identified to cause problems at certain process settings and has to be replaced by a more robust solution at future industrial applications. The MLR model was log-transformed by $10 \times \log(y)$ to increase the model quality. The model statistics presented in the summary of fit plot in Figure A-48 in Appendix A.5.3 show a medium model quality of the response compression time, which is why the observed results were verified with additional experiments.

The effect plot of the compression time model is presented in Figure 6-30(a). The only significant effect of the model is the compression force (f_c) while the other two factors, injection gap height (h_{ig}) and vent pressure (p_v), as well as all interactions are shown to be not significant. Figure 6-30(b) depicts the predicted factor-response correlation of the compression time model. The insignificant factors, gap height and vent pressure, are predicted to have a smaller impact on the response than the uncertainty of their prediction. However, the factor compression force is observed to significantly impact the response compression time in which an increased compression force results in a reduced compression time. A non-linear correlation between compression time and compression force is predicted.

Due to the limited model quality of the presented MLR model of the compression time model, the predicted correlation between compression time and force was anticipated to be verified by additional experiments. The additional experiments differ in their preform lay-up and some dependent process settings of the experiments performed for the MLR model. Therefore, the results of the flow visualization ex-

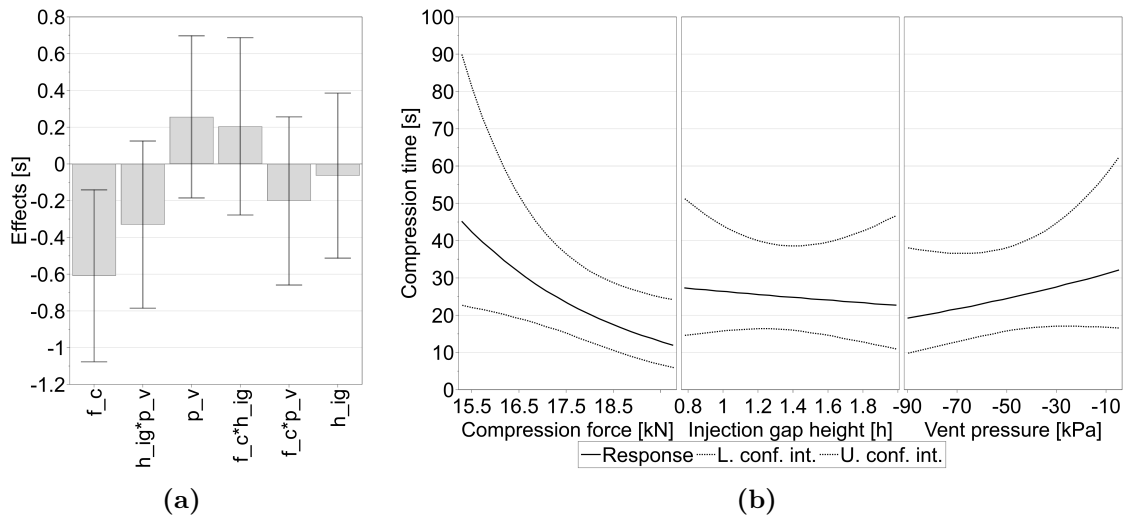


Fig. 6-30 (a) Effects of compression time model; (b) predictions of compression time model at medium factor setting ($f_c = 17.31$ kN, $p_v = -47.5$ kPa, $h_{ig} = 1.39$ mm).

periments are only qualitatively and not quantitatively comparable. However, the general non-linear correlation between compression time and force is expected to be validated. Three experimental settings were conducted each repeated three times as listed in Table 6-3.

Figure 6-31(a) shows the compression force over time after injection start for a representative experiment of each setting. The first setting was defined to be velocity-controlled (no force limit) while the second and third were force-controlled on two different force levels. Except for the first curve maxima at approximately two seconds (end of injection), the compression force curves of all three settings are overlapping each other during the compression phase due to the identical mold closing speed of 0.1667 mm/s. The curve of the velocity-controlled experiment vc-#1 (dotted black line) is observed to have the highest maximum recorded compression force and the shortest compression end time due to the experiment's mold closure at a constant speed of 0.1667 mm/s until complete mold closure. Both force-controlled experiments were intended to reduce their closing speed after a pre-defined force limit had been reached and subsequently regulate their closing speed to hold the closing force at a constant level as recorded in Figure 6-31(a) for experiment fc-#3 (blue dashed/dotted line) and fc-#6 (orange dashed line). Therefore, a longer compression end time is recorded for settings of lower maximum compression force at force-controlled mold closure. Furthermore, all experiments show a relaxation of compression force after their compression end times, indicating a viscoelastic behavior of the compression force during the FS-CRTM process. These observations correspond well with literature reports [35] of the compression force progression during the conventional CRTM process.

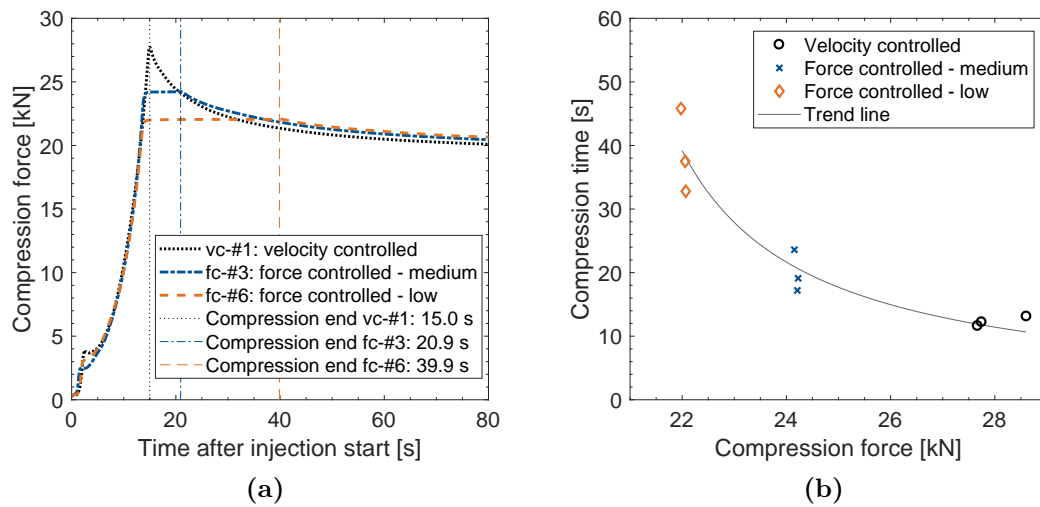


Fig. 6-31 (a) Compression force over time after injection start; (b) compression time over (maximum) compression force of additional experiments.

Figure 6-31(b) depicts the compression end time of the additional experiments over their recorded maximum compression force. The results as well as the plotted trend line show a non-linear decrease of compression time with increasing compression force. The results show that a reduction of the maximal compression force during FS-CRTM experiments by 20%, from approximately 28 kN to 22 kN, leads to an increase of the compression time by a factor of three, from 12.3 s to 37.9 s. The non-linear decreasing trend of the compression time with increasing compression force recorded for the additional experiments qualitatively correlates with the predictions of the compression time of the MLR model in Figure 6-30(b).

Compression and Holding Phase – Impregnation of Preform Bottom Side

While the fluid flow inside the injection gap was previously studied during the injection phase test series, the impregnation of the preform bottom side was investigated during the compression and holding phase. Three characteristic time steps were selected to be modeled in MODDE® to describe impregnation of the preform bottom side, first the time of initial through-thickness penetration (TITTP) of the fluid on the preform bottom side, second the time of 50%, and third the time of 90% area filling ratio (AFR) of the preform bottom side.

The TITTP of experiment #3 could not be identified because no pictures on the preform bottom side were recorded due to a malfunction of the data acquisition software. Further, the TITTP of experiment #13 could not be evaluated due to improper lighting conditions of the recorded pictures. Nevertheless, both experimental settings were conducted twice resulting in one valid experiment of each set-

ting which is included in the analysis of the TITTP response model. Figure A-49 in Appendix A.5.3 depicts the overview plot of the MLR model of the TITTP response including all factors and their interactions. The summary of fit indicates a low Q2 value and a low model validity. To improve the model quality the insignificant coefficients of factor interactions were removed from the MLR formula resulting in a well fitted model with increased Q2 value and improved model validity as presented in Figure A-50 in Appendix A.5.3.

Figures A-51 and A-52 in Appendix A.5.3 presents the overview plot of the models of the two responses (i) time of 50% and (ii) 90% AFR on preform bottom side, respectively. As for the TITTP model, experiment #3 could not be included in the two AFR response models due to a lack of recorded pictures. A large deviation of the replicates resulted in a negative reproducibility value for both AFR models depicted in their summary of fit plot. Furthermore, both models are characterized by a low R2 as well as Q2 value and none of the factors and interactions are listed as significant coefficients of the model. Therefore, the quality of both models are shown to be inadequate to draw conclusions on the factor-response correlation regarding the time of 50% and 90% AFR of the preform bottom side. Nevertheless, investigations on the impregnation pattern of the preform bottom side are presented in the following by discussing firstly the results of the TITTP response model and secondly the progression of the AFR of the preform bottom side of the additional experiments.

The effect plot of the TITTP model including all interactions is presented in Figure 6-32(a). The factors, injection gap height (h_{ig}) and vent pressure (p_v), are listed as significant effects of the MLR model while the compression force (f_c) and all interactions are not significant. The order of effects shows that the injection gap height is predicted to have the largest effect on the TITTP response. The findings of the significant factors correlate with the improved model without interactions (see Figure A-50 in Appendix A.5.3). Figure 6-32(b) presents the perdition plots of the factor-response correlations of the MLR model without interactions. The predicted effect of the compression force is shown to be within its uncertainty level and is therefore insignificant. Both significant effects, injection gap height and vent pressure, are predicted to have a linear correlation with the TITTP response. An increase of both factors is shown to result in an increased TITTP, while the injection gap height is observed to result in the largest change of TITTP over the investigated factor ranges. The correlation of the TITTP and vent pressure can be explained by an increased pressure gradient acting across the preform thickness at a reduced vent pressure setting. This increased through-thickness pressure gradient promotes the out-of-plane impregnation of the preform after the fluid is distributed above the preform surface inside the injection gap and results in an reduced TITTP.

The correlation of the TITTP and injection gap height can be explained by a reduced volume of the injection gap at reduced injection gap height. The reduced injection gap volume results in a larger remaining fluid volume which is injected after the injection gap is completely filled. After a complete injection gap filling, the fluid is forced to penetrate the preform below the injection gap already during the injection phase. Therefore, a reduced injection gap height promotes an early out-of-plane impregnation of the preform and results in a reduced TITTP.

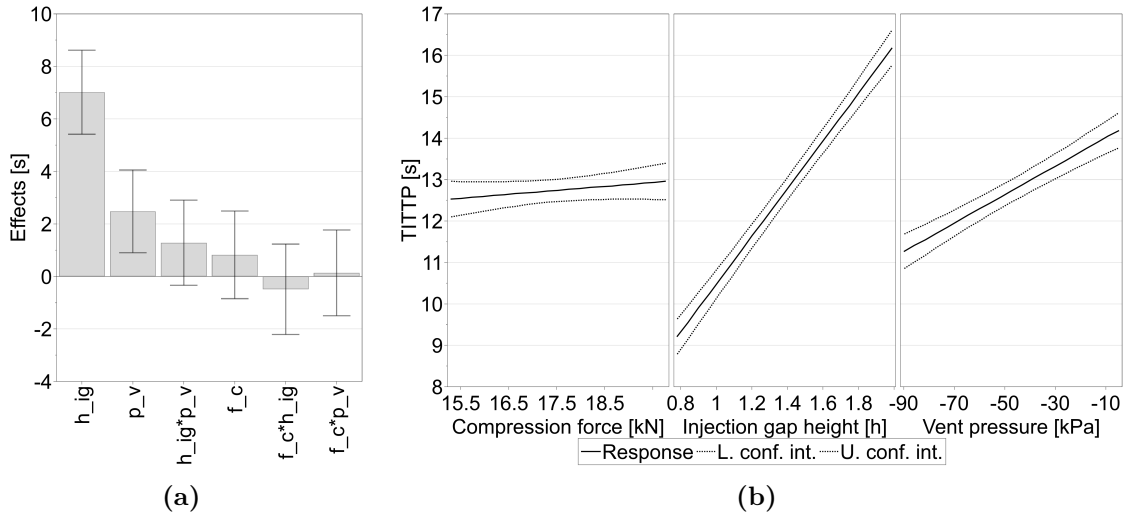


Fig. 6-32 (a) Effects of time of initial through-thickness penetration (TITTP) model; (b) predictions of TITTP model at medium factor setting ($f_c = 17.31$ kN, $p_v = -47.5$ kPa, $h_{ig} = 1.39$ mm).

Literature studies [37, 38] and numerical simulations in Chapter 4 report an out-of-plane preform impregnation during CRTM processing of preforms of small geometrical aspect ratios. Assuming a similar impregnation pattern for the FS-CRTM process, limitations of the used experimental method do not allow the monitoring of the the exact flow inside the preform but only the preform impregnation pattern on the preform top and bottom side. While the flow front arrival on the preform bottom side was characterized by the previously presented TITTP model, the impregnation pattern of the preform bottom side is investigated in the following by studying the additional experiments. Figure 6-33 depicts the progression of the AFR of the preform bottom side over time after injection start. The end time at 160 s corresponds to the gel time at 100 °C of the snap-cure resin system Araldite® LY 3585 / Aradur® 3475 (Huntsman, Salt Lake City, UT, USA) utilized for FRP manufacturing of automotive parts. If race-tracking in the preform corners is excluded, the AFR of the preform bottom side stays in Figure 6-33(a) at 0% for the first 12 s to 14 s after injection start. Subsequently, a linear increase of the AFR is recorded. The TITTP, or in other words time at which the AFR curve starts to rise, and the slope of the linear increase are similar for all experiments. However,

the point in time (transition point) in which the linear increase ends and the curve progresses with a decreasing slope until completely filled, is random, as observed in Figure 6-33(b). These observations indicate a potential reason why a MLR model could be set up for the TITTP but not for the responses of 50% and 90% AFR of preform bottom side, which are both observed to be inside the random slope-degression section of the AFR curve. Looking at the exact AFR progression curves of the repetition experiments of the full factorial design in Figure A-53 in Appendix A.5.3 shows a repeatable initiation of the rise of the AFR curve (TITTP) but a random progression towards complete filling, strengthening the previously stated assumption. Furthermore, the time delay of the the TITTP underlines the assumption that preforms of small geometrical aspect ratio are predominantly impregnated in out-of-plane direction during the FS-CRTM process, as described for the conventional CRTM process in literature [37, 38] and in Chapter 4. In Chapter 7, the irregular increase of the AFR on the preform bottom side after the linear increase is correlated to slight deformations of the test setup leading to an incomplete cavity closure at the compression end which relaxes during the holding phase. The relaxation and final mold closure is observed to happen simultaneously with the slope degression of the AFR curve on the preform bottom side ending at a complete preform impregnation at complete cavity closure.

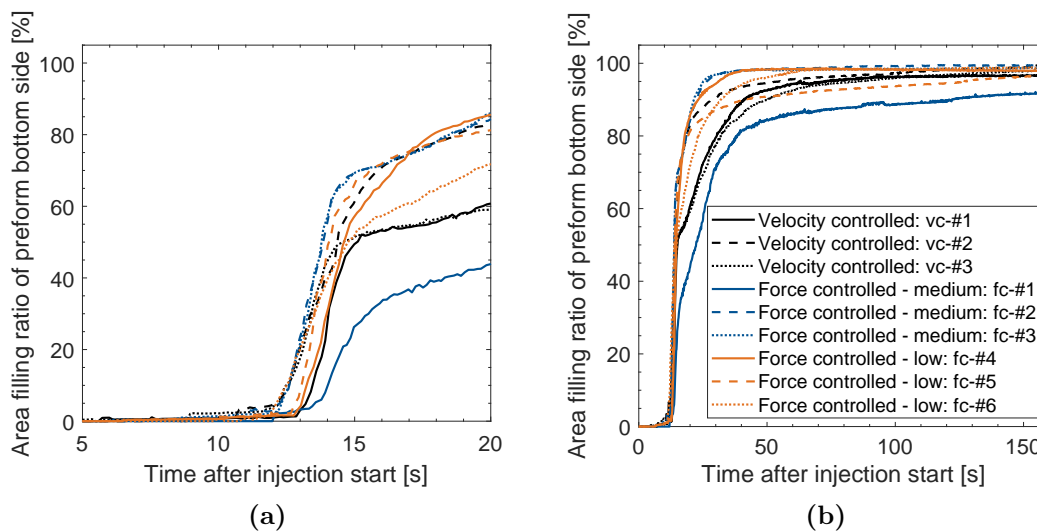


Fig. 6-33 Area filling ratio of preform bottom side of the additional experiments: (a) during the first 20 s of the process; (b) until gel time of representative snap-cure resin system. For legend of both plots see (b).

Figure 6-34 depicts the impregnation pattern on the preform bottom side at different points in time. The unimpregnated preform is shown as a dark, black section (neglecting the central stiffening cross section) while impregnated sections of the preform appear bright. The upper row in Figure 6-34 represents the preform impregnation pattern during the linear increase and the bottom row during the slope

degression of the AFR curve in Figure 6-33 of experiment vc-#1. Neglecting the race-tracking in the preform corners and the white vertical line on the right side due to an out-of-plane waviness of the preform, Figure 6-34(a) illustrates the TITTP by the first signs of out-of-plane flow front arrival in the center of the preform at 12.9 s. The second picture (b) shows that the fluid penetrates the preform bottom side first at stitching points at which out-of-plane flow channels are created due to the tension of the sewing thread. The impregnation pattern in (c) reveals that the fluid further impregnates the fiber structure between the initially impregnated stitching points. The observed out-of-plane impregnation pattern correlates with descriptions of similar NCF materials in literature [193]. While the steep linear increase of the AFR curve results in a fast filling of the first 49% of the preform bottom side in approximately 3 s, it takes another 135 s to completely impregnate the preform bottom side which happens during the slope degression of the AFR progression, shown in Figures 6-34(d) to (f).

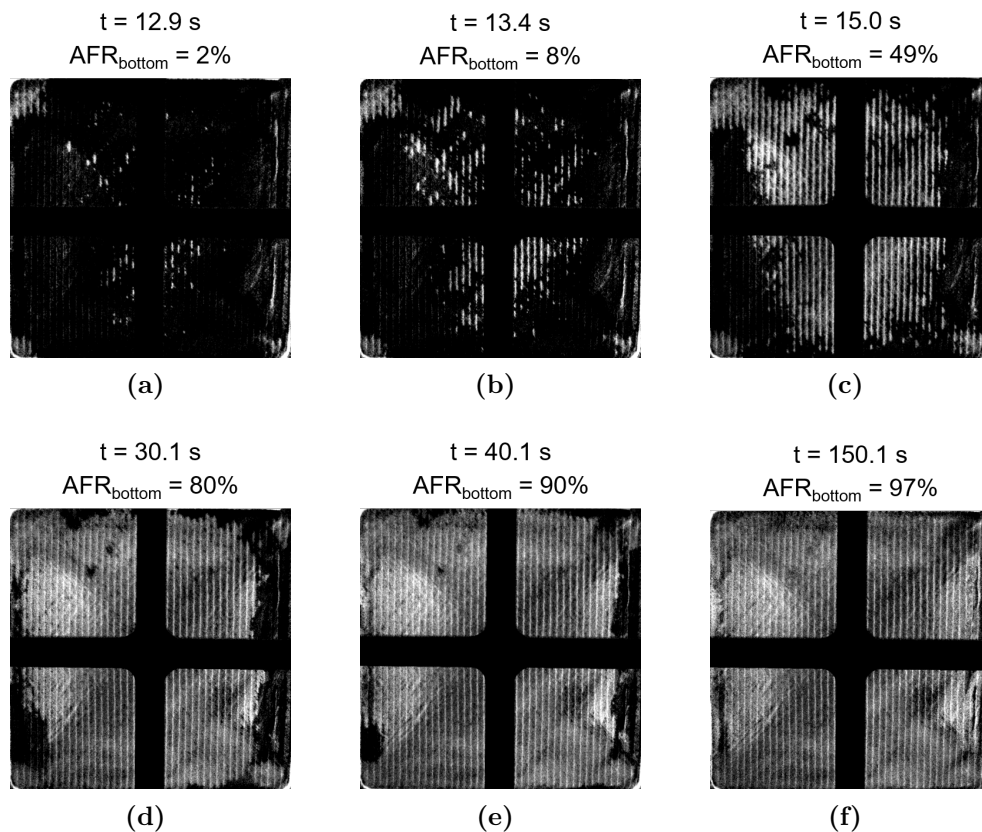


Fig. 6-34 Impregnation pattern on bottom side of preform of experiment vc-#1 (AFR_{bottom} = area filling ratio of preform bottom side).

6.3.3 Conclusions of the Factor-Response Study

The following subsection concludes the factor-response study. Two test series were conducted to investigate the injection as well as compression and holding phase of the FS-CRTM process by identifying dominant factors to provide guidelines on how to control the impregnation of preforms of small geometrical aspect ratio. Table 6-4 presents a summary of the identified factor-response correlations. The factors are listed in the first column, the responses in the first row and the intersecting cells present their specific correlation. While the two factors, vent pressure and injection gap height, were included in the investigations of both phases, the stagnation pressure and compression force are not present during the injection as well as compression and holding phase, respectively. Thus, the correlation of these two factors on the non-relevant responses were not investigated and marked with a “–” sign in the corresponding cells of Table 6-4. All recorded correlations are experimentally identified and valid inside the boundary conditions of the experimental design. Even though the presented correlations cannot be stated as generally applicable, they can be used as a guideline for future FS-CRTM process designs at which specific control strategies always have to be validated by preliminary manufacturing trials.

Tab. 6-4 Summary of factor-response correlations of the FS-CRTM process (factors listed in first column, responses listed in first row – AFR = area filling ratio, compr. = compression, TITTP = time of initial through-thickness penetration).

	Injection time	Flow rate	Injection pressure	AFR of preform top side	Compr. time	TITTP
Stagnation pressure	↓	↑	↑	↑	–	–
Vent pressure	○	○	○	○	○	↑
Injection gap height	(↓)	(↑)	↓	↓	○	↑
Compr. force	–	–	–	–	↓	○

↑ Increasing factor leads to increasing response.

↓ Increasing factor leads to decreasing response.

○ No significant factor-response correlation.

– Not investigated.

In Table 6-4 the stagnation pressure is listed as the first investigated factor of the FS-CRTM process. The stagnation pressure is a measure of the acting fluid pressure inside the feeding line of the inlet prior to injection start. The stagnation pressure

was identified as the dominant factor to control the injection time and the flow rate. An increased stagnation pressure was predicted to result in a reduced injection time as well as an increased flow rate. The observed non-linear factor-response correlation of the stagnation pressure and the injection time indicates that an optimal point of operation can be determined to balance the economical benefits of low cycle times and minimal investment costs for injection equipment needed to provide the required stagnation pressure. Furthermore, a near-linear correlation between stagnation pressure and flow rate was modeled. During the FS-CRTM flow experiments flow rates were recorded which are comparable to flow rates of industrial manufacturing processes but at much lower pressure level. While in industrial manufacturing processes flow rates of 20 cm³/s to 90 cm³/s are achieved via the high-pressure resin transfer molding (HP-RTM) processes by a mixing and injection pressure of up to 11000 kPa [10, 17, 23, 194], the flow rate model of the FS-CRTM process predicted flow rates of 15 cm³/s to 70 cm³/s at stagnation pressures of 100 kPa to 600 kPa. The high flow rates at low pressure during the FS-CRTM process are achieved by injecting the resin not into the preform, as during the conventional RTM or CRTM-1 process, but, as for the CRTM-2 process, into an empty space above the preform (injection gap) that bears marginal resistance to the flow during a FS-CRTM injection. This observation shows the benefit of the CRTM resin injection into an injection gap, enabling fast cycle times by high flow rates at low investment costs for low pressure injection equipment.

Furthermore, the stagnation pressure was identified to influence the fluid pressure acting between injection start and end, denoted as “injection pressure”. As listed in Table 6-4, an increase of the stagnation pressure at the investigated pressure-driven injection leads to an increase of the injection pressure. The recorded pressure progressions showed that a strong pressure drop occurs at the injection start from a high level of stagnation pressure before the injection start to a reduced injection pressure level during the filling of the injection gap. Additionally, the investigations showed that the injection pressure stays on a constant level during the filling of the injection gap and increases after the injection gap is completely filled. The reduced but constant value of the injection pressure is explained by the state of the fluid which is static prior to the injection and dynamic during the filling of the injection gap. After the injection gap is completely filled, the ongoing injection forces the fluid to impregnate the low-permeable preform, leading to recorded pressure increase.

During the investigations on the filling of the injection gap a correlation with the factor stagnation pressure was identified. The extend to which the injection gap was filled above the preform was indirectly measured by the area filling ratio (AFR) of the preform top side. As previously stated, the investigations revealed on the one hand that a higher stagnation pressure results in a higher injection

pressure. According to Darcy's law (Equation 2-1), an increased injection pressure results in a linearly faster impregnation of the preform. However, the previously discussed non-linear reduction of injection time with increasing stagnation pressure over-proportionally reduces the time in which the preform below the injection gap can be impregnated. Therefore, less resin penetrates the preform at an increased stagnation pressure and more resin fills the injection gap indirectly recorded by the AFR of the preform top side.

The factor vent pressure was observed to only influence the time of initial through-thickness penetration (TITTP) of the fluid observed on the preform bottom side. Based on literature reports [37, 38] and numerical simulations of the conventional CRTM process in Chapter 4, the impregnation pattern of preforms of small geometrical aspect ratio is known to take place via a predominantly in-plane filling of the injection gap and a subsequent predominantly out-of-plane impregnation of the preform. Knowing this, the TITTP response indicates the arrival time of the through-thickness flow on the preform bottom side which was predicted to linearly increase with increasing vent pressure. Therefore, a low vent pressure setting at the FS-CRTM process was shown to promote the out-of-plane impregnation of the preform.

The injection gap height was investigated as third factor during the factor-response study. Besides stagnation pressure, the injection gap height was the only significant factor on the two responses, injection time and flow rate. However, the impact was predicted to be minimal compared to the effect which the stagnation pressure has on these two responses. Therefore, the stagnation pressure is defined as the dominant factor to control the injection time and flow rate.

Besides stagnation pressure, the injection gap height was identified to influence the responses injection pressure and the AFR on the preform top side. An increase of the injection gap height is listed in Table 6-4 to result in a decrease of the two responses. The presented studies showed that for preforms of small geometrical aspect ratio, a threshold height of the injection gap exists at which the injection gap is completely filled during the injection. While an injection gap height above this threshold value results in an incomplete filling of the injection gap at injection end, an injection gap height below the threshold always results in a complete filling of the injection gap (100% AFR of preform top side). The response injection pressure is changed in two ways by the factor injection gap height. On the one hand, an increased injection gap height was observed to change the level of the injection pressure plateau during the filling of the injection gap. On the other hand, the investigations showed that a reduction of the injection gap height below its threshold value of complete gap filling leads to a steady increase of the injection pressure after the injection gap is completely filled.

Additionally, the injection gap height influences, alongside the vent pressure, the out-of-plane preform impregnation recorded by the TITTP response. A decreasing injection gap height was predicted to result in a decreased TITTP. While the effect of the vent pressure on the TITTP response was predicted to be smaller than for the injection gap height, both factors are recorded to have a significant influence. Therefore, both factors, injection gap height and vent pressure, are stated in Table 6-4 as dominant factors to control the FS-CRTM process in regard to the TITTP response.

The fifth and final investigated factor of the FS-CRTM process, which is listed in Table 6-4, is the compression force. It defines the pre-defined force limit during a force-controlled mold closure of the process. The compression force was identified to influence only the response compression time for which the compression force is listed as the dominant factor. During the force-controlled closure, the mold was closed at a constant closing speed until the compression force limit was reached. Subsequently, the closing speed was dynamically regulated to hold the control variable compression force at a constant level until the mold was completely closed. The investigations revealed that an increasing compression force results in a reduced compression time. This is explained by the control mechanism in which a lower compression force limit results in an earlier reduction of the mold closure speed. While in the presented control mechanism the velocity is dynamically reduced to remain at a constant compression force level, Baskaran [138] investigated a CRTM control mechanism in which the mold is closed at different intervals of constant closing speeds, showing also potential to reduce the final compression force. Future research has to compare the two approaches to find the best control strategy of the CRTM process which balances short compression time and low compression pressure for a cost-efficient FRP manufacturing of short cycle times and low investment costs of mold and press equipment.

7 Experimental Study on Edge Race-Tracking during FS-CRTM¹

Despite the extensive investigations of edge race-tracking effects during RTM, a knowledge gap still exists for edge race-tracking effects in the CRTM process as well as how effects can be controlled during CRTM processing. An initial investigation via numerical CRTM simulations was presented in Chapter 4, but no experimental validation has been conducted yet. Therefore, this chapter presents flow visualization experiments of the film-sealed compression resin transfer molding (FS-CRTM) process, studying the effect of edge race-tracking and investigating a passive flow control strategy to diminish edge race-tracking. Figure 7-1 illustrates the hypothesis of the anticipated flow pattern during the FS-CRTM experiments, considering the numerical results in Chapter 4. Due to spatial constraints of the test rig, preforms with small geometrical aspect ratio are used in this chapter to investigate the FS-CRTM process with injection gap. According to [37, 38, 140], an in-plane filling of the injection gap is anticipated during the injection phase followed by a through-thickness impregnation of the preform during the compression phase for experiments without a race-tracking channel as illustrated in Figure 7-1(a). By cutting the preform slightly smaller than the in-plane dimensions of the cavity, an edge race-tracking channel is created as shown in Figure 7-1(b). Due to the spatial connection between the injection gap and the race-tracking channel, it is anticipated that besides the injection gap, the channel is also filled during the injection phase. During the compression phase, the preform impregnation pattern is predicted to change to a superimposed flow of through-thickness flow from the injection gap above the preform and a simultaneously occurring in-plane flow from the race-tracking channel. To diminish the flow disturbing effect of edge race-tracking, attractive features of the FS-CRTM process are exploited, i.e. the injection gap is isolated from the edge race-tracking channel and the preform edge is pre-compacted to the final part thickness. During the suggested passive flow control strategy, the resin is distributed inside an injection gap that covers only the central section of the preform top surface as shown in Figure 7-1(c). Closing of the central tool segment above the localized injection gap initiates a flow pattern that is intended to impregnate the central preform section under the injection gap predominantly in the through-thickness direction, progressing further through the pre-compacted preform edge predominantly in the in-plane direction. Hence, the goal of the passive flow control strategy is to establish a robust FS-CRTM flow pattern that strategically directs the flow from the preform center towards its

¹ This chapter has been previously published in [26].

edge. A potential edge race-tracking channel is, therefore, filled late in the process and potential flow disturbing effects are diminished, as numerical simulations in Chapter 4 indicate.

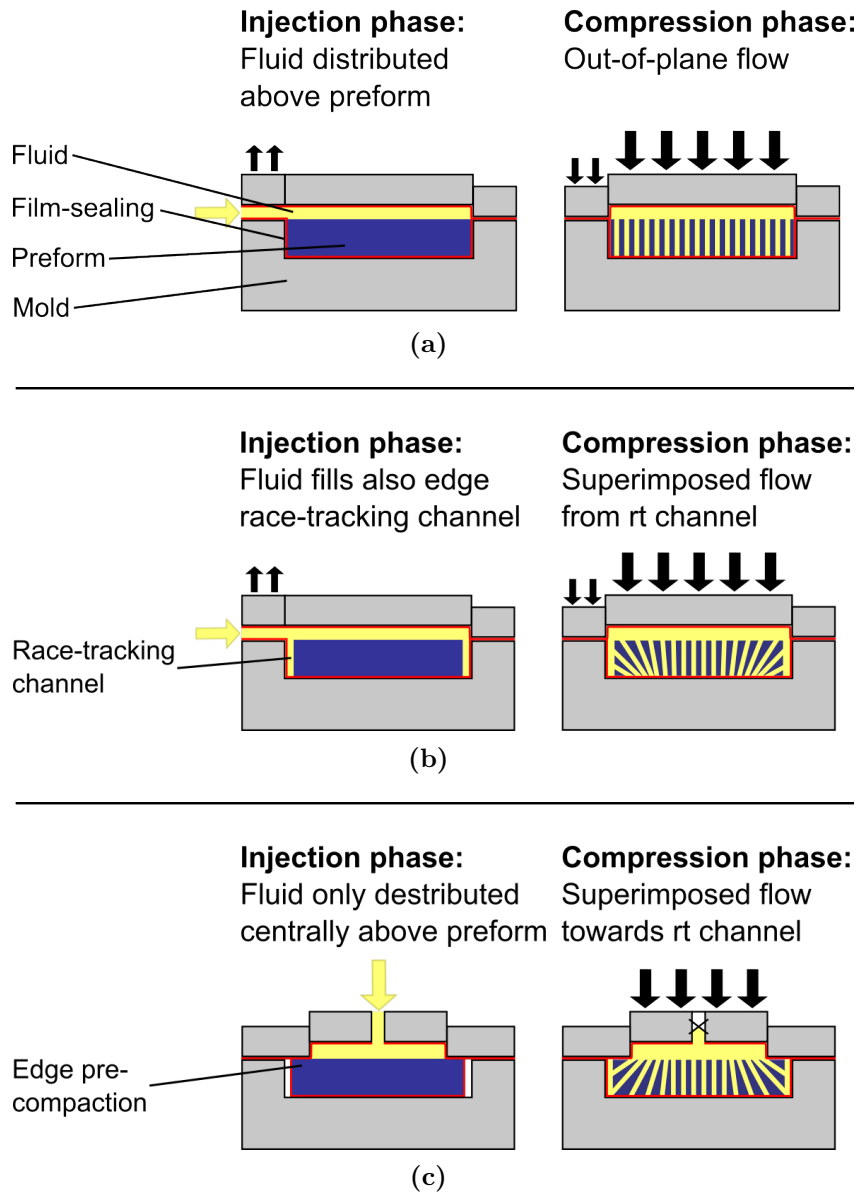


Fig. 7-1 Hypothesized FS-CRTM flow experiment scenarios of preforms of small geometrical aspect ratio: (a) without edge race-tracking (rt) channel; (b) with edge race-tracking channel; (c) applying a passive flow control strategy to diminish the edge race-tracking effect. [26]

7.1 Preforming and Experimental Plan of Race-Tracking and Flow Control Study

Materials

A common reinforcement structure for automotive applications is built of non-crimp fabric (NCF) containing carbon fibers [9, 10, 188, 189]. Thus, the stitched, biaxial NCF material SIGRATEX[®] C B310-45/ST-E214/5g manufactured by the SGL Group (Wiesbaden, Germany) was chosen for this study, containing the carbon fiber SIGRAFIL[®] C T50-4.4/255-E100 [143]. The NCF material has a nominal specific mass of 318 g/m² including a pre-applied powder binder of 5 g/m² on one side of the fabric. Two different batches of the SIGRATEX[®] NCF material formed the preforms used in two separate studies for this chapter. Due to manufacturing tolerances, the specific mass of the NCF batch used for studying edge race-tracking was measured to be 320 g/m² (SD = 1), and the batch used for studying the passive flow control strategy was 316 g/m² (SD = 1).

The preforms consisting of the NCF material were encapsulated in thermoplastic films. In Chapter 6.1, a cost-effective multilayer polyamide/polypropylene (PA/PP) film was developed for FS-CRTM production due to its favorable mechanical properties at process temperatures of 80 °C to 120 °C, chemical resistance to thermoset resin systems, low gas permeability of air, and good weldability. However, in the present investigation, flow visualization experiments were performed at room temperature to study the preform impregnation in the FS-CRTM process. Therefore, a thermomechanical characterization was performed to substitute the PA/PP film at process temperature with a film of comparable mechanical properties at room temperature (see Subsection 6.1.3). A polyethylene low-density (PE-LD) film manufactured by Sokufol (Limburg, Germany) was identified to be a suitable replacement. The film is 0.1 mm thick and optically transparent to enable an observation of the FS-CRTM preform impregnation.

The presented study focuses only on the mold filling of the FS-CRTM process. Thus, a reactive thermoset resin was substituted with a non-reactive fluid of comparable flow characteristics to ease the experimental procedure. Sunflower oil was chosen due to its comparable flow characteristics and its Newtonian behavior. Its viscosity was measured, as explained in Appendix A.1.1, with a cone-plate measuring system on a Modular Compact Rheometer (MCR) 302 (Anton Paar, Graz, Austria) at a shear rate of 100 s⁻¹ to be approximately 54 mPas at 25.5 °C.

Preform Preparation

Structural FRP parts for automotive applications are commonly designed to contain a fiber volume fraction (FVF) of 50% to 60% [17, 152]. Therefore, the preforms for the presented studies were composed of 15 layers of the SIGRATEx[®] NCF material [143] aiming at a FVF at the upper boundary of approximately 60%. The individual layers were cut to an oversized dimension of 30.2 mm larger than the final preform in-plane size of 209.8 mm × 209.8 mm for the edge race-tracking experiments and 227.8 mm × 227.8 mm for the flow control study experiments without a race-tracking channel. A symmetric lay-up was created by flipping and rotating the lower seven layers by 90°. The binder was activated at 170 °C ± 10 °C via infrared heating and debulked under vacuum pressure. To ensure a good quality cut of the preform edges, cutting of the individual layers as well as of the activated preform to its final dimensions was done using a CNC cutting table (M-1200 CV, Zünd, Altstätten, Germany). While it was observed that the cutting dimensions of individual NCF layers agreed well with the nominal dimensions, the cutting dimensions of thick preform stacks deviated by approximately 1 mm and 0.5 mm from the nominal dimensions depending on the principal axis. Due to the deviation of cutting dimensions, a constant target race-tracking channel of 2 mm and 4 mm could not be realized as initially anticipated for the race-tracking study. Correcting steps were implemented during the cutting of the preforms for the flow control study, which is why a more homogeneous theoretical channel width was realized for this test series. The exact dimensions and corresponding theoretical channel widths of all preforms are listed in Tables A-17 and A-18 in Appendix A.6.1 as well as in Tables A-21 and A-22 in Appendix A.6.2.

Experimental Plan

Two flow visualization test series are reported in this chapter. First, the effect of edge race-tracking on the preform impregnation of the FS-CRTM process was investigated. Second, a passive flow control strategy to diminish the race-tracking effect during FS-CRTM preform impregnation was studied. The first test series is herein referred to as “race-tracking study” or “RT study”, while the latter as “flow control study” or “FC study”. Both studies were performed using the same flow visualization setup with related boundary conditions, as described in Appendix A.4.2. The in-plane dimensions of the central slider are fixed at 210 mm × 210 mm with corner radii of 10 mm, while the cavity size below the central slider is adjustable. Since experiments for the RT study require an injection gap spanning over the entire cavity area, the cavity size was set to fit the in-plane dimensions of the central slider. Conversely, the FC study utilized a central injection gap in

combination with a pre-compaction of the preform edge to the final part thickness. Therefore, the cavity size was increased for the FC study to in-plane dimensions of 228 mm \times 228 mm with corner radii of 10 mm. The enlarged cavity was then covered by a partitioned upper mold. While the peripheral section of the cavity was covered by the static upper frame realizing the pre-compaction of the preform edge, the central part was covered by the movable central slider enabling a central, localized injection gap.

The preform in-plane dimensions were adjusted to fit the two different cavity sizes for the two test series. To study the natural preform impregnation pattern for each test design, reference experiments without a race-tracking channel were conducted in triplicate. Preliminary tests revealed that preforms cut to the nominal dimensions exhibited signs of edge race-tracking. To suppress randomly occurring edge race-tracking, the preforms of the reference configuration were cut slightly larger than the nominal dimensions as suggested in [190]. Further, two configurations of preforms with medium and wide race-tracking channels were cut for each test series as previously explained and illustrated in Figure A-25. Akin to the reference configuration, each experimental scenario with a race-tracking channel was conducted in triplicate. The exact preform dimensions and their theoretical race-tracking channel widths, neglecting placement tolerances, are listed in Tables A-17 and A-18 in Appendix A.6.1 as well as in Tables A-21 and A-22 in Appendix A.6.2.

In contrast to the varied preform dimensions, the process conditions were kept constant or were adapted to the changed cavity sizes of the two test studies. As listed in Table 7-1, the pressure pot was set to a target differential pressure of 370 kPa relative to ambient pressure. This setting was chosen to compensate for flow friction losses aiming at a differential stagnation pressure of 300 kPa at the inlet prior to fluid injection. Before each experiment, the target differential vent pressure was manually adjusted to -90 kPa relative to ambient pressure. The injected fluid volume was calculated based on the targeted fiber volume fraction of 60% and the cavity volume of the corresponding study at a target cavity height of 4.6 mm. The reported injected fluid volumes in Table 7-1 are the average and standard deviation of five metered and measured injections prior to each test series. To achieve complete filling of the injection gap during the injection and a subsequent through-thickness flow during the compression phase, the volume of the injection gap was set to 66% of the injected fluid volume. The corresponding target injection gap heights are listed for both studies in Table 7-1. The closing of the central slider was velocity-controlled at a target closing speed (\dot{h}_c) of 0.1667 mm/s. Preliminary tests revealed some deflections of the test rig. To compensate for this deflection, the target final closing position in the UTM control software was set -0.15 mm below the theoretical position of complete cavity closure for all experiments.

Tab. 7-1 Process conditions of experiments for the race-tracking (RTS) and flow control (FCS) studies. [26]

Target pot pressure ¹	Target vent pressure ¹	Injected fluid volume		Target injection gap height		Target closing speed
		RTS	FCS	RTS	FCS	
[kPa]	[kPa]	[ml]	[ml]	[mm]	[mm]	$[\frac{mm}{s}]$
370	-90	93.6 (SD = 0.5)	102.2 (SD = 0.5)	1.42	1.55	0.1667

¹ Differential value relative to ambient pressure.

7.2 Results and Discussion

The present section reports the findings from the test series conducted for the race-tracking (RT) study and the flow control (FC) study. The presented FS-CRTM flow visualization experiments followed the methodology as explained in Appendix A.4. The target process conditions, as presented in the previous section, were monitored and were found to be well within limits, as listed in Table A-19 in Appendix A.6.1 and Table A-23 in Appendix A.6.2. In the following, test data is presented in a sequence of graphs that are similar for both test series. First, the evolution of important process variables over time are depicted (see, e.g., Figure 7-2). Here, data for the gap height of the central slider, which was computed as the average of data from two laser triangulation sensors (LTS), are depicted in blue. The force acting on the central slider is shown by an orange curve, recorded via the load cell of the UTM. To draw conclusions on the preform impregnation, AFR histories of the preform top and bottom side as well as of the race-tracking channel, evaluated via post-processing of recorded images, are plotted as black curves. In addition to quantitative process information, qualitative information in the form of flow front progression visualizations for the preform top and bottom side is also presented (see, e.g., Figure 7-3). The experiments involve three phases. The injection phase takes place between the process start at 0 s and the “injection end”. The compression phase follows the injection phase and finishes at the “compression end”, which is simultaneous with the beginning of the holding phase. The three phases are distinguished by marked end times in the quantitative overview plots and are labeled in the legend of the qualitative flow front progression plots. Note that only one representative experiment for each configuration is presented in this section; remaining experiments are included in Appendix A.6.1 and A.6.2 of this work. Furthermore, an overview of recorded process responses is given for the RT study in

Table A-20 in Appendix A.6.1 and for the FC study in Table A-24 in Appendix A.6.2

7.2.1 Results and Discussion of the Race-Tracking Study

The race-tracking (RT) study investigates the edge race-tracking effect by quantitatively (Figure 7-2) and qualitatively (Figure 7-3) comparing FS-CRTM flow visualization experiments without a race-tracking channel (scenario (a), indicated by an identifier with the test number, e.g., “vc-#1” for the first test) with experiments with a medium (scenario (b), “mrt-#1”) and a wide race-tracking channel (scenario (c), “wrt-#1”). The experiments without a race-tracking channel have been also included in the investigations of the FS-CRTM preform impregnation in Chapter 6.3. Comparing the injection phase of all three experimental scenarios in Figure 7-2, the presence of a race-tracking channel is not seen to noticeably change the end time of the injection. Furthermore, it is observed that the AFR of the preform top sides of all three experimental scenarios increases linearly, with complete filling indicated before the end of the injection phase, which was the intent of the designed process. Recalling that the gap height was set to create an injection gap volume of 66% of the injected fluid volume, the injection gap volume was therefore filled before the complete fluid volume was injected, which was intended to produce a predominantly out-of-plane preform impregnation during the following process phases.

Towards the end of the injection phase, the force rises for all scenarios in Figure 7-2. Simultaneously, the gap height increases slightly, even though the UTM position control was programmed to hold the central slider in a constant position until the end of the injection phase. Both observations indicate an increase in cavity pressure between the complete filling of the preform top side and the end of the injection, resulting in an increased reaction force acting on the central slider and an associated deformation of the test rig. These effects are reduced with increased race-tracking channel width in scenarios (b) and (c) in Figure 7-2. As for the effects themselves, their reduction is also traced back to the process design, which keeps the cavity size constant and reduces the preform size to realize experiments with edge race-tracking. The injection gap, spanning over the complete cavity size, is spatially connected to the race-tracking channels. At the presence and increase of a race-tracking channel, the preform-free space inside the cavity is increased, which provides more space to distribute the injected fluid volume, reducing the cavity pressure increase after full filling of the injection gap and race-tracking channel.

The spatial connection between the injection gap and race-tracking channel also causes an early filling of the race-tracking channel as seen in scenarios (b) and

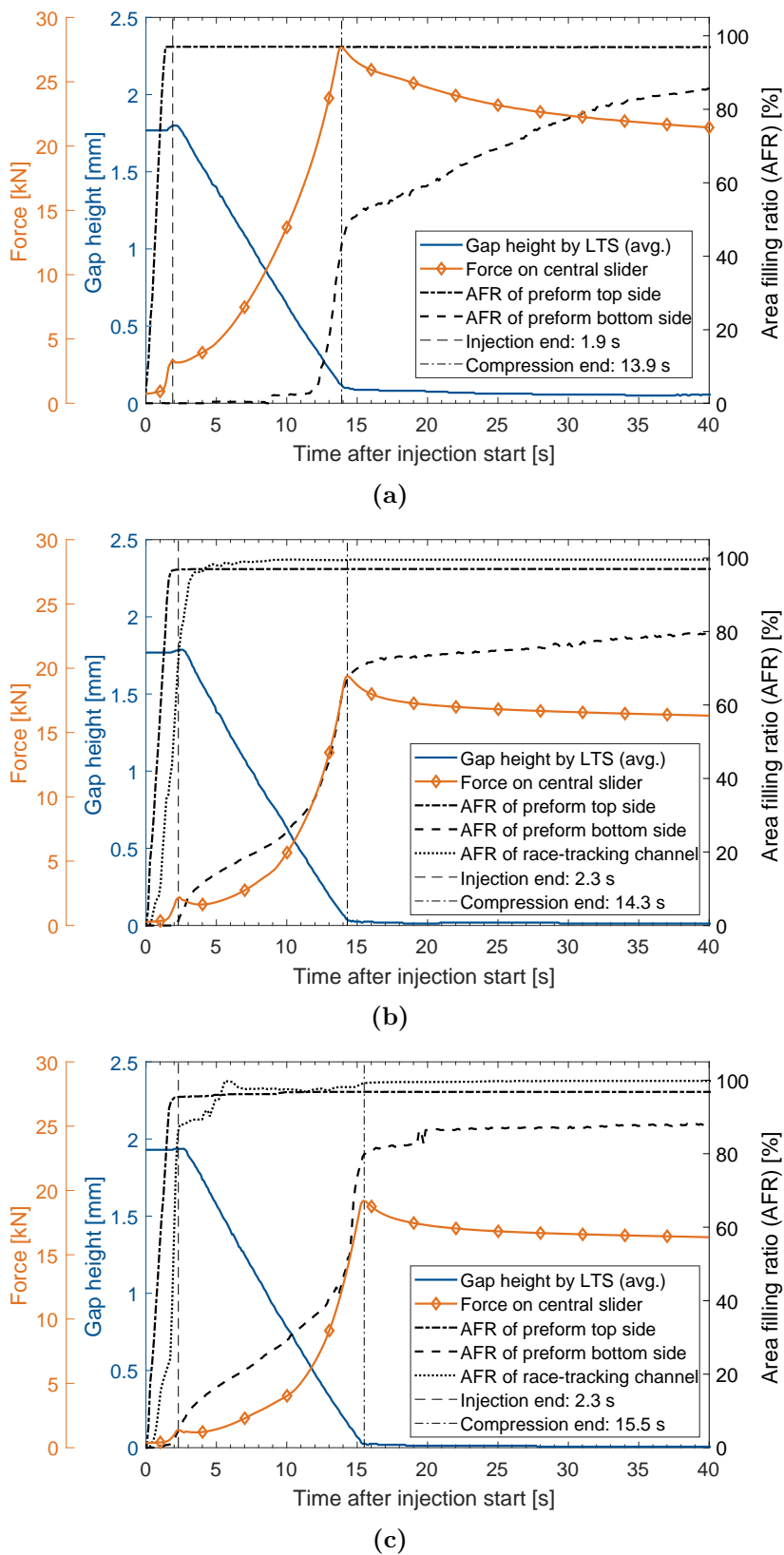


Fig. 7-2 Overview of important process variables during FS-CRTM experiments of the race-tracking study: (a) no race-tracking channel – vc-#3; (b) medium race-tracking channel width – mrt-#3; (c) wide race-tracking channel width – wrt-#1 (LTS = laser triangulation sensor). [26]

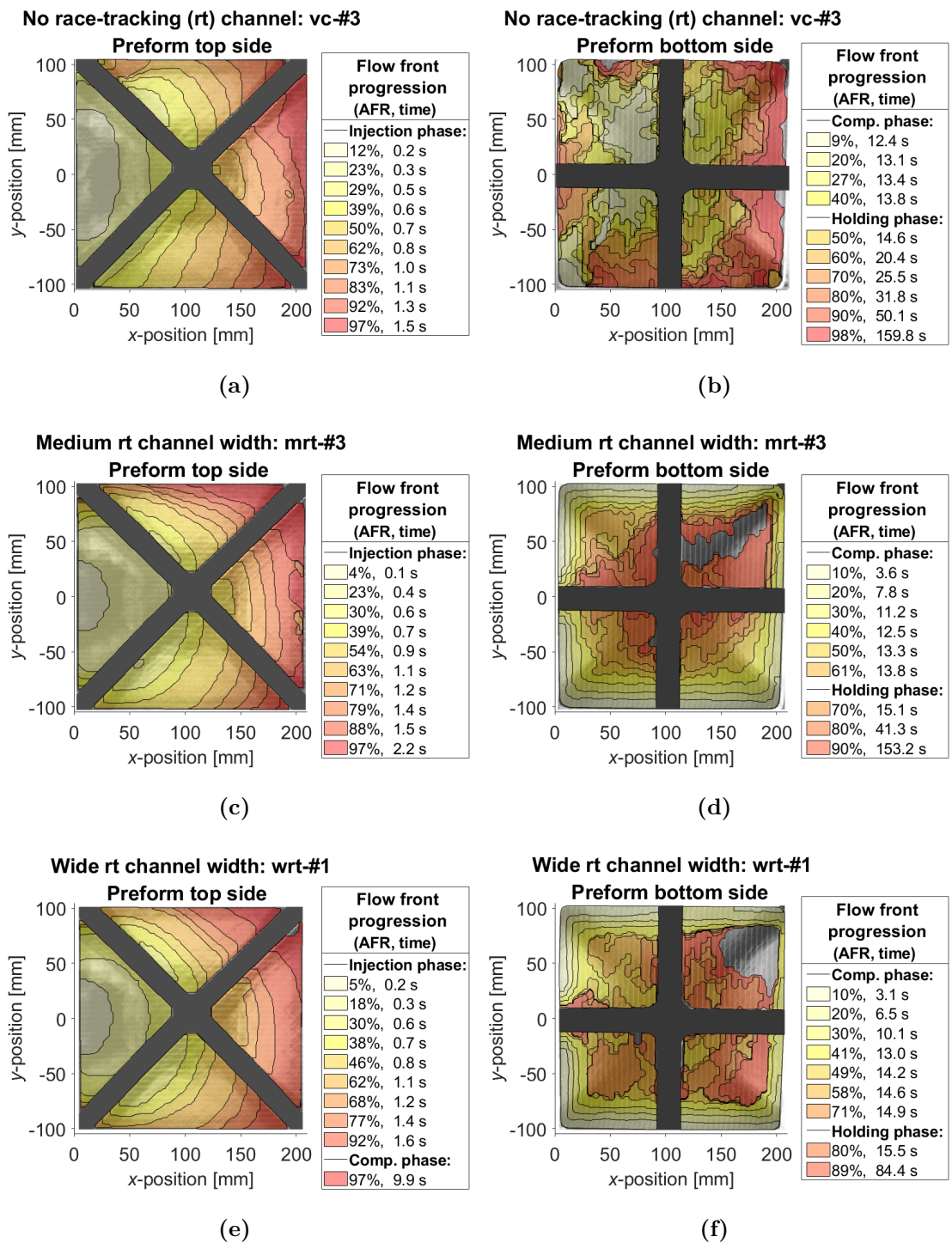


Fig. 7-3 Flow front progression of FS-CRTM experiments of the race-tracking study: (a,b) no race-tracking (rt) channel – vc-#3; (c,d) medium race-tracking channel width – mrt-#3; (e,f) wide race-tracking channel width – wrt-#1 (AFR = area filling ratio). [26]

(c) in Figure 7-2. The AFR of the race-tracking channels rises shortly after the injection start, increasing quickly, with the channel largely being filled at the end of the injection phase. The short time delay observed before the rise of the channel's AFR after the injection start is caused by the preform design, which incorporates the fluid transition zone to guide the fluid from the lateral inlet onto the preform, as illustrated in Figure A-25.

The flow front progression plots of Figure 7-3 show a similar filling pattern on the preform top side for all three experimental scenarios. Due to the injection of fluid into the injection gap above the preform, the shown flow front progression on top of the preform is correlated to the filling of the injection gap itself. Thus, the injection gap was filled from the inlet slider ($x = 0$, $-20 \text{ mm} < y < 20 \text{ mm}$), radially progressing towards the vent side ($x > 200 \text{ mm}$). A homogeneous, repeatable flow pattern was observed for all experiments with a race-tracking channel, while the flow front progressions of experiments without a race-tracking channel were slightly disturbed, which is explained as follows. To prevent edge race-tracking in experiments without a channel, the preforms were intentionally cut slightly larger than the cavity size. Cutting tolerances, which differed in the two principal directions of the CNC cutting table, resulted in out-of-plane wrinkles over the width of the preform after placing them in the cavity. The flow pattern in the associated experiments was slightly affected by the out-of-plane wrinkles as seen in Figure 7-3(a) and Figures A-56(a),(c) in Appendix A.6.1. Moreover, the image post-processing script misinterpreted sections of large wrinkles at, e.g., $x = 180 \text{ mm}$ of Figures A-56(a),(c) in Appendix A.6.1 to be filled too early, which thus need to be neglected during a general interpretation of the flow front progressions. Therefore, excluding these ambiguous sections of the flow front progression, a similar flow pattern inside the injection gap, from the inlet slider radially towards the vent side, was observed for all three experimental scenarios.

After the injection ended, the compression phase was initiated, which is indicated in Figure 7-2 by a decreasing gap height. Even though the UTM position was lowered to -0.15 mm as the final tool closing position to compensate for tool deformation, the measured gap height in scenario (a) is not completely closed at the end of the compression phase. The incomplete gap closure in combination with the lowered final tool closing position indicates a test rig deformation opposite to the closing direction. Due to this deformation, the closing speed was also slightly reduced from its targeted value of 0.1667 mm/s , evidenced by a departure of the gap height curve from perfectly linear during the compression phase. The non-linearity of the gap height curve towards the end of the compression phase correlates with a strong force increase, depicted in Figure 7-2(a). The recorded force acting on the central slider increased non-linearly with decreasing gap height and peaks at

the end of the compression phase. Applying Terzaghi's law [127] to the FS-CRTM preform impregnation, the recorded force is composed of two components. On the one hand, the fiber structure, i.e. the preform, is compacted to its final thickness, and, on the other hand, the fluid pressure is increased due to the occurring preform impregnation.

While the exact preform impregnation and its out-of-plane flow through the thickness of the preform cannot be observed by the current test method, the arrival of fluid at the preform bottom side can be recorded as indicated by its AFR shown as a dashed black line in Figure 7-2(a). Besides marginal race-tracking in the preform corners, a sudden and steep increase of the AFR of the preform bottom side was recorded towards the end of the compression phase. This near-linear increase in Figure 7-2(a) between 12 s to 14 s is visualized in the flow front progression plot of Figure 7-3(b) as a patchy arrival of fluid on the preform bottom side. It was observed that the fluid penetrates the preform during the time of the near-linear AFR increase first at the sewing threads in some areas of the preform, followed by the penetration of the adjacent fiber structure. At the end of the compression phase in Figure 7-2(a), the AFR curve on the preform bottom side changes its shape and progresses with a reduced slope towards full filling during the holding phase of the process. Simultaneously, the force curve relaxes during the holding phase, indicating a viscoelastic behavior of the FS-CRTM preform impregnation. Referring to the gap height after the incomplete gap closure at the end of the compression phase in Figure 7-2(a), it can be observed that the height further decreases during the holding phase and eventually stagnates at the complete gap closure. The observed elastic deformation of the test rig during the holding phase correlates with the viscoelastic behavior of the FS-CRTM preform impregnation. Therefore, it is presumed that the incomplete gap closure causes the incomplete filling of the preform bottom side at the end of the compression phase in Figure 7-2(a). This presumption is supported by the relaxation of the elastic test rig deformation during the holding phase and the simultaneous increase of the AFR of the preform bottom side.

In contrast to the AFR of the preform top side, which is nearly unchanged by the presence of a race-tracking channel, the AFR of the preform bottom side provides insight into the effect that edge race-tracking has on the preform impregnation during FS-CRTM. Comparing the AFR progression of the preform bottom side of the experiment without a race-tracking channel in Figure 7-2(a) with the experiments of medium (b) and wide race-tracking channel width (c), an earlier rise of the AFR curve in Figures 7-2(b),(c) can be observed at the injection end, followed by stagnation during the holding phase. To facilitate a more in-depth analysis, AFR data for the preform bottom side for all experiments are plotted in Figure 7-4

up to a process time of 160 s. The process end time at 160 s was experimentally determined as the gel point at 100 °C of the snap-cure resin system Araldite® LY 3585 / Aradur® 3475 (Huntsman, Salt Lake City, UT, USA) used for composite manufacturing in the automotive industry. Figure 7-4(a) shows that the AFR of the preform bottom side for experiments without a race-tracking channel remains approximately zero until a sudden increase at around 12 s to 13 s. In contrast, an early rise in the AFR of the preform bottom side (at approximately 2 s) can be observed for all experiments with a race-tracking channel. Considering the flow front progression of the preform bottom side shown in Figures 7-3(d),(f), the observed early increase in AFR can be correlated to the recorded lateral flow from the race-tracking channels toward the preform center.

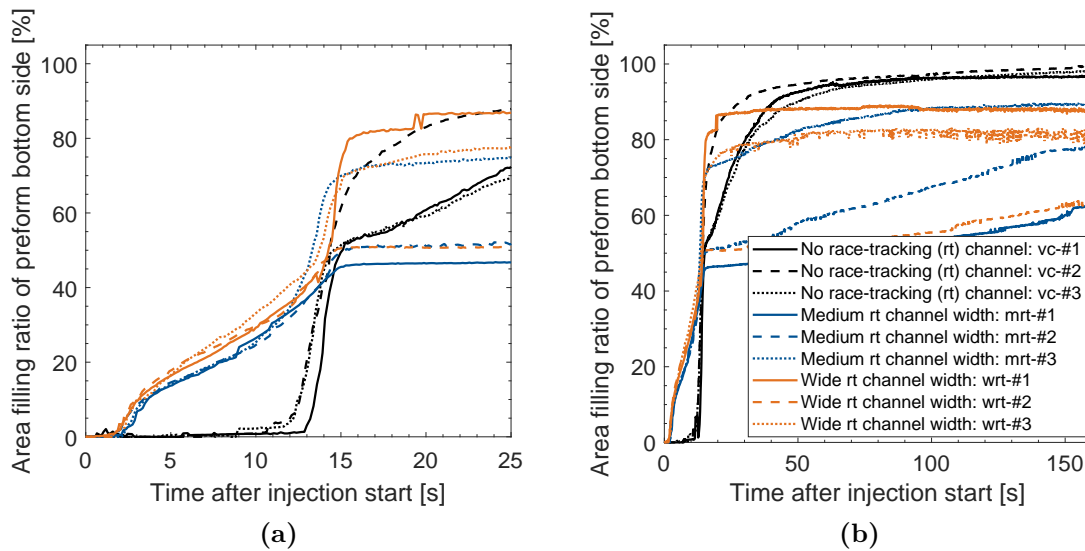


Fig. 7-4 Area filling ratio of preform bottom side: (a) during the first 25 s of the process; (b) until gel time of representative snap-cure resin system. For legend of both plots see (b). [26]

Two inhomogeneities of the lateral race-tracking flow are observed in Figures 7-3(d), (f) at the inlet section ($x = 0$, $-20 \text{ mm} < y < 20 \text{ mm}$) and at the vent side ($x > 200 \text{ mm}$). The first inhomogeneity can be explained by the design of the fluid transition zone, which is butt jointed to the cavity wall to guide the fluid onto the preform and prevents fiber washout as illustrated in Figure A-25. Thus, there is no race-tracking channel present at the inlet section of the preform, causing the observed inhomogeneity of the lateral flow. The second inhomogeneity at the vent side of the preform is explained by the lateral inlet design and the different theoretical race-tracking channel widths. As illustrated in Figures 7-3(c),(e), the fluid filled the injection gap radially from the inlet slider towards the vent side of the preform where it finally reached the race-tracking channel located there. Additionally, this portion of the race-tracking channel was the narrowest of all four preform sides due to inaccurate cutting dimensions as listed in Table A-18 in

Appendix A.6.1. The combination of both effects caused a delay in lateral preform filling from the race-tracking channel at the vent side ($x > 200$ mm) as observed for all race-tracking experiments of the RT study.

Following the lateral flow and its early AFR rise of the preform bottom side between 3 s to 11 s depicted in Figure 7-4(a), the various experiments with a race-tracking channel exhibit different progressions at the end of the compression phase. While one experiment with a medium and one with a wide race-tracking channel width immediately stagnate, the others increased further with a steeper slope comparable to the initial near-linear AFR increase of the experiments without a race-tracking channel. Looking at the flow front progression in Figures 7-3(d),(f) as well as in Figures A-57(b),(e) in Appendix A.6.1, the further AFR increase can be traced back to the arrival of an out-of-plane flow in the center of the preform. The fact that some experiments with a race-tracking channel experience an arrival of the central out-of-plane flow on the preform bottom side and others do not, led to a strong deviation of the recorded AFR at the end of the compression phase. While the AFR data for the preform bottom side in experiments without a race-tracking channel further increase during the holding phase towards 100%, the experiments with race-tracking show only a minor increase or complete stagnation of the AFR curves and stay below complete filling of the preform bottom side at 160 s after the process start, as seen in Figure 7-4(b).

The incomplete filling in the experiments with a race-tracking channel resulted in the formation of a macro void. As seen in Figures 7-3(d),(f), Figure A-56(f) and Figures A-57(b),(d),(e) in Appendix A.6.1, the macro void is always located on the preform bottom side in its central section, surrounded by the lateral race-tracking flow and, in some experiments, additionally by the out-of-plane flow. The void was caused by two effects: (i) the defined volume of fluid that was injected into the cavity and (ii) the increase of overall porosity inside the cavity when a race-tracking channel is present. With respect to (i), the injected fluid volume kept constant for the experiments, was determined by the fiber volume fraction of a preform without a race-tracking channel, i.e. the preform fills the complete cavity. For (ii), if the preform is cut significantly smaller than the cavity dimension, to create a race-tracking channel, then the overall porosity of the cavity increases, thus providing additional volume to be filled by the fluid. If the fluid volume is not adjusted to the increased porosity and the race-tracking channel is filled early in the process, then the injected amount of fluid is insufficient to completely impregnate the preform, resulting in the observed macro void.

The size of the macro voids at the end of the process varies largely between the various experiments with medium and wide race-tracking channels as seen in Figure 7-4(b). The strongly varying results prevent any correlation between the macro

void size and the race-tracking channel width. The reason for the strong variation of results may stem from limitations of the test method used. Given that the flow visualization test rig only allows the preform impregnation on the top and bottom side of the preform to be monitored, it gives no insight into the filling pattern over the preform thickness and, therefore, no knowledge of the three-dimensional shape and volumetric size of the formed voids. Assuming an identical void volume, the shape of a void could vary between two extremes of a thin and wide shape and a high and narrow shape. Certain inhomogeneity during the preform impregnation could cause different void shapes of identical volume for experiments of the same race-tracking width, leading to a varying observed area ratio of the void on the preform bottom side. Due to the use of a non-reactive fluid as flow media instead of reactive resins, the impregnated preform could not be cured and post-analyzed in order to inspect void volume and shape.

Comparing the experiment without a race-tracking channel in Figure 7-2(a) with the race-tracking experiments in Figures 7-2(b),(c), it is observed that the maximum recorded force at the end of the compression phase is reduced in the presence of a race-tracking channel. To further investigate this observation, the maximum recorded force for the three investigated scenarios is depicted in Figure 7-5 as dark blue bars as the mean value and with the standard deviation for three repetitions for each scenario. The results show that in the presence of a race-tracking channel, the mean of the maximum force is reduced by approximately 25%, and that there is statistically no difference between the two levels of race-tracking channel widths.

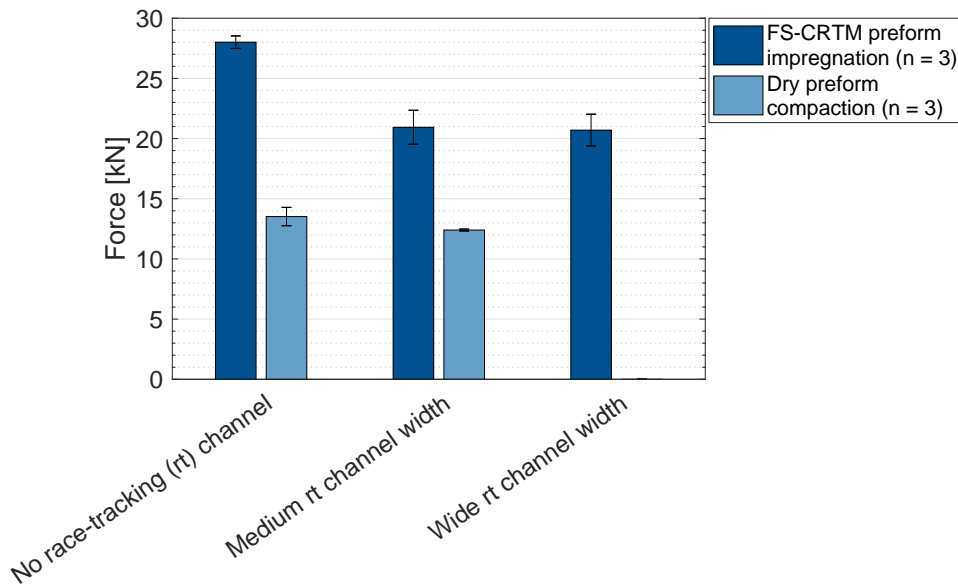


Fig. 7-5 Maximum recorded force of the three experimental scenarios of the race-tracking study. Bar heights give the mean value, and the error bars indicate the standard deviation of three repetitions. [26]

As previously mentioned, the one-dimensional laminate consolidation approach by Terzaghi [127] describes the recorded force during FS-CRTM impregnation experiments as a result of the combination of fluid pressure and preform compaction stress (Equation 2-15). While the preform compaction stress component certainly changes due to the reduced preform dimensions, the fluid pressure component is assumed to change too, due to an increased overall cavity porosity in the presence of an edge race-tracking channel. To investigate the change of these individual force components, additional experiments were performed for preforms without and with a medium race-tracking channel in which no fluid was injected, which permitted the pure preform compaction force to be measured. The recorded maximum forces are shown in light blue in Figure 7-5, again showing mean values and the standard deviation for experiments completed in triplicate. Comparing the recorded forces for experiments without a race-tracking channel with experiments with a medium race-tracking channel width in Figure 7-5, it is indicated that the dry preform compaction force reduces only by approximately 1 kN, while the maximum force during FS-CRTM impregnation experiments is reduced by approximately 7 kN. Considering that the dry preform compaction is comparable to the wet preform compaction component during impregnation, these observations suggest that the reduction of the fluid pressure component is far larger than the preform compaction component in the presence of race-tracking. The strong reduction of the fluid pressure component is explained by two effects, which occur due to the presence of edge race-tracking. First, the flow pattern changes from a predominantly out-of-plane flow for experiments without a race-tracking channel to a superimposed flow with an additional lateral in-plane flow for experiments with race-tracking. As seen in Figure A-4 in Appendix A.1.2, the in-plane permeabilities of the used NCF material [143] are approximately one order of magnitude higher than its out-of-plane component, resulting in a reduced flow resistance during the lateral preform impregnation and an overall reduced fluid pressure. Second, the presence of a race-tracking channel increases the overall porosity inside the cavity, which reduces the fluid stagnation pressure at the end of the compression phase. Hence, flow pattern changes and increased cavity porosity leads to a strong reduction of fluid pressure which is seen to have caused the majority of the recorded force reduction in the presence of edge race-tracking.

7.2.2 Results and Discussion of the Flow Control Study

Flow visualization experiments were performed during the flow control (FC) study to explore a passive flow control strategy to diminish the edge race-tracking effect during the FS-CRTM preform impregnation. The cavity in-plane dimensions were

increased from 210 mm \times 210 mm during the race-tracking (RT) study in the previous section to 228 mm \times 228 mm in the presented FC study. This was necessary to realize an experimental scenario with a localized injection gap covering only the area under the central slider with 210 mm \times 210 mm and circumferentially pre-compact the preform in the outer 9 mm of the cavity to the final part thickness. To explore the potential of a passive flow control strategy, experiments for three scenarios were again performed: without a race-tracking channel (indicated by an identifier with the test number, e.g., “fcs-#1” for the first test) and with medium (“fcs-mrt-#1”) and wide channel width (“fcs-wrt-#1”).

Figure 7-6 illustrates overview plots of important process variables of the three experimental scenarios performed during the FC study. Due to the increased preform in-plane dimensions, the injected fluid volume was adapted, leading to a longer injection time for flow control experiments at an identical injection pressure to that during the RT study. All three experimental scenarios of the FC study in Figures 7-6(a)-(c) show a steep linear increase of the AFR of the preform top side, initiating at the process start. Due to mirroring effects, the top camera of the test rig could only record the fluid flow in the area of the central slider and not in the outer cavity section of the pre-compacted edge. Therefore, the reported AFR of the preform top side provides information only on the filling of the localized injection gap, which is seen to be completely filled before the injection is finished. The flow front progression on the preform top side is shown in Figures 7-7(a),(c),(e). The herein shown filling pattern inside the injection gap progresses radially from the inlet slider ($x = 9$ mm, -20 mm $< y < 20$ mm) towards the vent side of the injection gap ($x = 219$ mm, -105 mm $< y < 105$ mm).

Similar to the experiments in the RT study, the force and gap height curve also increase at the end of the injection phase during the experiments of the flow control study (see Figure 7-6). The observed deflection of the curves is attributed to an increase in cavity pressure after the injection gap is completely filled, yet with remaining fluid being further injected. In contrast to the RT study, the force peaks during the FC study are reduced less when comparing the experiments without a race-tracking channel in Figure 7-6(a) with a channel in Figures 7-6(b),(c). This observation is correlated to the fact that during the flow control experiments, the fluid is injected into an isolated, central injection gap. Due to the applied passive flow control strategy, no direct spatial connection between the central injection gap and the edge race-tracking channel is established. Therefore, the presence of a race-tracking channel does not increase the empty space in which the fluid can discharge during the injection, which is identified as the cause for the peak reductions during the RT study.

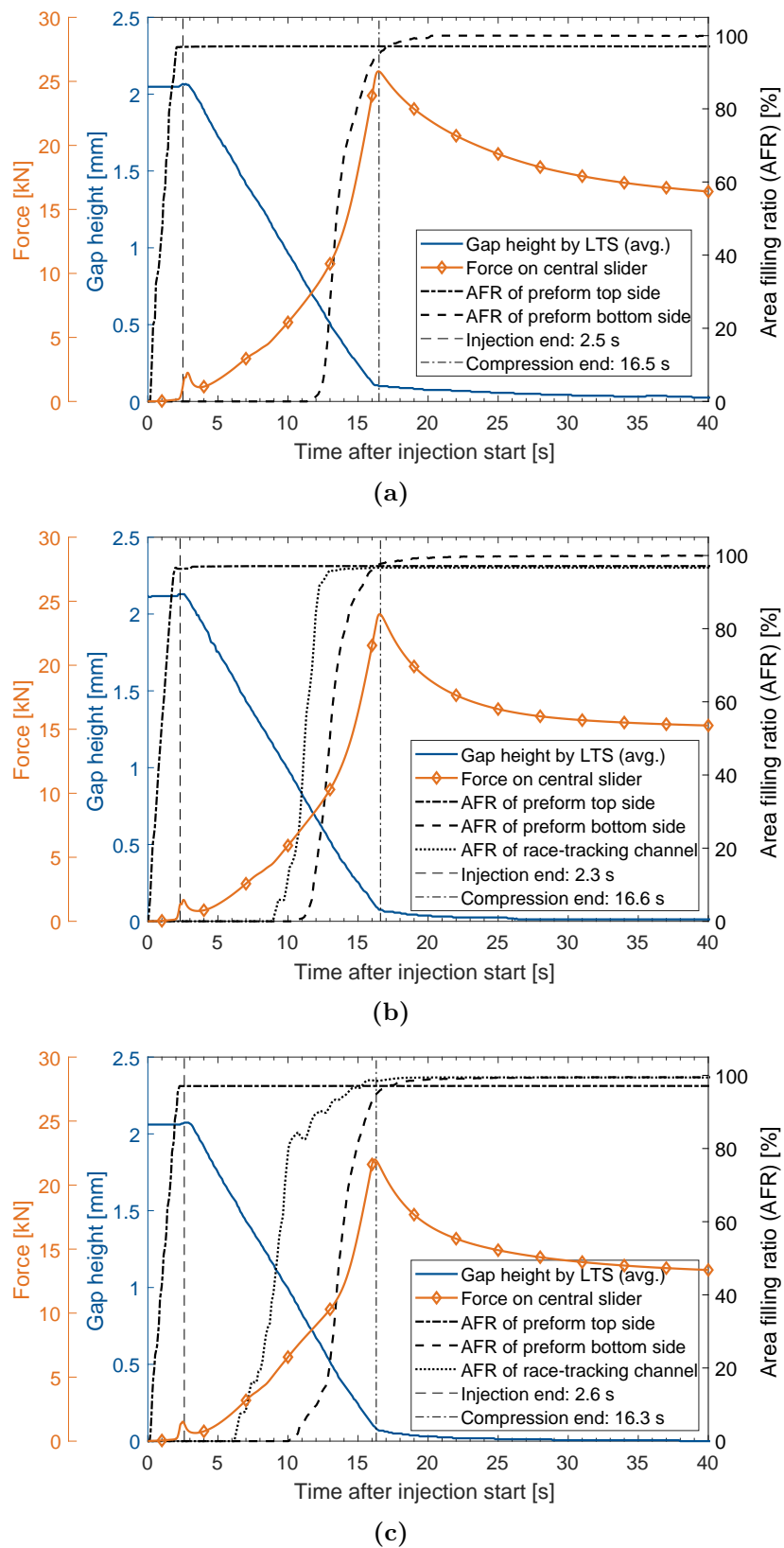


Fig. 7-6 Overview of important process variables during FS-CRTM experiments of the flow control study: (a) no race-tracking channel – fcs-#1; (b) medium race-tracking channel width – fcs-mrt-#3; (c) wide race-tracking channel width – fcs-wrt-#2 (LTS = laser triangulation sensor). [26]

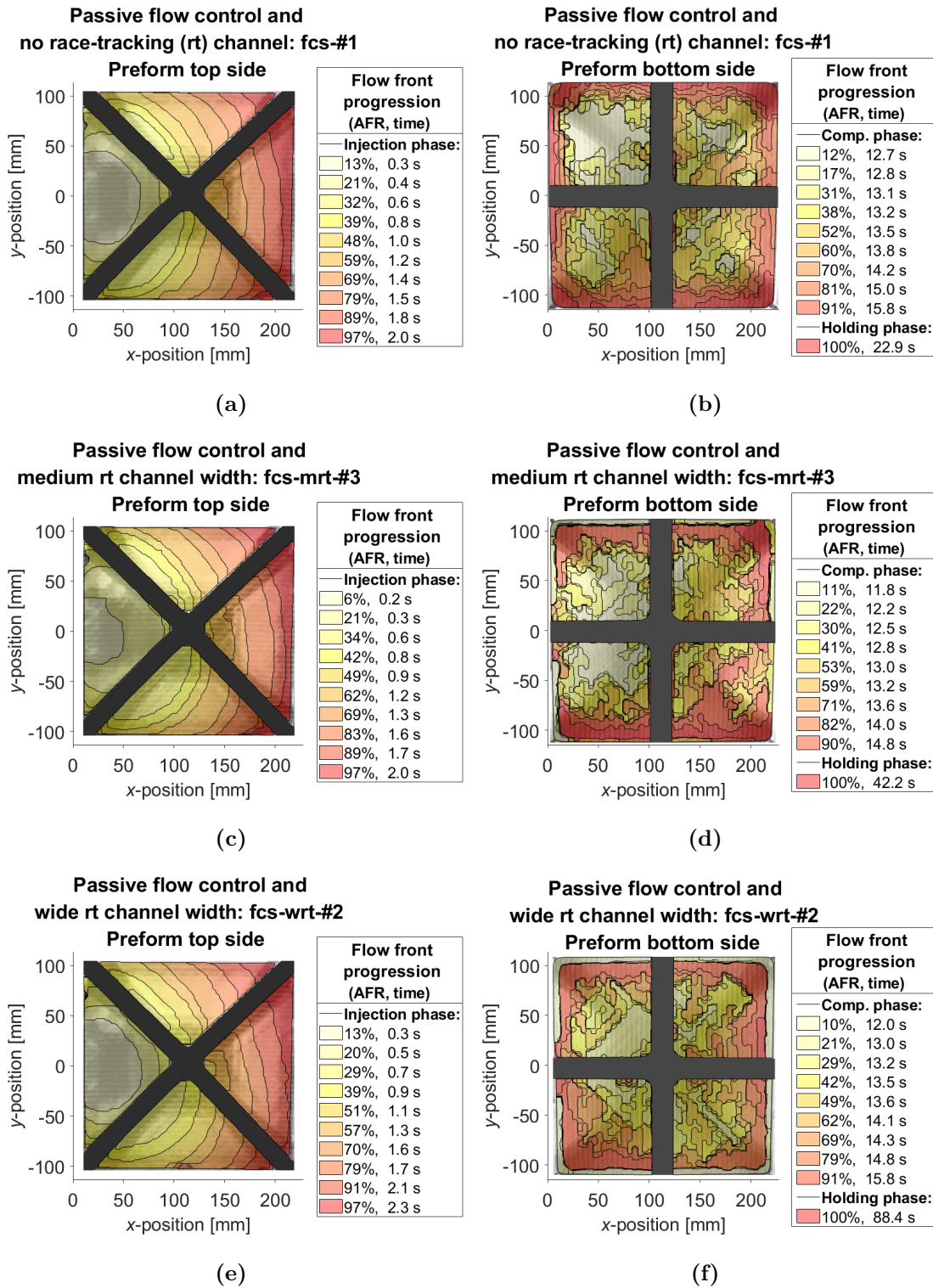


Fig. 7-7 Flow front progression of FS-CRTM experiments of the flow control study: (a,b) no race-tracking (rt) channel – fcs-#1; (c,d) medium race-tracking channel width – fcs-mrt-#3; (e,f) wide race-tracking channel width – fcs-wrt-#2 (AFR = area filling ratio). [26]

As in the injection phase, the compression phase is also longer for experiments in the FC study compared to the RT study, due to the increased height of the injection gap at an identical closing speed of the central slider. During the recorded gap height reduction in Figure 7-6, the force applied to the central slider increases and peaks at the end of the compression phase before it relaxes during the holding phase. The maximum recorded force during the FC study is reduced in the presence of a race-tracking channel as previously observed and discussed during the RT study.

The dashed black line in Figure 7-6(a) shows the AFR of the preform bottom side of the flow control experiment without race-tracking. The AFR stays constant at zero until approximately 12 s after the process start and rises rapidly afterwards before the slope decreases towards full filling during the holding phase at approximately 23 s. Looking at the qualitative flow front progression on the preform bottom side of the same experiment in Figure 7-7(b), it can be observed that the fluid fills the preform bottom side first in its center and then progresses towards the preform edges. These process observations in flow control experiments without race-tracking verify the intended flow manipulation of the passive flow control strategy to initiate a central through-thickness flow under the localized injection gap along with a subsequent lateral flow from the center towards the pre-compacted preform edge.

The initial rise of the AFR curve of the preform bottom side is defined as the “time of initial through-thickness penetration” (TITTP). Figure 7-8 depicts in the two dark blue bars TITTP mean values and standard deviations for three experiments without a race-tracking channel for the RT study and the FC study. Considering a predominantly out-of-plane flow in the preform center during the FC study, its TITTP should be comparable with the TITTP of the pure through-thickness impregnation of the RT study. Comparing the TITTP of the two studies in Figure 7-8, it is observed that the mean of the flow control experiments is slightly lower, even though the injection time of this study is marginally longer by 0.4 s. The small extension of the injection phase during the flow control experiments seems to be compensated by a slightly faster out-of-plane flow due to the marginally lower areal weight of the fabric used for the FC study and the resulting lower preform thickness as recorded in Table A-23 in Appendix A.6.2. Nevertheless, the injection time extension is low compared to the absolute value of the TITTP. The identical preform architecture and the similarity in TITTP between the two studies strengthen the conclusion of the previous paragraph, i.e. a predominantly out-of-plane flow is established in the preform center under the injection gap during the flow control experiments.

For experiments of the FC study, a faster progression until complete filling of the preform bottom side is recorded comparing the AFR of the preform bottom side of the FC study without a race-tracking channel in Figure 7-6(a) with the

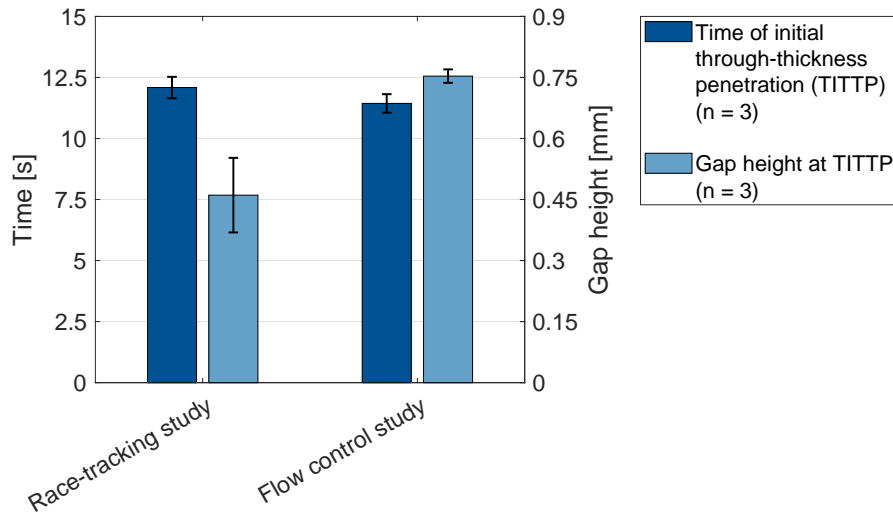


Fig. 7-8 Time of initial through-thickness penetration (TITTP) and corresponding gap height of FS-CRTM experiments without a race-tracking channel from the race-tracking study and the flow control study. Shown are mean values and standard deviations for experiments in triplicate. [26]

corresponding experiment of the RT study in Figure 7-2(a). The observed difference of AFR progression on the preform bottom side is correlated to process design changes and resulting flow manipulations due to the applied passive flow control strategy in the FC study. While the TITTP of the two studies is comparable, the compression phase is longer in the FC study due to the increased height of the injection gap. This results in a longer remaining time span between TITTP and the compression end and in an increased gap height at TITTP for the flow control experiments compared to experiments of the RT study as shown in Figure 7-8. With the larger remaining gap height of the central slider at TITTP, more fluid is distributed between the arrival of the flow front on the preform bottom side and the end of the compression phase, filling the observed preform bottom side quickly from its center towards the edges as seen in Figure 7-7(b).

Observing the flow control experiments with a race-tracking channel in Figures 7-6(b),(c), the black dotted AFR curve of the race-tracking channel stays at zero during the complete injection phase and for parts of the compression phase until it rises rapidly. The delayed filling of the race-tracking channel is explained by the flow manipulation of the applied passive flow control strategy. Due to the spatial isolation of the central injection gap from the edge race-tracking channel, the flow has to pass through the pre-compacted preform edge before it fills the race-tracking channel, causing the observed time delay of the rise in the channel's AFR. On the contrary, the process design during the RT study provides a spatial connection between the injection gap and the race-tracking channel, resulting in

an early filling of the race-tracking channel shortly after the injection start as seen in Figures 7-2(b),(c).

Comparing the flow control experiments with race-tracking in Figures 7-6(b),(c) with each other, the rise in the AFR of the race-tracking channel is recorded as starting earlier for experiments with larger race-tracking channel widths. The rise at different times for different channel widths is caused, on the one hand, by the difference in preform dimensions and, on the other hand, by the specific flow pattern of the passive flow control strategy. All experiments of the FC study were performed at identical in-plane dimensions of the cavity and of the central slider realizing the injection gap. The race-tracking channel was created by cutting the centrally placed preform smaller than the in-plane dimensions of the cavity. Therefore, the width of the race-tracking channel defines the width of the pre-compacted preform edge. For a wider channel width, a resulting narrower pre-compacted preform edge section needs to be penetrated by the fluid, flowing from the central injection gap towards the race-tracking channel. Therefore, a shorter flow path leads to the observed earlier filling of the race-tracking channel with increased channel width as shown in Figures 7-6(b),(c).

Figures 7-7(d),(f) show the flow front progression on the preform bottom side for experiments of the FC study with medium and wide race-tracking channel width, respectively. In both experiments, the out-of-plane flow under the central injection gap impregnates the preform bottom side from its center towards its edges, as previously discussed for the experiment without a race-tracking channel seen in Figure 7-7(b). Additionally, the experiments with race-tracking in Figures 7-7(d),(f) show a lateral flow from the race-tracking channel towards the preform center. Comparing these experiments with each other, the expansion of the lateral flow from the race-tracking channel towards the preform center increases with increasing channel width. On the one hand, this observation is explained by the earlier filling of the race-tracking channel for increased channel width, as discussed in the previous paragraph. On the other hand, the lateral flow is promoted by the acting fluid pressure inside the race-tracking channel. Generally, the fluid pressure during the compression phase is caused by the closure movement of the central slider leading to a high fluid pressure inside the injection gap. Due to the spatial disconnection between the injection gap and the race-tracking channel, the fluid has to flow through the pre-compacted preform edge to fill the race-tracking channel. Thus, the developing fluid pressure inside the race-tracking channel is reduced by the porous preform edge that the fluid flows through. The wider the race-tracking channel width, the narrower the pre-compacted preform edge and the higher the developing fluid pressure inside the channel, causing the extended lateral flow as observed by comparing Figures 7-7(d),(f).

The flow front progression plot in Figure 7-7(b) shows that the outer corner sections of the preform are filled last on the preform bottom side in experiments without race-tracking in the FC study. This is explained by the filling pattern of the flow control experiments, i.e. first the area on the preform bottom side under the injection gap is filled, followed by a lateral penetration towards the edges. Due to the geometrical design of the square injection gap with a side length of 210 mm and corner radii of 10 mm and of the square cavity with a side length of 228 mm and corner radii of 10 mm, the distances between the radii of the injection gap and cavity are the largest, and therefore, the outer preform corner sections are the last to be filled. The filling pattern overview of the flow control experiments with a race-tracking channel in Figures 7-7(d),(f) is not clear on this matter, for which reason additional flow front images are presented in Figure 7-9. The pictures show the preform bottom side at the time of complete filling at 23 s of the experiment without race-tracking in Figure 7-9(a) and the corresponding pictures of experiments with a medium and wide race-tracking channel at the same point in time in Figures 7-9(b),(c). The complete preform impregnation of the preform is delayed for experiments with race-tracking, observable by the unimpregnated preform sections in their corners. In contrast to the experiment without race-tracking, the sections filled last are not at the outer edge of the corner but located slightly inside the preform, entrapped between the two merging flows from the preform center and from the race-tracking channel.

A shift of the location of the lastly filled preform section is observed by comparing the flow control experiments with race-tracking with the corresponding experiments performed during the RT study. While the experiments of the RT study consistently show the lastly filled section in the center of the preform, the manipulated flow due to the passive flow control strategy of the FC study relocates

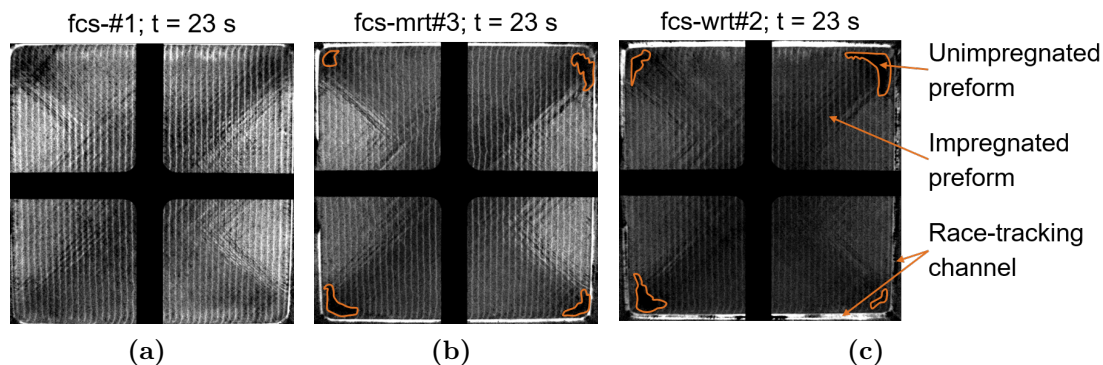


Fig. 7-9 Preform impregnation on the bottom side of the three experimental scenarios of the flow control study at 23 s: (a) complete filling of experiment without a race-tracking channel fcs-#1; unimpregnated corner sections of experiments with a medium fcs-mrt#3 (b) and wide fcs-wrt#2 (c) race-tracking channel. [26]

the lastly filled section towards the outer preform corners. This is traced back to the process design changes, which spatially disconnect the central injection gap from the edge race-tracking channels and initiate a preform impregnation from the preform center towards its edges. Therefore, the lastly filled preform sections and potential macro voids due to edge race-tracking shift towards the outer preform corners in experiments of the FC study. Manipulating the flow to locate potential manufacturing flaws, such as macro voids towards the edge section of the manufactured part, which is generally machined off, decreases the risk of scrap parts and highlights once more the benefit of the investigated passive flow control strategy for a robust FS-CRTM production.

7.3 Conclusions of the Race-Tracking and Flow Control Study

In this chapter, flow visualization experiments of the film-sealed compression resin transfer molding (FS-CRTM) process have been presented. Two studies were performed to investigate: (i) the effect of edge race-tracking and (ii) a passive flow control strategy to diminish edge race-tracking. Through the experimental observations, typical flow propagation scenarios are derived describing the impregnation of preforms of small geometrical aspect ratio without and with race-tracking as well as during the application of the investigated passive flow control strategy.

Figure 7-10(a) illustrates the first derived scenario of the preform impregnation during the FS-CRTM process without edge race-tracking. The observations from the flow visualization experiments revealed a fast distribution of fluid above the top preform surface inside the injection gap, which is fully filled during the injection phase. The tool closure movement during the compression phase initiates an out-of-plane flow propagation nearly parallel to the top preform surface. The out-of-plane flow was observed by a delayed arrival of the flow front on the preform bottom side. The general flow of the derived FS-CRTM scenario correlates with other studies in the technical literature for the conventional CRTM process of preforms with small geometrical aspect ratios [37, 38].

The second derived flow scenario of the FS-CRTM preform impregnation in the presence of edge race-tracking is shown in Figure 7-10(b). During the injection phase, the early filling of the injection gap is observed to be accompanied by the filling of the race-tracking channel due to their spatial connection. Based on the observations made, the preform impregnation during the compression phase is concluded to consist, in simplified terms, of three flow regions as illustrated in Figure 7-10(b). In region 1, at the edge of the preform, a predominantly in-plane

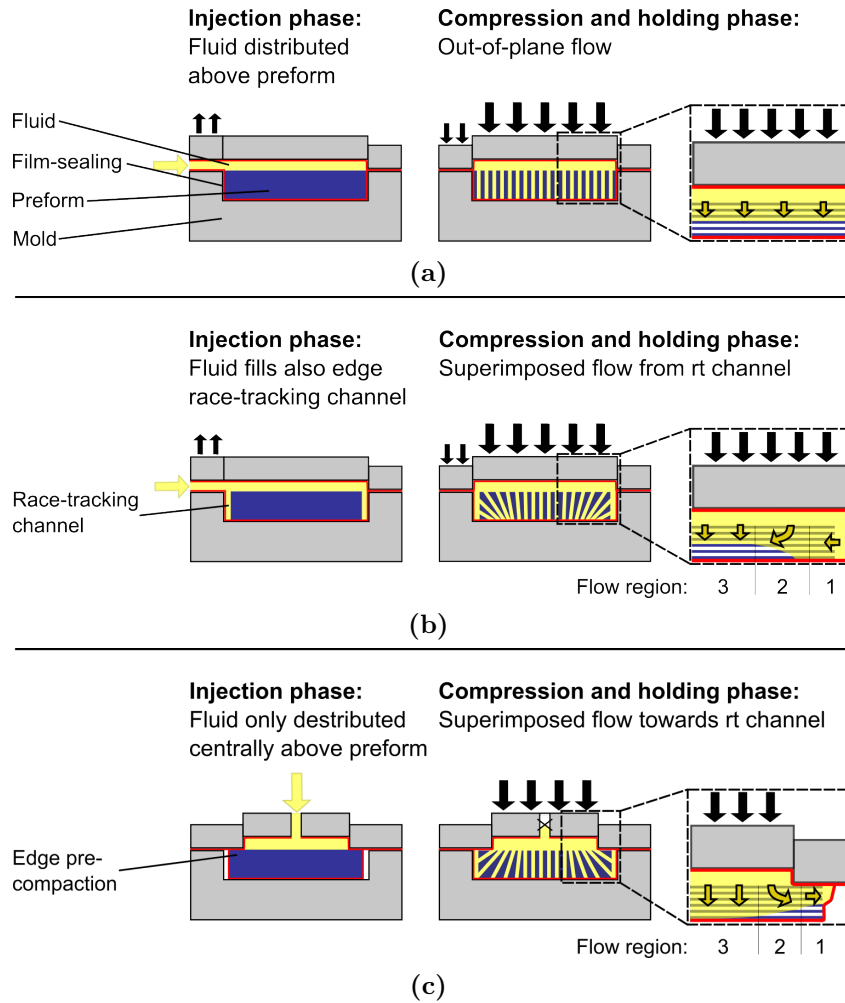


Fig. 7-10 Flow scenarios derived from FS-CRTM experiments: (a) without edge race-tracking (rt) channel; (b) with edge race-tracking channel; and (c) with applied passive flow control strategy of a localized, central injection gap and pre-compaction of the preform edge. [26]

flow develops from the race-tracking channel towards the preform center. In region 3, at the center of the preform, furthest away from the race-tracking channel, an undisturbed, predominantly out-of-plane flow is established from the preform top towards the bottom side. In region 2, the transition region, a superimposed flow of the neighboring in-plane and out-of-plane flows develops. The derived flow scenario demonstrates the change of flow pattern during the FS-CRTM preform impregnation in the presence of edge race-tracking, caused by the additional lateral in-plane flow from the race-tracking channel towards the center of the preform.

The experiments of the race-tracking (RT) study show that a FS-CRTM process design in which the fluid is injected into an injection gap that covers the complete preform top surface is sensitive to edge race-tracking. The direct spatial connection between the injection gap and the race-tracking channel leads to an early

filling of the race-tracking channel and a subsequent lateral in-plane flow from the race-tracking channel to the center of the preform. Considering that the in-plane permeabilities of a reinforcement structure are generally one order of magnitude higher than its out-of-plane permeability, the lateral in-plane flow will always significantly penetrate the preform before the out-of-plane flow saturates the preform in the through-thickness direction. As a result, macro void formation occurs, which was observed in all experiments with race-tracking during the RT study. In industrial production, such flaws lead to non-compliance of quality requirements (i.e. mechanical performance and surface quality) and require parts to be scrapped, which needs to be avoided.

The investigated passive flow control strategy provides a solution to diminish the edge race-tracking effect and increases the process robustness of the FS-CRTM process. Specifically, employed design changes manipulate the flow progression as shown in the third simplified flow scenario in Figure 7-10(c). During the injection phase, the fluid is distributed inside a localized injection gap. The injection gap spans only over the central preform section and is disconnected from a potential edge race-tracking channel by the pre-compacted outer preform edge. During the compression phase, a preform impregnation is initiated from the preform center towards its edges. The flow pattern, due to the applied passive flow control strategy, is simplified, described in three flow regions as illustrated in Figure 7-10(c). The closure of the central slider above the injection gap promotes a predominantly out-of-plane impregnation in the central preform section of flow region 3. In the neighboring region 2, the flow is transferred towards a predominantly in-plane flow in the outer part of the pre-compacted preform edge of region 1. Therefore, a superimposed flow is established in region 2 but now manipulated to flow from the preform center of the preform towards its edge, filling a potential edge race-tracking channel late in the process.

In the presence of a race-tracking channel, the experiments with an applied passive flow control strategy revealed that a lateral in-plane flow from the race-tracking channel towards the center of the preform is still developed but to a reduced extent compared to experiments without the passive flow control strategy. The reduction of the lateral flow is caused by the difference in process design between the two studies. For the process design in the RT study (without a passive flow control strategy), the injection gap and the edge race-tracking channel are spatially connected. This results, on the one hand, in an early filling of the race-tracking channel and, on the other hand, in a homogeneous pressure field between the fluid in the injection gap and the fluid inside the race-tracking channel. The consequences are an early start of a lateral preform impregnation and a fast lateral flow progression due to the large fluid pressure increase during the compression phase. For the process design in the

flow control (FC) study, the injection gap and the edge race-tracking channel are spatially disconnected due to the applied passive flow control strategy. Therefore, the fluid needs to flow through the pre-compacted preform edge before it fills the race-tracking channel. The delayed filling of the race-tracking channel results in a reduced time span in which the lateral race-tracking flow can penetrate the preform. Additionally, the pre-compacted preform edge acts as a pressure reducer between the high fluid pressure inside the injection gap and the adjusted, lower fluid pressure inside the race-tracking channel. The lowered fluid pressure inside the race-tracking channel leads to a reduced lateral flow propagation observed during the FC study. Therefore, comparison of the two studies emphasizes the effectiveness of the passive flow control strategy to diminish the edge race-tracking effect during the preform impregnation of the FS-CRTM process.

Besides changes in the flow pattern, edge race-tracking is identified as cause for a force reduction of up to 25% recorded at the central slider, which is directly correlated to the cavity pressure. The reduced cavity pressure during the tool closure is considered to be caused by the change from a pure out-of-plane to a superimposed preform impregnation with sections of out-of-plane and in-plane flow. Considering that in-plane permeabilities are generally one order of magnitude higher than the out-of-plane permeability of reinforcement structures, the developed fluid pressure during the preform impregnation reduces in the presence of edge race-tracking. The reduction of the stagnation pressure at the end of the compression phase is explained by an increased overall porosity inside the cavity in the presence of a race-tracking channel resulting from the reduced preform in-plane dimensions. Furthermore, a drop in the final stagnation pressure is also recorded for experiments with an applied passive flow control strategy and is therefore purely dependent on the existence of an edge race-tracking channel, and not on the preform impregnation pattern during FS-CRTM.

The presented RT and FC studies are an important step toward comprehensively understanding and controlling the preform impregnation during FS-CRTM processing. The studies show that: (i) edge race-tracking significantly alters the impregnation pattern of preforms of a small geometrical aspect ratio (50), and (ii), importantly, that the passive flow control strategy is an effective solution to diminish the race-tracking effect and establish a more robust FS-CRTM process.

8 Summary and Conclusions

The presented research investigates the edge race-tracking effect on the preform impregnation during the compression resin transfer molding (CRTM) process. Different studies were presented which aim to answer specific research questions targeting the overall research objective:

Increasing process robustness towards edge race-tracking during CRTM preform impregnation by investigating, enabling and validating a passive flow control strategy via the use of film-sealing and slider tooling.

In the following, the individual research questions are answered by summarizing and concluding the studies presented in the previous chapters. The first original study presented in this work is discussed in Chapter 4. Numerical flow simulations of the CRTM process with injection gap were performed in the commercial software PAM-RTM (ESI Group, Rungis, France). Models of different process configurations were set up to see how edge race-tracking affects the CRTM process at different process scenarios. Three process parameters (i) geometrical aspect ratio of the preform (length/width versus height), (ii) injection gap height, and (iii) inlet position were individually changed on two levels. Comparing the simulations of the different scenarios (without edge race-tracking) with each other, confirmed the complex character of the CRTM preform impregnation, as stated in literature [15], due to the combination of injection-driven and compression-driven flow.

The simulations presented in Chapter 4 showed that, during the CRTM injection phase, the resin is distributed mainly in in-plane direction above the preform due to the higher permeability of the injection gap compared to the preform. The extent of the preform impregnation during the injection phase is shown to be influenced by the injection time and the acting injection pressure which is, furthermore, influenced by the equivalent permeability of the injection gap above the preform. During the subsequent compression phase, two general compression-driven flow scenarios were observed. Firstly, simulations of preforms with small geometrical aspect ratio and large injection gap were observed to result in a complete filling of the injection gap and a subsequent predominantly out-of-plane impregnation of the preform, confirming literature reports of similar CRTM process scenarios [37, 38]. Secondly, preforms of (i) large geometrical aspect ratio and high injection gap height as well as (ii) small geometrical aspect ratio and low injection gap height were shown to be only partially overflowed at the time the upper mold gets in contact with the preform. In these process scenarios the compression-driven flow was observed to equalize over the preform thickness after the upper mold is in contact with the preform and subsequently impregnate the remaining unimpregnated preform sec-

tion predominantly in in-plane direction. While the observations for preforms of large geometrical aspect ratio with high injection gap height correlate well with CRTM literature studies [36, 37], the presented simulations unveil that the same compression-driven flow scenario also develops for preforms of small geometrical aspect ratio and low injection gap height.

During the race-tracking study in Chapter 4, the discussed CRTM simulations of ideal conditions (no edge race-tracking) were compared to simulations in which edge race-tracking occurred, to answer the first research question (RQ):

RQ 1: How does edge race-tracking impact the CRTM process?

To specify the investigations, the first research question is broken down in two research sub-questions. While the first research sub-question focuses on potential flow pattern changes inside the mold in the presence of edge race-tracking, the second aims to investigate the effect of edge race-tracking on CRTM process responses. Both are going to be answered in the following.

RQ 1.1: How does edge race-tracking impact the flow pattern at different CRTM process configurations?

In general, the conducted numerical study showed that edge race-tracking changes the preform impregnation pattern at all investigated process configurations. The presence of an edge race-tracking channel increases the complexity of the flow pattern inside the CRTM mold due to an additional third flow domain, the edge race-tracking channel, besides preform and injection gap. The conducted investigations showed that the flow pattern inside the mold changes depending on the permeability ratio between the individual flow domains. The preform permeability for structural parts is commonly multiple orders of magnitude lower than the equivalent permeability of the injection gap and the race-tracking channel. Therefore, the resin is primarily distributed inside the two highly-permeable flow domains, injection gap and edge race-tracking channel. However, depending on the CRTM process configuration, the permeability between these two flow domains can also significantly differ, which results in locally increased flow front velocities inside the mold. The observed advancing flow front in one of the flow domains results in a lateral impregnation of the other two flow domains and an overall changed preform impregnation pattern compared to simulations without edge race-tracking.

Furthermore, for all investigated process scenarios, the presence of an edge race-tracking channel is shown to cause an incomplete preform impregnation at process end. The increased porosity inside the mold due to the fiber-free race-tracking channel in combination with an injected constant fluid volume result in a macro void formation next to the lastly filled preform section. Depending on the process configuration, the shape and location of the macro void (unimpregnated preform

section) change, based on the developed compression-driven flow pattern. Due to the predominantly out-of-plane impregnation of the preform with small geometrical aspect ratio and large injection gap, macro voids were recorded to be of large in-plane and small out-of-plane dimensions. The final predominantly in-plane impregnation of preforms of (i) large geometrical aspect ratio and high injection gap height, as well as (ii) small geometrical aspect ratio and small injection gap height result in macro voids of small in-plane dimension which span over the complete preform thickness.

RQ 1.2: How does the severity of edge race-tracking affect CRTM process responses?

Three process responses were identified, which are influenced by edge race-tracking. Firstly, the injection pressure was observed to change at a constant flow rate injection as soon as the flow starts to fill the edge race-tracking channel. This is traced back to the difference in equivalent permeability of the different flow domains comprised of preform, injection gap and edge race-tracking channel. Furthermore, a wider race-tracking channel was identified to result in a decreased injection pressure during its filling due to the increased equivalent permeability of the channel according to the used Equation (2-12). Secondly, the maximum compression force acting on the upper mold at process end was recorded to decrease in the presence of edge race-tracking. The strongest compression force reduction was modeled comparing an ideal simulation without edge race-tracking with a simulation with edge race-tracking. The further increase of the edge race-tracking severity by increasing the width of the channel was recorded to result in a further reduction of the compression force but on a minor level. The recorded force reductions are traced back to a reduced fluid stagnation pressure at process end resulting of an increased mold porosity in the presence of a fiber-free race-tracking channel in combination with an injected constant fluid volume. Thirdly, the volume filling ratio (VFR) of the preform at process end was observed to decrease with increasing race-tracking severity. A decreased final VFR correlates with an increased macro void at process end. As for the maximum compression force, the decreased final VFR is also caused by the increased overall porosity inside the mold at increased race-tracking severity while the injected fluid volume is kept constant. These facts in combination with an complete filling of the race-tracking channels result in an incomplete preform impregnation at the end of the CRTM process.

In summary, the numerical race-tracking study confirmed the initial hypothesis stated in Chapter 3.1 that edge race-tracking changes the CRTM preform impregnation and that different geometrical preform and design parameters influence the alteration of the preform impregnation pattern differently. In general, the conventional CRTM design is identified to be sensitive to edge race tracking due to the

spatial connection between injection gap and edge race-tracking channel. Thus, the numerical race-tracking study revealed that in order to diminish edge race-tracking effects during CRTM, the filling of the race-tracking channel has to be delayed to a point at which the majority of the preform has already been impregnated. The two investigated CRTM process configurations of a (i) central inlet and small injection gap as well as of (ii) central inlet and large preform aspect ratio enable the design of the resin flow inside the injection gap so that the edge race-tracking channel is not reached before the upper mold is in contact with the preform. The subsequent equalization of the flow front over the preform thickness and final predominantly in-plane flow can help to impregnate the majority of the preform before the fluid fills the edge race-tracking channel. However, at the CRTM process configuration of large injection gap and small preform aspect ratio, a relocation of the inlet from a lateral to a central position was observed to be not sufficient enough to prevent a complete filling of the edge race-tracking channel early in the process.

A second numerical study, the numerical flow control study, was performed investigating a passive flow control strategy for the CRTM process configuration of large injection gap, small preform aspect ratio and central inlet to spatially separate the injection gap from the edge race-tracking channel. The spatial separation is enabled by a partitioned upper mold design which pre-compacts the preform edge and allows the injection of the resin into a localized, central injection gap. The numerical flow control study aimed to answer the second research question:

RQ 2: How does the passive flow control strategy impact the flow pattern during CRTM preform impregnation in the absence and presence of edge race-tracking?

The applied passive flow control strategy was observed to alter the ideal preform impregnation (no edge race-tracking) at the CRTM process configuration of large injection gap, small preform aspect ratio and central inlet position. While for the conventional mold design (without passive flow control strategy) the preform is predominantly impregnated in out-of-plane direction, the partitioned upper mold design of the passive flow control strategy is shown to result in a localized, predominantly out-of-plane preform impregnation in the area below the central injection gap and a subsequent predominantly in-plane impregnation of the pre-compacted preform edge. Due to the spatial disconnection between the central injection gap and the edge race-tracking channel at applied passive flow control strategy, the overall preform impregnation pattern does not change in the presence of an edge race-tracking channel resulting in a delayed filling of the channel close to process end. Therefore, the passive flow control strategy is modeled to prevent the lateral preform impregnation from the edge race-tracking channel towards the preform center observed at CRTM simulations without passive flow control strategy. Furthermore, the final VFR of the preform is shown to be increased at applied passive

flow control strategy and the locations of the formed macro voids are shifted towards the preform edge.

Concluding the numerical flow control study, the hypothesis stated in Chapter 3.1 is verified that a passive flow control strategy can be employed for the CRTM process in which a partitioned upper mold design separates a central, localized injection gap from a potential edge race-tracking channel by a pre-compacted preform edge. The simulations showed a modified flow pattern in which the preform impregnation is less dependent on the presence of an edge race-tracking channel and, therefore, highlight the potential of the investigated passive flow control strategy to diminish edge race-tracking during CRTM processing. The partitioned upper mold design, which is needed for the passive flow control strategy, can be put into effect by slider tooling technology (Chapter 2.1.4). However, slider tooling is known to increase the wear of conventional mold sealing concepts. Therefore, a seal-free CRTM mold design is sought in the context of this work by sealing the preform impregnation space inside the mold via film material, similar as done in literature [24] for a related process. To achieve this goal, the third research question is stated as follows:

RQ 3: How can film material be functionally integrated in the matched mold CRTM process to seal the preform impregnation space?

Aspects of the TRIZ methodology are used in Chapter 5.1 to analyze the CRTM process on an abstract level and identify the effect of a film integration. A function analysis showed that a film-sealing of the preform injection space physically separates the two components, preform and resin system, from the mold segments by having no more direct functional connection between these components. The abstract model of the film-sealed compression resin transfer molding (FS-CRTM) process revealed that the process enhancement brings advantages such as reduced risk of mold damages due to fiber-pinching, release agent free manufacturing, eliminated mold contamination due to release agent or resin residues, and enabling seal-free mold designs. The latter is needed in the context of this work to enable the studied passive flow control strategy during CRTM manufacturing via slider tooling. Furthermore, the abstract process analysis showed that the elimination or relocation of secondary process steps, such as mold cleaning and preform evacuation, bears the potential to reduce the mold cycle time during FS-CRTM by 20% to 30% compared to conventional CRTM manufacturing [152, 153].

In the context of the TRIZ methodology, the abstract solution of the FS-CRTM process is transferred back to a concrete process concept in Chapter 5.2 by defining principal process steps. Thus, the FS-CRTM process starts by encapsulating the preform with films which are sealed air- and liquid-tight via welding. The so-formed film-sealed preform package is evacuated prior to its placement in the mold. Inside

the mold, the film is penetrated to enable a resin injection into the film-sealed preform package. During the compression phase, either the complete upper mold or a local section of it closes to impregnate the preform before the resin is cured inside the film-sealing. In the context of this work, the film is intended to be used as a process aid material which is removed from the cured part after demolding.

The abstract analysis of the CRTM process enhancement by using film material to seal the preform injection space, revealed that besides enabling a seal-free tool design, other additional benefits arise showing the potential of the FS-CRTM process. The additional cost induced due the use of film material can, therefore, be compensated by, e.g., reduced maintenance cost due to worn sealing and damaged mold segments or an increased production rate due to a reduced mold cycle time by eliminating or relocating secondary process steps. However, specific cost calculations need to be performed for each business case and are not part of this thesis which investigates the integration of film material in the CRTM process solely to enable a passive flow control strategy by using slider tooling technology to enable a partitioned upper mold design.

Having the principle concept of the FS-CRTM process defined, the film integration bears a potential to change process characteristics by introducing an additional flexible material (the film) into the preform impregnation space. The film potentially influences the preform impregnation pattern, e.g., during the injection by either compacting the preform in unimpregnated sections or by lifting off the preform surface and expanding into the injection gap. Process characteristics could change based on the choice of the film material as well as the acting pressure gradient across the film. Therefore, the novel FS-CRTM process is characterized in the context of this work, by answering research questions four and five. In this context, research question four deals with the selection of the film material and is stated as follows:

RQ 4: Which film material is suitable to be used in FS-CRTM manufacturing and with which second film material can it be substituted in FS-CRTM flow visualization experiments?

Based on the defined concept of the FS-CRTM process, requirements on a suitable film material are defined in Chapter 6.1. The requirements of weldability and elasticity narrowed the type of polymer down to the groups of semi-crystalline thermoplasts and thermoplastic elastomers, both used at a temperature in their rubber-elastic state. Three thermoplastic mono-layer films made of polypropylene (PP), polyamide (PA), polyvinyl fluoride (PVF) and one thermoplastic elastomer (TPE) were selected and investigated in regard to the requirements of weldability, thermal stability (elasticity), low gas permeability of air, antistick properties to-

wards epoxy resin systems, and cost efficiency. The results showed that none of the investigated films fulfills all requirements, but a combination of PP and PA could do so. Therefore, a PA/PP multilayer film was designed and tested which verified its suitability to be integrated in the FS-CRTM process.

In the context of this work, the FS-CRTM process was studied on a laboratory scale by flow visualization experiments according to the developed methodology explained in Appendix A.4. However, the FS-CRTM flow visualization experiments were conducted at room temperature while industrial FS-CRTM manufacturing is done at an elevated process temperature between 80 °C to 120 °C. Therefore, a second film material was identified made of low-density polyethylene (PE-LD) to substitute the process film (PA/PP) during flow visualization experiments. The film was selected due to its characteristic of optical transparency, which is needed to monitor the flow front inside the film-sealed preform package during the experiments. Furthermore, the comparability of the mechanical properties, stiffness and stress relaxation, was verified by laboratory tests comparing the PE-LD film at room temperature with the PA/PP film at process temperature. Finally, the stiffness level of the films was investigated by unrestrained flow experiments in Chapter 6.2. The experiments verified an adequate stiffness level of the selected films which enable them to lift off the preform surface and adapt to the upper contour of the gap during fluid injection.

In conclusion, the identified cost-effective PA/PP multilayer film sets the baseline to industrialize the FS-CRTM process and enhance serial production of fiber-reinforced plastic (FRP) parts. However, the presented film selection did not include any real FS-CRTM production trials in the context of this work. Nevertheless, together with industrial partners, the FS-CRTM process was validated on an industrial scale in a post-thesis project by using a PA/PP multilayer film. Further information on the industrial FS-CRTM process verification is given in Chapter 9. In addition, the functionality of the substitution film (PE-LD) was demonstrated during laboratory tests in unrestrained flow visualization experiments and is therefore suitable to study the FS-CRTM preform impregnation by answering the fifth research question:

RQ 5: How does the preform impregnation during FS-CRTM take place and which are dominant process factors to control the preform impregnation?

Due to setup conditions of the used test methodology (Appendix A.4), the FS-CRTM process was characterized in the context of this work for preforms of small geometrical aspect ratio (length/width versus height). FS-CRTM flow visualization experiments were conducted via a pressure-controlled fluid injection of constant volume and a force-controlled mold closure. Dominant process factors to control

the preform impregnation were identified via two full-factorial test plans and derived multiple linear regression (MLR) models investigating the injection as well as the compression and holding phase of the FS-CRTM process. All identified factor-response correlations are presented in Table 6-4 in Chapter 6.3 and summarized by presenting dominant process factors to control the FS-CRTM preform impregnation in the following paragraphs.

The FS-CRTM process time was split in (i) the time between injection start and end, denoted “injection time”, and (ii) the time between injection end and complete mold closure, denoted “compression time”. The MLR models revealed that the injection time is dominantly affected by the fluid stagnation pressure, acting at the inlet prior to injection start, while the compression time is dependent on the compression force limit, pre-set for the force-controlled mold closure. Therefore, by disregarding resin curing, the FS-CRTM process time can be controlled by only two factors, the stagnation pressure and compression force. For both, the injection and compression time, a non-linear correlation to the factors, stagnation pressure and compression force, was respectively identified, showing that the process can be designed to be most cost-effective by balancing a low process time with low investment costs of process equipment needed to supply the required stagnation pressure and compression force.

Furthermore, the stagnation pressure was observed to correlate near-linearly with the flow rate. The recorded flow rates during the FS-CRTM flow visualization experiments were comparable with flow rates of industrial processes, such as HP-RTM described in literature [10, 17, 23, 194], but on a pressure level that is approximately one order of magnitude lower for FS-CRTM. The reduced injection pressure level is traced back to the initial distribution of the fluid above the preform inside the high-permeable injection gap which highlights another benefit of the investigated FS-CRTM design to reduce the investment cost of the needed injection equipment.

The acting pressure during the injection is dependent on the pre-defined pressure level prior to the injection, the stagnation pressure, and on the injection gap height, influencing the flow resistance inside the injection gap. Via the area filling ratio (AFR) of the preform top side, the extend, to which the injection gap was filled at injection end, was indirectly measured. It was shown to be primarily influenced by the gap height, due to its direct correlation to the overall volume of the injection gap. The investigations showed that a threshold value exists below which the injection gap is always completely filled and above which the extend to which the injection gap is filled decreases. If the injection gap is not completely filled, the stagnation pressure additionally influences the ratio of filled injection gap due to the shortened injection time, which limits the time the fluid can vanish the injection gap by penetrating the below located preform. The height of the injection

gap should therefore be chosen as high as possible to realize a minimal injection pressure and as low as possible to achieve a maximally filled injection gap at injection end. The described threshold value of the injection gap height, which sets the upper limit at which the injection gap is completely filled, defines the optimal point of balance between minimal injection pressure and maximal injection gap filling.

The FS-CRTM impregnation pattern of preforms of small geometrical aspect ratio was observed to correlate well with literature reports [37, 38] and numerical simulations (Chapter 4) of the conventional CRTM process. While the resin is first mainly distributed inside the injection gap predominantly in in-plane direction, the preform is subsequently impregnated in out-of-plane direction during mold closure. Based on the performed FS-CRTM experiments a MLR model was derived describing the time of the initial through-thickness penetration (TITTP) which is shown to be triggered by the acting vent pressure as well as the injection gap height. As previously stated, the injection gap height directly influences the overall volume of the injection gap and, therefore, also the time at which the injection gap is completely filled at a pressure-driven injection. After the injection gap is completely filled, the resin can only penetrate the permeable preform located below, which is why the injection gap height influences the starting point of a predominantly out-of-plane impregnation of the preform and, therefore, also of the measured TITTP. A low vent pressure is expected to initiate a pressure gradient in through-thickness direction of the preform, supporting the out-of-plane fluid flow from the preform top to bottom side, directly influencing the TITTP. However, while the TITTP was well predictable, no MLR model could be set up for the time of increasing preform impregnation due to recorded random impregnation patterns on the preform bottom side. A potential explanation is observed in Chapter 7, at which the out-of-plane deformation of the test setup was correlated to the filling pattern on the preform bottom side during the holding phase after complete mold closure. The observed limitation of the test setup is therefore expected to cause the observed random preform impregnation pattern on the preform bottom side but does not limit the drawn conclusions of the general preform impregnation pattern.

By having the ideal FS-CRTM preform impregnation (no edge race-tracking) characterized, the effect of edge race-tracking was studied by answering research question six:

RQ 6: How does edge race-tracking affect the preform impregnation during FS-CRTM processing?

By cutting the preform in-plane dimensions smaller than the cavity dimensions, edge race-tracking was provoked during velocity-controlled FS-CRTM flow visualization experiments of preforms of small geometrical aspect ratio according to the

methodology explained in Appendix A.4. The experiments presented in Chapter 7.2.1 showed that the direct spatial connection between injection gap and edge race-tracking channel results in an early filling of the channel. While the preform is predominantly impregnated in out-of-plane direction in FS-CRTM experiments without edge race-tracking, the early filling of the channel in the presence of edge race-tracking leads to an additional lateral flow from the race-tracking channel towards the preform center. Furthermore, the increased overall porosity inside the mold, due to the presence of an edge race-tracking channel in combination with an injected constant fluid volume, leads to a state in which the preform is not completely impregnated at process end. Thus, a macro void was observed in all FS-CRTM flow experiments with edge race-tracking located next to the lastly impregnated preform section.

Besides a change in preform impregnation pattern, a degradation of the maximum compression force acting on the upper mold was recorded in the presence of an edge race-tracking channel. The decreased compression force at process end was concluded to be mainly caused by a reduction of fluid pressure inside the mold at presence of an edge race-tracking channel and is recorded to decrease further with increased channel width.

Both observations, the changed preform impregnation pattern as well as the decreased maximum compression force in the presence of edge race-tracking, correlate well with results of numerical CRTM simulations of preforms with small geometrical aspect ratio, as discussed for research question one and presented in detail in Chapter 4. The results of Chapter 7.2.1 show that the FS-CRTM impregnation of preforms of small aspect ratio is sensitive to edge race-tracking. Without any prevention or control strategy, slight off-tolerances during the preform cutting or placement result in the creation of edge race-tracking channels which bear a high risk to drastically change the preform impregnation pattern and result in an unsuccessful preform impregnation. Therefore, the passive flow control strategy, investigated in Chapter 4 for the conventional CRTM process, was also applied during FS-CRTM processing and studied by answering the final research question seven of this work:

RQ 7: How effective is the attempt to diminish the edge race-tracking effect during FS-CRTM processing by applying the passive flow control strategy?

As discussed for research question one and six, the spatial connection between injection gap and edge race-tracking channel leads to an early filling of the channel for preforms of small geometrical aspect ratio. Therefore, the core idea of the studied passive flow control strategy is to spatially separate the injection gap and the edge race-tracking channel by a partitioned upper mold design. The numerical CRTM

simulations of Chapter 4 showed that by applying the passive flow control strategy, the flow is manipulated to initially impregnate the preform predominantly in out-of-plane direction in the section below the central injection gap and subsequently impregnate the preform edge predominantly in in-plane direction. The FS-CRTM flow experiments presented in Chapter 7.2.2 match the numerical CRTM simulations in some points, but not to the full extent. While the spatial separation of the central, localized injection gap and the edge race-tracking channels was recorded at the FS-CRTM flow experiments to delay the filling of the channel, the filling time of the channel was only delayed to approximately the middle of the compression phase and not to compression end as predicted by the CRTM simulations. Furthermore, the edge race-tracking channel was observed to be completely filled during the compression phase of the FS-CRTM flow experiments while the CRTM simulations predicted a reduced filling of the channel at compression end. These discrepancies are explained by assumptions of numerical CRTM flow simulations on a macro scale, which assume, e.g., the preform to be homogeneous. In reality, preform flaws such as local gaps inside individual fabric layer or variations of fabric grammage can lead to a reduced effectiveness in some sections of the edge pre-compaction. The increased preform permeability in these sections can, therefore, result in the observed earlier filling of the edge race-tracking channel in the FS-CRTM flow experiments compared to the numerical CRTM flow simulations which assume a homogeneous preform structure without local flaws. Nevertheless, the FS-CRTM flow experiments verified the overall effectiveness of the passive flow control strategy by the recorded delay of the filling time of the edge race-tracking channel.

Due to the earlier and complete filling of the edge race-tracking channel during the FS-CRTM flow experiments with applied passive flow control strategy, a lateral flow from the preform edge towards the preform center was observed which was not predicted by the numerical CRTM flow simulations. However, the extent of the lateral flow was significantly reduced in FS-CRTM flow experiments with applied passive flow control strategy compared to experiments without. This is explained by two facts. Firstly, as stated before, the filling time of the edge race-tracking channel is delayed, reducing the time span in which the flow can laterally penetrate the preform from the edge race-tracking channel towards the preform center. Secondly, the pre-compacted preform edge acts as a pressure reducer. While in the conventional mold design (without applied passive flow control strategy), the spatial connection between injection gap and edge race-tracking channel leads to an equally high fluid pressure inside both flow domains, the passive flow control strategy separates these domains by the pre-compacted preform edge leading to an area of high fluid pressure inside the central injection gap and an area of re-

duced fluid pressure inside the edge race-tracking channel. Thus, the FS-CRTM flow visualization experiments showed that the reduced pressure inside the edge race-tracking channel results in a decreased lateral in-plane penetration of the preform and a main out-of-plane preform impregnation from its top (injection gap) to bottom side.

In sum, this work shows that the CRTM as well as the FS-CRTM preform impregnation is sensitive to edge race-tracking. For both processes, the presence of edge race-tracking is identified to reduce the process robustness mainly due to a changed preform impregnation pattern and a formed macro void at process end. The spatial connection between the high permeable flow domains of injection gap and edge race-tracking channel is identified as the main issue of the conventional CRTM mold design in which the complete upper mold is actuated, spanning over the entire lower cavity. The initial hypothesis of this work provided a theoretical solution to spatially separate the injection gap and the edge race-tracking channel by partitioning the upper mold. Numerical CRTM as well as experimental FS-CRTM validation studies showed that the partitioned upper mold design manipulates the preform impregnation pattern flowing from the preform center towards its edges, filling an edge race-tracking channel late in the process. By applying the investigated passive flow control strategy, the CRTM as well as the FS-CRTM preform impregnation is identified to have a higher resistance to flow pattern changes in the presence of an edge race-tracking channel. Additionally, the lastly filled preform section as well as potentially formed macro voids are relocated to the edge of the part, which is often milled off during industrial manufacturing processes. Furthermore, the core idea of this work, to seal the preform impregnation space during CRTM, was validated on a laboratory scale, which enables the integration of slider tooling technology to enable the studied passive flow control strategy. Therefore, the overall research objective of this work is met by increasing the process robustness towards edge race-tracking during the CRTM process, by the use of films to seal the preform impregnation space and slider tooling technology to control the resin flow pattern.

9 Post-Thesis Achievements and Outlook

The present work investigates the preform impregnation pattern during the compression resin transfer molding (CRTM) process in the presence of edge race-tracking. Edge race-tracking is identified to change the preform impregnation pattern during CRTM. However, a passive flow control strategy is determined which uses slider tooling technology to manipulate the preform impregnation pattern to diminish edge race-tracking effects. To ease the use of slider tooling, needed to establish the passive flow control strategy during CRTM processing, the preform impregnation space is intended to be sealed by film material. Laboratory experiments validated the principle process concept of the film-sealed compression resin transfer molding (FS-CRTM) process, however, the validation on an industrial scale was not part of this work. Therefore, a post-thesis project was initiated which was funded by the German Federal Ministry for Economic Affairs and Energy (BMWi – funding number: ZF4004314TA9) as well as the Austrian Federal Ministry of Digital and Economic Affairs. Two research institutes, Polymer Competence Center Leoben GmbH and Technical University of Munich, as well as three industrial partners, DEKUMED Kunststoff- und Maschinenvertrieb GmbH & Co. KG, Alpex Technologies GmbH, and RAC GmbH – Riedmann Advanced Composite, collaborated in a bi-national project using results presented in this work as a starting point for the industrialization of the FS-CRTM process. [195]

Figure 9-1(a) shows the jointly developed manufacturing equipment of the industrialization project. Besides a press-free tooling system to actuate the partitioned upper mold, a penetration mechanism was developed to tap the film via the injection adapter placed on top of the preform inside the film-sealed package. The process was run according to the principal process steps explained in Chapter 5.2, except for the evacuation of the film-sealed preform package which was done via a tube and cord similar to the flow visualization experiments explained in Appendix A.4. Via a two-staged development plan, the FS-CRTM process behavior was first investigated by manufacturing plates as seen in Figure 9-1(a), while the determined optimal process settings were eventually validated by manufacturing a three-dimensional demonstrator part in the shape of an omega-stiffener, as shown in Figure 9-1(b). The project verified that the FS-CRTM process, as designed and studied on a laboratory scale in this work, is suitable to manufacture fiber-reinforced plastic (FRP) parts under industrial conditions of the automotive industry. [196]

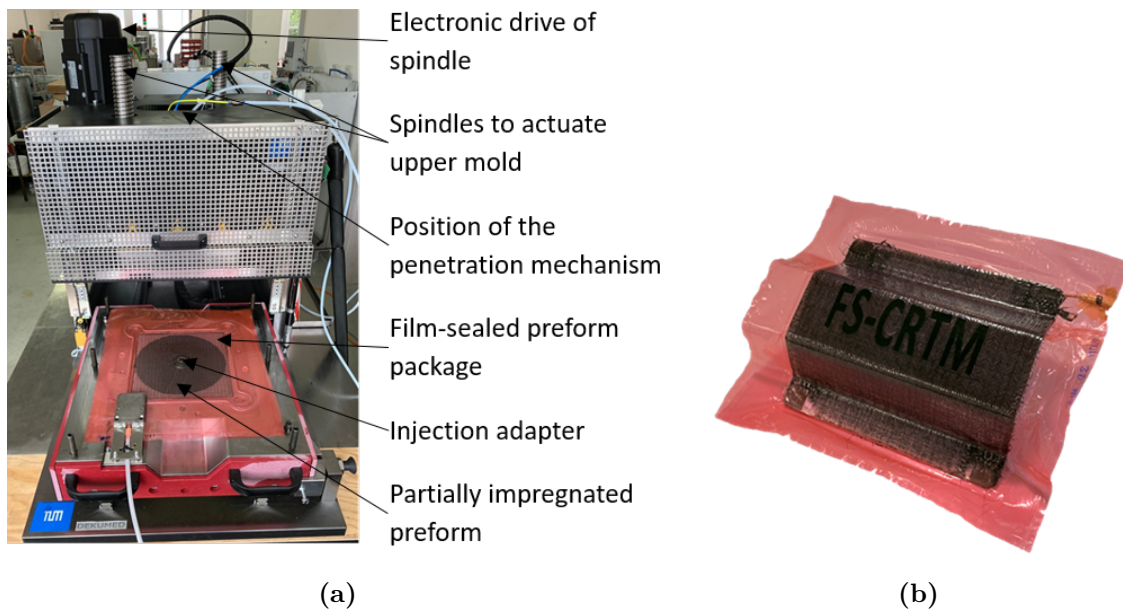


Fig. 9-1 (a) Tooling system and partially impregnated flat preform, (b) final three-dimensional demonstrator of post-thesis FS-CRTM industrialization project. [196]

Even though the post-thesis project contributes to future industrial applications of the FS-CRTM process, there are topics which need to be further investigated based on the groundwork presented in this thesis. Firstly, the edge race-tracking effect has been broadly studied via numerical simulations for different CRTM process conditions in Chapter 4. The presented results show that edge race-tracking is most severe for one of the four studied process scenarios, i.e. preforms of small geometrical aspect ratio and large injection gap. Thus, this process scenario was further studied via FS-CRTM experiments in Chapter 7 confirming the principle findings of the numerical CRTM simulations. However, future research has to be carried out to confirm the simulated effects which edge race-tracking causes in the other investigated CRTM process scenarios. Furthermore, experiments have to validate the conclusion drawn from the numerical simulations, that for these scenarios, the part as well as process can be designed so that the upper mold gets in contact with the preform before the flow inside the injection gap reaches the edge race-tracking channel. If the intended validation experiments show that this cannot be achieved for all cases, the suggested passive flow control strategy via an partitioned upper tool can also be applied to other process scenarios to spatially separate the injection gap from the edge race-tracking channel and, through this, diminish edge race-tracking effects.

Secondly, the functionalization of the film, used during FS-CRTM, has to be studied to further develop the manufacturing process as well as the produced part. Nowadays, many established sensors used during FRP manufacturing are integrated in

the mold structure due to their requirement to be in direct contact to the processed raw materials (i.e. fibers, resin system) to work properly. As identified in Chapter 5.1, the newly integrated film during FS-CRTM manufacturing separates the raw materials from the mold segments where sensors are commonly located. This separation could either confound the measured responses or even result in a dysfunction of the sensors. A potential solution can be to integrate sensors to monitor the FS-CRTM process into the film material and, therefore, be again in direct contact to the raw materials. Moreover, the film can be designed to adhere to the manufactured FRP part and to fulfill specific functions during the manufacturing or service life of the part. This idea is not new in composite manufacturing as, for example, Bruckbauer [31] studied the structural properties of adhered thermoplastic films and thermoset resin systems. Furthermore, Weimer et al. [197] suggested the integration of a functional film layer for FRP parts in an open-mold process and Häffelin [24] integrated a film in the closed mold RTM process to enhance the surface quality of the manufactured part. However, FS-CRTM provides the potential to industrialize this idea for application in different industries. Aerospace FRP applications can, for example, benefit from a functional film layer to protect the structure from lightning strike and precipitation static, needed in skin structures of airplanes [198] or propeller blades [199] and automotive FRP applications can be functionalized via an adhered, functional film layer to improve the electromagnetic shielding and flame protection needed, for example, for battery boxes of electric vehicles [200].

Finally, the FS-CRTM process can be further developed to expand the process limits of today's automated FRP production. In this context, the slider tooling technology can be used to manufacture complex part geometries with, e.g., undercuts in an automated way. A sophisticated use of the slider tooling technology during FS-CRTM can be designed to automatically place and remove inserts during the molding process to manufacture FRP parts with undercuts. Chapter 2.1.4 showed that slider tooling is already today used in FRP manufacturing but the film-sealing eases the use of slider tooling by enabling a seal-free mold design (see Chapter 5.1) which eliminates downtime due to sealing wear and helps to lower the production cost of complex shaped FRP parts.

Furthermore, manufacturing limitations can be overcome by combining different molding technologies such as the manufacturing of thermoset FRP parts with thermoplastic injection molding. Many thermoset-thermoplastic material combinations are difficult to combine due to adhesion problems when the two materials are processed in two separate process steps. This limitation can be overcome by using a thermoplastic film, such as PEI or PES, as process aid material during FS-CRTM manufacturing. Besides its use as process aid material, the film interacts with the

curing thermoset resin to permanently adhere to it. [31] The FS-CRTM manufacturing process can then be extended with a subsequent thermoplastic injection molding step during which the injected material melt has no problems to adhere to the FRP part due to its outer thermoplastic film surface that is meltable and can be fused with the injected thermoplastic melt. This combination of manufacturing techniques enables to increase the geometrical freedom of the manufactured part by, e.g., molding complex-shaped thermoplastic structures, such as stiffeners, on a thermoset FRP part or by over-molding of a thermoset FRP stiffening structure with thermoplastic material.

Eventually, issues and limitations during the preform impregnation process, which can result from complex part geometries or flow disturbing phenomena such as race-tracking, can be controlled in real time during part manufacturing. Based on the FS-CRTM process, an active flow control strategy can be designed by a combination of flow monitoring sensors integrated in the film in combination with the slider tooling technology. The latter can be used to design the upper mold to consist of numerous small sliders which can be individually actuated depending on an online flow pattern recognition via the sensors in the film. The core concept of the actuating sliders is similar to the concept of the articulated resin transfer molding process by Choi and Dharan [77, 78]. The individual sliders can be controlled to change their position to either promote the flow front by enabling a local injection gap, or to hinder it by locally decreasing the preform's permeability. Stewart [74] patented such a tooling method by using a flexible membrane, fixed inside the mold, which separates the sliders from the raw materials. This flexible membrane is redundant during FS-CRTM processing due to the film encapsulation of the preform impregnation space. While the passive flow control strategy, studied in this work, provides a solution to statically manipulate the resin flow during FS-CRTM processing, the here suggested active flow control strategy provides a more flexible solution by tracking the flow pattern inside the mold in real time and manipulating the preform impregnation pattern only if needed, to ensure a complete preform impregnation and, therefore, maximize the process' robustness.

Bibliography

- [1] United Nations, “Paris agreement,” 2015. [Online]. Available: https://unfccc.int/sites/default/files/english_paris_agreement.pdf
- [2] European Commission, “The European Green Deal sets out how to make Europe the first climate-neutral continent by 2050, boosting the economy, improving people’s health and quality of life, caring for nature, and leaving no one behind,” Brussels, Belgium, 11 December 2019. [Online]. Available: https://ec.europa.eu/info/strategy/priorities-2019-2024/european-green-deal_de
- [3] —, “Transport and the Green Deal: Providing efficient, safe and environmentally friendly transport.” [Online]. Available: https://ec.europa.eu/info/strategy/priorities-2019-2024/european-green-deal/transport-and-green-deal_en
- [4] D. Brown, M. Flickenschild, C. Mazzi, A. Gasparotti, Z. Panagiotidou, J. Dingemans, and S. Bratzel, “The future of the EU automotive sector: Study requested by the ITRE committee,” 2021. [Online]. Available: [https://www.europarl.europa.eu/RegData/etudes/STUD/2021/695457/IPOL_STU\(2021\)695457_EN.pdf](https://www.europarl.europa.eu/RegData/etudes/STUD/2021/695457/IPOL_STU(2021)695457_EN.pdf)
- [5] N. Lutsey, “Review of technical literature and trends related to automobile mass-reduction technology.” [Online]. Available: <https://escholarship.org/uc/item/85p4x0jn>
- [6] W. Siebenpfeiffer, *Leichtbau-Technologien im Automobilbau: Werkstoffe - Fertigung - Konzepte*, ser. ATZ/MTZ-Fachbuch. Wiesbaden: Imprint: Springer Vieweg, 2014.
- [7] G. Deinzer, “Leichtbau – Anforderungen und Potenziale aus Sicht der Automobilindustrie,” Proceedings of the Hybridica, Munich, 09 November 2010.
- [8] J. Starke, “Carbon composites in automotive structural applications.” Proceedings of the EuCIA: Composites and Sustainability, Brussels, 19 March 2016.
- [9] G. Tecklenburg and M. Ahlers, “Carbon Core: die neue BMW 7er Karosserie,” Proceedings of the Karosseriebautage, Hamburg, 2016, doi: 10.1007/978-3-658-14144-8_9.
- [10] D. Roquette, F. Meyer, and L. Herbeck, “High volume manufacturing of carbon fiber reinforced plastics for body in white,” Proceedings of the Materialien des Karosseriebaus, Bad Nauheim, 16 May 2017. [Online]. Available: http://voith.com/composites-en/20170516_Bad-Nauheim_Audi_Voith_Online.pdf

- [11] O. Berger, “Voith unveils fully digital production line for Audi A8 carbon fiber rear wall panel at JEC World 2018 expo in Paris,” Garching, Paris, 13 March 2018. [Online]. Available: http://voith.com/corp-en/news-room/press-releases_100233.html
- [12] BMW Group, “The first ever BMW iX,” 02 June 2021. [Online]. Available: <https://www.press.bmwgroup.com/global/article/detail/T0333569EN/the-first-ever-bmw-ix?language=en>
- [13] H. Mason, “BMW rolls out multi-material Carbon Cage with 2022 iX vehicle line: For its new battery-electric iX sports activity vehicle, BMW combines CFRP strategies from previous i3, i8 and 7-Series designs and adds CFRTP for a lightweight, rigid frame.” 22 December 2021. [Online]. Available: <https://www.compositesworld.com/articles/bmw-rolls-out-multi-material-carbon-cage-with-2022-ix-vehicle-line>
- [14] S. G. Advani and E. M. Sozer, *Process modeling in composites manufacturing*. New York: Marcel Dekker, 2003, vol. 59.
- [15] S. G. Advani and K.-T. Hsiao, Eds., *Manufacturing techniques for polymer matrix composites (PMCs): Chapter 11: Compression resin transfer moulding (CRTM) in polymer matrix composites*, Woodhead Publishing Limited, 2012, vol. Kapitel 11.
- [16] G. Deinzer, M. H. Kothmann, D. Roquette, and F. Diebold, “Audi Ultra-RTM: A technology for high performance and cost effective CRFP parts for high volume production,” Proceedings of the 17th European Conference on Composite Materials (ECCM17), Munich, Germany, 26 - 30 June 2016.
- [17] C. Koch, *Eigenschaftsprofil von Carbonfasergelegen und deren Wirkzusammenhänge in der automobilen Großserienproduktion*, PhD Thesis. Technical University of Munich, Munich, Germany, 24 August 2020. [Online]. Available: <https://mediatum.ub.tum.de/1506859>
- [18] K. Han and L. J. Lee, “Dry spot formation and changes in liquid composite molding: I-experimental,” *Journal of Composite Materials*, vol. 30, no. 13, pp. 1458–1474, 1996.
- [19] A. Hammami, R. Gauvin, F. Trochu, O. Touret, and P. Ferland, “Analysis of the edge effect on flow patterns in liquid composites molding,” *Applied Composite Materials*, vol. 5, no. 3, pp. 161–173, 1998.
- [20] S. Bickerton and S. G. Advani, “Characterization and modeling of race-tracking in liquid composite molding processes,” *Composites Science and Technology*, vol. 59, no. 15, pp. 2215–2229, 1999.

- [21] F. A. Martin, N. A. Warrior, P. Simacek, S. Advani, A. Hughes, R. Darlington, and E. Senan, "Simulation and validation of injection-compression filling stage of liquid moulding with fast curing resins," *Applied Composite Materials*, 2018, doi: 10.1007/s10443-018-9682-4.
- [22] L. Aretxabaleta, C. Rytka, L. Walker, J. Maldonado, M. Baskaran, and J. Aurrekoetxea, "Analysis of the manufacturing process of a car bonnet using compression resin transfer moulding (CRTM)," *Materiales Compuestos*, no. 3, pp. 60–67, 2019. [Online]. Available: <https://revista.aemac.org/materiales-compuestos/article/view/426/195>
- [23] P. Rosenberg, *Entwicklung einer RTM Prozessvariante zur kavitätsdruck-geregelten Herstellung von Faserverbundstrukturbauteilen*. PhD Thesis. Karlsruhe Institute of Technology (KIT), Karlsruhe, 13 September 2018.
- [24] D. Häffelin, *Erweiterung des RTM-Prozesses (resin transfer molding) durch die Integration von Folien*, PhD Thesis. Technical University of Munich, Munich, Germany, 2017. [Online]. Available: <https://mediatum.ub.tum.de/1314295>
- [25] M. Vollmer and S. Zaremba, "Enhancing composite production by integrating thermoplastic films in closed mold LCM processes," Proceedings of the 1. RTM Anwenderforum (AVK), Augsburg, Germany, 25 - 26 June 2019.
- [26] M. Vollmer, S. Zaremba, P. Mertiny, and K. Drechsler, "Edge race-tracking during film-sealed compression resin transfer molding," *Journal of Composites Science*, vol. 5, no. 8, p. 195, 2021. [Online]. Available: <https://www.mdpi.com/2504-477X/5/8/195>
- [27] M. Neitzel and P. Mitschang, Eds., *Handbuch Verbundwerkstoffe: Werkstoffe, Verarbeitung, Anwendung*. München and Wien: Hanser, 2004.
- [28] S. G. Advani and P. Simacek, "Liquid composite molding: Role of modeling and simulation in process advancement: A benchmark exercise," Proceedings of the 20th International Conference on Composite Materials, Copenhagen, Denmark, 19 - 24 July 2015.
- [29] S. Konstantopoulos, C. Hueber, I. Antoniadis, J. Summerscales, and R. Schledjewski, "Liquid composite molding reproducibility in real-world production of fiber reinforced polymeric composites: a review of challenges and solutions," *Advanced Manufacturing: Polymer & Composites Science*, vol. 5, no. 3, pp. 85–99, 2019.
- [30] T. S. Mesogitis, A. A. Skordos, and A. C. Long, "Uncertainty in the manufacturing of fibrous thermosetting composites: A review," *Composites Part A: Applied Science and Manufacturing*, vol. 57, pp. 67–75, 2014.

- [31] P. Bruckbauer, *Struktur-Eigenschafts-Beziehungen von Interphasen zwischen Epoxidharz und thermoplastischen Funktionsschichten für Faserverbundwerkstoffe*, PhD Thesis. Technical University of Munich, Munich, Germany, 25 July 2018. [Online]. Available: <https://mediatum.ub.tum.de/1427427>
- [32] W. Michaeli and K. Fischer, “Investigations on manufacturing of high-performance composite parts by the gap-impregnation process,” *Journal of Plastic Technology*, 2008.
- [33] J. B. Alms, S. G. Advani, and J. L. Glancey, “Liquid composite molding control methodologies using vacuum induced preform relaxation,” *Composites Part A: Applied Science and Manufacturing*, vol. 42, no. 1, pp. 57–65, 2011.
- [34] K. Potter, *Resin Transfer Moulding*. London: Chapman & Hall, 1997.
- [35] W. A. Walbran, *Experimental validation of local and global force simulations for rigid tool liquid composite moulding processes*, PhD Thesis. Center for Advanced Composite Materials, University of Auckland, New Zealand, 2011.
- [36] P. Simacek, S. G. Advani, and S. A. Iobst, “Modeling flow in compression resin transfer molding for manufacturing of complex lightweight high-performance automotive parts,” *Journal of Composite Materials*, vol. 42, no. 23, pp. 2523–2545, 2008.
- [37] J. Merotte, P. Simacek, and S. G. Advani, “Flow analysis during compression of partially impregnated fiber preform under controlled force,” *Composites Science and Technology*, vol. 70, no. 5, pp. 725–733, 2010.
- [38] —, “Resin flow analysis with fiber preform deformation in through thickness direction during compression resin transfer molding,” *Composites Part A: Applied Science and Manufacturing*, vol. 41, no. 7, pp. 881–887, 2010.
- [39] S. Zaremba, *Bypassströmungen im Füllprozess textiler Strukturen: Charakterisierung, Abbildung und Optimierung*, PhD Thesis. Technical University of Munich, Munich, Germany, 04 October 2018. [Online]. Available: <https://mediatum.ub.tum.de/1443169>
- [40] C. D. Rudd and K. N. Kendall, “Towards a manufacturing technology for high-volume production of composite components,” *IMechE*, no. 206, pp. 77–91, 1992. [Online]. Available: https://journals.sagepub.com/doi/pdf/10.1243/PIME_PROC_1992_206_060_02
- [41] M. Ishii, P. Mitschang, and F. Weyrauch, “Verfahren zur Herstellung faserverstärkter Verbundwerkstoffen,” Patent EP000 001 685 947A1, 2006.
- [42] P. Rosenberg, B. Thoma, and F. Henning, “Characterization of epoxy and polyurethane resin systems for manufacturing of high-performance composites

- in high-pressure rtm process,” Proceedings of the 15th Annual SPE Automotive Composites Conference & Exposition (ACCE), Novi, MI, USA, 09 - 11 September 2015.
- [43] S. Brack, W. Dauner, and T. Zimmermann, “Verfahren zum Herstellen eines faserverstärkten Kunststoffbauteils und Preform für ein faserverstärktes Kunststoffbauteil,” Patent DE102 013 006 770 A1, 2014.
- [44] P. Kistner, D. Könnicke, F. Diebold, and D. Roquette, “Verfahren zur Herstellung eines Faserverbundkunststoff-Bauteils,” Patent DE 10 2014 009 408 A1, 2015.
- [45] M. Graf and T. Fürst, “Verfahren und Anlage zum Herstellen eines faserverstärkten Kunststoffbauteils,” Patent DE102 012 110 353A1, 2014.
- [46] M. Schindelbeck, “RTM-Verfahren und dichtungsloses Werkzeug zur Herstellung von faserverstärkten Kunststoffformteilen,” Patent DE102 011 077 468A1, 2012.
- [47] S. Zaremba and P. Steib, “Verfahren zur Herstellung eines Bauteils aus einem Faserverbundwerkstoff,” Patent WO002 015 007 353A2, 2015.
- [48] D. Guittard, D. Soro, and J. M. Poignonec, “Verfahren zur Herstellung eines Gegenstandes aus Verbundwerkstoff durch Transfer-Spritzgießen von Kunstharz (R.T.M.) und dadurch hergestellter Gegenstand,” Patent DE000 069 607 445T2, 2000.
- [49] W. R. Rodgers and A. R. Aitharaju, “Resin transfer molding systems and control logic for manufacturing fiber-reinforced composite parts,” Patent US 2020/0 238 637 A1, 2020.
- [50] D. Kaiser, “RTM-Verfahren mit Zwischenfaserschicht,” Patent DE102 014 118 670A1, 2016.
- [51] R. Kaps, “Verfahren zur Herstellung eines Faserverbundbauteils,” Patent DE102 009 053 549A1, 2011.
- [52] M. Bitterlich, M. Drechsel, and T. Niederstadt, “Verfahren und Vorrichtung zum Herstellen eines Faserverbundbauteils und Fahrzeug mit einem Faserverbundbauteil,” Patent DE102 011 112 141A1, 2013.
- [53] D. R. Nielsen and R. Pitchumani, “Control of flow in resin transfer molding with real-time preform permeability estimation,” *Polymer Composites*, vol. 23, no. 6, pp. 1087–1110, 2002.
- [54] D. H. Lee, W. I. Lee, and M. K. Kang, “Analysis and minimization of void formation during resin transfer molding process,” *Composites Science and*

- Technology*, vol. 66, no. 16, pp. 3281–3289, 2006.
- [55] M. K. Kang, J. J. Jung, and W. I. Lee, “Analysis of resin transfer moulding process with controlled multiple gates resin injection,” *Composites Part A: Applied Science and Manufacturing*, vol. 31, no. 5, pp. 407–422, 2000.
- [56] S. Bickerton, H. C. Stadtfeld, K. V. Steiner, and S. G. Advani, “Design and application of actively controlled injection schemes for resin-transfer molding,” *Composites Science and Technology*, vol. 61, no. 11, pp. 1625–1637, 2001.
- [57] J. M. Lawrence, K.-T. Hsiao, R. C. Don, P. Simacek, G. Estrada, E. Sozer, H. C. Stadtfeld, and S. G. Advani, “An approach to couple mold design and on-line control to manufacture complex composite parts by resin transfer molding,” *Composites Part A: Applied Science and Manufacturing*, vol. 33, no. 7, pp. 981–990, 2002.
- [58] K.-T. Hsiao and S. G. Advani, “Flow sensing and control strategies to address race-tracking disturbances in resin transfer molding. Part I: Design and algorithm development,” *Composites Part A: Applied Science and Manufacturing*, vol. 35, no. 10, pp. 1149–1159, 2004.
- [59] J. M. Lawrence, P. Fried, and S. G. Advani, “Automated manufacturing environment to address bulk permeability variations and race tracking in resin transfer molding by redirecting flow with auxiliary gates,” *Composites Part A: Applied Science and Manufacturing*, vol. 36, no. 8, pp. 1128–1141, 2005.
- [60] M. Arnold, L. A. Medina, and P. Mitschang, “Varietherme Prozesse zur Herstellung von Hochleistungsverbundwerkstoffen,” *Lightweight Design*, vol. 8, no. 5, pp. 58–61, 2015.
- [61] J. Nentwig, “Kunststoff-Folien: Herstellung, Eigenschaften, Anwendung,” München [u.a.], 2006.
- [62] M. Kaßmann, Ed., *Grundlagen der Verpackung: Leitfaden für die fächerübergreifende Verpackungsausbildung*, 1st ed., ser. Studium Verpackung. Berlin: Beuth, 2011. [Online]. Available: <http://www.beuth.de/cmd?level=tpl-langanzeige&webservice=vlb&smoid=127205942>
- [63] L. W. McKeen, *Permeability properties of plastics and elastomers*, 3rd ed., ser. PDL handbook series. Amsterdam and Heidelberg: Elsevier, 2012.
- [64] C. Williams, J. Summerscales, and S. Grove, “Resin infusion under flexible tooling (RIFT): A review,” *Composites Part A: Applied Science and Manufacturing*, vol. 27, no. 7, pp. 517–524, 1996.

- [65] Solvay, Alpharetta, GA, USA, “Product portfolio – composites; vacuum bag film.” [Online]. Available: <https://www.solvay.com/en/search?f%5B0%5D=fchemicalcat%3A12761&f%5B1%5D=fsection%3AProducts>
- [66] AIRTECH EUROPE Sarl, Differdange, Luxembourg, *Catalogue – Product Portfolio*, 17 September 2018. [Online]. Available: <https://catalogue.airtech.lu/index.php?lang=EN>
- [67] A. G. Becker, “FlexPLAS-Trennfolie – Trennmittelfreie FVK-Bauteilherstellung in komplexen Heizpressen-Werkzeugen,” 05 March 2018. [Online]. Available: <https://www.ifam.fraunhofer.de/de/Presse/Archiv/2018/FlexPLAS.html>
- [68] Infiana, Forchheim, Germany, “Data sheet: Flexplas fm tpe - film,” July 2017.
- [69] C. Poppe, F. Albrecht, C. Krauß, and L. Kärger, “A 3D modelling approach for fluid progression during process simulation of wet compression moulding – motivation & approach,” *Procedia Manufacturing*, vol. 47, pp. 85–92, 2020. [Online]. Available: <http://www.sciencedirect.com/science/article/pii/S2351978920311975>
- [70] P. Bockelmann, *Process control in compression molding of composites*, PhD Thesis. Technical University of Munich, Munich, Germany, 2017.
- [71] Richmond Aerovac, CA, USA, “Data sheet: STRECH-VAC 250.”
- [72] E. Ruiz and F. Trochu, “Manufacture of composites by a flexible injection process using a double or multiple cavity mold,” Patent US 7.866,969 B2, 25 June 2004.
- [73] C.-Y. Chang, “Experimental analysis of mold filling in vacuum assisted compression resin transfer molding,” *Journal of Reinforced Plastics and Composites*, vol. 31, no. 23, pp. 1630–1637, 2012.
- [74] D. H. Stewart, “Method and machine for manufacturing molded structures using zoned pressure molding,” Patent US2003/0227107A1, 2003.
- [75] Alpex Technologies, “HP-RTM tool with sliders.” [Online]. Available: <https://www.alpex-tec.com/das-machen-wir/>
- [76] —, “Company profile 2019 - tooling systems for composites,” 2019.
- [77] J. H. Choi and C. K. H. Dharan, “Enhancement of resin transfer molding using articulated tooling,” *Polymer Composites*, vol. 23, no. 4, pp. 674–681, 2002.
- [78] —, “Mold fill time and void reduction in resin transfer molding achieved by articulated tooling,” *Journal of Composite Materials*, vol. 36, no. 19, pp.

- 2267–2285, 2002.
- [79] G. Menges, W. Michaeli, and P. Mohren, “Spritzgießwerkzeuge: Auslegung, Bau, Anwendung; mit 63 Tabellen,” München, 2007.
- [80] R. Dangel, *Spritzgießwerkzeuge für Einsteiger, 2.A.* [S.l.]: Carl Hanser Verlag, 2017.
- [81] H. Tan and K. M. Pillai, “Numerical simulation of reactive flow in liquid composite molding using flux-corrected transport (FCT) based finite element/control volume (FE/CV) method,” *International Journal of Heat and Mass Transfer*, vol. 53, no. 9, pp. 2256–2271, 2010. [Online]. Available: <https://www.sciencedirect.com/science/article/pii/S0017931009006632>
- [82] J. Samir, J. Echaabi, and M. Hattabi, “Control volume finite element methods for flow in porous media: Resin transfer molding,” in *Finite Element Analysis - Applications in Mechanical Engineering*, F. Ebrahimi, Ed. InTech, 2012; doi: 10.5772/46167.
- [83] A. Boccard, W. I. Lee, and G. S. Springer, “Model for determining the vent locations and the fill time of resin transfer molds,” *Journal of Composite Materials*, vol. 29, no. 3, pp. 306–333, 1995.
- [84] A. Shojaei, S. R. Ghaffarian, and S. M. H. Karimian, “Modeling and simulation approaches in the resin transfer molding process: A review,” *Polymer Composites*, vol. 24, no. 4, pp. 525–544, 2003.
- [85] P. Boisse, Ed., *Advances in composites manufacturing and process design*, ser. Woodhead publishing series in composites science and engineering. Cambridge, UK: Woodhead Publishing, 2015, vol. number 56. [Online]. Available: <http://www.sciencedirect.com/science/book/9781782423072>
- [86] B. Verleye, S. V. Lomov, A. Long, I. Verpoest, and D. Roose, “Permeability prediction for the meso–macro coupling in the simulation of the impregnation stage of resin transfer moulding,” *Composites Part A: Applied Science and Manufacturing*, vol. 41, no. 1, pp. 29–35, 2010.
- [87] H. Tan and K. M. Pillai, “Fast liquid composite molding simulation of unsaturated flow in dual-scale fiber mats using the imbibition characteristics of a fabric-based unit cell,” *Polymer Composites*, vol. 31, no. 10, pp. 1790–1807, 2010.
- [88] M. V. Brusckke and S. G. Advani, “A finite element/control volume approach to mold filling in anisotropic porous media,” *Polymer Composites*, vol. 11, no. 6, pp. 398–405, 1990.

- [89] W.-B. Young and C.-L. Lai, "Analysis of the edge effect in resin transfer molding," *Composites Part A: Applied Science and Manufacturing*, vol. 28, no. 9, pp. 817–822, 1997.
- [90] K. Han, J. Ni, J. Toth, L. J. Lee, and J. P. Greene, "Analysis of an injection/compression liquid composite molding process," *Polymer Composites*, vol. 19, no. 4, pp. 487–496, 1998.
- [91] M. K. Kang and W. I. Lee, "A flow-front refinement technique for the numerical simulation of the resin-transfer molding process," *Composites Science and Technology*, vol. 59, no. 11, pp. 1663–1674, 1999. [Online]. Available: <https://www.sciencedirect.com/science/article/pii/S0266353899000299>
- [92] —, "Analysis of resin transfer/compression molding process," *Polymer Composites*, vol. 20, no. 2, pp. 293–304, 1999. [Online]. Available: <http://dx.doi.org/10.1002/pc.10356>
- [93] P. Simacek and S. G. Advani, "Simulating three-dimensional flow in compression resin transfer molding process," *Revue Europeenne des Elements*, vol. 14, no. 6-7, pp. 777–802, 2005.
- [94] A. Shojaei, "A numerical study of filling process through multilayer preforms in resin injection/compression molding," *Composites Science and Technology*, vol. 66, no. 11–12, pp. 1546–1557, 2006.
- [95] —, "Numerical simulation of three-dimensional flow and analysis of filling process in compression resin transfer moulding," *Composites Part A: Applied Science and Manufacturing*, vol. 37, no. 9, pp. 1434–1450, 2006.
- [96] E. Ruiz, V. Achim, S. Soukane, F. Trochu, and J. BREARD, "Optimization of injection flow rate to minimize micro/macro-voids formation in resin transfer molded composites," *Composites Science and Technology*, vol. 66, no. 3-4, pp. 475–486, 2006. [Online]. Available: <https://www.sciencedirect.com/science/article/pii/S026635380500223X>
- [97] B. Verleye, W. A. Walbran, S. Bickerton, and P. A. Kelly, "Simulation and experimental validation of force controlled compression resin transfer molding," *Journal of Composite Materials*, vol. 45, no. 7, pp. 815–829, 2011.
- [98] W. A. Walbran, B. Verleye, S. Bickerton, and P. A. Kelly, "Prediction and experimental verification of normal stress distributions on mould tools during liquid composite moulding," *Composites Part A: Applied Science and Manufacturing*, vol. 43, no. 1, pp. 138–149, 2012.

- [99] M. S. Kandelousi and D. D. Ganji, “Control volume finite element method (CVFEM),” in *Hydrothermal Analysis in Engineering Using Control Volume Finite Element Method*. Elsevier, 2015, pp. 1–12.
- [100] F. Nusser, *Simulative comparison study of filling behavior during RTM and CRTM process at occurring race tracking: Development of the study approach, data basis and evaluation method*, Masters’ Thesis, Technical University of Munich, Munich, Germany, 14 January 2019.
- [101] B. Liu, S. Bickerton, and S. G. Advani, “Modelling and simulation of resin transfer moulding (RTM) – gate control, venting and dry spot prediction,” *Composites Part A: Applied Science and Manufacturing*, vol. 27, no. 2, pp. 135–141, 1996.
- [102] F. R. Phelan, “Simulation of the injection process in resin transfer molding,” *Polymer Composites*, vol. 18, no. 4, pp. 460–476, 1997.
- [103] X.-T. Pham, F. Trochu, and R. Gauvin, “Simulation of compression resin transfer molding with displacement control,” *Journal of Reinforced Plastics and Composites*, vol. 17, no. 17, pp. 1525–1556, 1998.
- [104] S. Bickerton and M. Z. Abdullah, “Modeling and evaluation of the filling stage of injection/compression moulding,” *Composites Science and Technology*, vol. 63, no. 10, pp. 1359–1375, 2003.
- [105] J. Ni, Y. Zhao, L. J. Lee, and S. Nakamura, “Analysis of two-regional flow in liquid composite molding,” *Polymer Composites*, vol. 18, no. 2, pp. 254–269, 1997.
- [106] A. Bley, *Untersuchung von Strömungsvorgängen bei Bypassituationen für den FRT Prozess*, Bachelor’s Thesis, Technical University of Munich, Germany, 2016.
- [107] L. Fong and L. J. Lee, “Preforming analysis of thermoformable fiber mats – preforming effects on mold filling,” *Journal of Reinforced Plastics and Composites*, vol. 13, no. 7, pp. 637–663, 1994.
- [108] K. Han, L. J. Lee, and M. Liou, “Fiber mat deformation in liquid composite molding: II modeling,” *Polymer Composites*, vol. 14, no. 2, pp. 151–160, 1993.
- [109] A. Hammami, R. Gauvin, and F. Trochu, “Modeling the edge effect in liquid composites molding,” *Composites Part A: Applied Science and Manufacturing*, vol. 29, no. 5, pp. 603–609, 1998.
- [110] C.-Y. Chang, L.-W. Hourng, and T.-Y. Chou, “Effect of process variables on the quality of compression resin transfer molding,” *Journal of Reinforced Plastics and Composites*, vol. 25, no. 10, pp. 1027–1037, 2006.

- [111] C.-Y. Chang, “A numerical study of filling process in resin injection/compression molding,” *Journal of Reinforced Plastics and Composites*, vol. 27, no. 8, pp. 781–795, 2008.
- [112] P. Bhat, J. Merotte, P. Simacek, and S. G. Advani, “Process analysis of compression resin transfer molding,” *Composites Part A: Applied Science and Manufacturing*, vol. 40, no. 4, pp. 431–441, 2009.
- [113] M. Baskaran, I. Ortiz De Mendibil, M. Sarrionandia, J. Aurrekoetxea, J. Acosta, U. Argarate, and D. Chico, “Manufacturing cost comparison of RTM, HP-RTM and CRTM for an automotive roof,” Proceedings of the 16th European Conference on Composite Materials, Seville, Spain, 2014.
- [114] A. Dereims, S. Zhao, H. Yu, P. Pasupuleti, M. Doroudian, W. Rodgers, and V. Aitharuaju, “Compression resin transfer molding (C-RTM) simulation using a coupled fluid-solid approach,” Proceedings of the 32nd ASC Technical Conference 2017, Indiana, USA, 2017.
- [115] M. Baskaran, L. Aretxabaleta, M. Mateos, and J. Aurrekoetxea, “Simulation and experimental validation of the effect of material and processing parameters on the injection stage of compression resin transfer molding,” *Polymer Composites*, vol. 0, no. 0, 2017.
- [116] J. Yang, Y. Jia, Y. Ding, H. He, T. Shi, and L. An, “Edge effect in RTM processes under constant pressure injection conditions,” *Journal of Applied Polymer Science*, vol. 18, pp. n/a–n/a, 2010.
- [117] F. M. White, *Viscous fluid flow*, 3rd ed., ser. McGraw-Hill series in mechanical engineering. Boston: McGraw-Hill, 2006.
- [118] Z. Tadmor and C. G. Gogos, *Principles of polymer processing*, 2nd ed. Hoboken: Wiley, 2006. [Online]. Available: <http://www.loc.gov/catdir/enhancements/fy0653/2006009306-d.html>
- [119] J. Sheard, V. Senft, S. C. Mantell, J. H. Vogel, and R. S. Maier, “Determination of corner and edge permeability in resin transfer molding,” *Polymer Composites*, vol. 19, no. 1, pp. 96–105, 1998.
- [120] esi group, “Infusion process simulation for large and/or complex composites with PAM-RTM.” [Online]. Available: http://www.aysplm.com/documentos/productos/pdf/pam_rtm_ays.pdf
- [121] P. Marquette, A. Dereims, T. Ogawa, and M. Kobayashi, “Numerical methods for 3D compressive RTM simulations,” Proceedings of the 17th European Conference on Composite Materials (ECCM17), Munich, Germany, 26.06.2016.

- [122] H. Grössing, N. Stadlmajer, E. Fauster, M. Fleischmann, and R. Schledjewski, “Flow front advancement during composite processing: predictions from numerical filling simulation tools in comparison with real-world experiments,” *Polymer Composites*, vol. 37, no. 9, pp. 2782–2793, 2015.
- [123] A. Dereims, S. Drapier, J.-M. Bergheau, and P. de Luca, “Industrial validation of an original method for liquid resin infusion simulation,” Proceedings of the SAMPE Conference, Seattle, WA, USA, 2014.
- [124] A. Vita, V. Castorani, and M. Germani, “Manufacturing, process simulation and mechanical tests of a thick component produced by compression-RTM process,” Proceedings of the 18th European Conference on Composite Materials, Athens, Greece, 2018.
- [125] Y. Lin, J. Liu, and M. Yang, “Finite volume element methods: An overview on recent developments,” *International Journal of Numerical Analysis Modeling Series B*, vol. 1, pp. 14–34, 2013. [Online]. Available: https://global-sci.org/intro/article_detail/ijnamb/244.html
- [126] esi group, “esi – PAM-Composites 2018.0: Release notes & installation guide,” 2018. [Online]. Available: https://myesi.esi-group.com/system/files/documentation/Composites%20Simulation%20Solution%2C%20PAM-COMPOSITES/2018/PAM-COMPOSITES-2018.0_ReleaseNotes.pdf
- [127] K. Terzaghi, *Theoretical soil mechanics*. New York and London: John Wiley and Sons, inc., 1943.
- [128] esi group, “3D C-RTM simulation tutorial.”
- [129] W. A. Walbran, S. Bickerton, and P. A. Kelly, “Evaluating the shear component of reinforcement compaction stress during liquid composite moulding processes,” *Journal of Composite Materials*, vol. 47, no. 5, pp. 513–528, 2012.
- [130] M. Vollmer, H. Baumann, L. Graßl, S. Zaremba, D. Schultheiß, P. Mertiny, and K. Drechsler, “Compression resin transfer molding simulation for process optimization: A user case study,” Proceedings of the 29th SICOMP Conference - Manufacturing and Design of Composites, Luleå, Sweden, 28-29 May 2018.
- [131] esi group, “esi – PAM-Composites 2020.0: Release notes,” 2020. [Online]. Available: https://myesi.esi-group.com/system/files/documentation/PAM-COMPOSITES/2020.0/PAM-COMPOSITES_2020-0_ReleaseNotes.pdf

- [132] ———, “esi – PAM-Composites 2018.5: Release notes & installation guide,” 2018. [Online]. Available: <https://myesi.esi-group.com/downloads/software/pam-composites-2018.5>
- [133] ———, “esi – PAM-Composites 2019.5: Release notes,” 2019. [Online]. Available: https://myesi.esi-group.com/system/files/documentation/PAM-COMPOSITES/2019.5/PAM-COMPOSITES_2019-5_ReleaseNotes.pdf
- [134] ———, “esi – PAM-Composites 2020.5: Release notes,” 2020. [Online]. Available: https://myesi.esi-group.com/system/files/documentation/PAM-COMPOSITES/2020.5/PAM-COMPOSITES_2020-5_ReleaseNotes.pdf
- [135] N. Ikegawa, H. Hamada, and Z. Maekawa, “Effect of compression process on void behavior in structural resin transfer molding,” *Polymer Engineering & Science*, vol. 36, no. 7, pp. 953–962, 1996.
- [136] C.-Y. Chang, L.-W. Hourng, and C.-S. Yu, “Analysis of flow phenomena during the filling stage of CTM,” *Journal of Reinforced Plastics and Composites*, vol. 23, no. 14, pp. 1561–1570, 2004.
- [137] S. Hsu, M. Ehrgott, and P. A. Kelly, “Optimisation of mould filling parameters of the compression resin transfer moulding process,” Proceedings of the 45th Annual Conference of the ORSNZ, Auckland, New Zealand, 29-30 November 2010.
- [138] M. Baskaran, *Optimización del proceso de Compression Resin Transfer Moulding (CRTM) mediante técnicas experimentales y simulación: Optimization of the compression resin transfer molding (CRTM) process through experimental techniques and simulation*, PhD Thesis. Mondragon University, Mondragon, Spain, 2017. [Online]. Available: <http://ebiltegia.mondragon.edu/xmlui/handle/20.500.11984/1204>
- [139] B. Yang, S. WANG, and Q. TANG, “Modeling and 3D simulation of the mould compression and resin flow for force-controlled compression resin transfer moulding,” *Materials Science*, vol. 25, no. 1, 2019.
- [140] M. Vollmer, F. Nusser, D. Bublitz, H. Baumann, L. Graßl, F. Masseria, S. Zaremba, P. Mertiny, and K. Drechsler, “Increasing process robustness of the compression resin transfer molding process towards edge race-tracking,” Proceedings of the SAMPE Europe Conference 2021, Baden, Switzerland, 28 - 30 September 2021; ISBN/EAN: 978-90-829101-3-1.
- [141] G. Gardiner, “Compression RTM for production of future aerostructures: Automated preforming and 5-min resin infiltration show a

- way forward for lower-cost CFRP primary structures.” 31 March 2020. [Online]. Available: <https://www.compositesworld.com/articles/compression-rtm-for-production-of-future-aerostructures>
- [142] Huntsmann Advanced Materials, “Data sheet: Araldite ly 3585 / aradur 3475: Warm curing epoxy system,” 2015.
- [143] SGL Group, Wiesbaden, Germany, “ata sheet: SIGRATEX C B310-45/ST-E214/5g - stitched, biaxial, carbon fiber fabric with powder binder,” June 2017.
- [144] D. Bublitz, M. Vollmer, and F. Nusser, “A novel method for the evaluation of compression RTM process simulations,” Proceedings of the ESI Forum 2019, Berlin, Germany, 07 November 2019.
- [145] C. D. Rudd, *Liquid moulding technologies: Resin transfer moulding, structural reaction injection moulding and related processing techniques*. Warrendale, PA.: Society of Automotive Engineers, 1997.
- [146] Z. Hua, J. Yang, S. Coulibaly, and B. Zhang, “Integration TRIZ with problem-solving tools: A literature review from 1995 to 2006,” *International Journal of Business Innovation and Research*, vol. 1, no. 1/2, p. 111, 2006.
- [147] U. Lindemann and P. Schrieverhoff, “Innovationsmethodik - TRIZ Basiswissen (Lecture Notes),” Technical University of Munich, 2019.
- [148] K. Gadd, *TRIZ for engineers: Enabling inventive problem solving*. Chichester, West Sussex, U.K and Hoboken, N.J: Wiley, 2011.
- [149] M. A. Orloff, *ABC-TRIZ: Introduction to creative design thinking with modern TRIZ modeling*. Cham: Springer, 2017.
- [150] T. S. Lundstrom, B. R. Gebart, and C. Y. Lundemo, “Void formation in RTM,” *Journal of Reinforced Plastics and Composites*, vol. 12, no. 12, pp. 1339–1349, 1993.
- [151] T. S. Lundström and B. R. Gebart, “Influence from process parameters on void formation in resin transfer molding,” *Polymer Composites*, vol. 15, no. 1, pp. 25–33, 1994.
- [152] P. Rosenberg, B. Thoma, and F. Henning, “Investigation and validation of a new cavity pressure controlled HP-RTM process variant (PC-RTM),” Proceedings of the 16th Annual SPE Automotive Composites Conference & Exposition (ACCE), Novi, MI, USA, 07 - 09 September 2016.
- [153] A. Hemmen, *Direktbestromung von Kohlenstofffasern zur Minimierung von Zykluszeit und Energieaufwand bei der Herstellung von Karbonbauteilen*, PhD

- Thesis. University of Augsburg, Germany, 2016.
- [154] M. Vollmer, D. König, I. Gilch, H. Waller-Ehrat, S. Zaremba, C. Hübner, P. Mertiny, and K. Drechsler, “Identification of a film to seal the preform impregnation during the compression resin transfer molding process,” Proceedings of the SAMPE Europe Conference 2021, Baden, Switzerland, 28 - 30 September 2021; ISBN/EAN: 978-90-829101-3-1.
- [155] G. W. Ehrenstein, G. Riedel, and P. Trawiel, *Praxis der thermischen Analyse von Kunststoffen*, 2nd ed. München: Hanser, 2003.
- [156] A. Frick and C. Stern, *DSC-Prüfung in der Anwendung*, 2nd ed. München: Hanser, 2013.
- [157] DIN EN ISO 11357-1, “Kunststoffe – Dynamische Differenz-Thermoanalyse (DSC),” February 2017.
- [158] H. Domininghaus and P. Eyerer, *Die Kunststoffe und ihre Eigenschaften*, 6th ed. Berlin: Springer, 2005.
- [159] G. W. Ehrenstein, *Polymer-Werkstoffe: Struktur - Eigenschaften - Anwendung*, 3rd ed. München: Hanser, 2011.
- [160] W. Grellmann, S. Seidler, and V. Altstädt, *Polymer testing*. München: Hanser, 2007.
- [161] DIN EN ISO 6721-1, “Kunststoffe – Bestimmung dynamisch-mechanischer Eigenschaften,” August 2011.
- [162] Cytec, Woodland Park, NJ, USA, “Data sheet: SM5142, sealant tape.”
- [163] C. Buchmann, S. Langer, J. Filsinger, and K. Drechsler, “Analysis of the removal of peel ply from CFRP surfaces,” *Composites Part B: Engineering*, vol. 89, pp. 352–361, 2016.
- [164] DIN EN 1939, “Klebebänder: Bestimmung der Klebkraft,” December 2003.
- [165] D. Häffelin, *Folienintegrierter RTM-Prozess (resin transfer molding) für endlosfaserverstärkte Schalenbauteile (Film-RTM)*, ser. Fortschritt-Berichte VDI. Reihe 5, Grund- und Werkstoffe/Kunststoffe. Düsseldorf: VDI Verlag, 2014, vol. Nr. 754.
- [166] ASTM F1929-12, “Standard test method for detecting seal leaks in porous medical packaging by dye penetration,” 2012.
- [167] DIN 53441, “Spannungsrelaxationsversuch,” Berlin, January 1984.
- [168] H. J. Fahrenwaldt, V. Schuler, H. Wittel, and J. Twdrek, *Praxiswissen Schweißtechnik: Werkstoffe, Prozesse, Fertigung ; mit 141 Tabellen*,

- 2nd ed., ser. Vieweg Praxiswissen. Wiesbaden: Vieweg, 2006. [Online]. Available: http://deposit.d-nb.de/cgi-bin/dokserv?id=2865947&prov=M&dok_var=1&dok_ext=htm
- [169] G. Bleisch, J.-P. Majschak, and U. Weiß, *Verpackungstechnische Prozesse*. Rehr's Verlag, 2011.
- [170] H. Domininghaus, P. Elsner, P. Eyerer, and T. Hirth, *Kunststoffe: Eigenschaften und Anwendungen*, 8th ed., ser. VDI-Buch. Heidelberg u.a: Springer, 2012.
- [171] Hexion Inc., Columbus, OH, USA, "Data Sheet: EPIKOTE™ Resin TRAC 06170; EPIKURE™ Curing Agent TRAC 06170; HELOXY™ Additive TRAC 06805," 2015.
- [172] —, "Data Sheet: EPIKOTE Resin 06000, EPIKURE Curing Agent 06130, HELOXY™ Additive TRAC 06805," 2015.
- [173] B. Carlowitz, *Kunststoff-Tabellen*, 3rd ed. München: Hanser, 1986.
- [174] A. Fukada, K. Kohama, T. Abe, and H. Okamoto, "A vacuum and/or pressure forming system using a prepreg sheet of FRP with a gel coat layer," *Journal of Reinforced Plastics and Composites*, vol. 14, no. 2, pp. 100–112, 1995.
- [175] Infiana Group, "Composites presentation," October 2016.
- [176] Du Pont, Buffalo, NY, USA, "Data sheet: Tedlar PVF film, technical information."
- [177] M. Bonnet, *Kunststoffe in der Ingenieur Anwendung: Verstehen und zuverlässig auswählen*, 1st ed., ser. Studium. Wiesbaden: Vieweg + Teubner, 2009.
- [178] P. Bruckbauer, *MAIfo - Entwicklung einer Prozesskette zur Herstellung von teilfolierten Faserverbundbauteilen: Abschlussbericht : Berichtszeitraum: 01.05.2013-30.04.2016*. Chair of Carbon Composites, Technical University of Munich, 2015.
- [179] G. Habenicht, *Kleben: Grundlagen, Technologien, Anwendungen ; mit 37 Tabellen*, 5th ed., ser. VDI-Buch. Berlin, Heidelberg: Springer-Verlag Berlin Heidelberg, 2006. [Online]. Available: <http://gbv.ebib.com/patron/FullRecord.aspx?p=323891>
- [180] W. Kaiser, *Kunststoffchemie für Ingenieure: Von der Synthese bis zur Anwendung*, 3rd ed. München: Hanser, 2011.
- [181] Cytec, "Product portfolio for process materials aerospace and industrial markets." [Online]. Available: <https://www.cytec.com/sites/default/files/>

- files/IM-7001-EN-Process_materials_Aformat_022514_sngl.pdf
- [182] W. Kaiser, *Kunststoffchemie für Ingenieure*. München: Carl Hanser Verlag GmbH & Co. KG, 2016.
- [183] D. König, *Bewertung thermoplastischer Folien hinsichtlich ihrer Eignung zur Integration in den RTM-Prozess duroplastischer CFK-Bauteile*, Term Thesis, Technical University of Munich, Munich, Germany, 30 October 2017.
- [184] A. Prenninger, *Process optimisation and investigation of the film behaviour during the injection phase of a film-sealed CRTM process*, Masters' Thesis, Technical University of Munich, Munich, Germany, 29 July 2019.
- [185] P. Laubichler, *Flow experiments of the film-sealed CRTM process*, Masters' Thesis, Technical University of Munich, Munich, Germany, 23 December 2019.
- [186] M. Vollmer, A. Prenninger, P. Laubichler, S. Zaremba, and K. Drechsler, "Effect of vent pressure variation during film sealed compression resin transfer molding (FS-CRTM)," Proceedings of the 5th International Composites Conference (ICC), Stuttgart, Germany, 10 - 12 September 2019.
- [187] DIN EN ISO 527-3, "Bestimmung der Zugeigenschaften: Teil 3: Prüfbedingungen für Folien und Tafeln," July 2003.
- [188] S. V. Lomov, *Non-crimp fabric composites: Manufacturing, properties and applications*, ser. Woodhead Publishing in materials. Oxford and Philadelphia: Woodhead Pub, 2011.
- [189] F. Dirschmid, "Die CFK-Karosserie des BMW i8 und deren Auslegung," in *Karosseriebautage Hamburg: 13. ATZ-Fachtagung*, G. Tecklenburg, Ed. Wiesbaden: Springer Fachmedien Wiesbaden, 2014, pp. 217–231.
- [190] M. Richardson and Z. Zhang, "Experimental investigation and flow visualisation of the resin transfer mould filling process for non-woven hemp reinforced phenolic composites," *Composites Part A: Applied Science and Manufacturing*, vol. 31, no. 12, pp. 1303–1310, 2000. [Online]. Available: <http://www.sciencedirect.com/science/article/pii/S1359835X00000087>
- [191] K. Siebertz, D. van Bebber, and T. Hochkirchen, *Statistische Versuchsplanung: Design of Experiments (DoE)*, 2nd ed., ser. VDI-Buch. Berlin, Germany: Springer Vieweg, 2017.
- [192] Sartorius Stedim Data Analytics, "User guide to MODDE: Version 12," 2017. [Online]. Available: <https://blog.umetrics.com/hubfs/Download%20Files/MODDE%2012.0.1%20User%20Guide.pdf>

- [193] D. Becker, *Transversales Imprägnierverhalten textiler Verstärkungsstrukturen für Faser-Kunststoff-Verbunde: PhD Thesis*, als manuskript gedruckt ed., PhD Thesis. Technische Universität Kaiserslautern, Kaiserslautern, Germany, 2015.
- [194] R. Chaudhari, *Characterization of high-pressure resin transfer molding process variants for manufacturing high-performance composites*. PhD Thesis. Karlsruhe Institute of Technology (KIT), Karlsruhe, Germany: Fraunhofer Verlag, 2014.
- [195] M. Vollmer, “SKR-FVK – increasing cost efficiency and robustness in the automated production of fiber-reinforced plastic parts: Characterization and validation of a novel CRTM process variant at which the preform is encapsulated by thermoplastic films to reduce process cycle time and equipment investment costs.” 2019. [Online]. Available: <https://www.asg.ed.tum.de/en/lcc/public-projects/processing-technologies/>
- [196] —, *SKR-FVK – increasing cost efficiency and robustness in the automated production of fiber reinforced plastic parts (ZIM-project): Final project report*, Chair of Carbon Composites, Technical University of Munich, January 2022.
- [197] C. Weimer, N. Bätge, P. Parlevliet, H. Luinge, and G. Wachinger, “Manufacturing process for composite material part comprising a functional finishing layer,” Patent, EP2345528A2, 2011.
- [198] R. Yadav, M. Tirumali, X. Wang, M. Naebe, and B. Kandasubramanian, “Polymer composite for antistatic application in aerospace,” *Defence Technology*, vol. 16, no. 1, pp. 107–118, 2020.
- [199] R. McCarthy, G. H. Haines, and R. A. Newley, “Polymer composite applications to aerospace equipment,” *Composites Manufacturing*, vol. 5, no. 2, pp. 83–93, 1994.
- [200] C. Schludi and J. Joos, “Lightweight and safe composite battery housings,” *Lightweight Design worldwide*, vol. 12, no. 6, pp. 44–47, 2019.
- [201] M. Vollmer, N. Tagscherer, S. Zaremba, D. Schultheiß, P. Mertiny, and K. Drechsler, “Material characterization for compression resin transfer molding process simulation,” Proceedings of the 18th European Conference on Composite Materials (ECCM18), Athens, Greece, 24 - 28 June 2018.
- [202] R. Meier, *Scherverdünnende Epoxidharzsysteme und vibrationsunterstützte Harzfiltrationsprozesse*, PhD Thesis. Technical University of Munich, Munich, Germany, 2017.

- [203] S. Bickerton, M. J. Buntain, and A. A. Somashekar, “The viscoelastic compression behavior of liquid composite molding preforms,” *Composites Part A: Applied Science and Manufacturing*, vol. 34, no. 5, pp. 431–444, 2003.
- [204] Huntsman Advanced Materials (Switzerland) GmbH, “A new step forward in composites mass production,” 2015. [Online]. Available: <https://www.compositesworld.com/cdn/cms/highlighta-new-step-forward-in-composites-mass-production-150310171900-conversion-gate01.pdf>
- [205] Huntsman, The Woodlands, Texas, United States, “Data Sheet: Araldite LY 3585 / Aradur 3475: Warm curing epoxy system,” vol. 10 April 2015.
- [206] T. Mezger, *Das Rheologie-Handbuch: Für Anwender von Rotations- und Oszillations-Rheometern*, 4th ed. Hannover: Vincentz Network, 2012.
- [207] R. Meier, A. Walbran, H. Christoph, S. Zaremba, and K. Drechsler, “Methods to determine the permeability of textile reinforcements,” *Journal of Plastic Technology*, 2014.
- [208] R. Arbter, J. M. Beraud, C. Binetruy, L. Bizet, J. Bréard, S. Comas-Cardona, C. Demaria, A. Endruweit, P. Ermanni, F. Gommer, S. Hasanovic, P. Henrat, F. Klunker, B. Laine, S. Lavanchy, S. V. Lomov, A. Long, V. Michaud, G. Morren, E. Ruiz, H. Sol, F. Trochu, B. Verleye, M. Wietgreffe, W. Wu, and G. Ziegmann, “Experimental determination of the permeability of textiles: A benchmark exercise,” *Composites Part A: Applied Science and Manufacturing*, vol. 42, no. 9, pp. 1157–1168, 2011.
- [209] N. Vernet, E. Ruiz, S. Advani, J. B. Alms, M. Aubert, M. Barburski, B. Barari, J. M. Beraud, D. C. Berg, N. Correia, M. Danzi, T. Delavière, M. Dickert, C. Di Fratta, A. Endruweit, P. Ermanni, G. Francucci, J. A. Garcia, A. George, C. Hahn, F. Klunker, S. V. Lomov, A. Long, B. Louis, J. Maldonado, R. Meier, V. Michaud, H. Perrin, K. Pillai, E. Rodriguez, F. Trochu, S. Verheyden, M. Wietgreffe, W. Xiong, S. Zaremba, and G. Ziegmann, “Experimental determination of the permeability of engineering textiles: Benchmark II,” *Composites Part A: Applied Science and Manufacturing*, vol. 61, pp. 172–184, 2014.
- [210] A. Aktas, G. Sims, C. Lira, and M. Stojkovic, “Survey of procedures in use for permeability measurements in liquid composite moulding processes,” May 2016. [Online]. Available: <http://www.npl.co.uk/content/ConPublication/7094>
- [211] S. Scholz, J. W. Gillespie, and D. Heider, “Measurement of transverse permeability using gaseous and liquid flow,” *Composites Part A: Applied Science*

- and Manufacturing*, vol. 38, no. 9, pp. 2034–2040, 2007.
- [212] M. Dickert, D. Berg, and G. Ziegmann, “Influence of binder activation and fabric design on the permeability of non-crimp carbon fabrics,” Proceedings of the 11th International Conference on Flow Processes in Composite Materials (FPCM11), Auckland, New Zealand, 9.-12.07.2011.
- [213] T. G. P. Gutowski, *Advanced composites manufacturing*. New York: Wiley, 1997.
- [214] Richmond Aerovac, CA, USA, “Data sheet: Raphold 1, high temperature double backed tape,” August 2010.
- [215] M. Schreiber, *Auslegung und Konstruktion eines Teststandes zur Untersuchung eines Folierungsprozesses von Preforms für den RTM-Prozess*, Term Thesis, Technical University of Munich, Munich, Germany, 29 March 2018.
- [216] Richmond Aerovac, CA, USA, “Data sheet: LTS90B/G, sealant tape,” August 2010.
- [217] Solvay, Alpharetta, GA, USA, “Data sheet: Flashtape1, adhesive tape,” August 2019.
- [218] J. Kil, *Entwicklung einer Testvorrichtung zur Prozessdatenaufzeichnung und Visualisierung des Harzflusses eines neuartigen LCM-Prozesses*, Masters’ Thesis, Technical University of Munich, Munich, Germany, 30 October 2017.
- [219] R. Ernhofer, *Programming a test rig for optical analysis of the RTM-injection-process for CFRP-manufacturing*, Masters’ Thesis, Technical University of Munich, Munich, Germany, 30 April 2018.
- [220] H. Baumann, *Implementation of a novel test rig for the optical analysis of the RTM-injection process for CFRP manufacturing*, Masters’ Thesis, Technical University of Munich, Munich, Germany, 15 November 2018.
- [221] L. Li, Y. Zhao, J. Yang, J. Zhang, and Y. Duan, “An experimental investigation of compaction behavior of carbon non-crimp fabrics for liquid composite molding,” *Journal of Materials Science*, vol. 50, no. 7, pp. 2960–2972, 2015.

A Appendix

A.1 Material Characterization¹

The resin flow in FRP manufacturing has generally been modeled obeying Darcy's law (Equation 2-1), which describes fluid flow through a porous medium. The flow of the fluid is hereby described by its volume averaged velocity vector \vec{v} , the permeability tensor \mathbf{K} of the porous medium, the driving pressure gradient ∇p , and the viscosity η of the fluid. While pressure is a process variable, viscosity and permeability are characteristics of the constituent materials and need to be thoroughly characterized prior to any simulation. [14]

Resin systems used in fiber-reinforced plastic (FRP) manufacturing commonly exhibit a non-Newtonian behavior. A higher process temperature generally lowers resin viscosity. Simultaneously, the resin curing increases viscosity over time. [202] As per Darcy's law (Equation 2-1), a low resin viscosity at elevated temperature is desired to minimize preform fill times. However, good knowledge of the temperature specific cure kinetics is essential to prevent a premature viscosity increase, risking incomplete preform filling [14]. Therefore, a characterization of the resin viscous behavior over time at process temperatures is essential to generate required input data for compression resin transfer molding (CRTM) simulation [130].

A non-reactive matrix material was used to reduce the complexity of permeability measurements and film-sealed compression resin transfer molding (FS-CRTM) flow visualization experiments presented in this work. Based on Darcy's law (Equation 2-1) the flow inside a porous medium is dependent on the viscosity of the fluid. Thus, the knowledge of the viscosity during an experiment is essential to characterize the fabric's permeability. Furthermore, a precise knowledge of the fluid's viscosity is of importance to adequately compare the flow characteristics observed in different flow visualization experiments.

Applying Darcy's law (Equation 2-1) in composite manufacturing simulation, a good understanding of the permeability of the reinforcement is required. During some FRP manufacturing processes, i.e. resin transfer molding (RTM), the preform impregnation of thin structures is dominated by in-plane resin flow at a constant mold thickness. Therefore, the permeability characterization for these processes can be narrowed down to in-plane permeability tests at one desired fiber volume fraction (FVF). Conversely, the preform impregnation at CRTM takes place during its injection and during its compaction phase. In the latter, the preform is

¹ Parts of the introduction have been previously published in [201].

compressed whereby its permeability is continuously changed. Additionally, a significant part of the preform impregnation during the compaction phase occurs by in-plane and through-thickness resin flow [15, 203]. These process specifics require an extensive reinforcement characterization, specifically, its in-plane and out-of-plane permeabilities over a wide range of FVFs, as input for CRTM simulation [15, 130].

In this work, the effect of edge race-tracking during CRTM is studied. Darcy's law (Equation 2-1) describes the flow through a homogeneous porous medium. Software packages, such as the used PAM-RTM of ESI Group, model the flow inside a cavity via Darcy's law. To be able to model a flow through a non-porous media, such as an edge race-tracking channel, the equivalent permeability approach (see Chapter 2.2.3) has to be applied. A variety of different equations are available in literature for the equivalent permeability of an edge race-tracking channel, providing the need to select a suitable equation and validate it.

In addition, the compaction behavior of the reinforcement is needed to model the CRTM process. During the CRTM compaction phase, the total loading acting on the mold σ_{tot} is, according to the one-dimensional laminate consolidation approach of Terzaghi (Equation 2-15), balanced by the fluid (resin) pressure p_f and the stress needed to compact the preform σ_p . [15, 127] To accurately predict mold forces and to model the resin flow resulting from the continuous change in permeability, the reinforcement's resistance to compaction σ_p has to be determined as input for CRTM simulation [130, 203].

The, in the previous paragraphs presented, material parameters are characterized throughout the following sections of this appendix chapter.

A.1.1 Matrix Material

Reactive Matrix Material – Resin²

Viscosity is defined as the resistance of a fluid against deformation or flow [14]. Therefore, a good knowledge about the resin's viscosity behavior is needed to accurately model the resin flow during the CRTM process. According to Advani and Sozer [14], the viscosity of most thermoset resins is a function of pressure, temperature, degree of cure and shear rate. In the following, a thermoset resin system is characterized by its isothermal viscosity development over time at constant shear rate.

² This subsection has been previously published in [201].

Experimental procedure: Viscosity measurements were performed on the Modular Compact Rheometer (MCR) 302 (Anton Paar, Graz, Austria). Isothermal rotatory measurements were performed at three process-relevant temperature levels: 80 °C, 100 °C and 120 °C. A cone-plate measurement setup (CP25-1) was used with radius $R_{CP} = 12.5$ mm and cone angle of $\alpha_{CP} = 1^\circ$ according to DIN 53019. A gap of 50 μm beneath the cone was calibrated for each temperature level. Based on preliminary tests, the shear rate for all measurements was set to $\dot{\gamma} = 100$ s^{-1} . Tests for each temperature level were repeated in triplicate for statistical relevance.

Material and sample preparation: An epoxy resin system from Huntsman (The Woodlands, Texas, United States) was chosen for the present study, typical for automotive applications [204]. The epoxy resin, Araldite[®] LY 3585, and the amine hardener, Aradur[®] 3475, were processed as per the manufacturer's data sheet [205]. The individual components were degassed, weighed and manually stirred at room temperature for approximately 45 s. The time measurement for the viscosity tests was initiated as soon as the evenly mixed resin system was dispensed onto the heated sample carrier of the rheometer. At the same time, the automatic closing of the rheometer was started, leading to a temporal offset between the start of the experiment and the first recorded data point.

Results and discussion: The diagram of Figure A-1(a) displays the measured viscosity (η) versus time (t) for the investigated epoxy system up to $\eta = 0.7$ Pas. The three displayed viscosity curves exhibit common characteristics in terms of initial viscosity at a low level, followed by an exponential rise in viscosity. Having the shear rate fixed for all measurements, the results show a clear temperature dependency of the viscosity, indicated by an earlier viscosity rise for tests at higher temperatures. The diagram of Figure A-1(b) depicts data points up to $\eta = 0.05$ Pas. Even though the first 30 s to 40 s of the measurements could not be recorded, the level of the initial viscosity at the first recorded data points is shown to be below 0.01 Pas for all three temperature levels.

The presented results indicate a strong dependency of viscosity behavior on the temperature. A higher temperature generally promotes curing of the resin system, leading to fast cross-linking of the prepolymer [14]. The process times of the CRTM simulations presented in Chapter 4 are all below 10 s, the time span at which the applied test method provided no measured viscosity values. Nevertheless, during this short time span after mixing, a low conversion degree is expected with a viscosity of below 0.01 Pas as observed in Figure A-1(b) independent of the investigated temperatures. Therefore, the CRTM simulations in Chapter 4, which are all below a process time of 30 seconds, are simulated with a conservative assumption of a constant resin viscosity of 0.01 Pas. Literature studies [21, 115], using similar resin systems for numerical flow simulations, support the choice of stated viscosity value.

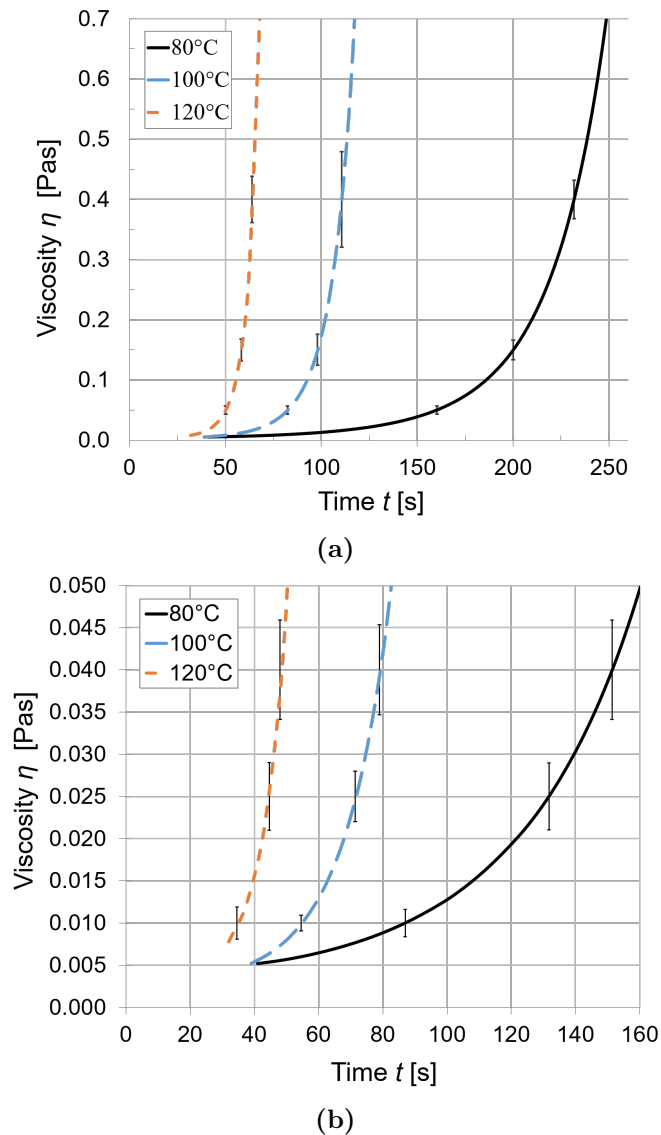


Fig. A-1 Isothermal viscosity measurements over time of three temperatures - epoxy resin system: Araldite[®] LY 3585 and Aradur[®] 3475 (mean of tests performed in triplicate; standard deviations shown as error bars). [201]

Overall, the reproducibility of the performed measurements was good, ensured by a strict and consistent measurement procedure, performed by the same operator. However, significant differences were identified comparing the measured viscosity values to the data provided by the manufacturer [205]. For the latter, the viscosity rises approximately 30% earlier in time for all measured temperature levels. These discrepancies can be explained by different mixing procedures, a different definition of the measurement start, and a different testing method or testing parameters, i.e. shear rate [206].

Non-Reactive Matrix Material – Sunflower Oil

A non-reactive matrix material, as substitutive fluid for reactive resin systems, was used during the permeability measurements [207] and the FS-CRTM flow visualization experiments presented in this work. This subsection presents the test method and material of the viscosity measurements of the non-reactive matrix material. Furthermore, general results are presented while specific viscosity values are given in the individual chapters of this work, at which the specific experiments are discussed.

Experimental procedure: As for the viscosity measurements of the reactive matrix material, the measurements of the non-reactive matrix material were performed on the Modular Compact Rheometer (MCR) 302 of Anton Paar. Two measurement procedures were performed for each fluid batch. First, the fluid was investigated in regards to its shear rate dependency with the goal to identify a shear rate at which Newtonian behavior is applicable. The viscosity was measured in a logarithmic ramp over a shear rate of 1 s^{-1} to 1000 s^{-1} at a constant temperature of $25 \text{ }^\circ\text{C}$. Secondly, the temperature dependent viscosity of the fluid was investigated via a temperature sweep of $\pm 5 \text{ }^\circ\text{C}$ around the average temperature of all experiments performed with the specific batch of fluid. Based on the recorded viscosity range of the temperature sweep, the viscosity of the experiment was identified by the recorded oil temperature of the specific experiment. All measurements of the non-reactive matrix material were performed with a cone plate measurement setup (CP25-1) with a radius $R_{CP} = 12.5 \text{ mm}$ and cone angle of $\alpha_{CP} = 1^\circ$ according to DIN 53019.

Material: According to the existing permeability measurement procedures of the Chair of Carbon Composites, Technical University of Munich, [207] sunflower oil manufactured by Vita D’Or was used as non-reactive matrix material for all presented permeability measurements. Additionally, this fluid was used for all FS-CRTM flow experiments presented in this work.

Results and discussion: The shear rate sweep of the sunflower oil showed a shear-rate independent Newtonian behavior at a shear rate of 100 s^{-1} at all performed measurements. Therefore, a constant shear rate of 100 s^{-1} was pre-set for all measurements of the temperature dependent viscosity of the sunflower oil. The exact values of the oil viscosity measurements of each experiment are presented in the corresponding chapters at which the experiment is discussed in detail.

A.1.2 Reinforcement Material

Permeability of Reinforcement Structure³

Generally, the permeability of a porous material is defined as the inverse of the quantity describing the medium's resistance to fluid flow. The general second order permeability tensor \mathbf{K} can be diagonalized, consisting of two principal in-plane permeabilities K_{11} and K_{22} and of one principal out-of-plane (or through-thickness) permeability K_{33} , as illustrated in Figure A-2(a). The principal in-plane permeabilities can be graphically described by an ellipsis as shown in Figure A-2(b), commonly defining K_{11} as of largest magnitude and rotated by the angle β relative to the coordinate system of the reinforcement. [14]

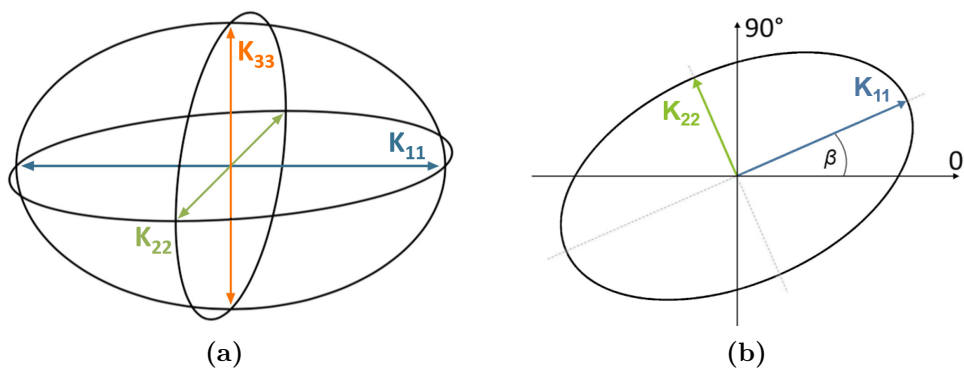


Fig. A-2 Principal permeability tensor as ellipsoid (a); in-plane permeabilities rotated by β (b). [201]

Besides its anisotropic nature, the permeability of reinforcement fabrics depends mainly on its textile type and on its FVF, thus the compaction of the reinforcement [14, 188]. In the following, the permeability tensor of a carbon fiber non-crimp fabric (NCF) is characterized for a FVF range of 40% to 60% to determine input data for CRTM simulation of Chapter 4.

Experimental Procedure: To this day, no specific method has been standardized to measure the permeability of reinforcement fabrics, therefore, a wide variety of experimental procedures exist [208–210]. For the present study, the permeability test facilities at the Chair of Carbon Composites, Technical University of Munich, were used [207].

Saturated, out-of-plane permeability measurements were carried out using the (one-dimensional) “1D Out-of-Plane Facility” explained by Meier et al. [207]. A 3 mm spacer was used for all tests, resulting in a consistent preform thickness of 3 mm

³ Parts of this subsection have been previously published in [201].

during testing. The fluid flow was evenly distributed over the 124 mm preform diameter by 340-hole perforated plates, each hole measuring a diameter of 4 mm.

Unsaturated, in-plane permeability measurements were performed via the (two-dimensional) “2D In-Plane Facility” as explained in [207]. In accordance to the out-of-plane permeability tests, all preforms were compressed to a thickness of 3 mm prior to in-plane measurements. The preform height during the experiments was controlled by the displacement control of the universal testing machine (UTM) Inspekt table 100 (Hegewald & Peschke, Nossen, Germany). In addition, more accurate measurements from two laser distance sensors were used during data post-processing. The development of the radial-flow-front was optically recorded and analyzed using MATLAB (MathWorks, Natick, Massachusetts, United States) in order to calculate K_{11} and K_{22} as well as their rotational angle β . All in-plane and out-of-plane permeability tests were performed in triplicate to ensure statistical relevance.

The variability of permeability measurements between two fabric batches can vary largely. The measurements of the pure fabric measurements and the determination of the equivalent permeability of the race-tracking channel were performed with two different batches of fabric. To correct the measured permeabilities for potential variation between these two batches, visual flow experiments were performed with the “1D In-Plane Facility” explained in [207] and superimposed by 2D RTM simulations in PAM-RTM of ESI Group (Rungis, France), at which all parameter settings were identical to the experiment. While the experiments were performed with fabric batch 2 of the equivalent permeability determination, the simulations were modeled with in-plane permeabilities determined for batch 1 used in the 2D in-plane permeability tests. If the superposition of the flow front propagation of the experiment and the simulation was observed to be dissimilar, the input values of the permeability for the simulations were iteratively adjusted to match the simulated flow progression with the experiment. Using this correction method, the in-plane permeabilities measured by one batch of fabric could be adjusted to another batch and aligned with the later presented determination of the equivalent permeability of the race-tracking channel. The applied approach of superimposing flow front progressions between experiment and simulation is based on attempts presented in literature [20, 100].

The RTM flow experiments with the “1D In-Plane Facility” were performed by Nusser [100] at a cavity height of 2.09 mm and 2.6 mm representing the maximal ($V_{f,p} = 51.4\%$) and minimal ($V_{f,p} = 41.2\%$) fiber volume fraction of the preform during CRTM simulations of Chapter 4. Further details on the superposition experiments are found in [100].

Material and sample preparation: A stitched, biaxial, carbon fiber NCF was chosen for the present study, manufactured by SGL Group (Wiesbaden, Germany) and denoted SIGRATEx[®] C B310/45-ST-E214/5g [143]. The fabric has a specific weight of 310 g/m² and 5 g powder binder, Araldite[®] LY 3366 (Huntsman), is sintered to its upper side.

All preforms used for test in the “1D Out-of-Plane Facility” and “2D In-Plane Facility” were tested at a height of 3 mm, for which the different FVFs for different test setups were adjusted by the number of reinforcement layers. Preforms consisting of 7, 8, 9 and 10 layers of material batch 1 were carefully cut and stacked, intending to measure permeabilities at fiber volume fractions $V_{f,p} = 41.7\%$, 47.7% , 53.8% and 59.6% , respectively. Preforms of 300 mm squares were binder-activated at $170\text{ °C} \pm 10\text{ °C}$ via infrared heating and debulked under vacuum prior to permeability testing, to be compliant to industrial manufacturing processes. Preliminary tests showed that preforms of less than 8 layers remained after debulking at heights lower than the desired testing thickness of 3 mm; therefore these preforms should have been excluded. To be able to measure at least one FVF lower than 47.7% (8 layers), it was decided to activate preforms of 7 layers only under heat without compaction, yielding adequate preform heights for testing.

Preforms of a length of 400 mm ($SD = 0.2$) and a width of 170 mm ($SD = 0.2$) were manufactured for the RTM flow experiments performed with the “1D In-Plane Facility”. Layers of material batch 2 were stacked to form a preform lay-up of $(\pm 45_6)_s$ and binder activated as described in the previous paragraph.

Non-reactive sunflower oil was used as test fluid for all permeability measurements. Its Newtonian behavior was verified and its viscosity was measured at 52.9 mPas, at 25.5 °C, as described in Chapter A.1.1.

Results and discussion: Radial, in-plane permeability measurements were conducted via the “2D In-Plane Facility” using material batch 1. Furthermore, RTM flow experiments were performed using material batch 2. To check for potential permeability variations between the two batches, 2D RTM simulations were conducted using the determined in-plane permeabilities of batch 1 and superimposed with the flow experiments conducted with preforms of batch 2, as shown in Figure A-3. The impregnated preform section appears in Figure A-3 in dark gray while the flow front of the simulation is presented as a green line. For both investigated FVFs the flow front of the experiment is ahead of the green simulated flow front—clearly visible from the second presented time step on. To adjust the simulated flow front propagation with one of the experiments, the input data of the in-plane permeabilities was equally increased for all FVFs in an iterative process. Neglecting a slight flow advancement due to edge race-tracking on the upper side of the preform for

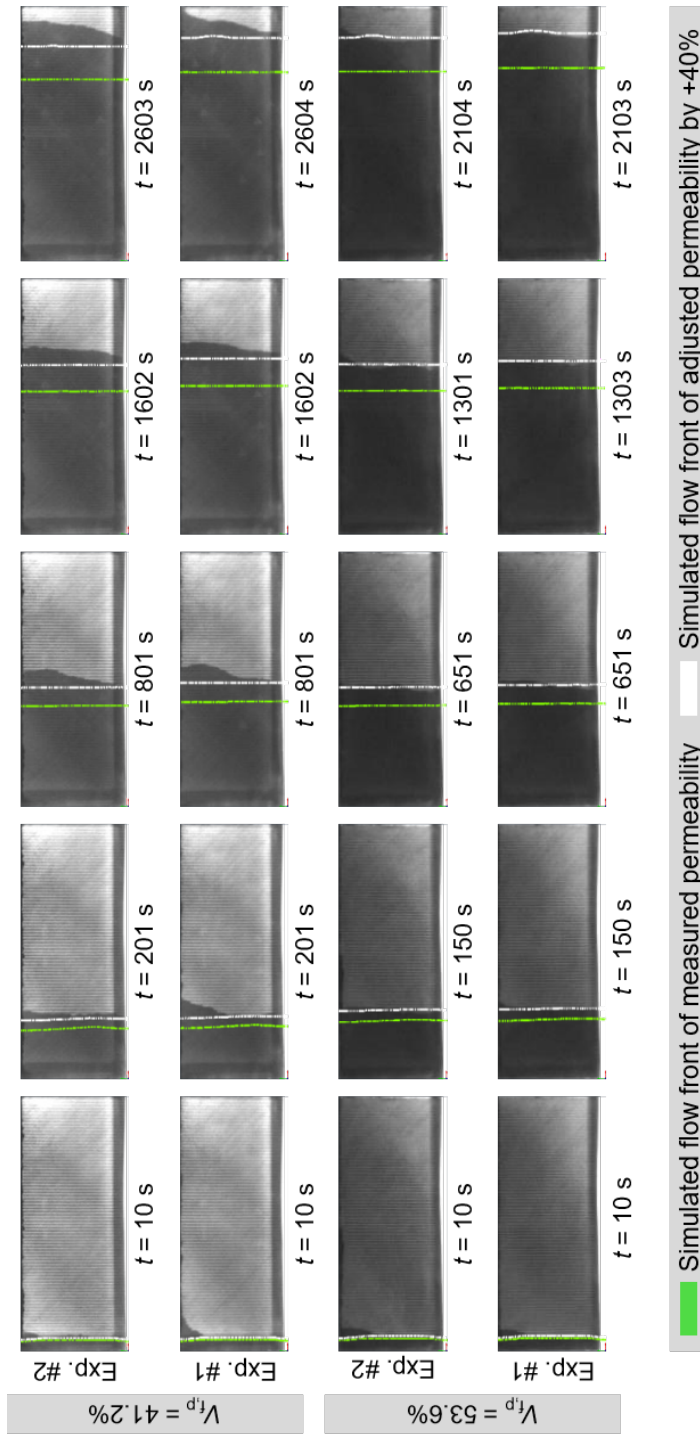


Fig. A-3 Superposition of flow front positions of RTM flow experiments with numerical simulations at different time steps.

experiments at $V_{f,p} = 41.2\%$, an adjustment of $+40\%$ showed best correspondence with the conducted flow experiments, as shown by the white lines in Figure A-3. Additionally, the adjustment of the permeability by $+40\%$ is verified by superposition experiments with preforms of batch 2 to verify the equivalent permeability of the edge race-tracking channel, presented in Figures A-8 and A-9.

The adjusted in-plane permeabilities by $+40\%$ (K_{11} and K_{22}) and measured (non-adjusted) out-of-plane permeability (K_{33}) are presented in Figure A-4 over a range of FVFs. The principle permeabilities in all three directions decrease linear in the semi-logarithmic plot of Figure A-4 with increasing FVF. Furthermore, the out-of-plane permeability is recorded to be approximately one order of magnitude lower than the corresponding adjusted in-plane permeabilities for comparable FVF. The observed relation between permeability and FVF correlates well with literature [14, 188, 211]. The reasons for some scatter in the results is seen to be the high amount of manual work during sample preparation as well as variance in the binder activation procedure for 7-layered preforms [212].

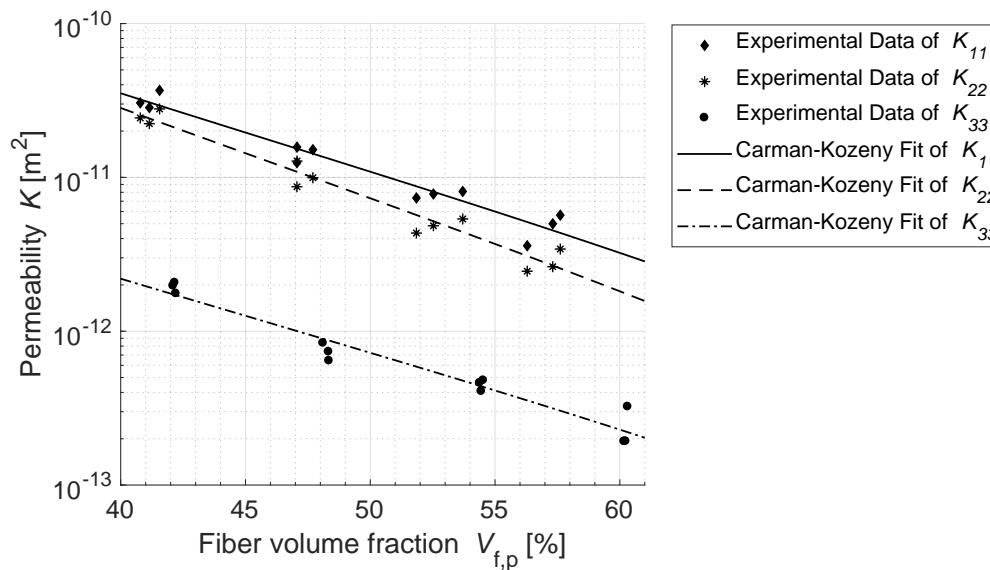


Fig. A-4 Measured out-of-plane and adjusted ($+40\%$) in-plane permeability of the reinforcement material [143]: Permeability over fiber volume fraction. [140]

In literature, the relationship between the permeability \mathbf{K} and the fiber volume fraction $V_{f,p}$ are mostly stated by purely empirical relations. One of the most commonly used is the Carman-Kozeny relation. Equation (A-1) presents a modified Carman-Kozeny relation [15, 213], which is used to model a continuous permeability function based on experimentally determined permeability values at different FVFs. The coefficients C and exponent m of Equation (A-1) are material parameters, which are listed in Table A-1 for the three determined principle permeabilities of the investigated NCF material. As illustrated in Figure A-4, the modified

Carman-Kozeny equation shows a good fit to the experimental data. Due to the equation's characteristic to provide a continuous function to fit the permeabilities over a wide range of FVFs, these functions were used to generate data input of the permeabilities for CRTM simulations in Chapter 4.

$$K = \frac{1}{C} \cdot \frac{(1 - V_{f,p})^{m+1}}{(V_{f,p})^m} \quad (\text{A-1})$$

Tab. A-1 Coefficient of the Carman-Kozeny Equation (A-1) for the determined principle permeabilities presented in Figure A-4.

	K_{11}	K_{22}	K_{33}
C	$4.5915682831 \times 10^{10}$	$6.8318173395 \times 10^{10}$	$6.9072025537 \times 10^{11}$
m	2.45	2.88	2.29

Figure A-5 presents the measured (non-adjusted) permeability angle β between the principle in-plane permeabilities K_{11} and the coordinate system of the reinforcement for different FVF. As shown in Figure A-5, the average of β varies between $+6^\circ$ and -7° while a strong fluctuation is recorded, indicated by large error bars. The strong fluctuation and variation of the permeability angle β indicates a high uncertainty. Theoretically, a symmetrical ($\pm 45^\circ$) NCF, as tested [143], is expected to show nearly identical principle in-plane permeabilities and an angle β of approximately 0° . The measured values of β , presented in Figure A-5, are observed to fluctuate around its theoretical value of 0° . Therefore, β was defined to be of a constant value of 0° over the relevant FVF-range for the CRTM simulations of Chapter 4.

Compaction Behavior of Reinforcement Structure⁴

The reinforcement compaction behavior describes its through-thickness resistance to deformation by compression stress. Various studies describe viscoelastic compaction behavior of fibrous reinforcement material used in FRP manufacturing. Reported viscoelastic behavior characteristics of reinforcements include strain rate dependency, stress relaxation and hysteresis [203, 207]. This subsection presents transverse compaction tests of the carbon fiber NCF, providing stress-strain curves up to a maximum fiber volume fraction 54.1%, which is required as input for CRTM simulation.

⁴ Parts of this subsection have been previously published in [201].

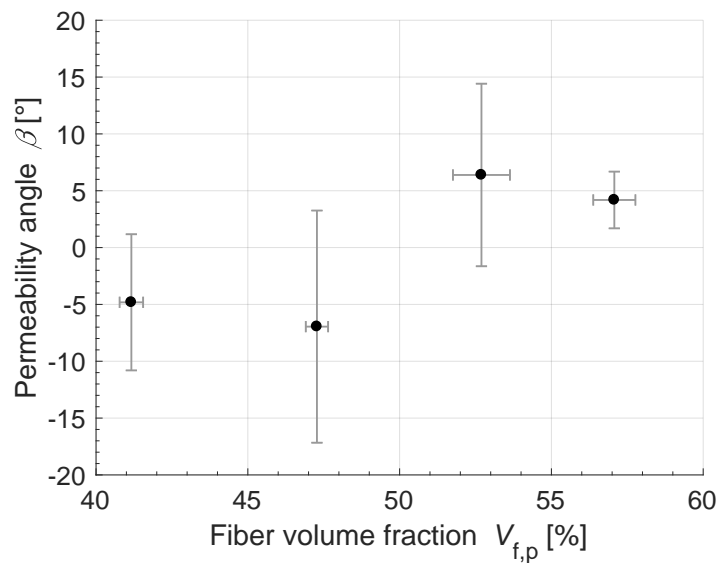


Fig. A-5 Permeability angle over fiber fiber volume fraction (mean of three measurements; standard deviations shown as error bars).

Experimental procedure: As for in-plane permeability tests, the “2D In-Plane Facility” [207] was utilized for the compaction tests. The test rig was mounted and operated on the universal testing machine (UTM) Inspekt table 100. During experiments, the compaction height h_p and velocity \dot{h}_p of the preform were adjusted by the displacement control of the UTM. The compaction force was measured via a 100 kN load cell. For statistical relevance, the test setup was performed in triplicate, always using a new, untested preform.

Materials and sample preparation: The same biaxial carbon fiber NCF (SIGRATEX® C B310/45-ST-E214/5g) [143], that was used for permeability characterization, was also used for compaction tests. Reinforcement layers were cut into 300 mm squares and ten layers were stacked ensuring identical biaxial fiber orientation. Preforms were binder-activated at $170\text{ °C} \pm 10\text{ °C}$ via infrared heating and debulked under vacuum pressure.

Results and discussion: Transverse compaction tests were performed at a closing velocity of $\dot{h}_c = 1\text{ mm/s}$. Each sample was compacted to a height of 3.3 mm, corresponding to maximum fiber volume fraction of 54.1%. The diagram in Figure A-6 shows the experimental stress-strain curve up to peak stress at maximum compaction of $V_{f,p} = 54.1\%$, as an average of three measurements. For this study, strain ϵ is defined as:

$$\epsilon = 1 - \frac{h_p}{h_{p,u}} \quad (\text{A-2})$$

where $h_{p,u}$ represents the preform height at compaction start, recorded at a load level of 50 N. The initial preform heights of the samples for the test series were $h_{p,u} = 4.70$ mm (SD = 0.00). The experimental curve in Figure A-6 shows a non-linear dependency between compaction stress and strain. The observed strain-rate dependent compaction behavior of the material corresponds to literature reports [203, 207].

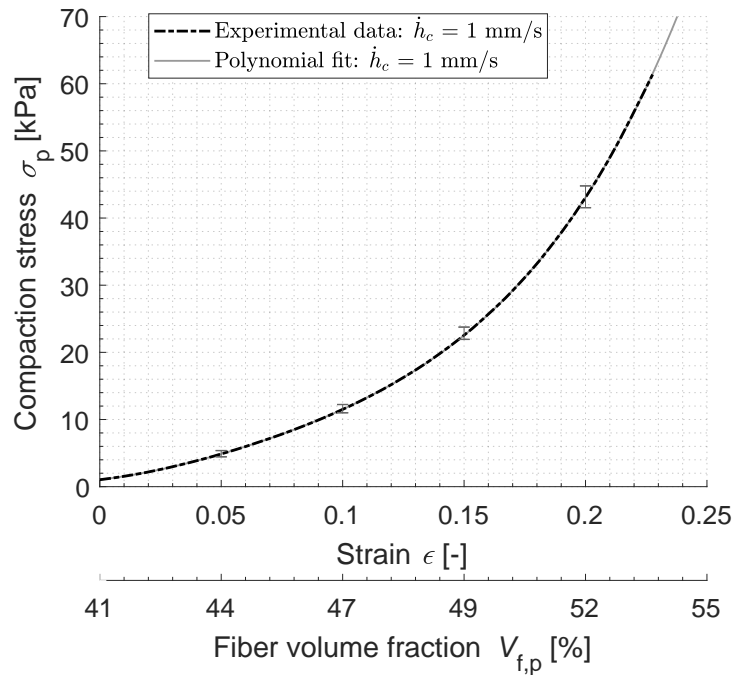


Fig. A-6 Compaction behavior of the reinforcement material [143]: Compaction stress over fiber volume fraction and strain (experimental data: mean of three measurements; standard deviations shown as error bars). cf. [140]

To generate input data for numerical CRTM simulations in ESI's PAM-RTM, a polynomial fit of fourth order, as presented in Equation (A-3), was applied. The polynomial fitting function, with an R^2 -value of 1.0, is plotted in Figure A-6.

$$f(x) = 1.857 \cdot 10^4 \cdot x^4 - 3851 \cdot x^3 + 689.3 \cdot x^2 + 33.69 \cdot x + 1.459 \quad (\text{A-3})$$

Equivalent Permeability to Model an Edge Race-Tracking Channel

The equivalent permeability approach is commonly applied to model edge race-tracking channels in numerical simulations which are based on Darcy's law (2-1) as in the used software package PAM-RTM. The literature review in Chapter 2.2.3 presents different formulas to simulate the longitudinal flow inside an edge race-tracking channel. For the two channel widths investigated in this work (2 mm

and 4 mm), Figures 2-11 and 2-12 show progressions of equivalent permeability curves over preform height of the different equations. The literature review (Chapter 2.2.3) revealed that Equation (2-10) is only applicable if transverse flow is neglectable [109], which is not the case for a preform impregnation in the presence of edge race-tracking. Therefore, this equation is not considered for the application in CRTM simulations of this work. No reported validation of Equation (2-13) could be found in literature, disregarding the use of this equation in this work. An adequate correlation between edge race-tracking simulations and experiments could only be found for Equations (2-11), (2-12) and (2-14) [20, 21, 116]. As seen in Figures 2-11 and 2-12, Equations (2-12) and (2-14) are identical for the determined preform permeabilities used in this work. Equation (2-11) is observed to be of low value compared to others. In the context of this work, Equation (2-12) was chosen due to (i) its proven validation in literature [20, 21], (ii) its medium level at the equations' comparison in Figures 2-11 and 2-12, and (iii) its reduced complexity of the formula compared to Equation (2-14) which was shown to result in identical equivalent permeability values as Equation (2-12) (see Figures 2-11 and 2-12).

Experimental procedure: RTM flow experiments with edge race-tracking, conducted by Nusser [100], were superimposed with 2D RTM simulations of identical process setting. The preforms for the experiments were placed inside the cavity of the “1D In-Plane Facility” to form edge race-tracking channels of 2 mm and 4 mm on the upper side of the preform. The flow front progression was optically tracked during the experiments to be able to identify (i) the flow front progression pattern and (ii) the time of full channel filling. Both are then compared to results of numerical RTM simulations performed with PAM-RTM. The experiments of both channel widths are performed at two FVFs, representing the upper and lower FVF limit of the preform during a CRTM simulation in Chapter 4. The experiments of all four scenarios (two FVFs at two channel widths) are repeated in triplicate for statistical relevance.

The literature review, presented in Chapter 2.2.3, showed limited information on attempts used to model the transversal equivalent permeability of a channel. Sheard et al. [119] reported good agreement between edge race-tracking experiments and simulation in which an equated longitudinal and transversal equivalent permeability ($K_{ch,eq;x} = K_{ch,eq;y}$) was modeled. Therefore, this attempt was also applied at the RTM simulations presented in the following and was validated by the superposition with RTM flow experiments. Detailed information on the performed RTM experiments is found in [100].

Materials and sample preparation: Preforms of the investigated NCF material (SIGRATEX® C B310/45-ST-E214/5g) [143] of batch 2 were stacked to a lay-up of $(\pm 45_6)_s$ and binder-activated at $170\text{ °C} \pm 10\text{ °C}$ via infrared heating as well

as debulked under vacuum. A precise in-plane dimensioning of the preforms is of high importance to ensure a precise and homogeneous edge race-tracking channel during the experiments. Therefore, the activated preforms were cut via a CNC cutting table (M-1200 CV, Zünd, Altstätten, Germany) to its final dimension of 400 mm (SD = 0.2) in length and 168 mm (SD = 0.2) as well as 166 mm (SD = 0.2) in width to enable an one-sided edge race-tracking channel width of 2 mm and 4 mm, respectively.

Results and discussion: The channel fill time and preform impregnation pattern between experiments and numerical simulations are compared in the following to validate the attempt to model an edge race-tracking channel via the equivalent permeability approach of Equation (2-12).

Figure A-7 presents the times at which the edge race-tracking channel was completely filled. Comparing the two simulations with 2 mm wide edge race-tracking channels with the ones with 4 mm show that a wider channel width results in lower filling time of the channel. Furthermore, a reduction of the FVF shows a clear reduction of filling time for the simulation with a 2 mm channel but only a minor reduction for the simulations with a 4 mm wide channel. The experiments with a 4 mm wide edge race-tracking channel support the conclusions of the corresponding simulations, while the experiments with a 2 mm channel are of uncertain potential filling time reduction at a higher FVF, due to the high standard deviation of the experiments especially at high FVF.

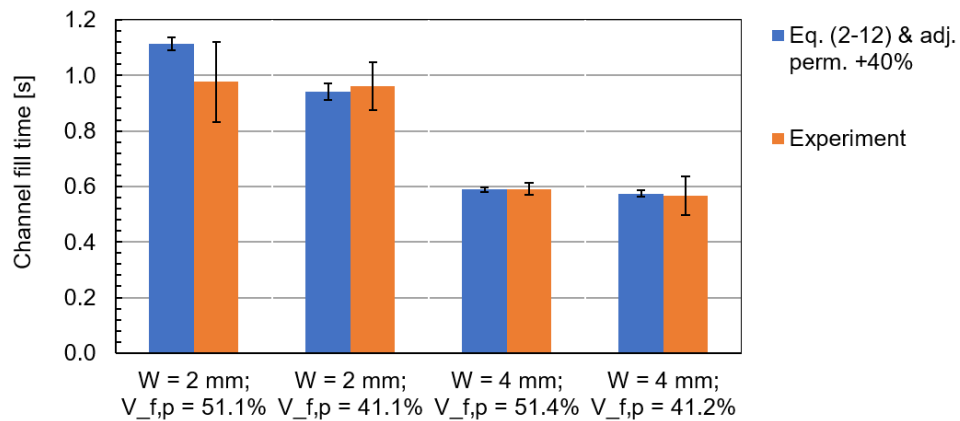


Fig. A-7 Fill time of edge race-tracking channel: Simulation result (blue) vs. experimental result (orange) for different channel width (W) and fiber volume fractions (V_{f,p}) (bar height represents mean of three experiments or numerical simulations; standard deviations shown as error bars).

To validate the equivalent permeability approach of Equation (2-12), the consistency of the channel fill times of the experiments and the corresponding numerical

simulations are of high interest. Figure A-7 shows good consistency between the experimental and simulated results, except for the scenario of 2 mm wide channel width at a FVF of 51.1%. In this scenario the mean channel fill time of the experiments is lower than the simulated value, but at the same time the standard deviation of the experiments shows the highest recorded fluctuation of all recorded scenarios. The extent of the standard deviation of the scenario of 2 mm channel width a FVF of 51.1% shows an uncertainty which is in the range of the corresponding simulated results, showing a consistency of the experiments and simulation within their uncertainties.

Figures A-8 and A-9 show superpositions of RTM flow experiments with RTM numerical simulations with a 2 mm and 4 mm wide edge racetracking channel, respectively. For each time step the picture in the background shows the experiment in which the dark gray section represents the impregnated preform section. The simulated flow front is plotted on top of the preform as a green and white line, representing a simulation with the originally measured in-plane permeability of batch 1 (green) and the adjusted permeability to match the permeability of batch 2 (white). As discussed two subsections ahead for the in-plane permeability measurements of the preform, the flow front of the experiment containing preforms of batch 2 shows to advance the flow front simulated with the measured in-plane permeability of batch 1, shown in green, but is adequately represented by the adjusted permeability (+40%), shown in white.

In comparison to the pure in-plane permeability verification experiments in Figure A-3, the flow fronts in Figures A-8 and A-9 are not equally progressing over the preform width but advance inside the edge race-tracking channel at the upper preform edge. Due to the fast channel filling in approximately 1 s for the scenarios with a 2 mm wide edge racetracking channel and approximately 0.6 s for the ones with a 4 mm wide channel (see Figure A-7), the preform is laterally impregnated from the edge race-tracking channel on the preform top side. The back-filling of the preform from the outlet side (on the right side) during the experiment is caused by the experimental setup, at which the fluid is collected at a reservoir on the outlet side before it exits the cavity. The so-caused back-filling from the reservoir into the preform at the outlet side is unintended and therefore not modeled during the simulations. Focusing on the main point of interest, the comparison of the simulated flow fronts in white with the flow fronts of the experiments shows good correspondence for both investigated channel widths and FVFs.

Therefore, the results of the channel fill time and of the superpositioned flow front progressions lead to the conclusion that the attempt to simulate the equivalent permeability of the edge race-tracking channel via Equation (2-12) is valid. Hence,

Equation (2-12) is used to simulate the flow in longitudinal and transversal direction of an edge racetracking channel during CRTM simulations in Chapter 4.

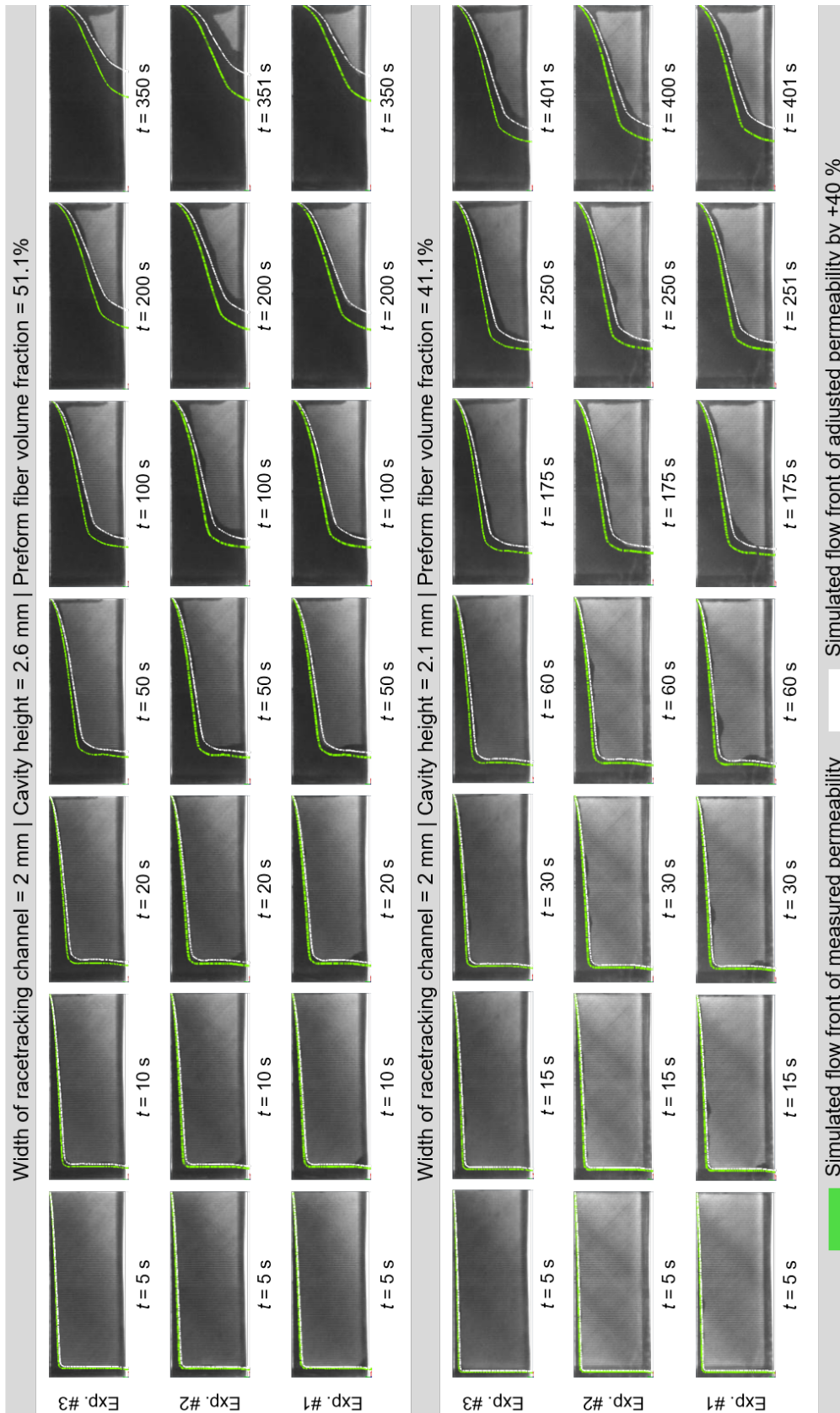


Fig. A-8 Superposition of RTM race-tracking flow experiments with numerical simulations: edge race-tracking channel width = 2 mm.

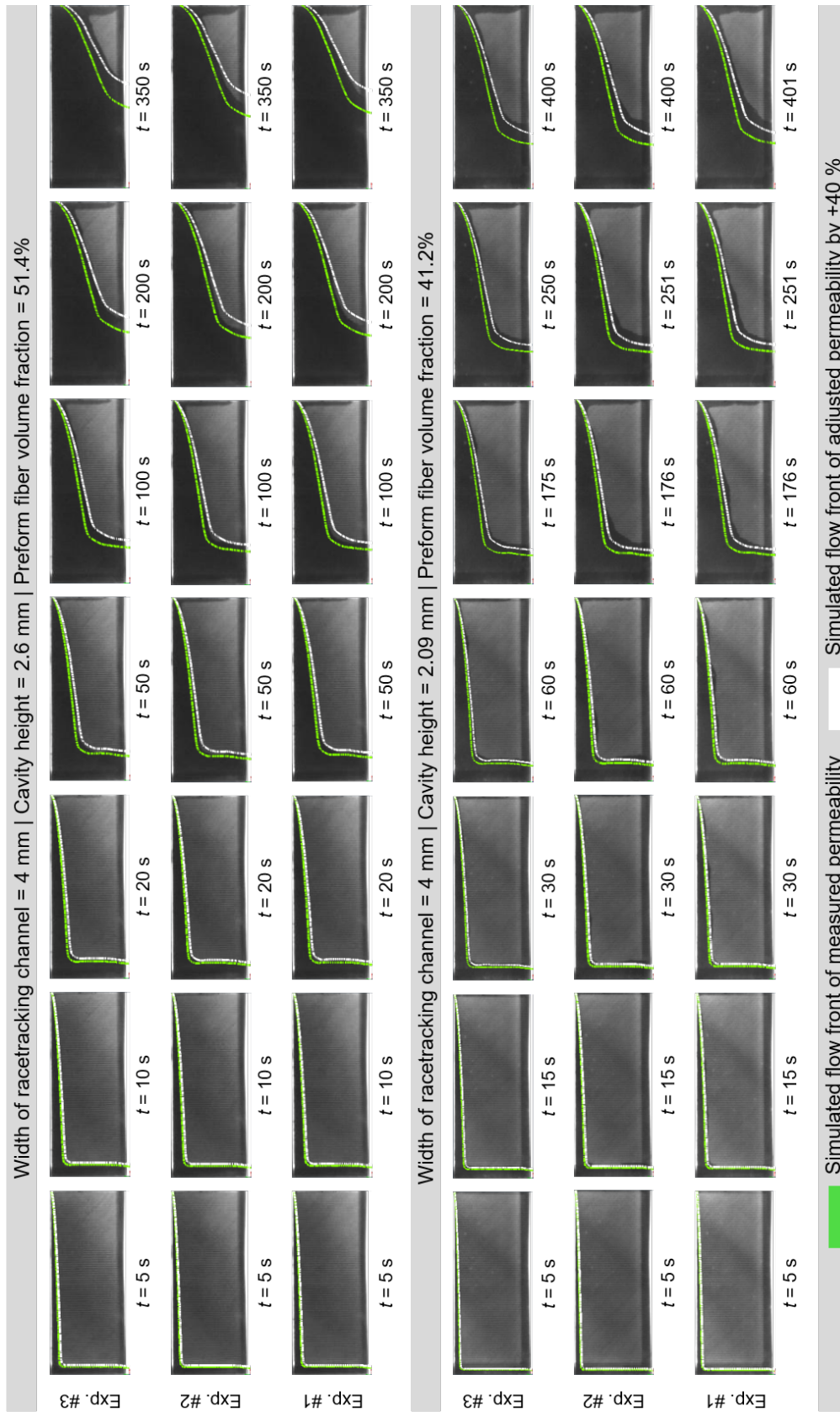


Fig. A-9 Superposition of RTM race-tracking flow experiments with numerical simulations: edge race-tracking channel width = 4 mm.

A.2 Appendix of Numerical Studies on Edge Race-Tracking during CRTM

A.2.1 Modeling Approach and Evaluation Method

Tab. A-2 Flow rate of CRTM simulations of the numerical race-tracking study (NRT study) and numerical flow control study (NFC study).

CRTM process configuration	Flow rate of simulations without race-tracking (rt)	Flow rate of simulations with 2 mm wide rt channel	Flow rate of simulations with 4 mm wide rt channel
	[m ³ /s]	[m ³ /s]	[m ³ /s]
1 (NRT study)	$1.36298 \cdot 10^{-05}$	$1.35721 \cdot 10^{-05}$	$1.35156 \cdot 10^{-05}$
2 (NRT study)	$1.36297 \cdot 10^{-05}$	$1.36009 \cdot 10^{-05}$	-
3 (NRT study)	$1.36298 \cdot 10^{-05}$	$1.35721 \cdot 10^{-05}$	-
4 (NRT study)	$1.36299 \cdot 10^{-05}$	$1.35722 \cdot 10^{-05}$	-
4 (NFC study)	$1.36475 \cdot 10^{-05}$	$1.36088 \cdot 10^{-05}$	-

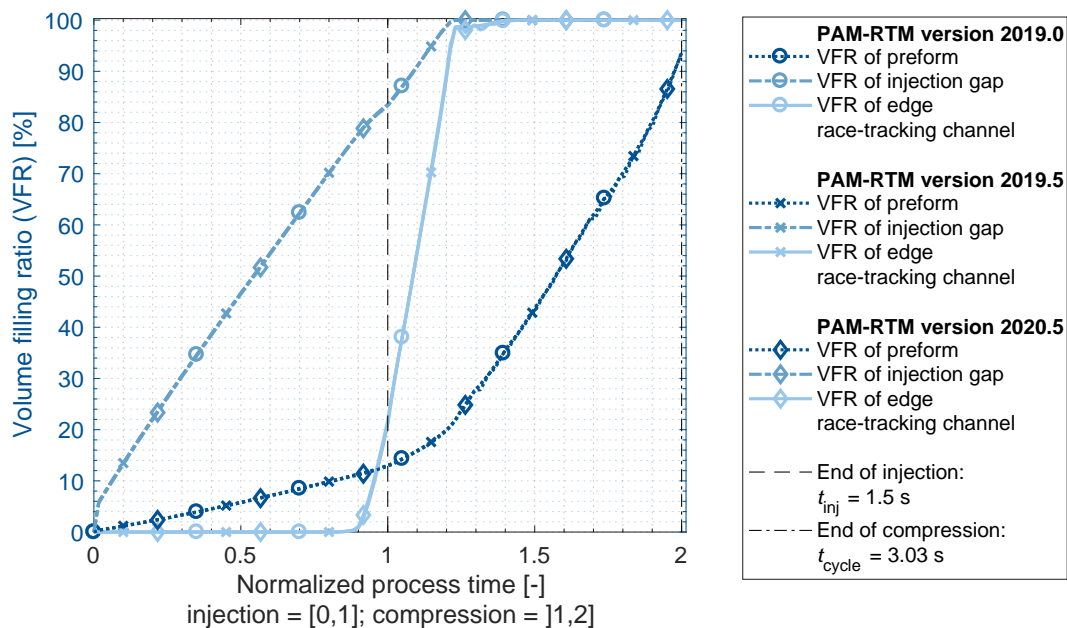


Fig. A-10 Comparison of CRTM simulation results calculated with different PAM-RTM versions 2019.0, 2019.5 and 2020.5, all used in this work – CRTM process configuration 4 of small geometrical aspect ratio, large injection gap and central inlet as well as with a 2 mm wide race-tracking channel.

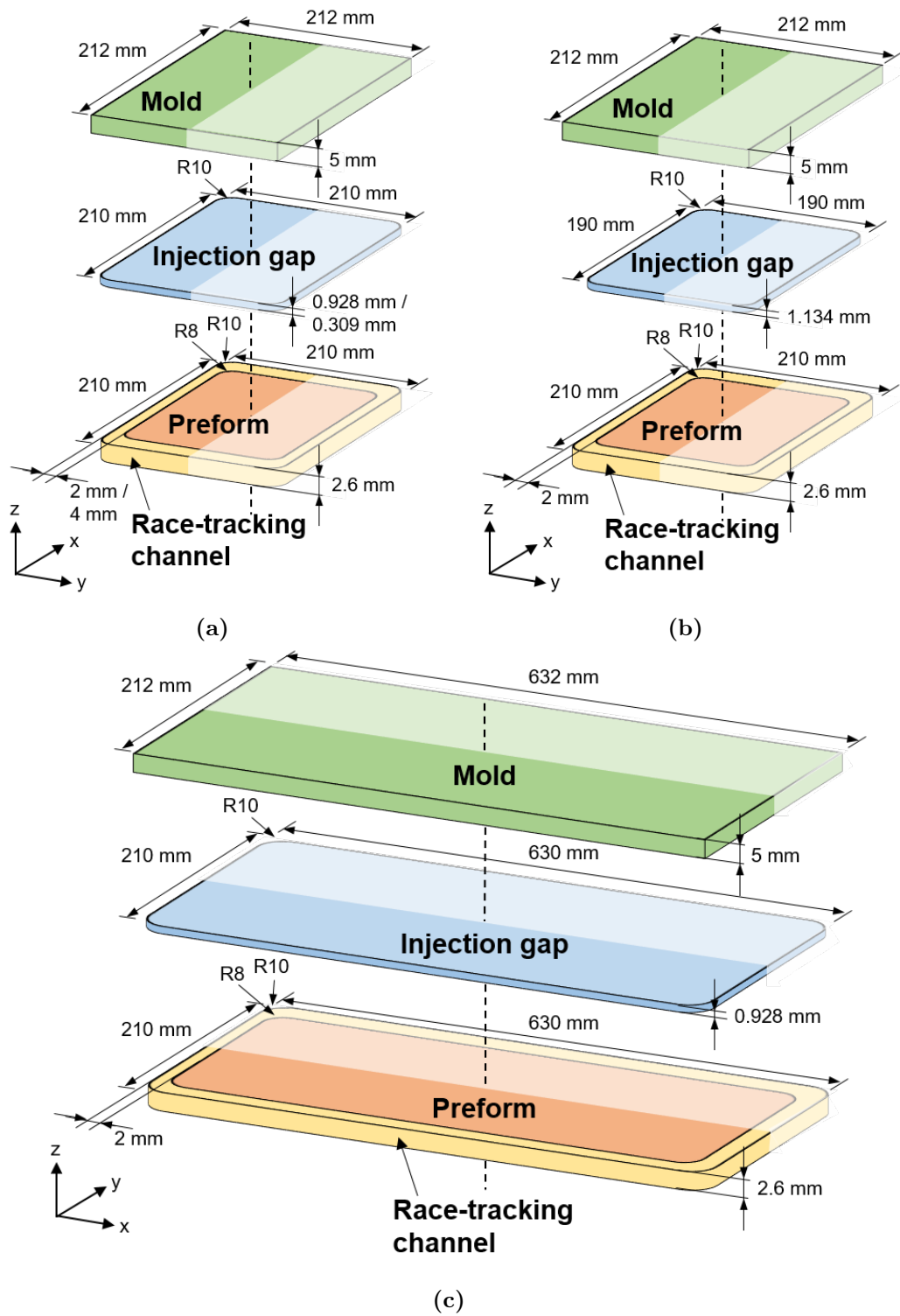


Fig. A-11 Geometry dimensions of simulation models at process start (simulated as half models) at which the channel domain is defined as preform domain for simulations without an edge race-tracking channel: (a) numerical race-tracking study – process configuration 1, 3 and 4 cf. [140]; (b) numerical flow control study [140]; (c) numerical race-tracking study – process configuration 2.

Tab. A-3 Coupling frequency between fluid and solid mechanics solver in PAM-RTM of CRTM simulations of the numerical race-tracking study (NRT study) and numerical flow control study (NFC study).

CRTM process configuration	Coupling frequency of simulations without race-tracking (rt)	Coupling frequency of simulations with 2 mm wide rt channel	Coupling frequency of simulations with 4 mm wide rt channel
	[s]	[s]	[s]
1 (NRT study)	0.05	0.05	0.05
2 (NRT study)	0.1	0.0875	-
3 (NRT study)	0.05	0.05	-
4 (NRT study)	0.05	0.075	-
4 (NFC study)	0.05	0.05	-

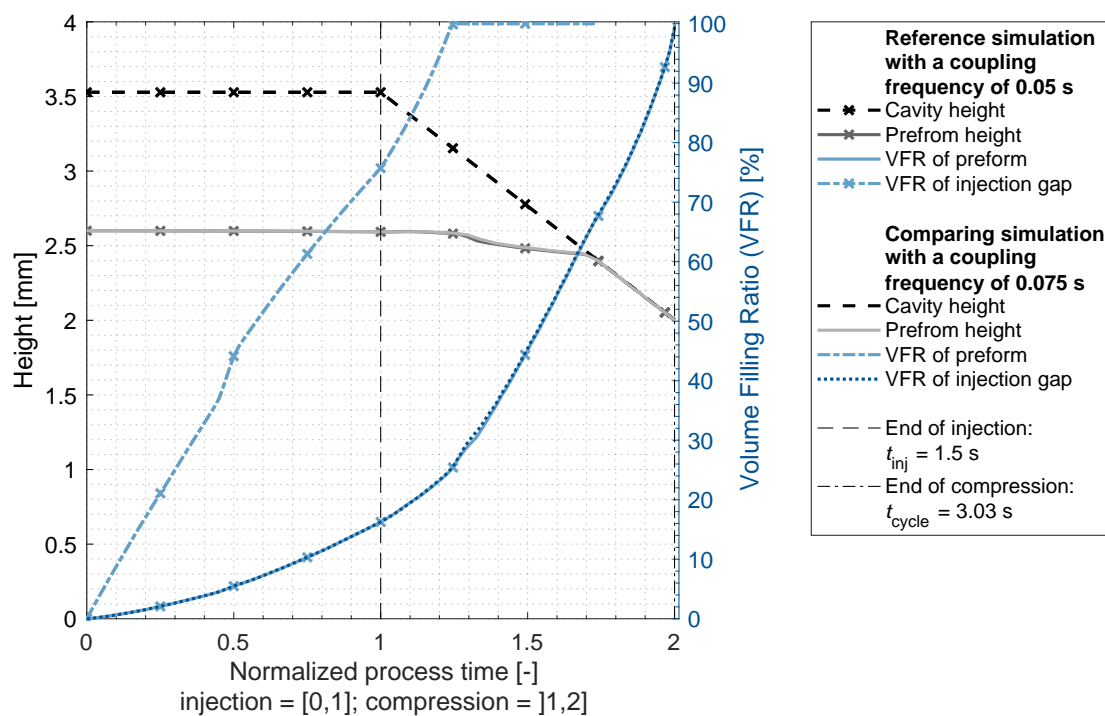


Fig. A-12 Comparison of CRTM simulation results calculated with a coupling frequency of 0.05 s and 0.075 s, the maximum deviation of coupling frequency between two comparing simulations in this work (see Table A-3) – CRTM process configuration 1 of small geometrical aspect ratio, large injection gap and lateral inlet.

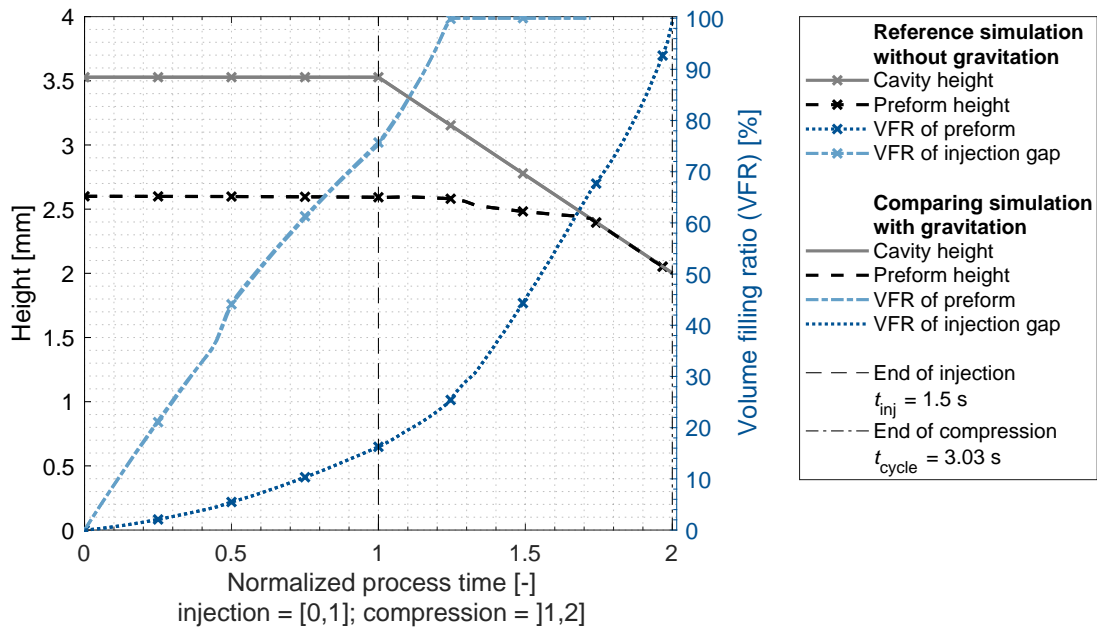


Fig. A-13 Comparison of CRTM simulation results calculated with and without gravitation – CRTM process configuration 1 of small geometrical aspect ratio, large injection gap and lateral inlet.

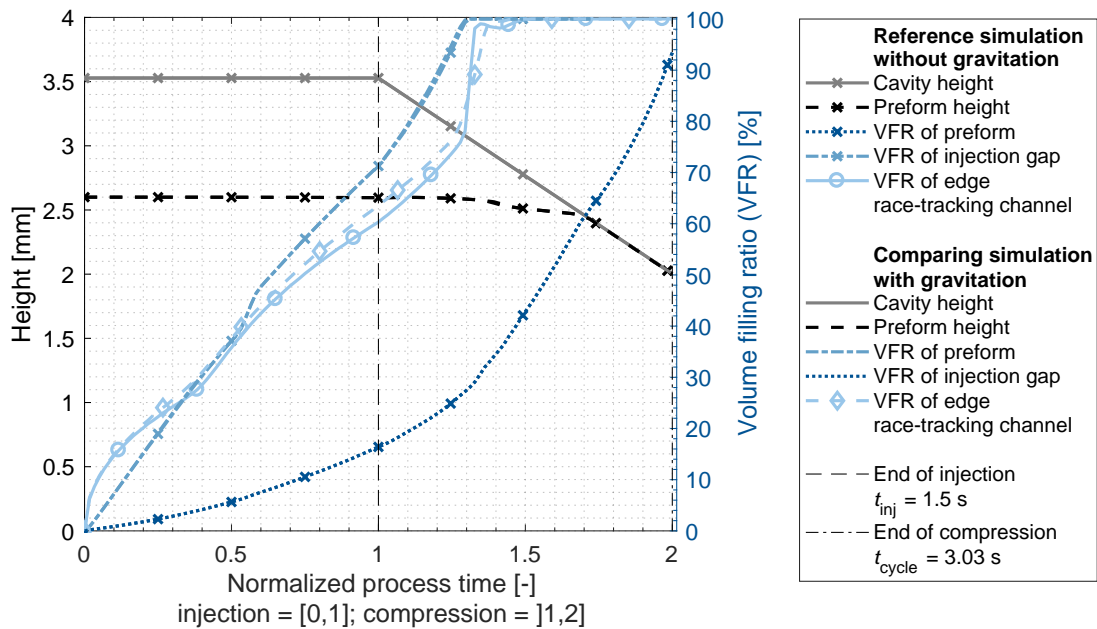


Fig. A-14 Comparison of CRTM simulation results at presence of edge race-tracking calculated with and without gravitation – CRTM process configuration 1 of small geometrical aspect ratio, large injection gap and lateral inlet.

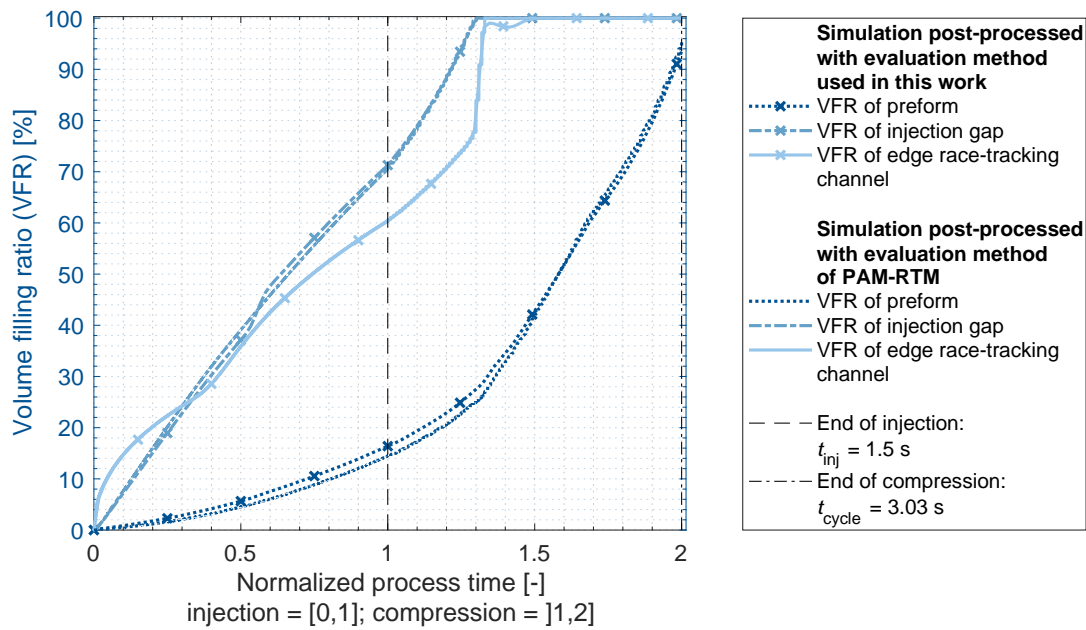


Fig. A-15 Comparison of evaluation methods – CRTM process configuration 1 of small geometrical aspect ratio, large injection gap and lateral inlet (both simulations calculated in PAM-RTM version 2020.5).

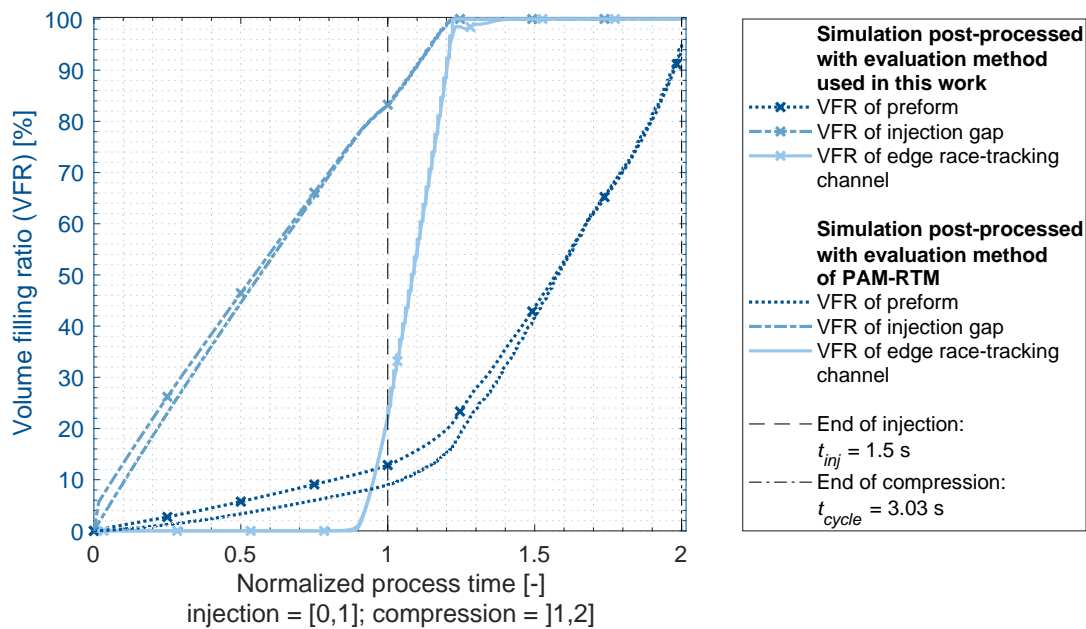


Fig. A-16 Comparison of evaluation methods – CRTM process configuration 4 of small geometrical aspect ratio, large injection gap and central inlet (both simulations calculated in PAM-RTM version 2020.5).

A.2.2 Numerical Race-Tracking Study

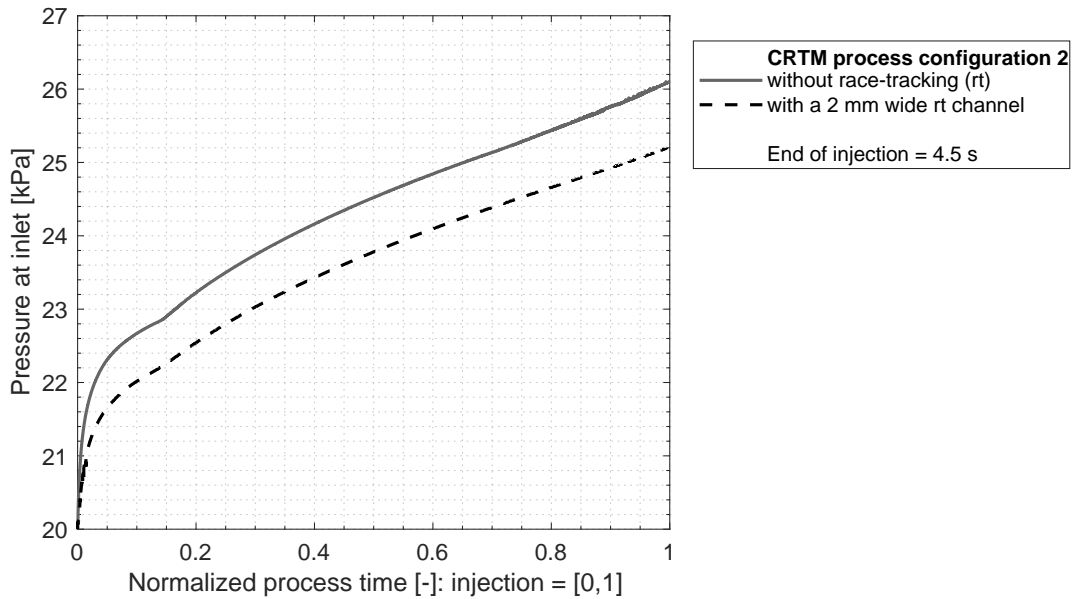


Fig. A-17 Pressure at inlet during the CRTM injection phase of numerical simulations of the CRTM process configuration 2 of large geometrical aspect ratio, large injection gap, and lateral inlet: without and with 2 mm wide edge race-tracking channel.

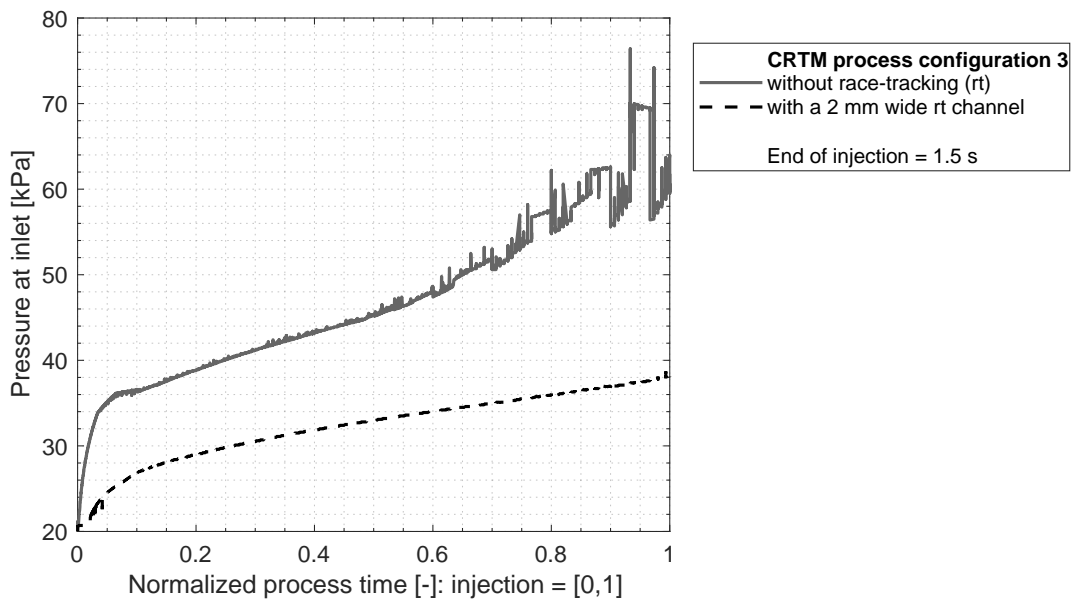


Fig. A-18 Pressure at inlet during the CRTM injection phase of numerical simulations of the CRTM process configuration 3 of small geometrical aspect ratio, small injection gap, and lateral inlet: without and with 2 mm wide edge race-tracking channel.

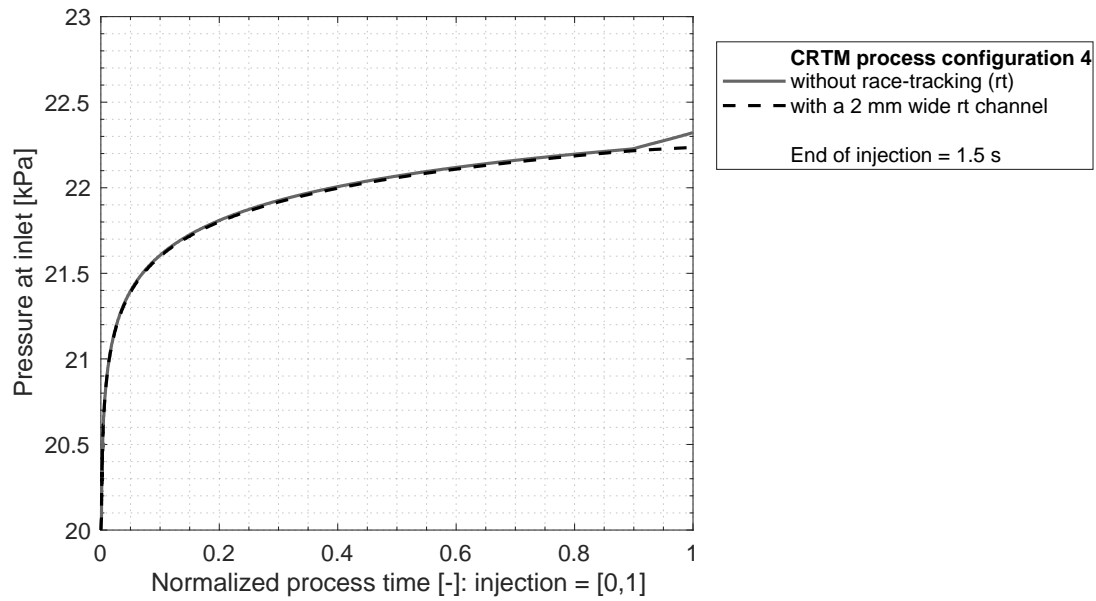


Fig. A-19 Pressure at inlet during the CRTM injection phase of numerical simulations of the CRTM process configuration 4 of small geometrical aspect ratio, large injection gap, and central inlet: without and with 2 mm wide edge race-tracking channel.

A.2.3 Numerical Flow Control Study

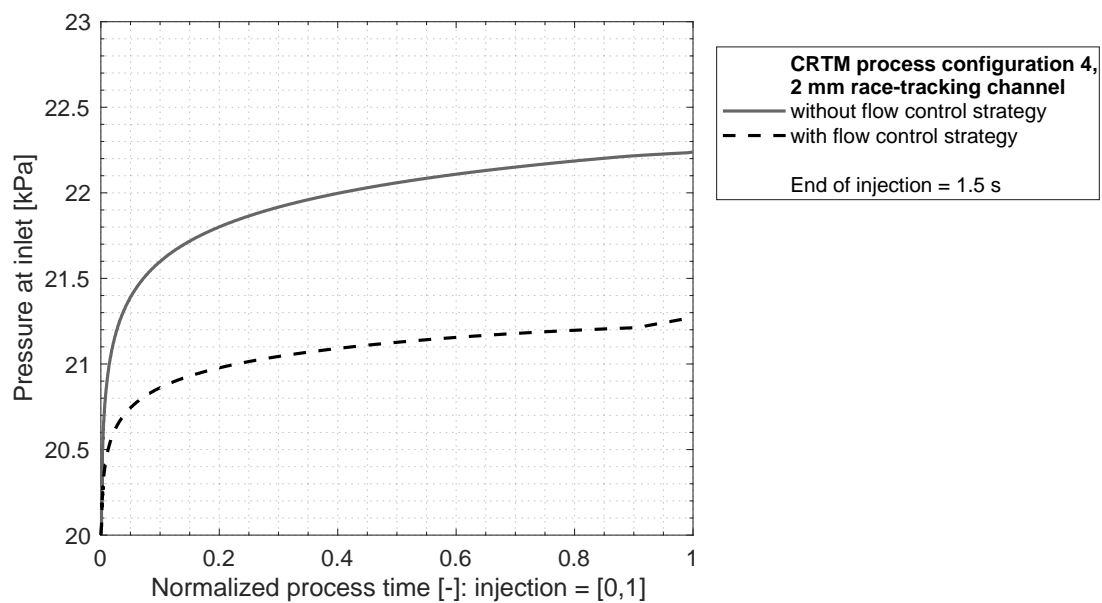


Fig. A-20 Pressure at inlet during the CRTM injection phase of numerical simulations of the CRTM process configuration 4 of small geometrical aspect ratio, small injection gap, and central inlet: without and with applied flow control strategy.

A.3 Appendix of Function Analysis of Film-Integration into CRTM

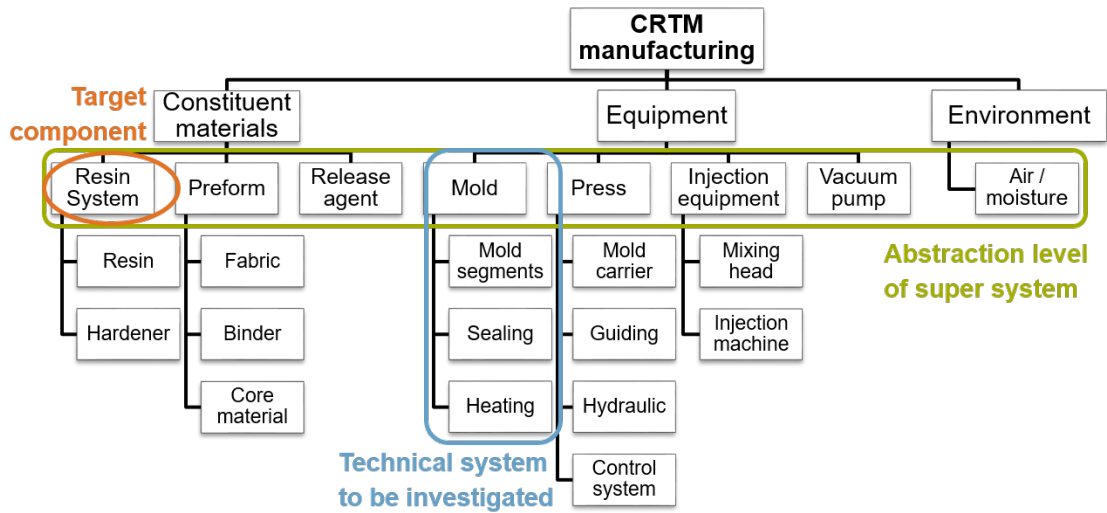


Fig. A-21 Abstraction of the system “CRTM manufacturing” and definition of the investigated technical system (blue), super system (green) and target component (orange). [25]

	Mold segments	Heating	Sealing	Resin system	Prefom	Release agent	Press	Injection equipment	Vacuum pump	Air / moisture
Mold segments	+	+	+	+	+	+	+	+	-	+
Heating	+	-	+	+	+	-	-	-	-	-
Sealing	+	+	-	+	-	+	-	-	-	+
Resin system	+	+	+	+	+	+	-	+	-	+
Prefom	+	+	-	+	-	+	-	-	-	-
Release agent	+	-	+	+	+	-	-	+	-	-
Press	+	-	-	-	-	-	-	-	-	-
Injection equipment	+	-	-	+	-	+	-	-	-	-
Vacuum pump	-	-	-	-	-	-	-	-	-	+
Air / moisture	+	-	+	+	-	-	-	-	+	-

Fig. A-22 Interactions of the components of the technical system (blue), target (orange), and super system (green); + interaction, - no interaction.

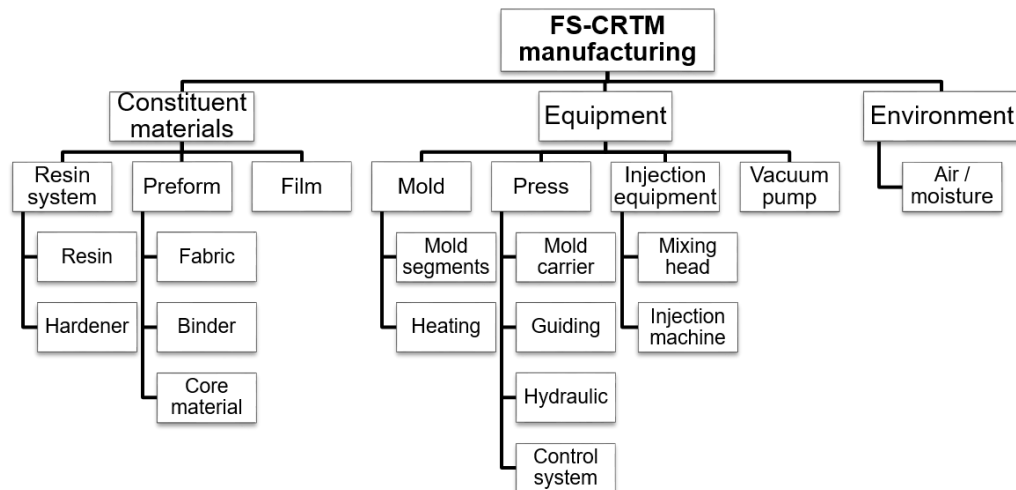


Fig. A-23 Abstraction of the system “FS-CRTM manufacturing”. [25]

A.4 Methodology of FS-CRTM Flow Visualization Experiments

In this work, a novel LCM process variant, the so-called film-sealed compression resin transfer molding (FS-CRTM) process is studied on a laboratory scale. Flow visualization experiments are conducted to characterize the FS-CRTM process in Chapter 6 and investigate its robustness towards edge race-tracking in Chapter 7. In the following, the methodology of FS-CRTM flow visualization experiments is presented. The process starts by film-sealing the preform which is explained in Subsection A.4.1. Novel test equipment was designed to perform FS-CRTM flow visualization experiments, explained in detail in Subsection A.4.2. Subsection A.4.3 presents the experimental procedure of the flow visualization experiments as performed in the present work.

A.4.1 Film-Sealing of Preforms⁵

The film-sealing of the preform is a critical step in the FS-CRTM process chain. While the film-sealed preform package needs to be air- and liquid-tight, it also needs to be free of wrinkles. In the preform section, wrinkles of the film could cause imprints on the part surface or result in out-of-plane wrinkles of the fiber structure. In the outer tool section, wrinkles of the two touching films could result in overlapped material that is thinned or even torn during closure of the upper frame. Thus, the

⁵ This subsection has been previously published in [26].

film-sealed preform package could leak, bearing a high risk of an unsuccessful preform impregnation. To minimize film wrinkling and to ensure a repeatable process, a film-sealing station was developed as shown in Figure A-24.

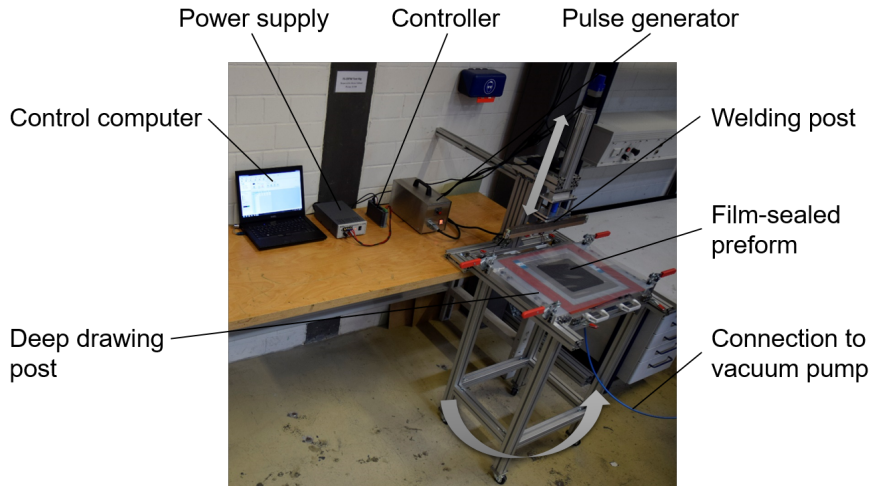


Fig. A-24 Components of the film-sealing station for preforms. [26]

At the beginning of the film-sealing process, a lower film sheet of 670 mm \times 420 mm is spanned on the deep drawing post. The film is then manually heated via a hot air gun while vacuum is applied below the film, deep drawing it into a negative form in the shape of the cavity of the flow visualization test rig. The preform is then placed on top of the lower film inside the cavity. The exact central positioning of the preforms for experiments with race-tracking channels is realized via 3D-printed spacer blocks placed between preform edge and deep drawn film at the cavity wall. Small 5 mm \times 5 mm squares of double backed tape [214] are applied near the preform edges as illustrated in Figure A-25 to affix the preform in its central position as well as to prevent any lift-off and flushing of the preform. To minimize a disturbed observation of the preform impregnation, the fixation points are placed above the stiffening structure of the lower cavity section not visible in the later post-processing of the flow visualization experiments. After covering the lower film and positioned preform with an upper film sheet, the two films are sealed on all four sides via impulse welding.

The film-sealing station is designed to adjust and control the pressure and heat application during the welding process [215]. Teflon films are placed between the thermoplastic films at the locations where the inlet and vent hose are later bonded via sealant tape [216]. An inlet passage is created to prevent lateral outflow of the fluid inside the film-sealed preform package between inlet hose location and injection gap. The inlet passage is realized by manually welding the films on both sides of the inlet and sealing the section on top of the fluid transition zone with

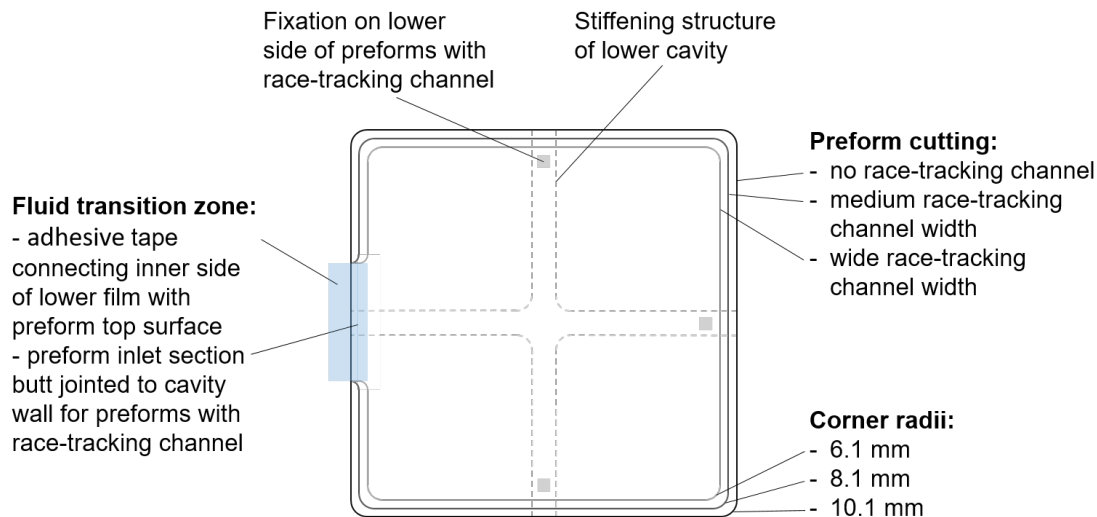


Fig. A-25 Schematic illustration of preform shapes including fluid transition zone and preform fixation on lower side of preforms with a race-tracking channel. [26]

sealant tape. To ensure a complete evacuation of the preform, a cord is threaded through the vent hose and fixed on the lower film connecting the vent with the preform. All features and components of the film-sealed preform package are shown in Figure A-26.

Preliminary tests exhibited severe fiber washout at the inlet section of the tested preform. The upper layers of the preform are pushed back or even flipped, which may lead to a disturbed fluid flow and increased compression forces due to a locally increased FVF. The cause of the fiber washout was traced back to the lateral inlet design. The fluid is guided inside the film-sealed preform package over the edge section of the lower cavity hitting the protruding layers of the uncompressed preform. To prevent fiber washout, a fluid transition zone of 60 mm width was implemented as illustrated in Figure A-25. Adhesive tape [217] was applied connecting the inner side of the lower film to the top surface of the preform guiding the fluid flow and preventing preform washout at the inlet section. For preforms of the factor-response study (Chapter 6.3) and the race-tracking study (Chapter 7), the overlap was determined to be 4 mm wide to balance a minimal disturbance of the through-thickness preform impregnation and sufficient tape adherence to prevent tape separation during preform and test preparation. For preforms of the flow control study (Chapter 7), the tape overlap of the transition zone was increased to 9 mm, representing the width of the pre-compacted preform edge. The impermeable character of the tape was intentionally used during the flow control study to avoid an impregnation of the preform edge during the injection and therefore simulate a direct injection into the isolated central injection gap. Due to the design

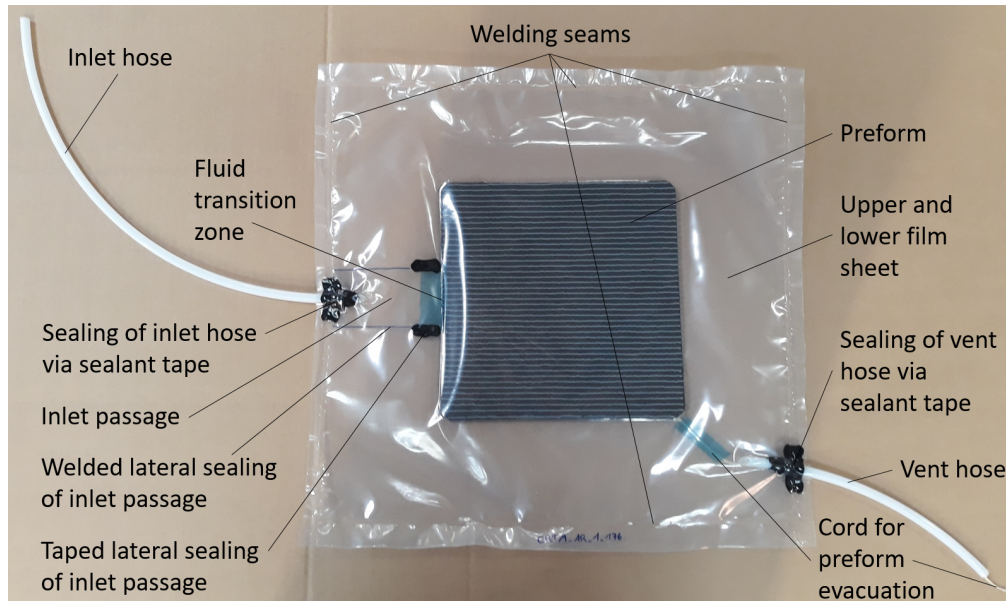


Fig. A-26 Features and components of a film-sealed preform package. [26]

of the test rig, the fluid can only be injected laterally, whereas, and hence, the intended central injection for some of the experiments in Chapter 7, as indicated in Figure 7-1(c), is simulated via a direct, lateral injection into the central injection gap created by the fluid transition zone and the applied impermeable tape in the section of the pre-compacted preform edge. The concept of a fluid transition zone was adapted to the experiments with a race-tracking channel by cutting the preforms to butt joint the cavity wall at the inlet over a width of 60 mm, neighboring the circumferential race-tracking channel as illustrated in Figure A-25.

A.4.2 Flow Visualization Setup⁶

A novel test rig was developed to perform the flow visualization experiments for the FS-CRTM process. Figure A-27 shows the test rig with its three main components: injection unit, cavity unit, and the control and data acquisition unit. The flow visualization test rig was designed to study the injection and compression phase of the FS-CRTM process on a laboratory scale [218]. A transparent mold design enables the preform impregnation on its top and bottom side to be observed. Sensors recording injection pressure, compression force, and tool gap height history facilitate the comprehensive investigation of the FS-CRTM process. A schematic depicting the test rig with its tubing and wiring is shown in Figure A-28. Addi-

⁶ This subsection has been previously published in [26].

tionally, Tables A-4 and A-5 list the manufacturers and types for all purchased components and sensors.

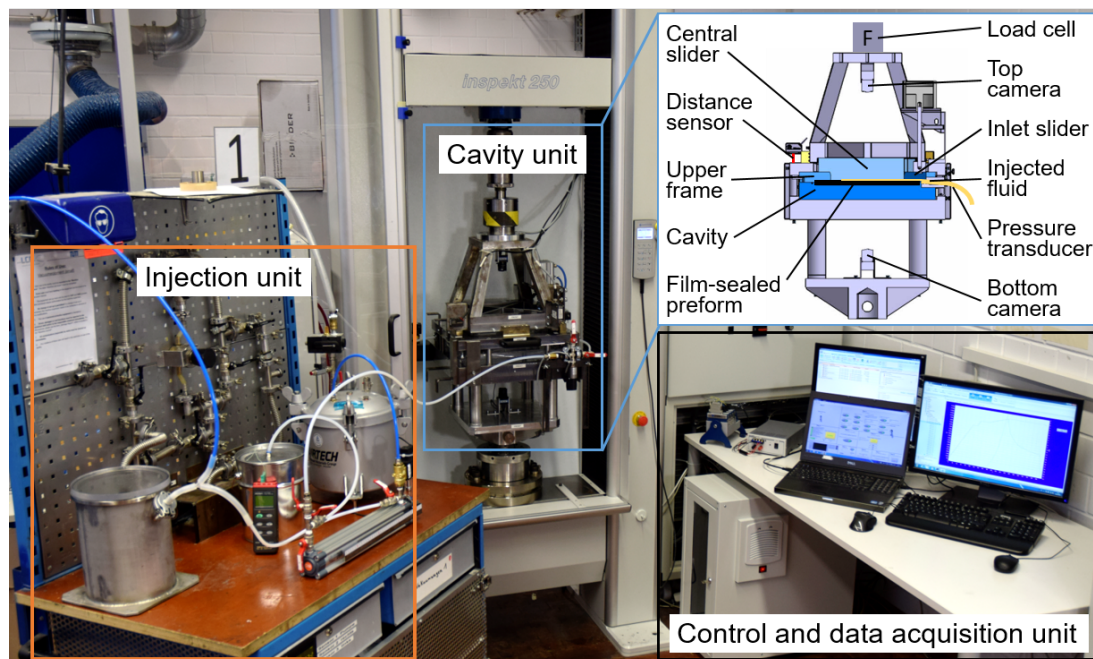


Fig. A-27 Flow visualization test rig grouped in its three main units. Inset on top right illustrates the cavity unit with labeling of its main components and sensors. [26]

The injection unit is designed to evacuate the preform to a defined pressure level and facilitate the injection of a constant fluid volume at a controlled pressure. Its main actuators are a vacuum pump and a pressure pot with the pneumatic-hydraulic converter (PHC), with the latter being a central component for this experimental setup. A system of tubes and valves ensures the PHC and all tubing between the PHC and the mold are filled with fluid prior to an experiment (see Figure A-28). Transparent tubing is used to allow visual control of a bubble-free filling. Tubes and PHC are filled shortly before every experiment with fluid from a temperature-controlled reservoir to ensure comparable fluid viscosities between the experiments. The PHC is equipped with an adjustable limit stop to manually set the volume of injected fluid with high reproducibility. The injection process is controlled and automated via a LabVIEW program (National Instruments Corp., Austin, TX, USA) that regulates the pressure applied to the PHC and opens and closes the inlet slider of the cavity [185, 219].

The preform impregnation takes place inside the cavity unit, which contains all of the main sensors to monitor the flow visualization experiment. The film-sealed preform package is placed in the transparent cavity and connected to the inlet and vent hoses of the injection unit. The cavity is designed to accommodate planar preforms of different in-plane and thickness dimensions by using different inlay spacers

[218]. The transparent upper tool, made of polymethylmethacrylate (PMMA), is composed of three components as seen in the sectional drawing in Figure A-27. It consists of a circumferential upper frame that compresses the outer film layers and pre-compacts the preform edge depending on the preform size. Inside the upper frame, the central slider can be moved vertically to create the active tool movement during the FS-CRTM process. The injection of the fluid is created via a lateral inlet, which is opened by the inlet slider, which is a movable 40 mm wide section of the upper frame. The cavity, upper frame, and central slider are stiffened by steel structures to minimize their deformation, thus resulting in local fiber volume changes inside of the transparent tool. The stiffening structure of the lower cavity is affixed to the lower, static portion of the universal testing machine (UTM), see Figure A-27. The upper frame and cavity are bolted together via their stiffening structures, and the inlet slider and its pneumatic actuator are attached to the stiffening structure of the upper frame. The central slider and its stiffening structure are connected to the movable crosshead of the UTM. Two cameras are mounted inside the stiffening structures of the central slider and lower cavity to monitor the preform impregnation. The injection pressure is logged via a pressure transducer in the feeding line of the inlet. The force applied to the central slider is recorded via the load cell of the UTM to enable the force history during the compression phase of the process to be recorded. Two laser triangulation sensors (LTS) record the gap height by measuring the distance between the stiffening structures of the movable central slider and the static upper frame.

The control and data acquisition unit is split in two parts, separately controlling the injection and compression phase of the FS-CRTM process. A detailed process control sequence is established and semi-automated via a LabVIEW program in which fluid injection is initiated by the operator and afterwards performed autonomously [185, 219]. Visible and acoustic signals at the end of the injection phase indicate to the operator to start the automated closure sequence of the central slider via the control software of the UTM, LabMaster (Hegewald & Peschke, Nossen, Germany). The established process control sequence enables a reproducible FS-CRTM process in which the idle time between the two manually initiated phases is reduced to only a fraction of the process time, specifically 0.5 s (SD =0.2) for all experiments of Chapter 7. Data acquisition from all main sensors is implemented into the LabVIEW program except for the force recording, which is recorded via LabMaster.

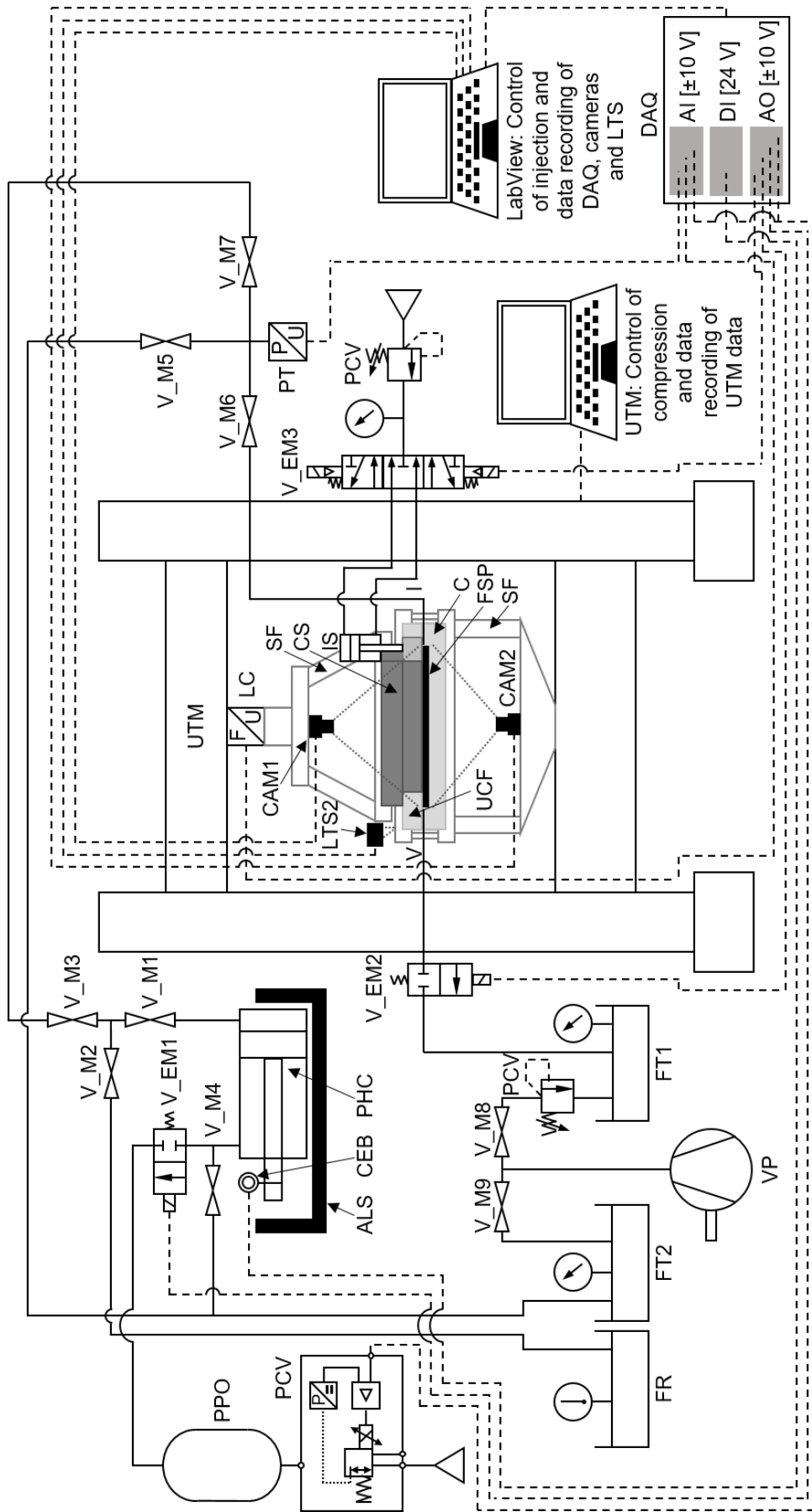


Fig. A-28 Schematic of flow visualization test rig. For a list of abbreviations and further details, see Tables A-4 and A-5. [26]

Tab. A-4 List of abbreviations (I / II) and further details on flow visualization setup of Figure A-28. [26]

Abbreviation	Name	Manufacturer	Type
ALS	Adjustable limit stop	-	-
AI	Analogue input	National Instruments	NI 9201
AO	Analogue output	National Instruments	NI 9236
C	Cavity (optically transparent)	-	-
CAM1 / 2	Industrial cameras with fish eye lens	- CAM1 / 2: The Imaging Source - Lens: computar	- CAM1: DMK 22AUC03 - CAM2: DMK 27AUR0135 - Lens: T2314FICS-3
CEB	Converter-empty button	-	-
CS	Central slider (optically transparent)	-	-
DAQ	Data acquisition unit	National Instruments	NI cDAQ™-9174
DI	Digital input	National Instruments	NI 9421
FR	Fluid reservoir	-	-
FT1/2	Fluid trap	-	-
FSP	Film-sealed preform package	-	-
I	Inlet	-	-
IS	Inlet slider incl. actuator LINER	- Actuator: Riegler	- Actuator: Kompaktzylinder ISO 21287 Ø 80 250 kN (10-003-327) optoNCDT ILD1302-50
LC	Load cell	Hegewald & Peschke micro-epsilon	VP5010BJ111H00
LTS1 / 2	Laser triangulation distance sensor	IMI Norgren	Zylinder ISO 15552 Ø 32 - 125 mm
PCV	Pressure control valve	IMI Norgren	psibar 1200 Series
PHC	Pneumatic-hydraulic converter	Riegler	-
PPO	Pressure pot	Airtech	-
PT	Pressure transducer	Gems	-
SF	Stiffening structure	-	-
UCF	Upper cavity frame	-	-

Tab. A-5 List of abbreviations (II / II) and further details on flow visualization setup of Figure A-28. [26]

Abbreviation	Name	Manufacturer	Type
UTM	Universal testing machine	Hegewald & Peschke	Inspekt 250 kN
V	Vent	-	-
V_M1 - 9	Manual valves	-	-
V_EM1 - 3	Electro-magnetic valves	- V_EM1: AirTAC - V_EM2: ODE - V_EM3: METAL WORK	- V_EM1: 2W050-15 - V_EM2: 21A2KT30 - V_EM3: 7010022200
VP	Vacuum pump	Oerlikon Leybold Vacuum	TRIVAC D25BCS

A.4.3 Experimental Procedure⁷

The experimental procedure of the flow visualization experiments is divided into three phases: preparatory work, experiment execution, and data post-processing. At the beginning of the preparatory work, the limit stop of the PHC is adjusted to the predefined fluid volume of the test series. The correct setting is checked by filling and metering the PHC five times prior to each test series. Afterwards, the limit stop setting is kept constant throughout the test series to ensure a reproducible injected fluid volume for each experiment. In the next step, the film-sealed preform package is evacuated to the desired vent pressure of the experiment and its thickness is measured. By knowing the thickness of the film-sealed preform package, the gap height of the central slider is calculated and entered into the control sequence for the central slider movement in the LabMaster software. Adjusting the gap height for each experiment of the test series ensured a constant injection gap between preform top side and the central slider. The injection pressure is adapted by defining the pressure inside the pressure pot via the LabVIEW program. The pressure pot level is set to an increased value to compensate for pressure losses inside the tubes and the PHC. Further, the cavity is adjusted to fit to the preform dimensions of the test series. First, the cavity height is adjusted by placing a transparent inlay plate. A thin layer of glycerin is applied between cavity bottom wall and inlay plate to improve the image quality for the lower camera. Second, inlay frames are inserted to adapt the cavity to the in-plane dimensions of the preform. Once the cavity is prepared, the film-sealed preform package is connected to the tubes of the injection unit, evacuated to the desired vent pressure of the experiment and placed inside the cavity. Special care is taken to precisely place the preforms for experiments with a race-tracking channel. First, the transition zone at the inlet section of the preform is butt joined to the inlay frame defining the race-tracking channel at the inlet and vent side. Second, an equal lateral race-tracking channel space is adjusted with the aid of 3D-printed spacers. The latter are removed after the preform was positioned. Now, the upper frame is placed by positioning it relative to both sliders to ensure smooth sliding during their vertical movements. The lighting conditions are checked and adjusted before each experiment to ensure a consistent high-quality process observation on the top and bottom side of the preform. Finally, the PHC and all tubes between the PHC and the inlet slider are evacuated and filled with fluid. In contrast to the fluid reservoir, the PHC and tubes are not temperature-controlled which is why this step was executed last in the preparatory work to minimize the time the fluid is exposed to a potential difference between defined fluid temperature and ambient temperature.

⁷ This subsection has been previously published in [26].

The actual flow visualization experiment is executed by launching the LabVIEW program, recording all sensor and camera data. Subsequently, the LabMaster program is started, which performed the lowering of the central slider to the gap height for the experiment. After double-checking the correctness of all set process parameters and the recording of all relevant data, the operator starts the fluid injection in LabVIEW. At the end of the injection, optical and acoustic signals indicate to the operator to initiate the closing sequence using the LabMaster program. LabMaster is programmed to move the central slider either at a constant closing speed until a pre-defined final closing position is reached or at a constant closing speed until a maximum force limit is reached at which point the closing speed is reduced to keep the force level constant until a pre-defined final closing position is reached. The closing sequence is held in the final closing position until the operator actively terminates the experiment after complete filling of the preform or a defined time.

The final phase, data post-processing, involves the following tasks. A data post-processing script was programmed using the software MATLAB[®] (MathWorks, Natick, MA, USA) [185, 220]. In a first step, the raw data files recorded by the LabVIEW and LabMaster programs are merged into a single dataset. The latter is combined with important process characteristics and calculated response data into a single output file. In a second step, images captured by the cameras during testing are post-processed to identify the flow front progression during the different phases of the FS-CRTM process and to calculate the area filling ratio (AFR) history for the race-tracking channel as well as for the top and bottom side of the preform. The AFR represents the filling of the preform surface excluding (i) the preform section that is hidden by the stiffening structures and (ii) the fluid transition zone of experiments with race-tracking channels. Due to limitations of the used post-processing algorithm, flow front features involving sharp corners (i.e. a non-differentiable point on a curve) cannot be detected. The diagonal stiffening structure on the preform top side introduces such features, and hence, complete filling of the preform top side is defined as a maximum AFR of approximately 97%. Calculating the AFR of the race-tracking channel proved to be challenging using the chosen methodology. While 80% to 90% of the channel area could be analyzed for experiments with medium race-tracking channel width, only a channel area approaching 50% could be assessed for experiments with the wide channel width in Chapter 7. Reasons for these challenges are optical artifacts caused by the reflective and translucent nature of the test fixture and disturbed lighting when the glycerin film below the PMMA inlay is disturbed. These issues can lead to AFR values below 100% and temporal reductions in the AFR progression for the race-tracking channel, which is physically incorrect. Consequently, any AFR data for the race-tracking channel must be interpreted with caution. Even so, qualitative information about the point

in time at which the race-tracking channel was filled, was verified manually and was therefore included in the analysis of Chapter 7.

A.5 Appendix of Characterization of the FS-CRTM Process

A.5.1 Film Specification for FS-CRTM

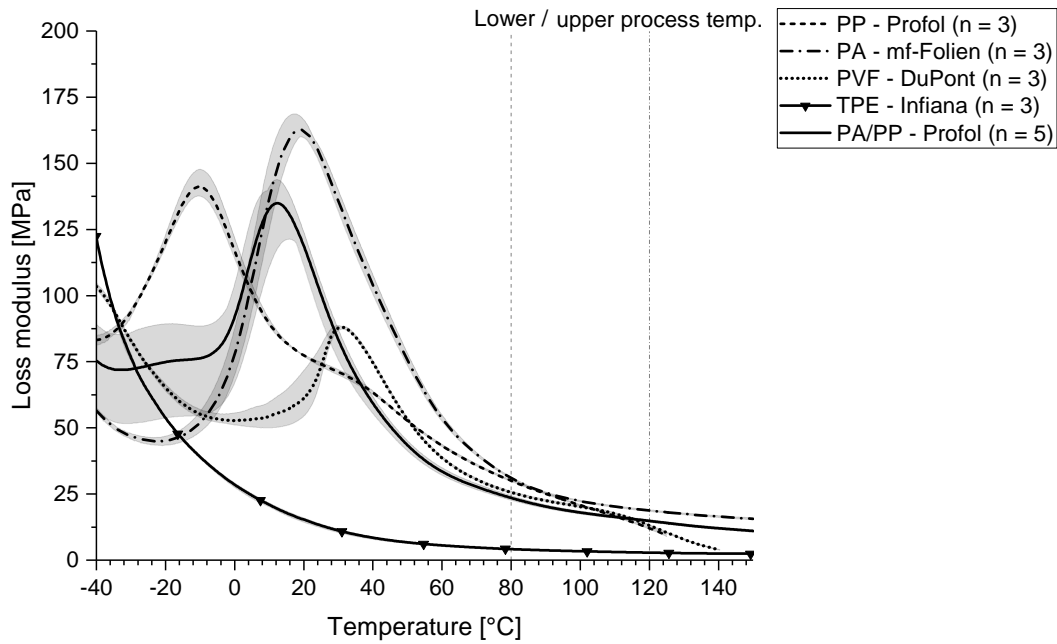


Fig. A-29 Loss modulus of monolayer films and PA/PP multilayer film (shown as average in black as well as spread between maximum and minimum measured values in gray).

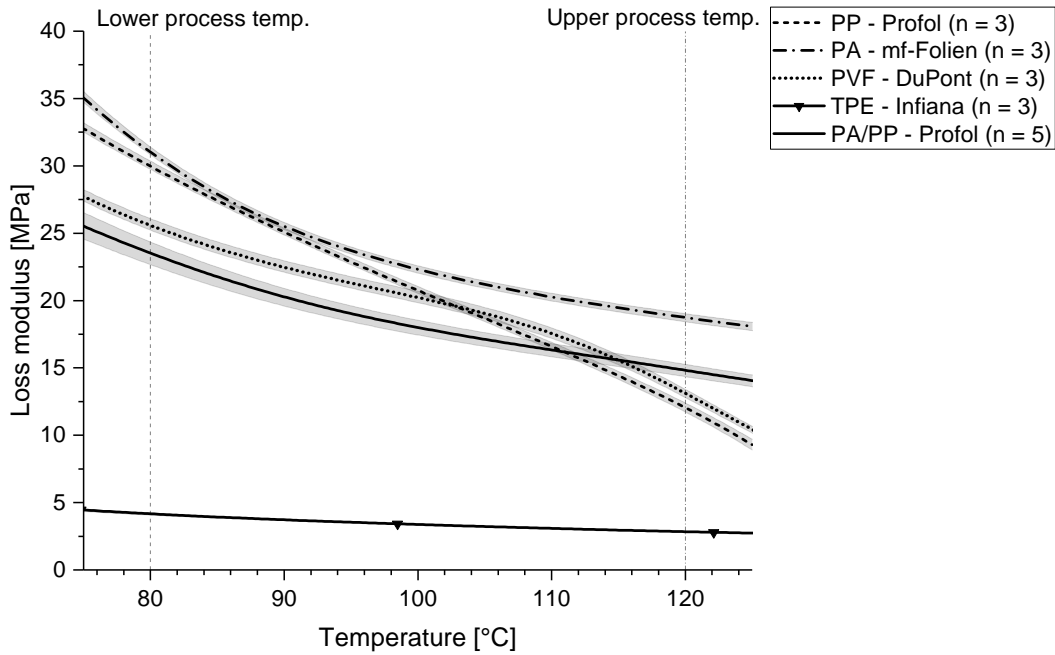


Fig. A-30 Loss modulus of monolayer films and PA/PP multilayer film - zoom in at process temperature range of FS-CRTM process (shown as average in black as well as spread between maximum and minimum measured values in gray).

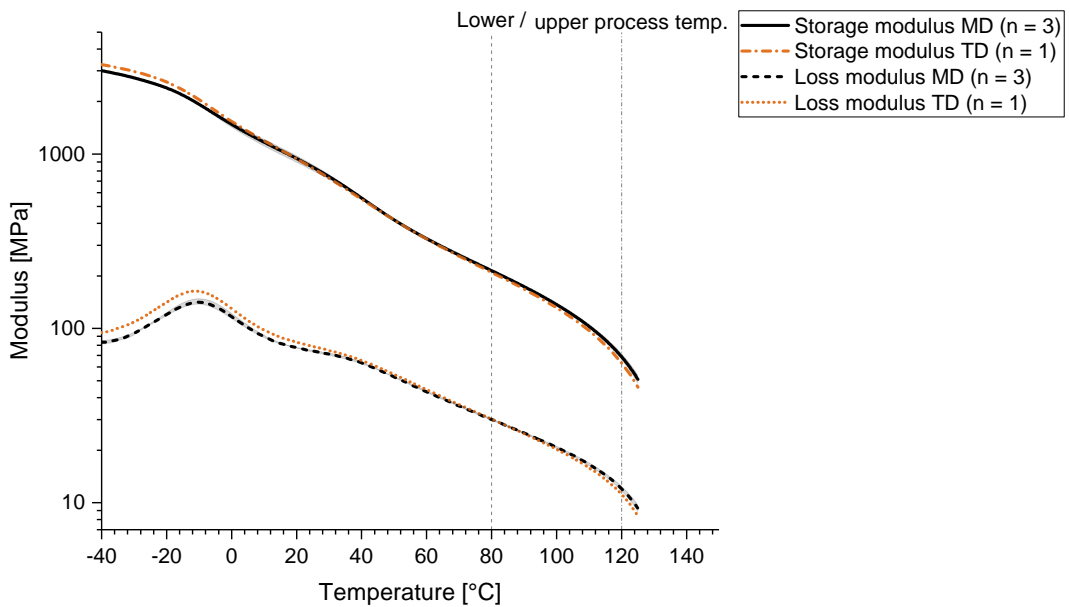


Fig. A-31 Storage and loss modulus of PP monolayer film manufactured by Profol - machine direction (MD) vs. transversal direction (TD) (shown as average in black as well as spread between maximum and minimum measured values in gray).

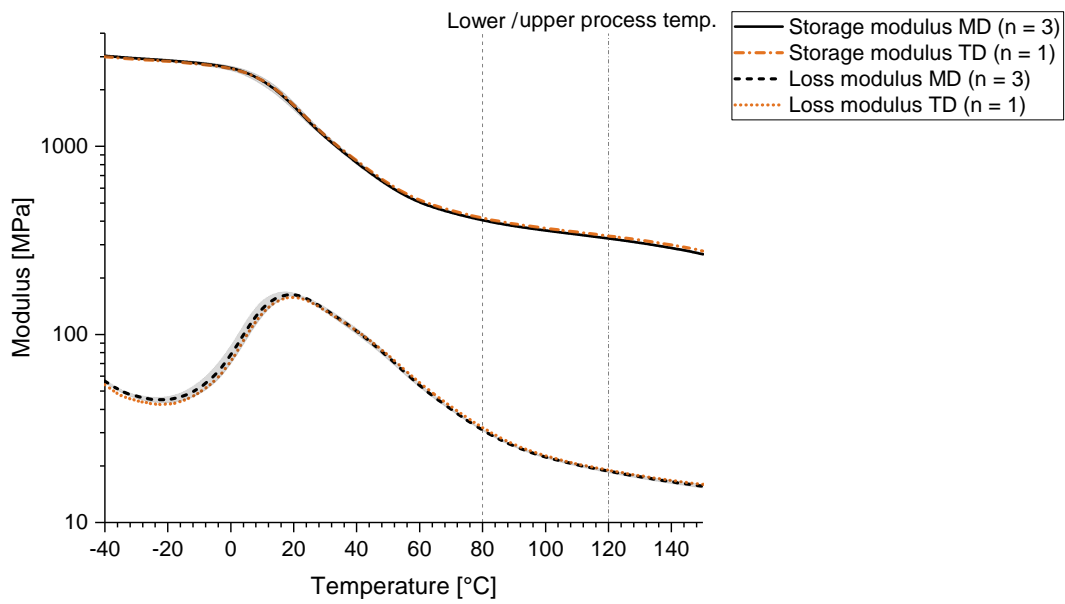


Fig. A-32 Storage and loss modulus of PA monolayer film manufactured by mf-Folien - machine direction (MD) vs. transversal direction (TD) (shown as average in black as well as spread between maximum and minimum measured values in gray).

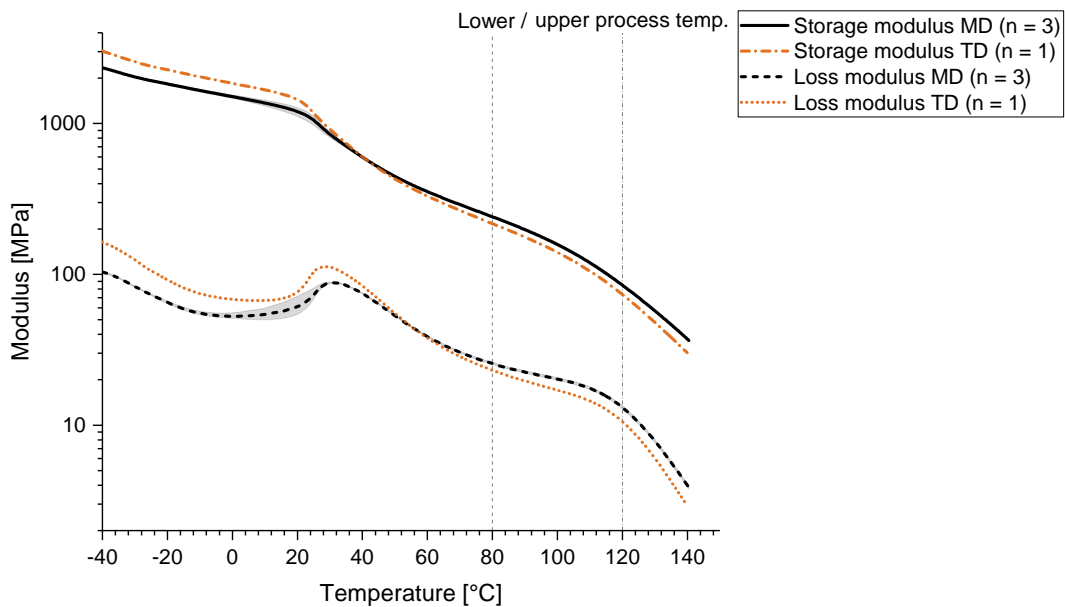


Fig. A-33 Storage and loss modulus of PVF monolayer film manufactured by DuPont - machine direction (MD) vs. transversal direction (TD) (shown as average in black as well as spread between maximum and minimum measured values in gray).

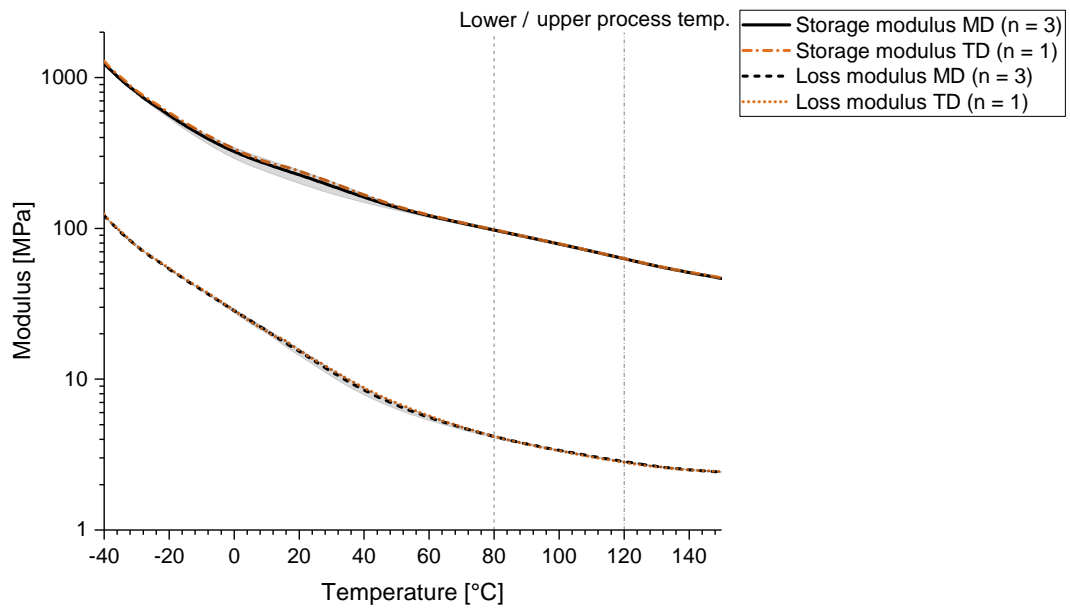


Fig. A-34 Storage and loss modulus of TPE monolayer film manufactured by Infiana - machine direction (MD) vs. transversal direction (TD) (shown as average in black as well as spread between maximum and minimum measured values in gray).

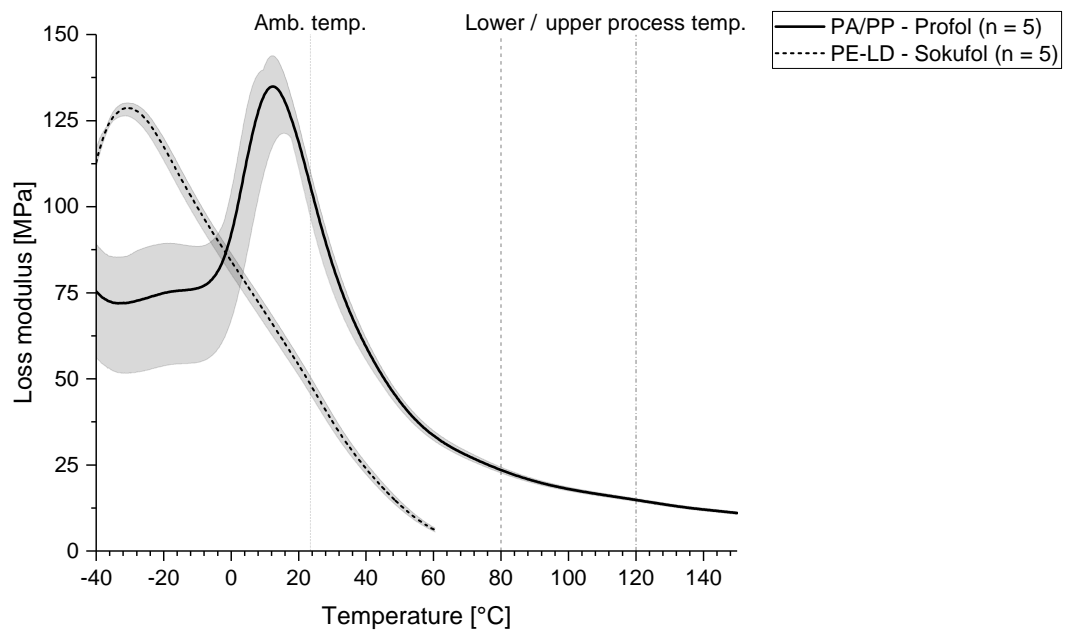


Fig. A-35 Loss modulus of PA/PP multilayer film for FS-CRTM at process temperature of 80 °C to 120 °C and substituting PE-LD film for FS-CRTM flow visualization experiments at ambient temperature (Amb. temp.) (shown as average in black as well as spread between maximum and minimum measured values in gray).

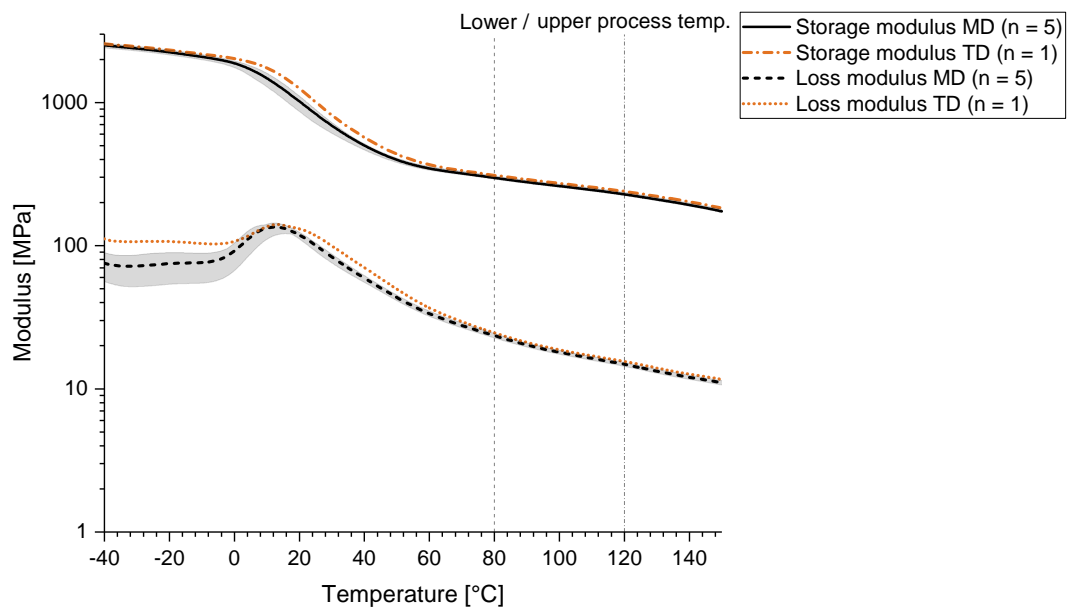


Fig. A-36 Storage and loss modulus of PA/PP multilayer film manufactured by Profol - machine direction (MD) vs. transversal direction (TD) (shown as average in black as well as spread between maximum and minimum measured values in gray).

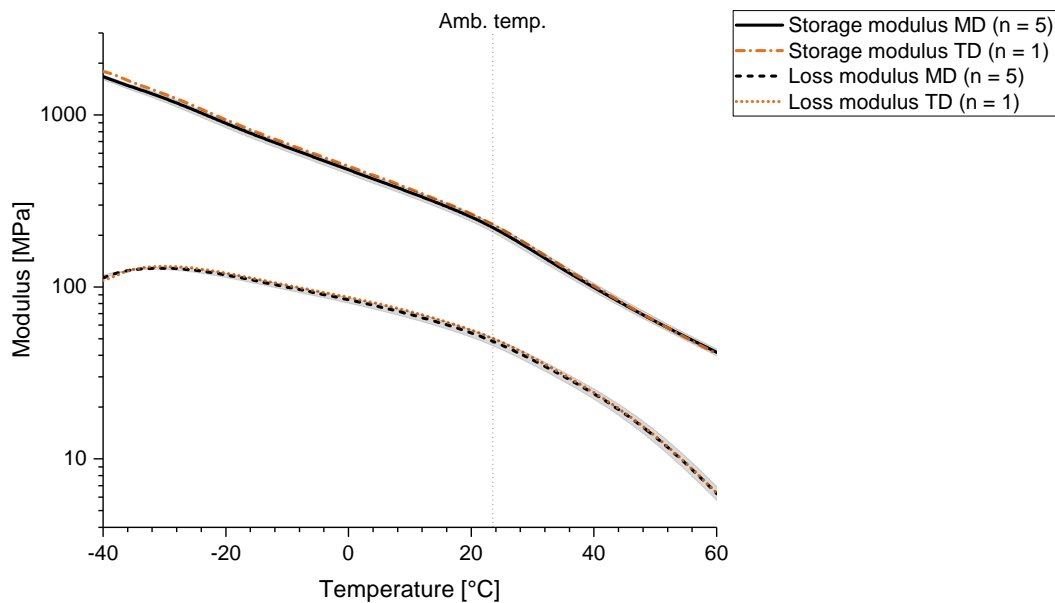


Fig. A-37 Storage and loss modulus of PE-LD monolayer film manufactured by Sokufol - machine direction (MD) vs. transversal direction (TD) (shown as average in black as well as spread between maximum and minimum measured values in gray).

A.5.2 Unrestrained Film Deformation Experiments

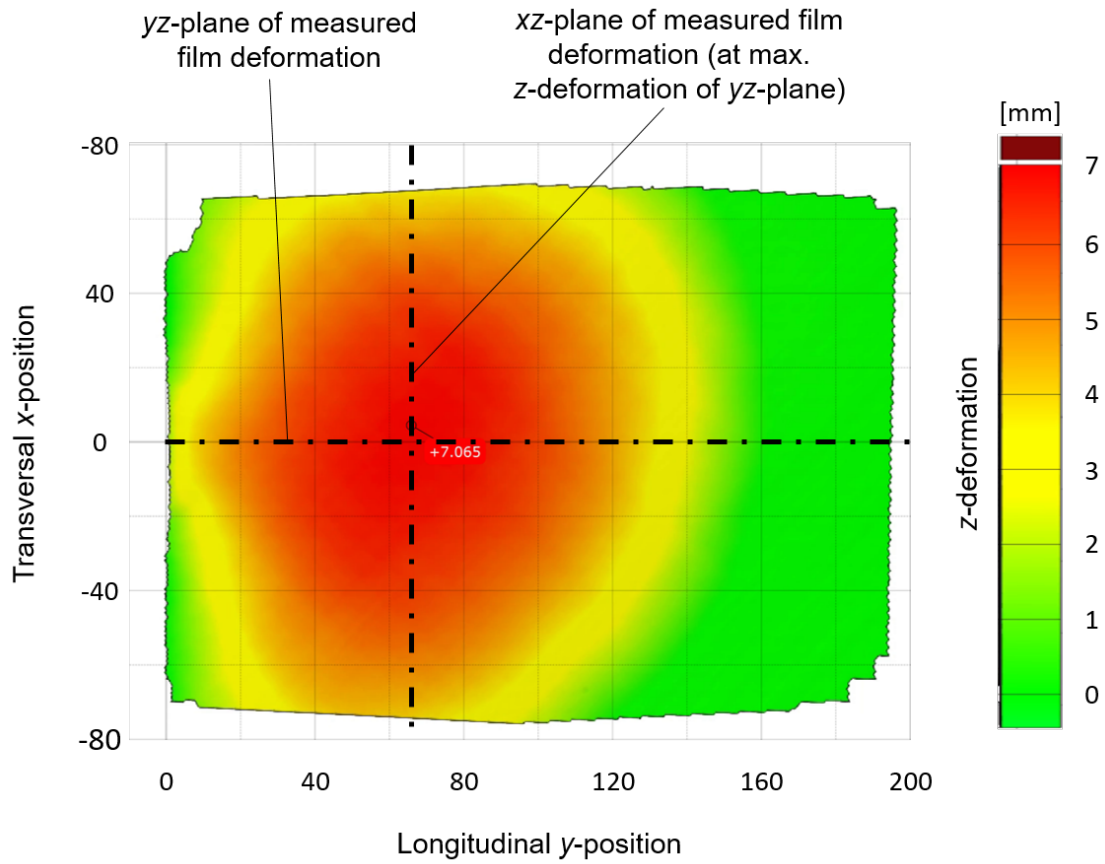


Fig. A-38 Three-dimensional z-deformation of ARAMIS measurement area of experiment #6 at injection end. cf. [185]

Tab. A-6 Preform data and process factors of the FS-CRTM experiments with unrestricted film deformation.

Experiment number and run order	Preform weight [g]	Injected fluid volume ^I [ml]	Viscosity of fluid ^{II} [mPas]	Pot pressure ^{III,IV} [kPa]	Vent pressure ^{III} [kPa]
1	164.5	123.9 (<i>SD</i> = 0.7)	61.0	344.9 (<i>SD</i> = 2.4)	-52
2	164.4	123.9 (<i>SD</i> = 0.7)	60.3	337.6 (<i>SD</i> = 1.7)	-99
3	164.2	123.9 (<i>SD</i> = 0.7)	59.3	585.5 (<i>SD</i> = 2.1)	-52
4	164.3	123.9 (<i>SD</i> = 0.7)	63.7	337.9 (<i>SD</i> = 2.0)	-52
5	165.0	123.9 (<i>SD</i> = 0.7)	65.1	337.4 (<i>SD</i> = 2.5)	-5
6	164.4	123.9 (<i>SD</i> = 0.7)	58.8	338.7 (<i>SD</i> = 1.9)	-52
7	164.0	123.9 (<i>SD</i> = 0.7)	62.6	87.4 (<i>SD</i> = 2.0)	-52

^I Mean and standard deviation (*SD*) of five metered and measured injections prior to the test series – manual injection piston setting (no limit stop). ^{II} Viscosity of fluid (sunflower oil) measured on a Modular Compact Rheometer (MCR) 302 of Anton Paar (Graz, Austria) with a cone-plate system (CP25-1) at specific temperature of experiment and shear rate of 100 s⁻¹ (see Chapter A.1.1). ^{III} Differential value relative to ambient pressure. ^{IV} Mean and *SD* measured during the injection phase of the experiment.

Tab. A-7 Process responses of the FS-CRTM experiments with unrestricted film deformation.

Experiment number and run order	Injection time [s]	Median injection pressure [kPa]	Maximum deformation of film in z -direction [mm]	Maximum velocity of film in z -direction [mm/s]	Minimum velocity of film in z -direction [mm/s]
1	3.8	64.4	7.2	20.5	-6.8
2	3.9	67.8	7.5	21.4	-5.8
3	2.3	111.2	7.1	22.6	-5.9
4	3.7	69.6	7.1	18.0	-5.3
5	3.9	69.3	9.0	18.0	-8.9
6	3.8	71.1	7.0	21.3	-5.4
7	18.8	28.9	8.0	12.8	-5.0

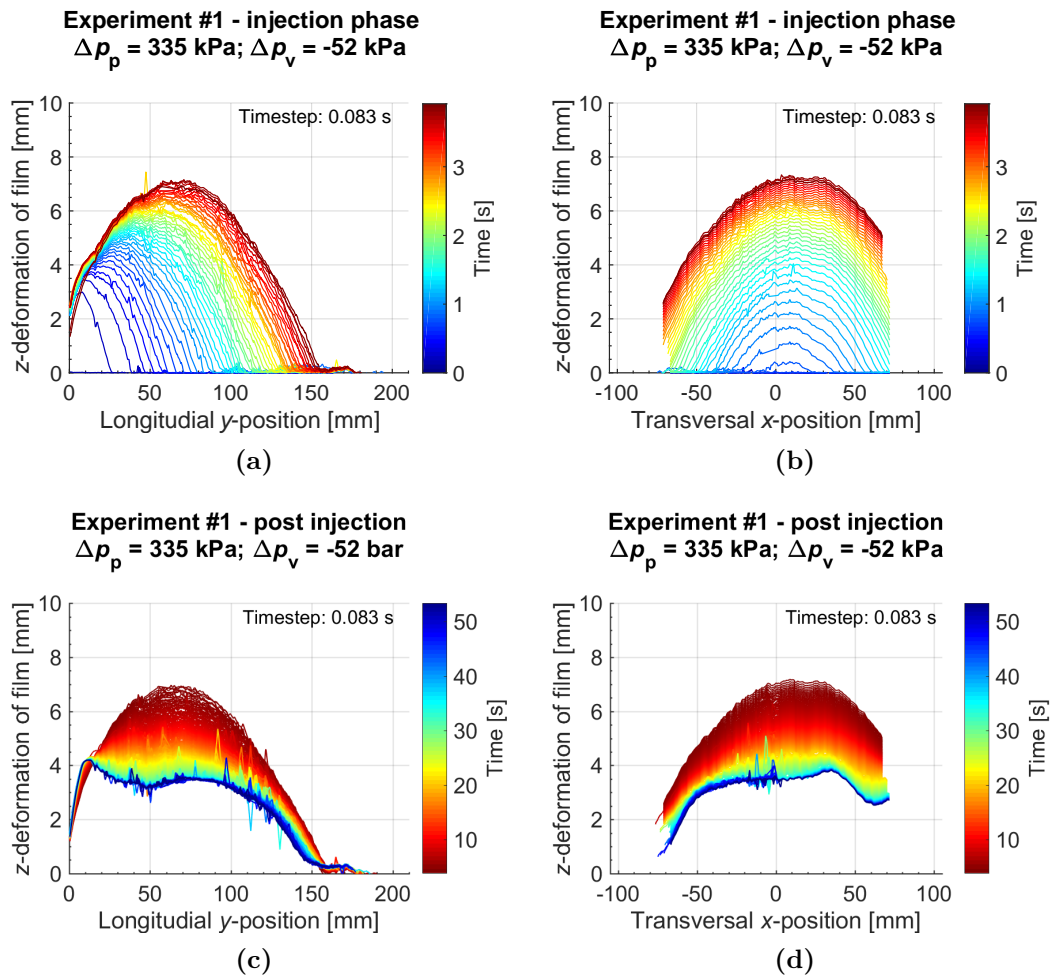


Fig. A-39 Illustration of the three-dimensional film deformation of experiment #1 over time during injection (top row) and after injection (bottom row) – depicted in the longitudinal yz -plane at the center of the inlet at $x = 0$ (left column) and at the transversal xz -plane at $y_{max} = 71.0 \text{ mm}$, position of maximum z -deformation recorded in the yz -plane (right column). cf. [185]

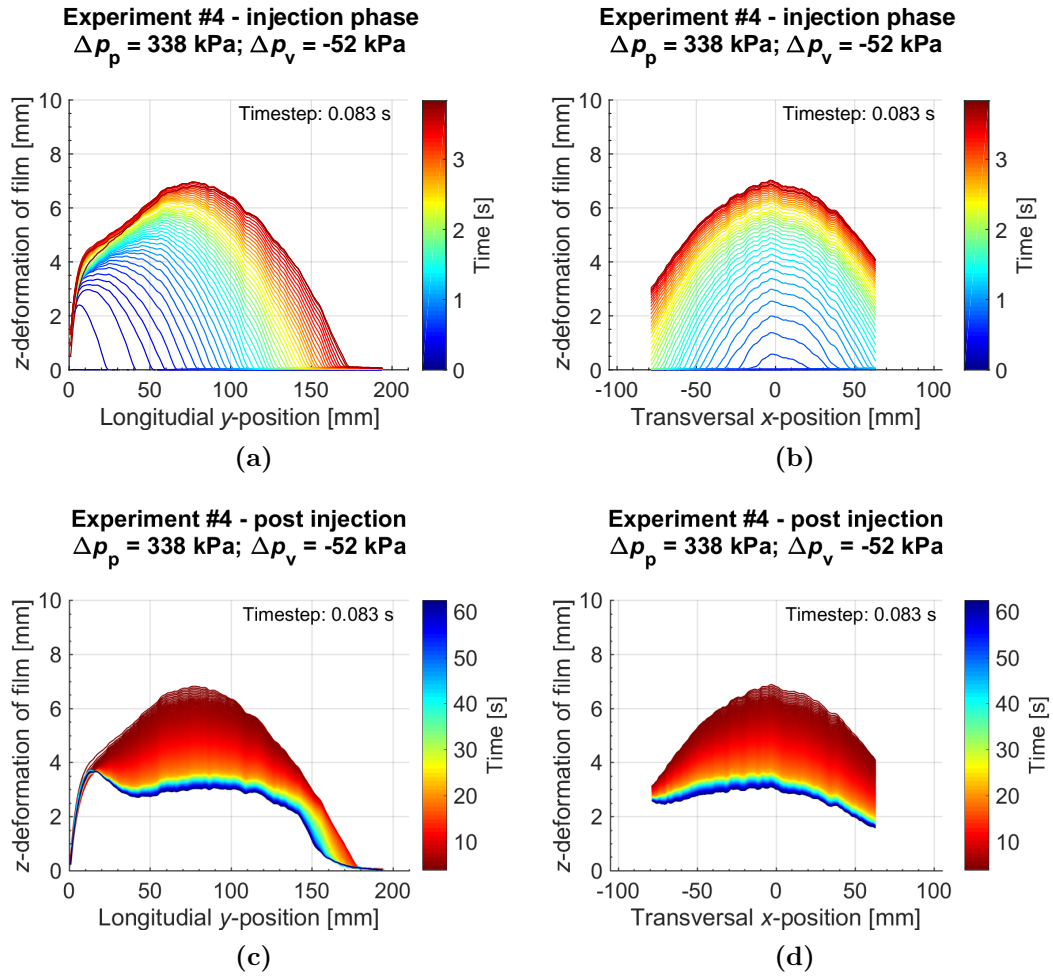


Fig. A-40 Illustration of the three-dimensional film deformation of experiment #4 over time during injection (top row) and after injection (bottom row) – depicted in the longitudinal yz -plane at the center of the inlet at $x = 0$ (left column) and at the transversal xz -plane at $y_{max} = 75.0 \text{ mm}$, position of maximum z -deformation recorded in the yz -plane (right column). cf. [185]

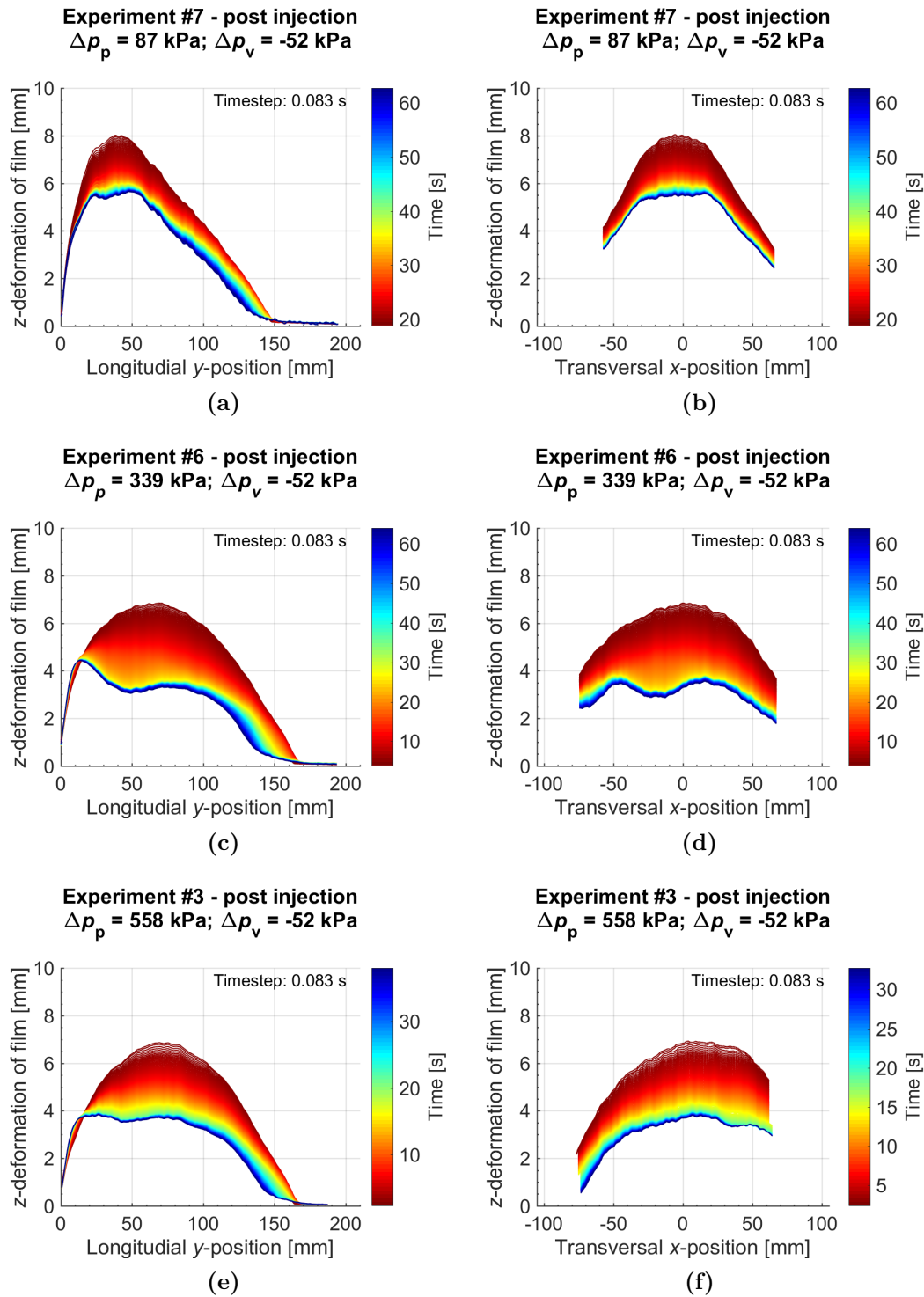


Fig. A-41 Effect of injection pressure variation on the out-of-plane film deformation after injection – depicted in the longitudinal yz -plane at the center of the inlet at $x = 0$ (left column) and at the transversal xz -plane position of maximum z -deformation recorded in the yz -plane at $y_{max}(\#7) = 38.1 \text{ mm}$, $y_{max}(\#6) = 70.6 \text{ mm}$ and $y_{max}(\#3) = 75.0 \text{ mm}$ (right column). cf. [185]

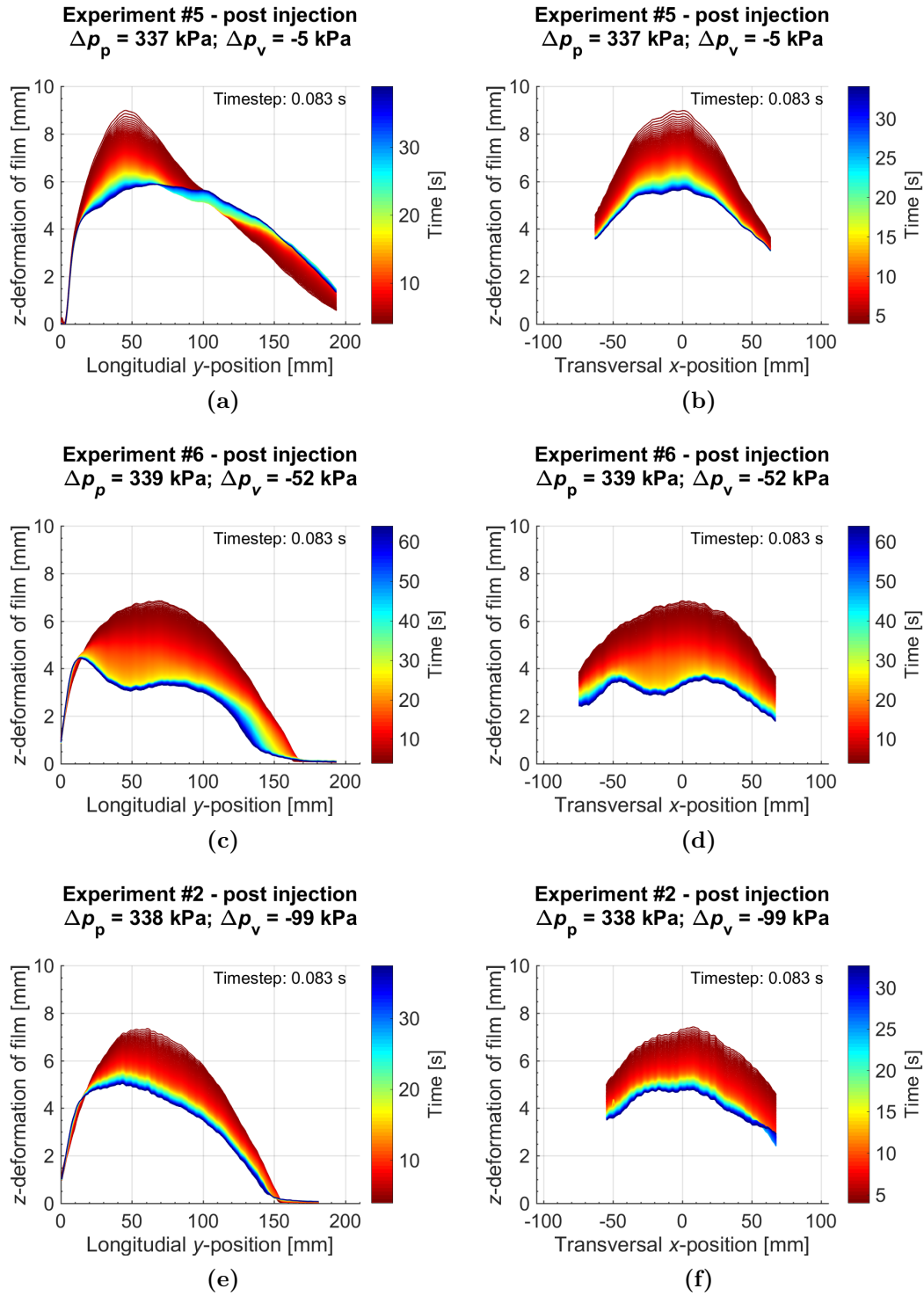


Fig. A-42 Effect of vent pressure variation on the out-of-plane film deformation after injection – depicted in the longitudinal yz -plane at the center of the inlet at $x = 0$ (left column) and at the transversal xz -plane position of maximum z -deformation recorded in the yz -plane at $y_{max}(\#5) = 44.8 \text{ mm}$, $y_{max}(\#6) = 70.6 \text{ mm}$ and $y_{max}(\#2) = 60.9 \text{ mm}$ (right column). cf. [185]

A.5.3 Factor-Response Study

Injection Phase

Tab. A-8 Preform data of the factor-response study investigating the injection phase of the FS-CRTM process.

Experiment number and run order	Preform weight [g]	Preform length [mm]	Preform width [mm]
1	167.9	210.6	210.3
2	167.8	210.5	210.4
3	167.6	210.5	210.4
4	167.7	210.5	210.4
5	167.9	210.5	210.4
6	167.6	210.5	210.4
7	167.4	210.3	210.2
8	167.6	210.4	210.2
9	167.7	210.5	210.5
10	168.1	210.5	210.3
11	167.7	210.5	210.4
12	168.1	210.5	210.4
13	167.4	210.4	210.4
14	168.1	210.4	210.5
15	167.9	210.4	210.2
16	168.1	210.7	210.4
17	167.8	210.6	210.4
18	167.5	210.5	210.5
19	167.6	210.3	210.4
20	167.0	210.2	210.2

Tab. A-9 Factors of flow visualization experiments investigating the injection phase of the FS-CRTM process.

Experiment number and run order	Preform thickness at vent pressure of experiment ^I [mm]	Viscosity of fluid ^{II} [mPas]	Pot pressure ^{III,IV} [kPa]	Stagnation pressure ^{III,V} [kPa]	Vent pressure ^{III} [kPa]	Injection gap height [mm]
1	3.8 (<i>SD</i> = 0.1)	49.2	752.8 (<i>SD</i> = 2.2)	599.8	-90.0	0.82
2	3.8 (<i>SD</i> = 0.0)	49.7	751.7 (<i>SD</i> = 1.9)	614.8	-90.0	1.97
3	3.9 (<i>SD</i> = 0.1)	49.5	129.4 (<i>SD</i> = 0.3)	98.7	-90.0	0.81
4	4.0 (<i>SD</i> = 0.1)	50.1	129.7 (<i>SD</i> = 0.3)	98.9	-90.0	1.99
5	4.1 (<i>SD</i> = 0.0)	49.9	440.5 (<i>SD</i> = 1.1)	355.2	-47.5	1.39
6	3.9 (<i>SD</i> = 0.1)	49.7	440.8 (<i>SD</i> = 1.1)	356.5	-47.3	1.40
7	4.3 (<i>SD</i> = 0.0)	49.9	130.4 (<i>SD</i> = 0.2)	94.6	-5.0	0.81
8	4.3 (<i>SD</i> = 0.1)	49.5	129.7 (<i>SD</i> = 0.3)	93.6	-5.2	2.00
9	4.3 (<i>SD</i> = 0.1)	50.5	753.5 (<i>SD</i> = 0.5)	608.2	-5.2	1.99
10	4.5 (<i>SD</i> = 0.1)	50.5	752.3 (<i>SD</i> = 2.0)	604.2	-5.1	0.82
11	4.0 (<i>SD</i> = 0.1)	49.5	440.7 (<i>SD</i> = 1.1)	357.3	-47.5	1.40
12	3.9 (<i>SD</i> = 0.0)	49.7	754.2 (<i>SD</i> = 1.3)	605.0	-90.0	0.82
13	4.0 (<i>SD</i> = 0.1)	49.9	753.9 (<i>SD</i> = 1.1)	604.0	-90.0	1.99
14	3.9 (<i>SD</i> = 0.0)	49.7	129.7 (<i>SD</i> = 0.2)	96.1	-90.0	0.81
15	4.4 (<i>SD</i> = 0.0)	50.1	752.6 (<i>SD</i> = 1.9)	595.5	-5.1	0.82
16	4.7 (<i>SD</i> = 0.1)	49.7	129.4 (<i>SD</i> = 0.3)	96.8	-5.0	0.81
17	4.3 (<i>SD</i> = 0.0)	49.9	129.7 (<i>SD</i> = 0.3)	100.0	-5.0	1.98
18	4.0 (<i>SD</i> = 0.1)	50.1	129.5 (<i>SD</i> = 0.3)	100.3	-90.0	2.00
19	4.5 (<i>SD</i> = 0.0)	49.5	754.0 (<i>SD</i> = 1.9)	614.8	-5.0	1.99
20	4.1 (<i>SD</i> = 0.1)	49.7	440.6 (<i>SD</i> = 1.2)	353.8	-47.5	1.40

^I Mean and standard deviation (*SD*) measured at four points of the preform; ^{II} based on the measured fluid temperature of the experiment the viscosity was measured with a cone-plate measuring system on a Modular Compact Rheometer (MCR) 302 of Anton Paar (Graz, Austria) at a shear rate of 100 s⁻¹ (see Chapter A.1.1); ^{III} differential value relative to ambient pressure; ^{IV} mean and *SD* measured during the injection phase of the experiment; ^V measured by pressure transducer in feeding line of inlet before injection start.

Tab. A-10 Responses of flow visualization experiments investigating the injection phase of the FS-CRTM process.

Experiment number and run order	Injection time	Flow rate of injection	Median injection pressure	Area filling ratio of preform top side at injection end
	[s]	[cm ³ /s]	[kPa]	[%]
1	1.1	71.1	243.2	97
2	1.0	78.1	151.0	83
3	6.0	13.0	36.7	97
4	5.2	15.0	27.8	67
5	1.6	48.9	89.1	97
6	1.6	48.9	90.3	97
7	6.9	11.3	40.5	94
8	5.4	14.5	31.3	72
9	1.1	71.1	166.5	90
10	1.2	65.2	190.5	97
11	1.7	46.0	102.8	97
12	1.2	65.2	200.3	97
13	1.1	71.1	139.6	79
14	6.2	12.6	40.5	97
15	1.2	65.2	212.8	97
16	5.7	13.7	34.8	97
17	5.0	15.6	31.6	78
18	5.1	15.3	27.9	64
19	1.1	71.1	172.4	82
20	1.6	48.9	85.6	97

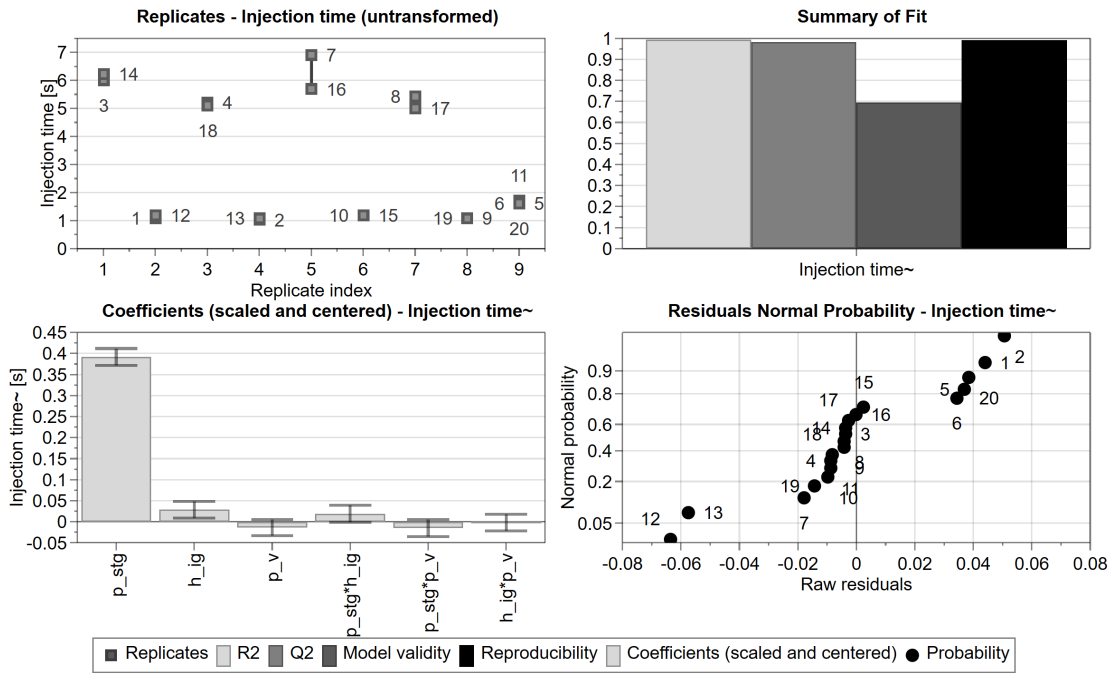


Fig. A-43 Overview plot of response model: injection time (p_stg = stagnation pressure, h_ig = injection gap height, p_v = vent pressure; ~ indicates the transformed model as described in Chapter 6.3.2).

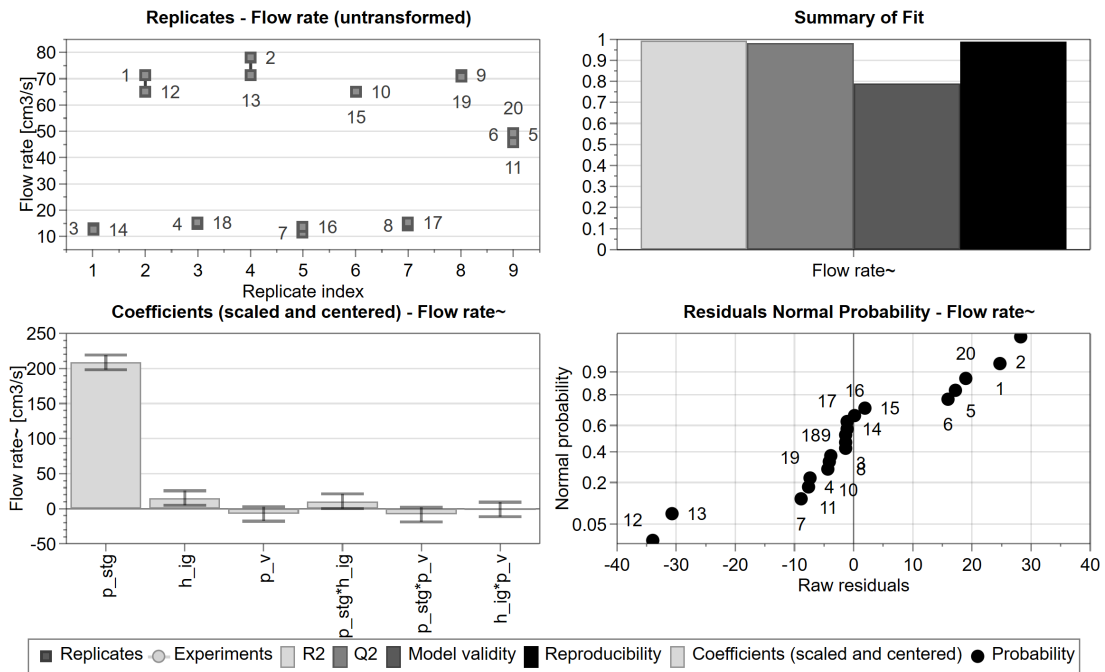


Fig. A-44 Overview plot of response model: flow rate (p_stg = stagnation pressure, h_ig = injection gap height, p_v = vent pressure; ~ indicates the transformed model as described in Chapter 6.3.2).

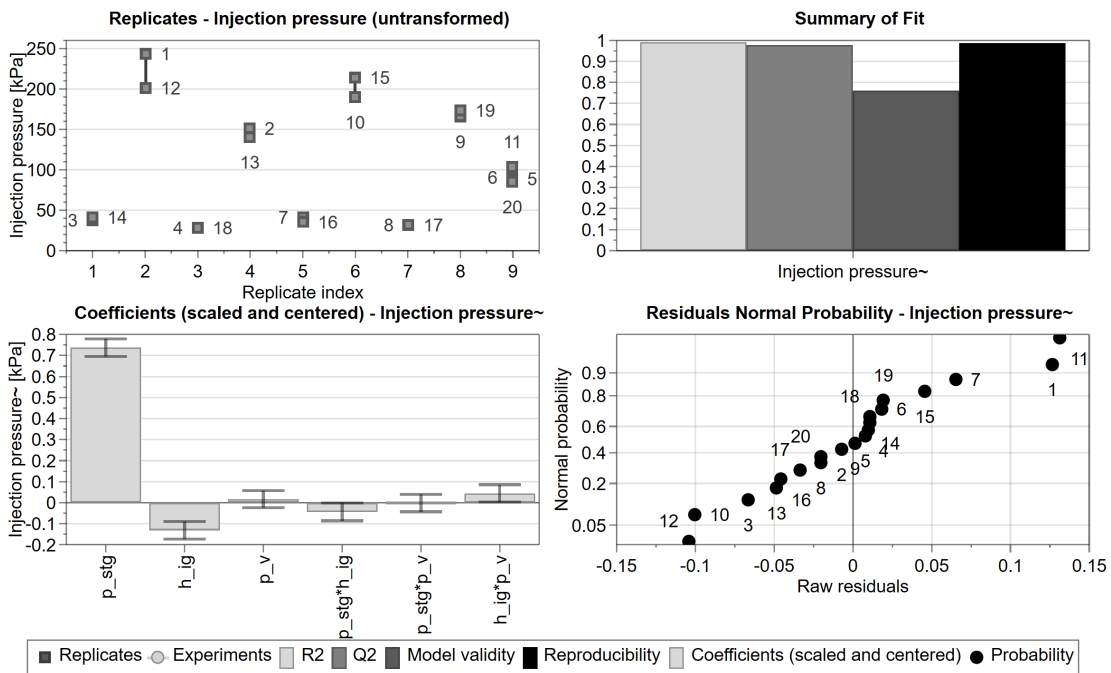


Fig. A-45 Overview plot of response model: injection pressure (p_{stg} = stagnation pressure, h_{ig} = injection gap height, p_v = vent pressure; \sim indicates the transformed model as described in Chapter 6.3.2).

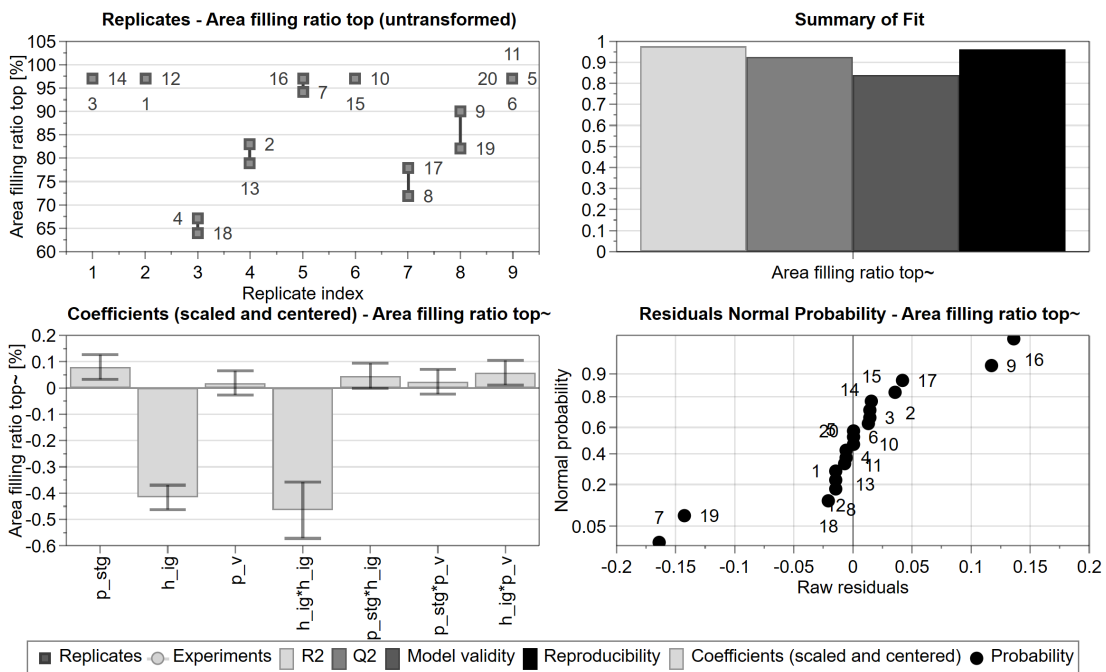


Fig. A-46 Overview plot of response model: area filling ratio on preform top side (p_{stg} = stagnation pressure, h_{ig} = injection gap height, p_v = vent pressure; \sim indicates the transformed model as described in Chapter 6.3.2).

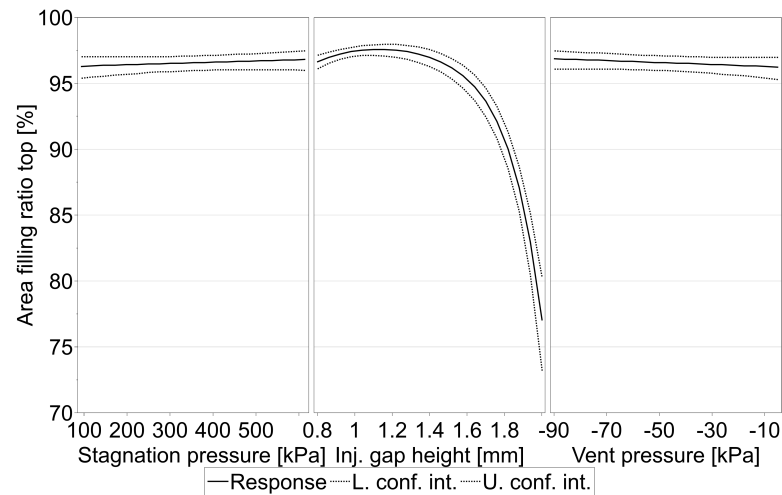


Fig. A-47 Predictions of ratio of injection gap filling model ($p_{stg} = 350$ kPa, $p_{vent} = -47.5$ kPa, $h_{ig} = 0.79$ mm).

Compression and Holding Phase

Tab. A-11 Preform data of the factor-response study investigating the compression and holding phase of the FS-CRTM process.

Experiment number and run order	Preform weight [g]	Preform length [mm]	Preform width [mm]
1	168.8	211.0	210.3
2	169.7	211.0	210.3
3	169.7	210.9	210.3
4	169.1	210.7	210.2
5	169.3	210.9	210.3
6	169.9	210.6	210.2
7	169.5	210.6	210.3
8	169.8	210.7	210.1
9	169.5	210.8	210.4
10	168.3	210.5	210.1
11	169.0	210.9	210.4
12	169.1	211.4	211.0
13	170.0	211.0	210.4

Tab. A-12 Factors of flow visualization experiments investigating the compression and holding phase of the FS-CRTM process.

Experiment number and run order	Preform thickness at vent pressure of experiment ^I [mm]	Viscosity of fluid ^{II} [mPas]	Pot pressure ^{III,IV} [kPa]	Stagnation pressure ^{III,V} [kPa]	Vent pressure ^{III} [kPa]	Injection gap height [mm]
1	4.6 ($SD = 0.0$)	54.2	368.3 ($SD = 0.9$)	293.5	-4.8	1.98
2	4.6 ($SD = 0.1$)	54.2	368.4 ($SD = 0.9$)	299.8	-5.0	0.79
3	4.1 ($SD = 0.0$)	54.2	368.3 ($SD = 0.9$)	298.0	-89.8	0.84
4	4.1 ($SD = 0.0$)	52.8	368.9 ($SD = 0.9$)	295.4	-47.5	1.37
5	4.5 ($SD = 0.0$)	53.3	368.6 ($SD = 0.9$)	297.3	-4.9	1.97
6	4.2 ($SD = 0.0$)	53.9	369.0 ($SD = 0.9$)	297.7	-47.5	1.39
7	4.5 ($SD = 0.0$)	52.0	368.4 ($SD = 0.9$)	298.9	-4.8	0.79
8	4.0 ($SD = 0.1$)	52.5	368.6 ($SD = 0.9$)	296.8	-90.0	1.98
9	4.2 ($SD = 0.1$)	53.1	368.4 ($SD = 0.9$)	297.5	-47.5	1.39
10	4.0 ($SD = 0.0$)	52.5	368.4 ($SD = 0.9$)	299.1	-90.0	0.80
11	4.1 ($SD = 0.1$)	53.3	368.9 ($SD = 0.9$)	297.4	-90.0	1.97
12	4.0 ($SD = 0.0$)	54.2	368.6 ($SD = 0.9$)	299.8	-90.0	0.80
13	4.4 ($SD = 0.0$)	52.5	368.6 ($SD = 0.9$)	297.7	-5.0	0.79

^I Mean and standard deviation measured at four points of the preform; ^{II} based on the measured fluid temperature of the experiment the viscosity was measured with a cone-plate measuring system on a Modular Compact Rheometer (MCR) 302 of Anton Paar (Graz, Austria) at a shear rate of 100 s^{-1} (see Chapter A.1.1); ^{III} differential value relative to ambient pressure; ^{IV} mean and standard deviation measured during the injection phase of the experiment; ^V measured by pressure transducer in feeding line of inlet before injection start.

Tab. A-13 Responses of flow visualization experiments investigating the compression and holding phase of the FS-CRTM process.

Experiment number and run order	Injection time [s]	Idle time [s]	Compression time [s]	Median injection pressure [kPa]	Avg. force during force plateau of compression [kN]	Time of initial thickness penetration (TITTP) [s]	Time at 50% area filling ratio of preform bottom side [s]	Time at 90% area filling ratio of preform bottom side [s]
1	1.8	0.8	29.0	79.0	15.4	17.7	33.8	202.1
2	1.9	0.8	11.6	97.7	19.7	11.0	38.3	249.8
3	2.5	0.8	13.4	165.5	19.8	-	-	-
4	1.8	0.7	13.9	86.2	17.5	12.2	69.0	243.2
5	1.7	0.5	17.5	81.4	19.5	18.1	24.2	39.5
6	1.8	0.7	16.6	87.3	17.6	12.8	225.5	468.0
7	1.7	0.7	118.4	91.1	15.3	10.3	164.0	349.9
8	1.7	0.7	14.2	81.0	19.5	14.7	53.5	121.4
9	1.8	0.7	18.6	88.0	17.6	12.2	37.0	176.5
10	1.9	0.7	18.2	126.6	15.4	8.1	46.0	134.1
11	1.7	0.5	53.8	93.9	15.4	14.4	29.3	61.3
12	2.3	0.7	7.7	161.4	19.6	8.3	58.6	93.3
13	2.0	0.9	294.6	124.0	15.3	-	280.6	719.8

Tab. A-14 Preform data of the factor-response study investigating the compression and holding phase of the FS-CRTM process – additional experiments.

Experiment	Preform weight	Preform length	Preform width
	[g]	[mm]	[mm]
vc-#1 ^{II}	213.2	211.1	210.5
vc-#2 ^{II}	213.2	211.1	210.5
vc-#3 ^{I,II}	212.0	211.2	210.6
fc-#1	213.6	211.1	210.5
fc-#2	213.1	211.3	210.5
fc-#3	212.6	210.7	210.4
fc-#4	213.4	211.2	210.3
fc-#5	213.4	211.2	210.5
fc-#6	213.4	211.1	210.5

^I Same preform was used for dry compaction, dryComp-#3, and FS-CRTM impregnation, vc-#3. During the film-sealing process and preparatory work prior to each experiment, all preforms were compacted five times under vacuum pressure. Literature [221] shows that elastically repeatable deformation is reached after the third compaction cycle. Therefore, it was assumed that the extra cycle of dry compaction of this preform would not change the FS-CRTM process, which has been proven by the comparable maximum force levels of experiments vc-#1, vc-#2 and vc-#3; ^{II} [26].

Tab. A-15 Factors of flow visualization experiments investigating the compression phase of the FS-CRTM process – additional experiments.

Experiment	Preform thickness at vent pressure of experiment ^I	Viscosity of fluid ^{II}	Pot pressure ^{III,IV}	Stagnation pressure ^{III,V}	Vent pressure ^{III}	Height of injection gap
	[mm]	[mPas]	[kPa]	[kPa]	[kPa]	[mm]
vc-#1 ^{VI}	5.0 (<i>SD</i> = 0.1)	49.9	368.2 (<i>SD</i> = 1.1)	293.6	-90.0	1.41
vc-#2 ^{VI}	5.1 (<i>SD</i> = 0.0)	49.9	368.4 (<i>SD</i> = 1.1)	295.9	-90.0	1.42
vc-#3 ^{VI}	5.0 (<i>SD</i> = 0.0)	51.0	368.2 (<i>SD</i> = 1.0)	297.0	-90.0	1.40
fc-#1	5.1 (<i>SD</i> = 0.1)	49.3	368.6 (<i>SD</i> = 1.1)	294.9	-90.0	1.39
fc-#2	5.0 (<i>SD</i> = 0.1)	50.1	368.1 (<i>SD</i> = 1.1)	297.1	-90.0	1.40
fc-#3	5.0 (<i>SD</i> = 0.1)	49.8	368.1 (<i>SD</i> = 1.1)	298.7	-90.0	1.38
fc-#4	5.0 (<i>SD</i> = 0.1)	49.7	369.3 (<i>SD</i> = 1.1)	298.7	-90.0	1.40
fc-#5	5.0 (<i>SD</i> = 0.1)	50.1	368.8 (<i>SD</i> = 1.1)	294.8	-90.0	1.39
fc-#6	5.0 (<i>SD</i> = 0.1)	49.5	368.7 (<i>SD</i> = 1.1)	297.1	-90.0	1.40

^I Mean and standard deviation (*SD*) measured at four points of the preform; ^{II} based on the measured fluid temperature of the experiment the viscosity was measured with a cone-plate measuring system on a Modular Compact Rheometer (MCR) 302 of Anton Paar (Graz, Austria) at a shear rate of 100 s⁻¹ (see Chapter A.1.1); ^{III} differential value relative to ambient pressure; ^{IV} mean and standard deviation measured during the injection phase of the experiment; ^V measured by pressure transducer in feeding line of inlet before injection start; ^{VI} [26].

Tab. A-16 Responses of flow visualization experiments investigating the compression and holding phase of the FS-CRTM process – additional experiments.

Exp.	Injection time [s]	Idle time [s]	Compr. time [s]	Median injection pressure [kPa]	Maximum force at injection end [kN]	Maximum force at compression end [kN]	Avg. force during force plateau of compression [kN]	Time of initial thickness penetration (TITTP) [s]	Gap height at TITTP [mm]
vc-#1	2.1	0.7	12.2	99.0	3.9	27.8	-	12.5	0.40
vc-#2	2.1	0.5	13.1	94.8	3.5	28.6	-	12.1	0.57
vc-#3	1.9	0.4	11.6	95.4	3.3	27.7	-	11.6	0.41
fc-#1	2.2	0.3	23.6	113.8	-	-	24.1	12.8	-
fc-#2	2.0	0.1	17.2	96.3	-	-	24.2	11.7	-
fc-#3	1.9	0.0	19.1	88.4	-	-	24.2	12.3	-
fc-#4	2.0	0.6	45.8	84.6	-	-	22.0	12.5	-
fc-#5	1.9	0.7	32.8	82.5	-	-	22.1	12.3	-
fc-#6	2.1	0.3	37.5	106.3	-	-	22.0	11.6	-

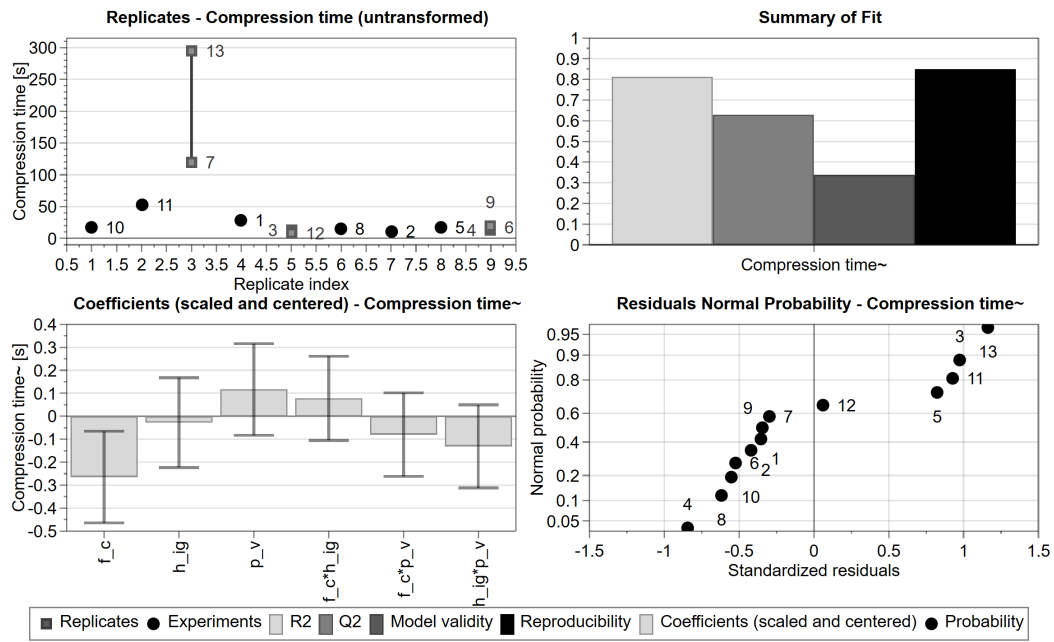


Fig. A-48 Overview plot of response model: compression time (f_c = compression force, h_{ig} = injection gap height, p_v = vent pressure; \sim indicates the transformed model as described in Chapter 6.3.2).

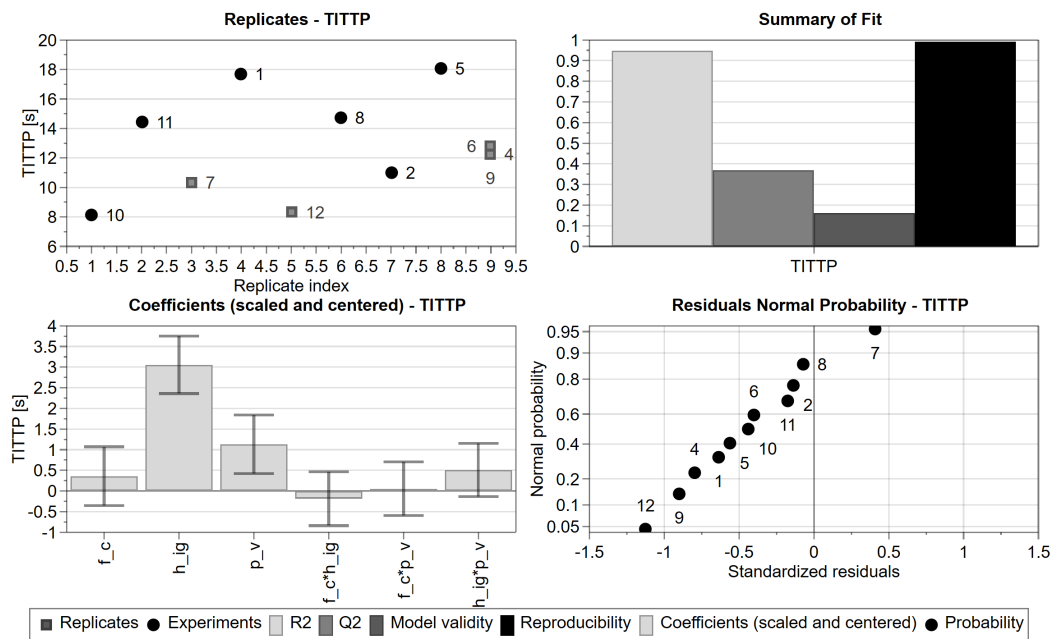


Fig. A-49 Overview plot of response model: time of initial through-thickness penetration (TITTP) (f_c = compression force, h_{ig} = injection gap height, p_v = vent pressure).

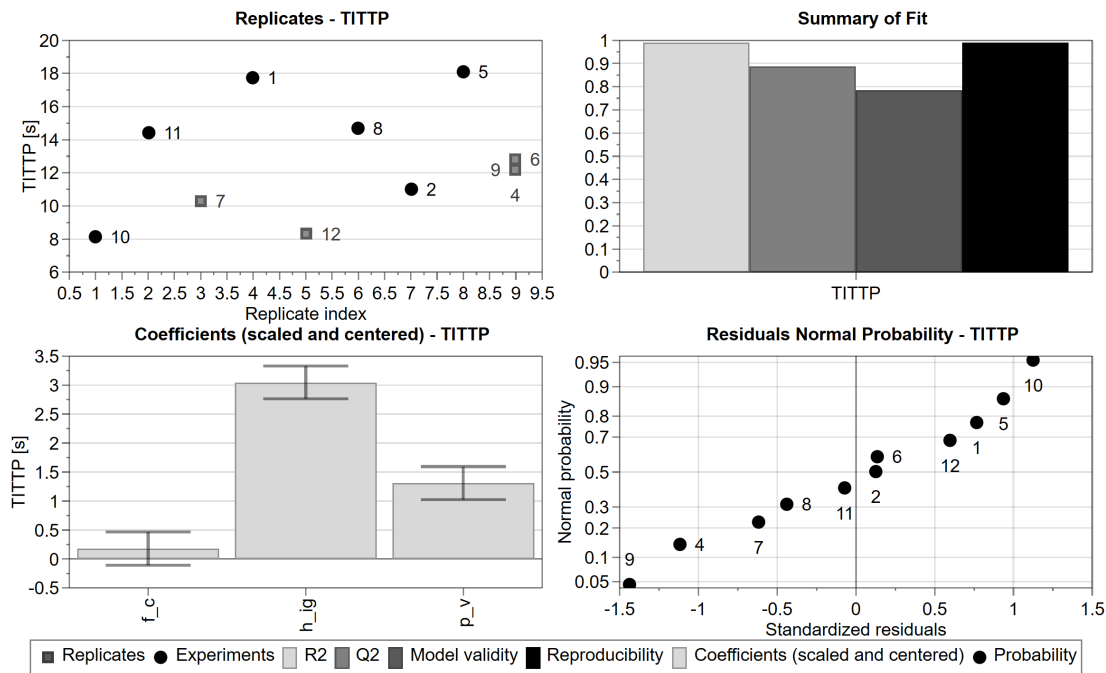


Fig. A-50 Overview plot of response model: time of initial through-thickness penetration (TITTP) (without factor interactions, f_c = compression force, h_ig = injection gap height, p_v = vent pressure).

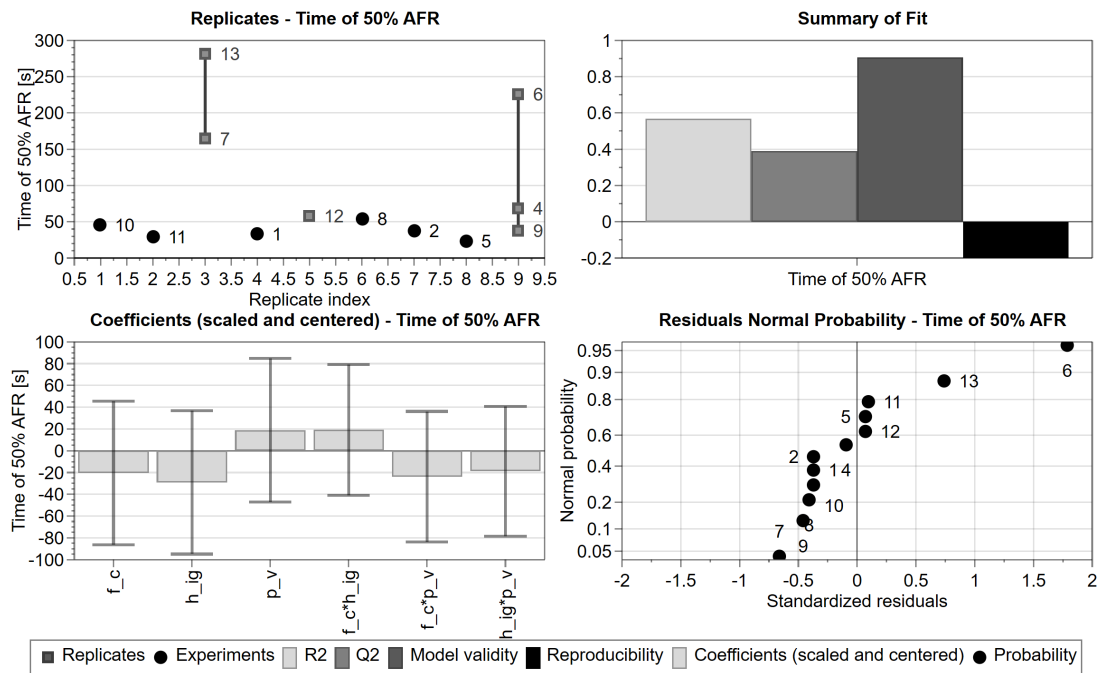


Fig. A-51 Overview plot of response model: time of 50% AFR on preform bottom side (f_c = compression force, h_ig = injection gap height, p_v = vent pressure).

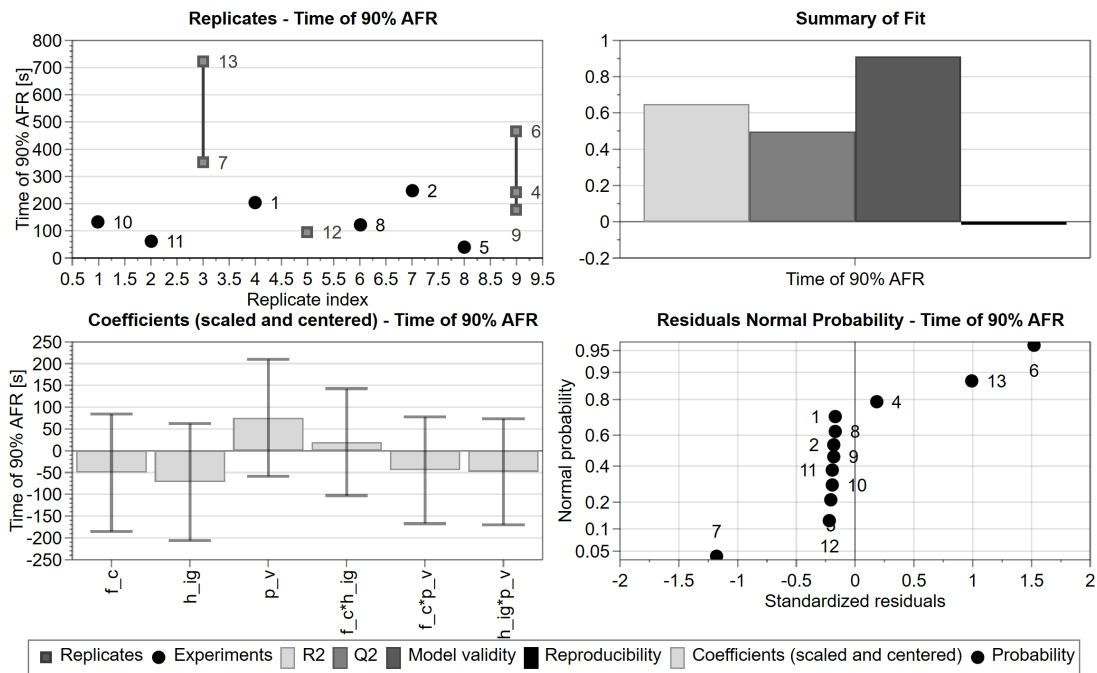


Fig. A-52 Overview plot of response model: time of 90% AFR on preform bottom side (f_c = compression force, h_{ig} = injection gap height, p_v = vent pressure).

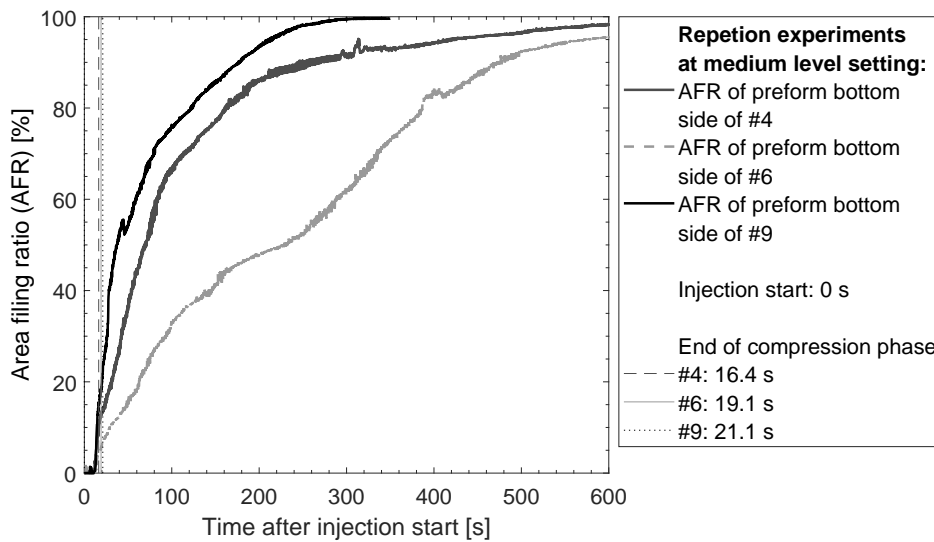


Fig. A-53 Area filling ratio of preform bottom side for repetition experiments of the full factorial experimental design investigating the compression and holding phase of the FS-CRTM process.

A.6 Appendix of Experimental Studies on Edge Race-Tracking during FS-CRTM

A.6.1 Race-Tracking Study

Tab. A-17 Preform data of experiments of the race-tracking study. [26]

Experiment	Preform weight	Preform length (incl. fluid transition zone)	Preform width
	[g]	[mm]	[mm]
mrt-#1	205.6	209.2	206.4
mrt-#2	205.5	209.4	206.7
mrt-#3	205.2	209.4	206.6
wrt-#1	197.9	207.5	202.7
wrt-#2	198.0	207.2	202.7
wrt-#3	199.2	206.2	202.6
dryComp-#1	210.8	211.1	210.4
dryComp-#2	210.7	211.4	210.3
dryComp-#3	212.0	211.2	210.6
dryComp-mrt-#1	205.7	209.1	206.5
dryComp-mrt-#2	205.7	209.4	206.4
dryComp-mrt-#3 ^I	205.2	208.9	206.6

^I Same preform was used for dry compaction, dryComp-#3, and FS-CRTM impregnation, vc-#3. During the film-sealing process and preparatory work prior to each experiment, all preforms were compacted five times under vacuum pressure. Literature [221] shows that elastically repeatable deformation is reached after the third compaction cycle. Therefore, it was assumed that the extra cycle of dry compaction of this preform would not change the FS-CRTM process, which has been proven by the comparable maximum force levels of experiments vc-#1, vc-#2 and vc-#3.

Tab. A-18 Theoretical race-tracking channel widths of preforms of the race-tracking study (neglecting preform placing tolerances). [26]

Experiment	Theoretical race-tracking channel on inlet side	Theoretical race-tracking channel on vent side	Theoretical lateral race-tracking channels
	[mm]	[mm]	[mm]
mrt-#1	1.9	0.6	1.7
mrt-#2	1.8	0.4	1.6
mrt-#3	2.2	0.4	1.6
wrt-#1	4.2	2.3	3.5
wrt-#2	4.0	2.6	3.6
wrt-#3	3.8	1.7	3.6
dryComp-mrt-#1	1.9	0.7	1.7
dryComp-mrt-#2	2.1	0.4	1.7
dryComp-mrt-#3	1.9	0.9	1.6

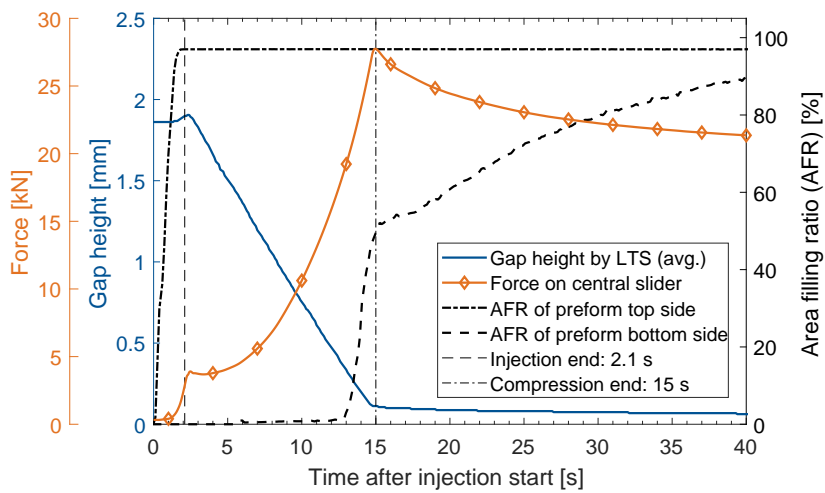
Tab. A-19 Process factors of experiments of the race-tracking study.

Experiment	Preform thickness at vent pressure of experiment ^I	Viscosity of fluid ^{II}	Pot pressure ^{III,IV}	Stagnation pressure ^{III,V}	Vent pressure ^{III}	Height of injection gap
	[mm]	[mPas]	[kPa]	[kPa]	[kPa]	[mm]
mrt-#1 ^{VI}	5.0 (<i>SD</i> = 0.0)	49.8	368.5 (<i>SD</i> = 1.1)	294.4	-90.0	1.40
mrt-#2 ^{VI}	5.0 (<i>SD</i> = 0.0)	49.8	368.2 (<i>SD</i> = 1.1)	297.0	-90.0	1.40
mrt-#3 ^{VI}	4.9 (<i>SD</i> = 0.1)	49.5	368.4 (<i>SD</i> = 1.1)	296.7	-89.9	1.41
wrt-#1 ^{VI}	5.0 (<i>SD</i> = 0.1)	49.9	368.5 (<i>SD</i> = 1.1)	298.2	-90.0	1.41
wrt-#2 ^{VI}	4.9 (<i>SD</i> = 0.1)	49.9	368.0 (<i>SD</i> = 1.1)	297.7	-89.9	1.40
wrt-#3 ^{VI}	5.0 (<i>SD</i> = 0.1)	49.5	368.6 (<i>SD</i> = 1.0)	298.7	-90.0	1.39
dryComp-#1	4.9 (<i>SD</i> = 0.0)	-	-	-	-90.1	-
dryComp-#2	4.8 (<i>SD</i> = 0.1)	-	-	-	-90.0	-
dryComp-#3	4.9 (<i>SD</i> = 0.0)	-	-	-	-89.9	-
dryComp-mrt-#1	5.0 (<i>SD</i> = 0.1)	-	-	-	-90.0	-
dryComp-mrt-#2	4.9 (<i>SD</i> = 0.0)	-	-	-	-90.0	-
dryComp-mrt-#3	5.0 (<i>SD</i> = 0.1)	-	-	-	-90.0	-

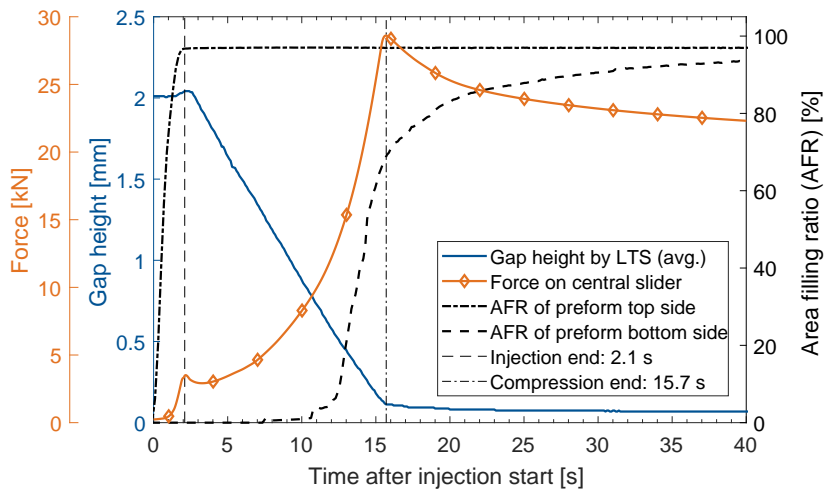
^I Mean and standard deviation measured at four points of the preform; ^{II} based on the measured fluid temperature of the experiment the viscosity was measured with a cone-plate measuring system on a Modular Compact Rheometer (MCR) 302 of Anton Paar (Graz, Austria) at a shear rate of 100 s⁻¹ (see Chapter A.1.1); ^{III} differential value relative to ambient pressure; ^{IV} mean and standard deviation measured during the injection phase of the experiment; ^V measured by pressure transducer in feeding line of inlet before injection start; ^{VI} [26].

Tab. A-20 Process responses of experiments of the race-tracking study.

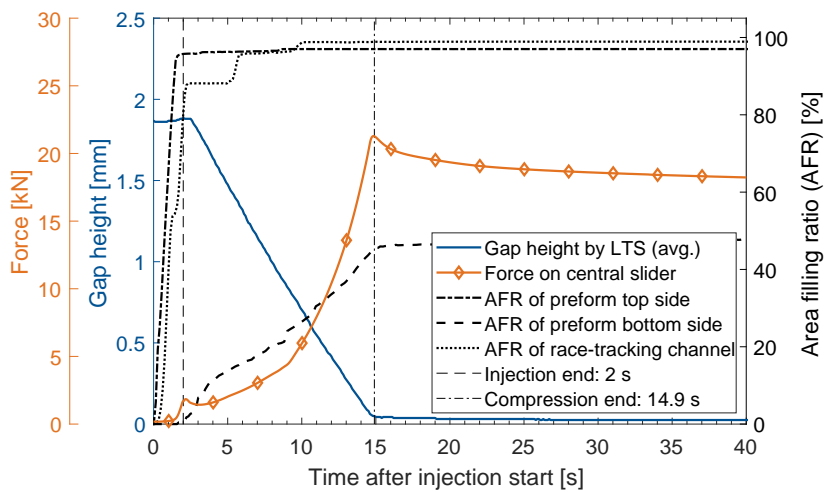
Experiment	Injection time [s]	Idle time [s]	Compression time [s]	Median injection pressure [kPa]	Maximum force at injection end [kN]	Maximum force at compression end [kN]
mrt-#1	2.0	0.6	12.3	84.6	1.8	21.3
mrt-#2	2.0	0.5	12.3	87.3	2.2	22.1
mrt-#3	2.3	0.5	11.5	121.1	2.2	19.4
wrt-#1	2.3	0.6	12.6	129.1	1.4	19.2
wrt-#2	2.1	0.6	12.0	109.2	1.6	21.3
wrt-#3	1.8	0.2	12.7	86.2	1.7	21.6
dryComp-#1	-	-	-	-	-	12.9
dryComp-#2	-	-	-	-	-	13.3
dryComp-#3	-	-	-	-	-	14.4
dryComp-mrt-#1	-	-	-	-	-	12.4
dryComp-mrt-#2	-	-	-	-	-	12.3
dryComp-mrt-#3	-	-	-	-	-	12.5



(a)

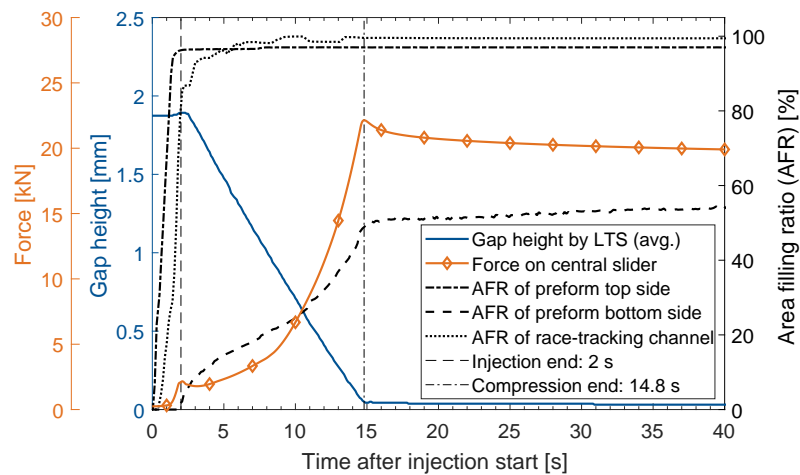


(b)

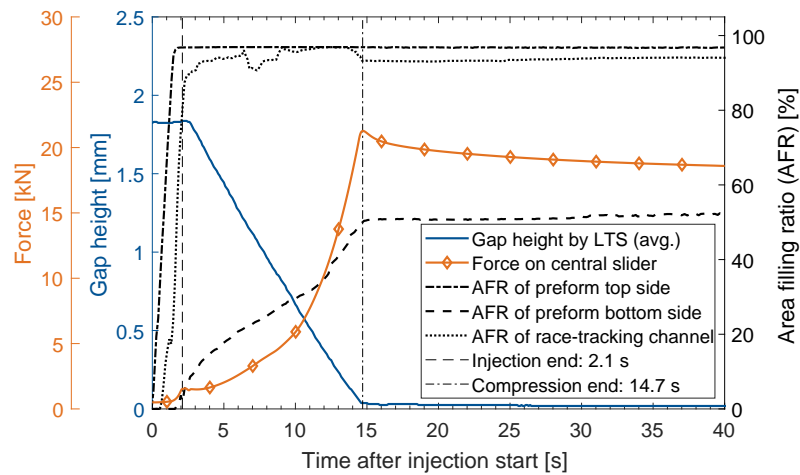


(c)

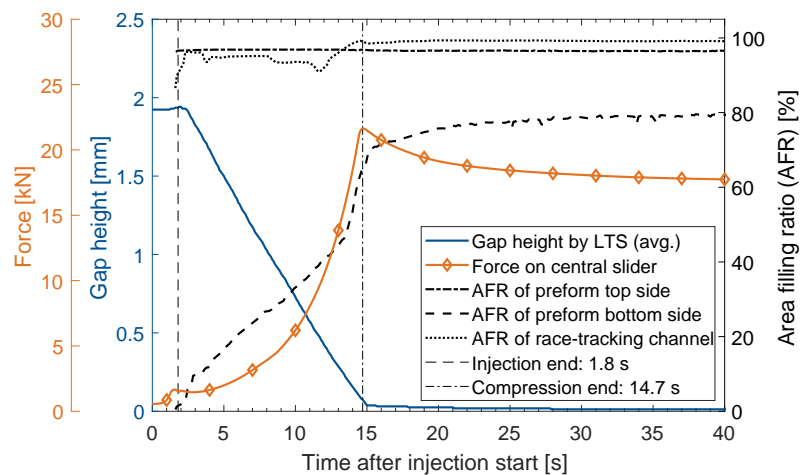
Fig. A-54 Overview of important process variables during FS-CRTM experiments of the race-tracking study: (a) no race-tracking channel – vc-#1; (b) no race-tracking channel – vc-#2; (c) medium race-tracking channel width – mrt-#1 (LTS = laser triangulation sensor). [26]



(a)



(b)



(c)

Fig. A-55 Overview of important process variables during FS-CRTM experiments of the race-tracking study: (a) medium race-tracking width – mrt-#2; (b) wide race-tracking width – wrt-#2; (c) wide race-tracking width – wrt-#3 – no pictures of the preform top side were recorded during the injection of wrt-#3 due to issues of the data acquisition equipment (LTS = laser triangulation sensor). [26]

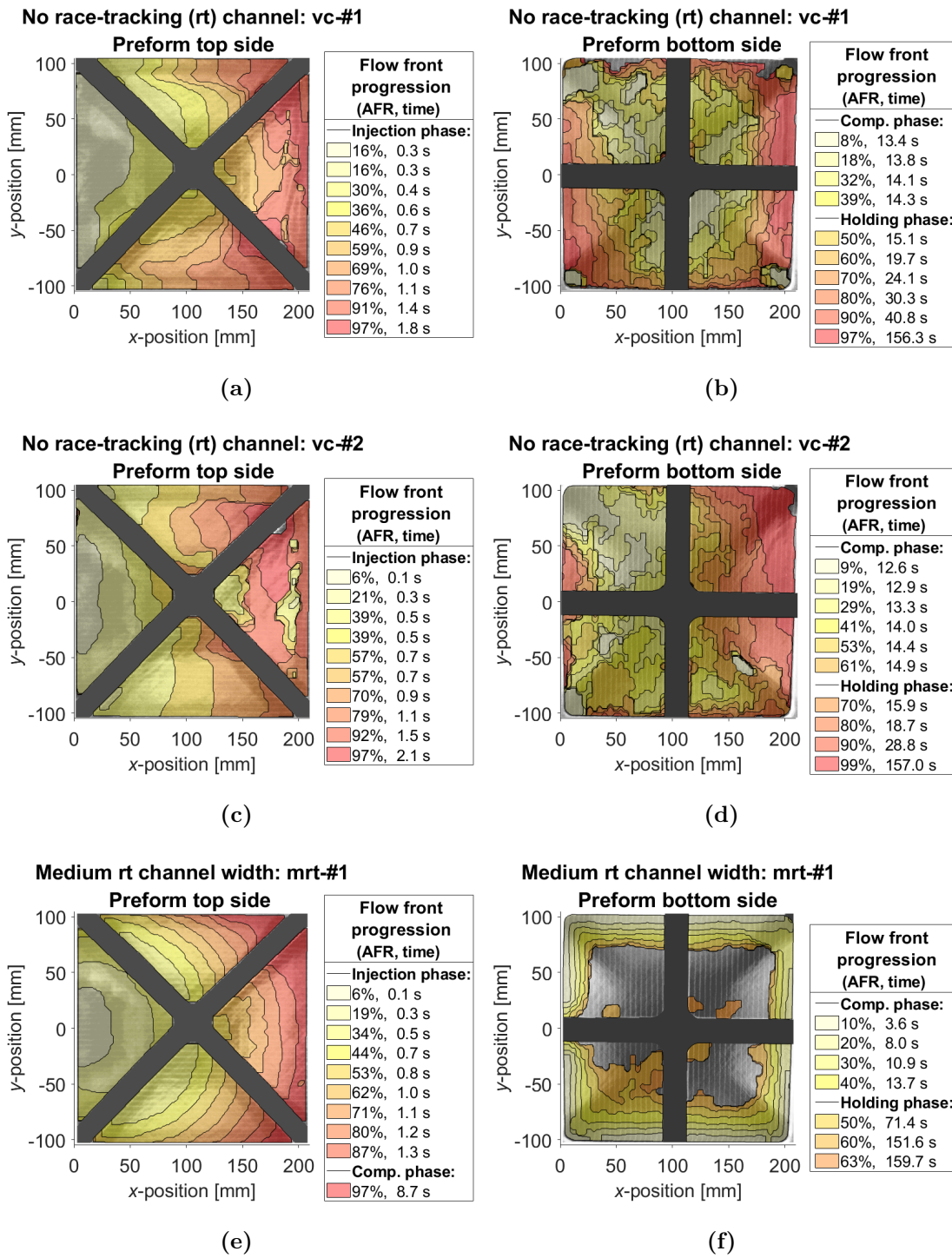


Fig. A-56 Flow front progression of FS-CRTM experiments of the race-tracking study: (a,b) no race-tracking (rt) channel – vc-#1; (c,d) no race-tracking channel – vc-#2; (e,f) medium race-tracking channel width – mrt-#1 (AFR = area filling ratio). [26]

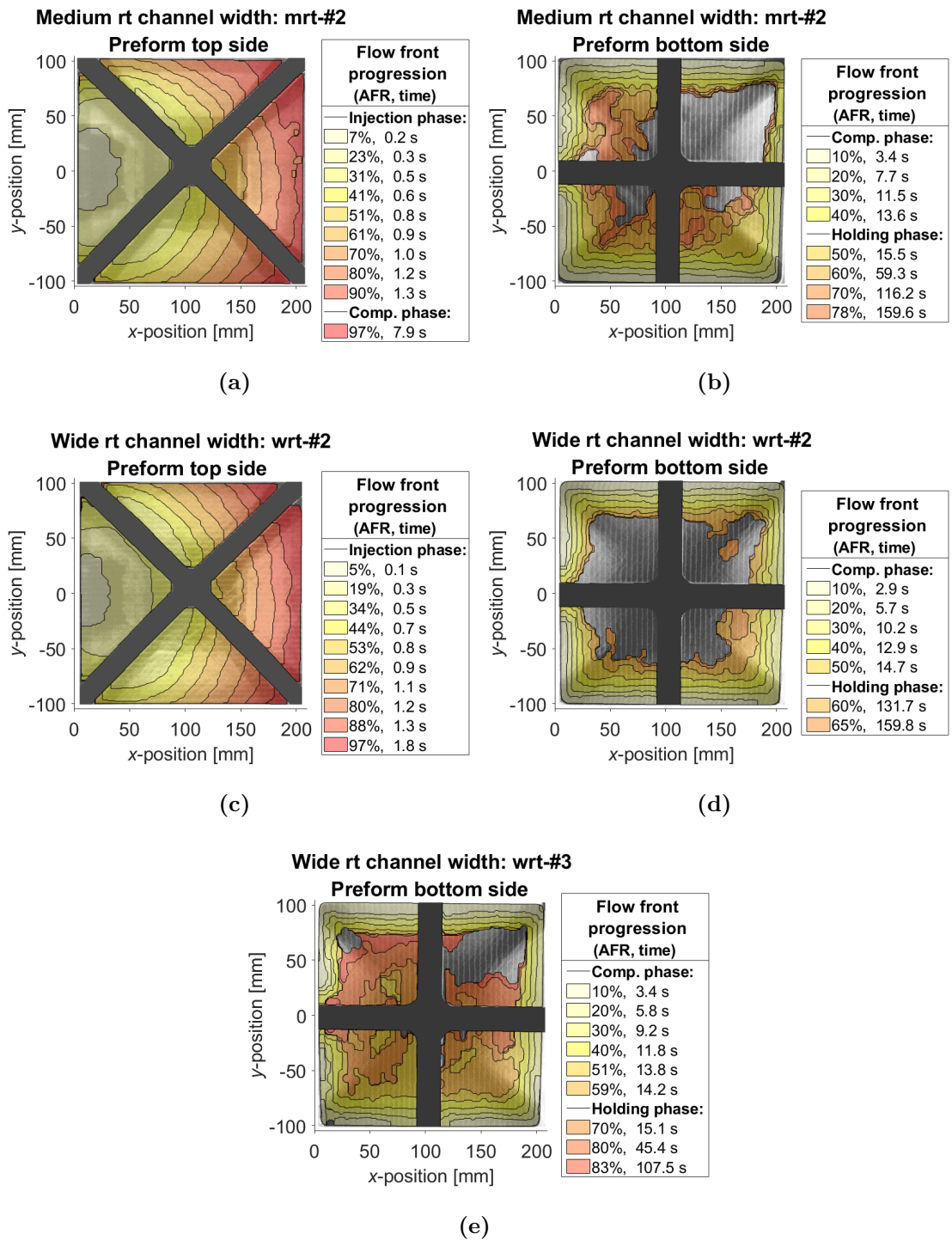


Fig. A-57 Flow front progression of FS-CRTM experiments of the race-tracking study: (a,b) medium race-tracking (rt) channel width – mrt-#2; (c,d) wide race-tracking channel width – wrt-#2; (e) wide race-tracking channel width – wrt-#3 – no pictures of the preform top side were recorded during the injection of wrt-#3 due to issues of the data acquisition equipment (AFR = area filling ratio). [26]

A.6.2 Flow Control Study

Tab. A-21 Preform data of experiments of the flow control study. [26]

Experiment	Preform weight	Preform length (incl. fluid transition zone)	Preform width
	[g]	[mm]	[mm]
fcs-#1	245.4	228.0	228.1
fcs-#2	245.6	228.1	228.1
fcs-#3	245.8	228.0	228.1
fcs-mrt-#1	237.6	226.1	224.2
fcs-mrt-#2	237.2	226.2	224.0
fcs-mrt-#3	237.1	225.9	223.8
fcs-wrt-#1	230.3	223.9	219.9
fcs-wrt-#2	229.6	223.8	220.0
fcs-wrt-#3	229.8	224.0	219.9

Tab. A-22 Theoretical race-tracking channel widths of preforms of the flow control study (neglecting preform placing tolerances). [26]

Experiment	Theoretical race-tracking channel on inlet side	Theoretical race-tracking channel on vent side	Theoretical lateral race-tracking channels
	[mm]	[mm]	[mm]
fcs-mrt-#1	2.0	1.7	1.8
fcs-mrt-#2	2.1	1.7	1.9
fcs-mrt-#3	2.0	1.9	2.0
fcs-wrt-#1	3.9	3.9	4.0
fcs-wrt-#2	3.9	4.0	3.9
fcs-wrt-#3	4.2	4.0	4.0

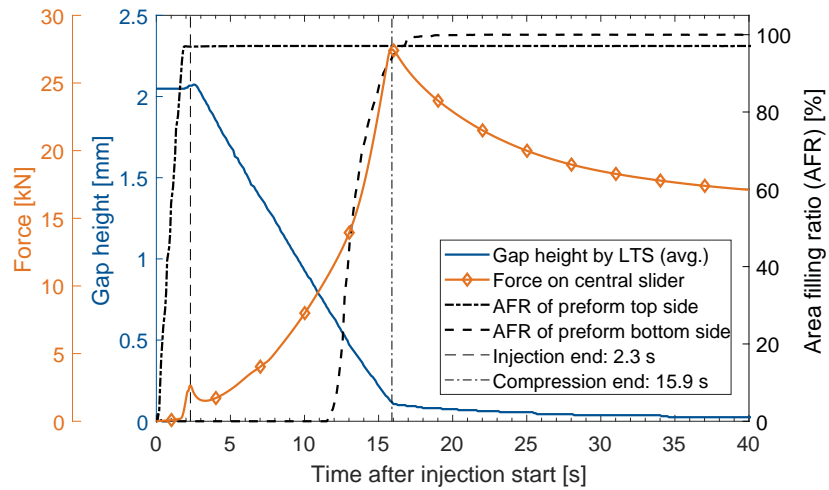
Tab. A-23 Process factors of experiments of the flow control study. [26]

Experiment	Preform thickness at vent pressure of experiment ^I	Viscosity of fluid ^{II}	Pot pressure ^{III,IV}	Stagnation pressure ^{III,V}	Vent pressure ^{III}	Height of injection gap
	[mm]	[mPas]	[kPa]	[kPa]	[kPa]	[mm]
fcs-#1	4.8 (<i>SD</i> = 0.0)	51.1	367.9 (<i>SD</i> = 1.2)	295.2	-90.0	1.55
fcs-#2	4.8 (<i>SD</i> = 0.0)	50.0	368.0 (<i>SD</i> = 1.2)	293.9	-90.0	1.54
fcs-#3	4.9 (<i>SD</i> = 0.1)	50.7	368.1 (<i>SD</i> = 1.2)	294.0	-90.0	1.55
fcs-mrt-#1	4.8 (<i>SD</i> = 0.1)	50.3	368.0 (<i>SD</i> = 1.1)	294.1	-90.0	1.54
fcs-mrt-#2	4.8 (<i>SD</i> = 0.1)	51.1	367.9 (<i>SD</i> = 1.2)	293.6	-90.0	1.56
fcs-mrt-#3	4.9 (<i>SD</i> = 0.0)	50.7	367.8 (<i>SD</i> = 1.2)	296.9	-90.0	1.54
fcs-wrt-#1	4.9 (<i>SD</i> = 0.1)	50.9	368.0 (<i>SD</i> = 1.2)	293.9	-90.0	1.54
fcs-wrt-#2	4.8 (<i>SD</i> = 0.1)	50.3	367.9 (<i>SD</i> = 1.2)	297.4	-90.0	1.54
fcs-wrt-#3	4.8 (<i>SD</i> = 0.1)	50.9	367.9 (<i>SD</i> = 1.2)	294.7	-90.0	1.55

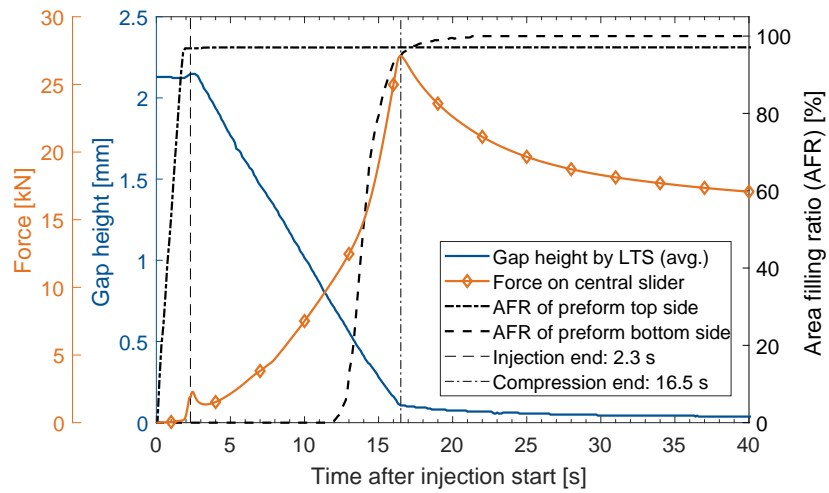
^I Mean and standard deviation measured at four points of the preform; ^{II} based on the measured fluid temperature of the experiment the viscosity was measured with a cone-plate measuring system on a Modular Compact Rheometer (MCR) 302 of Anton Paar (Graz, Austria) at a shear rate of 100 s⁻¹ (see Chapter A.1.1); ^{III} differential value relative to ambient pressure; ^{IV} mean and standard deviation measured during the injection phase of the experiment; ^V measured by pressure transducer in feeding line of inlet before injection start.

Tab. A-24 Process responses of experiments of the flow control study.

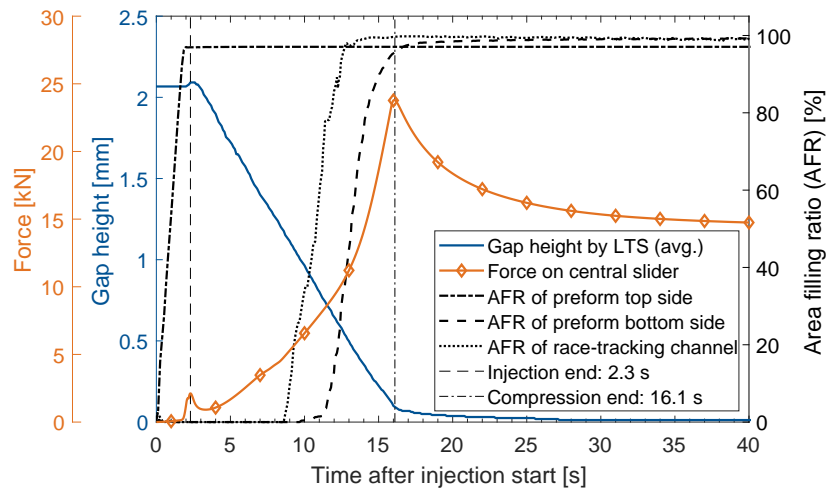
Experiment	Injection time [s]	Idle time [s]	Compr. time [s]	Median injection pressure [kPa]	Maximum force at injection end [kN]	Maximum force during force end [kN]	Time of initial through-thickness penetration (TITTP) [s]	Gap height at TITTP [mm]
fcs-#1	2.5	0.8	13.2	90.5	2.2	25.8	11.4	0.76
fcs-#2	2.3	0.3	13.3	72.2	2.6	27.5	11.1	0.77
fcs-#3	2.3	0.5	13.7	74.4	2.3	27.1	11.9	0.73
fcs-mrt-#1	2.3	0.4	13.4	73.7	2.1	23.8	-	-
fcs-mrt-#2	2.4	0.6	13.5	74.2	1.9	24.3	-	-
fcs-mrt-#3	2.3	0.6	13.7	73.8	1.7	24.0	-	-
fcs-wrt-#1	2.4	0.7	13.5	78.6	1.6	23.1	-	-
fcs-wrt-#2	2.6	0.3	13.4	108.3	1.5	22.0	-	-
fcs-wrt-#3	2.3	0.5	13.0	71.4	3.3	19.7	-	-



(a)

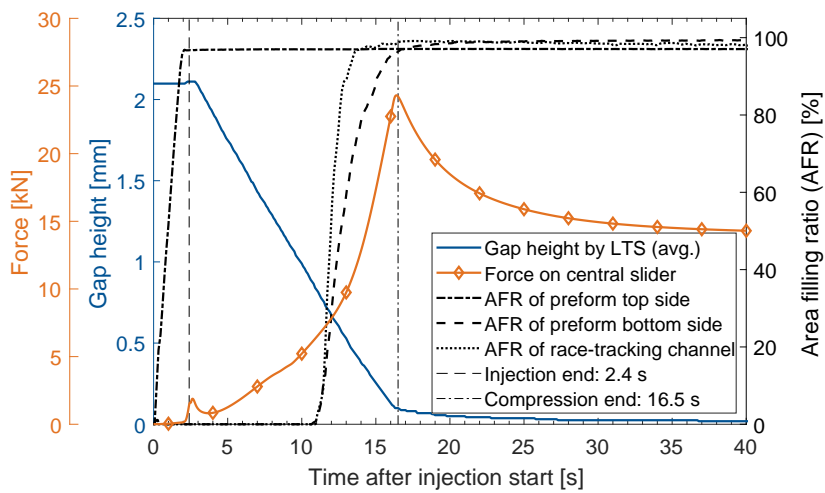


(b)

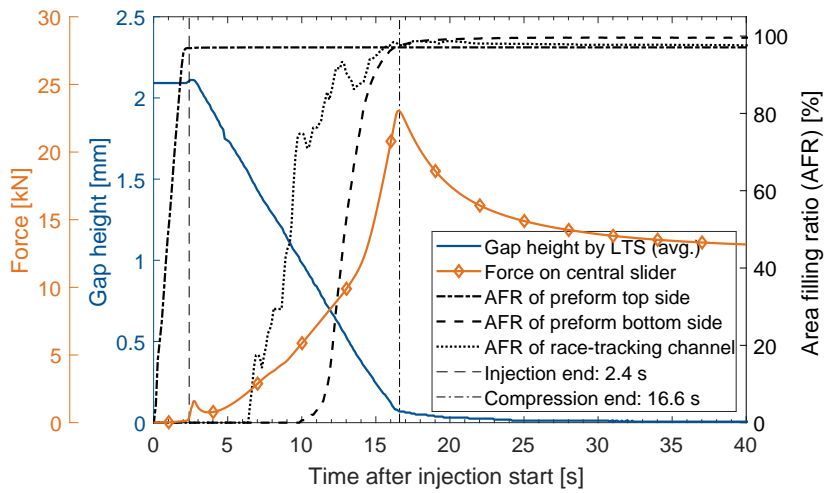


(c)

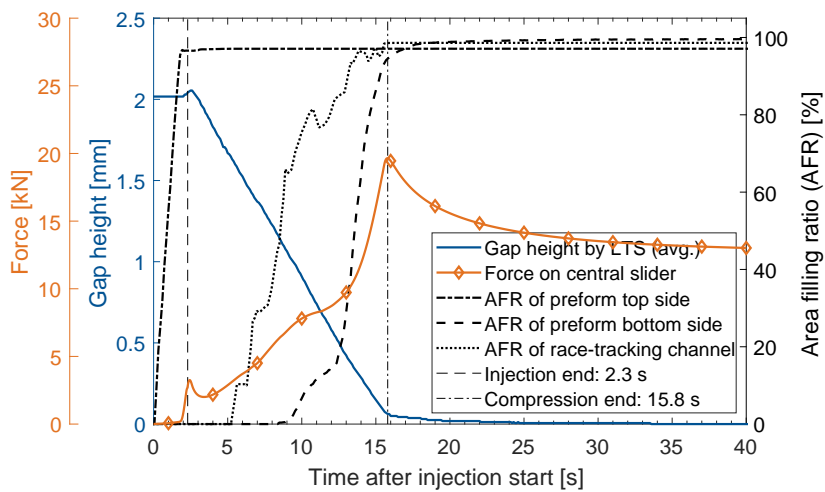
Fig. A-58 Overview of important process variables during FS-CRTM experiments of the flow control study: (a) no race-tracking channel – fcs-#2; (b) no race-tracking channel – fcs-#3; (c) medium race-tracking channel width – fcs-mrt-#1 (LTS = laser triangulation sensor). [26]



(a)



(b)



(c)

Fig. A-59 Overview of important process variables during FS-CRTM experiments of the flow control study: (a) medium race-tracking channel width – fcs-mrt-#2; (b) wide race-tracking channel width – fcs-wrt-#1; (c) wide race-tracking channel width – fcs-wrt-#3 (LTS = laser triangulation sensor). [26]

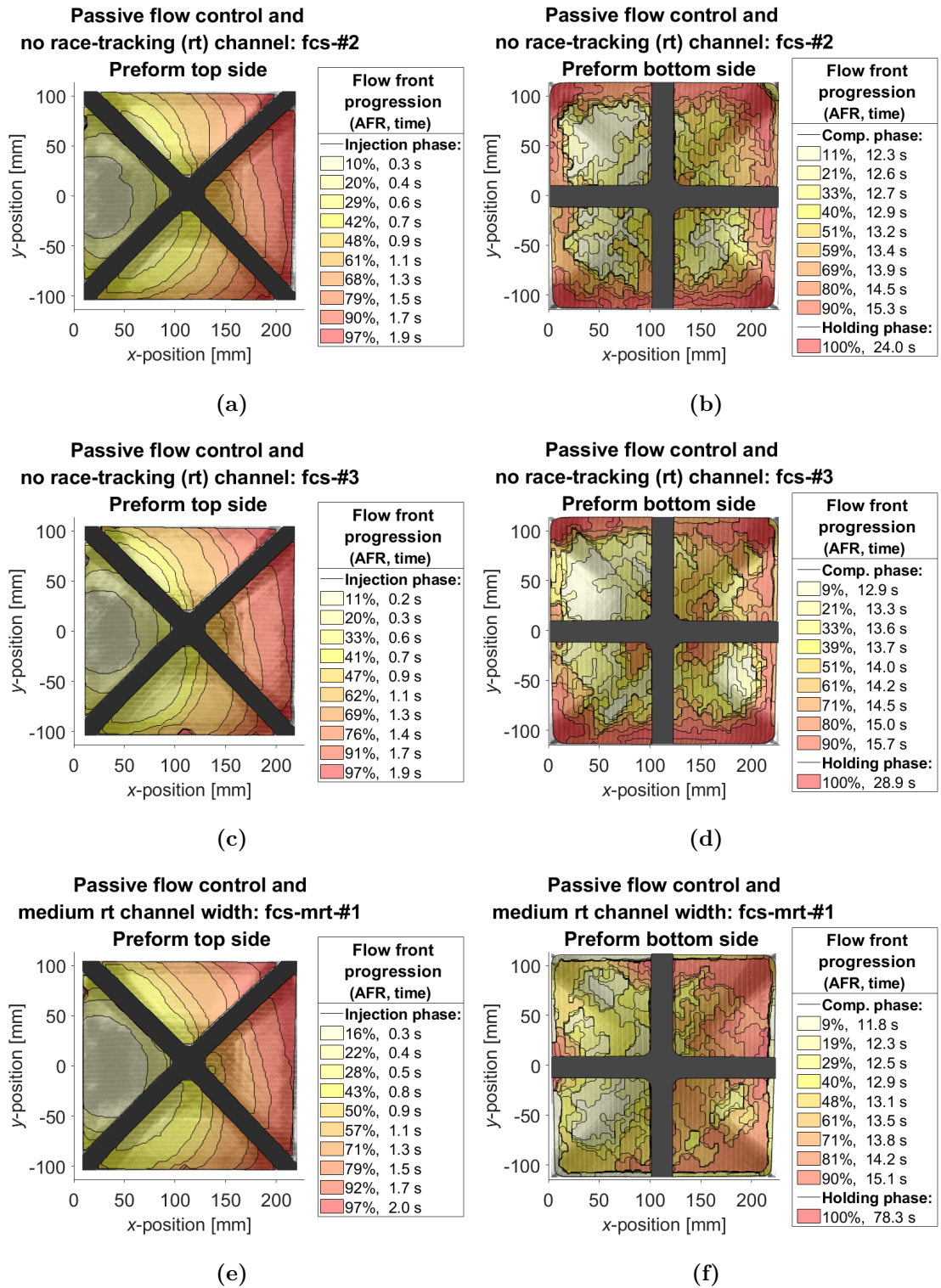


Fig. A-60 Flow front progression of FS-CRTM experiments of the flow control study: (a,b) no race-tracking (rt) channel – fcs-#2; (c,d) no race-tracking channel – fcs-#3; (e,f) medium race-tracking channel width – fcs-mrt-#1 (AFR = area filling ratio). [26]

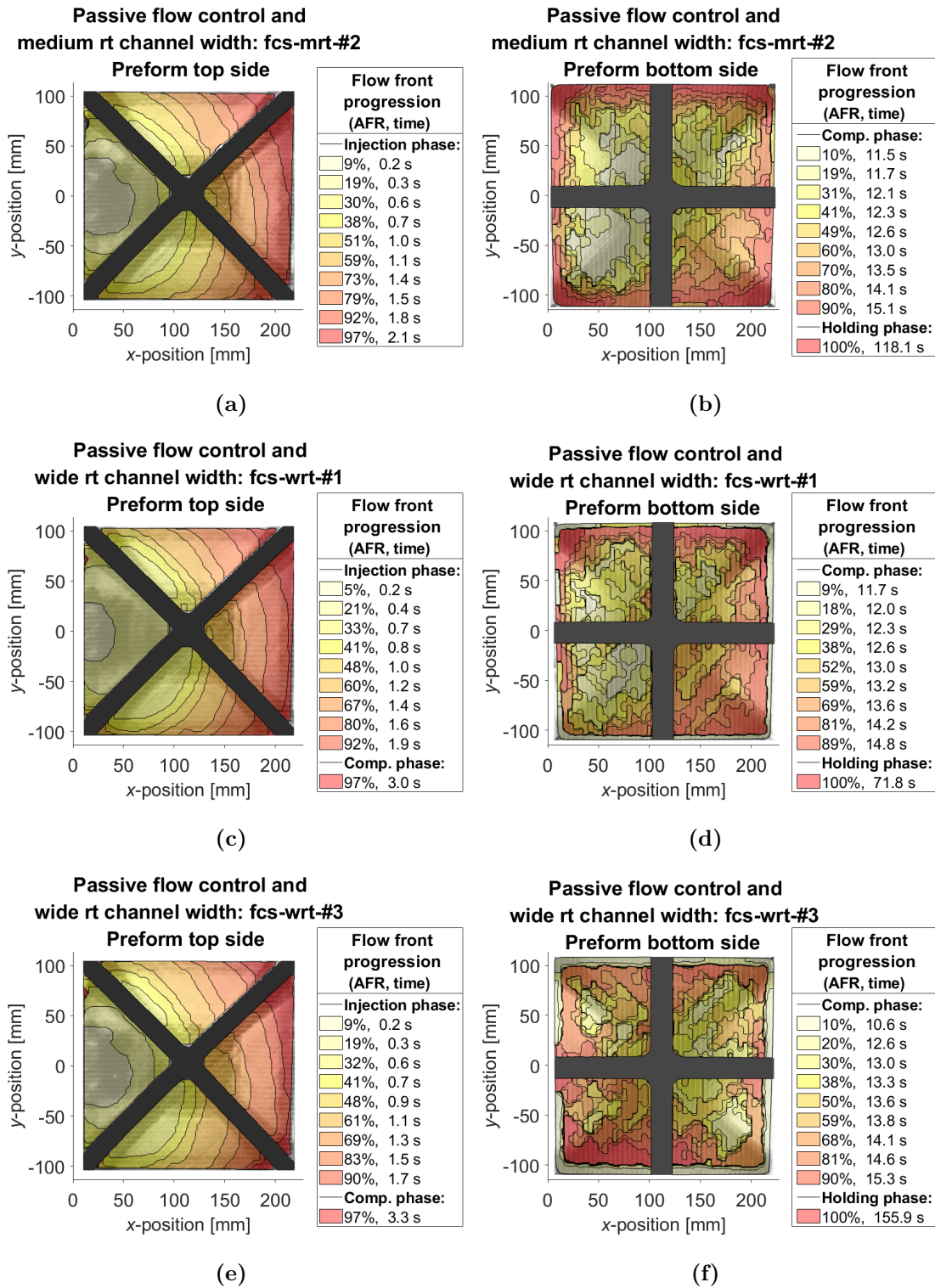


Fig. A-61 Flow front progression of FS-CRTM experiments of the flow control study: (a,b) medium race-tracking (rt) channel width – fcs-mrt-#2; (c,d) wide race-tracking channel width – fcs-wrt-#1; (e,f) wide race-tracking channel width – fcs-wrt-#3 (AFR = area filling ratio). [26]

B Publications

Scientific Journal Papers

- [P1] M. Vollmer, S. Zaremba, P. Mertiny and K. Drechsler, “Edge race-tracking during film-sealed compression resin transfer molding”, *Journal of Composites Science*, vol. 5, no. 8, p. 195, 2021. [Online]. Available: <https://www.mdpi.com/2504-477X/5/8/195>

Conferences

- [C1] M. Vollmer, H. Baumann, L. Graßl, D. Schultheiß, P. Mertiny and K. Drechsler, “Compression resin transfer molding simulation for process optimization: A user case study”, Proceedings of the 29th SICOMP Conference – Manufacturing and Design of Composites, Luleå, Sweden, 28 - 29 May 2018.
- [C2] M. Vollmer, N. Tagscherer, S. Zaremba, D. Schultheiß, P. Mertiny and K. Drechsler, “Material characterization for compression resin transfer molding process simulation”, Proceedings of the 18th European Conference on Composite Materials (ECCM18), Athens, Greece, 24 - 28 June 2018.
- [C3] M. Rieger, B. Nagarajan, M. Vollmer and P. Mertiny, “Determination of key influencing factors on thermal conductivity enhancement of graphene nanoplatelets reinforced epoxy”, Proceedings of the ASME 2018 International Mechanical Engineering Congress and Exposition, Pittsburgh, Pennsylvania, USA, 09 - 15 November 2018.
- [C4] M. Vollmer and S. Zaremba, “Enhancing composite production by integrating thermoplastic films in closed mold LCM processes”, Proceedings of the 1. RTM Anwenderforum (AVK), Augsburg, Germany, 25 - 26 June 2019.
- [C5] M. Vollmer, A. Prenninger, P. Laubichler, S. Zaremba and K. Drechsler, “Effect of vent pressure variation during film-sealed compression resin transfer molding (FS-CRTM)”, Proceedings of the 5th International Composites Conference (ICC), Stuttgart, Germany, 10 - 12 September 2019.
- [C6] D. Bublitz, M. Vollmer and F. Nusser, “A novel method for the evaluation of compression RTM process simulations”, Proceedings of the ESI Forum 2019, Berlin, Germany, 07 November 2019.
- [C7] M. Vollmer, D. König, I. Gilch, H. Waller-Ehrat, S. Zaremba, C. Hübner, P. Mertiny and K. Drechsler, “Identification of a film to seal the preform impregnation during the compression resin transfer molding process”, Proceedings of the SAMPE Europe Conference 2021, Baden, Switzerland, 28 - 30 September 2021; ISBN/EAN: 978-90-829101-3-1.

- [C8] M. Vollmer, F. Nusser, D. Bublitz, H. Baumann, L. Graßl, F. Masseria, S. Zaremba, P. Mertiny and K. Drechsler, “Increasing process robustness of the compression resin transfer molding process towards edge race-tracking”, Proceedings of the SAMPE Europe Conference 2021, Baden, Switzerland, 28 - 30 September 2021; ISBN/EAN: 978-90-829101-3-1.

C Supervised Student Theses

During his employment at the Chair of Carbon Composites of the Technical University of Munich, the author supervised the following student theses:

- [S1] R. Snajdr, *Untersuchung des Einflusses duromerer Matrixsysteme auf die Konsolidierung und die mechanischen Kennwerte gewickelter CFK-Prepregplatten*, Term Thesis in cooperation with Voith Composites GmbH & Co. KG, Technical University of Munich, Munich, Germany, 31 July 2017.
- [S2] H. Baumann, *Erstellung und Bewertung von Simulationsmodellen für einen neuartigen Compression RTM-Prozess*, Term Thesis, Technical University of Munich, Munich, Germany, 28 September 2017.
- [S3] J. Kil, *Entwicklung einer Testvorrichtung zur Prozessdatenaufzeichnung und Visualisierung des Harzflusses eines neuartigen LCM-Prozesses*, Masters' Thesis, Technical University of Munich, Munich, Germany, 30 October 2017.
- [S4] D. König, *Bewertung thermoplastischer Folien hinsichtlich ihrer Eignung zur Integration in den RTM-Prozess duroplastischer CFK-Bauteile*, Term Thesis, Technical University of Munich, Munich, Germany, 30 October 2017.
- [S5] N. Tagscherer, *Material characterization for a numerical compression resin transfer molding simulation*, Masters' Thesis, Technical University of Munich, Munich, Germany, 15 February 2018.
- [S6] I. Moll, *Thermische und thermisch-mechanische Foliencharakterisierung zur Integration in den RTM-Prozess*, Term Thesis, Technical University of Munich, Munich, Germany, 28 February 2018.
- [S7] M. Schreiber, *Auslegung und Konstruktion eines Teststandes zur Untersuchung eines Folierungsprozesses von Preforms für den RTM-Prozess*, Term Thesis, Technical University of Munich, Munich, Germany, 29 March 2018.
- [S8] L. Graßl, *Weiterentwicklung von Simulationsmodellen für einen neuartigen CRTM-Prozess*, Term Thesis, Technical University of Munich, Munich, Germany, 31 March 2018.
- [S9] M. Rieger, *Characterization of the thermal conductivity of graphene-modified epoxy composites via the hot disk method*, Masters' Thesis in cooperation with the University of Alberta, Technical University of Munich, Munich, Germany, 31 March 2018.

- [S10] R. Ernhofer, *Programming a test rig for optical analysis of the RTM-injection-process for CFRP-manufacturing*, Masters' Thesis, Technical University of Munich, Munich, Germany, 30 April 2018.
- [S11] H. Baumann, *Implementation of a novel test rig for the optical analysis of the RTM-injection process for CFRP manufacturing*, Masters' Thesis, Technical University of Munich, Munich, Germany, 15 November 2018.
- [S12] H. Waller-Ehrt, *Charakterisierung des Schälwiderstands zwischen thermoplastischen Folien und duroplastischen CFK-Oberflächen*, Masters' Thesis, Technical University of Munich, Munich, Germany, 21 December 2018.
- [S13] F. Nusser, *Simulative comparison study of filling behavior during RTM and CRTM process at occurring race tracking: Development of the study approach, data basis and evaluation method*, Masters' Thesis, Technical University of Munich, Munich, Germany, 14 January 2019.
- [S14] W. Jiang, *Einfluss des Trennmittels für Epoxidsysteme auf das Trennverhalten*, Masters' Thesis in cooperation with KDX Europe Composites R&D Center GmbH, Technical University of Munich, Munich, Germany, 02 May 2019.
- [S15] A. Prenninger, *Process optimisation and investigation of the film behaviour during the injection phase of a film-sealed CRTM process*, Masters' Thesis, Technical University of Munich, Munich, Germany, 29 July 2019.
- [S16] P. Laubichler, *Flow experiments of the film-sealed CRTM process*, Masters' Thesis, Technical University of Munich, Munich, Germany, 23 December 2019.
- [S17] Y. Jiang, *Thermisch-mechanische Charakterisierung von thermoplastischen Folien zur Composite-Herstellung*, Term Thesis, Technical University of Munich, Munich, Germany, 02 July 2020.
- [S18] J. Stockbauer, *Optimization of the film-sealing process of preforms for CRTM flow experiments*, Masters' Thesis, Technical University of Munich, Munich, Germany, 22 July 2020.
- [S19] T. Erschbaumer, *Customization of the preform architecture to control the flow front in RTM*, Masters' Thesis, Technical University of Munich, Munich, Germany, 18 November 2020.

Parts of the above listed theses contributed to the underlying dissertation as stated in the text.